Universitat Politècnica de València
Departamento de Máquinas y Motores Térmicos

Doctoral Thesis

Thermal Effects Influence on the Diesel Injector Performance through a Combined 1D Modelling and Experimental Approach

Presented by:
Marcos Carreres Talens

Supervised by:
Dr. Francisco Javier Salvador Rubio

in fulfillment of the requirements for the degree of
Doctor of Philosophy

Valencia, September 2016

PhD. Thesis

Thermal Effects Influence on the Diesel Injector Performance through a Combined 1D Modelling and Experimental Approach

Written by: Mr. Marcos Carreres Talens
Supervised by: Dr. Francisco Javier Salvador Rubio

Thesis committee:

Chairman:	Dr. Jesús Benajes Calvo
Secretary:	Dr. Octavio Armas Vergel
Member:	Dr. Angelo Onorati

Thesis committee substitutes:

Chairman:	Dr. Antonio José Torregrosa Huguet
Secretary:	Dr. Pedro Acisclo Rodríguez Aumente
Member:	Dr. Gianluca D'Errico

Valencia, September 27$^{\text{th}}$ 2016

Abstract

The injection system is one of the topics that has been paid most attention to by researchers in the field of direct injection diesel engines, due to its key role on fuel atomization, vaporization and air-fuel mixing process, which directly affect fuel consumption, noise irradiation and pollutant emissions.

The increasing injection pressures in modern engines have propitiated the need of studying phenomena such as cavitation, compressible flow or the effect of changes in the fuel properties along the process, whose relative importance was lower in early stages of the reciprocating engines development. The small dimensions of the injector ducts, the high velocities achieved through them and the transient nature of the process hinder the direct observation of these facts. Computational tools have then provided invaluable help in the field.

The objective of the present thesis is to analyse the influence of the thermal effects on the performance of a diesel injector. To this end, the fuel temperature variation through the injector restrictions must be estimated. The influence of these changes on the fuel thermophyisical properties relevant for the injection system also needs to be assessed, due to its impact on injector dynamics and the injection rate shape.

In order to give answer to the previous objectives, both experimental and computational techniques have been employed. A dimensional and a hydraulic experimental characterization of a solenoid-actuated Bosch CRI 2.20 injector has been carried out, including rate of injection measurements at a wide range of operating conditions, with special attention to the fuel temperature control. A 1D computational model of the injector has been implemented in order to confirm and further extend the findings from the experiments. Local variations of fuel temperature and pressure are considered by the model thanks to the assumption of adiabatic flow, for which the experimental characterization of the fuel properties at high pressure also had to be performed. The limits of the validity of this assumption have been carefully assessed in the study.

Results show a significant influence of the fuel temperature at the injector inlet on injection rate and duration, attributed to the effect of the variation of the fuel properties and to the fact that the injector remains in ballistic operation for most of its real operating conditions. Fuel temperature changes along the injector control orifices are able to importantly modify its dynamic behaviour. In addition, if the fuel at the injector inlet is at room temperature or above, the temperature at the nozzle outlet has not been proved to importantly change once steady-state conditions are achieved. However, a significant heating may take place for fuel temperatures at the injector inlet typical of cold-start conditions.

Resumen

El sistema de inyección es uno de los elementos que más interés ha despertado en la investigación en el campo de los motores diésel de inyección directa, debido a su papel clave en la atomización y vaporización del combustible así como en el proceso de mezcla, que afectan directamente al consumo y la generación de ruido y emisiones contaminantes.

Las crecientes presiones de inyección en motores modernos han propiciado la necesidad de estudiar fenómenos como la cavitación, flujo compresible o el efecto de los cambios de las propiedades del combustible a lo largo del proceso, cuya importancia relativa era menor en etapas tempranas del desarrollo de los motores alternativos. Las pequeñas dimensiones de los conductos del inyector, las altas velocidades a través de los mismos y la naturaleza transitoria del proceso dificultan la observación directa en estas cuestiones. Por ello, las herramientas computacionales han proporcionado una ayuda inestimable en el campo.

El objetivo de la presente tesis es analizar la influencia de los efectos térmicos en el funcionamiento de un inyector diésel. Para tal fin, se debe estimar la variación de la temperatura del combustible a lo largo de las restricciones internas del inyector. La influencia de estos cambios en las propiedades termofísicas del combustible más relevantes en el sistema de inyección también debe ser evaluada, debido a su impacto en la dinámica del inyector y en la forma de la tasa de inyección.

Para dar respuesta a estos objetivos, se han utilizado técnicas experimentales y computacionales. Se ha llevado a cabo una caracterización dimensional e hidráulica de un inyector Bosch CRI 2.20 actuado mediante solenoide, incluyendo medidas de tasa de inyección en un amplio rango de condiciones de operación, para lo que se ha prestado especial atención al control de la temperatura del combustible. Se ha implementado un modelo 1D del inyector para confirmar y extender las observaciones extraídas de los experimentos. El modelo considera variaciones locales de presión y temperatura del combustible gracias a la hipótesis de flujo adiabático, para lo cual también se ha tenido que llevar a cabo una caracterización experimental de las propiedades del combustible a alta presión. Los límites de la validez de esta hipótesis se han analizado cuidadosamente en el estudio.

Los resultados muestran una influencia significativa de la temperatura del combustible a la entrada del inyector en la tasa y duración de inyección, atribuida al efecto de la variación de las propiedades del combustible y al hecho de que el inyector permanece en operación balística para la mayoría de sus condiciones de funcionamiento. Los cambios en temperatura del combustible

a lo largo de los orificios de control del inyector son capaces de modificar su dinámica considerablemente. Además, si el combustible a la entrada del inyector se encuentra a temperatura ambiente o por encima, se ha observado que la temperatura a la salida de la tobera no varía de manera importante una vez se alcanzan condiciones estacionarias. No obstante, un calentamiento significativo puede tener lugar para temperaturas de entrada típicas de las condiciones de arranque en frío.

Resum

El sistema d'injecció és un dels elements que més interés ha despertat en la investigació en el camp dels motors dièsel d'injecció directa, degut al seu paper clau en l'atomització i vaporització del combustible, així com en el procés de mescla, que afecten directament el consum i la generació de soroll i emissions contaminants.

Les creixents pressions d'injecció en motors moderns han propiciat la necessitat d'estudiar fenòmens com la cavitació, flux compressible o l'efecte dels canvis de les propietats del combustible al llarg del procés, la importància relativa dels quals era menor en les primeres etapes del desenvolupament dels motors alternatius. Les menudes dimensions dels conductes de l'injector, les altes velocitats a través dels mateixos i la natura transitòria del procés dificulten l'observació directa en estes qüestions. Per això, les ferramentes computacionals han proporcionat una ajuda inestimable en el camp.

L'objectiu de la present tesi és analitzar la influència dels efectes tèrmics en el funcionament d'un injector dièsel. Per a tal fi, es deu estimar la variació de la temperatura del combustible al llarg de les restriccions internes de l'injector. La influència d'estos canvis en les propietats termofísiques del combustible més relevants en el sistema d'injecció també ha de ser avaluada, degut al seu impacte en la dinàmica de l'injector i en la forma de la tasa d'injecció.

Per tal de donar resposta a estos objectius, s'han utilitzat tècniques experimentals i computacionals. S'ha dut a terme una caracterització dimensional i hidràulica d'un injector Bosch CRI 2.20 actuat mitjançant solenoide, incloent mesures de tasa d'injecció en un ampli rang de condicions d'operació, per al que s'ha prestat especial atenció al control de la temperatura del combustible. S'ha implementat un model 1D de l'injector per tal de confirmar i estendre les observacions extretes dels experiments. El model considera variacions locals de pressió i temperatura del combustible gràcies a la hipòtesi de flux adiabàtic, per la qual cosa també s'ha hagut de dur a terme una caracterització experimental de les propietats del combustible a alta pressió. Els límits de la validesa d'esta hipòtesi s'han analitzat acuradament en l'estudi.

Els resultats mostren una influència significativa de la temperatura del combustible a l'entrada de l'injector en la tasa i duració d'injecció, atribuïda a l'efecte de la variació de les propietats del combustible i al fet que l'injector roman en operació balística per a la majoria de les seues condicions de funcionament. Els canvis en temperatura del combustible al llarg dels orificis de control de l'injector són capaços de modificar la seua dinàmica considerablement. A més, si el combustible a l'entrada de l'injector es troba a temperatura ambient o per damunt, s'ha observat que la temperatura a l'eixida de

la tobera no varia de manera important una vegada s'han assolit condicions estacionàries. No obstant això, un escalfament significatiu pot tenir lloc per a temperatures d'entrada típiques de les condicions d'arrancada en fred.

A mis padres
y hermanos

No quiero dejar pasar la oportunidad de expresar mi gratitud por todas aquellas personas que han hecho posible la consecución de este trabajo. Muchos os habéis cruzado conmigo en este largo camino y habéis dejado una huella imborrable en mi persona, por lo que os considero tan autores de esta Tesis como yo mismo. No en vano, estas son para mí sus páginas más importantes.

En primer lugar, quisiera darle las gracias a mi tutor y director Javier Salvador, no sólo por su inestimable consejo, dedicación y esfuerzo en mi formación como investigador, sino especialmente por su excepcional calidad humana. Amigo, no tengo la menor duda de que esta Tesis no habría sido posible sin tu aportación.

Asimismo, debo agradecer al Instituto CMT-Motores Térmicos, y en particular a Francisco Payri y José María Desantes, la oportunidad de permitirme formar parte de este prestigioso grupo de investigación. Sus recursos tecnológicos, económicos y humanos han posibilitado la realización de esta Tesis Doctoral.

En este sentido, también debo mencionar aquí a las personas que me acogieron para desarrollar sendas estancias en sus respectivos centros de investigación: Luigi Alloca (Istituto Motori), y Gerald Steinwender y Johannes Schagerl (BMW Steyr).

Mi gratitud a los miembros del equipo de Inyección de CMT, encabezado por Raúl Payri. Mención especial merece Jaime Gimeno por su paciencia para resolver mis interminables dudas sobre Matlab y las instalaciones experimentales. No me puedo olvidar del resto de profesores y doctorandos del equipo: Pedro (a quien también le debo agradecer su ayuda durante la carrera), Gabriela, Joaquín, Jorge, Óscar, Michele, Juan Pablo, David, Daniel, Alberto, Jesús, Mary, Sebas, Vincenzo, Santiago y Marco. Además, he tenido la oportunidad de trabajar con múltiples proyectandos que han tenido la difícil tarea de soportarme como "jefe". Por supuesto, tampoco puedo dejar de mencionar a José Enrique, a pesar de su peculiar sentido del humor, por su colaboración en la parte experimental de este trabajo.

Del mismo modo, ha habido mucha gente dentro de CMT que ha sido fundamental para mí a lo largo de estos años, pese a no estar directamente involucrados en mis investigaciones. Hablo de compañeros doctorandos como Ricardo, José Pedro (otro viejo amigo de la carrera), Juanra, Estepa, Vaquerizo o Diego. Integrantes de la Copa Ayudante como Pedro (nuevamente) y Roberto. Profesores con los que he compartido asignaturas, como Andrés (gracias por ser mi tutor "docente") y Luismi. Técnicos de Laboratorio. Personal de Secretaría. Y tantos otros dispuestos a echar una mano siempre que lo he requerido.

No me puedo olvidar de todas las personas que, ajenas a mi trabajo, han aportado o aportaron su granito de arena para mi bienestar y mi crecimiento personal tanto durante esta última etapa como en el pasado. Amigos de Sueca, amigos de la carrera, estas líneas van por vosotros. Además, quiero reconocer la importancia del grupo del volley y de los compañeros del fútbol, sin olvidarme de Antonio Moreno y su virtud para hacer grupo.

Me gustaría además reconocer la labor formadora que ha tenido en mi persona el Colegio Mayor San Juan de Ribera, con especial mención al que fue su director durante mi estancia allí, José Vicente Puig. Me siento muy agradecido a todos y cada uno de los compañeros riberitas con los que compartí en el "Tru" una etapa especialmente relevante de mi vida. Dudo haber escogido este camino de no ser por esta experiencia.

De manera especial debo agradecer a mi familia los valores que me ha inculcado y el apoyo incondicional que me ha prestado a lo largo de toda mi vida. Padres, hermanos, os debo absolutamente todo cuanto he alcanzado. Gracias por vuestro ánimo en los momentos más difíciles y en los que estén por venir. Sin vosotros no habría encontrado la fuerza. Gracias por la educación que me habéis brindado. Espero que os sintais tan orgullosos de este "logro" como yo lo estoy de formar parte de vosotros.

Por último, y no por ello menos importante: gracias, Nazaret. Gracias por estar a mi lado tanto en los buenos momentos como en los que no lo han sido tanto, y por construir esto en una etapa tan complicada. Gracias por ayudarme a ser quien soy hoy. Gracias por caminar junto a mí y hacer que sigamos buscando nuestra suerte.

Quisiera también disculparme por las personas a las que no alcancen estas palabras. Sois muchos los que habéis tenido vuestro impacto en mí y os estoy igualmente agradecido.

A todos vosotros, gracias.

Contents

List of Figures

List of Tables

Nomenclature

Acronyms

BC Boundary Condition.
CAD Crank Angle Degree.
CFD Computational Fluid Dynamics.
CIDI Compression-Ignition Direct Injection.
CI Compression-Ignition.
DAE Differential Algebraic Equations.
DI Direct Injection.
DT Dwell Time.
ECU Electronic Control Unit.
ELSA Eulerian-Lagrangian Spray Atomization.
ET Energizing Time.
FAME Fatty Acid Methyl Ester.
FEM Finite Element Method.
FT-IR Fourier-Transformed Infrared Spectrometry.
GTL Gas to Liquids.
HEM Homogeneous Equilibrium Model.
HRM Homogeneous Relaxation Model.
HVO Hydrotreated Vegetable Oil.
IDI Indirect Injection.
IRDCI Injection Rate Discharge Curve Indicator.
LDV Laser Doppler Velocimetry.
LES Large-Eddy Simulation.

LL Liquid Length.
LMM Linear Multistep Methods.
ODE Ordinary Differential Equations.
PDE Partial Differential Equations.
PDPA Phase Doppler Particle Analyzer.
PID Proportional-Integral-Derivative.
RME Rapeseed Oil Methyl Ester.
ROI Rate of Injection.
SEM Scanning Electron Microscope.
SMD Sauter Mean Diameter.
SOE Start of Energizing.
SOI Start of Injection.
UHC Unburned Hydrocarbon.
VCO Valve Covered Orifice.

Greek symbols

α Coefficient of thermal expansion.
α_b Ball seat angle.
α_c Cone angle.
α_k Thermal diffusivity.
α_L Line angle with respect to the horizontal.
α_m Mass angle with respect to the horizontal.
α_p Angle among a cone surface and a line perpendicular to the poppet.
α_s Seat angle.
α_t Tube thermal expansion coefficient.
β Bulk modulus (general).
β_f Fuel (liquid) bulk modulus.
β_S Isentropic bulk modulus.
β_T Isothermal bulk modulus.
β_t Tube compressibility coefficient.
β_{eff} Effective bulk modulus.
Δp Pressure difference.
ΔT Temperature difference.
η Dynamic viscosity.
η_0 Dynamic viscosity at atmospheric pressure.
η_b Fluid bulk viscosity.

η_f Fuel dynamic viscosity (liquid phase).
η_w Fluid viscosity at the wall.
γ Void fraction.
κ_S Isentropic coefficient of compressibility.
λ_{inj} Constant for the transient radial heat conduction through an injector duct.
μ Magnetic permeability.
μ_0 Magnetic permability of vacuum.
μ_r Material relative magnetic permeability.
ν Kinematic viscosity.
ν_f Fuel kinematic viscosity (liquid phase).
ν_{Po} Poisson's ratio.
Φ_B Magnetic flux.
$\phi_{visc,M}$ Major losses due to viscous dissipation.
$\phi_{visc,m}$ Minor losses due to viscous dissipation.
ϕ_{visc} Losses due to viscous dissipation.
ρ Density (general).
ρ_0 Density at atmospheric pressure.
ρ_f Fuel density (liquid phase).
σ Surface tension.
σ_f Surface tension (liquid phase).
τ_k Characteristic time of heat transfer due to conduction.
θ Temperature difference among the fluid and the wall.
θ_s Spray spreading angle.
ε Deviation among experimental and modelled results (generic).
ξ Viscous dissipation minor pressure losses coefficient.
ζ Magnetic flux distortion correction factor.

Latin symbols

$\dot{M}$ Momentum flux.
$\dot{m}$ Mass flow rate.
$\dot{M}_{th}$ Theoretical momentum flux.
$\dot{m}_{th}$ Theoretical mass flow rate.
$\dot{q}$ Heat flux.
$\dot{V}$ Volumetric flow rate.
$\mathcal{F}$ Magnetomotive force.

$\mathcal{P}$	Magnetic permeance.
$\mathcal{R}$	Magnetic reluctance.
A	Cross-sectional area.
a_f	Fuel (liquid) speed of sound.
a_G	Gaussian distribution coefficient.
A_i	Orifice inlet area.
A_o	Orifice outlet area.
A_P	Area submitted to heat transfer.
A_t	Tube cross-sectional area.
A_{eff}	Effective flow area.
Ad	Adiabatic number.
AR	Orifice area reduction.
B	Magnetic flux density.
b	Damping coefficient.
C_a	Area coefficient.
C_c	Contraction coefficient.
C_d	Discharge coefficient.
C_f	Darcy friction coefficient.
C_M	Momentum coefficient.
c_p	Specific heat capacity at constant pressure.
C_v	Velocity coefficient.
c_v	Specific heat capacity at constant volume.
C_{wall}	Wall compliance (total elasticity).
CN	Cavitation number (alternative definition).
D	Diameter.
D_b	Ball diameter.
d_d	Droplet diameter.
D_f	Fuel mass diffusivity.
D_h	Hydraulic diameter.
D_i	Orifice inlet diameter.
D_m	Orifice mid-section diameter.
D_o	Orifice outlet diameter.
D_s	Seat throat diameter.
D_{cl}	Clearance on diameter.
D_{eff}	Effective diameter.

D_{ext} Line external diameter.
D_{int} Line internal diameter.
D_{pist} Piston diameter.
DT_{crit} Critical dwell time to separate two subsequent injections.
E Young modulus.
e Specific internal energy.
e_k Specific kinetic energy.
F Force.
f Fanning friction factor.
$F_{\Delta p}$ Force due to the pressure difference at both sides of the needle.
F_{dyn} Dynamic friction force.
F_{ext} External force.
F_{fric} Friction force.
F_{needle} Resultant force on the needle.
F_{st} Static friction force.
G Shear modulus.
g Gravitational acceleration.
H Magnetic field intensity.
h Specific enthalpy.
h_c Convective heat transfer coefficient.
I Electric current.
J_0 Bessel function of first kind of order zero.
K Cavitation number.
k Thermal conductivity.
$k - factor$ Orifice conicity factor.
k_f Fuel thermal conductivity.
k_r Relative roughness.
k_s Spring stiffness.
K_{crit} Critical cavitation number.
k_{eq} Equivalent stiffness.
L Characteristic length.
l Lift.
L_0 Reference length.
m Mass.
m_i Total mass injected per cycle.

n	Unit vector normal to an orifice cross-section.
N_d	Number of droplets.
n_e	Engine speed (rpm).
N_s	Spring number of spires.
N_t	Coil number of turns.
Nu	Nusselt number.
Oh	Ohnesorge number.
P	Perimeter.
p	Pressure (general).
p_0	Reference pressure (atmospheric).
p_b	Discharge pressure.
p_i	Injection pressure.
p_v	Vapour pressure.
p_{dw}	Downstream pressure.
p_{up}	Upstream pressure.
Pr	Prandtl number.
Q	Net heat supplied to a thermodynamic system.
R	Electrical resistance.
r	Radial coordinate.
r_0	Cylinder internal radius.
r_b	Bubble radius.
r_i	Orifice rounding radius at the inlet.
r_l	Lower side orifice rounding radius.
R_s	Spray radius.
r_u	Upper side orifice rounding radius.
Re	Reynolds number.
Re_{th}	Theoretical Reynolds number.
S	Spray penetration.
Sc	Schmidt number.
St	Stanton number.
T	Temperature (general).
T_0	Reference temperature.
t_d	Delay among SOE and SOI.
T_f	Fuel (liquid) temperature.
T_i	Fuel temperature at the injector inlet.

T_w	Wall temperature.
t_{Ad}	Ratio among residence time and conduction characteristic time.
t_{aSOE}	Time after Start of Energizing.
t_{aSOI}	Time after Start of Injection.
t_{res}	Fuel residence time in the injector.
T_{dw}	Downstream temperature.
t_{inj}	Injection time.
T_{up}	Upstream temperature.
U	Flow velocity.
u	Flow velocity normal to an orifice cross-section.
U_b	Body velocity.
u_{eff}	Effective flow velocity.
u_{rel}	Relative velocity among the fuel droplets and the surrounding gas.
u_{th}	Theoretical flow velocity (according to the Bernoulli equation).
$U_{b,0}$	Body critical velocity.
V	Voltage.
v	Specific volume.
V_i	Volume (general).
W	Net work done by a thermodynamic system.
We	Weber number.
x	Position.
x_0	Spring initial compression.
Y_f	Fuel (liquid) concentration.
z	Elevation.

Chapter 1

Introduction

1.1 General context

Over the last few decades, the development of society and the consequent growth of energy consumption have led to an increasing concern for environmental protection. In an already fiercely competitive market such as the automotive industry, the stringent emissions regulations imposed by the governments (i.e. Euro VI [1]) have resulted in a growing interest by the scientific community on how to transform energy in a clean and efficient way without negatively affecting the economy.

In modern Diesel engines, combustion is the phenomenon that has received most attention by researchers, since its optimization directly influences the fuel consumption, noise irradiation and pollutant emissions [2, 3]. In this frame, the injection system has been widely studied due to its key role on fuel atomization, vaporization and air-fuel mixing process, setting the scenario in which combustion will take place, thus importantly affecting its characteristics [2–8].

Numerous studies, both theoretical and experimental, have been historically carried out in order to increase the knowledge about the injection phenomenon. These studies have paid attention to different features of the injection system. Thereby, the influence of the injector geometry (both in terms of internal ducts and nozzle orifices) on the internal flow characteristics, spray formation and fuel atomization has been deeply analysed [9–13]. Similarly, given the order of magnitude of the injection times and the need to inject rel-

atively large amounts of fuel in that time, it has always been sought to characterize and improve injector dynamics. Technical advances in this regard, with the appearance of both solenoid and piezoelectric valves, have allowed a very fast response and the development of powerful tools such as multi-injection strategies [6, 14–16]. The irruption of the common-rail system has also made it possible to progressively increase the injection pressure (currently above 250 MPa), generating higher injection rates [17–20]. However, the technical development has also increased the complexity of the problem, making it necessary to study the influence of phenomena such as compressible or cavitating flow in the nozzles and their effect on the injection process [21–26].

The studies in these matters have had the invaluable help of engineered techniques. On the one hand, experimental tools have made it possible, for instance, to geometrically characterize an injector or even to visualize the spray in both their liquid and gaseous phases [27–29]. On the other hand, several computational tools have allowed to model an injection system in order to predict its behaviour under different operating conditions [30, 31], or even to observe the flow patterns along the injector ducts and orifices through CFD techniques [13, 26, 32, 33].

Nevertheless, there are still certain considerations that have not been taken into account when studying the fuel injection phenomenon in diesel engines. The increasing injection pressures accelerate the injector internal flow to high speeds, especially through the control and nozzle orifices it encounters, due to their low diameters in the order of tenths of a millimiter [3]. The flow through these orifices may also induce changes in fuel temperature due to depressurization and viscous friction. These changes may modify the fuel properties given their strong dependence on temperature. Specifically, the viscosity, density and speed of sound, among others, are modified when the temperature rises [21, 34, 35]. However, this phenomenon has not been deeply analysed, and most studies consider the injection as an isothermal process, taking the fuel temperature value at the injector inlet as constant along the injection system. Some authors move one step further and assume the flow along the injector as adiabatic [36, 37], although attention has never been given to the assessment of the extension of the validity of this hypothesis, which may not be true under some real circumstances. Indeed, even though the temperature difference among the fuel and the injector walls may be high in some conditions, heat transfer to the surroundings could not be relevant in conditions where the flow velocity is high enough to lead to low residence times of a fuel particle within the injector. However, the adiabatic assumption may not hold if the fuel velocity is too low and there is enough time for the fuel to interact with the ambient.

1.2 Objectives and methodology

The purpose of this thesis is to shed light on the aforementioned issues in order to assess the influence of the thermal effects on the diesel injector performance. Fuel temperature and its local variations along the injector are deemed to play a key role on injector dynamics, given that diesel injectors are operated hydraulically.

The injector taken as a reference to carry out the investigation (a Bosch CRI 2.20 injector) is a solenoid-driven unit of ballistic nature [38], which means that the needle lift is not mechanically limited to a value usually achieved during its normal operation. Thus, the influence of the fuel properties on the dynamic behaviour is here expected to be of even more crucial importance, since the maximum lift reached by the needle will directly depend on its friction with the fuel due to viscous effects.

With all, the objectives of the present thesis may be summarized as follows:

- To estimate the actual fuel temperature variation through the injector restrictions. In this regard, once the isothermal assumption is discarded, the limits of the validity of the adiabatic flow hypothesis must be assessed and bounded. Otherwise, an order of magnitude of the temperature variations that could take place due to heat transfer to the surroundings depending on the injector operating conditions should be determined.
- To establish the influence of the aforementioned fuel temperature variations on the fuel thermodynamic properties that are expected to play a key role on the injection process, namely the fuel density, viscosity, speed of sound and bulk modulus.
- To determine and understand the impact of the induced variations in fuel properties on injector dynamics and the injection rate shape for a wide range of injection conditions (including cold start), given its consequences on the combustion phenomenon.

Ideally, the means employed for the attainment of these objectives would be purely experimental. However, there are a number of constraints that make it difficult to reproduce the problem characteristics in order to carry out their investigation:

- Small dimensions of the injector internal ducts and orifices (the typical length of nozzle orifices is in the order of millimiters, whereas their typical diameter is in the order of tenths of a millimiter).

- High flow velocities, reaching values in the order of hundreds of meters per second due to the high injection pressures that can be currently achieved.
- Transient nature of the process, which takes place cyclically in times of the order of milliseconds.

Therefore, the use of experimental tools has been combined with 1D computational tools (previously validated against experimental results) given their proved potential when studying the hydro-dynamic behaviour of injection systems. The use of these computational tools allows to have a look at the injector internal features (such as flow regime set in each of the internal orifices, pressure evolution in the relevant volumes ...) that are not accessible by a purely experimental approach. This makes it possible to determine not only the influence of the thermal effects on the injection rate, but also to understand the reasons behind that behaviour.

This work has been performed in the frame of the *Departamento de Máquinas y Motores Térmicos* at *Universitat Politècnica de València* (Spain), which has a long expertise in the study of the diesel injection process. Not in vain, numerous PhD theses about the topic have been defended in the last years [10, 30–33, 39–48], following experimental and computational approaches alike. From all these works, two are closely related to the topics dealt with in the present thesis, since they are focused on injection system modelling or the fuel properties influence on the injection process.

Specifically, Plazas [31] used 1D computational tools to model and analyse different generations of diesel injectors, both in solenoid and piezo-driven variants. His work focused on the differences among injector typologies and the influence of the different technologies on the injection rate shape. The use of 1D modelling combined with statistical models allowed him to establish the most critical parameters in injector design.

From the experimental point of view, Bracho [44] studied the injection process at cold start by means of injection rate and momentum flux determination together with spray visualization techniques in non-evaporative conditions. To this end, the existing facilities available at the department were adapted to low temperature conditions (between 255 and 273 K) and a new technique to determine the fuel properties in a wide range of temperatures and pressures (up to 180 MPa) was developed and implemented. She also applied a CFD approach to analyse the turbulent patterns of the internal nozzle flow at these extreme conditions.

1.3 Thesis outline

This thesis is organized in seven chapters including the present introduction (*Chapter 1*). In *Chapter 2*, the Diesel engine injection process is dealt with. The current injection system technologies are described, with special attention to their most determining component: the injector. Due to their relevance in the combustion process, the fundamentals of the internal flow along the *common-rail* injector and the resulting Diesel spray are presented as well.

Chapter 3 offers a detailed review on how the injection systems have been modelled by other authors through 1D tools and the evolution of these models as the injection systems themselves were upgraded. Considering its significance in the analysis carried out in the present investigation, a review of the studies about the influence of the fuel properties on the injection process is also offered. This kind of studies cannot be performed without an accurate knowledge of the evolution of these properties with the thermodynamic variables. For this reason, the most relevant works on fuel properties determination at the high pressures and temperatures representative of the Diesel injection process are also here outlined.

A description of the experimental tools on which this work is based is presented in *Chapter 4*. This includes those tools needed to perform a complete characterization of the injector, both in dimensional and hydraulic terms. Since a computational model needs to be implemented for the present investigation, the fuel properties need to be determined in a wide range of temperatures and pressures. The procedure to do so is also presented in this chapter. The experiments performed in each case are described in detail, highlighting the physical principles behind the measurements, discussing the implemented hardware and explaining how the data are gathered and processed.

Chapter 5 deals with the computational model used to reach the objective of the thesis. It offers a thorough explanation on the methodology followed to implement the 1D model of the reference injector so that the real physics behind the injection process is captured. A description of the code is given, with special attention to the different elements modelled and the hypotheses assumed for the injector internal flow. The validity of these assumptions is tested against the experimental measurements made available by the techniques described in *Chapter 4* in order to ensure that the actual behaviour of the injector is properly reproduced. The assessment of the extension of the validity of the adiabatic flow assumption is also dealt with in this chapter. This attempt at bounding the conditions at which the flow may or not be regarded to as adiabatic constitutes one of the most innovative contributions of this thesis.

The analysis of the results obtained from both the experimental and computational tools previously described is shown in *Chapter 6*. First, the purely experimental results from the mass flow rate measurements are discussed, establishing trends about the influence of the fuel temperature at the injector inlet on the shape of the rate of injection temporal evolution. Next, the thermal effects on the flow through the most important restrictions of the injector are evaluated thanks to the computational model. A detailed discussion on how these thermal effects influence the injection rate shape and therefore the injection process is also given in this chapter. In this case, the combination among experimental and computational tools shows its true potential, since the findings gathered experimentally are confirmed, justified and extended thanks to the use of the implemented 1D model.

The last chapter (*Chapter 7*) draws the main conclusions of this thesis synthesizing all the new information brought and indicating possible directions on which to orient future investigations in the topic.

References

[1] *On type-approval of motor vehicles and engines with respect to emissions from heavy duty vehicles (Euro VI) and on access to vehicle repair and maintenance information and amending Regulation (EC) No 715/2007 and Directive 2007/46/EC and repealing Directi*. Official Journal of the European Union. Regulation. 2009.

[2] HEYWOOD, J. B. *Internal Combustion Engine Fundementals*. McGraw Hill, 1988. ISBN: 007028637X.

[3] PAYRI, F. and DESANTES, J. M. *Motores de combustion interna alternativos*. Editorial Reverte, 2011. ISBN: 978-84-291-4802-2.

[4] NISHIMURA, T., SATOH, K., TAKAHASHI, S., and YOKOTA, K. "Effects of Fuel Injection Rate on Combustion and Emission in a DI Diesel Engine". *SAE Technical Paper 981929*. 1998. DOI: 10.4271/981929.

[5] SCHMIDT, D. P. and CORRADINI, M. L. "The internal flow of diesel fuel injector nozzles: a review". *International Journal of Engine Research*, vol. 2.1 (2001), pp. 1–22. ISSN: 1468-0874. DOI: 10.1243/1468087011545316.

[6] Park, S. H., Yoon, S. H., and Lee, C. S. "Effects of multiple-injection strategies on overall spray behavior, combustion, and emissions reduction characteristics of biodiesel fuel". *Applied Energy*, vol. 88.1 (2011), pp. 88–98. ISSN: 0306-2619. DOI: http://dx.doi.org/10.1016/j.apenergy.2010.07.024.

[7] Payri, R., Salvador, F. J., Gimeno, J., and De la Morena, J. "Influence of injector technology on injection and combustion development, Part 1: Hydraulic characterization". *Applied Energy*, vol. 88.4 (2011), pp. 1068–1074. ISSN: 0306-2619. DOI: 10.1016/j.apenergy.2010.10.012.

[8] Payri, R., Salvador, F. J., Gimeno, J., and De la Morena, J. "Influence of injector technology on injection and combustion development, Part 2: Combustion analysis". *Applied Energy*, vol. 88.4 (2011), pp. 1130–1139. ISSN: 0306-2619. DOI: 10.1016/j.apenergy.2010.10.012.

[9] Von Kuensberg Sarre, C., Kong, S.-c., and Reitz, R. D. "Modeling the effects of injector nozzle geometry on diesel sprays". *SAE Technical Paper 1999-01-0912*, 724 (1999). DOI: 10.4271/1999-01-0912.

[10] Salvador, F. J. "Estudio teórico experimental de la influencia de la geometría de toberas de inyección Diésel sobre las características del flujo interno y del chorro". PhD thesis. Universitat Politècnica de València, 2003.

[11] Payri, R., Garcia-Oliver, J. M., Salvador, F. J., and Gimeno, J. "Using spray momentum flux measurements to understand the influence of diesel nozzle geometry on spray characteristics". *Fuel*, vol. 84.5 (2005), pp. 551–561. ISSN: 00162361. DOI: 10.1016/j.fuel.2004.10.009.

[12] Payri, F., Payri, R., Salvador, F. J., and Gimeno, J. "Influence of Nozzle Geometry on Spray Characteristics in Non-Evaporative and evaporative conditions". *SAE Technical Paper 2007-24-0023* (2007). DOI: 10.4271/2007-24-0023.

[13] Som, S., Aggarwal, S. K., El-Hannouny, E. M., and Longman, D. E. "Investigation of nozzle flow and cavitation characteristics in a diesel injector". *Journal of Engineering for Gas Turbines and Power*, vol. 132 (2010), p. 42802. ISSN: 07424795. DOI: 10.1115/1.3203146.

[14] CATANIA, A. E., FERRARI, A., MANNO, M., and SPESSA, E. "Experimental Investigation of Dynamics Effects on Multiple-Injection Common Rail System Performance". *Journal of Engineering for Gas Turbines and Power*, vol. 130.3 (2008), p. 032806. ISSN: 07424795. DOI: 10.1115/1.2835353.

[15] ZHENG, M. and KUMAR, R. "Implementation of multiple-pulse injection strategies to enhance the homogeneity for simultaneous low-NOx and -soot diesel combustion". *International Journal of Thermal Sciences*, vol. 48.9 (2009), pp. 1829–1841. ISSN: 12900729. DOI: 10.1016/j.ijthermalsci.2009.02.009.

[16] MOHAN, B., YANG, W., and CHOU, S. K. "Fuel injection strategies for performance improvement and emissions reduction in compression ignition engines - A review". *Renewable and Sustainable Energy Reviews*, vol. 28.x (2013), pp. 664–676. ISSN: 13640321. DOI: 10.1016/j.rser.2013.08.051.

[17] ERLACH, H., CHMELA, F., CARTELLIERI, W., and HERZOG, P. "Pressure Modulated Injection and Its Effect on Combustion and Emissions Ofa Hd Diesel Engine". *SAE transactions*, 412 (1995). DOI: 10.4271/952059.

[18] GANSER, M. A. "Common rail injectors for 2000 bar and beyond". *SAE Technical Paper 2000-01-0706* (2000). DOI: 10.4271/2000-01-0706.

[19] GUMUS, M., SAYIN, C., and CANAKCI, M. "The impact of fuel injection pressure on the exhaust emissions of a direct injection diesel engine fueled with biodiesel–diesel fuel blends". *Fuel*, vol. 95.1 (2012), pp. 486–494. ISSN: 00162361. DOI: 10.1016/j.fuel.2011.11.020.

[20] AGARWAL, A. K. et al. "Effect of fuel injection pressure and injection timing of Karanja biodiesel blends on fuel spray, engine performance, emissions and combustion characteristics". *Energy Conversion and Management*, vol. 91 (2015), pp. 302–314. ISSN: 01968904. DOI: 10.1016/j.enconman.2014.12.004.

[21] PAYRI, R., SALVADOR, F., GIMENO, J., and BRACHO, G. "The effect of temperature and pressure on thermodynamic properties of diesel and biodiesel fuels". *Fuel*, vol. 90.3 (2011), pp. 1172–1180. ISSN: 00162361. DOI: 10.1016/j.fuel.2010.11.015.

[22] ARCOUMANIS, C., BADAMI, M., FLORA, H., and GAVAISES, M. "Cavitation in real-size multi-hole Diesel injector nozzles". *SAE Technical Paper 2000-01-1249* (2000). DOI: 10.4271/2000-01-1249.

[23] Payri, F., Bermúdez, V., Payri, R., and Salvador, F. J. "The influence of cavitation on the internal flow and the spray characteristics in diesel injection nozzles". *Fuel*, vol. 83.4-5 (2004), pp. 419–431. issn: 00162361. doi: 10.1016/j.fuel.2003.09.010.

[24] Gavaises, M. and Andriotis, A. "Cavitation Inside Multi-hole Injectors for Large Diesel Engines and Its Effect on the Near-nozzle Spray Structure". *SAE Technical Paper 2006-01-1114* (2006). doi: 10.4271/2006-01-1114.

[25] Suh, H. K. and Lee, C. S. "Effect of cavitation in nozzle orifice on the Diesel fuel atomization characteristics". *International Journal of Heat and Fluid Flow*, vol. 29 (4).4 (2008), pp. 1001–1009. issn: 0142727X. doi: 10.1016/j.ijheatfluidflow.2008.03.014.

[26] Salvador, F. J., Hoyas, S., Novella, R., and Martinez-Lopez, J. "Numerical simulation and extended validation of two-phase compressible flow in diesel injector nozzles". *Proceedings of the Institution of Mechanical Engineers, Part D: Journal of Automobile Engineering*, vol. 225.4 (2011), pp. 545–563. issn: 0954-4070. doi: 10.1177/09544070JAUTO1569.

[27] Naber, J. D. and Siebers, D. L. "Effect of gas density and vaporization on penetration and dispersion of Diesel sprays". *SAE Technical Paper 960034*, vol. 105.412 (1996), pp. 82–111. doi: 10.4271/960034.

[28] Siebers, D. L. "Liquid-phase fuel penetration in diesel sprays". *SAE Technical Paper 980809* (1998). doi: 10.4271/980809.

[29] Desantes, J. M., García-Oliver, J. M., Pastor, J. M., and Ramírez-Hernández, J. G. "Influence of nozzle geometry on ignition and combustion for high-speed direct injection diesel engines under cold start conditions". *Fuel*, vol. 90.11 (2011), pp. 3359–3368. issn: 00162361. doi: 10.1016/j.fuel.2011.06.006.

[30] Rodriguez, P. "Modelado del comportamiento hidrodinámico de sistemas de inyección directa Diesel". PhD thesis. Valencia: Universitat Politècnica de València, 2001.

[31] Plazas, A. H. "Modelado unidimensional de inyectores common-rail Diesel". PhD thesis. Valencia: Universitat Politècnica de València, 2005.

[32] Martínez López, J. "Estudio computacional de la influencia del levantamiento de aguja sobre el flujo interno y el fenómeno de la cavitación en toberas de inyección diésel". PhD thesis. Valencia (Spain): Universitat Politècnica de València, 2013. doi: 10.4995/Thesis/10251/29291.

[33] MARTÍ GÓMEZ-ALDARAVÍ, P. "Development of a computational model for a simultaneous simulation of internal flow and spray break-up of the diesel injection process". PhD thesis. Valencia (Spain): Universitat Politècnica de València, 2014. DOI: 10.4995/Thesis/10251/43719.

[34] RODRÍGUEZ-ANTÓN, L. M., CASANOVA-KINDELAN, J., and TARDAJOS, G. "High Pressure Physical Properties of Fluids used in Diesel injection systems". *SAE Paper 2000-01-2046*, vol. 2000-01-20 (2000). DOI: 10.4271/2000-01-2046.

[35] DERNOTTE, J., HESPEL, C., HOUILLE, S., FOUCHER, F., and MOUNAIM-ROUSSELLE, C. "Influence of Fuel Properties on the Diesel Injection Process in Nonvaporizing Conditions". *Atomization And Sprays*, vol. 22.6 (2012), pp. 461–492. ISSN: 1044-5110. DOI: 10.1615/AtomizSpr.2012004401.

[36] SEYKENS, X. and SOMERS, L. "Detailed modeling of common rail fuel injection process". *Journal of Middle European* (2005), pp. 30–39.

[37] CATANIA, A. E., FERRARI, A., and SPESSA, E. "Temperature variations in the simulation of high-pressure injection-system transient flows under cavitation". *International Journal of Heat and Mass Transfer*, vol. 51 (2008), pp. 2090–2107. ISSN: 00179310. DOI: 10.1016/j.ijheatmasstransfer.2007.11.032.

[38] ZEH, D. et al. "Bosch Diesel Injection Technology – Response for Every Vehicle Class Production : Light Vehicles 1) World by Region". *23 Aachener Kolloquium*. Aachen, 2014.

[39] ARRÈGLE, J. "Análisis de la estructura y dinámica interna de chorros Diesel". PhD thesis. Universitat Politècnica de València, 1997.

[40] RUIZ, S. "Estudio teórico-experimental de los procesos de atomización y de mezcla en los chorros Diesel D.I." PhD thesis. Valencia: E.T.S. Ingenieros Industriales. Universidad Politécnica de Valencia, 2003.

[41] GONZÁLEZ, C. A. "Estudio de la influencia de la geometría de la tobera de inyección en la combustión y emisión de contaminantes de un motor diesel". PhD thesis. Universitat Politècnica de València, 2005.

[42] HERMENS, S. "Influence of Diesel injector nozzle geometry on the injection and combustion process". PhD thesis. Universitat Politècnica de València, 2007.

[43] GIMENO, J. "Desarrollo y aplicación de la medida del flujo de cantidad de movimiento de un chorro Diesel". PhD thesis. Universitat Politècnica de València, 2008.

[44] Bracho, G. "Experimental and theoretical study of the direct diesel injection process at low temperatures". PhD thesis. Universitat Politècnica de València, 2011.

[45] De la Morena, J. "Estudio de la influencia de las características del flujo interno en toberas sobre el proceso de inyección Diesel en campo próximo". PhD thesis. Universidad Politécnica de Valencia, 2011.

[46] De la Garza, O. "Estudio de los efectos de la cavitación en toberas de inyección diesel sobre el proceso de inyección y el de formación de hollín". PhD thesis. Valencia (Spain): Universitat Politècnica de València, 2012. doi: 10.4995/Thesis/10251/18153.

[47] Bardi, M. "Partial needle lift and injection rate shape effect on the formation and combustion of the Diesel spray". PhD thesis. Valencia (Spain): Universitat Politècnica de València, 2014. doi: 10.4995/Thesis/10251/37374.

[48] Venegas, O. "Estudio del fenómeno de la cavitación en la inyección Diesel mediante la visualización del flujo interno en orificios transparentes." PhD thesis. Valencia (Spain): Universitat Politècnica de València, 2014. doi: 10.4995/Thesis/10251/37375.

Chapter 2

Fundamentals of the Diesel injection process

2.1 Introduction

Direct injection has become the most employed method to introduce the fuel into the combustion chamber of Diesel engines [1, 2], as a consequence of the increase in efficiency and the reduction of the engine head size resulting from the pre-chamber removal. Nevertheless, this method has a main drawback inherent to its definition: the fuel must be quickly atomized, mixed and ignited directly within the combustion chamber. This fact highlights the need for a high quality injection system, and has encouraged both the automotive industry and its research community to introduce continuous technical innovations and new injection strategies.

The present chapter is mainly focused on the fundamentals of *direct injection* (DI) for *compression-ignition* (CI) engines. The main injection system technologies that have emerged as an answer to the demanding requirements are described, emphasizing the critical achievements that resulted in a better performance along the last few decades. Special attention is given to the *common-rail* system, since it has become a standard in CIDI engines [2]. Among all the elements that comprise a common-rail system, the injector deserves major consideration. The internal flow through both its control and nozzle orifices play a key role in the injection process timing and the spray formation and development, finally affecting the combustion characteristics.

For this reason, the physical principles driving the injector internal flow and the Diesel spray are also explained in this chapter.

With regard to the injection process, the short time available in CI engines to form the air-fuel mixture imposes significant limitations. Hence, their engine speed is limited by the time needed to complete the fuel injection, atomization, mixture and combustion. The injection system is then of key importance to promote the rapid realization of those events.

Two different philosophies have been used to carry out the fuel delivery to the combustion chamber, as depicted in Figure 2.1: indirect injection (IDI) and direct injection (DI).

- In IDI systems (Figure 2.1(a)), the fuel is delivered into a pre-chamber where the air had been previously confined. The mixture takes place at this pre-chamber, where it is ignited and spread to the main combustion chamber. Thus, the air is responsible for generating the diffusive and convective fields necessary to promote the mixture, whereas the role of the fuel and the injection system is secondary. In this case, injectors with single-hole nozzles working with relatively low injection pressures (20-40 MPa) are generally used.
- In DI systems (Figure 2.1(b)), the fuel is directly injected into the combustion chamber. Hence, the fuel is responsible for generating the mixture. To this end, it must be injected at high pressure and properly atomized and spread. Therefore, the need for a high quality injection system in response to these demands becomes evident. The injectors are more complex and make use of multi-hole nozzles with orifice diameters around 100 µm and very high injection pressures, even greater than 250 MPa.

DI engines achieve a better performance thanks to their lower heat losses resulting from the lower surface-to-volume ratio when prescinding from the pre-chamber. For this reason, IDI systems have fallen into disuse [2]. Consequently, this thesis and the following subsections are focused on DI systems. Nozzle internal flow and Diesel spray are also dealt with since they are crucial to the air-fuel mixture in this kind of systems.

2.2 Diesel direct injection systems

By definition, the fuel delivery system must fulfill the following tasks [2]:

- To introduce the required amount of fuel into the combustion chamber according to a law that will define the behaviour of the different stages

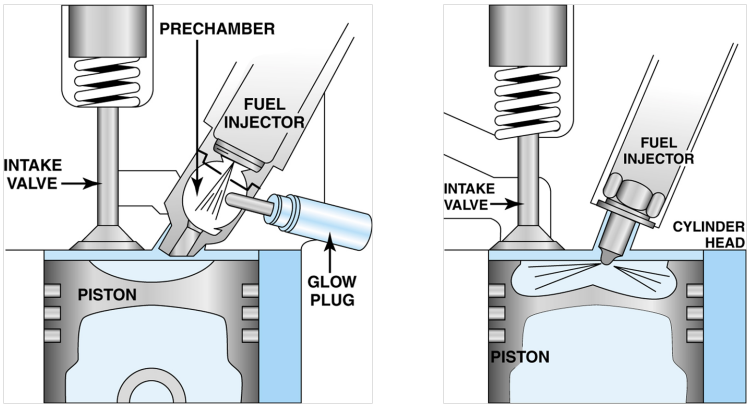

(a) IDI injection system (b) DI injection system

Figure 2.1: Methods to deliver fuel to the combustion chamber [3].

of the combustion process. This fuel delivery must be synchronized with the piston movement.

- To atomize the fuel in order to increase the surface in contact with the hot air after the compression stroke, thus accelerating the fuel evaporation process.
- To mix the fuel with the air available in the combustion chamber.

The DI systems for CI engines that have been mostly employed to give response to the previous requirements are listed below [4]:

- Rotary pump
  The first DI systems made use of a high-pressure pump in charge of delivering the fuel to the injector, whose mission merely consisted on its atomization. The main drawback of these systems was the impossibility of neither regulating the injection pressure in a proper way nor keeping it constant along the process, since it depended on the pump speed. They eventually fell into disuse for these reasons.
- Unit injector
  The pump and the injector are included in the same device, placed at the cylinder head. The pump plunger is driven either by the camshaft or through special joints. The start of injection (SOI) and the injection duration are controlled by means of a solenoid valve placed inside each injector. Then, the main advantages of this kind of systems are the possibility to electronically control the system through the Electronic Control Unit (ECU) and the high injection pressures reached.

- Unit pump
  Variant of the previous system in which the pump and the injector are connected through a short high-pressure line. It also allows high injection pressures and control over the SOI and injection duration through a solenoid valve placed into the pump associated to each cylinder.
- Accumulation systems
  They are based on storing fuel at a certain pressure in a volume placed between the pump and the injector. The fuel remains in this volume until injected. The pump, driven by the engine crankshaft, is exclusively in charge of raising the fuel pressure, whereas the injector is responsible for both its dosing and its atomization. Their great flexibility allows an easy control of the SOI and injection duration, the injection pressure, the amount of fuel injected and even rate shaping. In addition, the existence of this intermediate volume damps the pressure oscillations generated either by the pump or by the rapid evacuation of the fuel through the injector nozzle orifices. The *common-rail*, which has become the Diesel injection system with a higher market share for automotive applications, belongs to this kind of systems.

2.2.1 The common-rail Diesel injection system

Figure 2.2 shows the layout of a *common-rail* system. Its components may be classified into a low-pressure circuit (comprised by the fuel tank, a low-pressure pump, the pipes and a filter) and a high-pressure circuit (comprised by the high-pressure pump, the rail, the pressure regulator, the high-pressure lines and the injectors).

The low-pressure pump, generally housed in the fuel tank, feeds the fuel to the high-pressure pump. A filter is placed prior the high-pressure pump in order to remove any impurities or water traces that could damage the other components, especially the pump (where the water could cause corrosion) and the injectors (whose nozzle orifices could be blocked).

The high-pressure pump, mechanically connected to the engine through the crankshaft, provides a certain fuel mass flow rate abundantly higher than the average one required by the engine. The fuel is driven towards the rail, which is connected to the injectors. A flow valve in combination with a pressure sensor regulates the pressure of the fuel in the rail. Thus, if the rail pressure is higher than the desired value, the flow valve opens redirecting the part of the fuel that is not injected back to the fuel tank. On the contrary, if the rail pressure is lower than desired, the flow valve remains closed so that the pressure is raised thanks to the arrival of fuel from the pump.

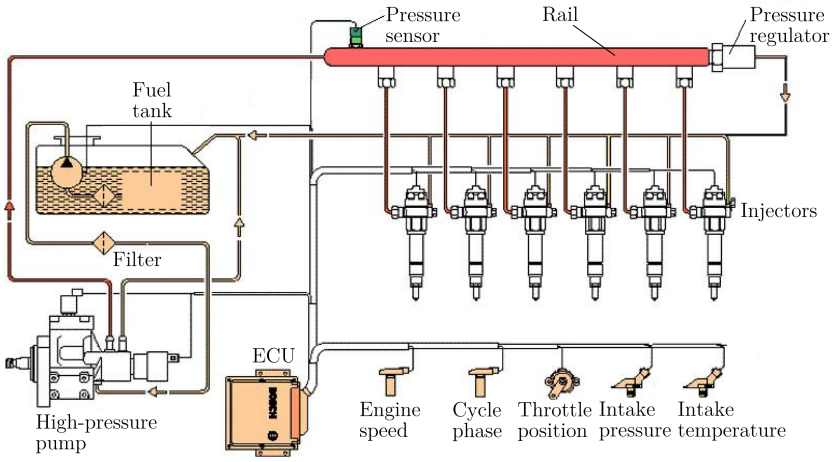

Figure 2.2: Components and layout of a typical common-rail system [2].

This way, a relatively high fuel volume is maintained at high and constant pressure. The rail acts as an accumulator that limits both the pressure fluctuations due to the high-pressure pump and the pressure drop induced by the opening of each injector [5]. The injectors, connected to the rail through short high-pressure lines (typically around 100 to 200 mm long), are independently actuated by the ECU. Most of the fuel entering the injectors is directly injected in the combustion chamber of each engine cylinder, whereas a small portion is used to hydraulically control the injector opening and closing and returns to the fuel tank after the injection event.

The main advantage of the *common-rail* system is that the rail pressure and injection timing are totally decoupled from the engine operating conditions and can be controlled electronically. In fact, the ECU is connected to several sensors (i.e. engine speed, cycle phase, throttle position, ...) that provide the information from the engine conditions. The independent control on the rail pressure and injection timing makes use of this information in order to adapt to each operating condition by means of different injection strategies [6–8].

Even when the first prototypes of this kind of system were presented in the late 1960s, they were first used in a production vehicle in Japan by the mid-1990s, specifically in a *Hino Rising Ranger* truck equipped by a Denso high pressure *common-rail* system [9]. At the same time, prototypes were being developed in collaboration between Fiat, Magneti Marelli and Elasis. When Bosch acquired the design by Fiat and refined it, its use was extended

for passenger cars. This way, the *Alfa Romeo 156 2.4 JTD* became the first passenger car that was equipped with a *common-rail* system in 1997.

2.2.2 The common-rail injector

Most efforts to improve the behaviour of the *common-rail* systems are focused on the development of the injectors, which certainly represent the most complex element in this environment. The latest advances in their technology have raised the maximum injection pressure limit to up to 300 MPa, thus increasing the capability of delivering fuel in a short time and indirectly enhancing the air-fuel mixing efficiency [10].

Common-rail injectors may be classified in two big groups: solenoid activated injectors and piezoelectric driven injectors. Their working principle is explained below taking the solutions implemented by Bosch as a reference, since they have been pioneers in the development of the *common-rail* system and the work carried out in this thesis mainly focuses on the Bosch CRI 2.20 injector.

Bosch solenoid activated injectors

The main elements composing a Bosch solenoid activated *common-rail* injector are shown in Figure 2.3 and can be classified into the following main components:

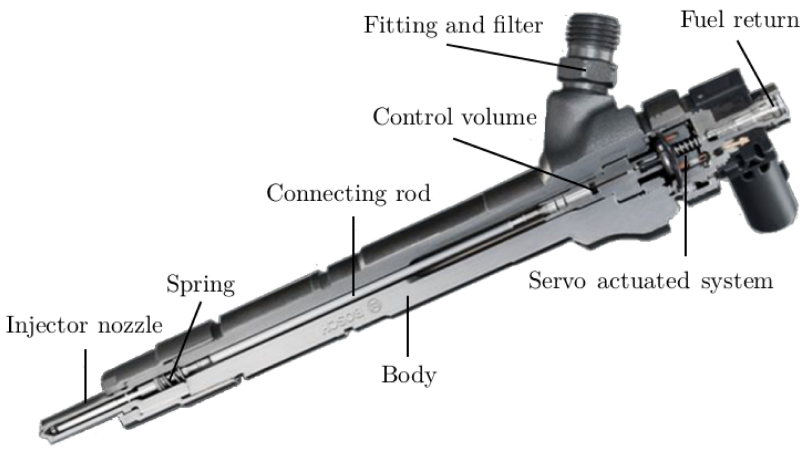

Figure 2.3: Solenoid activated common-rail injector (Bosch CRI 2.20).

- Servo-actuated system: this mechanism is composed of a solenoid actuator, a fuel valve and a control volume. This is the core of the injection and generates the forces needed to effectively move the needle during the injection. The working principle of this mechanism is explained below.
- Connecting rod: this element transmits the movement from the servo-actuated circuit to the needle. Hence, its bottom part pushes against the top of the needle.
- Injector nozzle: it is generally a multi-hole nozzle, with typycally 5 to 12 orifices in automotive applications. The needle can also be included in this element, since it is responsible for controlling the fuel flow through the nozzle orifices.

Figure 2.4 illustrates the working principle of a typical Bosch solenoid activated common-rail injector. The fuel coming from the rail enters the injector after being filtered, and is bifurcated in two ducts. One duct goes down towards the nozzle, whereas the other one leads the fuel through the so-called inlet orifice into the control volume, right above the connecting rod.

When the solenoid is not activated (Figure 2.4(a)), the connecting rod remains at its rest position. A small ball valve blocks the so-called control volume outlet orifice preventing fuel from leaving the injector through the return line. During this stage, the fuel pressure both at the control volume

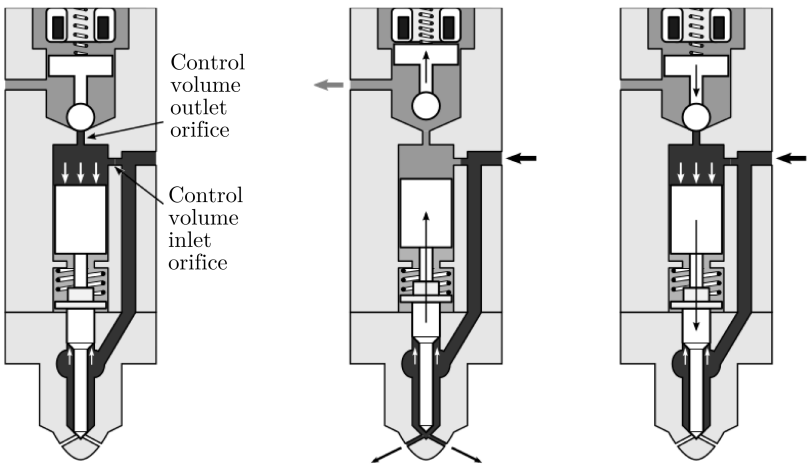

(a) Rest condition (b) Opening (c) Closing

Figure 2.4: Working principle of a typical solenoid activated common-rail injector [11].

and at the lower part of the injector is equal to the rail pressure. Considering that the area at the top of the connecting rod is higher than the one at the bottom of the needle, the resultant force pushes the rod-needle set downwards keeping the nozzle orifices locked and preventing the injection.

Once an injection is required, the ECU sends an electric pulse to the injector. The duration of this pulse controls the injection time and, consequently, the injected mass. This intensity through the solenoid coils generates a magnetic field that induces an ascending force on the ball valve, unlocking the control volume outlet orifice. In this situation (Figure 2.4(b)), the fuel flow evacuating the control volume induces a significant pressure drop in this region. As a consequence, since the pressure at the lower part of the needle is kept, a resultant force drives the rod-needle set upwards. Once the needle is lifted, fuel can flow through the nozzle orifices producing the start of the injection. This situation is kept as long as the solenoid remains excited by the ECU.

The end of the injection is triggered by the electric pulse extinction. At this moment, the ball valve returns to its rest position locking the control volume orifice (Figure 2.4(c)). The return flow is interrupted and the control volume is refilled by the fuel coming from the rail through the inlet orifice. The pressure in the control volume is then progressively re-established. When the initial conditions are reached again, the rod-needle set is pushed back towards its seat, blocking the fuel flow through the nozzle orifices and ending the injection.

Different solutions have been implemented along the years in order to enhance the accuracy and rapidity of the injector actuation. The reduction of the needle-rod inertia and the improvements on the actuator effectiveness have allowed to significantly reduce the delay among the solenoid start of energizing (SOE) and the SOI, enabling the introduction of a higher number of injections per engine cycle.

In this respect, the Bosch CRI 2.20 injector displayed in Figure 2.3 assembles both the needle and the rod together in a single piece, as opposed to the previous generations. Another interesting feature of the Bosch CRI 2.20 injector is the fact that its needle lift is mechanically limited to about 850 µm, unlike its predecessors, whose typical values of maximum needle lift are 250 µm. For this reason, the injector remains in ballistic operation (i.e. does not reach its maximum needle lift) during the whole injection event for the regular engine operating conditions.

Bosch piezoelectric driven injectors

Piezoelectric driven injectors also appeared in this search for accuracy and fastness. In these systems, some of the mobile elements of the control valve are replaced by a piezoelectric crystal, made up of wafers that compress or expand in function of the applied electric field. This allowed a substantial reduction of the needle-rod set inertia and a consequent improvement of the injector dynamic response [12, 13]. In this regard, the Bosch CRI 3.1 injector, displayed in Figure 2.5, dispenses with the connecting rod in favour of the introduction of an amplifier piston [13].

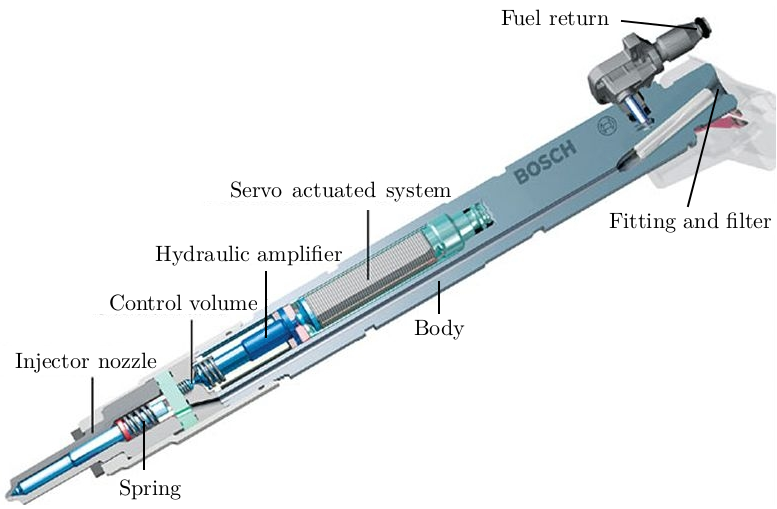

Figure 2.5: Piezoelectric driven common-rail injector (Bosch CRI 3.1).

Figure 2.6 depicts the internal components of this injector, namely the piezoelectric valve (consisting of a piezoelectric actuator, a hydraulic amplifier and a control valve), the injector holder (including a high-pressure fitting, the filter, fuel return to pump and injector body) and the nozzle. The components of the piezoelectric valve are also shown in detail in the figure. Unlike the typical solenoid injector previously described, the control volume is accessed by three orifices (an outlet orifice and two inlet orifices). The outlet orifice (OAZ) also works as an inlet orifice. On the other hand, the control volume is placed directly over the valve, improving the dynamic response of the injector and allowing an easier introduction of multiple injections.

In this injector, the actuator expands when it is activated, thus displacing the amplifier piston. This piston compresses the fuel located between its lower part and the upper part of the valve piston. This, in turn, amplifies the

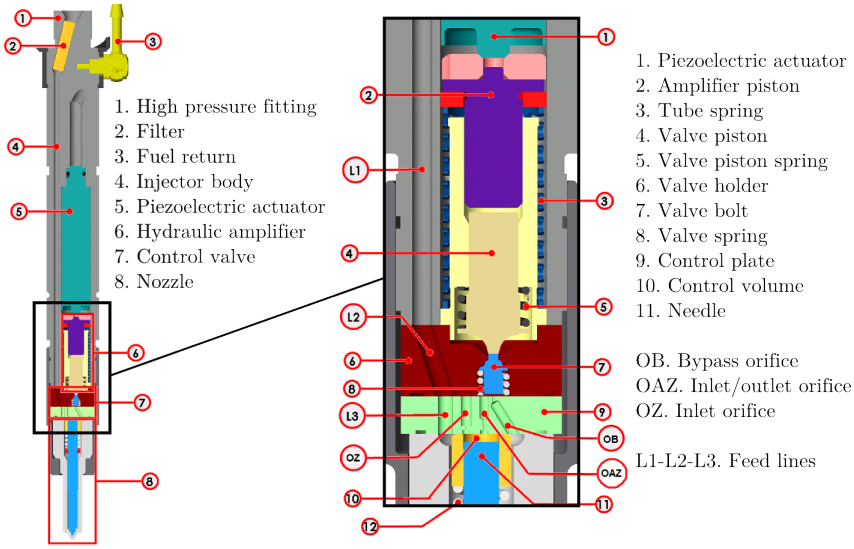

Figure 2.6: Detail on the internal components of a Bosch CRI 3.1 piezoelectric driven injector [13].

vertical displacement of the command piston, opening the upper side of the control valve (at the upper side of the valve bolt) and closing the lower one (at the lower side of the valve bolt), thus keeping the bypass orifice OB inactive. Once the upper side of the control valve is opened, the pressure downstream of the OAZ orifice is reduced so that the fuel at the control volume flows through it and the upper side of the valve bolt towards the fuel return duct. The pressure drop in the control volume lifts the needle up, resulting in the injection phenomenon.

When the actuator is deactivated, it returns to its initial length thanks to the tube spring. The upper side of the valve bolt closes against its upper seat due to the valve spring preload. The pressure in the control volume is then recovered as the fuel enters through the OZ orifice and the OAZ orifice, which becomes a new inlet orifice since it is connected to the now unlocked OB orifice. The needle is therefore pushed back against its seat, terminating the injection event.

The main advantages of this kind of injector can be summarized as follows:

- Fast response to opening and closing signals, allowing multiple injection strategies (up to 8 consecutive injections in one cycle).

- High accuracy. The piezoelectric crystal allows needle displacements in the order of nanometers by just changing the electric voltage applied.
- Absence of attrition after millions of cycles.

Other Diesel injector concepts

Some other improvements have been tested based on these two concepts (solenoid activated and piezoelectric driven injectors). The introduction of balanced-valves in traditional solenoid actuators allowed this technology to endure in the market and keep being installed in many commercial engines. This solution, employed by Delphi in the DFI1 concept [14], enables a reduction in the force on the actuator caused by the hydrostatic pressure of the fuel. In this way, the spring precharge on the solenoid valve can be decreased with a consequent improvement of the injector dynamic operation.

Furthermore, Denso introduced an innovative 3-way valve for its last generation solenoid actuated injector, the Denso G4S, which allowed to minimize the leakages, reduce the moving masses to improve hydraulic performance and increase the injection pressure up to 250 MPa, with the prospective of increasing it to 300 MPa in subsequent iterations [15, 16]. The operation of the Denso G4S injector is illustrated in Figure 2.7. At rest (Figure 2.7(a)), the control plate is kept at its upper position by the action of a spring, thus closing the inlet orifice. Once the control valve opens, the fuel in the control volume flows out through the outlet orifice and the needle moves upwards due to the lowered pressure in the control volume (Figure 2.7(b)). When the control valve closes, the pressure in the intermediate chamber increases bringing the control plate down (Figure 2.7(c)), consequently discovering the inlet orifice through which fuel flows into the control volume. The restituted pressure at this location pushes the needle back against its seat, ending the injection.

Despite the improvements brought by all these solutions, allowing a high control on the injection timing and duration, they do not allow an easy control on the mass flow rate profile. It remains a dependent parameter, related to the injection pressure above all. Even though the rail pressure can be properly controlled, it is difficult to adjust it in cycle-to-cycle timing and to accurately accommodate it to shape the injection profile.

The hydraulic amplifier or piston amplifier system allows a partial modulation of the mass flow rate during the injection. This solution, called Hydraulic Amplifier Diesel Injection System (HADIS) by Bosch [17, 18], has been adopted by several manufacturers and allows to inject fuel at two different pressure levels: the rail pressure and a higher pressure obtained thanks to

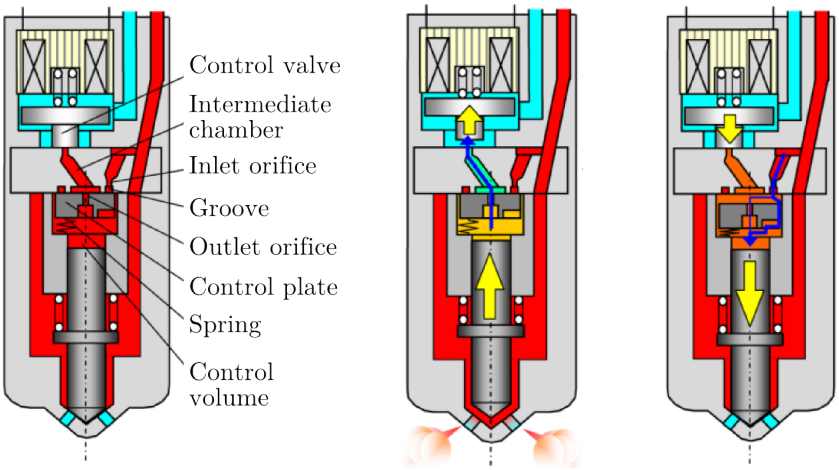

(a) Rest condition (b) Opening (c) Closing

Figure 2.7: Denso G4S injector structure and operation [15].

the action of an amplifier piston. However, its increased complexity together with its restricted flexibility limit the appeal of the solution.

Caterpillar adopted a similar system for its hydraulically actuated, electronically controlled unit injector (HEUI) [19]. This system can be operated in the standard non-amplified mode at the rail fuel pressure, or in an amplified mode. In this last case, an amplifier piston is driven by means of high-pressure oil. The movement of this piston can be modulated thanks to the actuation valve. The main drawback of this system is the need for high-pressure oil, which is not readily available in automotive vehicles.

Another relevant concept was introduced by Delphi in their DFI3 generation. They proposed a direct acting system that replaces the standard steps of the servo hydraulic technology (i.e. actuation of the solenoid/piezo, control valve opening, pressure drop in a control volume and needle opening) by a single step: the direct actuation of the needle through a hydraulic amplifier by a piezoelectric actuator [20]. Thus, the needle opening and closing stages are independent on the rail pressure. This fact makes it possible to electronically adapt the force change delivered by the actuator, leading to an improved multiple injection capability. In addition, the needle speed can be increased and made independent from the rail pressure, which makes it possible to keep fast opening rates even at low injection pressures [20, 21].

The Continental direct-acting (CDA) injector makes use of a similar con-

cept to the DFI3, although it provides a mechanical coupling among the piezoelectric crystal and the needle by means of a leverage system. This system amplifies the limited deformations of the piezoelectric actuator, causing a larger displacement of the needle. The needle position can then be controlled through the fast response of the piezoelectric crystal and the ECU capability to generate complex signals. Different partial needle lifts then act as a fuel flow throttle, leading to rate shaping capabilities [22, 23]. However, the voltage supplied to the piezoelectric crystal needs to be adjusted to any changes in the rail pressure in order to obtain a given needle lift. In addition, an accurate injector temperature control needs to be performed given the dependence of the crystal deformation on the temperature [24].

2.3 Internal flow

In order to understand injector dynamics and the air-fuel mixing process in Diesel engines it is necessary to know the flow conditions through the injector control orifices and the nozzle orifices, respectively. This section aims at the description of the main features of the flow through the internal passages of the injector. It is structured considering the path travelled by the fuel on its way from the injector inlet towards its discharge to the combustion chamber through the nozzle orifices.

2.3.1 Forced internal flow

Flow inside the injector channels and valves is driven by a pressure difference. The transformations involved are mainly variations in pressure and velocity, energy dissipation, and even the formation of vapour bubbles due to the presence of very low pressure regions (cavitation).

As a starting point, the application of the energy transport equation to the non-viscous flow of incompressible fluids leads to the Bernoulli equation:

$$\frac{p}{\rho} + \frac{u^2}{2} + gz = \text{const.} \tag{2.1}$$

Three different contributions can be identified in Equation (2.1): the static pressure, the dynamic pressure and the elevation, which can be usually neglected in automotive applications due to their low relative importance when compared to the high pressure variations that take place in *common-rail* systems. Equation (2.1) assumes an ideal flow in which the transformation from potential to kinetic energy can be completed without any viscous dissipation.

In real applications, however, viscous dissipation cannot be neglected and the flow evolution among two different points has to be written as follows:

$$\frac{p_1}{\rho} + \frac{u_1^2}{2} + \cancel{z_1} = \frac{p_2}{\rho} + \frac{u_2^2}{2} + \cancel{z_2} + \phi_{visc} \tag{2.2}$$

The viscous dissipation term, ϕ_{visc}, accounts for the total viscous losses of the flow, and is responsible for the head losses in pipe flow. The determination of this term is not trivial and its characterization has been approached by many researchers [25–29]. In general, ϕ_{visc} can be expressed as:

$$\phi_{visc} = \phi_{visc,M} + \phi_{visc,m} \tag{2.3}$$

where $\phi_{visc,M}$ and $\phi_{visc,m}$ represent the *major* and *minor* losses due to viscous dissipation, respectively. The minor losses ($\phi_{visc,m}$), also called singular pressure losses, are related to sudden changes in the shape or the direction of the channel driving the flow. In these cases, the fluid cannot completely follow the channel internal shape and the boundary layer may detach from its walls. As a consequence, a recirculation zone appears and restrains the flow in a smaller section, known as *vena contracta*. The flow speeds up and then slows down around the *vena contracta* causing energy dissipation and pressure losses. In the case of injector internal channels, these minor losses can be significant due to their complex geometries [13]. The pressure drop related to a minor loss (Δp_m) can be written as:

$$\Delta p_m = \xi \frac{\rho}{2} u^2 \tag{2.4}$$

where ξ is the coefficient of minor losses, which usually ranges from 0 (no losses) to 1 (pressure losses equal to the dynamic pressure), even though it may be greater than 1 for specific cases.

In order to accurately predict the pressure losses, the flow regime needs to be identified. Two flow regimes are commonly distinguished: *laminar* and *turbulent*, depending on the Reynolds number [30]. The Reynolds number is a dimensionless parameter that relates the inertial and viscous forces of a fluid and is defined as:

$$Re = \frac{\rho u L}{\eta} = \frac{u L}{\nu} \tag{2.5}$$

where L is a characteristic length (i.e. the hydraulic diameter in the case of flow through a pipe), η is the dynamic viscosity of the fluid and ν is its kinematic viscosity. For cylindrical straight ducts, experimental observations show that the flow is generally laminar for values of Reynolds number lower than $Re \approx 2300$ and turbulent for values above $Re \approx 4000$. For $2300 < Re < 4000$, the flow is said to be in a transitional regime, where both laminar and turbulent regimes are possible, depending on the pipe roughness. However, this is true for fully developed flows: any changes in the pipe section lead to perturbations that are dragged for a length equivalent to several diameters, known as *flow development length*. This distance needed for the flow to stabilize also depends on the flow regime, among other factors.

On the other hand, the major losses are induced by friction of the fuel with the channel wall. These losses depend on the length of the channel. For a circular pipe, the pressure drop related to a major loss (Δp_M) can be written as:

$$\Delta p_M = C_f \frac{L}{D} \frac{\rho u^2}{2} \tag{2.6}$$

where D is the section diameter and C_f is the Darcy friction coefficient, which also depends on the flow regime (i.e. the Reynolds number) and the surface roughness. For fully developed laminar flow, the wall roughness may be neglected and C_f can be calculated as:

$$C_f = \frac{64}{Re} \tag{2.7}$$

In turbulent regime, both the velocity profile and the interaction among the fluid and the wall are different. The surface roughness needs to be taken into account and the Darcy friction coefficient is described by:

$$C_f = f(Re, k_r/D) \tag{2.8}$$

where k_r is the wall roughness. Colebrook derived an analytical solution for C_f in turbulent flow [25], that can be solved iteratively to determine the major dissipation losses:

$$\frac{1}{\sqrt{C_f}} = -2 \log \left(\frac{2.51}{Re\sqrt{C_f}} \right) + \frac{k_r/D}{3.72} \tag{2.9}$$

Equations (2.6) to (2.9) may be extended to pipes with different cross-sections by using the concept of hydraulic diameter, D_h:

$$D_h = \frac{4A}{P} \tag{2.10}$$

where A is the cross-sectional area and P is the perimeter of the cross-section.

2.3.2 Upstream of the injector nozzle

Most efforts when studying the injector internal flow are focused on the nozzle itself, since it is the interface with the combustion chamber and it is directly related to the spray characteristics. However, attention must also be given to the flow through the internal ducts and passages of the injector, even though the fuel does not use to experience important pressure losses, given that it also affects the dynamic of the system [13].

Usually, the diameter of the injector feeding line is about 3 mm and its length depends on the arrangement of the injection system (it typically ranges from 300 to 700 mm for passenger cars). The flow velocity in this pipe during the injection process normally varies from 5 to 8 m/s with $Re \approx 10^4$. In these conditions and in accordance to the theory presented in Section 2.3.1, the pressure drop through the feeding line is expected to be less than 0.3 MPa, which is negligible when compared to the total available pressure drop in a diesel injector [31].

Nevertheless, the correct design of the feeding line is important in the view of the time required for a pressure wave to travel through the line (usually from 0.2 to 0.4 ms), which is of the same order of magnitude of the injection duration [32]. The propagation of the pressure waves could then have repercussions on the injection process or in successive injections if applying multi-injection strategies [13, 32].

On the other hand, the flow through the rest of internal channels also needs to be studied. Depending on the injector technology, this includes the injector control orifices, whose design has a crucial influence on injector dynamics [32–34]. In addition, the design of the injector internal channels can generate pressure waves that are eventually reflected by oscillations of the rate of injection. Since the pressure losses through these channels are difficult to measure directly without using intrusive techniques, the fuel flow within the injector has been traditionally estimated through simulation with 1D models [32, 35]. The study carried out in the present thesis also benefits from the use of this kind of tools.

2.3.3 Needle seat

Traditionally, the needle has not been considered to interfere much with the injector internal flow. Once the needle reaches a certain lift, its influence on the injection rate stops being appreciable [36–38]. For conventional injectors, this value is around 100 µm [36], which means that the nozzle is only effectively operating under the needle influence for a short period during the transient stages at the start and the end of the injection. Nevertheless, the increasing tendency to split one injection into several pilot and post injections is leading to a reduction in the duration of a single injection event. Thus, the injector is often working at partial needle lifts and the relative importance of the transient stages is increasing, also attracting the interest of the engine research community. In this regard, several studies have been performed to assess the influence of the needle seat type on the internal nozzle flow [39] and the spray development [40–43].

Figure 2.8 shows the two main typologies of needle seat that can be currently found according to their geometry: VCO (*Valve Covered Orifice*) and sac. A classification can also be established within this last group, finding mini-sac, micro-sac and even nano-sac nozzles.

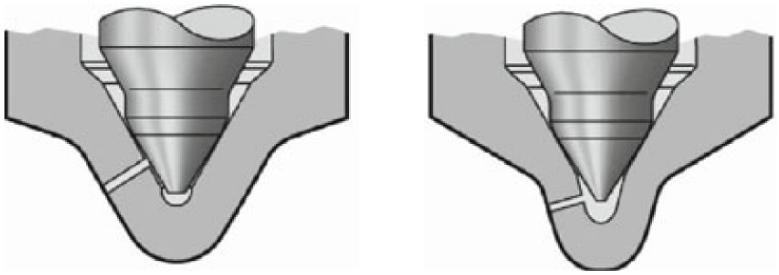

(a) VCO (b) Sac

Figure 2.8: Main needle seat types [4].

In VCO nozzles, as seen in Figure 2.8(a), the needle blocks the fuel passage by directly leaning over the nozzle holes. In practice, in case of needle eccentricity due to small manufacturing imperfections, this results in an uneven distribution of the fuel around the nozzle, leading to large variations in the internal flow and spray development among orifices, especially at low needle lifts [44, 45]. However, it presents a faster response to start delivering fuel.

In sac nozzles, represented in Figure 2.8(b), the fuel flow through the nozzle is not prevented by directly locking the holes, but by making the needle close

against the nozzle wall (needle seat) upstream of the discharge orifices. As a consequence, it leaves a small volume of fuel between the needle tip and the nozzle sac. This volume helps reducing the hole-to-hole dispersion in case of needle eccentricity. However, its drawback is that the residual fuel stored in this volume after needle closing may reach the combustion chamber, provoking small undesired and uncontrolled combustions that favour UHCs and soot formation.

The search for a trade-off among these typologies led to a reduction of the sac volume [46]. The consequence was the appearance of micro-sac nozzles, which lead to a more accurate fuel delivery with lower dispersion among orifices.

2.3.4 Nozzle orifices [1]

In the nozzle orifices, the fuel potential energy due to pressure is transformed into kinetic energy, accelerating the flow before entering the combustion chamber. Any microscopic feature of the orifices has its consequence in diesel spray characteristics and therefore in the air-fuel mixing process.

Figure 2.9 depicts the main geometrical parameters of a nozzle orifice in a direct injection system: inlet and outlet diameters (D_i and D_o, respectively), orifice length (L) and rounding radius at the orifice inlet (r_i). Some relevant dimensionless parameters can be defined from the previous ones so that any study involving nozzles can be generalized:

- length to diameter ratio: L/D_o.
- rounding radius to inlet diameter: r_i/D_i.
- inlet to outlet diameter ratio: D_i/D_o.

The last ratio gives a measure of the orifice degree of conicity, and equals the unity for cylindrical nozzles. An alternative parameter is commonly defined in the literature for the same purpose [46, 47]:

$$k\text{-}factor = \frac{D_i - D_o}{[10\,\mu m]} \tag{2.11}$$

However, according to this definition, an orifice with $D_i = 210\,\mu m$ and $D_o = 200\,\mu m$ has the same *k-factor* as an orifice with $D_i = 110\,\mu m$ and

[1] Given the fact that their behaviour is analysed in the present thesis, it is important to note that all the theory described hereinafter also applies to the injector internal orifices (i.e. control orifices), unless otherwise stated.

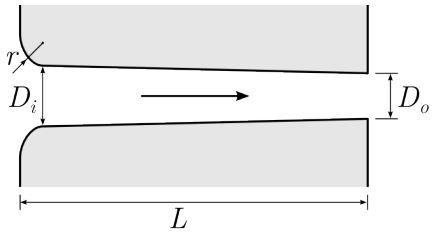

Figure 2.9: Nozzle orifice geometrical parameters.

$D_o = 100\,\mu m$, even though their cross-sectional areas and consequently their flow characteristics are completely different. For this reason, some researchers prefer to utilize the *area reduction* (AR) as a parameter to quanfity the conicity of an orifice [48]:

$$AR = \frac{A_i - A_o}{A_i} = \frac{D_i^2 - D_o^2}{D_i^2} \tag{2.12}$$

Table 2.1 shows the typical values of parameters found in diesel injection nozzle orifices. In view of the table and as stated in Section 1.2, the study of the internal flow in DI nozzles presents great difficulties given the small size of the holes, the transient nature of the injection process and the large velocities induced (even higher than 600 m/s in some cases) due to the high pressure gradients across the orifices.

Parameter	**Typical value**
Orifice outlet diameter (D_o)	80 - 250 µm
Inlet to outlet diameter ratio (D_i/D_o)	1 - 1.25
Orifice length (L)	0.6 - 1 mm
Length to diameter ratio (L/D_o)	4 - 10
Rounding radius (r_i)	0 - 50 µm
Area reduction (AR)	0 - 0.36
Number of orifices per nozzle	5 - 12
Injection pressure (p_i)	30 - 250 MPa
Discharge pressure (p_b)	3 - 9 MPa
Flow outlet velocity (u_o)	150 - 600 m/s
Reynolds number (Re)	6000 - 30000

Table 2.1: Typical values for the geometrical and operating parameters in diesel injection nozzle orifices for passenger cars.

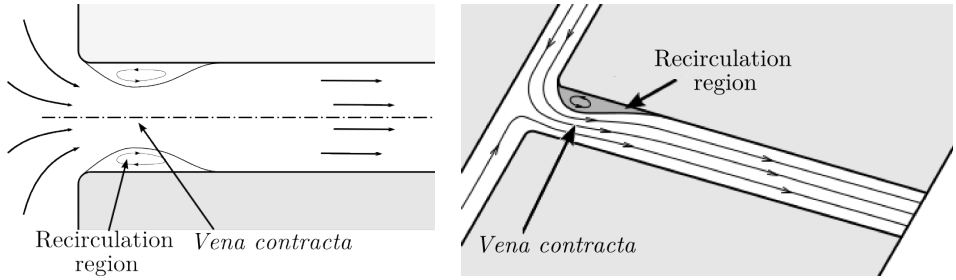

(a) Axisymmetric nozzle (b) Multi-hole nozzle

Figure 2.10: Flow structure in an injection nozzle orifice.

Flow morphology in injection orifices

Figure 2.10 shows the flow morphology in an injection nozzle orifice. In the case of axisymmetric nozzles [2], representative of the single-orifice nozzles usually employed for research purposes [11], the flow enters the orifice equally from all directions, as shown in Figure 2.10(a). Given the abrupt change in cross-section, the streamlines are deflected inducing the boundary layer detachment and the appearance of a recirculation region at the orifice inlet (the *vena contracta* previously introduced).

For multi-hole nozzles, commonly employed in automotive applications [49], the orifices axes form an angle with respect to the nozzle symmetry axis. Hence, the flow change in direction at the orifice entrance is higher. As depicted in Figure 2.10(b), the recirculation region seems to be generally restricted to the upper side of the orifice. However, Martínez-López [36] found that this region may appear at the lower side of the orifice for low values of needle lift. The size of the recirculation region depends mainly on the flow velocity and its geometry. Specifically, larger rounding radius and orifice conicity tend to minimize the flow deflection.

It is in the recirculation region where there is a local reduction in static pressure that, depending on the orifice geometry and under certain operating conditions, may fall below the fuel vapour pressure. This results in the formation of vapour bubbles (*cavitation*) that may even be dragged through the orifice to its outlet. This phenomenon is later analysed in more detail, since the existence of a two-phase flow through the discharge orifices emphasizes all the difficulties to study the orifices internal flow.

[2] This is also the usual flow morphology for the injector control orifices

Once the flow is past the recirculation region, it takes a certain distance for it to stabilize so that the boundary layer is reattached to the walls and the velocity profile is reorganized. In this situation, the flow is known to be *fully-developed*. It is generally considered that it takes a length equivalent to several diameters for the flow to reach these conditions again. The magnitude of this distance depends on the flow regime (laminar or turbulent). For laminar flow, Schlichting [50] established that this length can be estimated as a function of the Reynolds number:

$$\frac{L}{D} = 0.03Re \quad \text{if } Re < 2300. \tag{2.13}$$

Other authors [51] modify the coefficient in Equation (2.13) in a range from 0.03 to 0.06. In any case, if $Re = 2000$, the fully-developed flow would be achieved at a length of at least 60 times the diameter.

For turbulent flow, the mixing intensity induced by turbulence results in a shorter length needed to get a developed flow. White [51] proposes the following formulation:

$$\frac{L}{D} = 4.4Re^{1/6} \quad \text{if } Re > 4000. \tag{2.14}$$

In this case, for typical Reynolds numbers found in injection nozzle flow ($10^4 < Re < 10^5$), the fully-developed conditions would be found at a length equivalent to 20 or 30 times the diameter.

It is therefore clear that Diesel injection nozzle orifices are generally too short ($L/D \approx 10$, as shown in Table 2.1) for the boundary layer to be fully-developed either in the laminar or in the turbulent regime. Thus, the following considerations need to be taken into account when analysing the internal flow in injection orifices:

- The flow is mainly controlled by the orifice entrance effects (i.e. boundary layer detachment and local pressure losses).
- Given that the flow is not fully-developed, the boundaries traditionally accepted to determine whether the flow is laminar ($Re < 2300$) or turbulent ($Re > 4000$) are not valid [52]. This means that the Reynolds number is not enough to characterize the flow regime and the turbulence intensity by itself.
- Care must be taken when applying the classical fluid mechanics theories based on fully-developed flow. For instance, the velocity profiles at the

orifice outlet do not necessarily follow the Hagen-Poiseuille law for laminar regime, and may not be practically constant in the whole section for stabilized flow in the turbulent regime [51].

Hydraulic characterization

Given the difficulties when analysing the internal flow through the injection orifices, most works in the literature take the mean parameters at the orifice outlet as a reference. In this sense, one of the parameters most widely studied to characterize the hydraulic behaviour of an orifice is the *discharge coefficient* (C_d), a dimensionless coefficient defined as the ratio among the real mass flow rate and the theoretical mass flow rate through the orifice.

The continuity equation establishes that the mass flow rate through an orifice may be computed as:

$$\dot{m} = \int_A \rho \left(\boldsymbol{U} \cdot \boldsymbol{n} \right) \mathrm{d}A \tag{2.15}$$

where $(\boldsymbol{U} \cdot \boldsymbol{n})$ is the scalar product among the local velocity vector and the unit vector normal to the orifice outlet area. Considering only the axial velocity, Equation (2.15) can be rewritten as:

$$\dot{m} = \int_A \rho u \, \mathrm{d}A \tag{2.16}$$

As discussed earlier, it is not possible to accurately determine the flow axial velocity and density profiles. However, if the fluid is considered incompressible and inviscid (consequently with no boundary layer), Equation (2.16) can be simplified since the density and the velocity are constant across the orifice outlet section:

$$\dot{m}_{th} = \rho u_{th} A_o \tag{2.17}$$

where u_{th} is the theoretical velocity according to the Bernoulli equation (2.1) considering a negligible variation in elevation across the orifice ($z = const.$) and that, as a result of the large pressure drops, the velocity upstream of the orifice is very low compared to the one downstream of the orifice:

$$u_{th} = \sqrt{\frac{2\Delta p}{\rho}} \tag{2.18}$$

where Δp is the difference in pressure upstream and downstream of the orifice ($p_i - p_b$). Hence, for a given condition, the discharge coefficient can be calculated as:

$$C_d = \frac{\dot{m}}{\dot{m}_{th}} = \frac{\dot{m}}{A_o\sqrt{2\rho\Delta p}} \tag{2.19}$$

Equation (2.19) highlights the dependence among mass flow rate and the pressure difference across the nozzle. In addition, it underlines that the discharge coefficient evaluates the *efficiency* of the nozzle in terms of delivering fuel. For this reason, the behaviour of the discharge coefficient in orifices has been widely studied along the last decades [53–57]. In those studies, the discharge coefficient has been found to follow an asymptotic behaviour with the Reynolds number in non-cavitating conditions, as shown in Figure 2.11.

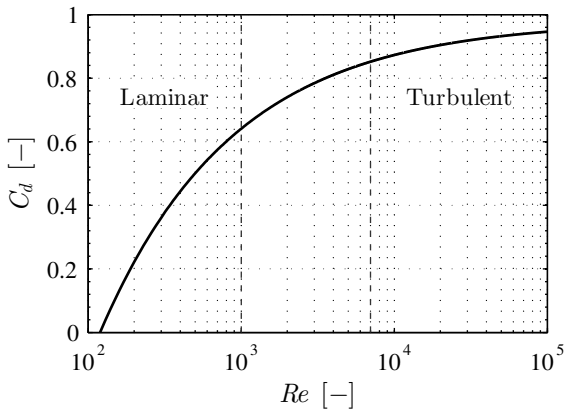

Figure 2.11: Discharge coefficient as a function of the Reynolds number.

The flow regime can be analysed according to this behaviour: the flow may be regarded as laminar while the discharge coefficient grows almost linearly with Re, whereas it can be considered turbulent once the asymptotic value of the discharge coefficient ($C_{d,max}$) is practically achieved. Among these two regions, the flow is transitional and the discharge coefficient grows with Re in a moderate way.

The way the discharge coefficient evolves with respect to the Reynolds number depends on the orifice geometry. Some empirical correlations have been developed to describe this dependency. A summary on several expressions proposed in the literature for non-cavitating conditions is shown in Table 2.2.

Author	Expression
Asihmin *et al.* [58]	$\frac{1}{C_d} = 1.23 + \frac{58L}{Re\,D_o}$
Nakayama [59]	$C_d = \frac{Re^{5/6}}{17.11\frac{L}{D_o}+1.65Re^{0.8}}$
Hall [60]	$C_d = 1 - 0.184\left(\frac{L}{D_o} - 1 + 1.11Re^{0.25}\right)^{0.8} Re^{-0.2}$
Lichtarowicz *et al.* [53]	$\frac{1}{C_d} = \frac{1}{C_{d,max}} + \frac{20}{Re}\left(1 + 2.25D_o^{-1}\right) - \frac{0.0015D_o^{-1}}{1+7.5[\log(0.000015Re)]^2}$
Benedict [61]	$C_d = 0.19 + 0.15\ln Re - 0.01\left(\ln Re\right)^2 + 0.0002\left(\ln Re\right)^3$
Salvador [57]	$C_d = 0.98 - 0.07\left(r^{-0.49}l^{-1.14}D_o^{1.2}AR^{-0.088}\right) - \frac{10.7}{Re^{0.5}}$

Table 2.2: Empirical correlations developed in the literature to describe the behaviour of C_d as a function of Re.

As it has been mentioned, the discharge coefficient measures the deviation of an orifice mass flow rate with respect to its maximum discharge capacity for certain pressure conditions. Hence, the mass flow rate through the orifice may be expressed as:

$$\dot{m} = C_d \rho u_{th} A_o \tag{2.20}$$

With this formulation, the discharge coefficient takes into account both the losses due to wall friction and the ones due to the presence of a non-uniform velocity profile, together with those related to cavitation if it appears. The real situation at the orifice outlet, as shown in Figure 2.12(a), consists of fuel crossing the outlet area (A_o) with non-uniform velocity and density profiles (ρ and u, respectively). However, as seen in Figure 2.12(b), it is possible to define an equivalent flow through an effective area (A_{eff}), with a constant effective velocity (u_{eff}) and a constant density (ρ_f, corresponding to the liquid phase), so that it preserves the same mass flow rate as the real flow [62]:

$$\dot{m} = \rho_f u_{eff} A_{eff} \tag{2.21}$$

This simplification of the flow also makes it possible to define a velocity coefficient (C_v) as the ratio among effective and theoretical velocity, so that it takes into account the energy or pressure losses:

$$C_v = \frac{u_{eff}}{u_{th}} \tag{2.22}$$

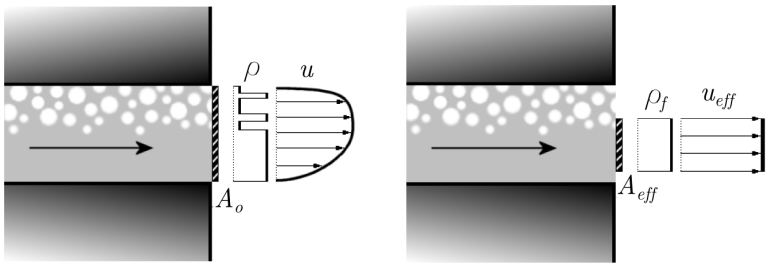

(a) Real flow (b) Simplified equivalent flow

Figure 2.12: Flow at the orifice outlet [62].

In an analogous way, an area coefficient (C_a) may also be defined so that it takes into account the loss of section due to a non-uniform velocity profile, cavitation bubbles reaching the exit area and flow separation from the wall (*hydraulic flip*):

$$C_a = \frac{A_{eff}}{A_o}\frac{\rho}{\rho_f} \approx \frac{A_{eff}}{A_o} \tag{2.23}$$

Combining Equations (2.20) and (2.21), the discharge coefficient may be expressed as a function of the area coefficient (C_a) and the velocity coefficient (C_v), so that the different contributions to the global losses of the flow can be independently analysed:

$$C_d = C_a C_v \tag{2.24}$$

These two coefficients have been used in the literature [62, 63] in applications where it is useful to define an equivalent uniform velocity profile. However, even though the discharge coefficient may be easily obtained experimentally from mass flow rate measurements, obtaining the individual C_a and C_v is not an easy task. The development of methodologies to determine the momentum flux at the orifice outlet [11, 45, 64–67] has helped solving this problem. The total momentum flux is defined as:

$$\dot{\boldsymbol{M}} = \int_A \rho \boldsymbol{U}(\boldsymbol{U}\cdot\boldsymbol{n})\,\mathrm{d}A \tag{2.25}$$

For the particular case of the outlet section of the orifice, considering only the velocity component normal to the orifice cross-section:

$$\dot{M} = \int_A \rho u^2 \, \mathrm{d}A \tag{2.26}$$

As it happened to the mass flow rate, Equation 2.26 can be simplified if the fluid is considered incompressible and inviscid:

$$\dot{M}_{th} = \rho u_{th}^2 A_o \tag{2.27}$$

A coefficient analogous to the discharge coefficient can also be defined for the spray momentum:

$$C_M = \frac{\dot{M}}{\dot{M}_{th}} \tag{2.28}$$

where the actual momentum flux may also be expressed in terms of the effective area and the effective velocity:

$$\dot{M} = \rho_f u_{eff}^2 A_{eff} \tag{2.29}$$

Equations (2.21) and (2.29) show the potential of combining the mass flow rate and spray momentum measurements, since it allows to extract the effective velocity:

$$u_{eff} = \frac{\dot{M}}{\dot{m}} \tag{2.30}$$

Similarly, replacing Equation (2.30) into Equation (2.21), the effective area can also be determined:

$$A_{eff} = \frac{\dot{m}^2}{\rho_f \dot{M}} \tag{2.31}$$

As a consequence, the dimensionless coefficients C_a and C_v can be calculated to complement the discharge coefficient C_d in order to fully characterize the internal flow through the orifice and its losses.

2.3.5 The cavitation phenomenon

Cavitation is the phase change phenomenon (liquid to vapour) that may take place in the region close to an orifice entrance radius, as a consequence of the way the fuel enters the orifice. As explained earlier, there is a recirculation zone together with a contraction near the orifice entrance (see Figure 2.10). That contraction (*vena contracta*) reduces the flow effective area, also resulting in a velocity increase. The acceleration acquired by the flow in the *vena contracta* entails a decrease in static pressure, which may fall below the vapour pressure. This results in a partial vaporization of the liquid, generating small vapour cavities (i.e. bubbles), known as *hydrodynamic cavitation*. The first time these bubbles appear inside an orifice is commonly known as *incipient cavitation*.

The formation of cavitation bubbles mainly depends on the fluid velocity (i.e. pressure drop across the orifice) and the orifice geometry. In particular, studies like the ones carried out by Nurick [68], Schmidt *et al.* [69] or Salvador [57] show that cavitation is more severe for low conicities, small rounding radius at the orifice inlet, higher inlet diameters or more accused surface roughness. The needle lift has also been found to influence the cavitation formation, which is enhanced at low needle lifts due to the restriction imposed to the flow [36].

Once a cavitation bubble has appeared, its diameter may increase or decrease according to the pressure field to which it is subject. A common expression to analyse this process is the Rayleigh-Plesset equation [70]:

$$r_b \frac{\mathrm{d}^2 r_b}{\mathrm{d}t^2} + \frac{3}{2}\left(\frac{\mathrm{d}r_b}{\mathrm{d}t}\right)^2 = \left(\frac{p_v - p}{\rho_f}\right) - \frac{4\nu_f}{r_b}\left(\frac{\mathrm{d}r_b}{\mathrm{d}t}\right) - \frac{2\sigma_f}{\rho_f r_b} \tag{2.32}$$

where r_b is the cavitation bubble radius, p is the pressure outside the bubble and ν_f and σ_f are the fuel kinematic viscosity and surface tension, respectively. According to this expression, the bubble grows if the pressure surrounding the bubble is lower than the vapour pressure, being reduced otherwise until its collapse. However, under some combinations of geometry and injection conditions, the time it takes for the bubbles to reduce their diameter to a minimum and collapse may be higher than their residence times (i.e. the time it takes for them to travel the whole orifice length). In these conditions, the cavitation region is thus extended to the orifice outlet. This phenomenon is known as *supercavitation* [71].

One of the first investigations of cavitation in the frame of Diesel injection was performed in 1959 by Bergwerk [72], who studied the influence of the

geometry of different nozzles on the flow behaviour. Bergwerk visualized the internal flow development by means of transparent orifices with diameters ranging from 0.2 to 2.5 mm. He noticed the presence of cavitation under certain conditions, reporting that the cavitation intensity was lower the higher the orifice rounding radius, needing a higher pressure drop along the orifice to get the cavitation to extend to the orifice outlet. The same was concluded with regard to the L/D ratio. Bergwerk also noticed the loss in discharge capabilities of the orifices under cavitating conditions. He showed that, in these conditions, the discharge coefficient is hardly affected by the Reynolds number and starts being influenced by the pressure ratio $(p_i - p_b)/(p_b)$ instead. In addition, Bergwerk reported the appearance of a phenomenon known as *hydraulic flip*. This phenomenon appears when the boundary layer detachment at the orifice entrance is extended along the whole orifice, resulting in the gas initially present at the discharge chamber flowing countercurrently to occupy the space between the orifice wall and the *vena contracta* [57].

In 1976, Nurick [68] carried out a similar study for a wide set of injection conditions. He observed that, once cavitation starts, the mass flow rate is independent from the pressure drop, as shown in Figure 2.13 for a sample orifice with cylindrical geometry. This phenomenon, which is known as *mass flow collapse*, has also been experimentally observed by several authors. Randall [73] had already reported it for venturi tubes, Soteriou *et al.* [56] found it for real and large scale nozzles, Salvador [57] and Gimeno [11] for real multi-orifice nozzles and De la Morena [74] for calibrated orifices at different injection pressure conditions.

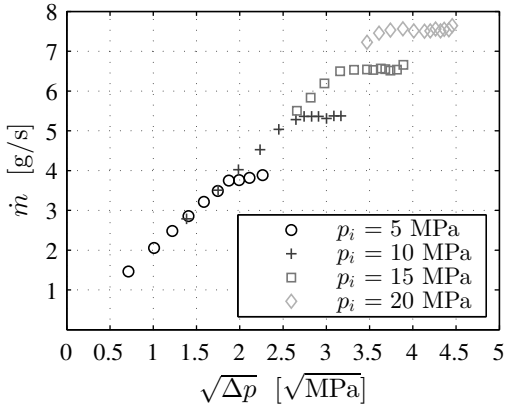

Figure 2.13: Mass flow provided by a cylindrical orifice for different injection conditions.

Based on these observations, Nurick proposed a one-dimensional model to explain the behaviour of the discharge coefficient in cavitating conditions. The model was validated against experimental measurements performed on orifices of different L/D ratios, rounding radius and a wide range of discharge pressures. Taking the simplified sketch shown in Figure 2.14 as a reference, Nurick defined three characteristic points: one point (i) upstream of the orifice inlet, far enough so that the flow velocity is negligible compared to the one that may be achieved inside the orifice; a second point (c) in the highest flow restriction (which leads to the maximum flow velocity and the minimum local pressure), coinciding with the *vena contracta*; and a third point (b) at the outlet section of the orifice.

Assuming that the fraction of the orifice section occupied by vapour remains constant, the remaining fraction of the orifice section is available for the liquid to flow through the *vena contracta*. Hence, at this location, it is possible to define a contraction coefficient (C_c) as:

$$C_c = \frac{A_c}{A_o} \tag{2.33}$$

This coefficient only depends on the orifice geometry, and its minimum value is estimated in 0.61 [75]. Assuming a constant velocity in the axial direction at the point c (u_c) and a density equal to the one of the liquid, the mass flow rate through the orifice may be determined as:

$$\dot{m} = \rho_f A_c u_c \tag{2.34}$$

Additionally, if it is assumed that the vapour does not generate shear stresses at the wall, the flow suffers no losses among points i and c. Given

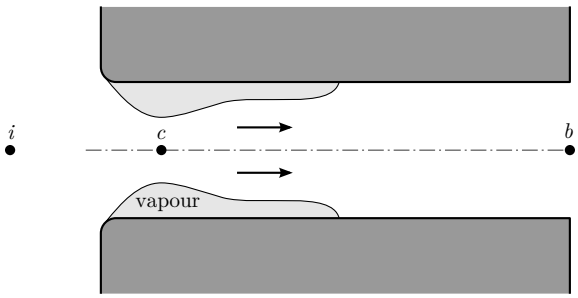

Figure 2.14: Sketch of the cavitation phenomenon in an axisymmetric orifice.

that there coexist both the liquid and vapour phases in the orifice cross-section at which point c is located, the pressure at this point is supposed to be equal to the vapour pressure (p_v). Applying the Bernoulli equation among points i and c with these assumptions:

$$p_i = p_v + \frac{1}{2}\rho_f u_c^2 \tag{2.35}$$

Combining Equations (2.33) to (2.35), the mass flow rate may be expressed as:

$$\dot{m} = A_o C_c \sqrt{2\rho_f \left(p_i - p_v\right)} \tag{2.36}$$

Equation (2.36) highlights the fact that the mass flow rate becomes independent of the discharge pressure at cavitating conditions, thus explaining the mass flow rate collapse introduced previously.

It is also interesting to analyse the consequences of cavitation on the discharge coefficient. Figure 2.11 showed its asymptotic behaviour with respect to the Reynolds number for non-cavitating conditions. This trend cannot be expected when the mass flow rate is collapsed. Figure 2.15 displays the results of the sample cylindrical orifice shown in Figure 2.13, now represented in terms of discharge coefficient against Reynolds number. For a given injection pressure, the discharge coefficient increases with *Re* (i.e. when the discharge pressure is reduced) following the usual trend in non-cavitating conditions. However, once cavitation appears and the mass flow collapses, the discharge coefficient falls abruptly and stops being importantly influenced by *Re*, as Bergwerk observed.

If Equation (2.36) is introduced into Equation (2.19), the discharge coefficient in cavitating conditions may be obtained as a function of the injection and discharge pressures:

$$C_d = C_c \sqrt{\frac{p_i - p_v}{p_i - p_b}} \tag{2.37}$$

in which the ratio among pressure differences corresponds to one of the definitions of the dimensionless parameter known as *cavitation number* (K), introduced by Nurick as:

$$K = \frac{p_i - p_v}{p_i - p_b} \approx \frac{p_i}{p_i - p_b} \tag{2.38}$$

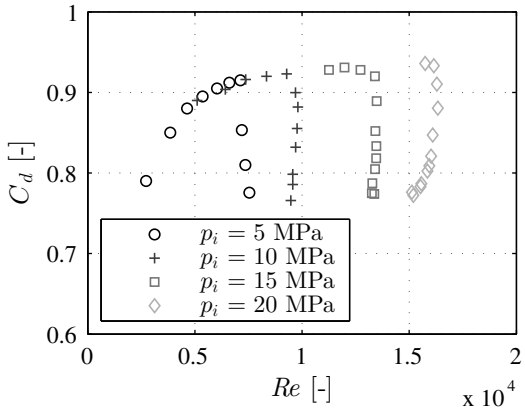

Figure 2.15: Sample of the evolution of the discharge coefficient against Re for a cylindrical orifice.

Given its use in this thesis, it is also important to note here that an alternative definition of the cavitation number (CN) was introduced by Soteriou *et al.* [56] based on the pressure ratio analysed by Bergwerk [72], as shown by Equation (2.39).

$$CN = \frac{p_i - p_b}{p_b - p_v} \approx \frac{p_i - p_b}{p_b} \tag{2.39}$$

so that K and CN are related as follows:

$$K = 1 + \frac{1}{CN} \tag{2.40}$$

As implied by their definitions, in case that cavitating conditions take place, both K and CN quantify the intensity of cavitation. Figure 2.16 shows an experiment of visualization of cavitation bubbles in an injection nozzle that illustrates this fact. For low values of CN (Figure 2.16(a)), the volume of the orifice ocuppied by vapour bubbles is relatively low, corresponding to *incipient cavitation*. For sufficiently high values of CN (Figure 2.16(b)) cavitation is enhanced and the vapour bubbles may even reach the orifice outlet (*supercavitation*).

According to Equations (2.37) to (2.40), the discharge coefficient may also be rewritten as:

$$C_d = C_c\sqrt{K} = C_c\sqrt{1 + \frac{1}{CN}} \tag{2.41}$$

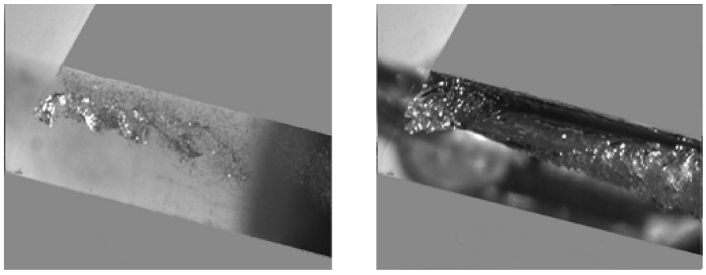

(a) $CN = 0.8$ (b) $CN = 4$

Figure 2.16: Cavitation appearance for different cavitation levels in a scaled VCO nozzle [76].

Equation (2.41) states that, under cavitating conditions, the discharge coefficient increases linearly with the square root of the cavitation number K, rather than being dominated by the Reynolds number. This trend is observed in Figure 2.17. As K grows (i.e. the discharge pressure increases or the injection pressure decreases), the conditions become less cavitating. At some point, the linear trend is not respected, since cavitation disappears in the orifice. The value of K for which the transition from cavitating to non-cavitating conditions takes place is known as critical cavitation number, K_{crit}. An analogous analysis could be carried out in terms of CN, considering that cavitation is favoured by large values of CN.

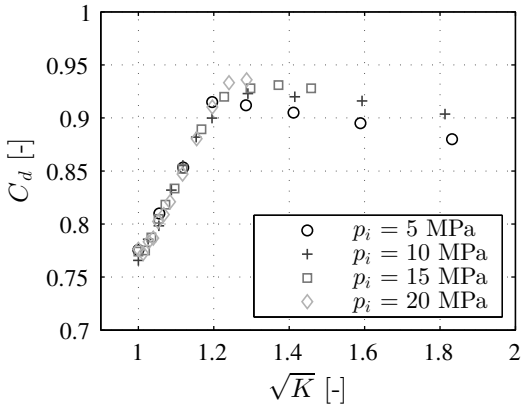

Figure 2.17: Sample of the evolution of the discharge coefficient with respect to the square root of K for a cylindrical orifice.

The critical cavitation number depends mainly on the orifice geometry. Macián *et al.* [77] carried out a study in which K_{crit} was investigated by varying several geometrical parameters like the orifice entrance radius, conicity and diameter. As it could be expected, they found that an increase in either rounding radius or orifice conicity results in a lower K_{crit}, consequently preventing the cavitation phenomenon. On the contrary, an increase in orifice diameter results in a higher K_{crit}. Some authors [47, 57, 77, 78] also pointed out the dependence of K_{crit} with the injection pressure, or more generally with the Reynolds number.

As seen earlier (Equation (2.24)), the losses taken into account by the discharge coefficient may be divided into the individual effects of the area contraction and the effective velocity at the orifice outlet (C_a and C_v, respectively). Payri *et al.* [62] performed mass flow rate and momentum flux measurements for both a cylindrical and a conical nozzle with similar permeability. They observed that, whereas the mass flow collapses in cavitating conditions provoking the fall of the discharge coefficient, the momentum flux is not affected by cavitation and keeps increasing when increasing the pressure drop. From those observations, in the view of Equation (2.30), it is implied that the effective velocity increases with the presence of cavitation (i.e. the velocity coefficient C_v increases). This increase in flow velocity, widely reported in the literature [62, 71, 79–82], is attributed to the loss of friction with the walls caused by the presence of vapour in their vicinities. However, the presence of vapour drastically reduces the effective flow section for the liquid. This means that the reduction of the area coefficient (C_a) exceeds the increase in effective velocity, leading to a net reduction of the discharge coefficient (C_d) as previously seen. A summary of the influence of cavitation on the dimensionless coefficients that define the flow behaviour is shown in Figure 2.18, adapted from [62].

Another effect of cavitation that has been reported in the literature is the increase in turbulence at the orifice outlet [83–85]. In these studies, velocity measurements were performed by means of LDV (*Laser Doppler Velocimetry*), noting the increased turbulence at cavitation conditions and the presence of a more uniform velocity profile at the outlet section. In fact, He *et al.* [83] observed that the turbulence generated downstream of the restriction is even higher than the one existing in the recirculation region close to the orifice inlet.

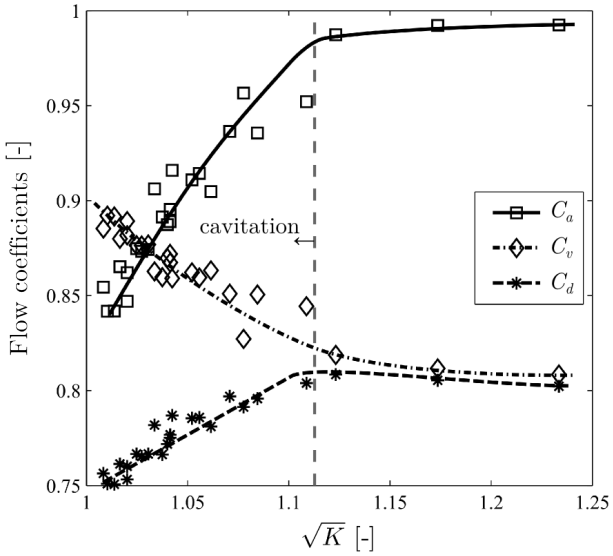

Figure 2.18: Sample of the evolution of the flow dimensionless coefficients with respect to the square root of K [62].

2.3.6 Influence of the orifice geometry on the internal flow

The geometry of an injection orifice has a strong influence on the internal flow. Studies have traditionally been conducted trying to link the orifice geometrical parameters to significant features such as the flow pattern or the proneness of the orifice to cavitate. The relevance of these features is not only restricted to the spray development in the case of the nozzle orifices, but is also key in the injector dynamics considering that the ability to evacuate or refill the injector control volume depends on the control orifices flow behaviour. The most significant and widely accepted generalities about the influence of the geometry of an orifice on its flow behaviour are then summarized in this section.

It is important to remark that even the small uncertainties due to tolerances in the manufacturing processes deserve consideration. Therefore, efforts have been made to develop experimental techniques to gather data from actual nozzle geometries in a non-destructive way. In this respect, Macián *et al.* [48] developed a technique based on extracting silicone moulds of the orifices internal geometry and visualizing them through a Scanning Electron Microscope (SEM). Lee *et al.* [86], in turn, used high-energy X-rays to visualize the orifices internal features. They were able to use this technique even to study the needle movement during the opening and closing stages of the injector in

operating conditions. More recently, X-ray tomography has also been used to measure the needle movement inside the injector [87], whereas the appearance of contact sensors of increasingly smaller size has allowed to obtain data from irregular features such as the wall surface roughness [88, 89]. However, this technique is limited to the vicinity of the outlet section and does not allow to obtain information from parameters such as the rounding radius or the orifice length.

Length to outlet diameter ratio, L/D_o

The effect of the length-to-diameter ratio on the internal flow is different depending on the presence of cavitation in the orifice. When there is no cavitation, an increase in L/D_o increases the losses due to friction with the orifice walls, which is expected to be reflected as a decrease in the discharge coefficient.

Lichtarowicz [53] collected data that had been gathered by multiple researchers from investigations on orifices with different L/D_o in non-cavitating conditions. Figure 2.19 summarizes these results with a representation of the maximum discharge coefficient ($C_{d,max}$) found depending on the value of L/D_o.

Two zones with different behaviour may be identified in the figure. On the one hand, for $L/D_o < 2$, flow separation is present [53] leading to lower

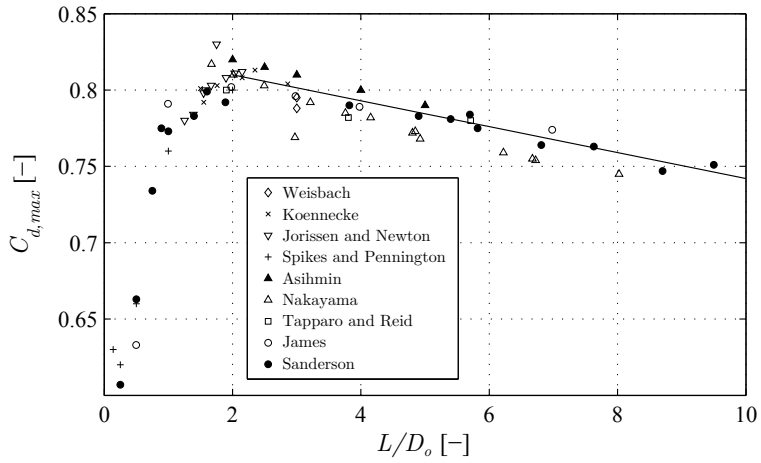

Figure 2.19: Variation of the maximum discharge coefficient with the length to diameter ratio [53].

values of $C_{d,max}$, since the effective area is reduced. For $L/D_o > 2$, without separation, $C_{d,max}$ descends when L/D_o is increased. This trend is expected according to Equation (2.6), and was also later confirmed by other researchers [90–92]

With regard to the appearance of cavitation, higher values of L/D_o lead to a lower K_{crit}, thus obstructing the appearance of cavitation [55, 77, 93, 94]. As can be appreciated in Figure 2.20, for a given mass flow rate and discharge pressure, the pressure at the orifice inlet is higher the higher the L/D_o ratio, due to the more important pressure losses associated. Hence, the odds of reaching the vapour pressure are diminished.

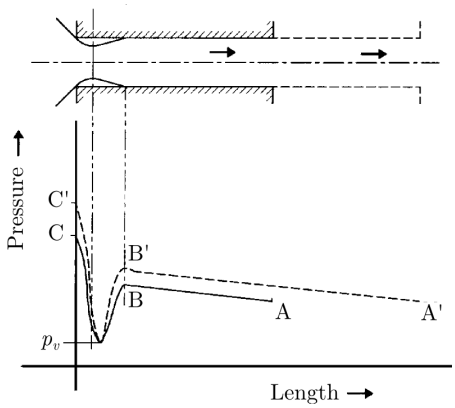

Figure 2.20: Variation of the static pressure along two orifices with different L/D_o [94].

Orifice conicity, D_i/D_o

According to the continuity equation, the reduction in area linked to a higher conicity produces an increase in velocity at the orifice outlet for subsonic flows. Therefore, in this kind of orifice, the flow acceleration is not concentrated at the orifice entrance as it happens for a cylindrical orifice. On the contrary, it is distributed along the orifice length. Since the mean flow velocity at the inlet is lower than the one at the outlet, convergence induces a higher static pressure at the orifice entrance as compared to the one that a cylindrical orifice would have.

This higher pressure at the orifice inlet has several consequences. With regard to cavitation, the higher pressure at the orifice inlet obstructs its appearance (lower values of K_{crit}), even completely avoiding it for the usual

pressure conditions. Hence, it has been widely reported that cylindrical orifices are prone to cavitate, whereas conicity inhibits this phenomenon [48, 57, 77, 78, 95–99]. In fact, the main utility of convergent orifices in injection systems is precisely to prevent the appearance of cavitation [46].

Another consequence of the convergence and the increased pressure at the orifice inlet, although less important, is the reduction of the pressure losses at the entrance of the hole as compared to a cylindrical orifice. Indeed, the pressure losses at the entrance depend on the velocity or the pressure drop at the inlet. Since this pressure drop is lower in a convergent orifice, so will be the pressure losses. Therefore, another effect of the orifice conicity is a greater discharge coefficient.

Orifice rounding radius at the inlet, r_i

The main cause of the pressure losses at the orifice is the separation of the boundary layer provoked by the high velocities and the abrupt change in direction to which the flow is submitted. A way to mitigate the detachment of the boundary layer is the introduction of a rounding radius to the orifice entrance. Hence, the higher the radius, the lower the pressure loss. Some authors like Idelchik [100] found that the boundary layer detachment may be even completely avoided for $r_i/D_o \geq 0.2$, with a consequent decrease in pressure losses, which may then be neglected.

Besides the reduction in pressure loss and the consequent increase in discharge coefficient, the introduction of higher rounding radius helps to inhibit cavitation [72, 77, 90, 99, 101, 102]. In fact, considering that higher values of r/D_o reduce the boundary layer detachment leading to a less pronounced flow contraction, the minimum pressure achieved at the orifice will be higher, diminishing or even preventing cavitation from occurring.

Recently, Brusiani *et al.* [103] analysed the consequences of the application of the hydrogrinding process to provide the orifices with a certain rounding radius. This parameter was investigated together with the orifice conicity. They concluded that a high rounding radius in a conical orifice could compensate for its reduced mass flow rate when compared to a cylindrical nozzle. Similarly, Salvador *et al.* [104] investigated the orifice rounding radius together with the inclination angle given to the orifices with respect to the nozzle axis. In their study they confirmed that lower inclination angles and higher rounding radius led to the higher discharge coefficient values and the less cavitating configurations. An interesting result from their work was the fact that, for low inclination angles, cavitation starts at the lower wall of the orifice instead

of appearing at the upper wall, and it tends to displace towards the orifice centre if the cavitation intensity grows larger.

Number of orifices

Another geometrical factor that must be taken into account when dealing with injection nozzles is the total number of orifices. Previous studies had shown its importance in spray development and combustion, since the jet spacing is expected to affect the air entrainment [105–107]. Hence, multirow nozzle concepts have been tested [21, 105] and their influence on the engine performance and emissions has been assessed.

However, the off-axis arrangement of multi-hole injectors can alter the internal flow pattern. Since all the orifices are fed from the same volume (i.e. the sac), the initial flow development may differ depending on the number of orifices. Attention had not been paid to this fact, until recently Moon *et al.* [108] applied an X-ray imaging technique to analyse the needle dynamics and flow characteristics for nozzles with different number of holes, keeping the same hole diameter in all cases. They found that, in general, the needle speed at the opening stage is reduced the higher the number of orifices, since their higher discharge flow rates decrease the degree of sac pressure rise during the opening. This results in a lower force trying to push the needle upwards once it is lifted from its seat. At the same time, this implies greater speeds during the closing the higher the number of orifices. With regard to the flow itself, they observed that multi-hole nozzles initially generate more turbulent flow with faster mixing, although the effect is not noticeable from a certain value of needle lift.

Alternative geometries

It is interesting to remark that attempts to provide alternatives to conventional geometry nozzles have also been reported. For instance, elliptical nozzles have shown shorter tip penetrations and wider spray cone angles, indicating a considerable increase in air entrainment downstream of the nozzle [109–113]. Molina *et al.* [114] used CFD techniques to assess the influence of this kind of geometries on the cavitation characteristics. Their findings confirm a better quality of the mixing process for elliptical nozzles if their major axis is oriented horizontally.

2.4 The Diesel spray

In CIDI engines, the fuel is introduced in the combustion chamber through the injector, specifically through the nozzle orifices. The fuel must be finely atomized so that it is disintegrated into small droplets. That facilitates its evaporation and mixture with the air in order to improve its subsequent combustion.

The parameters that significantly affect the spray atomization process include the fuel density, viscosity and flow velocity at the nozzle outlet [115]. This highlights the importance of the internal flow development.

This section includes a brief description of the Diesel spray, followed by an explanation of the atomization process and the main mechanisms involved in it. Finally, a review on the characteristic macroscopic and microscopic parameters employed in the definition of a Diesel spray is presented.

2.4.1 General description of the Diesel spray

The first phenomenon that takes place once the fuel leaves the nozzle and penetrates the ambient gas is the atomization of the liquid vein. From a given instant and at a certain axial location from the nozzle orifice (known as *intact core length*) this vein is transformed into a collection of ligaments and droplets in the so-called *primary atomization*. After this stage, these ligaments and droplets may keep breaking up and reducing their diameter (which is known as *secondary atomization*) or some of them may collide increasing their diameter (*coallescence*). At the end of the process a virtually heterogeneous distribution of droplet sizes is obtained.

This atomization process is important since it favours the physical process of mixing that takes place among the gas present in the combustion chamber and the fuel (*air entrainment*), strongly increasing the contact surface between them. It is precisely this entrainment of hot air coming from the compression in the cylinder prior to the injection event what triggers the fuel evaporation. The time needed for all these phenomena to take place constitutes the physical delay prior to the combustion process.

As far as the macroscopic appearance of the Diesel spray is concerned, a first incipient stage may be distinguished at the beginning of the injection, when the fuel is ejected at high velocity through the nozzle orifices against a more or less dense atmosphere depending on the ambient conditions. In this situation, the atomization process is started. As an example of this first stage, Figure 2.21 shows a spray during its incipient stage, with a field of view

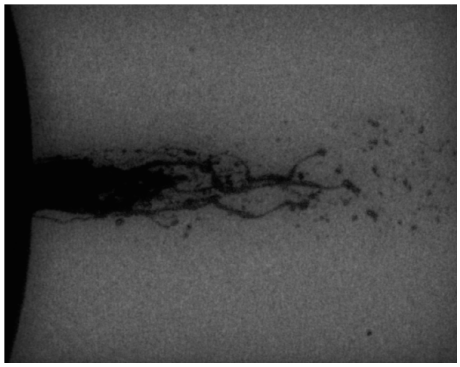

Figure 2.21: Image of a Diesel spray at its incipient stage. ($p_i = 80\,\text{MPa}$ and $p_b = 1\,\text{MPa}$. Field of vision $= 1.5\,\text{mm}$) [2].

of only 1.5 mm from the nozzle tip. As can be seen, some irregularities arise in the spray surface due to the interaction with the ambient gas, leading to the disgregation of the initial liquid vein. In this case, the spray is greatly influenced by injector needle dynamics, rather than being affected by the geometry of the nozzle orifice itself.

Once the transitional needle lifting stage is overcome, steady pressure conditions are achieved upstream of the nozzle discharge orifices. Hence, a more developed stage is reached and the macroscopic appearance of the spray substantially changes. Due to the atomization and air entrainment processes, the Diesel spray acquires the aspect of a cone with a semi-elliptical tip, as shown in Figure 2.22. In this figure, the evolution of the sprays of a 7-hole nozzle is represented for three different instants after the start of injection.

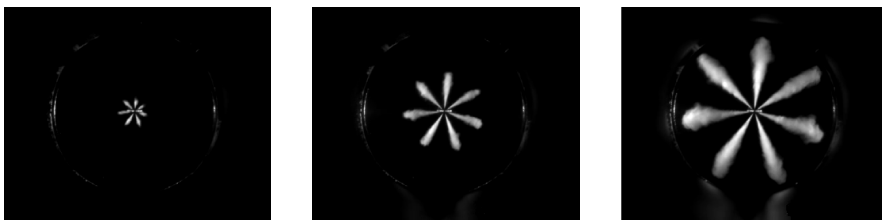

(a) $t_{aSOI} = 50\,\mu\text{s}$ (b) $t_{aSOI} = 225\,\mu\text{s}$ (c) $t_{aSOI} = 650\,\mu\text{s}$

Figure 2.22: Macroscopic appearance of the Diesel sprays of a 7-hole nozzle for different instants ($p_i = 180\,\text{MPa}$ and $p_b = 5\,\text{MPa}$) [2].

2.4.2 Diesel spray atomization process

Just when the fuel leaves the nozzle orifice, it starts to atomize shaping a conical spray. As stated in Section 2.4.1, a primary and a secondary atomization processes may be distinguished before a heterogeneous distribution of droplets is achieved. Each of these atomization processes is described in more detail below.

Primary atomization

The *primary atomization* process of a liquid spray is governed by different mechanisms depending on the velocity of the liquid with respect to the gas surrounding it and the properties of both fluids. The size of the droplets formed and the *intact core length* (distance from the nozzle tip to the point where the axial velocity is reduced with respect to the one at the nozzle orifices outlet, where the atomization starts being relevant) are the representative parameters of the process.

According to the study conducted by Reitz and Bracco [116] about round liquid jets, four different primary atomization regimes may be distinguished depending on the velocity of the liquid at the nozzle outlet (see Figure 2.23): Rayleigh regime, first and second regimes induced by aerodynamic interaction and atomization regime.

For low injection velocities (in the order of 10 m/s) the surface tension plays a key role on the atomization process, promoting the emergence and growth of waves on the jet surface that cause the rupture of the liquid phase

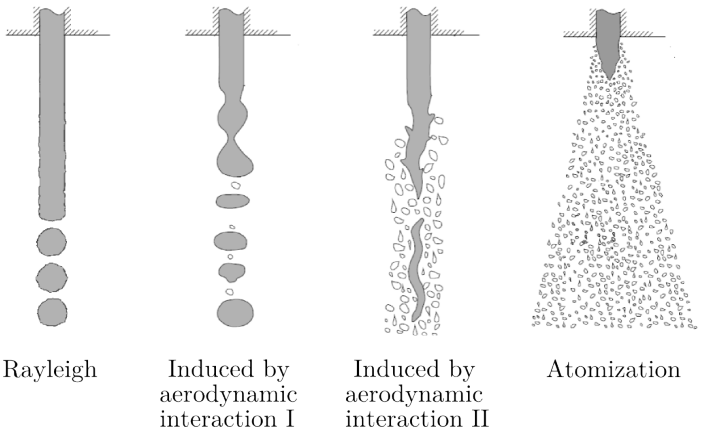

Figure 2.23: Scheme of the different primary atomization regimes.

into droplets (*Rayleigh regime*). This kind of atomization produces large size droplets, starting at a considerably long distance from the injector [117–119].

For higher injection velocities, the effect of the surface tension is amplified mainly due to the increase in relative velocity among the injected liquid and the gas surrounding it. In these conditions, specific from the *first regime induced by aerodynamic interaction*, the intact core length is reduced. The droplet diameter is also reduced, getting values close to the orifice size.

If the injection velocity is further increased, the effect of the aerodynamic forces starts being predominant (*second regime induced by aerodynamic interaction*) promoting the growth of small scale disturbances on the spray surface caused by the development of turbulence. These disturbances force the separation into fuel droplets of sizes smaller than the orifice diameter at a relatively short distance from the injector.

Finally, for very high injection velocities typical of the Diesel injection process, the spray primary atomization begins right at the nozzle outlet due to the huge difference in speed among the liquid and the gas, producing droplets of very small size (*atomization regime*).

Aiming at a quantitative characterization of the primary atomization of a spray, Ohnesorge [120] carried out measurements of the spray intact core length, showing that the atomization process could be described through the Reynolds number and the Weber number, the latter defined as:

$$We = \frac{\rho_f u^2 D}{\sigma_f} \tag{2.42}$$

where σ_f is the surface tension at the boundary among the liquid and the gas.

From these parameters, the Ohnesorge dimensionless number (Oh) was defined according to Equation (2.43), including all the relevant properties that intervene in the spray atomization: liquid density and viscosity, surface tension and orifice diameter.

$$Oh = \frac{\sqrt{We}}{Re} = \frac{\eta_f}{\sqrt{\rho_f \sigma_f D}} \tag{2.43}$$

These parameters allowed to determine the predominant regime in the atomization of a spray in steady conditions. In this sense, Figure 2.24 shows the accepted boundaries among regimes as a function of the Reynolds and

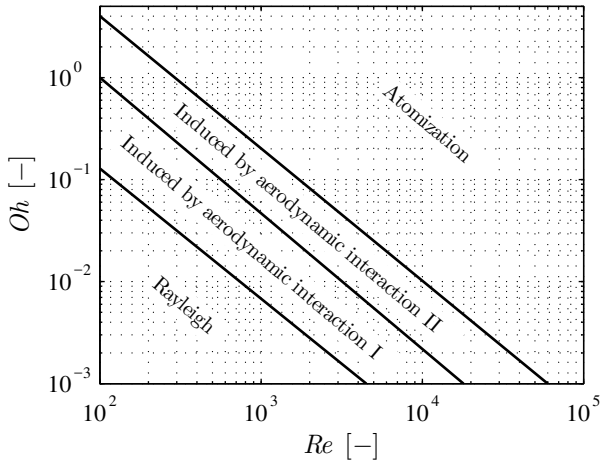

Figure 2.24: Boundaries among primary atomization regimes according to Re and Oh.

Ohnesorge numbers. Attending to the typical values of the parameters involved in Diesel injection (Table 2.1), a Diesel spray is clearly located at the atomization regime for most operating conditions.

However, this kind of diagram does not take into account the influence of the properties of the gas on which the fuel is injected. For instance, it neglects the effects of the gas density, which Torda [121] or Hiroyasu and Arai [122] demonstrated that may contribute to improve the spray atomization. For this reason, Reitz [123] converted the two-dimensional diagram from Ohnesorge into a three-dimensional diagram (Figure 2.25), including a new variable that represents the ratio among densities from the injected liquid and the surrounding gas.

Secondary atomization

After the initial break-up of the liquid jet into droplets and ligaments, the spray atomization continues with the emergence of new smaller droplets from the ones already existing, due to the aerodynamic forces provoked by the difference in speed among the droplets and the air surrounding them.

Nevertheless, the forces associated to surface tension try to counteract the deformation of the droplets, attempting to keep their original spherical shape. Thus, the smaller the droplet size, the more difficult it is to deform it due to its higher curvature and surface tension, a higher speed being required to produce its disintegration.

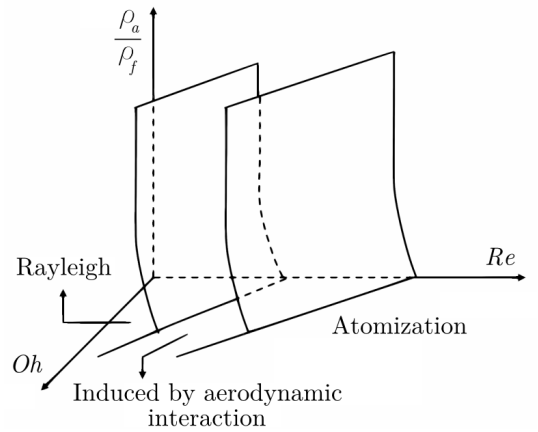

Figure 2.25: Boundaries among primary atomization regimes including the ratio among air and fuel density.

As in the primary atomization process, the secondary atomization may be characterized through the dimensionless Weber number, which relates the aerodynamic forces to the ones associated to surface tension. However, the gas density and the relative velocity among the droplets and the gas surrounding them are used in this case:

$$We = \frac{\rho_a u_{rel}^2 D}{\sigma_f} \tag{2.44}$$

Wierzba [124] distinguished five different secondary atomization regimes according to the values of *We*, as depicted in Figure 2.26. Following his classification, for Weber numbers lower than 12 the aerodynamic forces are not capable of causing the droplet breakup, provoking only small deformations. However, a small increase in the relative speed resulting in a Weber number close to 12 would propitiate the first breakup scheme, known as vibrational atomization. In this regime, the deformation of the droplet surface progressively grows until causing its division.

In the second breakup regime, corresponding to Weber numbers among 12 and 20, the droplet rupture is initially identified with a deformation that results in a sac or bag shape that ends up triggering the droplet disintegration into a large number of small size droplets. This mechanism of formation of new droplets holds a strong resemblance to the third secondary atomization regime. The only difference in this case is that, besides forming droplets

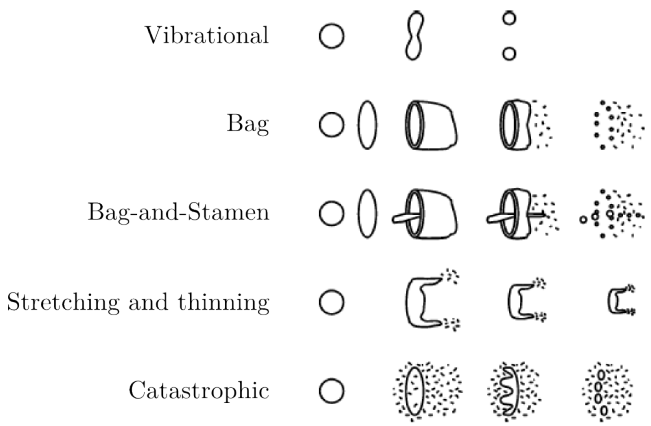

Figure 2.26: Scheme of the different secondary atomization regimes according to Wierzba [124].

from the bag shape, a ligament is created inside the bag giving birth to new droplets of relatively large size. These similarities among different atomization regimes are not observed for higher Weber numbers. As seen in the figure, the differences among the stretching and thinning regime (in which the formation of new droplets takes place due to deformation and disintegration of the ends of the initial droplet) and the catastrophic breakup regime are evident.

Arcoumanis *et al.* [125] also established boundaries among the five regimes proposed by Wierzba. The Weber values leading to transition among regimes according to Wierzba and Arcoumanis *et al.* are summarized in Table 2.3. A lack of agreement among the transitional values is observed, with notably large discrepancies in the regimes associated to high Weber numbers.

It is interesting to note the complexity of the secondary atomization of a Diesel spray. The primary atomization process is produced exclusively through

Regime	**Wierzba [124]**	**Arcoumanis *et al.* [125]**
Vibrational	≈ 12	≈ 12
Bag	< 20	< 18
Bag-and-stamen	< 50	< 45
Stretching and thinning	< 100	< 1000
Catastrophic	> 100	> 1000

Table 2.3: Weber numbers for the transition among the different secondary atomization regimes.

a single mechanism, whereas in the secondary atomization process all the regimes previously explained take place during a single injection event, since the velocity of the droplets varies substantially from the nozzle outlet to the spray tip.

Atomization mechanisms

Despite the large number of experimental studies conducted so far, the mechanisms associated to the liquid vein atomization process are partly unknown.

It is believed that atomization is due to the superposition of several independent mechanisms that may acquire more or less relative importance depending on the injection conditions. These mechanisms are explained below.

- Aerodynamic instabilities
  Once an unstable disturbance is generated at the interface among the liquid and the discharge gas, the relative velocity among the two fluids produces shear stresses that may cause its growth. In that case, the mechanism controlling the second regime induced by aerodynamic interaction is reproduced: the instabilities of the high frequency waves present at the vein surface due to local pressure variations in the gas and the liquid generate thin ligaments. The diameter of the liquid vein diminishes as it moves away from the injector, due to this portion of liquid being lost. The ligaments are broken by the action of surface tension forces and/or aerodynamic interaction with the ambient gas. This mechanism has been studied theoretically by several authors, like Reitz and Bracco [116] or Ruiz [126]. These authors mainly based their studies on the linear analysis of Rayleigh-Taylor [127]. For relatively low injection velocities, close to the second regime induced by aerodynamic interaction, this linear analysis agrees with the experimental results. However, as the injection velocity is increased, the atomization rate and the spray opening angles theoretically estimated are lower than the ones experimentally observed, pointing out that there exist other important effects that promote the atomization process. Additionally, the aerodynamic theory does not consider the influence of the orifice geometry.
  Consequently, it is not possible to explain the Diesel spray atomization phenomenon solely through the analysis of the instabilities on the surface of the liquid vein.
- Turbulence
  In another study, Ruiz [128] described the turbulence as a major cause of atomization. This turbulence would be generated in the nozzle discharge orifices. Inside the orifices, the radial component of the turbulent

velocity is contained by the walls. However, at the injector outlet, the radial component of the turbulent fluctuations expels some fuel out of the liquid vein, causing atomization.
This mechanism allows to explain the atomization of sprays injected into vacuum, for which there is no possible aerodynamic interaction with the environment. It is also evident that it is not the only mechanism responsible for the atomization of a Diesel spray, since it is independent from the large variations in the spray behaviour as a function of the gas density.

- Reorganization of the velocity profile
  Another mechanism that causes the atomization of the liquid vein is the modification of the velocity profile right at the orifice outlet. The viscous effects due to the presence of the orifice walls disappear, and the fuel close to the liquid vein surface is accelerated producing instabilities. According to the mechanism proposed by Brennen [129], this change in velocity produces disturbances in the liquid surface that promote the atomization. In the case of laminar flow in the orifice, the velocity profile corresponds to a Poiseuille flow. When the walls disappear, this profile becomes uniform. According to the momentum conservation, this velocity profile reorganization entails a decrease of the liquid vein kinetic energy, resulting in the generation of radial velocities that favour atomization.

- Cavitation
  The influence of the cavitation phenomenon on the atomization process is due to three main reasons. On the one hand, the cavitation appearance usually causes flow separation from the orifice wall. In the event of collapse, this separation and the subsequent reattachment of the flow would generate an increase in turbulence that would in turn favour the atomization, as above stated. In fact, numerous published experimental studies show how cavitation in Diesel injection nozzles contributes to the spray atomization, originating sprays of short penetration and wide spreading angle [56, 57, 74, 130–134]. This enhanced atomization is mainly based on the increased turbulence levels due to the augmented speed fluctuations caused by the reduction of effective area, and the implosion or disintegration of bubbles in the vicinity of the spray surface [135].
  On the other hand, the presence of vapour bubbles within the fuel, in the case of reaching the orifice outlet, would induce discontinuities in the liquid favouring the spray breakup in ligaments and droplets. Besides,

the arrival of bubbles to the orifice outlet reduces the effective area for the fuel flow, increasing its mean velocity and modifying the velocity profile. However, Chaves and Obermeier [136] demonstrated that it is not necessary for the bubbles to reach the orifice outlet in order to modify the velocity profile.
In addition, as shown by De la Morena [74], cavitation causes an increased level of irregularities in the spray profile. This results in a greater magnitude of the oscillations (defined as the averaged deviation of the spray contour with respect to its mean contour) and a lower distance among consecutive peaks or valleys. This result is indicative of the significant influence of cavitation on the atomization process, visibly influenced by the fluctuations in the liquid-gas interface.

2.4.3 Diesel spray characterization

When characterizing a Diesel spray there are several parameters that allow to know both its appearance and its structure. These parameters may be classified attending to the basic geometric characteristics of the spray (*macroscopic description*) or attending to its internal properties (*microscopic description*).

Macroscopic characterization

The macroscopic description of the Diesel spray focuses on the parameters that allow to evaluate its interaction with the surrounding air. It is usual to characterize it through four parameters: the spray penetration (S), the spreading angle (θ_s), the entrained air volume and the intact core length.

- Spray penetration
  The penetration of a spray is defined as the distance among the orifice outlet and the spray tip (see Figure 2.27). This parameter is an important indicator of the mixing process and of the possibility that the spray tip impinges the walls of the combustion chamber, factors that strongly influence the development of the combustion process and the formation of emissions [137, 138].

  There is a multitude of works devoted to the study of spray penetration in which several correlations have been obtained, one of the first being performed by Wakuri *et al.* [139]. Dent [140] in 1971 and Hay and Jones [141] in 1972 performed a comprehensive review on most of the correlations available at the time for a free jet in steady conditions. From these investigations it follows that the factors on which penetration mainly depends are:

- The momentum of the fuel when it is injected. Sprays with greater momentum exhibit a higher penetration speed into the chamber. However, the momentum flux is not always readily available, and its effect in the correlations is usually considered through parameters such as the difference among the injection pressure and the discharge pressure, the orifice diameter or the fuel density.
- The density at the discharge chamber. The higher the density, the more important the aerodynamic effects that tend to slow the progress of the spray into the chamber.
- The time lapsed from the start of injection. In particular, the previous studies show that the spray advances proportionally to the square root of the time.

More recently, other studies have been devoted to the obtaining of spray penetration correlations. In general, all of them still underline the dependence of the spray penetration with the difference among the injection pressure and the discharge pressure, the nozzle characteristics (orifice diameter and discharge coefficient), the density ratio among gas and fuel, the spray spreading angle and the time [11, 63, 78, 122, 142–144].

In this sense, Desantes *et al.* [145] proposed a correlation for the penetration of a non-evaporative Diesel spray. Considering the conservation of momentum flux in the axial direction, they derived the scaling law for the spray penetration shown in Equation (2.45).

$$S(t) \propto \dot{M}^{1/4}\, \rho_a^{-1/4}\, \tan^{-1/2}(\theta_s/2)\, t^{1/2} \tag{2.45}$$

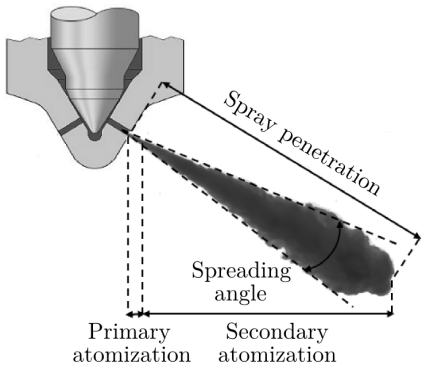

Figure 2.27: Scheme of the Diesel spray macroscopic appearance.

Besides, taking into account that the momentum flux may be written as follows:

$$\dot{M} = \dot{m} u_{eff} = \frac{\pi}{4} \rho_f D_{eff}^2 u_{eff}^2 = \frac{\pi}{4} \rho_f D_{eff}^2 C_v^2 u_{th}^2 = \frac{\pi}{2} D_{eff}^2 C_v^2 \Delta p \qquad (2.46)$$

the penetration law can be rewritten as:

$$S(t) \propto \rho_a^{-1/4} \Delta p^{1/4} D_{eff}^{1/2} \tan^{-1/2}(\theta_s/2)\, t^{1/2} \qquad (2.47)$$

As can be seen from Equation (2.47), the penetration of a Diesel spray is a direct function of the orifice diameter and the pressure drop along the orifice, and is inversely proportional to the ambient gas density and the tangent of the spray half angle.

In the case of an evaporative Diesel spray, Naber and Siebers [63] found that the spray vaporization may reduce its penetration up to a 20% compared to a non-evaporative spray. According to them, this reduction is mainly due to an increase in the density of the mixture among the ambient gas and the fuel vapour within the spray, since it cools down on account of its evaporation.

Finally, under reactive conditions, the spray penetration increases mainly due to the heat release that causes a significant increase in the specific volume within the spray. In these conditions, it is assumed that the relation given by Equation 2.47 only allows to evaluate the influence of the ambient gas density on the spray penetration qualitatively.

- Spray spreading angle
  The spreading angle together with the penetration are the most usual parameters used for the macroscopic spray description. The former is commonly defined as the angle between two straight lines delimiting the spray contour and intersecting at the nozzle outlet. As it happens for the penetration, it is a function of the injection conditions, the properties of both the injected fuel and the gas present in the combustion chamber, and the orifice geometry [63, 146–150].

  Naber and Siebers [63] conducted an extensive review about the different expressions proposed by several authors to relate the spray angle to the operating conditions for non-evaporative sprays. They state that, for high injection pressures and considering a single fuel, the spray spreading angle depends on the geometrical parameters of the nozzle orifices and the ratio among the densities of the ambient gas and the fuel.

In fact, the density ratio is found in all the correlations reported in the literature, with an associated exponent ranging from 0.2 to 0.5. According to the experimental results by Naber and Siebers, this exponent should take a value of 0.19, as shown in Equation (2.48)

$$\tan\left(\frac{\theta_s}{2}\right) \propto \left(\frac{\rho_a}{\rho_f}\right)^{0.19} \tag{2.48}$$

While it seems that there is a shrinkage phenomenon in the spray angle similar to the one described for the penetration [63], in general it may be assumed that the gas density is a parameter that influences the spray angle both in non-evaporative and evaporative conditions. This influence may be quantified through the value of the exponent associated to the ratio of densities, assuming a constant density for the fuel.

Nevertheless, there are differences when it comes to quantifying these effects. In part, the differences may be due to the uncertainties associated to the angle determination, generally obtained by spray visualization. The angle values reported are considerably sensitive to the visualization technique used, the quality of the illumination or the processing of the obtained images.

With regard to reactive sprays, experimental evidence has been found about an increase in spreading angle as a consequence of the heat release associated to the combustion process. The scaling factor among the angle for inert sprays and the one for reactive sprays may be obtained considering that the increase in specific volume due to the heat release produces a radial expansion within the spray.

- Entrained air volume
  The volume of air entrained allows to quantify the mixing process of the fuel with the air surrounding it. It is a clear indicator of the fuel overall concentration and a key factor in the spray evaporation process. This parameter may be directly obtained from the previous two.

- Intact core length
  It is defined as the distance between the nozzle orifice and the point of the spray where the axial velocity starts decreasing. This velocity reduction is a consequence of the interaction of fuel and air due to air entrainment. Hence, atomization starts being relevant at this position, from which the first droplets start to appear. Numerous studies have shown the variability of the intact core length depending on the ratio of densities among the fuel and the gas [63, 74, 122, 151–155], the diameter and

diameter-to-length ratio of the orifice [74, 156, 157], the temperatures of both fluids [155] or the physical and chemical properties of the fuel [155, 158].

Microscopic characterization

In order to carry out a complete characterization of the spray, it is necessary to attend not only to purely geometrical parameters, but also to those that allow to know its internal structure in detail, such as the size of the droplets that shape it or the velocity and concentration distributions.

- Droplet size
  One of the parameters that defines the degree of atomization of the spray in a better way is the droplet diameter. However, the size of the droplets that form the jet is not uniform, existing great variability both spatially and temporally. Therefore, a representative mean diameter is often used. Its value may be obtained from Equation (2.49), proposed by Mugele and Evans [159], where d_i represents the diameter of one droplet and $N_{d,i}$ the total number of droplets with size d_i.

$$d_{d,jk} = \left(\frac{\sum_{i=1}^{N_d} N_{d,i}\, d_{d,i}^{j}}{\sum_{i=1}^{N_d} N_{d,i}\, d_{d,i}^{k}} \right)^{\frac{1}{j-k}} \tag{2.49}$$

  From Equation (2.49), several kinds of diameter may be defined depending on the values given to a and b. The diameters mostly employed in Diesel sprays characterization are the arithmetic diameter (for $a = 1$ and $b = 0$) and the Sauter Mean Diameter (SMD, for $a = 3$ and $b = 2$). The SMD represents the diameter of the droplets of a monodisperse spray with the same volume-to-surface ratio as the characterized polydisperse spray. Hence, the lower the SMD, the higher the droplet surface with respect to its volume, thus leading to a greater efficiency of the mixing and evaporation processes.

- Droplet velocity and concentration distributions
  The velocity distribution is closely linked to the droplet size distribution. Its profile is isomorphic, exhibiting a Gaussian appearance. For this reason, in the practice it is usually represented through an exponential profile [145], as shown in Equation (2.50).

$$u(x, r) = u_{axis}(x) \exp\left[-a_G \left(\frac{r}{R_s(x)} \right)^2 \right] \tag{2.50}$$

where R_s represents the radius of a cone to which the spray can be approximated and a_G is a Gaussian distribution coefficient. The velocity profile can be extended to a concentration profile [160] by means of the *Schmidt* number (Sc), defined as the relation between the momentum diffusion to the mass diffusion:

$$Sc = \frac{\eta}{\rho D_f} \tag{2.51}$$

where D_f is the fuel mass diffusivity. Hence, the concentration profile can be expressed as follows:

$$Y_f(x,r) = Y_{f,axis}(x) \exp\left[-a_G\, Sc \left(\frac{r}{R_s(x)}\right)^2\right] \tag{2.52}$$

Even though the radial evolution of both the velocity and the concentration are relatively easy to characterize, as observed, the axial characterization of both parameters is more complex. There are some models in the literature that allow their estimation. For further details on this topic, the reader may refer to the works by Desantes *et al.* [160, 161] and Salvador *et al.* [162].

References

[1] Heywood, J. B. *Internal Combustion Engine Fundementals*. McGraw Hill, 1988. ISBN: 007028637X.

[2] Payri, F. and Desantes, J. M. *Motores de combustion interna alternativos*. Editorial Reverte, 2011. ISBN: 978-84-291-4802-2.

[3] Halderman, J. and Linder, J. *Automotive Fuel and Emissions Control Systems*. Prentice Hall, 2011. ISBN: 978-0132542920.

[4] Mollenhauer, K. and Tschoke, H. *Handbook of Diesel Engines*. Ed. by K. Mollenhauer and H. Tschöke. 1st ed. Berlin, Heidelberg: Springer Berlin Heidelberg, 2010, p. 636. ISBN: 978-3-540-89082-9. DOI: 10.1007/978-3-540-89083-6.

[5] Boehner, W. and Hummel, K. "Common rail injection system for commercial Diesel vehicles". *SAE Technical Paper 970345* (1997). DOI: 10.4271/970345.

[6] PARK, S. H., YOON, S. H., and LEE, C. S. "Effects of multiple-injection strategies on overall spray behavior, combustion, and emissions reduction characteristics of biodiesel fuel". *Applied Energy*, vol. 88.1 (2011), pp. 88–98. ISSN: 0306-2619. DOI: http://dx.doi.org/10.1016/j.apenergy.2010.07.024.

[7] ZHENG, M. and KUMAR, R. "Implementation of multiple-pulse injection strategies to enhance the homogeneity for simultaneous low-NOx and -soot diesel combustion". *International Journal of Thermal Sciences*, vol. 48.9 (2009), pp. 1829–1841. ISSN: 12900729. DOI: 10.1016/j.ijthermalsci.2009.02.009.

[8] MOHAN, B., YANG, W., and CHOU, S. K. "Fuel injection strategies for performance improvement and emissions reduction in compression ignition engines - A review". *Renewable and Sustainable Energy Reviews*, vol. 28.x (2013), pp. 664–676. ISSN: 13640321. DOI: 10.1016/j.rser.2013.08.051.

[9] KATO, T., KOYAMA, T., SASAKI, K., and MORI, K. K. "Common Rail Fuel Injection System for Improvement of Engine Performance on Heavy Duty Diesel Engine". *SAE Technical Paper 980806* (1998). DOI: 10.4271/980806.

[10] JOHNSON, T. V. "Vehicular Emissions in Review". *SAE International Journal of Engines*, vol. 5.2 (2012), pp. 2012–01–0368. ISSN: 1946-3944. DOI: 10.4271/2012-01-0368.

[11] GIMENO, J. "Desarrollo y aplicación de la medida del flujo de cantidad de movimiento de un chorro Diesel". PhD thesis. Universitat Politècnica de València, 2008.

[12] LEE, J. W. et al. "Effect of piezo-driven and solenoid-driven needle opening of common-rail diesel injectors on internal nozzle flow and spray development". *International Journal of Engine Research*, vol. 7.6 (2006), pp. 489–502. ISSN: 1468-0874. DOI: 10.1243/14680874JER00806.

[13] SALVADOR, F. J., PLAZAS, A. H., GIMENO, J., and CARRERES, M. "Complete modelling of a piezo actuator last-generation injector for diesel injection systems". *International Journal of Engine Research*, vol. 15.1 (2014), pp. 3–19. ISSN: 1468-0874. DOI: 10.1177/1468087412455373.

[14] Dober, G. et al. "The Impact of Injection Strategies on Emissions Reduction and Power Output of Future Diesel Engines". *SAE Technical Paper 2008-01-0941*, vol. 2008.724 (2008). doi: 10.4271/2008-01-0941.

[15] Matsumoto, S., Yamada, K., and Date, K. "Concepts and Evolution of Injector for Common Rail System". *SAE Technical Paper 2012-01-1753* (2012). doi: 10.4271/2012-01-1753.

[16] Matsumoto, S. et al. "4 th Generation Diesel Common Rail System: Realizing Ideal Structure Function for Diesel Engine". *SAE Technical Paper 2013-01-1590* (2013). doi: 10.4271/2013-01-1590.

[17] Dohle, U., Kampmann, S., Hammer, J., Wintrich, T., and Hinrichsen, C. "Advanced Diesel Common Rail Systems for Future Emission Legislation". *International Conference on Automotive Technologies-ICAT* (2004), pp. 109–113.

[18] Benajes, J., Payri, R., Molina, S., and Soare, V. "Investigation of the Influence of Injection Rate Shaping on the Spray Characteristics in a Diesel Common Rail System Equipped with a Piston Amplifier". *Journal of Fluids Engineering*, vol. 127.6 (2005), p. 1102. issn: 00982202. doi: 10.1115/1.2062767.

[19] Glassey, S. F., Stockner, A. R., and Flinn, M. A. "HEUI - A New Direction for Diesel Engine Fuel Systems". *SAE Technical Paper 930270* (1993). doi: 10.4271/930270.

[20] Schöppe, D. et al. "Delphi Common Rail system with direct acting injector". *MTZ worldwide*, vol. 69.10 (2008), pp. 32–38. issn: 2192-9114. doi: 10.1007/BF03226918.

[21] Dober, G., Guerrassi, N., and Karimi, K. "Mixture Preparation and Combustion Analysis , a Key Activity for Future Trends in Diesel Fuel Injection Equipment". *SIA Diesel Powertrain International Conference*. Rouen, 2012.

[22] Payri, R., Gimeno, J., Viera, J. P., and Plazas, A. H. "Effect of Partial Needle Lift on the Hydraulic and Evaporative Performance Characteristics of a Common rail Diesel Fuel Injector". *THIESEL 2012 Conference on Thermo- and Fluid Dynamic Processes in Diesel Engines*. Valencia, Spain, 2012, pp. 1–19.

[23] Bardi, M. "Partial needle lift and injection rate shape effect on the formation and combustion of the Diesel spray". PhD thesis. Valencia (Spain): Universitat Politècnica de València, 2014. doi: 10.4995/Thesis/10251/37374.

[24] ALTIERI, L. and TONOLI, A. "Piezoelectric Injectors for Automotive Applications: Modeling and Experimental Validation of Hysteretic Behavior and Temperature Effects". *Journal of Dynamic Systems, Measurement, and Control*, vol. 135.1 (2012), p. 011005. ISSN: 0022-0434. DOI: 10.1115/1.4006627.

[25] COLEBROOK, C. F. "Turbulent flow in pipes, with particular reference to the transition region between the smooth and rough pipe laws". *Journal of the Institution of Civil Engineers*, 4 (1939), pp. 133–156. ISSN: 0368-2455. DOI: 10.1680/ijoti.1939.13150.

[26] JUDY, J., MAYNES, D., and WEBB, B. W. "Characterization of frictional pressure drop for liquid flows through microchannels". *International Journal of Heat and Mass Transfer*, vol. 45.17 (2002), pp. 3477–3489. ISSN: 00179310. DOI: 10.1016/S0017-9310(02)00076-5.

[27] XU, B., OOI, K. T., MAVRIPLIS, C., and ZAGHLOUL, M. E. "Evaluation of viscous dissipation in liquid flow in microchannels". *Journal Of Micromechanics And Microengineering*, vol. 13.1 (2003), pp. 53–57. ISSN: 0960-1317. DOI: 10.1088/0960-1317/13/1/308.

[28] KOO, J. and KLEINSTREUER, C. "Viscous dissipation effects in microtubes and microchannels". *International Journal of Heat and Mass Transfer*, vol. 47.14-16 (2004), pp. 3159–3169. ISSN: 00179310. DOI: 10.1016/j.ijheatmasstransfer.2004.02.017.

[29] HAN, D. and LEE, K.-J. "Viscous dissipation in micro-channels". *Journal of Mechanical Science and Technology*, vol. 21.12 (2007), pp. 2244–2249. ISSN: 1738-494X. DOI: 10.1007/BF03177486.

[30] REYNOLDS, O. "An Experimental Investigation of the Circumstances Which Determine Whether the Motion of Water Shall Be Direct or Sinuous, and of the Law of Resistance in Parallel Channels". *Philosophical Transactions of the Royal Society of London*, vol. 174 (1883), pp. 935–982.

[31] LOPEZ, J. J., SALVADOR, F. J., GARZA, O. A. DE LA, and ARRÈGLE, J. "Characterization of the pressure losses in a common rail diesel injector". *Proceedings of the Institution of Mechanical Engineers Part D-Journal of Automobile Engineering*, vol. 226.D12 (2012), pp. 1697–1706. ISSN: 0954-4070. DOI: 10.1177/0954407012447020.

[32] Salvador, F. J., Gimeno, J., De la Morena, J., and Carreres, M. "Using one-dimensional modeling to analyze the influence of the use of biodiesels on the dynamic behavior of solenoid-operated injectors in common rail systems: Results of the simulations and discussion". *Energy Conversion and Management*, vol. 54.1 (2012), pp. 122–132. issn: 01968904. doi: 10.1016/j.enconman.2011.10.007.

[33] Coppo, M., Dongiovanni, C., and Negri, C. "Numerical Analysis and Experimental Investigation of a Common Rail-Type Diesel Injector". *Journal of Engineering for Gas Turbines and Power*, vol. 126.4 (2004), pp. 874–885. issn: 07424795. doi: 10.1115/1.1787502.

[34] Payri, R., Salvador, F. J., Marí-Aldaraví, P., and Martínez-López, J. "Using one-dimensional modeling to analyze the influence of the use of biodiesels on the dynamic behavior of solenoid-operated injectors in common rail systems: Detailed injection system model". *Energy Conversion and Management*, vol. 54.1 (2012), pp. 90–99. issn: 01968904. doi: 10.1016/j.enconman.2011.10.007.

[35] Bianchi, G. M., Falfari, S., Parotto, M., and Osbat, G. "Advanced modeling of common rail injector dynamics and comparison with experiments". *SAE Technical Paper 2003-01-0006* (2003). doi: 10.4271/2003-01-0006.

[36] Martínez López, J. "Estudio computacional de la influencia del levantamiento de aguja sobre el flujo interno y el fenómeno de la cavitación en toberas de inyección diésel". PhD thesis. Valencia (Spain): Universitat Politècnica de València, 2013. doi: 10.4995/Thesis/10251/29291.

[37] Salvador, F. J., Martínez-López, J., Caballer, M., and De Alfonso, C. "Study of the influence of the needle lift on the internal flow and cavitation phenomenon in diesel injector nozzles by CFD using RANS methods". *Energy Conversion and Management*, vol. 66 (2013), pp. 246–256. issn: 01968904. doi: 10.1016/j.enconman.2012.10.011.

[38] Desantes, J. M., Salvador, F. J., Carreres, M., and Martinez-Lopez, J. "Large-eddy simulation analysis of the influence of the needle lift on the cavitation in diesel injector nozzles". *Proceedings of the Institution of Mechanical Engineers, Part D: Journal of Automobile Engineering*, vol. 229.4 (2014), pp. 407–423. issn: 0954-4070. doi: 10.1177/0954407014542627.

[39] SALVADOR, F. J., CARRERES, M., JARAMILLO, D., and MARTÍNEZ-LÓPEZ, J. "Comparison of microsac and VCO diesel injector nozzles in terms of internal nozzle flow characteristics". *Energy Conversion and Management*, vol. 103 (2015), pp. 284–299. ISSN: 01968904. DOI: 10.1016/j.enconman.2015.05.062.

[40] BAE, C., YU, J., KANG, J., KONG, J., and LEE, K. O. "Effect of Nozzle Geometry on the Common-Rail Diesel Spray". *SAE Technical Paper 2002-01-1625* (2002). DOI: 10.4271/2002-01-1625.

[41] PAYRI, R., GIL, A., PLAZAS, A. H., and GIMENEZ, B. "Influence of Nozzle Seat Type on Internal Flow of Convergent Nozzles". *SAE Technical Paper 2004-01-2010* (2004). DOI: 10.4271/2004-01-2010.

[42] BERMUDEZ, V., PAYRI, R., SALVADOR, F. J., and PLAZAS, A. H. "Study of the influence of nozzle seat type on injection rate and spray behavior". *ImechE. Journal of automobile engineering*, vol. 219.5 (2005), pp. 677–689. ISSN: 0954-4070. DOI: 10.1243/095440705X28303.

[43] GAVAISES, M., ANDRIOTIS, A., PAPOULIAS, D., MITROGLOU, N., and THEODORAKAKOS, A. "Characterization of string cavitation in large-scale Diesel nozzles with tapered holes". *Physics of Fluids*, vol. 21.5 (2009), p. 052107. ISSN: 10706631. DOI: 10.1063/1.3140940.

[44] ARCOUMANIS, C., FLORA, H., GAVAISES, M., KAMPANIS, N., and HORROCKS, R. "Investigation of cavitation in a vertical multi-hole Diesel injector". *SAE Technical Paper 1999-01-0524* (1999). DOI: 10.4271/1999-01-0524.

[45] LINDSTRÖM, M. "Injector Nozzle Hole Parameters and their Influence on Real DI Diesel Performance". PhD thesis. KTH, 2009.

[46] POTZ, D., CHIRST, W., and DITTUS, B. "Diesel nozzle: The determining interface between injection system and combustion chamber". *THIESEL 2000 Conference on Thermo and Fluid-dynamic Processes in Diesel Engines*. Valencia, Spain, 2000.

[47] PAYRI, R., GUARDIOLA, C., SALVADOR, F. J., and GIMENO, J. "Critical cavitation number determination in Diesel injection nozzles". *Experimental Techniques*, vol. 28.3 (2004), pp. 49–52. DOI: 10.1111/j.1747-1567.2004.tb00164.x.

[48] MACIAN, V., BERMUDEZ, V., PAYRI, R., and GIMENO, J. "New technique for determination of internal geometry of a Diesel nozzle with the use of silicone methodology". *Experimental Techniques*, vol. 27.April (2003), pp. 39–43. ISSN: 0732-8818. DOI: 10.1111/j.1747-1567.2003.tb00107.x.

[49] Payri, R., Salvador, F. J., Gimeno, J., and De la Morena, J. "Effects of nozzle geometry on direct injection diesel engine combustion process". *Applied Thermal Engineering*, vol. 29.10 (2009), pp. 2051–2060. ISSN: 13594311. DOI: 10.1016/j.applthermaleng.2008.10.009.

[50] Schlichting, H. and Gersten, K. *Boundary layer theory*. 4th editio. McGraw-Hill, 1979. ISBN: 0-07-055334-3.

[51] White, F. M. *Fluid mechanics*. 5th editio. McGraw-Hill, 2003. ISBN: 9780071215664.

[52] Gravesen, P., Branebjerg, J., and Jensen, O. S. "Microfluidics-a review". *Journal of Micromechanics and Microengineering*, vol. 3.4 (1993), pp. 168–182. ISSN: 0960-1317. DOI: 10.1088/0960-1317/3/4/002.

[53] Lichtarowicz, A., Duggins, R. K., and Markland, E. "Discharge coefficients for incompressible non-cavitating flow through long orifices". *Journal of Mechanical Engineering Science*, vol. 7.2 (1965), pp. 210–219. ISSN: 0022-2542. DOI: 10.1243/JMES_JOUR_1965_007_029_02.

[54] Kent, J. C. and Brown, G. M. "Nozzle Exit Flow Characteristics for Square-edged and Rounded Inlet Geometries". *Combustion Science and Technology*, vol. 30.1-6 (1983), pp. 121–132. ISSN: 0010-2202. DOI: 10.1080/00102208308923615.

[55] Fox, T. A. and Stark, J. "Discharge coefficients for miniature fuel injectors". *Proceedings of the Institution of Mechanical Engineers, Part G: Journal of Aerospace Engineering*, vol. 203.17 (1989), pp. 75–78. ISSN: 0954-4100. DOI: 10.1243/PIME_PROC_1989_203_056_01.

[56] Soteriou, C., Andrews, R., and Smith, M. "Direct Injection Diesel Sprays and the Effect of Cavitation and Hydraulic Flip on Atomization". *SAE Technical Paper 950080* (1995). DOI: 10.4271/950080.

[57] Salvador, F. J. "Estudio teórico experimental de la influencia de la geometría de toberas de inyección Diésel sobre las características del flujo interno y del chorro". PhD thesis. Universitat Politècnica de València, 2003.

[58] Asihmin, V. I., Geller, Z. I., and Skobel'cyn, Y. A. "Discharge of a real fluid from cylindrical orifices". *Oil Industry*, vol. 9 (1961), pp. 135–172.

[59] NAKAYAMA, Y. "Action of the Fluid in the Air-Micrometer : 1st Report, Characteristics of Small-Diameter Nozzle and Orifice". *Bulletin of JSME*, vol. 4.15 (1961), pp. 507–515. ISSN: 1881-1426. DOI: 10.1299/jsme1958.4.507.

[60] HALL, G. W. "Analytical determination of the discharge characteristics of cylindrical-tube orifices". *Journal of Mechanical Engineering Science*, vol. 5.1 (1963), pp. 91–97. ISSN: 0022-2542. DOI: 10.1243/JMES_JOUR_1963_005_013_02.

[61] BENEDICT, R. *Fundamentals of temperature, pressure and flow measurements*. Ed. by W.-I. PUBLICATION. 3rd. USA, 1984. ISBN: 0-471-89383-8.

[62] PAYRI, R., GARCIA-OLIVER, J. M., SALVADOR, F. J., and GIMENO, J. "Using spray momentum flux measurements to understand the influence of diesel nozzle geometry on spray characteristics". *Fuel*, vol. 84.5 (2005), pp. 551–561. ISSN: 00162361. DOI: 10.1016/j.fuel.2004.10.009.

[63] NABER, J. D. and SIEBERS, D. L. "Effect of gas density and vaporization on penetration and dispersion of Diesel sprays". *SAE Technical Paper 960034*, vol. 105.412 (1996), pp. 82–111. DOI: 10.4271/960034.

[64] GANIPPA, L. C., ANDERSSON, S., and CHOMIAK, J. "Transient measurements of discharge coefficients of Diesel nozzles". *SAE Technical Paper 2000-01-2788* (2000). DOI: 10.4271/2000-01-2788.

[65] KULL, E. and KRÜGER, G. "Correlation of spray symmetry with mass and momentum of multihole diesel nozzles". *THIESEL 2004 Conference on Thermo and Fluid-dynamic Processes in Diesel Engines*. Valencia, Spain, 2004, pp. 7–10.

[66] HUSBERG, T., MANENTE, V., EHLESKOG, R., and ANDERSSON, S. "Fuel Flow Impingement Measurements on Multi-Orifice Diesel Nozzles". *SAE Technical Paper 2006-01-1552* (2006). DOI: 10.4271/2006-01-1552.

[67] SANGIAH, D. K. and GANIPPA, L. C. "Application of spray impingement technique for characterisation of high pressure sprays from multi-hole diesel nozzles". *International Journal of Thermal Sciences*, vol. 49.2 (2010), pp. 409–417. ISSN: 12900729. DOI: 10.1016/j.ijthermalsci.2009.08.001.

[68] NURICK, W. H. "Orifice Cavitation and Its Effect on Spray Mixing". *Journal of Fluids Engineering*, vol. 98.4 (1976), p. 681. ISSN: 00982202. DOI: 10.1115/1.3448452.

[69] Schmidt, D. P., Rutland, C. J., and Corradini, M. L. "A numerical study of cavitating flow through various nozzle shapes". *SAE Technical Paper 971597* (1997). doi: 10.4271/971597.

[70] Plesset, M. "The Dynamics of Cavitation Bubbles". *ASME Journal of Applied Mechanics*, vol. 16 (1949), pp. 277–282.

[71] Chaves, H., Knapp, M., Kubitzek, A., and Obermeier, F. "Experimental study of cavitation in the nozzle hole of diesel injectors using transparent nozzles". *SAE Technical Paper 950290* (1995). doi: 10.4271/950290.

[72] Bergwerk, W. "Flow pattern in diesel nozzle spray holes". *Proceedings of the Institution of Mechanical Engineers*, vol. 173 (1959), pp. 655–660. issn: 0020-3483. doi: 10.1243/PIME_PROC_1959_173_054_02.

[73] Randall, L. N. "Rocket Applications of the Cavitating Venturi". *Journal of the American Rocket Society*, vol. 22.1 (1952), pp. 28–38. issn: 1936-9964. doi: 10.2514/8.4412.

[74] De la Morena, J. "Estudio de la influencia de las características del flujo interno en toberas sobre el proceso de inyección Diesel en campo próximo". PhD thesis. Universidad Politécnica de Valencia, 2011.

[75] Schmidt, D. P. and Corradini, M. L. "The internal flow of diesel fuel injector nozzles: a review". *International Journal of Engine Research*, vol. 2.1 (2001), pp. 1–22. issn: 1468-0874. doi: 10.1243/1468087011545316.

[76] Arcoumanis, C., Badami, M., Flora, H., and Gavaises, M. "Cavitation in real-size multi-hole Diesel injector nozzles". *SAE Technical Paper 2000-01-1249* (2000). doi: 10.4271/2000-01-1249.

[77] Macian, V., Payri, R., Margot, X., and Salvador, F. J. "A CFD analysis of the influence of diesel nozzle geometry on the inception of cavitation". *Atomization and Sprays*, vol. 13 (2003), pp. 579–604. issn: 1045-5110. doi: 10.1615/AtomizSpr.v13.i56.80.

[78] Payri, F., Bermúdez, V., Payri, R., and Salvador, F. J. "The influence of cavitation on the internal flow and the spray characteristics in diesel injection nozzles". *Fuel*, vol. 83.4-5 (2004), pp. 419–431. issn: 00162361. doi: 10.1016/j.fuel.2003.09.010.

[79] Schmidt, D. P. "Cavitation in Diesel Fuel Injector Nozzles". PhD thesis. Wisconsin: University of Wisconsin - Madison, 1997.

[80] DESANTES, J. M., PAYRI, R., SALVADOR, F. J., and GIMENO, J. "Measurements of spray momentum for the study of cavitation in diesel injection nozzles". *SAE Technical Paper 2003-01-0703*, vol. 2003-01-07 (2003). DOI: 10.4271/2003-01-0703.

[81] DESANTES, J. M., PAYRI, R., PASTOR, J. M., and GIMENO, J. "Experimental characterization of internal nozzle flow and diesel spray behavior. Part I: Nonevaporative conditions". *Atomization And Sprays*, vol. 15.5 (2005), pp. 489–516. ISSN: 1044-5110. DOI: 10.1615/AtomizSpr.v15.i5.20.

[82] PAYRI, R., MOLINA, S., SALVADOR, F. J., and GIMENO, J. "A study of the relation between nozzle geometry, internal flow and sprays characteristics in diesel fuel injection systems". *KSME International Journal*, vol. 18.7 (2004), pp. 1222–1235. ISSN: 1226-4865. DOI: 10.1007/BF02983297.

[83] HE, L. and RUIZ, F. "Effect of cavitation on flow and turbulence in plain orifices for high-speed atomization". *Atomization and Sprays*, vol. 5 (1995), pp. 569–584. DOI: 10.1615/AtomizSpr.v5.i6.30.

[84] ROTH, H., GAVAISES, M., and ARCOUMANIS, C. "Cavitation initiation, its development and link with flow turbulence in diesel injector nozzles." *SAE Technical Paper 2002-01-0214* (2002). DOI: 10.4271/2002-01-0214.

[85] SOU, A., TOMIYAMA, A., HOSOKAWA, S., NIGORIKAWA, S., and MAEDA, T. "Cavitation in a Two-Dimensional Nozzle and Liquid Jet Atomization (LDV Measurement of Liquid Velocity in a Nozzle)". *JSME International Journal Series B*, vol. 49.4 (2006), pp. 1253–1259. ISSN: 1340-8054. DOI: 10.1299/jsmeb.49.1253.

[86] LEE, W.-K. K., FEZZAA, K., and WANG, J. "Metrology of steel micronozzles using x-ray propagation-based phase-enhanced microimaging". *Applied Physics Letters*, vol. 87.8 (2005), p. 84105. ISSN: 00036951. DOI: 10.1063/1.2034099.

[87] KASTENGREN, A. L. et al. "Engine Combustion Network (ECN): Measurements of Nozzle Geometry and Hydraulic Behavior". *Atomization and Sprays*, vol. 22.12 (2012), pp. 1011–1052. ISSN: 1044-5110. DOI: 10.1615/AtomizSpr.2013006309.

[88] KAO, C.-C. and SHIH, A. J. "Form measurements of micro-holes". *Measurement Science and Technology*, vol. 18.11 (2007), pp. 3603–3611. ISSN: 0957-0233. DOI: 10.1088/0957-0233/18/11/045.

[89] Peiner, E., Balke, M., and Doering, L. "Form measurement inside fuel injector nozzle spray holes". *Microelectronic Engineering*, vol. 86.4-6 (2009), pp. 984–986. issn: 01679317. doi: 10.1016/j.mee.2008.12.016.

[90] Von Kuensberg Sarre, C., Kong, S.-c., and Reitz, R. D. "Modeling the effects of injector nozzle geometry on diesel sprays". *SAE Technical Paper 1999-01-0912*, 724 (1999). doi: 10.4271/1999-01-0912.

[91] Sou, A., Hosokawa, S., and Tomiyama, A. "Cavitation in Nozzles of Plain Orifice Atomizers with Various Length-To-Diameter Ratios". *Atomization and Sprays*, vol. 20.6 (2010), pp. 513–524. issn: 1044-5110. doi: 10.1615/AtomizSpr.v20.i6.30.

[92] Payri, R., Salvador, F. J., Gimeno, J., and Garcia, A. "Flow regime effects over non-cavitating diesel injection nozzles". *Proceedings of the Institution of Mechanical Engineers, Part D: Journal of Automobile Engineering*, vol. 226.1 (2012), pp. 133–144. issn: 0954-4070. doi: 10.1177/0954407011413056.

[93] Fox, T. A. and Stark, J. "Characteristics of Miniature Short-Tube Orifice Flows". *Proceedings of the Institution of Mechanical Engineers, Part C: Journal of Mechanical Engineering Science*, vol. 203.5 (1989), pp. 351–358. issn: 0954-4062. doi: 10.1243/PIME_PROC_1989_203_124_02.

[94] Ramamurthi, K. and Nandakumar, K. "Characteristics of flow through small sharp-edged cylindrical orifices". *Flow Measurement and Instrumentation*, vol. 10.3 (1999), pp. 133–143. issn: 09555986. doi: 10.1016/S0955-5986(99)00005-9.

[95] Desantes, J. M., Arrègle, J., Lopez, J. J., and Hermens, S. "Experimental Characterization of Outlet Flow for Different Diesel Nozzle Geometries." *SAE Technical Paper 2005-01-2120*, 2005-01-2120 (2005). doi: 10.4271/2005-01-2120.

[96] Benajes, J., Molina, S., González, C., and Donde, R. "The role of nozzle convergence in diesel combustion". *Fuel*, vol. 87.10-11 (2008), pp. 1849–1858. issn: 00162361. doi: 10.1016/j.fuel.2007.12.016.

[97] Payri, R., Salvador, F. J., Gimeno, J., and De la Morena, J. "Study of cavitation phenomena based on a technique for visualizing bubbles in a liquid pressurized chamber". *International Journal of Heat and Fluid Flow*, vol. 30.4 (2009), pp. 768–777. issn: 0142727X. doi: 10.1016/j.ijheatfluidflow.2009.03.011.

[98] PAYRI, F., PAYRI, R., SALVADOR, F., and MARTÍNEZ-LÓPEZ, J. "A contribution to the understanding of cavitation effects in Diesel injector nozzles through a combined experimental and computational investigation". *Computers & Fluids*, vol. 58 (2012), pp. 88–101. ISSN: 00457930. DOI: 10.1016/j.compfluid.2012.01.005.

[99] SOM, S., RAMIREZ, A. I., LONGMAN, D. E., and AGGARWAL, S. K. "Effect of nozzle orifice geometry on spray, combustion, and emission characteristics under diesel engine conditions". *Fuel*, vol. 90.3 (2011), pp. 1267–1276. ISSN: 00162361. DOI: 10.1016/j.fuel.2010.10.048.

[100] IDELCHIK, I. E. *Memento des pertes de charge*. Eyrolles Paris, 1968.

[101] KAMPMANN, S., DITTUS, B., MATTES, P., and KIRNER, M. "The influence of hydro grinding at VCO nozzles on the mixture preparation in a D.I. diesel engine". *SAE Technical Paper 960867* (1996). DOI: 10.4271/960867.

[102] SOM, S., E., D., I., A., and AGGARWAL, S. "Influence of Nozzle Orifice Geometry and Fuel Properties on Flow and Cavitation Characteristics of a Diesel Injector". *Fuel Injection in Automotive Engineering*. InTech, 2012. ISBN: 978-953-51-0528-2. DOI: 10.5772/38900.

[103] BRUSIANI, F., FALFARI, S., and PELLONI, P. "Influence of the diesel injector hole geometry on the flow conditions emerging from the nozzle". *Energy Procedia*, vol. 45 (2014), pp. 749–758. ISSN: 18766102. DOI: 10.1016/j.egypro.2014.01.080.

[104] SALVADOR, F. J., CARRERES, M., JARAMILLO, D., and MARTÍNEZ-LÓPEZ, J. "Analysis of the combined effect of hydrogrinding process and inclination angle on hydraulic performance of diesel injection nozzles". *Energy Conversion and Management*, vol. 105 (2015), pp. 1352–1365. ISSN: 0196-8904. DOI: 10.1016/j.enconman.2015.08.035.

[105] BERGSTRAND, P. and DENBRATT, I. "The Effects of Multirow Nozzles on Diesel Combustion". *SAE Technical Paper 2003-01-0701* (2003). DOI: 10.4271/2003-01-0701.

[106] SAYIN, C., GUMUS, M., and CANAKCI, M. "Influence of injector hole number on the performance and emissions of a di diesel engine fueled with biodiesel-diesel fuel blends". *Applied Thermal Engineering*, vol. 61.2 (2013), pp. 121–128. ISSN: 13594311. DOI: 10.1016/j.applthermaleng.2013.07.038.

[107] Bazyn, T. and Koci, C. "The Effect of Jet Spacing on the Combustion Characteristics of Diesel Sprays". *THIESEL 2014 Conference on Thermo- and Fluid Dynamic Processes in Direct Injection Engines*. Valencia, Spain, 2014.

[108] Moon, S. et al. "Effect of the number and position of nozzle holes on in- and near-nozzle dynamic characteristics of diesel injection". *Fuel*, vol. 150 (2015), pp. 112–122. ISSN: 00162361. DOI: 10.1016/j.fuel.2015.01.097.

[109] Ho, C.-M. and Gutmark, E. "Vortex induction and mass entrainment in a small-aspect-ratio elliptic jet". *Journal of Fluid Mechanics*, vol. 179 (1987), p. 383. ISSN: 0022-1120. DOI: 10.1017/S0022112087001587.

[110] Hussain, F. and Husain, H. S. "Elliptic jets. Part 1. Characteristics of unexcited and excited jets". *Journal of Fluid Mechanics*, vol. 208 (1989), p. 257. ISSN: 0022-1120. DOI: 10.1017/S0022112089002843.

[111] Yunyi, G., Changwen, L., Yezhou, H., and Zhijun, P. "An Experimental Study on Droplet Size Characteristics and Air Entrainment of Elliptic Sprays". *SAE Technical Paper 982546* (1998). DOI: 10.4271/982546.

[112] Lee, C.-w., Kim, I., Koo, K.-w., Park, J., and Lee, Y. "Experimental study of the effects of nozzle hole geometry for a DI diesel engine". *ICLASS 2006*. Kyoto, 2006.

[113] Hong, J. G., Ku, K. W., Kim, S. R., and Lee, C. W. "Effect of cavitation in circular nozzle and elliptical nozzles on the spray characteristic". *Atomization and Sprays*, vol. 20.10 (2010), pp. 877–886. ISSN: 10445110. DOI: 10.1615/AtomizSpr.v20.i10.40.

[114] Molina, S., Salvador, F. J., Carreres, M., and Jaramillo, D. "A computational investigation on the influence of the use of elliptical orifices on the inner nozzle flow and cavitation development in diesel injector nozzles". *Energy Conversion and Management*, vol. 79 (2014), pp. 114–127. ISSN: 01968904. DOI: 10.1016/j.enconman.2013.12.015.

[115] Lefebvre, A. H. *Atomization and Sprays*. CRC Press, 1988. ISBN: 9780891166030.

[116] Reitz, R. D. "Mechanism of atomization of a liquid jet". *Physics of Fluids*, vol. 25.10 (1982), p. 1730. ISSN: 00319171. DOI: 10.1063/1.863650.

[117] Yuen, M.-C. "Non-linear capillary instability of a liquid jet". *Journal of Fluid Mechanics*, vol. 33.01 (1968), p. 151. ISSN: 0022-1120. DOI: 10.1017/S0022112068002429.

[118] NAYFEH, A. H. "Nonlinear Stability of a Liquid Jet". *Physics of Fluids*, vol. 13.4 (1970), p. 841. ISSN: 00319171. DOI: 10.1063/1.1693025.

[119] RUTLAND, D. and JAMESON, G. "Theoretical prediction of the sizes of drops formed in the breakup of capillary jets". *Chemical Engineering Science*, vol. 25.11 (1970), pp. 1689–1698. ISSN: 00092509. DOI: 10.1016/0009-2509(70)80060-4.

[120] OHNESORGE, W. V. "Formation of Drops by nozzles and the breakup of liquid jets". *ZAMM - Journal of Applied Mathematics and Mechanics*, vol. 16.6 (1936), pp. 355–358. ISSN: 00442267. DOI: 10.1002/zamm.19360160611.

[121] TORDA, T. P. "Evaporation of drops and breakup of sprays". *Astronautica Acta*, vol. 18 (1973), pp. 383–393.

[122] HIROYASU, H. and ARAI, M. "Structures of Fuel Sprays in Diesel Engines". *SAE Technical Paper 900475* (1990). DOI: 10.4271/900475.

[123] REITZ, R. D. "Atomisation and other breakup regimes of a liquid jet". PhD thesis. Ph.D. Thesis, Princeton University, 1978.

[124] WIERZBA, A. "Deformation and breakup of liquid drops in a gas stream at nearly critical Weber numbers". *Experiments in Fluids*, vol. 9.1-2 (1990), pp. 59–64. ISSN: 0723-4864. DOI: 10.1007/BF00575336.

[125] ARCOUMANIS, C., GAVAISES, M., and FRENCH, B. "Effect of fuel injection processes on the structure of Diesel sprays". *SAE Technical Paper 970799* (1997). DOI: 10.4271/970799.

[126] RUIZ, F. "A few useful relations for cavitating orifices". *In Proceedings of International Conference on Liquid Atomizations and Spray System. ICLASS-91, Gaithersburg, Maryland, 15-18 July.* 1991, pp. 595–602.

[127] SURHONE, L. M., TENNOE, M. T., and HENSSONOW, S. F. *Rayleigh-Taylor Instability.* Vdm Verlag, 2010. ISBN: 9786131104077.

[128] RUIZ, F. "Turbulence inside a cavitating injector orifice: a different animal". *ILASS-Americas.* 1998, pp. 133–137.

[129] BRENNEN, C. "An oscillating-boundary-layer theory for ciliary propulsion". *Journal of Fluid Mechanics*, vol. 65.04 (1974), pp. 799–824. ISSN: 0022-1120. DOI: 10.1017/S0022112074001662.

[130] ARAI, M., SHIMIZU, M., and HIROYASU, H. "Similarity between the breakup lengths of a high speed liquid jet in atmospheric and pressurized conditions". *In ICLASS-91, Gaithersburg, Maryland.* 1991.

[131] Bode, J. "Zum Kavitationseinfluss auf den Zerfall von Flüssigkeitsstrahlen". PhD thesis. Göttingen, Germany, 1991.

[132] Hiroyasu, H. "Spray breakup mechanism from the hole-type nozzle and its applications". *Atomization and Sprays*, vol. 10.3-5 (2000), pp. 511–527. issn: 1044-5110. doi: 10.1615/AtomizSpr.v10.i3-5.130.

[133] Tamaki, N., Shimizu, M., and Hiroyasu, H. "Enhancement of the atomization of a liquid jet by cavitation in a nozzle hole". *Atomization and Sprays*, vol. 11.2 (2001), p. 14. issn: 1044-5110. doi: 10.1615/AtomizSpr.v11.i2.20.

[134] Sou, A., Hosokawa, S., Tomiyama, A., and Akio, T. "Effects of cavitation in a nozzle on liquid jet atomization". *International Journal of Heat and Mass Transfer*, vol. 50.17-18 (2007), pp. 3575–3582. doi: 10.1016/j.ijheatmasstransfer.2006.12.033.

[135] Eifler, W. "Untersuchungen zur Struktur des instationären Dieselöleinspritzstrahles in Düsennahbereich mit der Methode der Hochfrequenz-Kinematografie". PhD thesis. Universität Kaiserslautern, Germany, 1990.

[136] Chaves, H. and Obermeier, F. "Correlation between light absortion signals of cavitating nozzle flow within and outside of the hole of a transparent Diesel injection nozzle". *Proc. 15th ILASS-Europe, Toulouse, July 5-7.* 1999, pp. 224–229.

[137] Takeda, Y., Keiichi, N., and Keiichi, N. "Emission characteristics of premixed lean Diesel combustion with extremely early staged fuel injection". *SAE Technical Paper 961163* (1996). doi: 10.4271/961163.

[138] Liu, B., Jia, M., and Peng, Z. "An investigation of multiple-injection strategy in a Diesel PCCI combustion enginee". *SAE Technical Paper 2010-01-1134* (2010). doi: 10.4271/2010-01-1134.

[139] Wakuri, Y. et al. "Studies of the penetration of a fuel spray in a Diesel Engine". *Bulletin of JSME*, vol. 3.9 (1960), pp. 123–130. issn: 0029-0270. doi: 10.1299/kikai1938.25.820.

[140] Dent, J. C. "A basis for comparison of various experimental methods for studying spray penetration". *SAE Technical Paper 710571* (1971). doi: 10.4271/710571.

[141] Hay, P. and Jones, P. L. "Comparison of the various correlations for spray penetration". *SAE Technical Paper 720776* (1972). doi: 10.4271/720776.

[142] CORREAS, D. "Estudio teórico-experimental del chorro libre Diesel isotermo". PhD thesis. Valencia: E.T.S. Ingenieros Industriales. Universidad Politécnica de Valencia, 1998.

[143] WAN, Y. and PETERS, N. "Scaling of spray penetration with evaporation". *Atomization and Sprays*, vol. 9.2 (1999), pp. 111–132. DOI: 10.1615/AtomizSpr.v9.i2.10.

[144] PAYRI, F., PAYRI, R., BARDI, M., and CARRERES, M. "Engine combustion network: Influence of the gas properties on the spray penetration and spreading angle". *Experimental Thermal and Fluid Science*, vol. 53.September 2015 (2014), pp. 236–243. ISSN: 08941777. DOI: 10.1016/j.expthermflusci.2013.12.014.

[145] DESANTES, J., PAYRI, R., SALVADOR, F., and GIL, A. "Development and validation of a theoretical model for diesel spray penetration". *Fuel*, vol. 85.7-8 (2006), pp. 910–917. ISSN: 00162361. DOI: 10.1016/j.fuel.2005.10.023.

[146] RANZ, W. E. "Some experiments on orifice sprays". *The Canadian Journal of Chemical Engineering*, vol. 36.4 (1958), pp. 175–181. ISSN: 00084034. DOI: 10.1002/cjce.5450360405.

[147] REITZ, R. D. and BRACCO, F. B. "On the dependence of spray angle and other spray parameters on nozzle design and operating conditions". *SAE Technical Paper 790494* (1979). DOI: 10.4271/790494.

[148] WU, K.-J., SU, C.-C., STEINBERGER, R. L., SANTAVICCA, D. A., and BRACCO, F. V. "Measurements of the Spray Angle of Atomizing Jets". *Journal of Fluids Engineering*, vol. 105.4 (1983), p. 406. ISSN: 00982202. DOI: 10.1115/1.3241019.

[149] DELACOURT, E., DESMET, B., and BESSON, B. "Characterisation of very high pressure Diesel sprays using digital imaging techniques". *Fuel*, vol. 84.7-8 (2005), pp. 859–867. DOI: 10.1016/j.fuel.2004.12.003.

[150] DESANTES, J. M., PASTOR, J. V., PAYRI, R., and PASTOR, J. M. "Experimental characterization of internal nozzle flow and diesel spray behavior. Part II: Evaporative conditions". *Atomization and Spray*, vol. 15.5 (2005), pp. 517–543. ISSN: 1044-5110. DOI: 10.1615/AtomizSpr.v15.i5.20.

[151] ARAI, M., TABATA, M., HIROYASU, H., and SHIMIZU, M. "Disintegrating Process and Spray Characterization of Fuel Jet Injected by a Diesel Nozzle". *SAE Technical Paper 840275* (1984). DOI: 10.4271/840275.

[152] Chehroudi, B., Chen, S.-H., Bracco, F. V., and Onuma, Y. "On the Intact Core of Full-Cone Sprays". *SAE Technical Paper 850126* (1985). DOI: 10.4271/850126.

[153] Espey, C. and Dec, J. E. "The effect of TDC temperature and density on the liquid-phase fuel penetration in a D.I. Diesel engine". *SAE Technical Paper 952456* (1995). DOI: 10.4271/952456.

[154] Canaan, R., Dec, J., Green, R., and Daly, D. "The influence of fuel volatility on the liquid-phase fuel penetration in a heavy-duty D.I. Diesel engine". *SAE Technical Paper 980510* (1998). DOI: 10.4271/980510.

[155] Siebers, D. L. "Liquid-phase fuel penetration in diesel sprays". *SAE Technical Paper 980809* (1998). DOI: 10.4271/980809.

[156] Ha, J. Y. et al. "Investigation on the initial part and the spray formation delay of Diesel spray". *SAE Technical Paper 830451* (1983). DOI: 10.4271/830451.

[157] Xu, M. and Hiroyasu, H. "Development of a new optical technique for measuring Diesel spray penetration". *SAE Technical Paper 902077* (1990). DOI: 10.4271/902077.

[158] Siebers, D. L. "Scaling liquid-phase fuel penetration in diesel sprays based on mixing-limited vaporization". *SAE Technical Paper 1999-01-0528* (1999). DOI: 10.4271/1999-01-0528.

[159] Mugele, R. A. and Evans, H. D. "Droplet Size Distribution in Sprays". *Industrial & Engineering Chemistry*, vol. 43.6 (1951), pp. 1317–1324. DOI: 10.1021/ie50498a023.

[160] Desantes, J. M., Payri, R., Garcia-Oliver, J. M., and Salvador, F. J. "A contribution to the understanding of isothermal diesel spray dynamics". *Fuel*, vol. 86.7-8 (2007), pp. 1093–1101. ISSN: 00162361. DOI: 10.1016/j.fuel.2006.10.011.

[161] Desantes, J. M., Salvador, F. J., Lopez, J. J., and De la Morena, J. "Study of mass and momentum transfer in diesel sprays based on X-ray mass distribution measurements and on a theoretical derivation". *Experiments in Fluids*, vol. 50.2 (2011), pp. 233–246. ISSN: 07234864. DOI: 10.1007/s00348-010-0919-8.

[162] Salvador, F. J., Ruiz, S., Gimeno, J., and De la Morena, J. "Estimation of a suitable Schmidt number range in diesel sprays at high injection pressure". *International Journal of Thermal Sciences*, vol. 50.9 (2011), pp. 1790–1798. ISSN: 12900729. DOI: 10.1016/j.ijthermalsci.2011.03.030.

Chapter 3

Literature review

3.1 Introduction

The present thesis explores the influence of the fuel temperature changes along the injector on the injection process by means of a combined experimental and computational approach. The fundamentals of the Diesel injection process were presented in *Chapter 2*. However, some more specific details need to be reviewed in depth before being able to undertake the tasks leading to the fulfillment of the objectives of the investigation.

Computational modelling has emerged as a tool of great value to understand and improve the behaviour of CIDI engines injection systems. Since the present thesis benefits from the potential of 1D modelling techniques, a review on the most relevant works in the literature that have applied these tools for the specific purpose of simulating the behaviour of injection systems is performed in the present chapter.

The fuel temperature changes along the injector are deemed to play a key role in the injection process, both in the internal flow and spray development. The rate of injection is expected be affected, both in its steady-state and transient stages, mostly due to the changes induced in the fuel properties (i.e. density, viscosity, speed of sound, ...). Hence, a review on the influence of the fuel properties on the injection process is also carried out in the present chapter. This important influence also highlights the fact that the potential of the computational modelling is not fully exploited unless the properties of the working fluid are known. Given the high pressures reached by the fuel in

the *common-rail* system (above 250 MPa), gathering knowledge about the fuel properties at the CIDI engines typical operating conditions is not an easy task. Therefore, a review regarding the existing works to determine the properties of diesel fuels at wide ranges of temperatures and pressures is presented as well.

3.2 Modelling of Diesel injection systems

Researchers have always sought ways to improve globally extended technologies like the internal combustion engine. An obvious way to do so is through experiments. However, this approach is extremely time-consuming and expensive. Simulation enables to reduce the number of experimental tests, shortening the development times, avoiding the instalation of costly measuring devices or even allowing to know the characteristics of the system at locations not accessible to realizable sensors. This is especially relevant in diesel injection systems, due to the already mentioned difficulties added by the small dimensions of the ducts and orifices, the high velocities achieved through them or the transient nature of the process. For instance, determining the pressure at the injector sac is hardly achievable through experiments, mainly due to the miniaturization of sensors that would be required in that location. A theoretical model previously validated with experimental measurements at regions easily accessible by sensors would allow to estimate this information avoiding the difficult instrumentation issues.

Numerical simulation is therefore a research tool complementary to experimentation. It allows to acquire a better understanding of the complex unsteady processes that occur in the injection systems, such as cavitation. With this knowledge, it is easier to determine the performance of the system under different operating conditions.

This section provides works carried out by several authors from the early models to our days. The authors have sequentially modelled the injection system providing substantial improvements over their predecessors. This study will determine which have been the main assumptions and simplifications taken through history, providing a clear vision of the state of the art and evolution of these models. This review will provide a good starting point for the model implemented in this thesis. The section has been divided by the historical milestone that supposed the emergence of the *common-rail* system, which allowed a great increase in the achieved injection pressures.

3.2.1 Before the appearance of the common-rail

Even though the first injection systems did not offer the possibility of reaching the high injection pressures of the *common-rail*, the authors of their models already had to face problems that became relevant for the modern systems. Thus, their experience in terms of the best numerical methods to solve the associated equations, how to model several phenomena involved (such as cavitation) or what is the relevance of the fluid properties variation, is highly valuable for current modellers.

The flow in an injection system is time-dependent and compressible. Pressure waves are formed in the system and travel along it, governing the dynamics of the internal elements. Initially, simple injection system models that assumed the fuel to be incompressible were used for dimensioning the components. Alliévi and Dubs [1] may have been the first authors to derive motion and continuity partial differential equations (PDE) for one-dimensional time-dependent pipe flow, assuming it to be frictionless. When these equations are solved, they result in general wave equations, which have been commonly used for calculating the time-dependent flow in a high-pressure pipe. According to the solution, the pressure in an arbitrary cross-section of the pipe is comprised of a constant pressure and two pressure waves travelling in different directions.

Later, in 1937, DeJuhasz [2] used a graphical method to solve the flow, assuming a constant speed of the pressure pulse and frictionless flow. This kind of method was practically abandoned due to the irruption of calculation methods intended for computers, that allowed approximations to give solution to Alliévi's equations. These approximations could take into account viscous friction or other phenomena by means of corrections.

It is from the 1960s that the numerical models start bearing fruits thanks to the use of digital computers. Numerical methods were applied to solve general wave equations, usually implementing *finite difference methods*. The pipe is divided into parts so that the boundary conditions between parts are solved. Generally, the time taken by the pressure wave to progress from one end of a pipe to the other was used as the time step. This approach was used by Knight [3] to predict the performance of an injection system, with special attention to avoiding secondary injections and dribble. This model was able to simulate oscillations propagated from one injection to the next one, but did not account for cavitation. The fuel properties were assumed to be constant along a simulation.

Other authors improved Knight's model by including extra features. In 1967, Brown and McCallion [4] introduced the possibility of cavitation in the

dead volumes and the variations of fuel viscosity with the pressure. Becchi [5] considered that the pressure waves could be attenuated due to friction and changes in the fuel bulk modulus due to the presence of vapour in the case of cavitation. Temperature variations were still not considered. In fact, it was not until 1990 when Ficarella *et al.* [6] took into account fuel temperature changes due to the pump regime, but they still did not consider temperature spatial variations along the system, thus assuming isothermal flow.

Another approach commonly taken to perform injection systems simulations involves the *method of characteristics*, which allows to reduce the governing partial differential equations to ordinary differential equations (ODE). From 1971 to 1973, Wylie *et al.* carried out several studies [7–9], including the PhD thesis by El-Erian [10] comparing and combining several numerical methods. On the one hand, they tried to describe the problem through systems of differential algebraic equations (DAE). On the other hand, they tried to solve the ODEs through Runge-Kutta or predictor-corrector methods. Finally, they applied the method of characteristics. Other interesting contributions of their work were the introduction of the friction losses as a function of the Reynolds number and the implementation of discharge coefficients for internal and nozzle orifices dependent on the Reynolds number (as opposed to the previous works, which always considered them to be constant), although based on steady conditions. They also assumed the fuel properties to be dependent on the pressure.

With regard to these two approaches, the ones based on general wave equations discretized through *finite difference methods* present more issues with the boundary conditions. Some efforts have been made to implement strategies that automatically readapt the time step along the simulation depending on the instantaneous residuals of the equations. On the contrary, the models that take profit of the *method of characteristics* solve the issues with the boundary conditions [11], but are numerically more time-consuming and their validity when dealing with cavitation has been questioned [12–14].

The following relevant works prior to the appearance of the *common-rail* systems are summarized in Table 3.1 together with their more significant features and contributions. As important milestones, Yamaoka *et al.* [15] were the first to consider the influence of dissolved air in the fuel properties, being imitated by other authors later [16–18]. Some researchers also found that these fuel properties play a key role on the propagation of the pressure waves and the SOI [5, 19, 20]. Goyal [16] was the first of many to adopt a modular approach, also known as *universal model* since it allowed to combine several predefined components to model any injection system. This approach was

later followed by Wannenwetsch [21], Sobel and Lehrach [17] Fairbrother [18] or Arcoumanis *et al.* [22, 23]. This last author was also pioneer in modelling the internal leakages among elements [20]. Some authors initiated the trend to evaluate the discharge coefficient as a function of the Reynolds number and the needle lift [24], even trying experimental approaches to determine these laws [25]. The consideration of the elasticity and deformations of the high-pressure line or the rest of mechanical elements was also an interesting contribution by some researchers [17].

The fact that some authors already made an effort to evaluate the fuel properties at the corresponding pressures and temperatures, even when they were not modified along a simulation (i.e. taking the assumption of isothermal flow), highlights the fact that their influence on the injection system performance cannot be neglected. This statement is further emphasized considering the relatively narrow range of variation of these conditions during the regular operation of the injection systems of the time. In this sense, Ficarella *et al.* [6] considered maximum pressures of 100 MPa, still far from the ones of the current *common-rail* systems. These authors were also the first to consider cavitation inside the nozzle orifices and to model orifices with variable area depending on the stage of the injection process.

Special consideration must be given to the work by Rodríguez-Antón [26], who successfully applied the *Bond-graph* technique to represent the behaviour of a fuel injection system, as done in the present thesis. In addition, he made a particular effort to experimentally determine the evolution of the fuel properties with respect to the temperature and pressure. Despite maintaining the isothermal hypothesis, this evolution was implemented in his model to yield more accurate results.

Hence, even though the characteristics of the injection systems of the time differ greatly from the current ones, these first experiences in modelling were useful to determine the relevant phenomena and hypotheses that must be considered when describing an injection system on the one hand, and to know the most proper numerical methods to solve the equations involved on the other.

Author	Year	Fuel properties	Numerical method	Other relevant features
Knight [3]	1960	Isothermal All properties constant	Finite differences	Cavitation avoided Rigid walls assumed
Brown and McCallion [4]	1967	Isothermal Id. as Knight with $\eta_f = f(p)$ $p = const.$ at a given location	Finite differences	Cavitation possible in dead volumes
Becchi [5]	1971	Isothermal Id. as Knight with $\beta_f = f(\gamma)$	Finite differences	Pressure waves attenuated by friction
Wylie *et al.* [7–10]	1971 to 1973	Isothermal Function of p	Algebraic equations Runge-Kutta Predictor-corrector Method of characteristics	Considered friction losses as a function of Re Considered $C_d = f(Re)$ based on steady-state
Yamaoka *et al.* [15, 27]	1973	Isothermal Function of p and T $p = const.$ at a given location $T = const.$ along the system	Not reported	Considered dissolved air in the fuel props. Experimentally determined fuel properties Modelled seat elasticity to simulate rebounds
Matsuoka *et al.* [19]	1976	Isothermal Only $a_f = f(p)$ $p = const.$ along the process	Not reported	Influence of η_f on pressure waves damping p losses along the ducts by Darcy's $C_f = f(Re)$ $C_d = const.$ for all the elements
Goyal [16]	1978	Isothermal $\rho_f = f(p, \gamma)$ and $\beta_f = f(p, \gamma)$ p updates at each t and location	Runge-Kutta Method of characteristics	Modular approach, valid for different systems $C_d = f(Re)$
Kumar *et al.* [12]	1983	$\rho_f = f(p)$ and $\beta_f = f(p)$	Finite differences Method of characteristics Leap-Frog / Lax-Wendrof Runge-Kutta Newton-Raphson	Inadequacy of the method of characteristics with cavitation
Marcic and Kovacic [24]	1985	Isothermal $\rho_f = f(T, p)$ and $\beta_f = f(T, p)$ $a_f = const.$	Runge-Kutta Inst. error controls t step	Use $C_d = f(l)$ Modelled the complete inj. system later [28, 29]
Wannenwestch [21]	1985	Not reported	Method of characteristics Euler Runge-Kutta Implicit	Modular approach More stability with implicit methods
Muñoz [30]	1987	Isothermal $\nu_f = f(T, p)$ and $\beta_f = f(T, p)$ $a_f = const.$	Not reported	Measured $\beta_f = f(p)$ Similar to Yamaoka *et al.*
Sobel and Lehrach [17]	1987	$a_f = f(p, \gamma)$ and $\beta_f = f(p, \gamma)$	Runge-Kutta 4^{th} order Method of characteristics	Universal model First to consider line elasticity and deformations Demonstrated the relevance of p and γ on a Cavitation and C_d treatment based on Wylie *et al.*

Continued on next page

Author	Year	Fuel properties	Numerical method	Other relevant features
Ficarella *et al.* [6, 31, 32]	1988 to 1993	Isothermal $a_f = f(p, T, \gamma)$ $\beta_f = f(p, T, \gamma)$ $\rho_f = f(p, \gamma)$	ODEs through Euler Predictor-corrector Runge-Kutta 2^{nd} order Method of characteristics	Wide range of T (330 to 440 K) Wide range of p (up to 100 MPa) Studied the injection system geometry Modelled elasticity of the needle, spring and shims Cavitation in the nozzle orifices Both rotary and in-line pumps considered Modelled orifices with variable area Stated the fuel props. as source of errors
Catania *et al.* [25, 33, 34]	1992 to 1996	Isothermal Function of p and T	Implicit methods Newton-Raphson	Different treatment of cavitation, affecting a_f Both rotary and in-line pumps considered Considered line elasticity Modelled friction and mech. losses among elements $C_d = f(Re, l)$, experimentally determined
Arcoumanis *et al.* [20, 22, 23]	1992 to 1997	Isothermal Function of p and T	Finite differences Runge-Kutta Method of characteristics	Universal model Studied the injection system geometry Modelled elastic deformations of mechanical elements Considered pressure and energy losses along the lines Modelled the internal leakages Influence of leakages, a_f and β_f on SOI
Fairbrother [18]	1994	Isothermal $\beta_f = f(p, \gamma)$ Dow and Fink $\rho_f = f(p, \gamma)$	Runge-Kutta Method of characteristics	Modular approach Friction through Darcy-Weisbach factor Considered elasticity of movable elements
Kegl [35]	1995	Isothermal Function of p and γ	Runge-Kutta 5^{th} order	Snubber valve consideration
Rakopoulos *et al.* [36]	1996	$\beta_f = f(p)$ $\rho_f = f(\beta_f)$	Mod. predictor-corrector Method of characteristics	Did not model elastic deformations
Gu *et al.* [37, 38]	1996	Isothermal $a_f = f(p, T)$ and $\rho_f = f(p, T)$ $\eta_f = f(T)$	Runge-Kutta Adaptive control of t step	Needle model Analysis of impact among needle and seat Elastic deformations of elements considered Cavitation not considered
Rodríguez-Antón [26]	1996	Isothermal Function of p and T	Bond-Graph approach	First to apply Bond-Graph for this problem Diesel properties experimentally measured Preferred isothermal β_f rather than isentropic β_f Internal friction and leakages model acc. to Moody
Palomar and Ruiz [39]	1997	Not reported	Not reported	Emphasized the importance of considering cavitation when modelling a_f

Table 3.1: Works on modelling of injection systems prior to the common-rail.

3.2.2 Common-rail systems modelling

The first reported model corresponding to a *common-rail* injection system was published in 1994 by Digesu *et al.* [40, 41]. Their work dealt with an innovative electro-injector patented by Elasis (within the Fiat group) before the acquisition of the design by Bosch. This injector was able to achieve maximum injection pressures of 120 MPa. The authors, among which Ficarella (recall Table 3.1) is found, applied the experience from previous models giving importance to the transmission of the pressure waves along the injector, the elastic deformations and collision of the mechanical components or the cavitation phenomenon, also considering the fuel leakage among elements by assuming laminar flow through their clearances. In addition, they considered isothermal flow with fuel properties dependent on the pressure and the vapour fraction. Due to the novelty of the injector, the magnet-driven electrovalve was modelled through a Finite Element Method (FEM) supported by experimental measurements. Still, the resulting equations were solved through the method of characteristics and an explicit first order Runge-Kutta scheme, approach that had also been taken by their predecessors.

Later on, Amoia *et al.* [42] and Ficarella *et al.* [43] took this model as a basis, including the dependence of the fuel properties on the temperature (although still considering isothermal flow), in order to perform parametric studies to determine the influence of several parameters on the injection process. They applied *Design of Experiments* (DoE) techniques for the first time in order to assess the response of the system to the modification of operating parameters (such as the injection pressure or energizing time) and geometrical factors (dimensions of internal pieces or their manufacturing tolerances), among others.

In fact, this way of proceeding has been the general trend after the appearance of the *common-rail*: once the foundations on which modelling is based were established, efforts stopped being focused on the numerical methods to solve the equations and have been rather placed on implementing a more accurate reproduction of the physics behind the diverse processes involved. Software programmers have developed modular commercial multidomain applications for simulation (such as Simulink, AMESim or GT-Suite) which already incorporate reliable solvers, so that the modellers can focus on the generation of practical results through the exploitation of the models. Table 3.2, which summarizes the main modelling works on *common-rail* injection systems, proves this statement.

The potential of *common-rail* systems, which enabled higher injection pressures and the delivery of larger amounts of fuel in shorter times, resulted in

the application of multiple injection strategies, increasing the transience of the injection process. As a consequence, the complexity of the injection system (and particularly the injector) started growing. This, in turn, resulted in more demanding requirements for the models, which needed great accuracy in order to properly catch the injector behaviour. Thereby, the authors started considering the simulation of phenomena that had been neglected at earlier stages, both in the electromagnetic, hydraulic and mechanical fields.

Due to its importance in injector dynamics, some authors focused on the accurate replication of the electrovalve behaviour, mainly through FEM approaches supported by experiments [40, 41, 44, 45]. Other researchers paid attention to a proper implementation of the dynamics of the movable elements. In this sense, most modellers considered the elasticity of the internal mechanical components, on one hand due to the influence of their deformations (mainly those of the needle) on the actual start of injection once the control valve is energized, and on the other hand to detect rebounds that may lead to fuel internal leakages or even secondary injections. In this sense, Desantes *et al.* [46] or Lee *et al.* [47] established a methodology to model the internal mobile components of the injector as an equivalent spring whose stiffness can be determined merely through geometrical parameters. The friction among this kind of elements was also generally considered in the models.

Nevertheless, the harder efforts were perhaps made on the correct implementation of the flow hydraulic parameters. Several authors identified the information about the discharge coefficients of the hydraulic restrictions (i.e. control and nozzle orifices) of the injector as the most sensitive to obtain a reliable model. Bianchi *et al.* [48, 49] used CFD techniques to determine the discharge coefficient as a funcion of the flow Reynolds number, whereas Payri *et al.* [50–52] or Coppo *et al.* [53] proposed a complete hydraulic experimental characterization to that end, complementing a basic injector metrology. This also included the characterization of the cavitation critical conditions. Other authors also insist on the need for including the instantaneous flow areas of the restrictions as a function of the valves and needle lift [54].

Another fact that has been paid attention to in the literature is the implementation of the fuel properties. Even when most works introduce them as a function of pressure and temperature, and despite the growing injection pressures, local changes in temperature are still not usually considered, thus regarding the flow as isothermal. In 2002, Catalano *et al.* [55] were the first to consider temperature variations along the injector, although they neglected relevant terms in the related equation. Later, in 2004, Catania *et al.* [56–58] developed an adiabatic model and stated the importance of the temperature

changes on the model predictions due to the modified fuel properties. They introduced the energy equation and a barotropic flow model, claiming temperature raises higher than 5 K for pressure changes of 40 MPa. Seykens *et al.* [59, 60] or Belmon *et al.* [61] also followed this approach for non-cavitating flow. However, although undoubtedly more accurate than the isothermal assumption, an exclusive assessment of the limits of the validity of the adiabatic hypothesis has never been performed. In addition, the range of fuel temperatures on which these models have been tested is narrow (293 to 333 K).

Many works have been oriented to the proper reproduction of the injector behaviour under multiple injections [43]. This is ensured if the elastic deformations of the elements are accurately replicated and the pressure waves are correctly transmitted (both along one injector and along the rail when several injectors are working alternatively [48, 62]), which has been guaranteed from the aforementioned studies. As stated earlier, models have recently been used to generate practical results to propose improvements to the existing technologies. From this basis, Bianchi *et al.* [48, 63] proposed some improvements to the injector technology in order to enhance the response of the injection system to multiple injections. A similar approach was followed by Payri *et al.* [52, 64], who investigated the effects of the biodiesel fuel properties on the multiple injection capabilities of the injector (i.e. minimum dwell time among injections) and proposed internal modifications to achieve the same behaviour with this fuel than with regular diesel fuel.

Similarly, models have been used to assess and compare the performance of different injector technologies arisen. Kiss *et al.* [45] made use of a model implemented in Matlab-Simulink to compare 2-way and 3-way valve injectors in terms of multiple injections performance and internal leakages. Plazas [65] modelled *common-rail* Bosch injectors from the 1^{st} to the 3^{rd} generation and compared their behaviour. This included piezoelectric injectors, which have been the most analyzed lately due to their novelty [62, 66–69].

These comparisons among technologies and the proposal of improvements have been possible by using parametric studies and DoE techniques, mainly applied to the injector internal geometry [47, 70, 71], but also to the hydraulic parameters of the most important restrictions to the flow [65, 70].

Finally, the latest trends include the usage of 1D modelling to provide boundary conditions to 3D nozzle internal flow simulations [71, 72] that are in turn used as a starting point to analyse the spray behaviour. The simulations have even been coupled so that the 1D codes provide online information about the instantaneous needle position, sac pressure and mass flow rate to the 3D solvers [67, 73], increasing their accuracy.

Author	Year	Fuel props.	Max. p_i	Numerical method	Other relevant features
Digesu *et al.* [40, 41]	1994	Isothermal $\beta_f = f(p, \gamma)$ $\rho_f = f(p, \gamma)$	120 MPa	Method of characteristics Runge-Kutta 1^{st} order	FEM supp. by experiments to model the electrovalve Wave transmission, cavitation and leak. among elements
Amoia *et al.* [42]	1997	Isothermal $a_f = f(p, T, \gamma)$ $\rho_f = f(p, T, \gamma)$	120 MPa	Same as above	Application of DoE
Ficarella *et al.* [43]	1999	Same as above	130 MPa	Same as above	Capability of multiple injections Pressure fluctuations at the control valve Elastic deformation of the needle
Desantes *et al.* [46]	1999	Isothermal $\rho_f = f(T)$ $\beta_f = f(T)$ $a_f = f(\rho_f, \beta_f)$	110 MPa	Runge-Kutta 4^{th} order	Modular approach Exp. characterization of fuel props. and geometry Analysed influence of geometry Elastic def. of needle and friction losses
Favennec [74]	1999	Isothermal $\rho_f = f(p, T, \gamma)$ $\eta_f = f(p, T, \gamma)$ $\beta_f = f(p, t, \gamma)$	110 MPa	Implicit method	Bond graph approach (AMESim) $C_d = f(Re)$ for hydr. restrictions Friction among mechanical elements Elastic def. due to contact forces Exp. characterization of fuel props.
Arcoumanis *et al.* [54]	1999	Isothermal Function of p	150 MPa	Finite differences Runge-Kutta Method of characteristics	Modular approach based on their previous models Predicted heating due to Δp, not applied on fuel props. Variable C_d Used modelling to show advantages of *common-rail*
Rodríguez [70]	2001	Isothermal Same as Desantes *et al.*	140 MPa	Runge-Kutta 4^{th} order	Modular approach Used hydraulic exp. information Importance of proper t step Parametric studies Attributed errors to fuel props. not correctly implemented (no local changes)
Catalano *et al.* [55]	2002	Isentropic $\beta_f = f(p, T)$ $\rho_f = f(p, T)$	120 MPa	MacCormack 2^{nd} order Predictor-corrector	Included T changes along the injector, although important terms are neglected Analysed Δp among rail and nozzle Proposed new design to reduce that Δp
Lee *et al.* [47]	2002	Isothermal Same as Gu *et al.*	160 MPa	Runge-Kutta	Equivalent spring to model needle deformations Related needle dynamics to secondary injections Parametric study Interesting contributions about bouncing dynamics

Continued on next page

Author	Year	Fuel props.	Max. p_i	Numerical method	Other relevant features
Bianchi *et al.* [48, 49, 63, 75, 76]	2002 to 2005	Isothermal ISO4113 f. of p and T	160 MPa	Not reported	Start based on a previous electrovalve model [44] Impl. in Matlab-Simulink, later migrated to AMESim Electromagnetic circuit simulated through FEM Cavitation only considered in the nozzle Highlighted importance of knowing C_d of each restriction Used CFD techniques to get $C_d = f(Re)$ of each restriction Flow areas function of valve lift New squish submodels Considered influence of line deformations on β_f Application to improve response to multiple injections Pressure waves interaction on multiple injections
Gullaksen [77]	2004	Isothermal f. of p and T	90 MPa	Method of characteristics Backward differentiation	Modular, implemented in Matlab $C_d = const.$, with no cavitation considered
Mullemane *et al.* [78]	2004	Isothermal ISO4113	135 MPa	Not reported	Implemented in AMESim Used to investigate different geometries
Kiss *et al.* [45]	2004	Isothermal $\beta_f = const.$	30 MPa	Finite volume method Runge-Kutta 4^{th} order Time step of 0.5 μs	Implemented in Matlab/Simulink FEM for the electromagnetic valve Comparison among 2 and 3-way valve injectors Focused on multiple injections performance
Catania *et al.* [56–58, 79]	2004 to 2008	Adiabatic ISO4113 f. of p and T	140 MPa	ODEs: finite volume backward differentiation PDEs: Implicit scheme Newton-Raphson	1^{st} to consider thermal effects, incl. cavitation Attributed high influence of T changes on fuel props. T changes along the injector not validated Claimed $\Delta T > 5$ K for $\Delta p = 40$ MPa Energy equation and barotropic flow model Wave dynamics with multiple injections
Seykens *et al.* [59, 60]	2004 to 2005	Adiabatic f. of p and T 293 to 313 K	140 MPa	Not reported	Implemented in AMESim Influence of fuel props. through different fuels Study on how the elements deformations control the SOI
Payri *et al.* [50, 51]	2004 to 2005	Isothermal f. of p and T	135 MPa	Two linear multistep Two-step backward diff. Two-step Adams Moulton Method of characteristics	Impl. in AMESim and Flowmaster, modular and flexible Dimensional and hydraulic exp. characterization Compared 1^{st} and 2^{nd} gen. *common-rail* injectors
Plazas [65]	2005	Same as above	180 MPa	Same as above	Compared 1^{st} to 3^{rd} gen. *common-rail* injectors Parametric studies
Falfari and Pelloni [71]	2006	Same as Bianchi *et al.*	140 MPa	Same as Bianchi *et al.*	AMESim model by Bianchi *et al.* Complex and simplified models Focused on giving BC for 3D simulations Parametric analysis of geometry of 2 solenoid injectors

Continued on next page

Author	Year	Fuel props.	Max. p_i	Numerical method	Other relevant features
Coppo *et al.* [53]	2007	Isothermal ISO4113 f. of p and T	140 MPa	ODEs: implicit 2^{nd} order PDEs: finite diff. Lax-Friedrichs	Implemented in Simulink Constant p at the inlet Nozzle $C_d = f(Re)$ experimentally measured Silicone moulds for internal geometry
Belmon *et al.* [61]	2009	Adiabatic AMESim data Not validated	140 MPa	Not reported	Complete injection system model in AMESim High temperature changes in the system: 30 K among parts and 30 K after long operations Investigation on improvements to cool down the fuel
Arpaia *et al.* [66]	2010	Isothermal f. of p and T	180 MPa	Not reported	Implemented in AMESim Analysis of the piezoelectric inj. technology
Marcer *et al.* [73]	2010	Not reported	160 MPa	Not reported	AMESim needle model coupled with 3D CFD (EOLE) Rigid body dynamics and constant p at the rail
Altieri and Tonoli [80]	2012	Not reported	-	Not reported	Piezo actuator model with T effects and hysteresis
Keskinen *et al.* [81]	2012	Not reported	140 MPa	Not reported	Implemented in GT-Suite Compared 2 solenoid inj. for heavy-duty and marine engines Measured in-cylinder p used as BC for p_b Giffen-Muraszew-Schmitt flow model
Payri *et al.* [52, 64]	2012	Isothermal Single T $\beta_f = f(p)$ $a_f = f(p)$	180 MPa	Same as earlier	Implemented in AMESim Detailed geometrical and hydraulic characterization Determined $C_d = f(Re)$ and cavitation Influence of fuel properties on solenoid injector Diesel vs biodiesel multiple injection capabilities Mod. proposed to operate injector with biodiesel
Caika *et al.* [67]	2013	Not reported	160 MPa	Not reported	1D/2D/3D integrated model AVL Hydsim + FIRE Bosch piezoelectric injector Comparison among centered vs eccentric needle
Plamondon and Seers [62]	2014	Isothermal f. of p and T	130 MPa	Not reported	Piezo injector model implemented in Matlab Influence of visc. damping coeff. on needle dynamics Multiple injection performance Model improves with variable C_d and fuel props.
Salvador *et al.* [68]	2014	Isothermal f. of p and T	160 MPa	Same as Payri *et al.*	Piezo injector model implemented in AMESim Detailed experimental characterization
Pogulyaev *et al.* [69]	2015	Not reported	160 MPa	D'Alembert method	Piezo injector model implemented in Matlab/Simulink Constant C_d determined with Ansys CFX 3D simulations
Marcic *et al.* [82]	2016	Isothermal Function of p	140 MPa	Runge-Kutta 4^{th} order Variable t step	Pressure fluctuations introduced as an input

Table 3.2: Works on modelling of common-rail injection systems.

3.3 Fuel properties determination

As shown in Section 3.2, several modellers tried to include the values of the fuel properties in their simulations according to the operating conditions of the injection system, even when most of them did not consider their local changes. This points out the need to know the dependency of the fuel properties on the relevant thermodynamic variables (i.e. temperature and pressure). The simulations in this thesis involve the assumption of adiabatic flow with updates on the values of the fuel properties at each location and time step, further emphasizing this need.

The dependency of the fuel properties on the temperature at low pressures has been extensively dealt with in the literature. In general, there exist commercial devices that make it possible to perform measurements on liquid samples at atmospheric pressure. Thanks to these measurements and theoretical derivations, tabulated data and correlations for monocomponent fuels such as alkanes are readily available. Nevertheless, the obtaining of the fuel properties at the high pressure conditions typical of the *common-rail* systems operation offers more difficulties. In the case of pure liquids, theoretical derivations have been carried out to predict them through several methods. For instance, Bell *et al.* [83] used multiparameter Helmholtz-energy-explicit-type formulations to obtain some thermodynamic properties and used correlations for the prediction of other thermophysical properties. However, this kind of approach is not valid for commercial diesel fuels, which consist of a mixture of hydrocarbon chains usually not known beforehand.

The main works available in the literature about the experimental determination of fuel properties at pressures relevant for *common-rail* systems are summarized in Table 3.3 and commented in the present Section. These studies benefit from the principles of high pressure physics established by Bridgman [84], who introduced a special type of seal that allowed to keep devices at high pressure. At first, most works focused on pure substances due to the available data either to calibrate or to validate the measurement methodology. From 2000 onwards, these methodologies started being applied for commercial diesel fuels. As it can be seen, several works have also dealt with biodiesel fuels and blends. It is important to note that the term biodiesel originally denoted esterified rape oil (rapeseed oil methyl ester or RME). Since its esterification improved its properties, this term has been expanded to include esterified fatty acids (FAME -fatty acid methyl ester-, vegetable oils, animal fats and used cooking oils) [85].

Author	Year	Property	Method	Fluid	Max. p [MPa]	T range [K]
Irving and Barlow [86]	1971	Viscosity	Falling cylinder viscometer	Diethylhexyl phthalate	1400	303
Dymond *et al.* [87–89]	1980 to 1985	Viscosity	Falling body viscometer	n-Hexane n-Octane n-Dodecane n-Hexadecane	500	298 to 373
Dandridge and Jackson [90]	1981	Viscosity	Falling body viscometer with LDV	2 polyisobutenes	250	Room T
Kashiwagi and Makita [91]	1982	Viscosity	Torsionally vibrating crystal method	5 alkanes 6 aromatics Cyclohexane	110	298 to 348
Chan and Jackson [92]	1985	Viscosity	Falling body viscometer with LDV	n-Octane n-Decane n-Dodecane n-Tetradecane	250	291
Ye *et al.* [93]	1990	Speed of sound	Ultrasonic cell	n-Decane n-Hexadecane	100	Room T
Ruzicka *et al.* [94]	1991	Heat capacities	Calorimetric methods	18 alkanes	0.1	90 to 500
Saint-guirons *et al.* [95]	1992	Viscosity	Falling body viscometer	9 alkanes	100	293 to 373
Assael *et al.* [96]	1992	Viscosity	Vibrating-wire viscometer	n-Heptane	250	303 to 348
Oliveira and Wakeham [97]	1992	Viscosity	Vibrating-wire viscometer	Toluene n-Pentane n-Hexane n-Octane n-Decane	250	303 to 348
Daridon *et al.* [98]	1998	Speed of sound Density Compressibilities	Ultrasonic cell Oscillating U-tube densimeter (atm. p)	Tridecane system Heptadecane system	150 100	293 to 373
Tat *et al.* [99]	2000	Speed of sound Density Bulk Modulus	Ultrasonic cell	2 diesel fuels 2 biodiesels	35	294
Rodríguez-Antón *et al.* [100]	2000	Speed of sound Density Compressibilities Viscosity	Vibrant tube densimeter	2 biodiesel fuels ISO4113 Test Fluid	140	293 to 353

Continued on next page

Author	Year	Property	Method	Fluid	Max. p [MPa]	T range [K]
Belonenko *et al.* [101]	2000	Density	Micro-pVT apparatus	n-Hexane + n-Hexadecane	500	263 to 333
Ball and Trusler [102]	2001	Speed of sound	Ultrasonic cell	n-Hexane n-Hexadecane	100	298 to 373
Audonnet and Pádua [103]	2001	Density Viscosity	Vibrating-wire instrument	n-Pentane	100	298 to 383
Dauge *et al.* [104]	2001	Viscosity	Falling body viscometer	Methane + Decane	140	293 to 373
Khasanshin *et al.* [105, 106]	2001 to 2003	Speed of sound Density Heat capacities	Ultrasonic cell Theoretical derivation	n-Dodecane	140	293 to 433
Dindar and Kiran [107]	2002	Viscosity	Falling body viscometer	n-Pentane	50	323 to 398
Boehman *et al.* [108]	2004	Bulk Modulus	Viscometer with pycnometer	n-Octadecane 1 diesel fuel 4 biodiesel blends 1 paraffinic	30	311
Caudwell *et al.* [109, 110]	2004 to 2009	Viscosity Density	Vibrating-wire instrument	4 alkanes 3 pure hydrocarbons	200	298 to 473
Dechoz and Rozé [111]	2004	Surface tension	Capillary waves method	Diesel fuel Gasoline n-Heptane	10	298 to 348
Dzida and Prusakiewicz [112]	2008	Speed of sound Density Heat capacity	Ultrasonic cell Oscillating U-tube densimeter Diff. scanning calorimeter	1 diesel fuel 2 biodiesel blends	101	273 to 363
Rodríguez Antón *et al.* [113]	2008	Specific volume Speed of sound Compressibilities	Designed exp. device	1 diesel fuel 1 biodiesel	350	288 to 328
Dávila and Trusler [114]	2009	Speed of sound Density Heat capacity Th. expansivity	Ultrasonic cell Oscillating U-tube densimeter Microcalorimeter (atm. p)	N-methyl-2-pyrrolidinone Methanol	60	298 to 343
Paton and Schaschke [115]	2009	Viscosity	Falling body viscometer	2 diesel fuels 3 biodiesels	140	293
Zeng and Schaschke [116]	2009	Density Viscosity	Falling body viscometer	n-Dodecane	132	Not reported

Continued on next page

Author	Year	Property	Method	Fluid	Max. p [MPa]	T range [K]
Fukui *et al.* [117]	2010	Viscosity	Dynamic Light Scattering	Ethanol + Water	400	Room T
Peleties *et al.* [118, 119]	2010 to 2011	Speed of sound Density Viscosity Heat capacity	Ultrasonic cell Pycnometer (atm. p) Vibrating-wire viscometer	Di-isodecyl phthalate	140	273 to 423
Duncan *et al.* [120, 121]	2010 to 2012	Viscosity	Axially oscilating piston viscometer	1 diesel fuel 5 biodiesel blends	131	283 to 373
Payri *et al.* [122, 123]	2011	Speed of sound Density Bulk Modulus	Propagating wave in a common-rail system	1 diesel fuel 1 arctic fuel 1 biodiesel	180	298 to 343
Aquing *et al.* [124]	2012	Viscosity	Multidimensional gas chromatography Theoretical derivation	12 diesel fuels 2 kerosenes	300	288 to 423
Ndiaye *et al.* [125]	2012	Speed of sound Density Compressibilities Viscosity	Ultrasonic cell Oscillating U-tube densimeter Falling body viscometer	ISO4113 Test Fluid	200	283 to 353
Chorazewski *et al.* [126]	2013	Vapour pressure Thermal expansion Heat capacity Compressibilities	Static apparatus Scanning transitiometry	ISO4113 Test Fluid	200	273 to 463
Nikolic *et al.* [127]	2013	Speed of sound Density	Ultrasonic cell	1 diesel fuel 2 biodiesel blends	160	293
Schaschke *et al.* [128]	2013	Density Viscosity	Micro-pVT device Falling body viscometer	5 diesel fuels	500	298 to 373
Freitas *et al.* [129]	2014	Viscosity	Vibrating-wire viscometer	3 biodiesels	140	293 to 393
Kielczynski *et al.* [130]	2015	Speed of sound Density Compressibilities	Ultrasonic cell	Diacylglycerol oil	210	293 to 323
Armas *et al.* [131]	2016	Bulk modulus Density (atm. p)	Rate of Injection in a common-rail system	1 commercial diesel HVO biodiesel GTL fuel	7.2	290 to 330

Table 3.3: Measurements of fuel properties at high pressure.

3.3.1 Speed of sound

The measurement of the speed of sound in a fluid at atmospheric pressure is easily achievable in any modern laboratory by transmitting a wave through the desired medium. However, its determination for a liquid at high pressures is more challenging. Most authors have made use of ultrasonic cells for this purpose [93, 98, 99, 102, 114, 118, 119, 125, 127, 130]. A sample of this kind of device is shown in Figure 3.1. The strategy consists of transmitting an ultrasonic pulse through a fluid confined in a high-pressure vessel by means of a transducer (normally piezoelectric). Parallel plates located at a known distance from the transducer reflect the echo of this pulse, which returns to the transducer. By recording the time it takes for the pulse to travel to the reflector and return to the transducer, it is possible to compute the speed of sound. A calibration procedure is required to account for variations in the distance among transducer and reflector due to deformations in the container when it is pressurized. An alternative arrangement makes use of two transducers arranged opposite to each other, so that the pulse is transmitted by one of them and received by the other. Locating the ultrasonic cell in a thermostatic bath allows to carry out measurements at controlled temperatures.

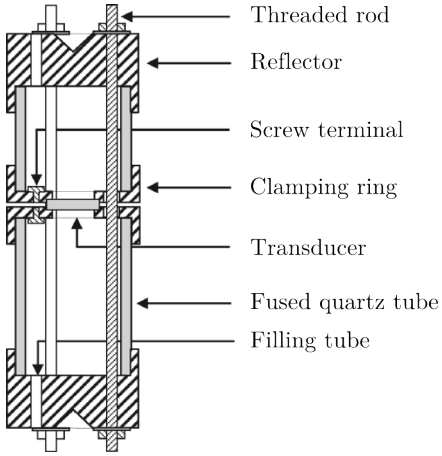

Figure 3.1: Cross-sectional view of an ultrasonic cell [118].

Payri *et al.* [122], on the contrary, took advantage of the pressure wave generated by a *common-rail* injector once it is actuated, and transmitted this wave through a high-pressure line. By measuring the same pressure peak at two different locations along this line, they were able to determine the speed of sound of several diesel and biodiesel fuels. A similar approach has been followed in the present thesis, as it will be explained in Chapter 4.

About the evolution of the speed of sound with the thermodynamic variables, all the authors have reported that it increases with increasing pressures and decreases almost linearly when the temperature increases.

3.3.2 Density

Fuel density has traditionally been measured at atmospheric pressure with hydrometers or pycnometers [118, 119]. More recently, it has also been determined on the basis of the principle of flexural vibration [98, 112, 114]. To do so, a tube bent into a U-shape is filled with a small amount of the fuel under test, as shown in Figure 3.3.2. Vibrations are induced in the tube and the resultant resonant frequency is measured and converted into a density value.

At high pressure, however, this kind of devices is not practical, since their instruments are usually made of glass and not able to bear pressurization stresses. Nevertheless, Ndiaye *et al.* [125] used an oscillating U-tube densimeter equipped with a high pressure cell that made it possible to perform measurements up to 140 MPa.

A number of alternatives is possible if the fluid density at atmospheric pressure is known. Belonenko *et al.* [101] patented a micro-pVT apparatus able to measure densities up to 500 MPa whose application to fuels has been attempted by some authors [101, 128]. It consists of forcing a metal rod through a seal into a closed cylinder containing the liquid. The pressure in the fluid is obtained directly from a pressure sensor within the cell and the volume change is determined from the displacement of the rod. Densities at elevated pressure are calculated from this volume change and the initial volume at atmospheric pressure. Similarly, some viscometers reported in the

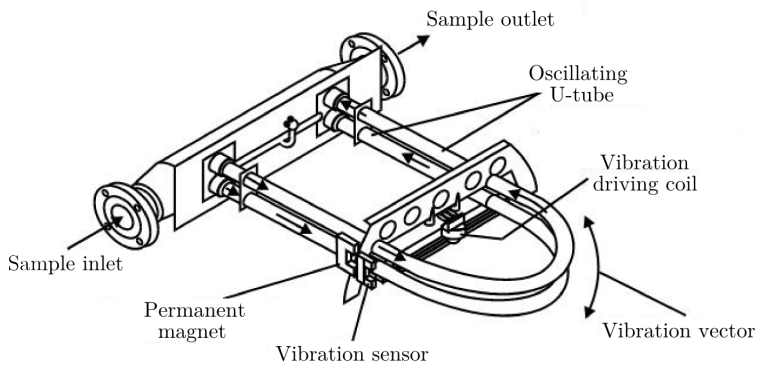

Figure 3.2: Sketch of the oscillating U-tube in a density meter.

literature make use of a cell with variable volume that allows the simultaneous measurement of density and viscosity, as will be presented in Section 3.3.4.

On the other hand, several authors theoretically derived the fuel density at high pressure from speed of sound data considering that the isothermal compressibility coefficient, described by $(\partial\rho/\partial p)_T$, is related to the speed of sound through the specific heat and the thermal expansion coefficient [98, 106, 112, 114, 118, 119, 122, 125] and performing numerical integration of the partial derivative along different isothermal lines. This approach is followed in this thesis and will be explained in more detail in Chapter 4.

Most authors fit the density data to a Tait-like equation, which establishes their dependency on the pressure and temperature:

$$\frac{1}{\rho} - \frac{1}{\rho_0} = C_1(T) \ln\left[\frac{C_2(T) + p}{C_2(T) + p_0}\right] \tag{3.1}$$

where p_0 and ρ_0 are the atmospheric pressure and its corresponding density, respectively, whereas C_1 and C_2 are temperature-dependent coefficients representative of the fluid.

The fuel density has been reported to increase when increasing the pressure and to decrease with growing temperatures.

3.3.3 Bulk modulus

Hayward reviewed the compressibility equations for liquids [132] and established the adequate way to measure its relevant magnitudes, that he determined for water and mercury [133]. A more recent review on the topic was performed by Douhéret *et al.* [134]. The isentropic bulk modulus β_S (hereinafter referred to as *bulk modulus*, β) is defined as the inverse of the isentropic coefficient of compressibility κ_S:

$$\beta_S = \beta = \frac{1}{\kappa_S} = \rho\left(\frac{\partial p}{\partial \rho}\right)_S = \rho a^2 \tag{3.2}$$

Hence, the bulk modulus of a liquid (or its compressibility coefficient) may be obtained directly by combining the speed of sound and density measurements, as several authors have done in the past [98–100, 122, 125, 130].

Alternatively, Boehman *et al.* [108] used a high-pressure viscometer in which they directly measured the change of volume of the fluid with respect to the pressure thanks to the use of a pycnometer tube, thus obtaining $(\partial\rho/\partial p)_S$ to apply Equation (3.2).

More recently, Armas *et al.* [131] estimated the bulk modulus by means of the usual experimental setup to measure fuel injection rates from *common-rail* injection systems.

It has been found that the bulk modulus of diesel fuels increases with the pressure and decreases linearly with the temperature.

3.3.4 Viscosity

For a considerable time, liquid viscosity measurements near ambient conditions have been performed with high precision in a variety of capillary viscometers, as the one illustrated in Figure 3.3(a). Based on the assumption of Poiseuille flow, valid for a capillary (laminar regime and low Re), the viscosity is determined through the observation of the time taken for a defined volume of liquid to flow through the capillary. Even though several designs of pressurized capillary viscometers have been introduced, they have not been generally used for liquid fuels.

Bridgman [84] introduced the high pressure falling body viscometer, through which he measured the viscosities and compressibilities of several lubricants up to 1200 MPa. This instrument was improved by Irving and Barlow [86] and more recent designs have been used by several researchers for the measurement of viscosity at high pressure [87–89, 95, 104, 107, 115, 116, 125, 128]. A sample of this kind of viscometer is shown in Figure 3.3(b). It consists of a vertical tube into which a sample of the pressurized liquid is sealed. A close-fitting sinker with an embedded magnetic core falls through the liquid due to gravity, acquiring a terminal velocity that is a balance among gravitational pull, buoyancy and shear stress within the gap between the sinker and the tube wall. Therefore, the fluid viscosity is inversely proportional to this terminal velocity, which is acquired from the time taken for the sinker to descend a fixed distance down the tube between two detection coils. Similar devices make use of a rotating or an oscillating body instead of a falling one, considering that the viscous torque or the oscillation period, respectively, are proportional to the fluid viscosity.

Other researchers have made use of vibrating-wire viscometers [96, 97, 118, 119, 129]. They consist of a metallic wire (usually tungsen or stainless steel) that is tensioned by a mass suspended from the lower end or clamped between two rigid supports. A current is passed through the tensioned wire, which is forced to move by the action of a permanent magnetic field perpendicular to its length. The decay of the amplitude or velocity of this oscillating movement when the wire is immersed in a viscous medium gives a measure of its

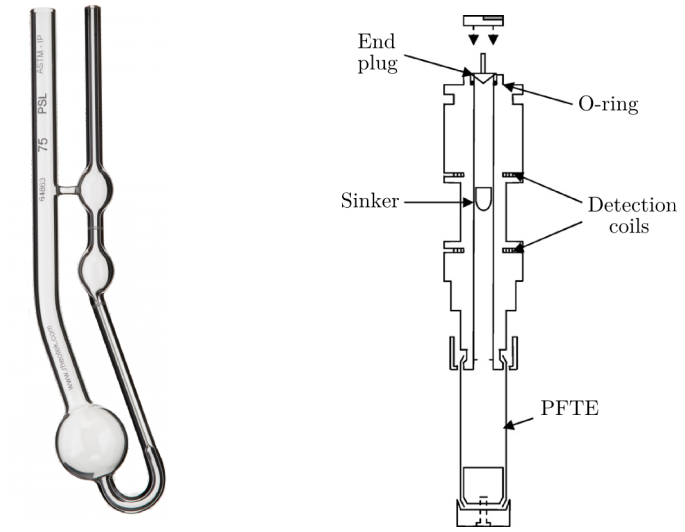

(a) Capillary viscometer (b) Falling body viscometer [115]

Figure 3.3: Sample of devices used for the measurement of fluid viscosity.

viscosity. The development of these devices has allowed to obtain the fluid density simultaneously [103, 109, 110]

Viscosity may also be determined by means of optical techniques, such as LDV [90, 92] or dynamic light scattering [117]. Alternatives involve the determination of the fuel composition and the estimation of the viscosity through theoretical derivations, like Aquing *et al.* [124] did through multidimensional gas chromatography.

The evolution of the viscosity with temperature and pressure has also been traditionally described through Tait-like equations [91]:

$$\ln\left(\frac{\eta}{\eta_0}\right) = C_1\left(T\right)\ln\left[\frac{C_2\left(T\right)+p}{C_2\left(T\right)+p_0}\right] \tag{3.3}$$

where η_0 is the dynamic viscosity at atmospheric pressure and C_1 and C_2 are temperature-dependent coefficients representative of the fluid. Other authors have tried to explain the variation of the viscosity of liquids with respect to the pressure by introducing the so-called *pressure-viscosity coefficient*, that they correlated with the evolution of the viscosity at atmospheric

pressure [135–139]. The most popular expression to explain this behaviour was introduced by Kouzel [140]:

$$\log\left(\frac{\eta}{\eta_0}\right) = \frac{p - p_0}{1000}\left(-1.48 + 5.86\eta_0^{0.181}\right) \tag{3.4}$$

These approaches allow to estimate the viscosity at any pressure and temperature condition if its evolution with the temperature at atmospheric pressure is known, without the need to carry out measurements at high pressure. However, they lead to less accurate results (Equation (3.4) is reported to be reliable up to 138 MPa, with an average error of approximately 10%).

As an example, Figure 3.4 shows the evolution of the viscosity of an ISO4113 Test Fluid with respect to the temperature and pressure. As it can be seen, the viscosity decreases exponentially when the temperature increases, whereas it increases importantly when the pressure increases.

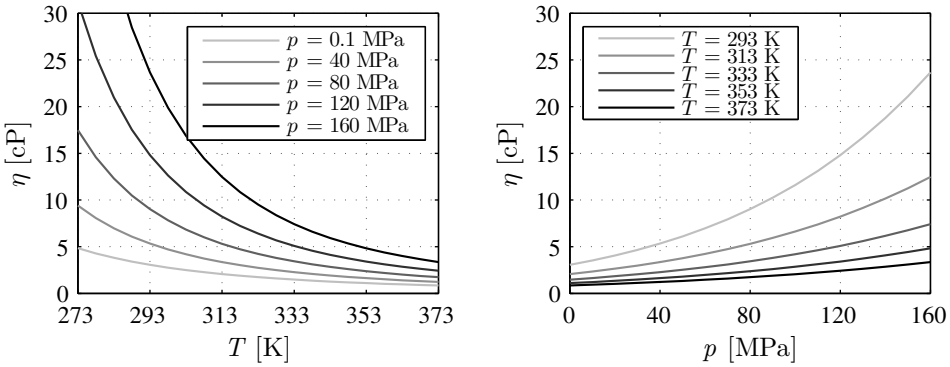

(a) $\eta = f(T)$ (b) $\eta = f(p)$

Figure 3.4: Evolution of the ISO4113 Test Fluid viscosity with the temperature and pressure [125].

3.3.5 Other properties

Effort has also been made to determine other properties of the liquid fuels. However, unlike the fuel speed of sound, density or viscosity, the variations of these other properties with the temperature and pressure have not been found to importantly affect the performance of injection systems. Therefore, the number of studies in this sense is scarce and is generally limited to pure hydrocarbons. Most researchers and modellers assume these results of pure

hydrocarbons to be valid for their studies in complex mixtures, given the low significance of the error comitted through this assumption.

A property that has been given attention to is the specific heat capacity at constant pressure, c_p, which can be determined through calorimeters that allow to measure the heat needed to increase the temperature of a certain fluid volume or mass in one degree. Ruzicka *et al.* [94, 141] reviewed and tabulated the results of variations of heat capacities with respect to the temperature at atmospheric pressure. This work was more recently updated by Zabransky *et al.* [142, 143]. Huang *et al.* analysed the evolution of this thermodynamic variable with the temperature as a function of the carbon chain length for linear and cyclic alkanes. With regard to the variation of c_p with the pressure, some authors use a theoretical derivation to determine $(\partial c_p/\partial p)_T$ by numerically solving a system of equations that also involves $(\partial \rho/\partial p)_T$ for an isothermal line. This procedure is described in detail by Khasanshin *et al.* [106] and other authors that modified the method to solve the system of equations [112, 114, 118].

With regard to the surface tension, Dechoz and Rozé [111] implemented an experimental setup to carry out its measurement on fuels and alkanes at high pressure based on the transmission of capillary waves. These waves are scanned using an He-Ne laser beam focused on the interface.

For more details on the general methods and common apparatus for the measurement of other thermophysical properties of liquids, such as the thermal conductivity, the reader may refer to the work by Leidenfrost [144].

3.4 Fuel properties effect on the injection process

Considering the purpose of this thesis, which aims at the study of the injector flow for a wide range of temperature and pressure conditions, it is interesting to review the works in the literature that have analysed the influence of the fuel properties on the injection process.

This problem has been widely reported in the literature, mainly due to two circumstances that triggered the interest on the field. On the one hand, the problem of cold start and the need to run the engine at low temperatures in some locations requires a deep knowledge of this topic due to the strong influence of temperature on the fuel properties [145]. On the other hand, the irruption of biodiesel as an alternative fuel called for some analysis about the implications of running a CI engine fuelled with this kind of substance. Not in vain, it has been observed that its different compressibility properties may

lead to an advanced injection timing of 1 crank angle degree (CAD) when used in a DI system, consequently increasing NO_x emissions [146–150].

Most works have approached these topics from an experimental point of view. Even though modellers also share these concerns, their main studies have dealt with the assessment of the impact of introducing inaccurate values of the fuel properties into their simulations. This is also a common concern for the attainment of the goals of the present thesis.

3.4.1 Experimental works

The most relevant experimental works about the influence of the fuel properties in operating conditions relevant for *common-rail* injection systems are compiled in Table 3.4. While the works aiming at the investigation of cold start were specifically based on the modification of the fuel temperature, the studies about biodiesel carried out tests with different fuels at the same conditions. This implies that different ranges of variation of the fuel properties have been tested, but their conclusions generally remain the same.

One of the first investigations was performed in 1997 by Chang and Farrell [151], who carried out tests with three different fuels in order to analyse the effect of the viscosity on the diesel spray. The fact that the measurements were only performed at a medium injection pressure made it difficult to extract general conclusions, although a small influence on spray penetration and SMD was detected.

One year later, Desantes *et al.* [152] studied the effect of the fuel density and viscosity on both the internal flow and the spray development by using 7 fuels of varied properties at a given condition. From rate of injection measurements, they concluded that the mass flow rate at steady conditions was linear with the density, as expected, whereas the influence of viscosity was not significant. A dependence with the fuel density was also found for the injection duration and the total mass injected. From the spray observations they did not find a significant influence of the fuel properties on the spray penetration or spreading angle, but a strong influence of the fuel viscosity on the SMD was reported. This influence was attributed to the different Weber numbers achieved at the tested conditions, which could change the atomization regime in extreme cases. The influence was more accused when the needle had not reached its maximum lift.

Similar works were carried out some years later, confirming some of the evidences pointed out by Desantes *et al.* and finding new ones thanks to the investigation of higher fuel viscosities (i.e. lower fuel temperatures). Given

the high volume of studies regarding comparisons among diesel and biodiesel fuels, it is interesting to remark here that, for a given condition of temperature and pressure, biodiesel exhibits a higher density, viscosity, speed of sound and bulk modulus than a standard diesel fuel [122]. The main findings from the works available in the literature, both in terms of internal flow and spray development, are summarized below.

Internal flow

- Rate of injection
  Both the fuel density and fuel viscosity may govern the rate of injection (ROI). The former affects the ROI in a direct way, whereas the latter may control the discharge coefficient of the nozzle orifices through the flow regime defined by the Reynolds number (recall Figure 2.11). For this reason it has been found that, at temperatures greater than room temperature, the ROI generally increases with the biodiesel content in the fuel [153–155], since it is governed by density. However, at low injection pressures, the effects of fuel density and flow regime compensate [155, 156]. On the other hand, for a given fuel, low temperatures lead to a lower ROI, especially at low pressure [157–161]. Even when the fuel density is higher at low temperatures, the low Reynolds numbers induced by both the increased fuel viscosity (recall Figure 3.4) and the low pressure drop across the nozzle orifices are enough to overcome the density effect. For medium injection pressures and above, the pressure drop across the orifice gets high enough to modify the fuel regime and compensate for the fuel temperature effect. Dernotte *et al.* [162–164] established a value of 85 MPa as a general guideline.
- Momentum flux
  Payri *et al.* [158] compared the momentum flux at a low fuel temperature and room fuel temperature. They found a lower momentum flux in the former case, which is also justified from the point of view of the flow regime induced in the nozzle orifices by the high fuel viscosity attained in these conditions (see Table 3.4).
  Other authors that carried out momentum flux measurements like Desantes *et al.* [153, 154] or Salvador *et al.* [155] did not find a significant influence of the fuel properties on the momentum flux at the nozzle orifices outlet. However, their studies focused on comparisons among diesel and biodiesel fuels, whose fuel properties do not importantly differ in the range of temperatures they tested and therefore do not substantially modify the flow regime.

- Injection delay
  Several authors found that biodiesel generates an advance in injection timing [108, 165–167] that is responsible for a higher NO_x generation. Boehman *et al.* [108] attributed this fact to the higher bulk modulus of the biodiesel fuel affecting how the pressure wave generated at the injector inlet is propagated to the injector nozzle. However, this propagation starts once the injector effectively opens and should only affect the timing of subsequent injections. Instead, the fact that the injection delay is lower for biodiesel fuels may be attributed to their higher viscosities, as analysed by Salvador *et al.* [64] through one-dimensional modelling techniques. This can be justified considering the lower flow regime induced in the flow through the control volume orifices. Hence, a higher fuel viscosity results in a lower discharge coefficient of the control orifices, inducing higher pressure losses across them. Therefore, for a given operating condition, the pressure in the control volume drops more abruptly once the injector is energized, leading to an earlier rise of the injector needle.
  Following the previous reasoning, an injection advance would also be expected at low temperature for a given fuel, considering the increase in fuel viscosity when decreasing the fuel temperature. However, several authors reported the opposite trend [158, 160, 161]. Paradoxically, this behaviour is also attributed to fuel viscosity, since it generates forces opposing the control valve and needle lift during the injector opening stage [157, 158, 161]. Again, this effect of fuel viscosity was not reported by the authors that compared diesel and biodiesel fuels given their different range of viscosities tested.
  In addition, some authors expect reduced leakages among movable elements when the fuel viscosity is increased, thus leading to a higher development of the pressure differential needed to discover the nozzle orifices and start the injection [165].
  With all, it seems that it is not possible to establish a universal trend about the injection delay, since it is also affected by the dynamics of the movable elements and, therefore, by the injector technology (i.e. maximum needle lift, direct or indirect actuation, etc.). Therefore, it is not easy to account for all the counteracting effects of the fuel properties on the injection delay beforehand. This fact constitutes an example of the potential of computational modelling techniques when studying the diesel injection process, approach followed in the present thesis in order to explore the injector internal behaviour.

- Injection duration
  The total injection duration for a given energizing time (and the total mass injected, by extension) is also affected by the fuel properties, mainly due to the effect of the fuel viscosity on the friction forces among mechanical elements. However, for the same reasons stated above, authors have found different trends depending on the injector technology. While Kegl and Hribernik [166], Park *et al.* [160] or Wang *et al.* [161] found lower injection durations at low temperature using solenoid operated injectors, Tinprabath *et al.* [156] reported an increase in injection duration for a piezoelectric injector the higher the biodiesel content in the fuel. This same observation was noted by Agarwal *et al.* [150].
- Cavitation
  The relation among fuel properties and cavitation has also been investigated. Suh *et al.* [168] found that, for the same flow rate conditions, biodiesel generated higher critical cavitation numbers. They attributed this finding to the higher viscosity increasing the nozzle wall friction. Vergnes *et al.* [159] also identified the fact that, for the same conditions, n-heptane led to cavitating conditions whereas non-cavitating flow was found for arctic diesel. In addition, Wang *et al.* [161] saw that cavitation intensity diminished at low temperatures. The explanation resides in the fact that the critical cavitation number depends on the Reynolds number [169–171]. In the case of the biodiesel fuel, the higher fuel viscosity results in a lower Reynolds number for a given pressure drop, leading to a lower cavitation intensity in the same operating conditions.
- Multiple injection strategies
  As a consequence of the injection delay findings, the behaviour under multiple injections may also be affected by the fuel properties. Again, the fuel speed of sound and bulk modulus affect the interaction among injections, whereas the fuel viscosity influences the friction forces generated against the injector internal movable elements. Therefore, a different minimum dwell time among the injections is needed to totally split them depending on the fuel properties. This was analysed by Wang *et al.* [161], who noticed a lower interaction among injections the lower the fuel temperature. Low fuel temperatures were also found to lead to lower minimum dwell times to split the injections. This was attributed to the high fuel viscosities induced, which result in a slower needle opening that in turn leads to lower maximum lifts. Hence, the needle falls from a lower position, cutting the injection earlier and letting a new injection begin.

Spray development

- Spray penetration and spreading angle
  Even though Desantes *et al.* did not find a significant influence of the fuel properties on the spray penetration and spreading angle in their first study [152], later studies showed that biodiesel generates a slightly greater spray penetration and lower spreading angle than standard diesel fuel [153–155, 172]. This is attributed to both its higher fuel density and viscosity, as shown independently by Dernotte *et al.* [163, 164]. However, for a given fuel, Payri *et al.* [157, 158] reported shorter penetrations at low temperatures in the transient stage. They analysed that the differences were not justified by the sole effect of fuel density, since the fuel viscosity influence through the flow regime was significant as well due to the low discharge coefficients induced. As it happened for the internal flow studies, this apparent contradiction may be due to the wider range of viscosities involved in the cold start studies, that leads to the fuel viscosity overcoming the effects of fuel density.
- Sauter Mean Diameter (SMD)
  Desantes *et al.* [152] already found a strong dependency of the SMD on the fuel viscosity. This same result has been confirmed later by other authors [150, 164, 172].
- Liquid Length (LL)
  In 2012, Payri *et al.* [173] analysed the effect of the fuel temperature on the diesel spray also in reacting conditions. They found that an increase in fuel temperature led to a lower LL, which is justified by the fact that a lower amount of heat needs to be transferred to the fuel droplets in order to evaporate them than to the ones at low temperature.

Another fuel property that has deserved attention from the researchers is the surface tension. Although obviously relevant in the atomization event, Desantes *et al.* [152–154] have shown that its variability among fuels in the operating range of *common-rail* systems is not large enough for it to attain a significant role in the injection process. This is due to the fact that, as stated in Section 2.4.2, the high pressures achieved in these systems induce the complete atomization regime regardless the fuel surface tension.

Author	**Year**	**Measurement**	**Fuel**	p **range** [MPa]	T_f **range** [K]	ρ **range** [kg/m^3]	ν **range** [mm^2/s]
Chang and Farrell [151]	1997	Rate of Injection Spray visualization	3 diesel fuels	90	Room T	827 to 832	2.33 to 10.39
Desantes *et al.* [152]	1998	Rate of Injection Spray visualization PDA	7 diesel fuels	Not reported	Not reported	787 to 852	2.48 to 7.34
Tat and Van Gerpen [165]	2003	Injection line p	1 diesel fuel 21 biodiesel blends	0.1 to 34.5	293 to 373	790 to 900	Not reported
Boehman *et al.* [108]	2004	Spray visualization	1 diesel fuel 4 biodiesel blends 2 paraffinic fuels	0.1 to 30	310	Not reported	Not reported
Kegl and Hribernik [166, 167]	2008	Rate of Injection	1 diesel fuel 4 biodiesel blends	0.1 to 60	258 to 293	810 to 896	Not reported
Suh *et al.* [168]	2008	Flow visualization	1 diesel, 1 biodiesel	Not reported	293	823 to 872	4.25 to 6.88
Payri *et al.* [123, 157, 158]	2009	Rate of Injection Momentum flux Spray visualization	1 winter diesel	30 to 180	255 to 298	823 to 851	3.44 to 13.64
Desantes *et al.* [153, 154]	2009	Rate of Injection Momentum flux Spray visualization	1 diesel fuel 2 biodiesel blends	30 to 160	Room T	831 to 879	2.38 to 4.47
Vergnes *et al.* [159]	2009	Rate of Injection	2 alkanes 1 arctic diesel	25 to 120	253 to 293	684 to 870	0.73 to 20.69
Wang *et al.* [172]	2010	Spray visualization	1 diesel fuel 2 biodiesels	100 to 300	Room T	830 to 885	3.36 to 5.53
Dernotte *et al.* [162–164]	2012	Rate of Injection Spray visualization	2 alkanes 5 diesel fuels	30 to 180	Room T	660 to 875	0.5 to 7.3
Payri *et al.* [173]	2012	Spray visualization	n-dodecane	50 to 150	331 to 391	677 to 722	0.43 to 0.83
Salvador *et al.* [155]	2013	Rate of Injection Momentum flux Spray visualization	3 biodiesel blends	30 to 160	288 to 323	831 to 879	2.38 to 4.47
Agarwal *et al.* [150]	2015	Rate of Injection PDPA Single cylinder eng.	1 diesel fuel 4 biodiesel blends	30 to 100	293	831 to 881	2.78 to 4.42
Park *et al.* [160]	2015	Rate of Injection Spray visualization	1 winter diesel	30 to 100	243 to 313	800 to 850	2.3 to 23
Tinprabath [156]	2015	Rate of Injection	5 fuels	30 to 60	265 to 293	835 to 900	4.23 to 19.72
Wang *et al.* [161]	2015	Rate of Injection	Winter diesel	35 to 100	255 to 298	Not studied	2.51 to 6.63

Table 3.4: Experiments on the influence of the fuel properties on DI systems.

3.4.2 Computational works

Most of the works that have been referred in Section 3.4.1 did not account for the variation of the fuel properties with the high pressures involved in *common-rail* systems, and only considered them at ambient pressure when drawing conclusions. Modellers have tried to account for this consideration and confirm the observations gathered in the experiments.

In 2009, Boudy and Seers [174] took profit of the 1D injector model implemented by Payri *et al.* in 2004 [50, 51] to explore the impact of the biodiesel properties on the injection process by comparing its ROI with the one obtained with the ISO4113 test fluid. They analysed the behaviour under multiple injections at room temperature, by having a look at the synchronization among the pressure wave and the injector activation (which may generate different instantaneous pressures at the nozzle in the moment of the injection), the friction coefficient established according to the Moody chart and the amplitude of the pressure wave transmitted along the injector, which depends on this friction coefficient. They concluded that an increase in fuel density or bulk modulus affects the post injections due to the effect of the pressure waves generated by the main injection. The fuel viscosity was not reported to play a major role in their analysis, probably due to the relatively low range of variation explored for this parameter.

Later, between 2010 and 2012, Som *et al.* [175, 176] used CFD tools to analyse the three-dimensional behaviour of the nozzle internal flow and spray development depending on whether diesel or biodiesel was used. They found that, for the same conditions, biodiesel led to lower cavitation intensity than diesel, fact also confirmed by Salvador *et al.* [177] as seen in Figure 3.5. It also led to a lower discharge coefficient, attributed to the higher losses at the near-wall region induced by the higher fuel viscosity. The potential of the numerical tool was utilized to obtain further results not achievable by experimental approaches, such as the fact that biodiesel leads to lower injection velocity and turbulence at the orifice outlet. With regard to the spray behaviour, Som *et al.* found that biodiesel led to slightly higher fuel penetrations and lower spreading angles than regular diesel, in accordance to the observations made by experimentalists (Section 3.4.1). They also reported a higher liquid length for biodiesel. For this reason, they proposed to increase the injection fuel temperature about 60 K when using this kind of fuel so as to reduce its liquid length (as according to Payri *et al.* [173]) and approach its atomization behaviour to the one of diesel fuel.

Among 2012 and 2014, Theodorakakos *et al.* [178, 179] started considering the influence of the fuel properties due to pressurization. In their study of

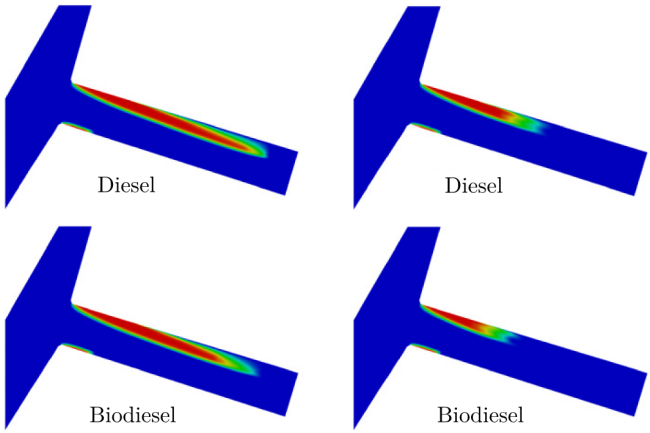

(a) $p_b = 17\,\text{MPa}$ (b) $p_b = 18\,\text{MPa}$

Figure 3.5: Vapour field comparison among diesel and biodiesel (p_i = 80 MPa) [177].

internal flow with fixed needle lift, a comparison among the assumptions of isothermal flow, adiabatic flow and flow considering heat exchange with the surroundings was carried out. They found that the friction heating close to the nozzle walls leads to a lower fuel viscosity, thus increasing the nozzle discharge coefficient and the mass flow rate through it. Only an initial inlet fuel temperature of 353 K was considered. This work has been complemented by Strotos *et al.* [180, 181], who included the variable needle lift and saw that cavitation may also lead to a local cooling.

Shi *et al.* [182] also investigated the effect of the fuel properties on the internal flow and the spray behaviour of a cylindrical and a conical nozzle at injection pressures up to 200 MPa and temperature ranges among 316 and 403 K. In this case, they coupled an AMESim 1D model of a Delphi DFI 1.20 injector to a 3D CFD code for the nozzle internal flow and another 3D code for the spray. In their work, supported by experiments, they also performed simulations with fuel properties that were modified at each location and every time step according to the local conditions of temperature and pressure. These simulations were compared to the assumptions of isothermal flow and properties not modified by the pressure. They found that, especially in the case of the cylindrical nozzle, the behaviour of the discharge coefficient with respect to the Reynolds number was not properly reproduced unless variable fuel properties were considered.

3.5 Conclusions about the current state of knowledge

An extensive review of the existing works regarding computational modelling of injection systems has been performed. As a result, it has been noticed that most modellers assume the flow along the system as isothermal, whereas only a few researchers have implemented a local variation of the fuel temperature and pressure. However, attention has never been paid to the assessment of the extension of the validity of the temperature changes derived from the assumption of adiabatic flow, which may not hold under some real circumstances. For instance, conditions with important pressure gradients among the fuel and the ambient or injections at low pressure that result in low flow velocities and higher residence times of the fuel particles in the injector may favour the heat exchange with the surroundings. Efforts should then be placed on establishing the boundaries on which these effects start gaining significance.

In any case, it has been seen that the local changes in both fuel temperature and pressure are expected to induce important variations in the fuel properties relevant for the injection process, namely speed of sound, density, bulk modulus and viscosity. The consideration of these variations implies a need to correctly measure or estimate them. In this regard, a review on the most commonly used techniques for the experimental measurement of the thermodynamic properties at a wide range of temperatures and pressures has been carried out. With these studies in mind, the measurement of the speed of sound, density and bulk modulus at the conditions relevant for a *common-rail* injector operation was performed as part of the present thesis, whereas the viscosity at high pressure was estimated. These topics will be dealt with in Chapter 4.

Indeed, the knowledge of the correct fuel properties depending on the operating condition is deemed to be crucial for the understanding of the diesel injection process. As reviewed, numerous authors have found a strong influence of the fuel properties on the internal flow (rate of injection, momentum flux, cavitation pattern and appearance, injection delay and duration, etc.) and spray development (spray penetration, spreading angle, droplet size, liquid core length, etc.), especially at very low temperatures. The injector technology has also been found to affect the way in which the fuel properties influence the injection process. In this sense, the injector object of study in the present thesis (Bosch CRI 2.20) remains in ballistic operation for most of the injection event. Hence, the effects of the fuel viscosity on its opening and closing stages are expected to be magnified, and consequently its local variations should not be neglected.

References

[1] ALLIÉVI, L. and DUBS, R. *Allgemeine Theorie über die veränderliche Bewegung des Wassers in Leitungen*. Ed. by R. DUBS and V. BATAILLARD. Berlin, Heidelberg: Springer Berlin Heidelberg, 1909. ISBN: 978-3-642-51953-6. DOI: 10.1007/978-3-642-52015-0.

[2] DEJUHASZ, K. J. "Graphical analysis of transient phenomena in linear flow". *Journal of the Franklin Institute*, vol. 223.5 (1937), pp. 643–654. ISSN: 00160032. DOI: 10.1016/S0016-0032(37)91917-3.

[3] KNIGHT, B. E. "Fuel-Injection system calculations". *Proceedings of the Institution of Mechanical Engineers, Automobile Division*, vol. 14.1 (1960), pp. 25–33. ISSN: 0367-8822. DOI: 10.1243/PIME_AUTO_1960_000_009_02.

[4] BROWN, G. W. and MCCALLION, H. "Simulation of an injection system with delivery pipe cavitation using a digital computer". *Proceedings of the Institution of Mechanical Engineers, Conference Proceedings*, vol. 182.12 (1967), pp. 206–216. ISSN: 0367-8849. DOI: 10.1243/PIME_CONF_1967_182_374_02.

[5] BECCHI, G. A. "Analytical Simulation of Fuel Injection in Diesel Engines". *SAE Technical Paper 710568* (1971). DOI: 10.4271/710568.

[6] FICARELLA, A., LAFORGIA, D., and CIPOLLA, G. "Investigation and Computer Simulation of Diesel Injection System With Rotative Pump". *Journal of Engineering for Gas Turbines and Power*, vol. 112.3 (1990), pp. 317–323. ISSN: 07424795. DOI: 10.1115/1.2906497.

[7] WYLIE, E. B., BOLT, J. A., and EL-ERIAN, M. F. "Diesel Fuel Injection System Simulation and Experimental Correlation". *SAE Technical Paper 710569* (1971). DOI: 10.4271/710569.

[8] EL-ERIAN, M. F., WYLIE, E. B., and BOLT, J. A. "Analysis and Control of the Transient Flow in the Diesel Injection System. Part I - The Analytical Control Method.pdf". *SAE Technical Paper 730661* (1973). DOI: 10.4271/730661.

[9] EL-ERIAN, M. F., WYLIE, E. B., and BOLT, J. A. "Analysis and Control of the Transient Flow in the Diesel Injection System. Part II - Design Results of Controlled After-Injection". *SAE Technical Paper 730662* (1973). DOI: 10.4271/730662.

[10] EL-ERIAN, M. F. "Simulation and control of transient flow in the diesel injection system". PhD thesis. University of Michigan, 1972.

[11] Onorati, A. "Prediction of the Acoustical Performances of Muffling Pipe Systems by the Method of Characteristics". *Journal of Sound and Vibration*, vol. 171.3 (1994), pp. 369–395. issn: 0022460X. doi: 10.1006/jsvi.1994.1127.

[12] Kumar, K., Gaur, R. R., Garg, R. D., and Gajendra Babu, M. K. "A Finite Difference Scheme for the Simulation of a Fuel Injection System". *SAE Technical Paper 831337* (1983). doi: 10.4271/831337.

[13] Moreno, E. "Contribución a la simulación del sistema de inyección de combustible de un motor diesel de inyección indirecta". PhD thesis. Universidad Politécnica de Madrid, 1999. isbn: 8482402609.

[14] Kiijärvi, J. "Diesel fuel injection system simulation". PhD thesis. Helsinki University of Technology, 2003. isbn: 9512266571.

[15] Yamaoka, K. and Saito, A. "Computer Technique for Evaluation of Cavitation Characteristics of Certain Phases of Fuel Injection in Fuel Injection System". *SAE Technical Paper 730663* (1973). doi: 10.4271/730663.

[16] Goyal, M. "Modular Approach to Fuel Injection System Simulation". *SAE Technical Paper 780162* (1978). doi: 10.4271/780162.

[17] Sobel, D. R. and Lehrach, R. P. C. "A Hydro-Mechanical Simulation of Diesel Fuel Injection Systems". *SAE Technical Paper 870432* (1987). doi: 10.4271/870432.

[18] Fairbrother, R. J. "Computer Simulation of Fuel Injection for Direct-Injection Diesel Engines". PhD thesis. Imperial College London, 1994.

[19] Matsuoka, S., Yokota, K., Kamimoto, T., and Igoshi, M. "A Study of Fuel Injection Systems in Diesel Engines". *SAE Technical Paper 760551* (1976). doi: 10.4271/760551.

[20] Arcoumanis, C., Gavaises, M., Yamanishi, M., and Oiwa, J. "Application of a FIE Computer Model to an In-Line Pump-Based Injection System for Diesel Engines". *SAE Technical Paper 970348* (1997). doi: 10.4271/970348.

[21] Wannenwetsch, P. and Egler, W. "A User-Friendly Program System for Digital Simulation of Hydraulic Equipment". *SAE Technical Paper 850532* (1985). doi: 10.4271/850532.

[22] ARCOUMANIS, C. and FAIRBROTHER, R. J. "Computer Simulation of Fuel Injection Systems for DI Diesel Engines". *SAE Technical Paper 922223* (1992). DOI: 10.4271/922223.

[23] ARCOUMANIS, C., GAVAISES, M., BOSTOCK, P. G., and HORROCKS, R. W. "Evaluation of Pump Design Parameters in Diesel Fuel Injection Systems". *SAE Technical Paper 950078* (1995). DOI: 10.4271/950078.

[24] MARCIC, M. and KOVACIC, Z. "Computer Simulation of the Diesel Fuel Injection System". *SAE Technical Paper 851583* (1985). DOI: 10.4271/851583.

[25] CATANIA, A. E., DONGIOVANNI, C., MITTICA, A., NEGRI, C., and SPESSA, E. "Study of Automotive Diesel Injection-System Dynamics Under Control". *SAE Technical Paper 962020* (1996). DOI: 10.4271/962020.

[26] RODRÍGUEZ-ANTÓN, L. M. "Simulación de sistemas de inyección Diesel mediante la técnica del Bond Graph". PhD thesis. Universidad Politécnica de Madrid, 1996.

[27] YAMAOKA, K., SAITO, A., ABE, N., and OKAZAKI, M. "Analysis of Bypass Control Fuel Injection Systems for Small Diesel Engines by Digital Computer". *SAE Technical Paper 730664* (1973). DOI: 10.4271/730664.

[28] MARCIC, M. "Computer Simulation of the Diesel Fuel Injection Nozzle". *SAE Technical Paper 930925* (1993). DOI: 10.4271/930925.

[29] MARCIC, M. "Calculation of the Diesel Fuel Injection Parameters". *SAE Technical Paper 952071* (1995). DOI: 10.4271/952071.

[30] MUÑOZ, A. "Análisis y Simulación de los Sistemas de Inyección de Combustible de los Motores Diesel Equipados con Bomba en Línea". PhD thesis. Universidad Politécnica de Madrid, 1987.

[31] FICARELLA, A. and LAFORGIA, D. "Contribution To The Simulation Of Injection System For Reciprocating Internal Combustion Engines". *SAE Technical Paper 885016* (1988). DOI: 10.4271/885016.

[32] FICARELLA, A. and LAFORGIA, D. "Injection characteristics simulation and analysis in Diesel engines". *Meccanica*, vol. 28.3 (1993), pp. 239–248. ISSN: 0025-6455. DOI: 10.1007/BF00989127.

[33] CATANIA, A. E., DONGIOVANNI, C., and MITTICA, A. "Implicit Numerical Model of a High-Pressure Injection System". *Journal of Engineering for Gas Turbines and Power*, vol. 114.3 (1992), pp. 534–543. ISSN: 07424795. DOI: 10.1115/1.2906622.

[34] Catania, A. E., Dongiovanni, C., Mittica, A., Badami, M., and Lovisolo, F. "Numerical Analysis Versus Experimental Investigation of a Distributor-Type Diesel Fuel-Injection System". *Journal of Engineering for Gas Turbines and Power*, vol. 116.4 (1994), pp. 814–830. issn: 07424795. doi: 10.1115/1.2906890.

[35] Kegl, B. "An Improved Mathematical Model of Conventional FIE Processes". *SAE Technical Paper 950079* (1995). doi: 10.4271/950079.

[36] Rakopoulos, C. and Hountalas, D. "A simulation analysis of a DI diesel engine fuel injection system fitted with a constant pressure valve". *Energy Conversion and Management*, vol. 37.2 (1996), pp. 135–150. issn: 01968904. doi: 10.1016/0196-8904(95)00176-E.

[37] Gu, F. and Ball, A. D. "Diesel injector dynamic modelling and estimation of injection parameters from impact response Part 1: modelling and analysis of injector impacts". *Proceedings of the Institution of Mechanical Engineers, Part D: Journal of Automobile Engineering*, vol. 210.44 (1996), pp. 293–302. issn: 0954-4070. doi: 10.1243/PIME_PROC_1996_210_276_02.

[38] Gu, F., Ball, A. D., and Rao, K. K. "Diesel injector dynamic modelling and estimation of injection parameters from impact response part 2: prediction of injection parameters from monitored vibration". *Proceedings of the Institution of Mechanical Engineers, Part D: Journal of Automobile Engineering*, vol. 210.44 (1996), pp. 303–312. issn: 0954-4070. doi: 10.1243/PIME_PROC_1996_210_277_02.

[39] Palomar, J. M. and Ruiz, J. J. "Análisis y Predicción del Comportamiento de una Bomba de Inyección Rotativa en Función de las Actuaciones Sobre Sus Parámetros Fundamentales". *Anales de Ingeniería Mecánica*, vol. 11.1 (1997), pp. 143–150.

[40] Digesu, P., Ficarella, A., Laforgia, D., Bruni, G., and Ricco, M. "Diesel Electro-injector: A Numerical Simulation Code". *SAE Technical Paper 940193* (1994). issn: 07424795. doi: 10.1115/1.2815466.

[41] Digesu, P. and Laforgia, D. "Diesel Electro-injector: A Numerical Simulation Code". *Journal of Engineering for Gas Turbines and Power*, vol. 117.4 (1995), pp. 792–798. issn: 07424795. doi: 10.1115/1.2815466.

[42] AMOIA, V., FICARELLA, A., and LAFORGIA, D. "A Theoretical Code to Simulate the Behavior of an Electro-injector for Diesel Engines and Parametric Analysis". *SAE Technical Paper 970349* (1997). DOI: 10.4271/970349.

[43] FICARELLA, A., LAFORGIA, D., and LANDVISCINA, V. "Evaluation of Instability phenomena in a common rail injection system for high speed Diesel engines". *SAE Technical Paper 1999-01-0192*, 724 (1999). DOI: 10.4271/1999-01-0192.

[44] BIANCHI, G. M., PELLONI, P., FILICORI, F., and VANNINI, G. "Optimization of the Solenoid Valve Behavior in Common-Rail Injection Systems". *SAE Technical Paper 2000-01-2042* (2000). DOI: 10.4271/2000-01-2042.

[45] KISS, T. and WOLVERTON, M. A. "Analytical Comparison of 2 and 3 Way Digital Valves for Use on Direct Needle Control Fuel Injectors". *SAE Technical Paper 2004-01-0032* (2004). DOI: 10.4271/2004-01-0032.

[46] DESANTES, J. M., ARRÈGLE, J., and RODRÍGUEZ, P. J. "Computational model for simulation of Diesel Injection systems". *SAE Technical Paper 1999-01-0915* (1999). DOI: 10.4271/1999-01-0915.

[47] LEE, J. H., CHO, S., LEE, S. Y., and BAE, C. "Bouncing of the diesel injector needle at the closing stage". *Proceedings of the Institution of Mechanical Engineers, Part D: Journal of Automobile Engineering*, vol. 216.8 (2002), pp. 691–700. ISSN: 0954-4070. DOI: 10.1177/095440700221600807.

[48] BIANCHI, G. M., FALFARI, S., PAROTTO, M., and OSBAT, G. "Advanced modeling of common rail injector dynamics and comparison with experiments". *SAE Technical Paper 2003-01-0006* (2003). DOI: 10.4271/2003-01-0006.

[49] BIANCHI, G. M., FALFARI, S., BRUSIANI, F., and PELLONI, P. "Advanced Modelling of a New Diesel Fast Solenoid Injector and Comparison with Experiments". *SAE Technical Paper 2004-01-0019* (2004). DOI: 10.4271/2004-01-0019.

[50] PAYRI, R., CLIMENT, H., SALVADOR, F. J., and FAVENNEC, A. G. "Diesel Injection System Modelling. Methodology and Application for a First-generation Common Rail System". *Proceedings of the Institution of Mechanical Engineers, Part D: Journal of Automobile Engineering*, vol. 218.1 (2004), pp. 81–91. ISSN: 0954-4070. DOI: 10.1243/095440704322829191.

[51] Payri, R., Tormos, B., Salvador, F., and Plazas, A. "Using one-dimensional modelling codes to analyse the influence of diesel nozzle geometry on injection rate characteristics". *International Journal of Vehicle Design*, vol. 38.1 (2005), p. 58. issn: 0143-3369. doi: 10.1504/IJVD.2005.006605.

[52] Payri, R., Salvador, F. J., Marí-Aldaraví, P., and Martínez-López, J. "Using one-dimensional modeling to analyze the influence of the use of biodiesels on the dynamic behavior of solenoid-operated injectors in common rail systems: Detailed injection system model". *Energy Conversion and Management*, vol. 54.1 (2012), pp. 90–99. issn: 01968904. doi: 10.1016/j.enconman.2011.10.007.

[53] Coppo, M. and Dongiovanni, C. "Experimental Validation of a Common-Rail Injector Model in the Whole Operation Field". *Journal of Engineering for Gas Turbines and Power*, vol. 129.2 (2007), pp. 596–608. issn: 07424795. doi: 10.1115/1.2432889.

[54] Arcoumanis, C., Gavaises, M., Abdul-Wahab, E., and Moser, V. "Modeling of Advanced High-Pressure Fuel Injection Systems for Passenger Cars Diesel Engines". *SAE Technical Paper 1999-01-0910* (1999). doi: 10.4271/1999-01-0910.

[55] Catalano, L. A., Tondolo, V. A., and Dadone, A. "Dynamic rise of pressure in the common-rail fuel injection system". *SAE Technical Paper 2002-01-0210* (2002). doi: 10.4271/2002-01-0210.

[56] Catania, A. E., Ferrari, A., Manno, M., and Spessa, E. "Thermal Effect Simulation in High-Pressure Injection System Transient Flows". *SAE Technical Paper 2004-01-0532* (2004). doi: 10.4271/2004-01-0532.

[57] Catania, A. E., Ferrari, A., and Spessa, E. "Temperature variations in the simulation of high-pressure injection-system transient flows under cavitation". *International Journal of Heat and Mass Transfer*, vol. 51 (2008), pp. 2090–2107. issn: 00179310. doi: 10.1016/j.ijheatmasstransfer.2007.11.032.

[58] Catania, A. E., Ferrari, A., and Manno, M. "Development and Application of a Complete Multijet Common-Rail Injection-System Mathematical Model for Hydrodynamic Analysis and Diagnostics". *Journal of Engineering for Gas Turbines and Power*, vol. 130.6 (2008), p. 062809. issn: 07424795. doi: 10.1115/1.2925679.

[59] SEYKENS, X., SOMERS, L., and BAERT, R. "Modelling of common rail fuel injection system and influence of fluid properties on process". *In: Proceedings of VAFSEP, Dublin, Ireland; July 6-9,* July (2004), pp. 6–9.

[60] SEYKENS, X. and SOMERS, L. "Detailed modeling of common rail fuel injection process". *Journal of Middle European* (2005), pp. 30–39.

[61] BELMON, L., GONARD, R., and CLARENC, P. "Simulation of Thermal Behaviour of Closed Loop Common Rail Injection Systems". *Diesel- und Benzindirekteinspritzung V*. Ed. by H. TSCHOKE. Essen: Haus der Technik, 2009. Chap. 6. ISBN: 978-3-8169-2867-6.

[62] PLAMONDON, E. and SEERS, P. "Development of a simplified dynamic model for a piezoelectric injector using multiple injection strategies with biodiesel/diesel-fuel blends". *Applied Energy*, vol. 131 (2014), pp. 411–424. ISSN: 03062619. DOI: 10.1016/j.apenergy.2014.06.039.

[63] BIANCHI, G. et al. "Numerical Investigation of Critical Issues in Multiple-Injection Strategy Operated by a New CR Fast-Actuation Solenoid Injector". *SAE Technical Paper 2005-01-1236* (2005). DOI: 10.4271/2005-01-1236.

[64] SALVADOR, F. J., GIMENO, J., DE LA MORENA, J., and CARRERES, M. "Using one-dimensional modeling to analyze the influence of the use of biodiesels on the dynamic behavior of solenoid-operated injectors in common rail systems: Results of the simulations and discussion". *Energy Conversion and Management*, vol. 54.1 (2012), pp. 122–132. ISSN: 01968904. DOI: 10.1016/j.enconman.2011.10.007.

[65] PLAZAS, A. H. "Modelado unidimensional de inyectores common-rail Diesel". PhD thesis. Valencia: Universitat Politècnica de València, 2005.

[66] ARPAIA, A., CATANIA, A., FERRARI, A., and SPESSA, E. "Development and Application of an Advanced Numerical Model for CR Piezo Indirect Acting Injection Systems". *SAE Technical Paper 2010-01-1503* (2010). DOI: 10.4271/2010-01-1503.

[67] CAIKA, V., SAMPL, P., and GREIF, D. "Integrated 1D/2D/3D Simulation of Fuel Injection and Nozzle Cavitation". *SAE Technical Paper 2013-24-0006*, vol. 2013-24-00 (2013), pp. 1544–1552. ISSN: 19463936. DOI: 10.4271/2013-24-0006.

[68] Salvador, F. J., Plazas, A. H., Gimeno, J., and Carreres, M. "Complete modelling of a piezo actuator last-generation injector for diesel injection systems". *International Journal of Engine Research*, vol. 15.1 (2014), pp. 3–19. issn: 1468-0874. doi: 10.1177/1468087412455373.

[69] Pogulyaev, Y., Baitimerov, R., and Rozhdestvenskii, Y. "Detailed Dynamic Modeling of Common Rail Piezo Injector". *Procedia Engineering*, vol. 129 (2015), pp. 93–98. issn: 18777058. doi: 10.1016/j.proeng.2015.12.014.

[70] Rodriguez, P. "Modelado del comportamiento hidrodinámico de sistemas de inyección directa Diesel". PhD thesis. Valencia: Universitat Politècnica de València, 2001.

[71] Falfari, S. et al. "Assessment of a Simplified Model of Common Rail Injector for Getting Proper Boundary Conditions for 3D Simulations of the Combustion Process in HSDI Diesel Engines". *61 Congresso Nazionale ATI - Perugia 12-15 Settembre 2006*. 2006, pp. 3–7.

[72] Martínez López, J. "Estudio computacional de la influencia del levantamiento de aguja sobre el flujo interno y el fenómeno de la cavitación en toberas de inyección diésel". PhD thesis. Valencia (Spain): Universitat Politècnica de València, 2013. doi: 10.4995/Thesis/10251/29291.

[73] Marcer, R. et al. "Coupling 1D System AMESim and 3D CFD EOLE models for Diesel Injection Simulation Renault". *ILASS - Europe 2010, 23rd Annual Conference on Liquid Atomization and Spray Systems*. September. 2010, pp. 1–10.

[74] Favennec, A. G. "Analyse d'un Système d'Injection Directe Diesel de Type Common Rail". PhD thesis. Université de Lyon, 1999.

[75] Bianchi, G. M., Falfari, S., Pelloni, P., Filicori, F., and Milani, M. "A Numerical and Experimental Study Towards Possible Improvements of Common Rail Injectors". *SAE Technical Paper 2002-01-0500* (2002). doi: 10.4271/2002-01-0500.

[76] Bianchi, G., Falfari, S., Pelloni, P., Kong, S.-C., and Reitz, R. D. "Numerical Analysis of High-Pressure Fast-Response Common Rail Injector Dynamics". *SAE Technical Paper 2002-01-0213* (2002). doi: 10.4271/2002-01-0213.

[77] Gullaksen, J. "Simulation of Diesel Fuel Injection Dynamics Using MATLAB". *SAE Technical Paper 2004-01-2966* (2004). doi: 10.4271/2004-01-2966.

[78] MULEMANE, A. et al. "Comparing cavitation in Diesel injectors based on different modeling approaches". *SAE Technical Paper 2004-01-0027* (2004). DOI: 10.4271/2004-01-0027.

[79] CATANIA, A. E. and FERRARI, A. "Advanced Mathematical Modeling of Electronic Unit-Injector Systems for Heavy Duty Diesel Engine Application". *SAE International Journal of Commercial Vehicles*, vol. 1.1 (2008), pp. 134–151. ISSN: 1946391X. DOI: 10.4271/2008-01-1195.

[80] ALTIERI, L. and TONOLI, A. "Piezoelectric Injectors for Automotive Applications: Modeling and Experimental Validation of Hysteretic Behavior and Temperature Effects". *Journal of Dynamic Systems, Measurement, and Control*, vol. 135.1 (2012), p. 011005. ISSN: 0022-0434. DOI: 10.1115/1.4006627.

[81] KESKINEN, K., KAARIO, O., TILLI, A., HULKKONEN, T., and LARMI, M. "Improving the Accuracy of 1-D Fuel Injection Modeling". *SAE Technical Paper 2012-01-1256* (2012). DOI: 10.4271/2012-01-1256.

[82] MARCIC, S., MARCIC, M., and PRAUNSEIS, Z. "Computer Simulation of the Common Rail Accumulator Fuel-Injection System". *Journal of Mechanical and Automobile Engineering*, vol. 1.1 (2016), pp. 1–15.

[83] BELL, I. H., WRONSKI, J., QUOILIN, S., and LEMORT, V. "Pure and pseudo-pure fluid thermophysical property evaluation and the open-source thermophysical property library coolprop". *Industrial and Engineering Chemistry Research*, vol. 53.6 (2014), pp. 2498–2508. ISSN: 08885885. DOI: 10.1021/ie4033999.

[84] BRIDGMAN, P. W. *The physics of high pressure*. Dover Publications, 1931. ISBN: 9780486627120.

[85] MOLLENHAUER, K. and TSCHOKE, H. *Handbook of Diesel Engines*. Ed. by K. MOLLENHAUER and H. TSCHÖKE. 1st ed. Berlin, Heidelberg: Springer Berlin Heidelberg, 2010, p. 636. ISBN: 978-3-540-89082-9. DOI: 10.1007/978-3-540-89083-6.

[86] IRVING, J. B. and BARLOW, A. J. "An automatic high pressure viscometer". *Journal of Physics E: Scientific Instruments*, vol. 4.3 (1971), pp. 232–236. ISSN: 0022-3735. DOI: 10.1088/0022-3735/4/3/017.

[87] DYMOND, J. H., YOUNG, K. J., and ISDALE, J. D. "Transport properties of nonelectrolyte liquid mixtures-II. Viscosity coefficients for the n-hexane + n-hexadecane system at temperatures from 25 to 100°C at pressures up to the freezing pressure or 500 MPa". *International Journal of Thermophysics*, vol. 1.4 (1980), pp. 345–373. ISSN: 0195928X. DOI: 10.1007/BF00516563.

[88] Dymond, J. H., Robertson, J., and Isdale, J. D. "Transport Properties of Nonelectrolyte Liquid Mixtures - III. Viscosity Coefficients for the n-Octane + n-Dodecane and Equimolar Mixtures of n-Octane + n-Dodecane and n-Hexane + n-Dodecane from 25 to 100°C at Pressures up to the Freezing Pressure or 500 M". *International Journal of Thermophysics*, vol. 2.2 (1981), pp. 133–154. ISSN: 0195928X.

[89] Dymond, J. H., Glen, N. F., and Isdale, J. D. "Transport properties of nonelectrolyte liquid mixtures-VII. Viscosity coefficients for isooctane and for equimolar mixtures of isooctane + n-octane and isooctane + n-dodecane from 25 to 100??C at pressures up to 500 MPa or to the freezing pressure". *International Journal of Thermophysics*, vol. 6 (1985), pp. 233–250. ISSN: 0195928X. DOI: 10.1007/BF00522146.

[90] Dandridge, A. and Jackson, D. A. "Measurements of viscosity under pressure: a new method". *Journal of Physics D: Applied Physics*, vol. 14.5 (1981), pp. 829–831. ISSN: 0022-3727. DOI: 10.1088/0022-3727/14/5/012.

[91] Kashiwagi, H. and Makita, T. "Viscosity of twelve hydrocarbon liquids in the temperature range 298-348 K at pressures up to 110 MPa". *International Journal of Thermophysics*, vol. 3.4 (1982), pp. 289–305. ISSN: 0195928X. DOI: 10.1007/BF00502346.

[92] Chan, R. K. Y. and Jackson, D. A. "An automated falling-cylinder high pressure laser-Doppler viscometer". *Journal of Physics E: Scientific Instruments*, vol. 18.6 (1985), pp. 510–515. ISSN: 0022-3735. DOI: 10.1088/0022-3735/18/6/011.

[93] Ye, S. et al. "Réalisation d'un dispositif de mesure de la vitesse et de l'atténuation d'ondes ultrasonores dans des liquides sous pression". *Revue de Physique Appliquée*, vol. 25.6 (1990), pp. 555–565. ISSN: 0035-1687. DOI: 10.1051/rphysap:01990002506055500.

[94] Růžička, V., Zábranský, M., and Majer, V. "Heat capacities of organic compounds in liquid state II. C1 to C18 n-alkanes". *Journal of Physical and Chemical Reference Data*, vol. 20.2 (1991), p. 405. ISSN: 00472689. DOI: 10.1063/1.555883.

[95] Saint-guirons, H., Alliez, J., Lagourette, B., and Xans, P. "High pressure guided falling body viscometer. Representation of alkanes viscosity as a function of temperature and pressure". *High Pressure Research*, vol. 8.1-3 (1992), pp. 419–422. ISSN: 0895-7959. DOI: 10.1080/08957959108260694.

[96] ASSAEL, M. J., OLIVEIRA, C. P., PAPADAKI, M., and WAKEHAM, W. A. "Vibrating-Wire Viscometers for Liquids at High Pressures". *International Journal of Thermophysics*, vol. 13.4 (1992), pp. 593–615. ISSN: 0195928X. DOI: 10.1007/BF00501943.

[97] OLIVEIRA, C. M. B. P. and WAKEHAM, W. A. "The viscosity of five liquid hydrocarbons at pressures up to 250 MPa". *International Journal of Thermophysics*, vol. 13.5 (1992), pp. 773–790. ISSN: 0195-928X. DOI: 10.1007/BF00503906.

[98] DARIDON, J., LAGRABETTE, A., and LAGOURETTE, B. "Speed of sound, density, and compressibilities of heavy synthetic cuts from ultrasonic measurements under pressure". *The Journal of Chemical Thermodynamics*, vol. 30.5 (1998), pp. 607–623. ISSN: 00219614. DOI: 10.1006/jcht.1997.0330.

[99] TAT, M. E. et al. "The speed of sound and isentropic bulk modulus of biodiesel at 21°C from atmospheric pressure to 35 MPa". *Journal of the American Oil Chemists' Society*, vol. 77.3 (2000), pp. 285–289. ISSN: 0003-021X. DOI: 10.1007/s11746-000-0047-z.

[100] RODRÍGUEZ-ANTÓN, L. M., CASANOVA-KINDELAN, J., and TARDAJOS, G. "High Pressure Physical Properties of Fluids used in Diesel injection systems". *SAE Paper 2000-01-2046*, vol. 2000-01-20 (2000). DOI: 10.4271/2000-01-2046.

[101] BELONENKO, V. "Application of a Micro- (p, V, T) apparatus for measurement of liquid densities at pressures up to 500 MPa". *The Journal of Chemical Thermodynamics*, vol. 32 (2000), pp. 1203–1219. ISSN: 00219614. DOI: 10.1006/jcht.1999.0604.

[102] BALL, S. J. and TRUSLER, J. P. M. "The speed of Sound and derived thermodynamic properties of n-hexane and n-hexadecane at temperatures between 298 K and 373 K and pressures up to 100 MPa". *International Journal of Thermophysics*, vol. 22.2 (2001), pp. 427–443.

[103] AUDONNET, F. and PÁDUA, A. A. H. "Simultaneous measurement of density and viscosity of n-pentane from 298 to 383 K and up to 100 MPa using a vibrating-wire instrument". *Fluid Phase Equilibria*, vol. 181.1-2 (2001), pp. 147–161. ISSN: 03783812. DOI: 10.1016/S0378-3812(01)00487-3.

[104] Dauge, P., Baylaucq, A., Marlin, L., and Boned, C. "Development of an Isobaric Transfer Viscometer Operating up to 140 MPa. Application to a Methane + Decane System". *Journal of Chemical & Engineering Data*, vol. 46.4 (2001), pp. 823–830. issn: 0021-9568. doi: 10.1021/je000371v.

[105] Khasanshin, T. S. and Shchemelev, A. P. "Sound Velocity in Liquid n-Alkanes". *High Temperature*, vol. 39.1 (2001), pp. 60–67. issn: 0018151X. doi: 10.1023/A:1004170530517.

[106] Khasanshin, T. S., Shchamialiou, A. P., and Poddubskij, O. G. "Thermodynamic Properties of Heavy n-Alkanes in the Liquid State: n-Dodecane". *International Journal of Thermophysics*, vol. 24.5 (2003), pp. 1277–1289. issn: 0195928X. doi: 10.1023/A:1026199017598.

[107] Dindar, C. and Kiran, E. "Reliable method for determination of the velocity of a sinker in a high-pressure falling body type viscometer". *Rev. Sci. Instrum.* Vol. 73.10 (2002), pp. 3664–3670. issn: 0034-6748. doi: 10.1063/1.1505100.

[108] Boehman, A. L., Morris, D., Szybist, J., and Esen, E. "The Impact of the Bulk Modulus of Diesel Fuels on Fuel Injection Timing". *Energy & Fuels*, vol. 18.6 (2004), pp. 1877–1882. issn: 0887-0624. doi: 10.1021/ef049880j.

[109] Caudwell, D. R., Trusler, J. P. M., Vesovic, V., and Wakeham, W. A. "The viscosity and density of n-dodecane and n-octadecane at pressures up to 200 MPa and temperatures up to 473 K". *International Journal of Thermophysics*, vol. 25.5 (2004), pp. 1339–1352. issn: 0195928X. doi: 10.1007/s10765-004-5742-0.

[110] Caudwell, D. R., Trusler, J. P. M., Vesovic, V., and Wakeham, W. A. "Viscosity and Density of Five Hydrocarbon Liquids at Pressures up to 200 MPa and Temperatures up to 473 K". *Journal of Chemical Engineering Data*, vol. 54 (2009), pp. 359–366. issn: 0021-9568. doi: 10.1021/je800417q.

[111] Dechoz, J. and Rozé, C. "Surface tension measurement of fuels and alkanes at high pressure under different atmospheres". *Applied Surface Science*, vol. 229.1-4 (2004), pp. 175–182. issn: 01694332. doi: 10.1016/j.apsusc.2004.01.057.

[112] Dzida, M. and Prusakiewicz, P. "The effect of temperature and pressure on the physicochemical properties of petroleum diesel oil and biodiesel fuel". *Fuel*, vol. 87.10-11 (2008), pp. 1941–1948. issn: 00162361. doi: 10.1016/j.fuel.2007.10.010.

[113] RODRÍGUEZ-ANTÓN, L. M., APARICIO, C., GUIGNON, B., and SANZ, P. D. "Volumetric properties at high pressure of waste oil methyl ester compared with diesel oil". *Fuel*, vol. 87.10-11 (2008), pp. 1934–1940. ISSN: 00162361. DOI: 10.1016/j.fuel.2007.10.006.

[114] DÁVILA, M. J. and MARTIN TRUSLER, J. "Thermodynamic properties of mixtures of N-methyl-2-pyrrolidinone and methanol at temperatures between 298.15K and 343.15K and pressures up to 60MPa". *The Journal of Chemical Thermodynamics*, vol. 41.1 (2009), pp. 35–45. ISSN: 00219614. DOI: 10.1016/j.jct.2008.08.003.

[115] PATON, J. M. and SCHASCHKE, C. J. "Viscosity measurement of biodiesel at high pressure with a falling sinker viscometer". *Chemical Engineering Research and Design*, vol. 87.11 (2009), pp. 1520–1526. ISSN: 02638762. DOI: 10.1016/j.cherd.2009.04.007.

[116] ZENG, M. and SCHASCHKE, C. "High Pressure Falling Sinker Liquid Viscosity Determination without Supplementary Density Data: A New Approach". *International Journal of Chemical Engineering* (2009), pp. 1–8. ISSN: 1687-806X. DOI: 10.1155/2009/747592.

[117] FUKUI, K., ASAKUMA, Y., and MAEDA, K. "Determination of liquid viscosity at high pressure by DLS". *Journal of Physics: Conference Series*, vol. 215 (2010), p. 012073. ISSN: 1742-6596. DOI: 10.1088/1742-6596/215/1/012073.

[118] PELETIES, F., SEGOVIA, J. J., TRUSLER, J. P. M., and VEGA-MAZA, D. "Thermodynamic properties and equation of state of liquid di-isodecyl phthalate at temperature between (273 and 423) K and at pressures up to 140 MPa". *Journal of Chemical Thermodynamics*, vol. 42.5 (2010), pp. 631–639. ISSN: 00219614. DOI: 10.1016/j.jct.2009.12.002.

[119] PELETIES, F. and TRUSLER, J. P. M. "Viscosity of liquid di-isodecyl phthalate at temperatures between (274 and 373) K and at pressures up to 140 MPa". *Journal of Chemical and Engineering Data*, vol. 56.5 (2011), pp. 2236–2241. ISSN: 00219568. DOI: 10.1021/je101256z.

[120] DUNCAN, A. M. et al. "High-pressure viscosity of biodiesel from soybean, canola, and coconut oils". *Energy & Fuels*, vol. 24.10 (2010), pp. 5708–5716. ISSN: 08870624. DOI: 10.1021/ef100382f.

[121] Duncan, A. M., Pavlicek, N., Depcik, C. D., Scurto, A. M., and Stagg-Williams, S. M. "High-pressure viscosity of soybean-oil-based biodiesel blends with ultra-low-sulfur diesel fuel". *Energy and Fuels*, vol. 26.11 (2012), pp. 7023–7036. issn: 08870624. doi: 10.1021/ef3012068.

[122] Payri, R., Salvador, F., Gimeno, J., and Bracho, G. "The effect of temperature and pressure on thermodynamic properties of diesel and biodiesel fuels". *Fuel*, vol. 90.3 (2011), pp. 1172–1180. issn: 00162361. doi: 10.1016/j.fuel.2010.11.015.

[123] Bracho, G. "Experimental and theoretical study of the direct diesel injection process at low temperatures". PhD thesis. Universitat Politècnica de València, 2011.

[124] Aquing, M. et al. "Composition analysis and viscosity prediction of complex fuel mixtures using a molecular-based approach". *Energy & Fuels*, vol. 26.4 (2012), pp. 2220–2230. issn: 08870624. doi: 10.1021/ef300106z.

[125] Ndiaye, E. H. I., Bazile, J. P., Nasri, D., Boned, C., and Daridon, J. L. "High pressure thermophysical characterization of fuel used for testing and calibrating diesel injection systems". *Fuel*, vol. 98 (2012), pp. 288–294. issn: 00162361. doi: 10.1016/j.fuel.2012.04.005.

[126] Chorazewski, M. et al. "Thermophysical properties of Normafluid (ISO 4113) over wide pressure and temperature ranges". *Fuel*, vol. 105 (2013), pp. 440–450. issn: 00162361. doi: 10.1016/j.fuel.2012.05.059.

[127] Nikolić, B. D., Kegl, B., Marković, S. D., and Mitrović, M. S. "Determining the speed of sound, density, and bulk modulus of rapeseed oil, biodiesel, and diesel fuel". *Thermal Science*, vol. 16.2 (2013), pp. 505–514. issn: 03549836. doi: 10.2298/TSCI120426187N.

[128] Schaschke, C., Fletcher, I., and Glen, N. "Density and Viscosity Measurement of Diesel Fuels at Combined High Pressure and Elevated Temperature". *Processes*, vol. 1.2 (2013), pp. 30–48. issn: 2227-9717. doi: 10.3390/pr1020030.

[129] Freitas, S. V. D. et al. "Measurement and prediction of high-pressure viscosities of biodiesel fuels". *Fuel*, vol. 122 (2014), pp. 223–228. issn: 00162361. doi: 10.1016/j.fuel.2014.01.031.

[130] KIEŁCZYŃSKI, P. et al. "Ultrasonic evaluation of thermodynamic parameters of liquids under high pressure". *IEEE Transactions on Ultrasonics, Ferroelectrics, and Frequency Control*, vol. 62.6 (2015), pp. 1122–1131. ISSN: 0885-3010. DOI: 10.1109/TUFFC.2015.007053.

[131] ARMAS, O., MARTÍNEZ-MARTÍNEZ, S., MATA, C., and PACHECO, C. "Alternative method for bulk modulus estimation of Diesel fuels". *Fuel*, vol. 167 (2016), pp. 199–207. ISSN: 00162361. DOI: 10.1016/j.fuel.2015.11.067.

[132] HAYWARD, A. T. J. "Compressibility equations for liquids: a comparative study". *British Journal of Applied Physics*, vol. 18.7 (1967), pp. 965–977. ISSN: 0508-3443. DOI: 10.1088/0508-3443/18/7/312.

[133] HAYWARD, A. T. J. "How to measure the isothermal compressibility of liquids accurately". *Journal of Physics D: Applied Physics*, vol. 4.7 (1971), pp. 938–950. ISSN: 00223727. DOI: 10.1088/0022-3727/4/7/308.

[134] DOUHÉRET, G., DAVIS, M. I., REIS, J. C. R., and BLANDAMER, M. J. "Isentropic Compressibilities—Experimental Origin and the Quest for their Rigorous Estimation in Thermodynamically Ideal Liquid Mixtures". *ChemPhysChem*, vol. 2.3 (2001), pp. 148–161. ISSN: 1439-4235. DOI: 10.1002/1439-7641(20010316)2:3<148::AID-CPHC148>3.0.CO;2-J.

[135] APPELDOORN, J. K. "A Simplified Viscosity-Pressure-Temperature Equation". *SAE Paper 630139* (1963). DOI: 10.4271/630139.

[136] FRESCO, G. P., KLAUS, E. E., and TEWKSBURY, E. J. "Measurement and Prediction of Viscosity-Pressure Characteristics of Liquids". *Journal of Lubrication Technology*, vol. 91.3 (1969), pp. 451–457. ISSN: 00222305. DOI: 10.1115/1.3554960.

[137] SO, B. Y. C. and KLAUS, E. E. "Viscosity-Pressure Correlation of Liquids". *A S L E Transactions*, vol. 23.4 (1980), pp. 409–421. ISSN: 0569-8197. DOI: 10.1080/05698198008982986.

[138] SARGENT, L. B. "Pressure-Viscosity Coefficients of Liquid Lubricants". *A S L E Transactions*, vol. 26.1 (1983), pp. 1–10. ISSN: 0569-8197. DOI: 10.1080/05698198308981471.

[139] WU, C. S., KLAUS, E. E., and DUDA, J. L. "Development of a Method for the Prediction of Pressure-Viscosity Coefficients of Lubricating Oils Based on Free-Volume Theory". *Journal of Tribology*, vol. 111.1 (1989), p. 121. ISSN: 07424787. DOI: 10.1115/1.3261861.

[140] Kouzel, B. "How pressure affects liquid viscosity". *Hydrocarbon Process. Petrol Refiner*, vol. 44 (3) (1965), p. 120.

[141] Růžička, V. and Domalski, E. S. "Estimation of the Heat Capacities of Organic Liquids as a Function of Temperature using Group Additivity. I. Hydrocarbon Compounds". *Journal of Physical and Chemical Reference Data*, vol. 22.3 (1993), p. 597. issn: 00472689. doi: 10.1063/1.555923.

[142] Zábranský, M. "Heat Capacity of Liquids: Critical Review and Recommended Values. Supplement I". *Journal of Physical and Chemical Reference Data*, vol. 30.5 (2001), p. 1199. issn: 00472689. doi: 10.1063/1.1407866.

[143] Zábranský, M., Kolská, Z., Růžička, V., and Domalski, E. S. "Heat capacity of liquids: Critical review and recommended values. Supplement ii". *Journal of Physical and Chemical Reference Data*, vol. 39.1 (2010), pp. 3–404. issn: 00472689. doi: 10.1063/1.3182831.

[144] Leidenfrost, W. "Measurements of thermophysical properties". *Measurements in Heat Transfer*. Ed. by E. R. G. Eckert and R. J. Goldstein. 2nd editio. New York: Hemisphere Publishing Corporation, 1976. Chap. 11. isbn: 0-89116-652-1.

[145] Brunner, M. and Ruf, H. "Contribution to the problem of starting and operating diesel vehicles at low temperatures". *Proceedings of the Institution of Mechanical Engineers, Automobile Division*, vol. 13.1 (1959), pp. 124–154. issn: 0367-8822. doi: 10.1243/PIME_AUTO_1959_000_019_02.

[146] Heywood, J. B. *Internal Combustion Engine Fundementals*. McGraw Hill, 1988. isbn: 007028637X.

[147] Monyem, A., Van Gerpen, J. H., and Canakci, M. "The Effect of Timing and Oxidation on Emissions from Biodiesel-Fueled Engines". *Transactions of the ASAE*, vol. 44.1 (2001), pp. 35–42. issn: 2151-0059. doi: 10.13031/2013.2301.

[148] Lapuerta, M., Armas, O., and Rodríguez-Fernández, J. "Effect of biodiesel fuels on diesel engine emissions". *Progress in Energy and Combustion Science*, vol. 34.2 (2008), pp. 198–223. issn: 03601285. doi: 10.1016/j.pecs.2007.07.001.

[149] Gumus, M., Sayin, C., and Canakci, M. "The impact of fuel injection pressure on the exhaust emissions of a direct injection diesel engine fueled with biodiesel–diesel fuel blends". *Fuel*, vol. 95.1 (2012), pp. 486–494. issn: 00162361. doi: 10.1016/j.fuel.2011.11.020.

[150] AGARWAL, A. K. et al. "Effect of fuel injection pressure and injection timing of Karanja biodiesel blends on fuel spray, engine performance, emissions and combustion characteristics". *Energy Conversion and Management*, vol. 91 (2015), pp. 302–314. ISSN: 01968904. DOI: 10.1016/j.enconman.2014.12.004.

[151] CHANG, C. T. and FARRELL, P. V. "A study on the effects of fuel viscosity and nozzle geometry on high injection pressure Diesel spray characteristics". *SAE Technical Paper 970353* (1997). DOI: 10.4271/970353.

[152] DESANTES, J. M., ARRÈGLE, J., PASTOR, J. V., and DELAGE, A. "Influence of the fuel characteristics on the injection process in a D.I. Diesel engine". *SAE Technical Paper 980802* (1998). DOI: 10.4271/980802.

[153] DESANTES, J. M., PAYRI, R., GARCIA, A., and MANIN, J. "Experimental Study of Biodiesel Blends' Effects on Diesel Injection Processes". *Energy & Fuels*, vol. 23.6 (2009), pp. 3227–3235. ISSN: 0887-0624. DOI: 10.1021/ef801102w.

[154] DESANTES, J. M., PAYRI, R., SALVADOR, F. J., and MANIN, J. "Influence on Diesel Injection Characteristics and Behavior Using Biodiesel Fuels". *SAE Technical Paper 2009-01-0851*, vol. 4970.2009-01-0851 (2009). DOI: 10.4271/2009-01-0851.

[155] SALVADOR, F. J., RUIZ, S., SALAVERT, J., and DE LA MORENA, J. "Consequences of using biodiesel on the injection and air-fuel mixing processes in diesel engines". *Proceedings of the Institution of Mechanical Engineers, Part D: Journal of Automobile Engineering*, vol. 227.8 (2013), pp. 1130–1141. ISSN: 09544070. DOI: 10.1177/0954407012463667.

[156] TINPRABATH, P., HESPEL, C., CHANCHAONA, S., and FOUCHER, F. "Influence of biodiesel and diesel fuel blends on the injection rate under cold conditions". *Fuel*, vol. 144 (2015), pp. 80–89. ISSN: 00162361. DOI: 10.1016/j.fuel.2014.12.010.

[157] PAYRI, R., SALVADOR, F. J., GIMENO, J., and BRACHO, G. "Effect of fuel properties on diesel spray development in extreme cold conditions". *Proceedings of the Institution of Mechanical Engineers. Part D, Journal of Automobile Engineering*, vol. 222.9 (2008), pp. 1743–1753. ISSN: 0954-4070. DOI: 10.1243/09544070JAUTO844.

[158] Payri, R., Salvador, F. J., Gimeno, J., and Bracho, G. "Understanding Diesel Injection Characteristics in Winter Conditions". *SAE Technical Paper 2009-01-0836* (2009). doi: 10.4271/2009-01-0836.

[159] Vergnes, C., Foucher, F., and Mounaim-Rousselle, C. "Discharge coefficients for a diesel injector during cold starting conditions". *Atomization and Sprays*, vol. 19.7 (2009), pp. 621–631. issn: 1044-5110. doi: 10.1615/AtomizSpr.v19.i7.20.

[160] Park, Y. et al. "Effects of diesel fuel temperature on fuel flow and spray characteristics". *Fuel*, vol. 162 (2015), pp. 1–7. issn: 00162361. doi: 10.1016/j.fuel.2015.09.008.

[161] Wang, Z., Ding, H., Wyszynski, M. L., Tian, J., and Xu, H. "Experimental study on diesel fuel injection characteristics under cold start conditions with single and split injection strategies". *Fuel Processing Technology*, vol. 131 (2015), pp. 213–222. issn: 03783820. doi: 10.1016/j.fuproc.2014.10.003.

[162] Dernotte, J., Hespel, C., Foucher, F., Houillé, S., and Mounaïm-Rousselle, C. "Influence of physical fuel properties on the injection rate in a Diesel injector". *Fuel*, vol. 96 (2012), pp. 153–160. issn: 00162361. doi: 10.1016/j.fuel.2011.11.073.

[163] Dernotte, J. et al. "Experimental Study of the Influence of Fuel Properties on the Diesel Injection Process in Non-Vaporizing Conditions". *ILASS - Europe 2011, 24th European Conference on Liquid Atomization and Spray Systems*. Estoril, Portugal, 2011, pp. 1–10.

[164] Dernotte, J., Hespel, C., Houille, S., Foucher, F., and Mounaim-Rousselle, C. "Influence of Fuel Properties on the Diesel Injection Process in Nonvaporizing Conditions". *Atomization And Sprays*, vol. 22.6 (2012), pp. 461–492. issn: 1044-5110. doi: 10.1615/AtomizSpr.2012004401.

[165] Tat, M. E. and Van Gerpen, J. H. *Measurement of Biodiesel Speed of Sound and Its Impact on Injection Timing*. Tech. rep. 4. National Renewable Energy Laboratory (NREL), 2003.

[166] Kegl, B. and Hribernik, A. "Experimental Analysis of Injection Characteristics Using Biodiesel Fuel". *Energy & Fuels*, vol. 20.5 (2006), pp. 2239–2248. issn: 0887-0624. doi: 10.1021/ef060285m.

[167] Kegl, B. "Biodiesel usage at low temperature". *Fuel*, vol. 87 (2008), pp. 1306–1317. issn: 00162361. doi: 10.1016/j.fuel.2007.06.023.

[168] SUH, H. K., PARK, S. H., and LEE, C. S. "Experimental investigation of nozzle cavitating flow characteristics for diesel and biodiesel fuels". *International Journal of Automotive Technology*, vol. 9.2 (2008), pp. 217–224. ISSN: 1229-9138. DOI: 10.1007/s12239-008-0028-3.

[169] SALVADOR, F. J. "Estudio teórico experimental de la influencia de la geometría de toberas de inyección Diésel sobre las características del flujo interno y del chorro". PhD thesis. Universitat Politècnica de València, 2003.

[170] PAYRI, F., BERMÚDEZ, V., PAYRI, R., and SALVADOR, F. J. "The influence of cavitation on the internal flow and the spray characteristics in diesel injection nozzles". *Fuel*, vol. 83.4-5 (2004), pp. 419–431. ISSN: 00162361. DOI: 10.1016/j.fuel.2003.09.010.

[171] PAYRI, R., GUARDIOLA, C., SALVADOR, F. J., and GIMENO, J. "Critical cavitation number determination in Diesel injection nozzles". *Experimental Techniques*, vol. 28.3 (2004), pp. 49–52. DOI: 10.1111/j.1747-1567.2004.tb00164.x.

[172] WANG, X., HUANG, Z., KUTI, O. A., ZHANG, W., and NISHIDA, K. "Experimental and analytical study on biodiesel and diesel spray characteristics under ultra-high injection pressure". *International Journal of Heat and Fluid Flow*, vol. 31.4 (2010), pp. 659–666. ISSN: 0142727X. DOI: 10.1016/j.ijheatfluidflow.2010.03.006.

[173] PAYRI, R., GARCIA-OLIVER, J. M., BARDI, M., and MANIN, J. "Fuel temperature influence on diesel sprays in inert and reacting conditions". *Applied Thermal Engineering*, vol. 35 (2012), pp. 185–195. ISSN: 1359-4311. DOI: 10.1016/j.applthermaleng.2011.10.027.

[174] BOUDY, F. and SEERS, P. "Impact of physical properties of biodiesel on the injection process in a common-rail direct injection system". *Energy Conversion and Management*, vol. 50.12 (2009), pp. 2905–2912. ISSN: 01968904. DOI: http://dx.doi.org/10.1016/j.enconman.2009.07.005.

[175] SOM, S., LONGMAN, D., RAMÍREZ, A., and AGGARWAL, S. "A comparison of injector flow and spray characteristics of biodiesel with petrodiesel". *Fuel*, vol. 89.12 (2010), pp. 4014–4024. ISSN: 00162361. DOI: 10.1016/j.fuel.2010.05.004.

[176] SOM, S., E., D., I., A., and AGGARWAL, S. "Influence of Nozzle Orifice Geometry and Fuel Properties on Flow and Cavitation Characteristics of a Diesel Injector". *Fuel Injection in Automotive Engineering*. InTech, 2012. ISBN: 978-953-51-0528-2. DOI: 10.5772/38900.

[177] Salvador, F. J., Martínez-López, J., Romero, J., and Roselló, M. "Influence of biofuels on the internal flow in diesel injector nozzles". *Mathematical and Computer Modelling*, vol. 54.7-8 (2011), pp. 1699–1705. ISSN: 08957177. DOI: 10.1016/j.mcm.2010.12.010.

[178] Theodorakakos, A., Mitroglou, N., and Gavaises, M. "Simulation of heating effects in cavitating flows through Diesel fuel injectors caused by extreme fuel pressurisation". *8th international symposium on cavitation*. Singapore, 2012.

[179] Theodorakakos, A., Strotos, G., Mitroglou, N., Atkin, C., and Gavaises, M. "Friction-induced heating in nozzle hole microchannels under extreme fuel pressurisation". *Fuel*, vol. 123.x (2014), pp. 143–150. ISSN: 00162361. DOI: 10.1016/j.fuel.2014.01.050.

[180] Strotos, G., Koukouvinis, P., Theodorakakos, A., and Wang, L. "Fuel heating in high pressure diesel nozzles". *THIESEL 2014 Conference on Thermo- and Fluid Dynamic Processes in Direct Injection Engines*. Valencia, Spain, 2014.

[181] Strotos, G., Koukouvinis, P., Theodorakakos, A., Gavaises, M., and Bergeles, G. "Transient heating effects in high pressure Diesel injector nozzles". *International Journal of Heat and Fluid Flow*, vol. 51 (2015), pp. 257–267. ISSN: 0142727X. DOI: 10.1016/j.ijheatfluidflow.2014.10.010.

[182] Shi, J., Guerrassi, N., Dober, G., Karimi, K., and Meslem, Y. "Complex physics modelling of diesel injector nozzle flow and spray supported by new experiments". *THIESEL 2014 Conference on Thermo- and Fluid Dynamic Processes in Direct Injection Engines*. Valencia, Spain, 2014.

Chapter 4

Experimental tools

4.1 Introduction

As already stated, this thesis aims at the study of the influence of the fuel temperature and its changes along a solenoid-driven *common-rail* ballistic injector (Bosch CRI 2.20) on the injection process through a combined experimental and computational approach. Hence, on the one hand, experimental tools have been used to directly assess the effects of the fuel temperature on the injection process. On the other hand, since a 1D model has been implemented to serve as a tool to predict the performance of the injector and analyse its internal behaviour, experiments were needed both to correctly implement the model and to ensure its validity over a wide range of injector operating conditions. The present chapter focuses on the description of these experiments and the equipment used to perform them. Partial results are also shown given their importance to better understand some of the tools used and the model implementation described in Chapter 5.

The need for a detailed characterization of the injector in order to obtain a reliable model was already pointed out in Section 3.2.2 in the view of the previous works by modellers of *common-rail* injection systems. Therefore, the experimental methodology to completely characterize the injector is presented first in this chapter. This includes both a dimensional and a hydraulic characterization methodology. The former allowed to determine the internal geometry of the injector, whereas the latter included the description of the individual behaviour of the most important flow restrictions of the in-

jector (namely the control and the nozzle orifices) by obtaining the evolution of their discharge coefficients with the flow regime thanks to continuous flow measurements. The temperature variation the fuel suffered across them was determined as well.

In addition, the hydraulic behaviour of the complete injector was also characterized by means of rate of injection measurements, in which special attention was paid to the fuel temperature control. These measurements constitute the basis to analyse the temperature effects on the injection process and have also been used to validate the computational model developed in the present thesis.

The fuel used for the hydraulic characterization is also presented in this chapter. As justified in Chapter 3, the proper knowledge of the fuel properties at the injector operating conditions is essential to understand the injection process. Thus, the fuel speed of sound, density and bulk modulus were experimentally determined at a wide range of temperatures and pressures, representative of those found in the operating range of the studied injector. The methodology to obtain those properties has been validated by applying it for a pure alkane, whose properties at those conditions are readily available. The fuel viscosity was estimated from works previously reported in the literature. The computational model implemented in this thesis has been provided with these data in order to properly vary the fuel properties during a simulation, since local changes in temperature and pressure have been taken into account.

4.2 Injector dimensional characterization

The dimensional characterization involves gathering information about the internal lines, orifices, volumes and movable elements of the system. In the present thesis, the geometry of the internal ducts and orifices of the injector was determined by inserting a silicone into the injector body. The silicone methodology to determine nozzle geometries in a non-destructive way was first introduced by Macián *et al.* [1] and has been extended to other parts of the injector.

The general procedure followed for the Bosch CRI 2.20 injector dimensional characterization is shown in Figure 4.1. Silicone moulds of the different internal passages of the injector were extracted and visualized by either an optical microscope or a SEM (Scanning Electron Microscope), depending on the size of the samples. Thus, the moulds corresponding to larger internal ducts could be introduced in the optical microscope. Other large parts of the

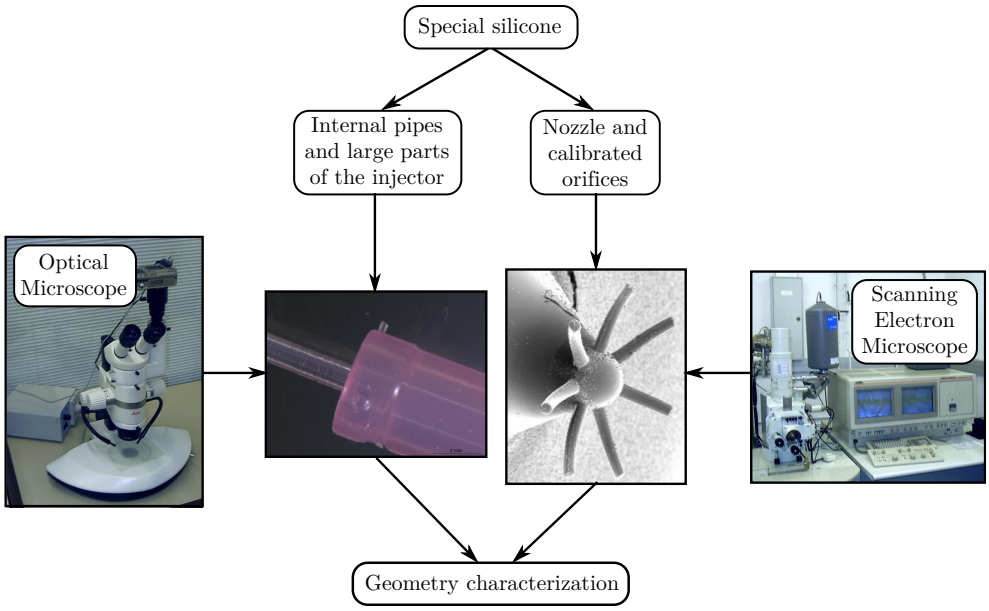

Figure 4.1: Injector dimensional characterization through the silicone methodology.

injector, such as the internal springs, could also be directly visualized in this microscope. Moulds of the small calibrated orifices (i.e. the control volume inlet and outlet orifices) and the injector nozzle were visualized in the SEM, which allowed a magnification from 30X to 1000X. Due to the SEM working principle, a gold coating needed to be applied to the silicone samples so that they were able to evacuate the energy of the electron beam. This gold coating is thin enough (in the order of nanometres) not to affect the geometry determination.

In the case of the nozzle orifices, pictures in the SEM may be taken from multiple perspectives by rotating the sample. Examples obtained for one of the orifices of the Bosch CRI 2.20 injector studied are shown in Figure 4.2. Digital pictures of the samples taken from both the optical microscope and the SEM were processed with a CAD software in order to perform the proper measurements. The magnification rate of the pictures shown in Figure 4.2 is 80X, kept for illustrative purposes. However, pictures with higher magnification rates were obtained to increase the accuracy of the measurements. As validated in several investigations [1–3], this technique leads to deviations lower than 2%.

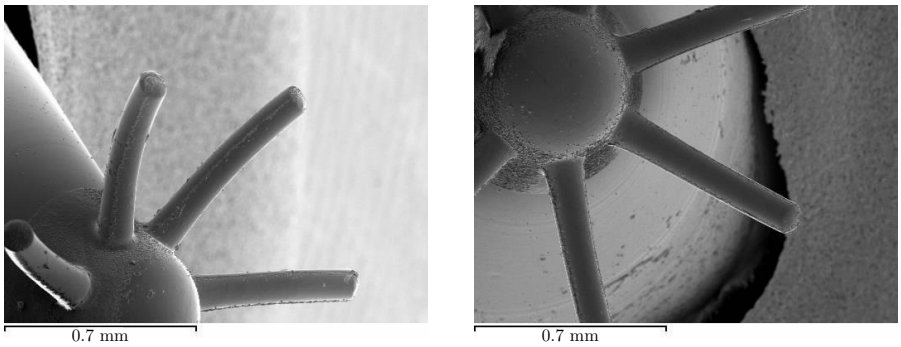

(a) Side view (b) Bottom view

Figure 4.2: Bosch CRI 2.20 nozzle orifices images obtained through the SEM (80X magnification).

The following dimensions may be determined for each of the orifices, as sketched in Figure 4.3:

- φ: Angle among the nozzle vertical axis and the orifice axis.
- r_{iu}: Upper side orifice rounding radius at the inlet.
- r_{il}: Lower side orifice rounding radius at the inlet.
- D_{si}: Orifice inlet diameter determined from the side view.
- D_{sm}: Orifice mid-section diameter determined from the side view.
- D_{so}: Orifice outlet diameter determined from the side view.
- D_{bi}, D_{bm}, D_{bo}: Diameter values analogous to the previous ones, but determined from the bottom view pictures.
- D_i, D_m, D_o: Geometric mean values of each of the previous diameters, defined from the two views as $D = \sqrt{D_s D_b}$.

The values of these parameters obtained for each of the orifices of the nozzle studied in the present thesis are compiled in Table 4.1 together with the average values of all the orifices. Values of the *k-factor*, defined in Section 2.3.4 and reproduced in Equation (4.1), are also shown in the table.

$$k\text{-}factor = \frac{D_i - D_o}{[10\,\mu m]} \tag{4.1}$$

Silicone moulds of the control volume orifices of the Bosch CRI 2.20 injector were also obtained and introduced in the SEM. The corresponding pictures are shown in Figure 4.4.

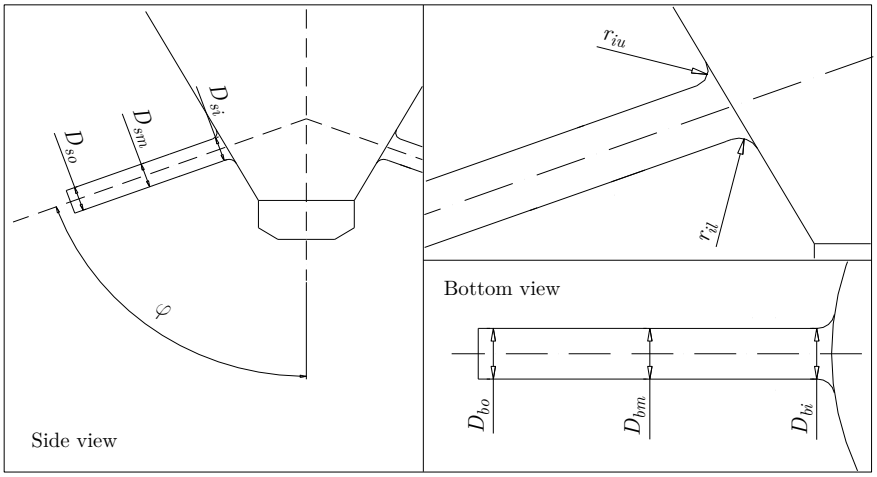

Figure 4.3: Nozzle geometrical parameters obtained through the SEM.

Orif.	D_i [µm]	D_m [µm]	D_o [µm]	r_u [µm]	r_l [µm]	***k-factor*** [µm]
1	145	125	119	25	26	2.6
2	146	123	117	39	11	2.9
3	150	123	118	28	16	3.1
4	145	125	118	59	19	2.7
5	144	123	117	34	17	2.7
6	144	123	115	31	21	2.9
7	146	123	117	36	18	2.9
Mean	146±2	124±1	117±1	36±11	18±5	2.8±0.2

Table 4.1: Geometrical parameters obtained for the studied nozzle.

A summary of the geometrical parameters obtained for the control volume orifices of the injector through this methodology is shown in Table 4.2. Values of the control orifices for the Denso G4S injector[1] (Figure 2.7) are also given, since their hydraulic characterization was also performed for this thesis in order to further examine the validity of the temperature changes through injection orifices estimated by the implemented model.

The *k-factor* values obtained, together with the ones shown in Table 4.1, highlight the high degree of convergence of the Bosch CRI 2.20 control volume inlet orifice and the nozzle orifices, as well as the Denso G4S outlet orifice.

[1]As stated in Section 2.2.2, the Denso G4S is a 3-way valve solenoid injector

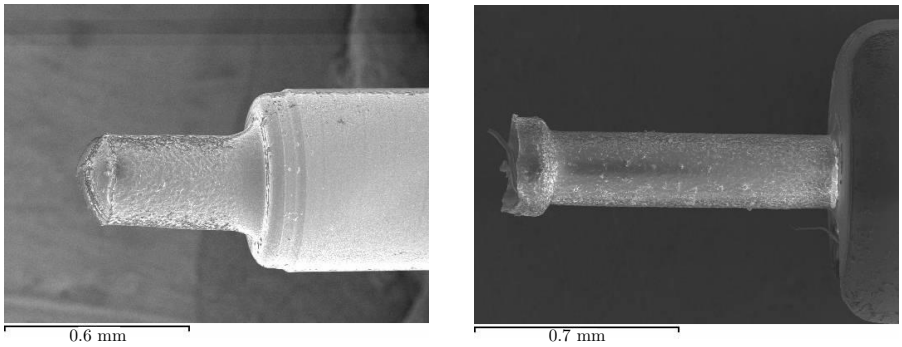

(a) Inlet orifice (90X) (b) Outlet orifice (85X)

Figure 4.4: SEM images of the Bosch CRI 2.20 control volume orifices.

Injector	**Orifice**	D_i [µm]	D_o [µm]	L [mm]	***k-factor*** [µm]
Bosch CRI 2.20	Inlet	308	290	1.47	1.8
	Outlet	256	259	1.48	−0.3
Denso G4S	Inlet	274	274	0.8	0
	Outlet	110	102	0.84	0.8
	Control Valve	199	198	0.75	0.1

Table 4.2: Summary of the control volume orifices geometrical parameters.

On the other hand, the Bosch CRI 2.20 control volume outlet orifice and the Denso G4S inlet and control valve orifices are essentially cylindrical. As explained in Section 2.3.6, this means that the former orifices are not prone to cavitate, as opposed to the latter. This finding should be confirmed by the hydraulic characterization (Section 4.3) through the detection of mass flow collapse.

4.3 Injector hydraulic characterization

As stated in Section 4.1, the main purpose of the hydraulic characterization of a single orifice or the complete injector is to determine its flow behaviour depending on the operating conditions.

With regard to the nozzle and control volume orifices, their individual behaviour may be characterized by imposing continuous flow through the studied orifice under several conditions of upstream and downstream pressure. Critical parameters for the model implementation were obtained through this

measurement, mainly to describe the evolution of the discharge coefficient as a function of the Reynolds number. In the case of the control volume orifices, in addition, the fuel temperature change across them was also experimentally determined depending on the pressure drop. In following chapters, this temperature change will be compared to the one expected for an adiabatic expansion in order to assess the extension of the validity of this assumption, used by the computational model to predict the temperature changes along the injector.

Concerning the injector as a whole, the characterization involves the measurement of instantaneous mass flow rate (rate of injection or ROI) for pulsed flow, allowing the assessment of the influence of the fuel temperature on the injection event on the one hand and providing data for the validation of the computational model developed in the present thesis on the other.

Experiments were carried out with a winter diesel fuel given the low fuel temperatures imposed for some of the ROI measurements. This fuel was also characterized as part of the present thesis. Details on the fuel properties determination at high pressure are given in Section 4.4.

4.3.1 Flow through the injector internal orifices

In order to characterize the injector hydraulic restrictions, continuous flow may be imposed through them under several conditions of controlled upstream and downstream pressure. To this end, an experimental setup was implemented and slightly modified to accomodate either the nozzle or the control volume orifices, as described in the following subsections.

Nozzle orifices characterization

The setup for the nozzle orifices characterization is shown in Figure 4.5. A sketch of a mobile trolley containing some of the elements that comprised the experimental setup is shown in Figure 4.6.

Two electrically-driven fuel pumps extracted fuel from a tank and pressurized it after making it flow through a filter, providing continuous flow. The arrangement of the fuel pumps, in parallel, was chosen in order to increase the maximum flow rate that could be achieved in the measurements. Since the fuel heated up due to its pressurization, a fuel-water heat exchanger was used to cool down the flow before it reached a commercial *common-rail*, in

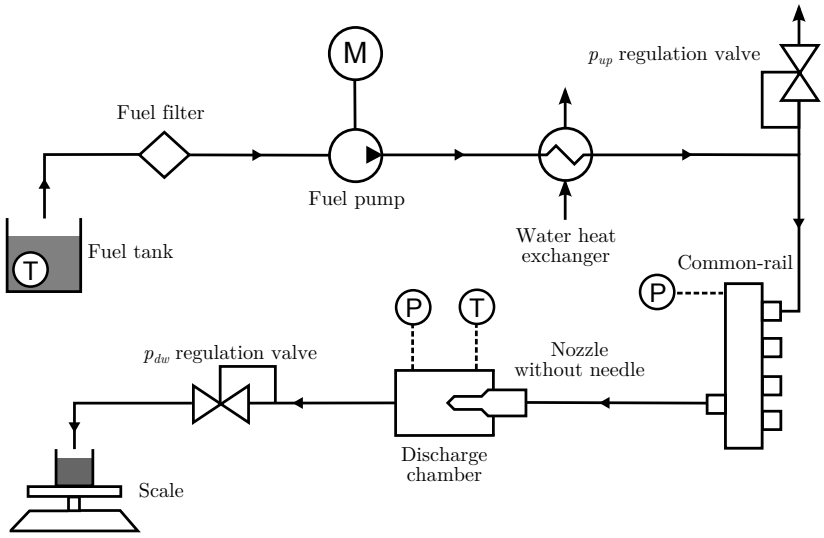

Figure 4.5: Setup for the hydraulic characterization of the nozzle orifices.

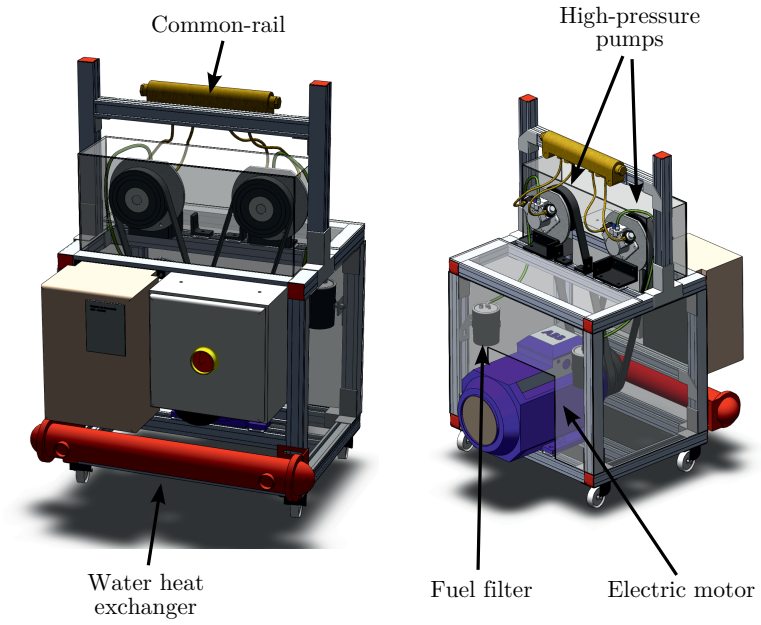

(a) Front view (b) Rear view

Figure 4.6: Sketch of the mobile trolley containing some of the elements used for the hydraulic characterization setup.

which the pressure p_{up}[2] was controlled by means of a manual pressure relief valve. The nozzle was fitted to a discharge chamber and sealed without the needle. During the measurements, this chamber totally filled with fuel and its pressure, p_{dw}, could be controlled by means of another manual regulation valve placed downstream. The temperature in this chamber was measured to accordingly compute the fuel properties and the Reynolds number. Finally, the fuel was injected into a glass in which the mass flow $\dot{m}_f$ could be measured in real time thanks to a scale connected to a computer.

The mass flow measurement was recorded for each tested condition after a short stabilization time by averaging it for a period of 80 s. This measurement made it possible to determine the orifices discharge coefficient for the tested operating conditions, as stated by Equation (4.2):

$$C_d = \frac{\dot{m}}{\dot{m}_{th}} = \frac{\dot{m}}{A_o\sqrt{2\rho_f\left(p_{up} - p_{dw}\right)}} \tag{4.2}$$

Control volume orifices characterization

The setup for the control volume orifices characterization is shown in Figure 4.7. In this case, the orifice to be tested was fitted inside a specifically built test rig located downstream of the rail. The purpose of this test rig was to isolate the corresponding restriction so that fuel flowed in the adequate direction through the orifice and was not leaked through any other paths that could be possible during the normal operation of the complete injector.

Figure 4.8 shows a detail of the Bosch CRI 2.20 control volume orifices test rig together with the injector control volume itself. There are two different configurations in which the test rig could be mounted in the experimental setup described in Figure 4.7. In order to characterize the inlet orifice, the port at the upper side of the test rig in Figure 4.7(b) was locked, and the test rig was mounted on the experimental setup so that the fuel flowed from the inlet orifice entrance to the lower part of the test rig. The same test rig could be used for the outlet orifice characterization by locking the lateral port of the test rig and making the fuel flow from the bottom of the control volume to the top.

Similarly, a sample of an on-purpose test rig for the Denso G4S outlet orifice is shown in Figure 4.9 together with the injector piece. In this case,

[2]The pressures upstream and downstream of the orifices in the continuous flow tests have been denoted as p_{up} and p_{dw} to avoid confusion, since the values reached are not in the order of the ones achieved in a pulsed injection in a real engine, p_i and p_b.

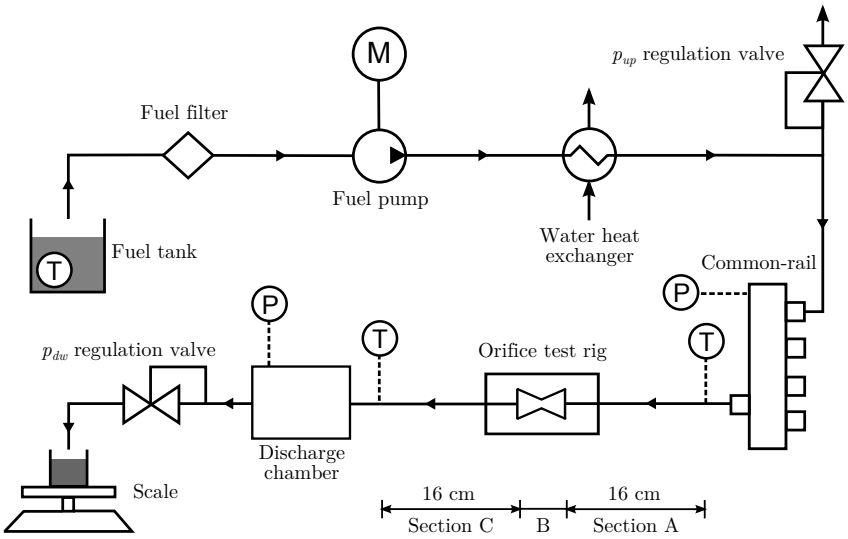

Figure 4.7: Setup for the hydraulic characterization of the control volume orifices.

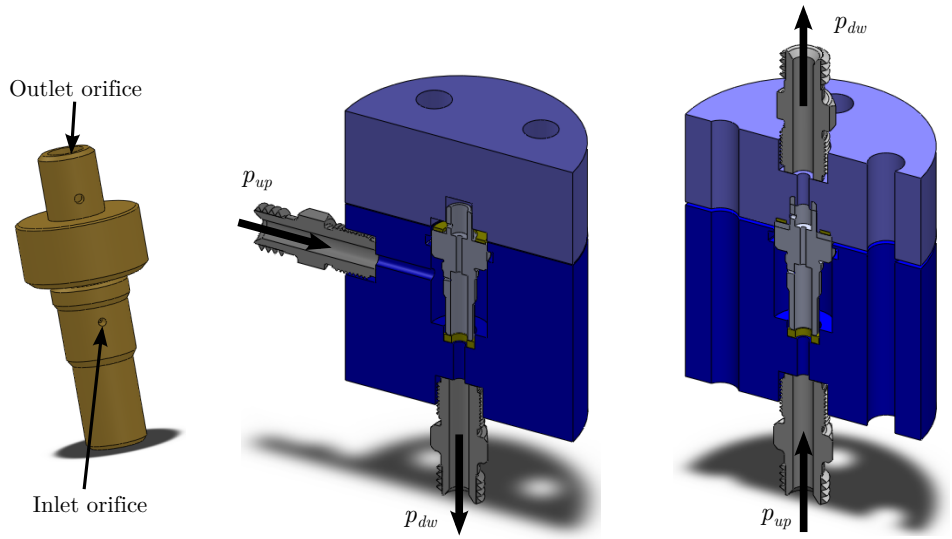

(a) Control volume (b) Inlet orifice configuration (c) Outlet orifice configuration

Figure 4.8: Test rig for the hydraulic characterization of the Bosch CRI 2.20 control volume orifices.

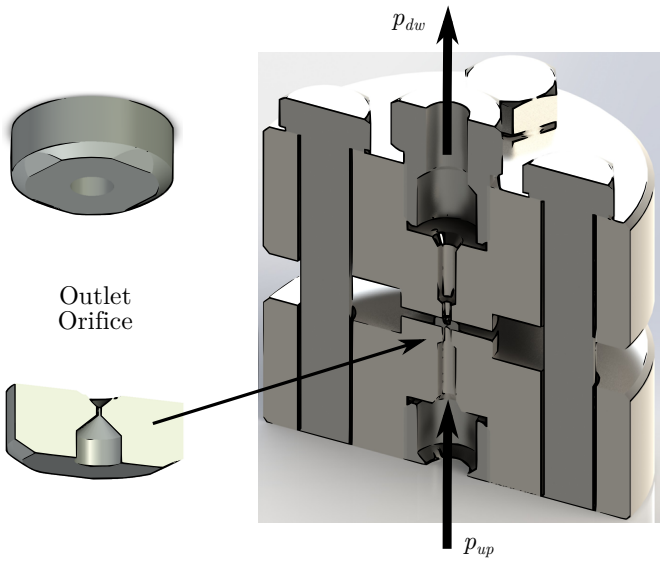

Figure 4.9: Test rig for the hydraulic characterization of the Denso G4S outlet orifice.

the end of the test rig was not to lock any orifice, but rather to drive the flow through the restriction to be characterized.

The temperature jump across the orifice was determined from fuel temperature measurements carried out by type K thermocouples inserted at two locations of the high-pressure lines at which the flow was assumed to develop and attain a similar velocity: right after the rail and before the discharge chamber (i.e. 16 cm upstream and downstream of the orifice). Values of fuel density and viscosity needed to compute the discharge coefficient (Equation (4.2)) and the Reynolds number were taken at a mean temperature and a mean pressure by averaging the values of these conditions upstream and downstream of the orifice.

An air-conditioning unit was used in order to control the ambient temperature and keep it below the temperature upstream of the orifice so that, in case that the heat transfer with the surroundings was relevant, it would take place in the same direction (from the fluid to the surroundings) for all the tested operating conditions, thus enabling comparability among tests. This ambient temperature was chosen at 293 K.

Hydraulic characterization test matrix

Table 4.3 depicts the operating conditions experimentally tested for the control volume orifices. The highest value of p_{up} was chosen corresponding to the maximum mass flow rate supplied by the high-pressure pumps, which was about 20 g/s. Hence, values of p_{up} range from 5 to 60 MPa in the case of the control volume orifices, whereas a maximum p_{up} of 40 MPa could be achieved for the nozzle orifices.

For each value of p_{up} tested, a sweep of p_{dw} was performed in order to ensure that each orifice worked for a wide range of Re values, so that all flow regimes (laminar, turbulent and transitional) were considered. The maximum value of p_{dw} tested was 12 MPa due to mechanical limitations of the discharge chamber.

$\boldsymbol{p_{up}}$ [MPa]	$\boldsymbol{p_{dw}}$ [MPa]
5	0.5 - 1 - 1.5 - 2 - 2.5 - 3 - 3.5 - 4 - 4.2 - 4.4 - 4.6 - 4.8
10	0.5 - 1 - 1.5 - 2 - 2.5 - 3 - 4 - 5 - 6 - 7 - 8 - 9
20, 30, 40, 50, 60	0.5 - 1 - 1.5 - 2 - 2.5 - 3 - 4 - 5 - 6 - 7 - 8 - 9 - 10 - 11 - 12

Table 4.3: Values of p_{dw} tested for each p_{up} considered in the hydraulic characterization measurements.

Hydraulic characterization results

Results of the hydraulic characterization for the Bosch CRI 2.20 nozzle orifices are shown in Figure 4.10.

Figure 4.10(a) shows the mass flow rate against the square root of the imposed pressure drop. A linear trend is observed for these orifices. The fact that a mass flow rate collapse is not seen points out that they do not cavitate for any of the pressure conditions tested in the experiments, confirming what has been stated in Sections 2.3.6 and 4.2 as suggested by their high $k-factor$ [4].

Figure 4.10(b), in turn, depicts the behaviour of the discharge coefficient with respect to the Reynolds number. The asymptotic trend expected from the literature [5], as explained in Section 2.3.4, is also guessed from the experimental results.

Analogously, results for the Bosch CRI 2.20 and Denso G4S control volume orifices are shown in Figures 4.11 to 4.13.

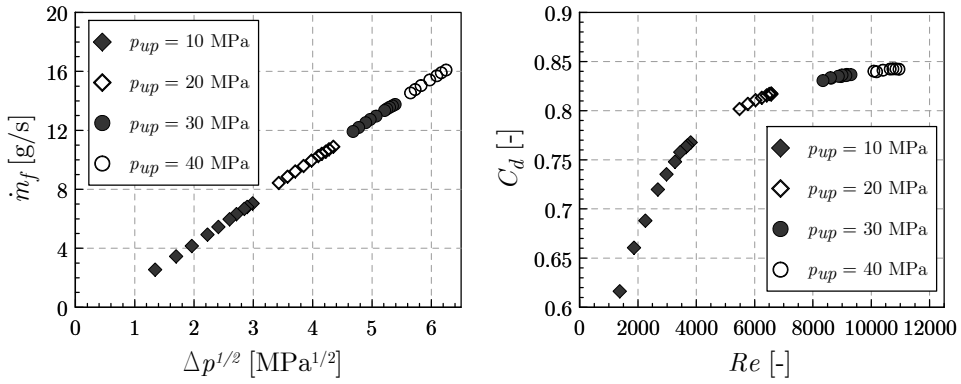

(a) Mass flow rate results

(b) Discharge coefficient results

Figure 4.10: Results of the hydraulic characterization for the Bosch CRI 2.20 nozzle orifices.

As done for the Bosch CRI 2.20 nozzle orifices, the mass flow rate results are depicted against the square root of the pressure drop in Figure 4.11. Focusing on the Bosch CRI 2.20 injector (Figure 4.11(a)), a mass flow rate collapse is not seen for this orifice, also confirming its low proneness to cavitate due to its $k - factor$. In the case of the outlet orifice, a linear trend with $\sqrt{\Delta p}$ is also observed until the mass flow rate collapse is noticed for each upstream pressure tested, indicating cavitation inside the orifice as expected due to its cylindrical shape reported in Table 4.2. Figure 4.11(b) shows that the Denso G4S injector inlet and control valve orifices are also prone to cavitate due to their cylindrical nature. Concerning the outlet orifice, cavitation appears in the less favourable conditions (higher pressure drops for each p_{up} value tested) despite its conical shape. This behaviour is attributed to its relatively low $k - factor$, which does not enable the complete inhibition of the cavitation phenomenon.

Figure 4.12 depicts the behaviour of the discharge coefficient with respect to the Reynolds number for these orifices. In the case of the non-cavitating orifices, the discharge coefficient always increases with the Reynolds number following the expected asymptotic trend. However, for the orifices in which cavitation takes place, the discharge coefficient drops abruptly for each upstream pressure once the orifice starts cavitating.

Table 4.4 summarizes the information of the hydraulic characterization provided to the one-dimensional model implemented, as will be explained in Chapter 5. The Reynolds number indicating the transition from laminar

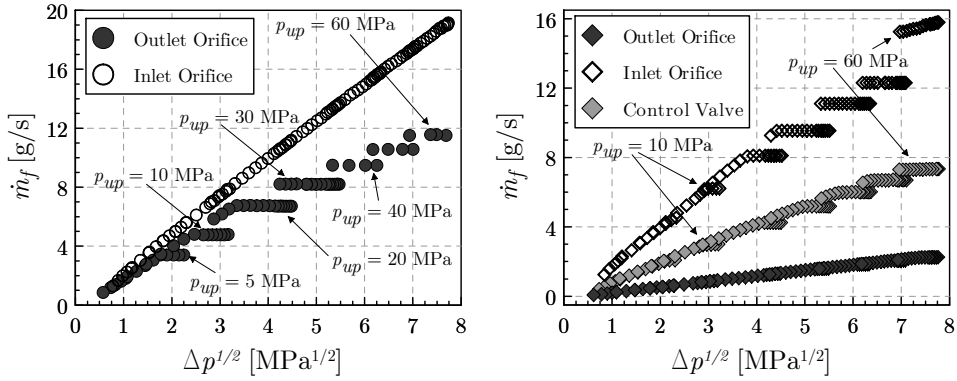

(a) Bosch CRI 2.20 injector (b) Denso G4S injector

Figure 4.11: $\dot{m}_f$ as a function of the square root of Δp for the control volume orifices.

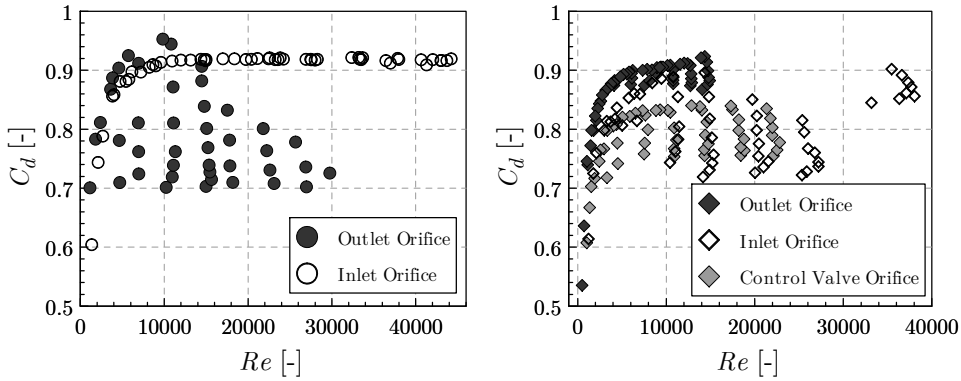

(a) Bosch CRI 2.20 injector (b) Denso G4S injector

Figure 4.12: C_d as a function of Re for the control volume orifices. For illustrative purposes, only half of the tested points are shown.

to turbulent flow, Re_{crit}, was determined considering the criterion used by AMESim [6] due to its importance to build the model. Hence, it was considered as the Re value at which C_d takes a value corresponding to 95% of $C_{d,max}$. The abrupt drop in discharge coefficient once the critical cavitation conditions are achieved highlights the need to properly describe them in order to predict the injector behaviour in an accurate way. Taking into account that CN_{crit} slightly depends on the upstream pressure considered [2, 7], the critical cavitation conditions were determined from the mass flow rate choking at the

Injector	Orifice	$C_{d,max}$ [-]	Re_{crit} [-]	CN_{crit} [-]	C_c [-]
Bosch CRI 2.20	Nozzle	0.86	5800	-	-
	Inlet	0.92	4600	-	-
	Outlet	0.96	5000	1.14	0.71
Denso G4S	Inlet	0.91	6800	1.72	0.73
	Outlet	0.92	4100	13.54	0.87
	Control Valve	0.84	3400	4.53	0.76

Table 4.4: Summary of the tested orifices hydraulic parameters.

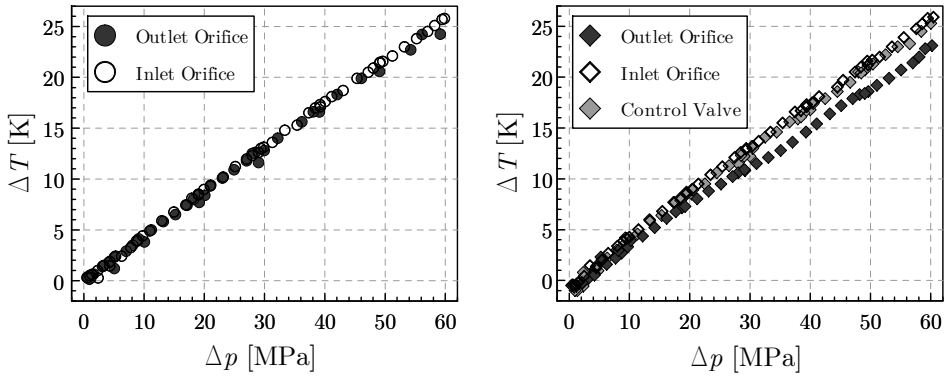

(a) Bosch CRI 2.20 injector

(b) Denso G4S injector

Figure 4.13: ΔT as a function of Δp for the control volume orifices. For illustrative purposes, only half of the tested points are shown.

highest value of upstream pressure at which it could be detected. According to Figure 4.11, this value is 20 MPa for the Bosch CRI 2.20 outlet orifice and 40 MPa for the Denso G4S injector orifices.

The temperature increase experimentally observed across each orifice as a function of the pressure drop is shown in Figure 4.13. As it can be seen, this temperature increase grows almost linearly with the pressure drop for most orifices. Figure 4.13(b) shows that, for the same pressure drop across the orifice, the Denso G4S outlet orifice leads to lower values of temperature increase across it. This could be attributed to the fact that this orifice has the lower diameter (102 µm, as shown in Table 4.2). Even though low diameters result in a lower area for heat exchange, the reduction in cross-sectional area leads to a higher portion of the flow effectively being within the boundary layer. The reduction of flow velocity in this region also acts in the sense of favouring

heat losses to the ambient. Hence, part of the theoretical temperature increase through the orifice could be ceded to the ambient instead of being kept by the fuel flow. In any case, this statement will be confirmed in Chapter 5, where the values of temperature increase here presented are compared to the theoretical ones corresponding to an isenthalpic (i.e. adiabatic) expansion in order to assess the limits of the assumption of adiabatic flow through the Bosch CRI 2.20 internal orifices.

4.3.2 Rate of injection measurement

As opposed to the hydraulic characterization of a single orifice, the determination of the injector mass flow rate signal requires to gather pulsed flow data. The device employed in the present thesis to measure and record the ROI temporal evolution during an individual injection event was a commercial Injection Rate Discharge Curve Indicator (IRDCI) from IAV. This device, illustrated in Figure 4.14, makes use of the Bosch long tube method [8], whose working principle is based on the theory of pressure wave propagation in a liquid column.

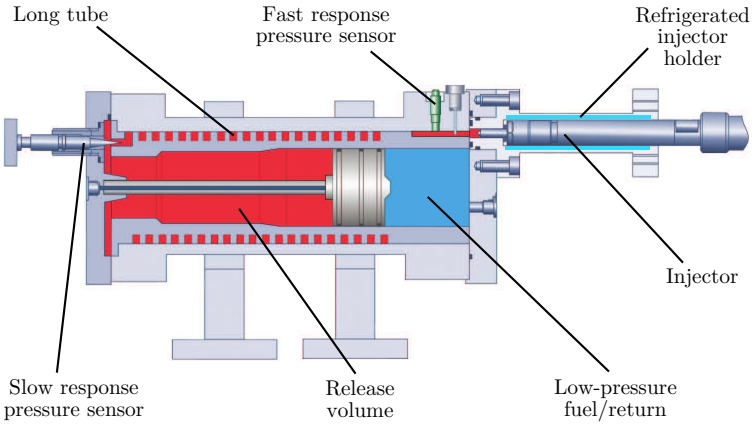

Figure 4.14: Sketch of the IRDCI main components.

As seen in the figure, the injector was introduced in the IRDCI by means of a refrigerated injector holder. This piece was part of the setup to ensure fuel temperature control, which is described in the following sections. The IRDCI internal volume is comprised by a long tube and a deposit, which were filled with fuel prior to the injection event in order to guarantee an accurate control on the pressure wave propagation. The pressure inside this volume can be adjusted to simulate the pressure inside an engine combustion chamber by

means of a flow valve controlled by a PID, which relies on the reading from a slow response pressure sensor.

When fuel is injected in the tube, a pressure wave is generated. This wave travels at the speed of sound from the injector nozzle orifices to the volume at the end of the tube, where it is damped. During each injection, the fast response pressure sensor (a piezoelectric pressure transducer) registers the pressure variation provoked by the initial pressure wave. From this signal it is possible to obtain the instantaneous mass flow rate corresponding to the injection event.

Considering a control volume constituted by a cylinder of cross-sectional area A_t in which the pressure wave is transmitted and neglecting the gravity effects, the only forces on the control volume are the pressure ones. The momentum conservation equation applied on this control volume results in:

$$(p + \Delta p)\, A_t - pA_t = \rho_f A_t a_f \Delta u_f \tag{4.3}$$

where Δu_f is the variation of liquid flow velocity in the tube. Equation (4.3) may be simplified:

$$\Delta p = \rho_f a_f \Delta u_f \tag{4.4}$$

As stated earlier, the pressure variation induced by the pressure wave (Δp) is registered by the piezoelectric sensor. This sensor must be located as close as possible to the nozzle tip in order to avoid a delay between the injection event and the acquisition time, on one hand, and to avoid friction attenuation effects that could affect the measurement, on the other. When the wave enters the release volume, the change in diameter in the duct induces a reflected wave that travels in the opposite direction of the main wave. This secondary wave may alter the shape of the measured signal. Hence, it is necessary to avoid its interaction with the primary wave. This may be achieved by using a tube sufficiently long. It is also convenient to attenuate the second wave in a fast way. Its amplitude depends on the system geometry and the injection conditions. The IRDCI control valve allows to change the flow cross-sectional area to control the effect of the reflected waves on the measurement depending on the working condition.

From the continuity equation, the variation of fuel mass flow rate through the tube as the pressure wave travels along it may be expressed as:

$$\dot{m}_f = \rho_f A_t \Delta u_f \tag{4.5}$$

Combining Equations (4.4) and (4.5), the instantaneous mass flow rate may be linked to the pressure change induced by the transmitted wave:

$$\dot{m}_f = \frac{A_t}{a_f}\Delta p \tag{4.6}$$

Hence, the rate of injection may be determined by knowing the cross-sectional area of the IRDCI tube and the fuel speed of sound. As stated in Section 4.1, this last magnitude was experimentally determined, as will be explained in Section 4.4.

Setup for the control of the injection conditions

In order to achieve the goals of the present thesis, the fuel pressure and temperature must be accurately controlled. Figure 4.15 shows a scheme of the experimental setup in which the IRDCI was introduced in order to perform the measurements with an appropriate control in the range from 253 to 373 K thanks to the use of a climatic chamber. Some of the elements that comprised the experimental setup are shown in Figure 4.16.

A *common-rail* high-pressure pump driven by an electric motor extracted and pressurized the fuel contained in a tank after being filtered. Water was recirculated around the fuel to cool it down after the heating suffered due to pressurization in the high-pressure pump. It is important to note that water was only recirculated when it was needed to mantain a relatively low temperature, but not when the climatic chamber was in use. After this heat exchange, the fuel travelled through a high-pressure flexible line, around which a coolant (glycol) at a proper temperature was also recirculated before the fuel entered the *common-rail*. The rail was connected to the injector through a 300 mm long high-pressure rigid line, which was also conveniently cooled or heated by glycol. The fuel inlet temperature and pressure conditions of the tests (hereinafter referred to as T_i and p_i, respectively) were measured in this high-pressure rigid line, right upstream of the injector (30 mm away from its inlet), where a thermocouple and a pressure sensor were located (see Figures 4.15 and 4.16). The injector was connected to the IRDCI device through an in-built intermediate piece. This piece, also shown in Figure 4.14, fell 52 mm upstream of the nozzle tip and made it possible to refrigerate the injector holder as well thanks to a glycol inlet and an outlet. An extra thermocouple was introduced at this location in order to measure the glycol temperature (see Figure 4.15). The glycol came from an electric heater where it was heated by a resistance if the fuel temperature needed to be increased.

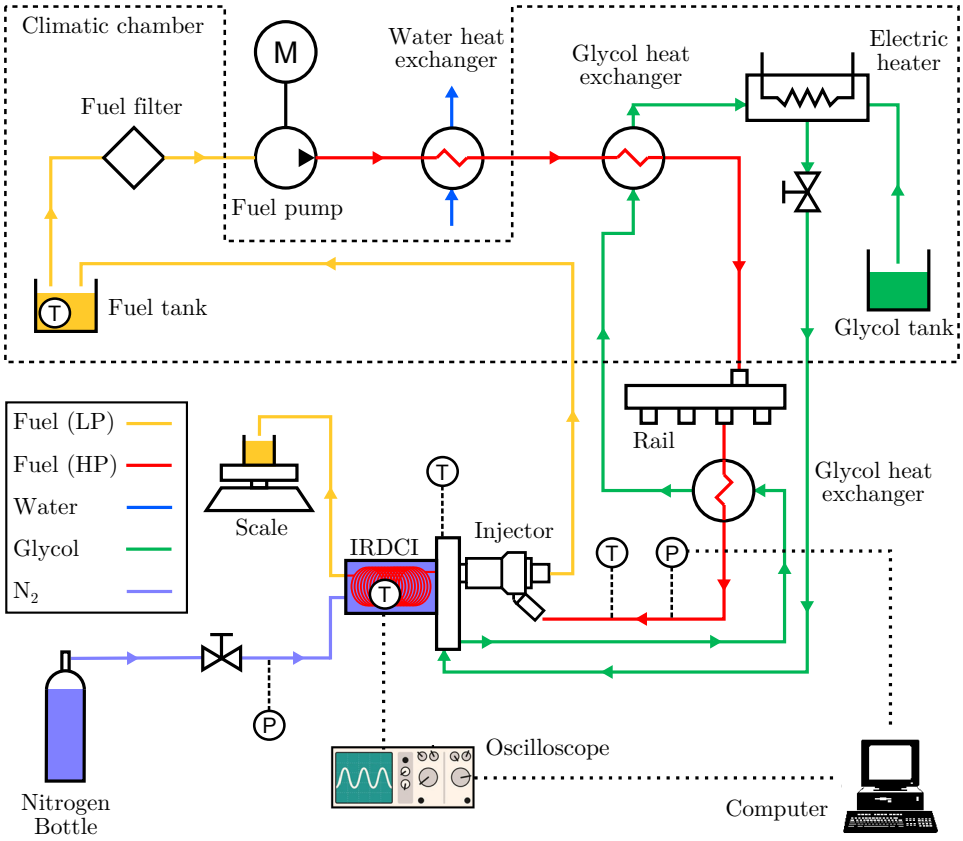

Figure 4.15: Setup for the ROI measurements. The thermocouple and pressure sensor locations are shown in the diagram.

PIDs were used as regulators, acting on the fuel pump (for the pressure) and the glycol heat exchanger (for the temperature).

Both the fuel and glycol tanks, the glycol electric heater and most of the high-pressure flexible line were placed in a climatic chamber (where temperatures down to 248 K could be achieved) with optical access for the coldest fuel temperatures tested (253 and 273 K). The high-pressure pump and the IRDCI were kept out of the climatic chamber since otherwise they would have operated out of their acceptable temperature range. In those conditions, the water cooling system was shut down and all the components upstream of the IRDCI were covered by an insulating material that prevented heat losses to the surroundings.

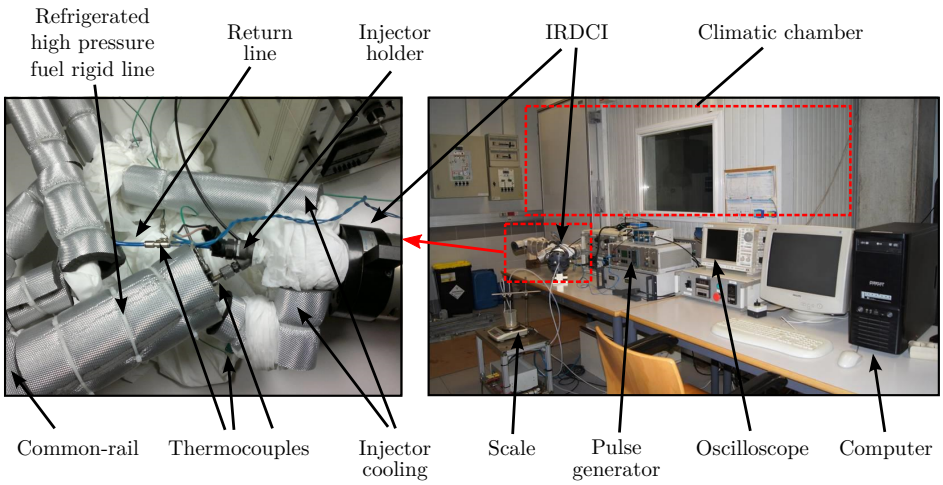

Figure 4.16: Actual elements of the experimental setup for the ROI measurements.

With this setup, in the least favourable case (253 K) it was possible to keep a controlled value of fuel temperature at the inlet (T_i), with differences among this temperature and the glycol temperature at the injector holder lower than 2 K, ensuring uniform and stable temperature conditions in the injector. The injector holder was tried to be kept at the same temperature that the fuel at the injector inlet attempting to minimize the heat exchange with the surroundings. This procedure was chosen in order to study the thermal effects purely related to the fuel evolution inside the injector and to ensure the suitability of the computational model (which treats the fuel flow as adiabatic) in order to complement the findings experimentally obtained. In any case, remarks about the extension of the validity of the assumption of adiabatic flow, both in these controlled experiments and in real engine operating conditions, will be given in Chapter 5.

The IRDCI made it possible to regulate the fuel discharge pressure with nitrogen, setting the desired value with the help of a valve downstream of a nitrogen bottle. Fuel from the injector return line was brought back to the fuel tank, whereas the fuel effectively injected in the IRDCI was discharged to a scale. The use of this scale allowed to record the total mass injected per stroke.

Signal treatment

The Bosch CRI 2.20 injector was driven by a Genotec pulse generator (Figure 4.16), which replaced the engine ECU. An injection frequency of 10 Hz was chosen so that a particular injection event was prevented from being influenced by the previous one. Once the operating conditions for a given test point were achieved, the injection was run by at least 100 s before recording the measurements, giving a minimum of 1000 warm-up injections so that stable conditions were attained.

The pressure signal from the IRDCI piezoelectric sensor was amplified, visualized in a Yokogawa DL708 digital oscilloscope and recorded in a computer together with the pressure signal in the high-pressure line and the corresponding temperature values. 50 injections per operating point were recorded, averaging both the mass flow rate and pressure signal curves. A second set of 50 injections was also measured to ensure no dispersion nor anomalous data in the results.

An example of an averaged mass flow rate curve together with its corresponding energizing signal and the recorded pressure at the high-pressure line is shown in Figure 4.17. The criteria to extract information from the curve are shown in the figure. The SOI was determined by calculating the opening slope where the mass flow was among the 10% and the 50% of the maximum achieved and intersecting the resulting curve with the value of null mass flow rate. This gave the injection delay (time difference among SOE and SOI), t_d, as shown. The time of injector closing was determined in an analogous way, leading to the injection time, t_{inj}. The steady-state stage was established as the stage on which the mass flow rate was above 95% of its maximum value. The average of the mass flow rate in the steady-state stage was computed for the longest points tested, allowing to calculate the injector discharge coefficient as shown in Equation (4.7), as derived in Section 2.3.4:

$$C_d = \frac{\dot{m}}{\dot{m}_{th}} = \frac{\dot{m}}{A_o\sqrt{2\rho_f\left(p_i - p_b\right)}} \tag{4.7}$$

where the area A_o was computed from the number of nozzle orifices and the orifices outlet diameter D_o (recall Table 4.1).

It is important to note that the averaged ROI curve shown in Figure 4.17 was already treated to compensate for two different effects.

On the one hand, the integral of the ROI curve should match the total fuel mass injected per cycle obtained thanks to the measuring scale, knowing

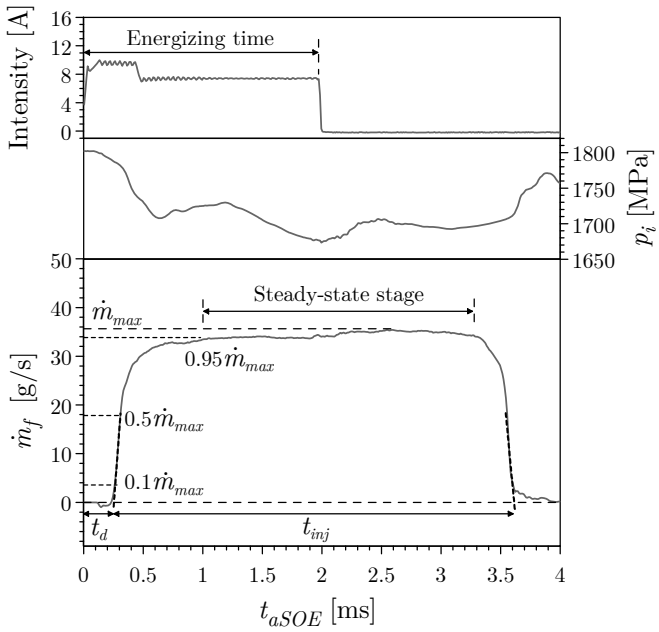

Figure 4.17: Generic averaged ROI curve together with its corresponding energizing and pressure signals.

the injection frequency. Deviations in this sense were corrected by applying the corresponding proportionality factor to the ROI curve.

On the other hand, a cumulative phenomenon has been noticed when using IRDCI devices based on the Bosch long tube. An example of this phenomenon is shown in Figure 4.18(a), where two ROI signals obtained in the same conditions of injection and discharge pressures but with different energizing time (ET) are represented. The cumulative phenomenon induces an increase in mass flow rate with the time in both curves, even though quasi-steady conditions are achieved (i.e. the maximum needle lift is reached). As a result, the mass flow rate is not zero once the injection event is finished. As it can be seen, this effect is more important the longer the duration of the energizing pulse. In addition, the two curves do not match each other in the first part of the injection, as would be expected.

The method proposed by Payri *et al.* [9] was employed to correct this phenomenon in the measurements. This method is based on the decomposition of the measured ROI curve into two signals. The first one accounts for the injection itself, whereas the second one adds the accumulation term. Fig-

ure 4.18(b) shows an example of the resulting ROI curves once the correction through this method is applied.

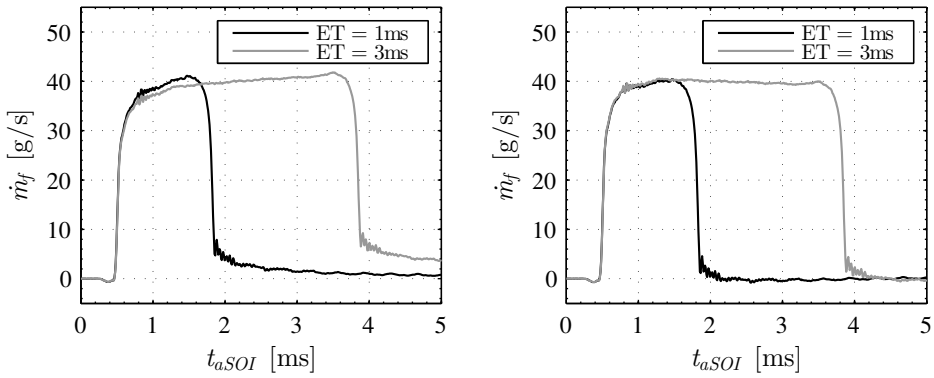

(a) Not corrected (b) Corrected

Figure 4.18: ROI signals to illustrate the correction of the cumulative phenomenon (p_i = 160 MPa and p_b = 6 MPa).

Test matrix

The conditions tested in the study are listed in Table 4.5. They were chosen so that most engine-like operating conditions are covered. This includes from cold start to a long engine run (for which the whole *common-rail* system heats up), both low, intermediate and high typical injection pressure values and both short and long injections. The longest energizing times of 2 ms ensured a long period of stabilized mass flow rate so that the injector discharge coefficient could be accurately determined. The discharge pressure was selected to match a representative average value of those found inside the cylinder of a real engine during the injection event.

All the combinations among variables were tested, leading to a total of 80 operating points. The wide range of conditions tested ensured a reasonable basis for both the direct study of the influence of the inlet fuel temperature on the injection event and the validation of the computational model used to assess the thermal effects on the injector internal behaviour.

4.4 Fuel properties determination at high pressure

In this section, the methodology to experimentally determine some of the most influencing thermodynamic properties of diesel fuels (namely speed of

Property	Values tested
Fuel inlet temperature, T_i [K]	253 - 273 - 303 - 353 - 373
Injection pressure, p_i [MPa]	40 - 70 - 120 - 180
Energizing time, ET [ms]	0.25 - 0.5 - 1 - 2
Discharge pressure, p_b [MPa]	4

Table 4.5: Experimental ROI measurements test matrix.

sound, density and bulk modulus, as seen in Section 3.4) at a wide range of temperatures (from 303 to 353 K) and pressures (up to 200 MPa), representative of *common-rail* systems, is presented. Given the almost linear relation of these properties with the temperature and pressure, they were extrapolated to lower temperatures for the implementation of the computational model. The viscosity at high pressure was estimated from ambient pressure measurements by means of correlations available in the literature.

The methodology to determine the fuel speed of sound consisted of transmitting a pressure wave along a high-pressure line and measuring the time it took for the wave to travel a given distance. The speed of sound for different conditions could be determined as established by Equation (4.8):

$$a_f = \frac{L}{\Delta t} \tag{4.8}$$

The density values were then theoretically derived from the speed of sound measurements, also leading to the isothermal bulk modulus determination. The installation was calibrated with an alkane (n-dodecane) whose properties are known and readily available for a wide range of temperatures and pressures. The measurements were also validated with another known alkane (n-heptane). Finally, the methodology was tested for a reference diesel fuel and its winter variation, which was the fuel used for all the measurements carried out in the present thesis given its adequacy to work at low temperatures due to its lower viscosity when compared to standard diesel fuels. Correlations were found to explain the dependence of the properties of both fuels with pressure and temperature.

Details about both tested fuels are given in Table 4.6. The fuel flash point and the water content were determined in accordance to the ISO 2719 and 12937 standards [10, 11], respectively, whereas the FAME volume percentage was quantified based on the ASTM D7806-12 standard [12], using Fourier-Transformed Infrared Spectrometry (FT-IR). For this last measurement, a

calibration curve was first obtained with known concentrations of FAME in pure conventional fuel. After that, samples of the tested fuels were compared to that calibration curve.

Fuel property	Reference diesel	Winter diesel
Flash point [K]	339.15	337.15
Water content [mg/kg]	29.56	31.74
FAME [% volume]	2.4	2.3

Table 4.6: Water content and FAME volume percentage for the tested fuels.

4.4.1 Speed of sound measurement facility

As reviewed in Section 3.3.1, several methods have been used to determine the speed of sound at pressures higher than the atmospheric, including the ultrasonic cell method [13]. In the present thesis, a setup that allows to couple the facility to the *common-rail* injection system was used, with the consequent simplicity to test diesel fuels. An antecedent of this setup was used by Payri *et al.* [14] and Bracho [15], but some modifications were implemented in order to increase the reliability of the measurement by ensuring a more accurate and stable temperature and pressure control.

Figure 4.19 shows a sketch of the experimental facility and its setup, where it can be seen how the injection system was used. A picture of the actual setup is shown in Figure 4.20. Fuel was extracted from the tank by a high-pressure pump that raised its pressure and delivered it to a rail, where the pressure was controlled. Before reaching the injector, the fuel travelled through a long high-pressure pipe, which constituted the basis for the measurement since it was the line through which the measured pressure wave travelled. In order to measure the pressure wave, two piezo-resistive Kistler pressure sensors (able to work under pressures up to 300 MPa) were located in different points of the high-pressure line, defining the measuring section, as seen in Figure 4.21. The length of this section needed to be long enough to allow for a clear acquisition, but short enough to minimize signal attenuation. In the end, the length between sensors was established as 4 m. The internal diameter of the pipe needed to be small in order to ensure a one-dimensional tranmission of the wave, and was set to 2 mm. After the high-pressure line, the fuel reached the injector and, in the case of an injection event, was discharged in an IRDCI, where the injected mass flow rate was determined using the Bosch long tube method and registered to check the proper operation of the facility.

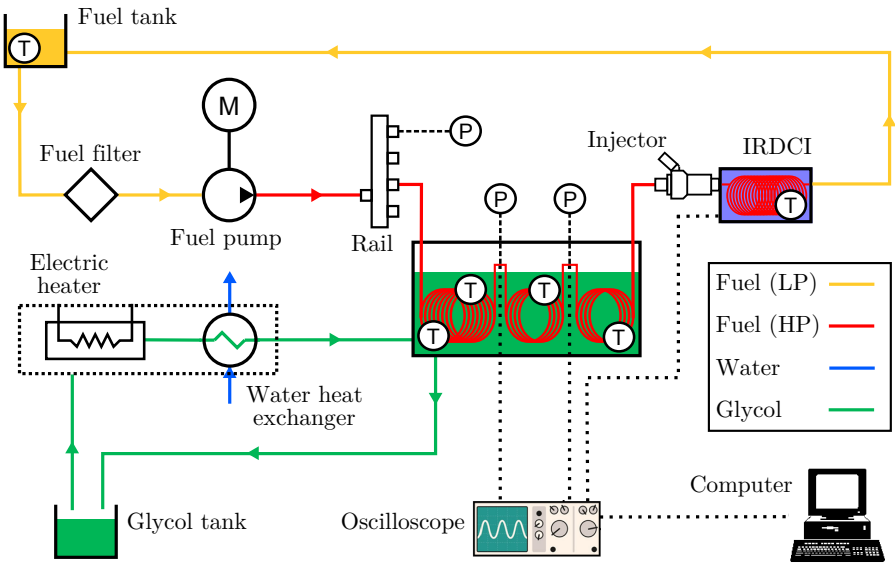

Figure 4.19: Setup for the speed of sound measurements. The thermocouple and pressure sensor locations are shown in the diagram.

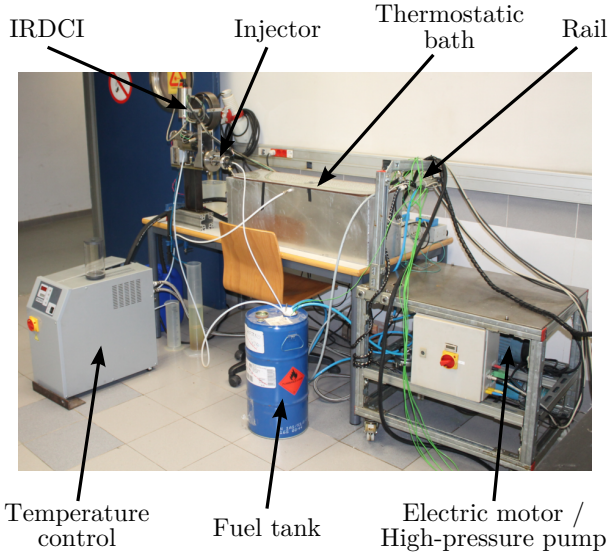

Figure 4.20: Actual elements of the experimental setup for the speed of sound measurements.

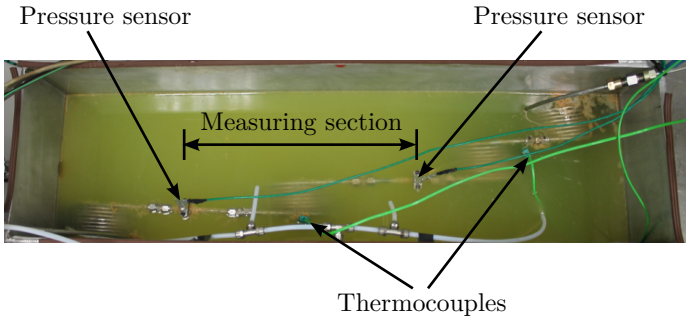

Figure 4.21: Glycol thermostatic bath containing the measuring section.

With this setup, a pressure disturbance is produced with an injection event due to the depression generated in the tube by the injector opening, resulting in the fuel being discharged in the IRDCI. This pressure disturbance was measured at two positions of the high-pressure line where the pressure sensors were located. An example of the acquired signals is shown in Figure 4.22. The injections were carried out at a small frequency (0.1 Hz) in order to avoid interaction among the waves of successive injections. It is also important to note that a long segment of high-pressure line (about 8 m, which corresponds to twice the length of the measuring section) was left between the measuring section and the injector (recall Figure 4.19) so that, for a certain injection, the rebound of the pressure wave did not interact with the perturbation being measured, which would have interfered with the signal acquisition. The signal acquisition was performed by means of a Yokogawa DL708 digital oscilloscope and recorded in a personal computer for processing purposes.

In order to control the temperature, the high-pressure lines were immersed in a thermostatic bath filled with glycol, as seen in Figure 4.21. Temperature was measured by means of 4 thermocouples at different locations to ensure temperature uniformity along the bath. The glycol was recirculated and its temperature electronically regulated by a device (Figure 4.20) that either heated it with an electrical resistance or cooled it down with external water, as needed. The maximum temperature deviations found between thermocouple locations were 1 K, confirming good temperature uniformity. In addition, fuel temperature was also measured in the fuel tank, rail, injector return line and IRDCI.

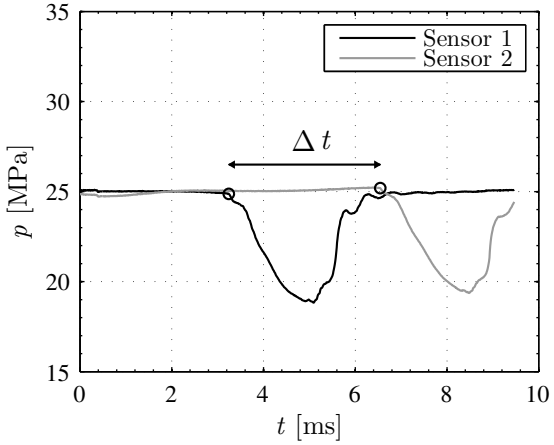

Figure 4.22: Example of the pressure signals captured by the pressure sensors at two different locations of the high-pressure lines.

Signal treatment, calibration and processing

For each operating point, 25 repetitions were taken. The pressure signals at the two locations were recorded for each of the repetitions and processed in order to obtain the travel time of the pressure wave (Δt) between sensors. Finally, an averaged value of Δt was accepted as the result due to the small dispersion among repetitions, quantified as $\pm$ 0.5%.

Recalling Equation (4.8), the proposed methodology implies that the speed of sound was calculated from the Δt value measured experimentally and the length L between sensors. However, it is important to note that this length changes in a certain magnitude (ΔL) with the ambient temperature and pressure:

$$\Delta L = L_0 \left[\alpha_t \left(T - T_0\right) + \beta_t \left(p - p_0\right)\right] \tag{4.9}$$

where L_0 is the theoretical length at a reference temperature (T_0) and a reference pressure (p_0), whereas α_t and β_t are the coefficients of thermal expansion and compressibility for the pipe material (stainless steel), respectively. Thus, for any tested operating condition, the length L used to compute the speed of sound through Equation (4.8) was:

$$L = L_0 + \Delta L \tag{4.10}$$

A calibration procedure to establish an accurate value of L_0 was performed with n-Dodecane, a pure alkane whose speed of sound values are known at different conditions of temperature and pressure. Measurements were performed at three different temperatures (303, 323 and 343 K) and several pressures up to 100 MPa. The length L_0 was then calibrated by comparing the n-Dodecane measurements to the data theoretically derived from Helmholtz-energy-explicit-type formulations by Bell *et al.* [16]. The value of L_0 at a reference point of $T_0 = 298\,\text{K}$ and $p_0 = 0.1\,\text{MPa}$ that led to the best fitting of all the measurements at different temperatures and pressures was accepted as the calibrated length.

Therefore, for any fuel to be characterized, once Δt and L were obtained for a given condition, the fuel speed of sound a_f could be calculated according to Equation (4.8).

Before actually applying the methodology for the tested fuels of unknown properties (i.e. the reference and winter diesel fuels), the calibrated value of L_0 was also validated by performing measurements for n-Heptane and comparing them to the CoolProp library [16], as outlined next.

Test matrix

Measurements were performed for n-Dodecane in order to calibrate the reference length L_0, n-Heptane to validate the methodology, and a reference diesel fuel and its winter variation for the purposes of this thesis. The operating points tested for each fuel are shown in Table 4.7.

Fuel	**Temperatures** [K]	**Pressures** [MPa]
n-Dodecane n-Heptane	303 - 323 - 343	25 - 30 - 40 - 50 - 60 - 70 - 80 - 90 - 100
Reference diesel Winter diesel	303 - 313 - 323 - 333 - 343 - 353	50 - 60 - 70 - 80 - 90 - 100 - 110 - 120 - 130 - 140 - 150 - 160 - 170 - 180 - 190 - 200

Table 4.7: Experimental speed of sound measurements test matrix.

It is important to note that the method has a limitation at low pressures, for which it was not possible to regulate the pressure at the rail. Hence, the lower pressure tested for each fuel was the minimum that allows an acceptable pressure regulation in the rail. Also, n-Dodecane and n-Heptane were only tested at pressures up to 100 MPa. Even though an increase in pressure leads to higher viscosities, it also generates an important temperature increase in

the fuel pump that induces a reduction in viscosity. The resulting consequence of these two opposed effects for the n-Dodecane and n-Heptane measurements was a net decrease in viscosity, reaching values way lower than those achieved with diesel fuel, thus strongly affecting the pump lubrication. For this reason, tests at higher pressures were not performed in order to prevent the fuel pump from being damaged.

Methodology validation

As already stated, the validity of the methodology needed to be assessed once the facility was calibrated with n-Dodecane. To do so, measurements were performed with n-Heptane at the conditions depicted in Table 4.7. Figure 4.23 shows the comparison of the n-Heptane experimental results with the theoretical data reported by Bell *et al.* [16].

In Figure 4.23(a), the evolution of the speed of sound with the temperature is shown for the several isobaric curves experimentally tested. On the other hand, Figure 4.23(b) shows the evolution of the property against the pressure for the tested isothermal curves. The comparison shows good agreement of the experimental data with the theoretical values, with a 1.24% maximum deviation, found at the lowest pressures and temperatures. This validates the speed of sound facility and the calibration procedure performed with n-Dodecane.

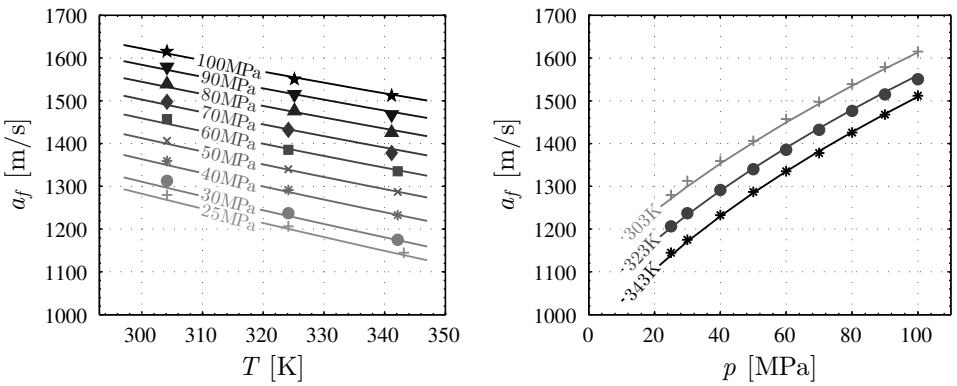

(a) Isobaric curves

(b) Isothermal curves

Figure 4.23: Speed of sound curves for n-Heptane compared to theoretical data from [16]. Experimental results are shown as symbols, whereas data from [16] are represented as continuous lines.

The observed evolution of the speed of sound with the temperature and pressure is as expected from previous works [17, 18] and reported in Section 3.3.1: it increases when the pressure increases, and decreases when the temperature increases. It is also important to state that the dependency with the temperature is found to be nearly linear, whereas the pressure dependency shows a different behaviour.

In order to quantify these trends and dispose of suitable data for the computational model implementation, the speed of sound values for each tested fuel have been fitted to a polynomial expression as a function of temperature and pressure:

$$a_f(p,T) = A_1 + A_2(T - T_0) + A_3(p - p_0) + A_4(p - p_0)^2 + A_5(T - T_0)(p - p_0) \quad (4.11)$$

The term corresponding to the dependency with the squared temperature was omitted in the view of the previous observations. The coefficients of this expression for each tested fuel are collected in Table 4.8 together with the statistical R^2 values. The high values of R^2 confirm the reliability of this regression and the fact that the speed of sound is virtually linear with respect to the temperature.

Fuel	$\boldsymbol{A_1}$ [-]	$\boldsymbol{A_2}$ [-]	$\boldsymbol{A_3}$ [-]	$\boldsymbol{A_4}$ [-]	$\boldsymbol{A_5}$ [-]	$\boldsymbol{R^2}$ [-]
n-Heptane	1152.6	-3.6694	6.6762	-0.016345	0.0070950	0.99980
Reference	1363.0	-3.0832	4.2798	-0.0061149	0.0072006	0.99959
Winter	1350.6	-3.1485	4.4928	-0.0069612	0.0074022	0.99959

Table 4.8: Coefficients for the speed of sound correlation of Equation (4.11) *for the different fuels tested. Reference:* $T_0 = 298\,\mathrm{K}$; $p_0 = 0.1\,\mathrm{MPa}$.

Tested fuels results

Figure 4.24 represents the experimental results for the winter diesel fuel at the different isothermal lines tested, plotted together with the values obtained through the polynomial expression to which they have been fitted. As the high values of R^2 suggested, there is good agreement among the experimental data and the values predicted by the correlation. The fact that the isothermal lines are equally spaced highlights again the linear dependency of the speed of sound with respect to the temperature.

Figure 4.25, in turn, shows a comparison among the reference and the winter diesel fuels, considering only the values predicted by their respective

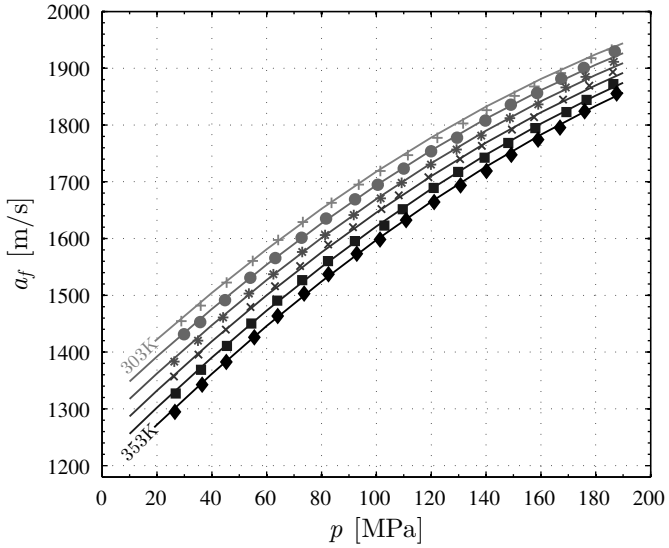

Figure 4.24: Speed of sound isothermal curves for the winter diesel fuel. Experimental results are shown as symbols, whereas the values corresponding to the regression from Equation (4.11) *and Table 4.8 are represented as continuous lines.*

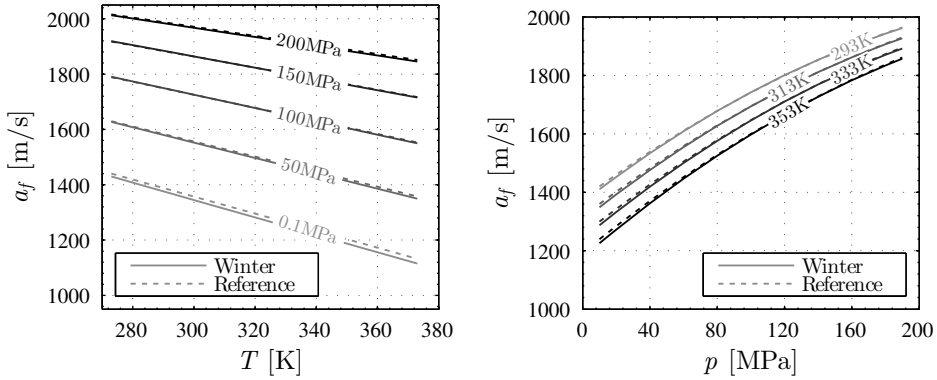

(a) Isobaric curves

(b) Isothermal curves

Figure 4.25: Speed of sound correlated curves for the reference and the winter diesel fuels.

correlations. It can be seen that both fuels present almost the same speed of sound for most of the conditions of pressure and temperature relevant for diesel injection engine operation. Slight differences are only observed at low pressures. This is an interesting result considering that the industry seeks for winter fuels with the same properties of standard fuels but with the ability of working at extremely low temperatures due to their reduced viscosities in those conditions.

4.4.2 Density determination

As reviewed in Section 3.3.2, the density values at high pressure may be derived from speed of sound measurements due to the relations among thermodynamic variables.

Let us consider the definitions of fuel isentropic and isothermal bulk modulus (β_S and β_T, respectively):

$$\beta_S = \rho_f \left(\frac{\partial p}{\partial \rho_f} \right)_S \tag{4.12}$$

$$\beta_T = \rho_f \left(\frac{\partial p}{\partial \rho_f} \right)_T \tag{4.13}$$

Both definitions of bulk modulus are related to each other as stated by Hayward [19]:

$$\frac{1}{\beta_T} = \frac{1}{\beta_S} + \frac{T\alpha^2}{\rho_f c_p} \tag{4.14}$$

where α is the coefficient of thermal expansion. As stated in Section 3.3, the isentropic bulk modulus and the speed of sound are linked through the density [19]:

$$a_f^2 = \frac{\beta_S}{\rho_f} \tag{4.15}$$

Hence, combining Equations (4.12) to (4.15):

$$\left(\frac{\partial \rho_f}{\partial p} \right)_T = \frac{1}{a_f^2} + \frac{T\alpha^2}{c_p} \tag{4.16}$$

Equation (4.16) can be solved for an isothermal line, thus obtaining the relation among the fuel density and speed of sound:

$$\rho_f(p,T) = \rho_f(p_0,T) + \int_{p_0}^{p} \frac{\mathrm{d}p}{a_f^2} + T\int_{p_0}^{p}\left(\frac{\alpha^2}{c_p}\right)\mathrm{d}p \tag{4.17}$$

The first term at the right side of Equation (4.17) corresponds to the density at the reference pressure, which is taken as the atmospheric pressure. This is convenient since ρ_f at p_0 can then be directly measured with a hydrometer. The other terms of the equation are the deviation to take into account the effect of pressure on the density at a given pressure. The second term can be evaluated from the evolution of the speed of sound with the pressure for a given isothermal line. Thus, this term can be evaluated from the speed of sound measurements, given that enough pressures are tested for a certain temperature. Finally, the last term is related to the difference between specific heat capacities (c_p and c_v) for the fluid. This difference is not significant for liquids [17, 19, 20], which leads to this last term being the smallest contribution to the density.

With all, it was possible to determine the density at any pressure and temperature condition only by measuring the density at atmospheric pressure and processing the speed of sound measurements presented in Section 4.4.1.

Density measurement at atmospheric pressure

According to Equation (4.17), density measurements needed to be performed at different temperatures for a reference pressure, which was taken as the atmospheric.

The elements to realize the measurements are shown in Figure 4.26. A standard hydrometer was used according to the ASTM D1298 standard [21]. The accuracy of the hydrometer was determined to be $\pm 5 \times 10^{-4}\mathrm{kg/m^3}$ upon calibration, also carried out in accordance to this standard. The hydrometer was fitted inside a test tube in which the diesel specimen was introduced. Measurements were taken at different temperatures ranging from 300 to 350 K, in steps of 5 K. Temperature control was achieved by means of a thermostatic bath. The temperature of the diesel sample was measured by a thermometer and regulated accordingly thanks to a temperature regulator (PID) that acted on an electrical resistance that heated the thermostatic bath.

These tests were also validated by measuring the density through a second procedure, using a pycnometer and following the method established in the

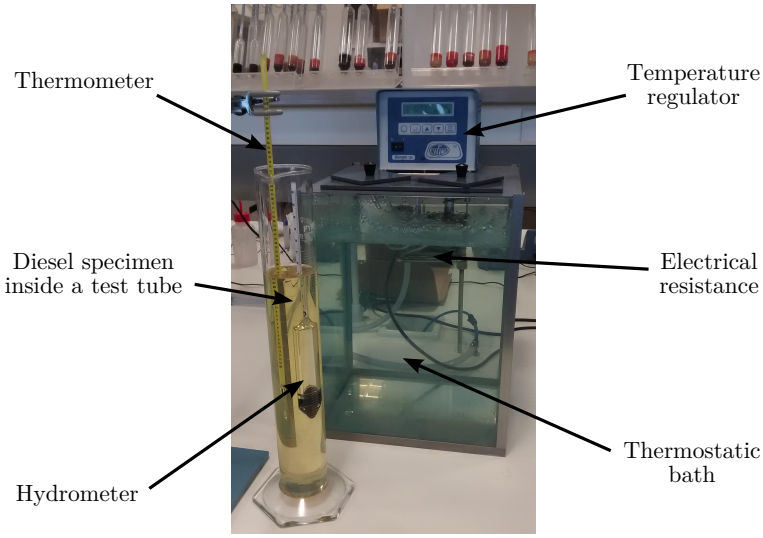

Figure 4.26: Elements for the measurement of the fuel density at atmospheric pressure.

ASTM D1217 standard [22]. A volume of 10 ml was used, with an accuracy of $\pm 1.16 \times 10^{-4}$ml estimated during its calibration.

It is known that the behaviour of the density with respect to the temperature at atmospheric pressure is linear. In order to have a practical expression to be introduced in Equation (4.17), data for each fuel were fitted to a linear function:

$$\rho_f\left(p_0, T\right) = B_1 + B_2 T \tag{4.18}$$

The coefficients obtained for both the reference and the winter diesel fuels are represented in Table 4.9 together with the corresponding R^2 values. The results of the measurements for both fuels are shown in Figure 4.27. The trends predicted by the correlation of Equation (4.18) are also represented. It can be observed that the fuel density evolution with the temperature is nearly identical for both fuels (as confirmed by the coefficients B_2 of Table 4.9), and the only difference among fuels is seen at the reference temperature and pressure (about $3\,\mathrm{kg/m^3}$). This fact confirms the evidence stated in Section 4.4.1 about both fuels trying to present the same properties regardless the operating conditions.

Fuel	B_1 [-]	B_2 [-]	R^2 [-]
Reference	1128.1	-1.0179	0.99932
Winter	1125.7	-1.0194	0.99594

Table 4.9: Coefficients for the density correlation at atmospheric pressure of Equation (4.18) *for the different fuels tested.*

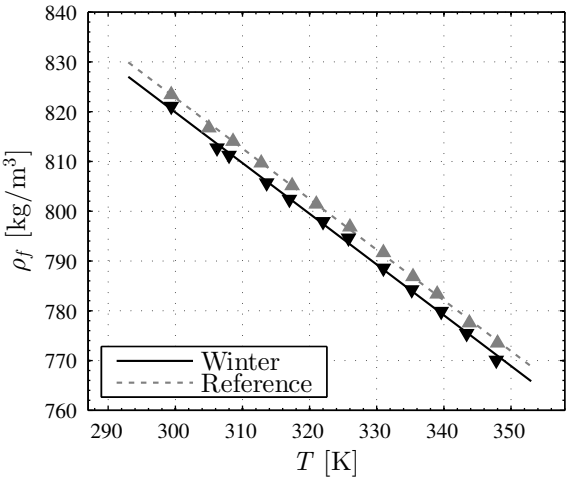

Figure 4.27: Density as a function of temperature for the reference and winter diesel fuels at atmospheric pressure. Experimental results are shown as symbols, whereas the values corresponding to the regression from Equation (4.18) *and Table 4.9 are represented as continuous lines.*

Density determination at high pressure

The next step to determine the density at any operating condition was to solve the second term of the right side of Equation (4.17). Therefore, it was needed to express the fuel speed of sound as a function of pressure for each isothermal line measured. A polynomial expression was chosen for this purpose:

$$a_f(p) = C_1 + C_2 p + C_3 p^2 + C_4 p^3 \tag{4.19}$$

The coefficients of Equation (4.19) for the isothermal curves tested for each fuel are shown in Table 4.10. The high values of R^2 show that this correla-

T [K]	C_1 [-]	C_2 [-]	$C_3 \cdot 10^3$ [-]	$C_4 \cdot 10^5$ [-]	R^2 [-]
n-Heptane					
303	1143.9	5.9723	−4.4777	−5.7752	0.99986
323	1049.0	7.2026	−20.690	1.2303	0.99988
343	871.02	14.975	−178.15	1.0185	0.99874
Reference diesel					
303	1309.7	5.4502	−16.752	2.9538	0.99986
313	1295.1	5.1006	−13.161	2.1344	0.99985
323	1241.2	5.8121	−18.525	3.5589	0.99989
333	1212.6	5.8715	−19.262	4.0063	0.99995
343	1163.7	6.4894	−23.649	4.9716	0.99994
353	1114.7	7.1147	−28.915	6.4891	0.99975
Winter diesel					
303	1312.2	5.2858	−15.751	2.5482	0.99995
313	1281.9	5.3342	−14.774	2.5496	0.99991
323	1247.3	5.5259	−16.164	3.0151	0.99994
333	1215.2	5.7518	−17.641	3.3736	0.99993
343	1185.2	5.6490	−15.665	2.7323	0.99982
353	1146.5	6.0103	−18.819	3.6888	0.99994

Table 4.10: Coefficients for the speed of sound correlations of Equation (4.19) *at each isothermal line for the different fuels tested.*

tion was suitable to be substituted in Equation (4.17) without introducing a significant error in the calculations.

Finally, considering its small influence in the result (its contribution to the total density represents around 1 to 2%), the last term of Equation (4.17) was approximated considering that α and c_p do not depend on the pressure for diesel fuels. As an example to support this fact, Chorazewski *et al.* [23] showed that c_p is hardly affected by pressure for the ISO4113 test fluid, whose thermophysical properties are similar to those of diesel fuels. Therefore, Equation (4.17) was rewritten as:

$$\rho_f(p,T) = B_1 + B_2 T + \int_{p_0}^{p} \frac{\mathrm{d}p}{\left(C_1 + C_2 p + C_3 p^2 + C_4 p^3\right)^2} + T\frac{\alpha^2}{c_p}(p - p_0) \quad (4.20)$$

where the coefficients C_1, C_2, C_3 and C_4 were computed for the corresponding isothermal line of interest. With regard to the last term of the equation,

$c_p = f(T)$ was assumed to take the same values of the ISO4113 test fluid reported by Chorazewski *et al.* [23]. On the other hand, $\alpha = f(T)$ was computed from the density measurements at atmospheric pressure in accordance to Equation (4.21):

$$\alpha = \frac{1}{v}\left(\frac{\partial v}{\partial T}\right)_p = -\frac{1}{\rho_f}\left(\frac{\partial \rho_f}{\partial T}\right)_p \tag{4.21}$$

Considering the usual variations of c_p and α among diesel fuels on the studied range of temperatures and pressures [16, 23] and the small contribution of the third term of Equation (4.17) to their density, the maximum impact of the assumptions concerning these variables was estimated to be 0.32% of the total density values finally obtained.

Methodology validation

In an analogous way to the analysis for the speed of sound reported in Section 4.4.1, Figure 4.28 shows the comparison of the n-Heptane experimental results with the data from [16] in order to check the validity of the methodology.

In Figure 4.28(a), the evolution of the density with the temperature is shown for the different isobaric curves tested. Figure 4.28(b), in turn, shows

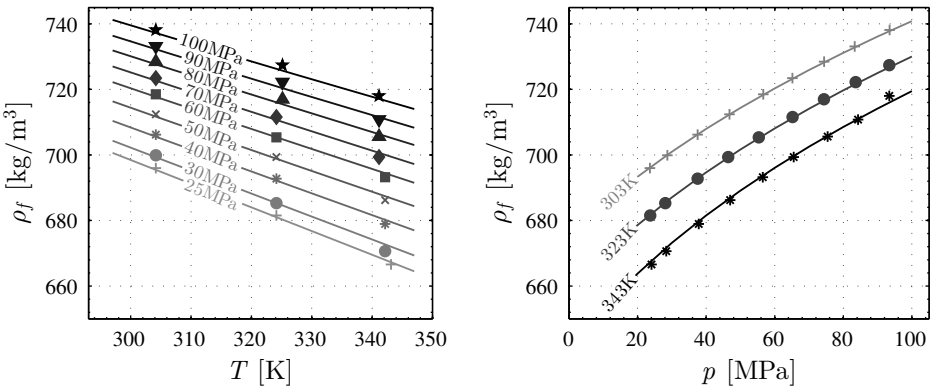

(a) Isobaric curves (b) Isothermal curves

Figure 4.28: Density curves for n-Heptane compared to theoretical data from [16]. Experimental results are shown as symbols, whereas data from [16] are represented as continuous lines.

the evolution of the density with respect to the pressure for the three isothermal curves. The comparisons show good agreement of the experimental data with the theoretical values, with a 0.5% maximum deviation that highlights the validity of the methodology implemented to determine diesel fuel densities at high pressure from the speed of sound measurements.

The evolution of the density with the temperature and pressure was found to be as expected from previous works [17, 24] and reported in Section 3.3.2: it increases when the pressure increases and decreases when the temperature increases.

As shown for the speed of sound in Section 4.4.1, in order to quantify the density trends with the temperature and pressure and dispose of suitable data for the computational model implementation, the density results have been fitted to a polynomial expression:

$$\rho_f(p,T) = D_1 + D_2(T-T_0) + D_3(T-T_0)^2 + D_4(p-p_0) + D_5(p-p_0)^2 + D_6(T-T_0)(p-p_0) \quad (4.22)$$

Note that, in this case, the term gathering the dependency of the property with the squared temperature has been kept. As opposed to the speed of sound, a small non-linearity of density with respect to the temperature was found. The coefficients of this expression for each fuel are collected in Table 4.11 together with the statistical R^2 values. These values are close to 1, which highlights the ability of the polynomial correlation to reproduce the density trends.

Fuel	$\boldsymbol{D_1}$	$\boldsymbol{D_2}$	$\boldsymbol{D_3 \cdot 10^3}$	$\boldsymbol{D_4}$	$\boldsymbol{D_5 \cdot 10^4}$	$\boldsymbol{D_6 \cdot 10^3}$	$\boldsymbol{R^2}$
n-Heptane	680.7	-0.6376	−3.630	0.8536	-2.267	2.486	0.9998
Reference	830.6	-1.0210	1.531	0.5657	-6.415	1.254	0.9997
Winter	826.5	-1.0217	1.251	0.6035	-8.265	1.441	0.9995

Table 4.11: Coefficients for the density correlation of Equation (4.22) *for the different fuels tested. Reference:* $T_0 = 298\,\mathrm{K}$; $p_0 = 0.1\,\mathrm{MPa}$.

Tested fuels results

Figure 4.29 represents the experimental results for the winter fuel at the different isothermal lines tested. Results are plotted together with the corresponding values obtained through the polynomial expression of Equation (4.22). Again, there is good agreement among the experimental data and the values predicted by the correlation, as the high values of R^2 suggest.

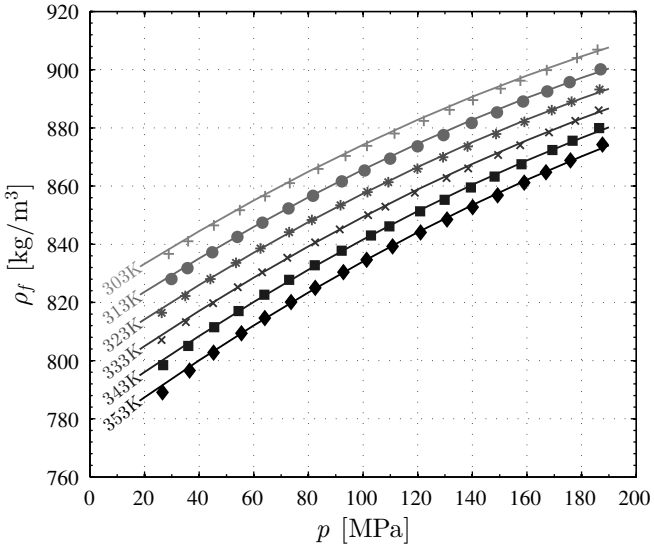

Figure 4.29: Density isothermal curves for the winter diesel fuel. Experimental results are shown as symbols, whereas the values corresponding to the regression from Equation (4.22) *and Table 4.11 are represented as continuous lines.*

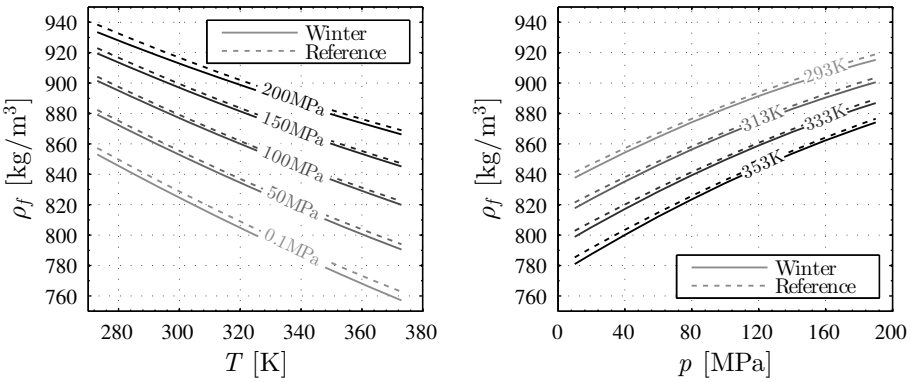

(a) Isobaric curves

(b) Isothermal curves

Figure 4.30: Density correlated curves for the reference and the winter diesel fuels.

Figure 4.30, in turn, shows a comparison among the reference and the winter diesel fuels, considering only the values predicted by their respective correlations. Densities take very similar values for both fuels. Differences can be mostly attributed to the differences at atmospheric pressure, as it was seen in Figure 4.27. These differences only get higher at low pressures, due to the discrepancies in the speed of sound values among fuels at these pressures (recall Figure 4.25). However, the density remains at similar values for both fuels, which highlights the possibility of interchanging both fuels in a real diesel engine without substantially affecting the quantity of diesel fuel mass injected in the cylinder.

4.4.3 Bulk modulus determination

The fuel isentropic bulk modulus β_S (here referred to as fuel *bulk modulus*, β_f) can be directly obtained from both the speed of sound and the density through Equation (4.15), rearranged as follows:

$$\beta_f = \beta_S = \rho_f a_f^2 \tag{4.23}$$

Even though a quadratic dependency of the fuel density with temperature has been reported (Equation (4.22) and Table 4.11), the quadratic contribution of the temperature was not found to be significant on the bulk modulus, as other authors implied as well [14, 24, 25]. A quadratic contribution of the pressure was noticed, however. Hence, results have been fitted to a polynomial expression with the following terms:

$$\beta_f\,(p,T) = E_1 + E_2\,(T - T_0) + E_3\,(p - p_0) + E_4\,(p - p_0)^2 \tag{4.24}$$

The coefficients of this expression for each fuel are collected in Table 4.12 together with the corresponding statistical R^2 values. The fact that these

Fuel	$\boldsymbol{E_1 \cdot 10^{-9}}$ [-]	$\boldsymbol{E_2 \cdot 10^{-6}}$ [-]	$\boldsymbol{E_3 \cdot 10^{-7}}$ [-]	$\boldsymbol{E_4}$ [-]	$\boldsymbol{R^2}$ [-]
n-Heptane	0.918 65	-7.6150	1.1994	-8523.0	0.99924
Reference	1.5146	-8.7413	1.1685	-6173.9	0.99979
Winter	1.4891	-8.7661	1.1986	-7461.3	0.99976

Table 4.12: Coefficients for the bulk modulus correlation of Equation (4.24) *for the different fuels tested. Reference:* $T_0 = 298\,\mathrm{K}$; $p_0 = 0.1\,\mathrm{MPa}$.

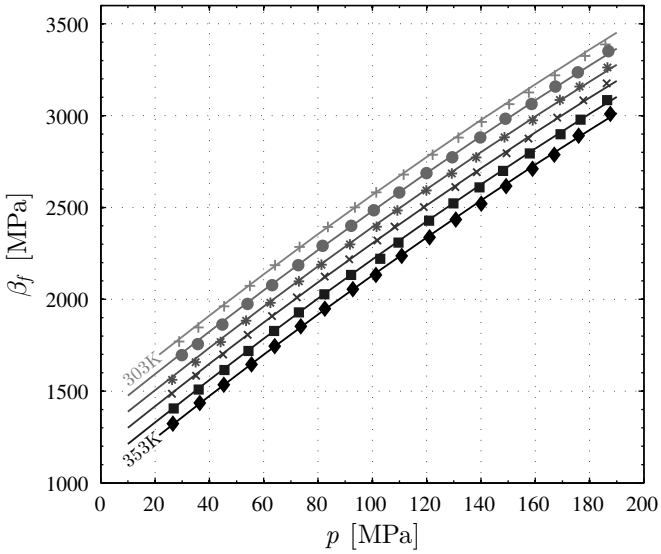

Figure 4.31: Isentropic bulk modulus isothermal curves for the winter diesel fuel. Experimental results are shown as symbols, whereas the values corresponding to the regression from Equation (4.22) *and Table 4.11 are represented as continuous lines.*

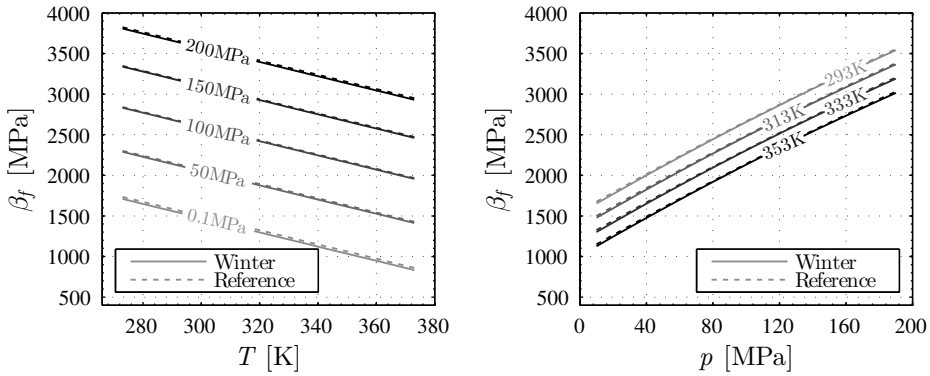

(a) Isobaric curves

(b) Isothermal curves

Figure 4.32: Isentropic bulk modulus correlated curves for the reference and winter diesel fuels.

values remain high confirms the linear tendency of the bulk modulus with temperature and quadratic with pressure.

Figure 4.31 shows the results for the winter diesel fuel at the different isothermal lines tested. Data are represented together with the values obtained through the polynomial expression of Equation (4.24). Results for n-Heptane are omitted since the validity of the methodology has already been proved for speed of sound and density, the bulk modulus depending directly on both of them. It can be seen that the bulk modulus grows almost linearly with the pressure, although a significant contribution of the quadratic term was confirmed. Several authors have reported that this increase of the bulk modulus with the pressure is related to an extra resistance to compression when the fuel is already compressed, since the molecules are closely packed together [17].

Figure 4.32 represents the bulk modulus comparison for the reference and winter diesel fuels, taking the data reported by the correlations of Equation (4.24) for both fuels. The results for both fuels are very similar again, as it was expected since the bulk modulus depends directly on both the speed of sound and density, that were already found to be alike. In addition, Figure 4.32 shows that the bulk modulus decreases with the temperature, although it is mostly influenced by pressure.

4.4.4 Viscosity estimation

In general, fuel viscosity has a relevant effect on the injection process, as stated in Section 3.4. Moreover, the Bosch CRI 2.20 injector studied in the present thesis remains in ballistic operation for the majority of the injection event. As a consequence, the effects of fuel viscosity on injector dynamics are deemed to be even more important. Hence, viscosity data needed to be supplied to the computational model implemented in order to properly mimic the injector behaviour.

Due to technological limitations, viscosity values were only measured at atmospheric pressure. The evolution of this thermodynamic property with the pressure was estimated from correlations available in the literature, as introduced in Section 3.3.4.

Viscosity measurement at atmospheric pressure

The kinematic viscosity of the fuels, ν_f, was determined by means of a commercial Cannon-Fenske viscometer. This device, a type of capillary viscometer (see Section 3.3.4), was used following the procedure specified in the ASTM

Fuel	F_1 [-]	F_2 [-]	R^2 [-]
Reference	3.4571	-0.028314	0.98748
Winter	3.2158	-0.026279	0.99061

Table 4.13: Coefficients for the viscosity correlation at atmospheric pressure of Equation (4.26) *for the different fuels tested. Reference:* $T_0 = 298\,\mathrm{K}$.

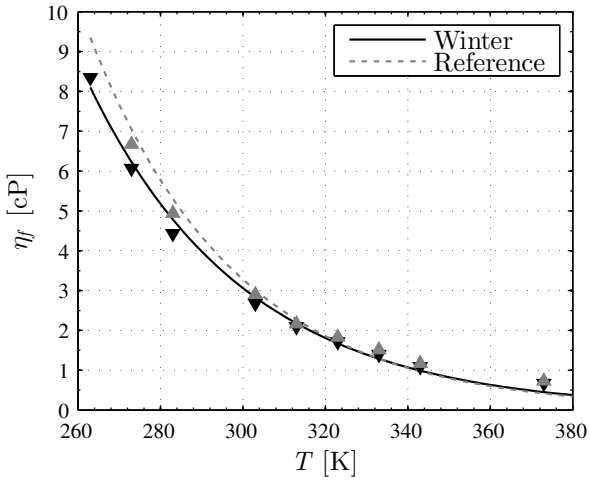

Figure 4.33: Viscosity as a function of temperature for the reference and winter diesel fuels at atmospheric pressure. Experimental results are shown as symbols, whereas the values corresponding to the regression from Equation (4.26) *and Table 4.13 are represented as continuous lines.*

D445 standard [26] in order to obtain an empirical expression for the viscosity as a function of the temperature at atmospheric pressure. In an analogous way to the fuel density determination at atmospheric pressure, a thermostatic bath was in charge of controlling the fuel temperature. The dynamic viscosity, η_f was determined through Equation (4.25) using the density data reported in Section 4.4.2.

$$\eta_f = \rho_f \nu_f \tag{4.25}$$

The experimental results were fitted to an exponential equation as follows:

$$\eta_f = F_1 e^{F_2 (T - T_0)} \tag{4.26}$$

The coefficients obtained for both the reference and the winter diesel fuels are represented in Table 4.13 together with the corresponding R^2 values. The results of the measurements for both fuels are shown in Figure 4.33. The trends predicted by the correlation of Equation (4.26) are also represented in the figure. It can be observed that the viscosity is nearly identical for both fuels from a temperature of about 300 K. However, the exponential increase of viscosity when reducing the temperature is less accused for the winter diesel, which therefore exhibits a lower viscosity at low temperatures as desired for its cold start capabilities.

Viscosity estimation at high pressures

The viscosity values at high pressure were estimated from the expression introduced by Kouzel [27], presented in Section 3.3.4 and reproduced here for illustrative purposes:

$$\log\left(\frac{\eta_f}{\eta_{f,0}}\right) = \frac{p - 0.10133}{1000}\left(-1.48 + 5.86\eta_{f,0}^{0.181}\right) \tag{4.27}$$

where $\eta_{f,0}$ was introduced from the correlation of Equation (4.26) at atmospheric pressure.

The resulting values are represented for both reference and winter diesel fuels in Figure 4.34. As it can be seen, the exponential growth of fuel viscosity

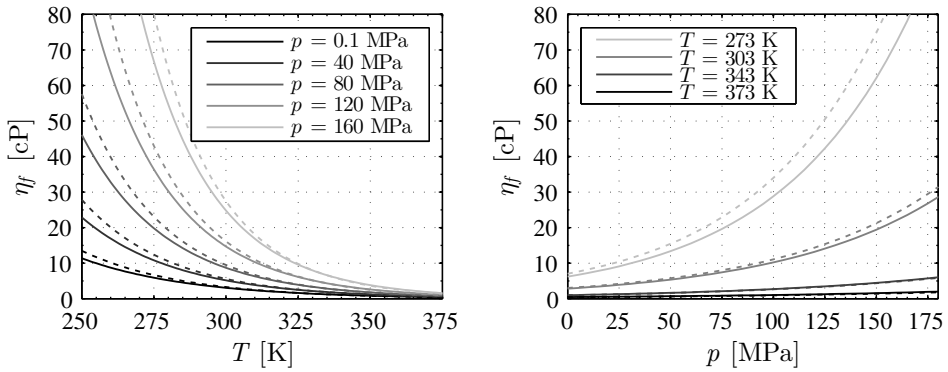

(a) $\eta = f(T)$ (b) $\eta = f(p)$

Figure 4.34: Estimated evolution of the dynamic viscosity for the reference (dashed line) and winter (continuous line) diesel fuels.

observed when the fuel temperature decreases is even more accused the higher the fuel pressure. This fact is key to understand the diesel injection process in cold conditions, considering the combined effect of both low temperatures and high pressures. On the other hand, deviations among fuels are also more accused the lower the fuel temperature and the higher the pressure. In these conditions, the viscosity of the reference fuel grows higher than the one of its winter variation. Hence, the discrepancies found in Figure 4.33 are further enhanced by the effect of pressure. This fact justifies the use of winter fuels for the operation of *common-rail* systems at cold temperatures.

References

[1] MACIAN, V., BERMUDEZ, V., PAYRI, R., and GIMENO, J. "New technique for determination of internal geometry of a Diesel nozzle with the use of silicone methodology". *Experimental Techniques*, vol. 27.April (2003), pp. 39–43. ISSN: 0732-8818. DOI: 10.1111/j.1747-1567.2003.tb00107.x.

[2] SALVADOR, F. J. "Estudio teórico experimental de la influencia de la geometría de toberas de inyección Diésel sobre las características del flujo interno y del chorro". PhD thesis. Universitat Politècnica de València, 2003.

[3] PLAZAS, A. H. "Modelado unidimensional de inyectores common-rail Diesel". PhD thesis. Valencia: Universitat Politècnica de València, 2005.

[4] PAYRI, F., BERMÚDEZ, V., PAYRI, R., and SALVADOR, F. J. "The influence of cavitation on the internal flow and the spray characteristics in diesel injection nozzles". *Fuel*, vol. 83.4-5 (2004), pp. 419–431. ISSN: 00162361. DOI: 10.1016/j.fuel.2003.09.010.

[5] LICHTAROWICZ, A., DUGGINS, R. K., and MARKLAND, E. "Discharge coefficients for incompressible non-cavitating flow through long orifices". *Journal of Mechanical Engineering Science*, vol. 7.2 (1965), pp. 210–219. ISSN: 0022-2542. DOI: 10.1243/JMES_JOUR_1965_007_029_02.

[6] LMS. *Imagine.Lab AMESim v.10. User's manual*. 2010.

[7] MACIAN, V., PAYRI, R., MARGOT, X., and SALVADOR, F. J. "A CFD analysis of the influence of diesel nozzle geometry on the inception of cavitation". *Atomization and Sprays*, vol. 13 (2003), pp. 579–604. ISSN: 1045-5110. DOI: 10.1615/AtomizSpr.v13.i56.80.

[8] Bosch, W. "The Fuel Rate Indicator: a New Measuring Instrument for Display of the Characteristics of Individual Injection". *SAE Technical Paper 660749* (1966). doi: 10.4271/660749.

[9] Payri, R., Salvador, F. J., Gimeno, J., and Bracho, G. "A new methodology for correcting the signal cumulative phenomenom on injection rate measurements". *Experimental Techniques*, vol. 32.February (2008), pp. 46–49. issn: 07328818. doi: 10.1111/j.1747-1567.2007.00188.x.

[10] *ISO 2719:2002, Determination of flash point – Pensky-Martens closed cup method*. Geneva, 2002.

[11] *ISO 12937:2000, Petroleum products – Determination of water – Coulometric Karl Fischer titration method*. Geneva, 2000.

[12] *ASTM D7806-12, Standard Test Method for Determination of the Fatty Acid Methyl Ester (FAME) Content of a Blend of Biodiesel and Petroleum-Based Diesel Fuel Oil Using Mid-Infrared Spectroscopy*. West Conshohocken, PA, 2012. doi: 10.1520/D7806-12.

[13] Ye, S. et al. "Réalisation d'un dispositif de mesure de la vitesse et de l'atténuation d'ondes ultrasonores dans des liquides sous pression". *Revue de Physique Appliquée*, vol. 25.6 (1990), pp. 555–565. issn: 0035-1687. doi: 10.1051/rphysap:01990002506055500.

[14] Payri, R., Salvador, F., Gimeno, J., and Bracho, G. "The effect of temperature and pressure on thermodynamic properties of diesel and biodiesel fuels". *Fuel*, vol. 90.3 (2011), pp. 1172–1180. issn: 00162361. doi: 10.1016/j.fuel.2010.11.015.

[15] Bracho, G. "Experimental and theoretical study of the direct diesel injection process at low temperatures". PhD thesis. Universitat Politècnica de València, 2011.

[16] Bell, I. H., Wronski, J., Quoilin, S., and Lemort, V. "Pure and pseudo-pure fluid thermophysical property evaluation and the open-source thermophysical property library coolprop". *Industrial and Engineering Chemistry Research*, vol. 53.6 (2014), pp. 2498–2508. issn: 08885885. doi: 10.1021/ie4033999.

[17] Daridon, J., Lagrabette, A., and Lagourette, B. "Speed of sound, density, and compressibilities of heavy synthetic cuts from ultrasonic measurements under pressure". *The Journal of Chemical Thermodynamics*, vol. 30.5 (1998), pp. 607–623. issn: 00219614. doi: 10.1006/jcht.1997.0330.

[18] BALL, S. J. and TRUSLER, J. P. M. "The speed of Sound and derived thermodynamic properties of n-hexane and n-hexadecane at temperatures between 298 K and 373 K and pressures up to 100 MPa". *International Journal of Thermophysics*, vol. 22.2 (2001), pp. 427–443.

[19] HAYWARD, A. T. J. "How to measure the isothermal compressibility of liquids accurately". *Journal of Physics D: Applied Physics*, vol. 4.7 (1971), pp. 938–950. ISSN: 00223727. DOI: 10.1088/0022-3727/4/7/308.

[20] BOEHMAN, A. L., MORRIS, D., SZYBIST, J., and ESEN, E. "The Impact of the Bulk Modulus of Diesel Fuels on Fuel Injection Timing". *Energy & Fuels*, vol. 18.6 (2004), pp. 1877–1882. ISSN: 0887-0624. DOI: 10.1021/ef049880j.

[21] *ASTM D1298-12b, Standard Test Method for Density, Relative Density, or API Gravity of Crude Petroleum and Liquid Petroleum Products by Hydrometer Method*. West Conshohocken, PA, 2012. DOI: 10.1520/D1298-12B.

[22] *ASTM D1217-15, Standard Test Method for Density and Relative Density (Specific Gravity) of Liquids by Bingham Pycnometer*. West Conshohocken, PA, 2015. DOI: 10.1520/D1217-15.

[23] CHORAZEWSKI, M. et al. "Thermophysical properties of Normafluid (ISO 4113) over wide pressure and temperature ranges". *Fuel*, vol. 105 (2013), pp. 440–450. ISSN: 00162361. DOI: 10.1016/j.fuel.2012.05.059.

[24] RODRÍGUEZ-ANTÓN, L. M., CASANOVA-KINDELAN, J., and TARDAJOS, G. "High Pressure Physical Properties of Fluids used in Diesel injection systems". *SAE Paper 2000-01-2046*, vol. 2000-01-20 (2000). DOI: 10.4271/2000-01-2046.

[25] ARMAS, O., MARTÍNEZ-MARTÍNEZ, S., MATA, C., and PACHECO, C. "Alternative method for bulk modulus estimation of Diesel fuels". *Fuel*, vol. 167 (2016), pp. 199–207. ISSN: 00162361. DOI: 10.1016/j.fuel.2015.11.067.

[26] *ASTM D445-15a, Standard Test Method for Kinematic Viscosity of Transparent and Opaque Liquids (and Calculation of Dynamic Viscosity)*. West Conshohocken, PA, 2015. DOI: 10.1520/D0445-15A.

[27] KOUZEL, B. "How pressure affects liquid viscosity". *Hydrocarbon Process. Petrol Refiner*, vol. 44 (3) (1965), p. 120.

Chapter 5

Diesel injector computational modelling

5.1 Introduction

A computational model of the Bosch CRI 2.20 injector has been implemented as part of this thesis in order to confirm and explain the findings resulting from the experimental mass flow rate measurements performed at different conditions of fuel inlet temperature. This strategy allows an analysis of the physical processes behind the dynamic behaviour of this kind of injector by having a look at the injector internal characteristics. In this sense, the influence of the fuel temperature on key features such as the pressure drop established in the control volume due to the control orifices performance or the forces on the needle due to viscous friction, which cannot be directly assessed through the experimental measurements, may be studied by means of the computational model. Due to the relevant changes in temperature along the injector and the induced variations in the fuel properties significantly affecting the injection process as seen in Chapter 3, the implemented model takes the adiabatic flow assumption with local changes of pressure and temperature rather than the isothermal approach.

The present chapter aims at the description of the cited computational model, which has been implemented in the commercial AMESim platform [1]. This platform, based on the Bond Graph technique for modelling engineering systems, is first described together with its particular way of representing each

of the physical processes involved in the *common-rail* injector internal flow. The numerical resolution of the resulting set of state equations is also treated.

Next, the application for the Bosch CRI 2.20 injector is presented, offering a detail of the different parts being modelled and the information supplied from the injector experimental characterization described in Chapter 4.

Finally, the validation of the model is described. A satisfactory validation ensures the suitability of the computational model to study the injection process complementing the purely experimental observations. The validation was performed both individually for each of the most important injector internal restrictions (i.e. nozzle and control volume orifices) and for the injector as a whole. To do so, the simulated mass flow rate through each of the restrictions and through the injector outlet are here respectively compared to the experimental results described in Chapter 4.

In addition, the limits of the extension of the validity of the adiabatic flow assumption have also been assessed in this chapter. On the one hand, the temperature variations experimentally determined across the injector internal orifices are compared with the ones theoretically found for an isenthalpic expansion across them, in order to ensure the proper reproduction of the injector behaviour in the controlled laboratory conditions for which the experimental results were obtained. Additionally, remarks are given on the applicability of this assumption to study the injection process under real engine-like conditions.

5.2 Common-rail injection systems 1D modelling with AMESim

LMS®Imagine.Lab AMESim (*Advanced Modelling Environment for Simulation*) is a commercial simulation software for the one-dimensional modelling and analysis of multi-domain systems. In this section, the approach followed by this platform in order to simulate *common-rail* injectors is presented.

AMESim is based on the Bond Graph technique and makes use of predefined libraries that have been implemented for the different physical domains, so that the following phenomena can be modelled:

- Mechanical phenomena: masses, springs and dampers, friction among elements, elastic deformations, impacts.
- Hydraulic phenomena: flow through ducts, hydraulic lines, constant section orifices, variable section orifices, cavitation ....

- Electromechanical phenomena: electromagnetism and piezoelectric effect.

Each library consists of several elements (i.e. masses, springs, pistons, orifices, hydraulic lines ...). These elements, referred to as *components*, are described by some governing equations derived under certain assumptions. The phenomena modelled through these equations are dealt with in the present section. The coefficients of the governing equations depend on parameters that need to be introduced from the experimental characterization.

The different components in AMESim may be connected to each other in order to model real systems. Being a multi-domain tool, components from different domains are allowed to interact with each other in AMESim. The interaction among components takes place with certain causality relations. In the end, a set of equations needs to be solved to simulate the system behaviour along time. Hence, the calculation scheme and the numerical resolution of the system state equations are also treated in this section.

5.2.1 The Bond Graph technique

Bond graphs are a method to graphically represent physical systems. In a bond graph, a set of elements are connected together in a structure that is somewhat representative of the modelled system. Each *element* has a certain number of *ports* from which it can be connected to other elements. These connections are represented by arrows and referred to as *bonds*. The bonds identify power flow paths, through which two kinds of variables are transmitted among elements: *effort* and *flow*. In each physical domain, effort and flow correspond to different specific variables. For instance, in mechanical systems, force and velocity correspond to effort and flow, respectively, whereas in electrical systems these variables are voltage and current. However, the fact that there is an analogy between the different physical domains in terms of effort and flow allows a bond graph to represent multi-domain systems.

The multi-domain analogy also makes it possible to classify the different elements of a bond graph as *resistive* (which dissipate energy), *capacitive* (store energy), *inertial* (where the integral of the effort is directly related to the flow by a constitutive law) and effort or flow *sources*.

Bonds departing from different elements join at a junction represented either by a number 0 or a number 1. In a *0-junction*, the flows sum to zero and the efforts are equal. In a *1-junction*, the efforts sum to zero and the flows are equal. Half arrows in a bond may indicate the direction in which the power is transmitted. Bond graphs also give a notion of causality, indicating the side

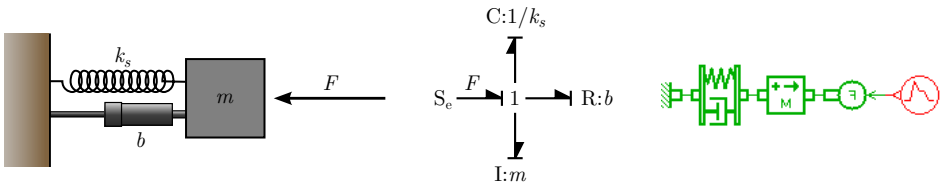

(a) Physical representation (b) Bond graph (c) AMESim representation

Figure 5.1: Mass-Spring-Damper system.

of a bond that defines the instantaneous effort and the side that defines the instantaneous flow. For this purpose, a stroke at one end of the power bond indicates that that end is defining the flow, whereas the opposite end defines the effort. Finally, it is possible from a bond graph to directly formulate the dynamic equations that describe the system. Causality relations then allow to identify the independent and the dependent variable for each element. Thus, some rules apply to causality in order for the model to be realizable.

As an example to illustrate the aforementioned concepts, consider the simple mass-spring-damper system represented in Figure 5.1(a). Its equivalent bond graph representation is depicted in Figure 5.1(b). The four elements that constitute the system (namely a mass, a spring, a damper and a force) are represented with a bond graph notation (inertial, capacitive, resistive and effort source, respectively). The bonds depart from each system joining at a 1-junction, since the efforts (forces) sum to zero at the junction and the flows (velocities) are equal for all the elements. The causality relations are also indicated, and thus it is immediate to derive the dynamic equations of the system and simulate its behaviour.

The different libraries of AMESim (hydraulic, mechanical, electromechanical, etc.) contain the components whose constitutive equations have been predefined. These components include several ports in order to connect them to others. The bonds are omitted in general so that the representation is more visual, whereas the causality relations can be specified by the user depending on how the different components are connected. The AMESim representation of the mass-spring-damper system of the example is shown in Figure 5.1(c).

The purpose of the following sections is to give an overview on the different physical phenomena that need to be modelled when simulating *common-rail* diesel injectors, outlining the assumptions introduced by AMESim and the equations resulting from these assumptions. For further reference on bond graph modelling itself, the reader may refer to the work by Karnopp *et al.* [2].

5.2.2 Mechanical phenomena modelled

Masses

Masses of the injector movable elements and their friction forces are taken into account. Figure 5.2 shows a mass on an inclined plane subject to an external force and friction. The total force exerted on that mass in the direction of the plane can be calculated as:

$$F = F_{ext} - F_{fric} - mg \sin \alpha_m \tag{5.1}$$

where F_{ext} and F_{fric} denote the external and friction forces, respectively, whereas α_m is the angle formed by the mass axis with respect to the horizontal.

The friction force is taken into account through a static friction term that needs to be overcome prior to the mass movement and a dynamic term (Coulumb's friction):

$$F_{fric} = F_{dyn} + (F_{st} - F_{dyn})\, e^{\frac{|U|}{3U_0}} \tag{5.2}$$

where F_{st} and F_{dyn} are the static and dynamic friction force terms, respectively, whereas U is the mass velocity and U_0 is the mass critical velocity that defines the threshold from which there is only dynamic friction. The fact that the friction force varies with the mass velocity is known as Stribeck effect. This model is known as the Karnopp friction model [3].

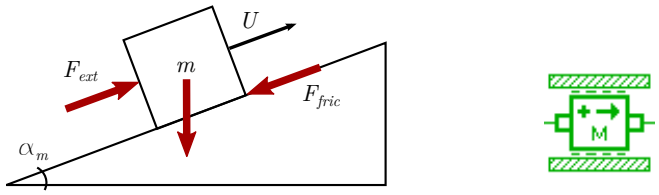

(a) Mass (b) AMESim representation

Figure 5.2: Mass subject to an external force and friction with its AMESim component representation.

The mass acceleration is then computed from Newton's second law. The velocity and position are in turn obtained by successively integrating the acceleration.

Springs and dampers

The physical representation of these elements and their corresponding AMESim subcomponent was introduced in Figures 5.1(a) and 5.1(c). In this case, the total force exerted on the body is:

$$F = k_s x + b\,(U_{b,1} + U_{b,2}) \tag{5.3}$$

where b is the damping coefficient, U_b is the body velocity, whereas 1 and 2 denote the two ports of the component. The spring compression is computed as:

$$x = x_0 + x_1 + x_2 \tag{5.4}$$

where x_0 is the initial deformation of the spring (precompression). The spring stiffness can be computed from the geometrical dimensions of the spring assuming it has an helicoidal shape, as stated by Adler and Bauer [4]:

$$k_s = \frac{G D_{spire}^4}{8 D_{spring}^3 N_s} \tag{5.5}$$

where G is the material shear modulus, N_s the spring total number of spires, D_{spire} the diameter of a single spire of the spring (i.e. its thickness) and D_{spring} the diameter of the spring as a whole.

Due to the high operating pressures in *common-rail* injectors, the elastic deformations of the internal elements may reach the same order of magnitude of their displacements. For instance, in the case of the needle, these deformations are especially relevant prior to the injection event, when the needle is closed against its seat and its deformation needs to be recovered before the needle can effectively open once the injector is energized. Therefore, the elastic deformations have been accounted for through the method defined by Desantes *et al.* [5]. It consists on representing these deformations by a spring with an equivalent stiffness (k_{eq}) defined from the geometry (longitude and cross-section) of the parts of the element with changes in cross-section:

$$\frac{1}{k_{eq}} = \frac{1}{E} \sum_{i=1}^{n} \frac{L_i}{A_i} \tag{5.6}$$

As an illustrative example, Figure 5.3 shows the needle-rod set of a Bosch CRI 2.20 injector where the changes in cross-sectional area are highlighted.

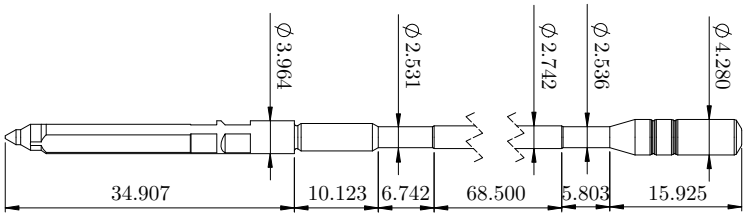

Figure 5.3: Drawing of the Bosch CRI 2.20 needle-rod set.

5.2.3 Hydraulic phenomena modelled

Hydraulic lines

Modelling high pressure lines (around 250 MPa in the case of *common-rail* injectors) is complex since it is needed to reduce the governing partial differential equations (PDEs) to ordinary differential equations (ODEs) or differential algebraic equations (DAEs), as seen in Section 3.2.

It is common to assume that the variations of the parameters along the line are negligible and thus to calculate only its variations with respect to the time. However, this assumption is not valid when the lines are long, since pressure variations may be important due to several factors such as pressure waves effects, compressibility variations of the fluid, fluid inertia, friction, etc. Alternatively, a series of nodes may be considered along the line. The pressure in these nodes is calculated by using finite differences or finite element methods (see Figure 5.4).

Compressibility effects are taken into account by applying Equation (5.7):

$$\frac{\partial p}{\partial t} = -\frac{\beta_{eff}}{A}\frac{\partial \dot{V}}{\partial x} \tag{5.7}$$

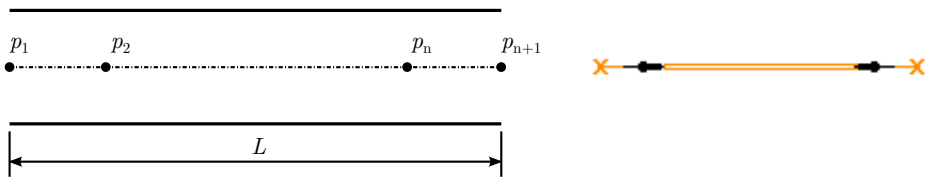

(a) Hydraulic line (b) AMESim representation

Figure 5.4: Node distribution of a hydraulic line with its AMESim component representation.

where A is the line cross-sectional area, $\dot{V}$ the volumetric flow rate through the line and β_{eff} the effective bulk modulus, which takes into account the influence of the elastic deformation of the hydraulic line in the following way:

$$\frac{1}{\beta_{eff}} = \frac{1}{\beta_f} + C_{wall} \tag{5.8}$$

where C_{wall} can be associated to the total elasticity of the line wall and is defined as:

$$C_{wall} = \frac{2}{E}\left(\frac{D_{ext}^2 + D_{int}^2}{D_{ext}^2 - D_{int}^2} + \nu_{Po}\right) - \frac{2\nu_{Po}}{E}\left(\frac{2D_{ext}^2}{D_{ext}^2 - D_{int}^2}\right) \tag{5.9}$$

where E and ν_{Po} are the line wall Young modulus and the Poisson coefficient, respectively. In order to consider the friction in the lines, the flow mean velocity through the line is calculated from:

$$\Delta p + \rho_f L g \sin\alpha_L = \frac{f L \rho_f u^2}{2D_{int}} \tag{5.10}$$

where α_L is the line angle with respect to the horizontal and f is the Fanning friction factor, related to the Darcy friction coefficient C_f introduced in Section 2.3 as established by Equation (5.11). AMESim determines the Fanning friction factor f through empirical relations that link it to the pressure loss Δp as derived from the Moody diagram [6].

$$f = \frac{C_f}{4} \tag{5.11}$$

In addition, if the fluid inertia is considered, the volumetric flow rate is calculated from:

$$\frac{\mathrm{d}\dot{V}}{\mathrm{d}t} = \frac{A\Delta p}{\rho_f L} - Ag\sin\alpha_L - \frac{fAu^2}{2D_{int}}\,\mathrm{sgn}(\dot{V}) \tag{5.12}$$

Different line subcomponents are found in AMESim in order to enable or disable friction and inertia. For each of these subcomponents, there are three possibilities in order to define the causality relations with other elements. Thus, it is possible to define whether the line receives the pressure as an input and computes the volumetric flow rate as an output or if it proceeds on the opposite way.

Orifices

Hydraulic orifices are resistive elements where the pressure is an input at each port and a flow rate is computed as an output. AMESim computes the volumetric flow rate from the continuity equation, assuming the velocity as Bernoulli's theoretical velocity:

$$\dot{V} = C_d A \sqrt{\frac{2\Delta p}{\rho_f}} \tag{5.13}$$

As shown in Section 2.3, the discharge coefficient C_d depends on the Reynolds number. AMESim introduces a non-dimensional parameter that can be interpreted as the theoretical Reynolds number (Re_{th}), since it includes Bernoulli's theoretical velocity in its definition:

$$Re_{th} = \frac{D_h}{\nu_f} \sqrt{\frac{2\Delta p}{\rho_f}} \tag{5.14}$$

where the fuel properties ν_f and ρ_f are evaluated for a mean pressure in the orifice and the upstream temperature, whereas the hydraulic diameter D_h is defined in Equation (5.15) as a function of the orifice cross-sectional area A and the associated wetted perimeter, P. It must be noted that, in the case of a circular orifice, the hydraulic diameter is equal to the orifice diameter.

$$D_h = \frac{4A}{P} \tag{5.15}$$

For non-cavitating orifices, AMESim expresses the discharge coefficient as a function of the theoretical Reynolds number as follows:

$$C_d = C_{d,max} \tanh\left(\frac{2Re_{th}}{Re_{th,crit}}\right) \tag{5.16}$$

The critical theoretical Reynolds number, $Re_{th,crit}$ is defined as the theoretical Reynolds number that leads to a discharge coefficient equal to 95% of $C_{d,max}$. An example of this behaviour is illustrated in Figure 5.5. It can be seen that, as opposed to the typical evolution described in Section 2.3 (see Figure 2.11), the discharge coefficient quickly reaches its maximum value (for theoretical Reynolds numbers close to the critical one). Hence, the mass flow rate is expected to be slightly overestimated when the modelled orifice works at flow regimes close to the transitional one.

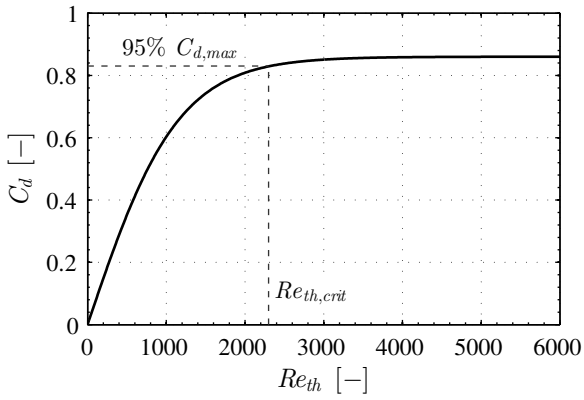

Figure 5.5: Modelled discharge coefficient behaviour as a function of the theoretical Reynolds number for a non-cavitating orifice.

Cavitation can also be considered in AMESim. Its description of the phenomenon is based on the one-dimensional flow theory established by Nurick [7] and introduced in Section 2.3. Hence, in an orifice prone to cavitate and for each operating condition established during the simulation, AMESim calculates the cavitation number CN defined by Soteriou *et al.* [8] so that:

- If CN is lower than the critical cavitation number CN_{crit}, the orifice is working under non-cavitating conditions and the behaviour of the discharge coefficient is calculated as a function of Re_{th} according to Equation (5.16).
- If CN is higher than CN_{crit}, the orifice is working under cavitating conditions and the discharge coefficient behaviour is a function of CN, as established by Equation (5.17):

$$C_d = C_c\sqrt{1+\frac{1}{CN}} \tag{5.17}$$

This behaviour is represented in Figure 5.6 for a sample orifice. The left side of the figure corresponds to the behaviour under non-cavitating conditions, whereas the right side corresponds to the cavitating conditions, for which the discharge coefficient asymptotically tends to the orifice contraction coefficient C_c. The plots have been overlapped to represent the loss of discharge capabilities under cavitating conditions. However, it must be noted that this loss does not necessarily appear once the maximum discharge coefficient is already reached.

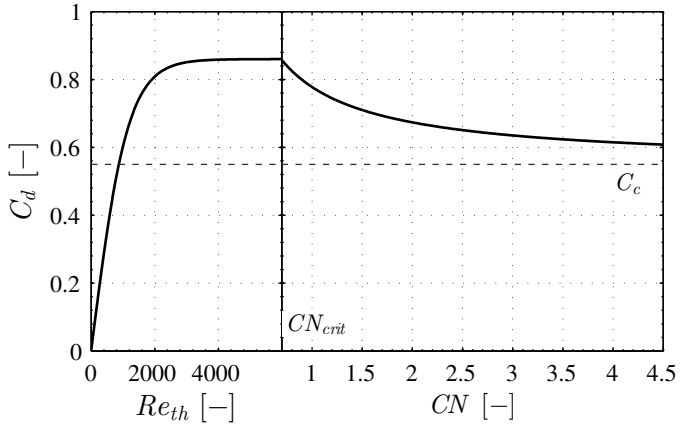

Figure 5.6: Modelled discharge coefficient behaviour for a cavitating orifice. Evolution as a function of Re_{th} for $CN < CN_{crit}$ (left) and as a function of CN for $CN > CN_{crit}$ (right).

Temperature change through a hydraulic restriction

The temperature change through a restriction to the flow is predicted under the assumption of adiabatic flow, with no heat transfer to the surroundings. According to the first law of thermodynamics and in the absence of external work, such an assumption implies that:

$$\Delta\left(h + e_k\right) = \cancelto{0}{Q} - \cancelto{0}{W} \tag{5.18}$$

where h is the specific enthalpy of the flow, e_k the specific kinetic energy of the flow defined in Equation (5.19), Q the net heat supplied to the system and W the net work done by it. The first two terms of Equation (5.18) constitute the stagnation enthalpy of the flow.

$$e_k = \frac{1}{2}u^2 \tag{5.19}$$

Therefore, under the previous assumptions, the first law establishes that the stagnation enthalpy is conserved along a hydraulic restriction.

If the reference locations upstream and downstream of the restriction at which the pressure is considered to be established are located far enough from the orifice and the hydraulic diameter at these locations is identical, the flow velocity is unchanged among them. Consequently, in this particular case,

there is no kinetic energy change and the specific enthalpy of the flow can be assumed to remain constant along the process. This is the case of the experimental setup for the hydraulic characterization of the injector orifices described in Section 4.3.1 (Figure 4.7). Hence, if the flow among sections A and C in the figure is regarded to as adiabatic, it may also be considered to be isenthalpic.

The fact that the specific enthalpy is unchanged across the restriction implies that, if it is possible to express the fuel specific enthalpy as a function of T and p, the temperature downstream of the restriction may be determined as long as both the temperature upstream of it and the pressure variation are known:

$$h\left(T_{dw}, p_{dw}\right) = h\left(T_{up}, p_{up}\right) \tag{5.20}$$

In the case of the nozzle orifices, however, the flow importantly accelerates from the inlet to the outlet and the variation of kinetic energy cannot be neglected. While the fuel is inside the orifice, the stagnation enthalpy is preserved and the specific enthalpy needs to balance the change in kinetic energy, according to Equation (5.18). This assumption stops being valid once the fuel leaves the injector and the atomization process starts, since an important amount of heat starts being supplied from the atmosphere of the combustion chamber.

In such a case, the theoretical temperature at the outlet of the nozzle orifices may still be determined under the assumption of adiabatic flow and no work exchange among the nozzle and other components of the system (please note that this assumption is acceptable once steady conditions are achieved, but does not hold for low values of needle lift for which the needle may exchange mechanical work with the nozzle) by considering the velocity change across it:

$$h\left(T_{dw}, p_{dw}\right) = h\left(T_{up}, p_{up}\right) - \frac{1}{2}\Delta u^2 \tag{5.21}$$

Assuming that the inlet velocity is small compared to the outlet one, Equation (5.21) may be rewritten:

$$h\left(T_{dw}, p_{dw}\right) = h\left(T_{up}, p_{up}\right) - \frac{1}{2}u_{dw}^2 \tag{5.22}$$

Furthermore, if Bernoulli's theoretical velocity is taken as a reference, Equations (2.22) and (2.18) allow to write:

$$h\left(T_{dw}, p_{dw}\right) = h\left(T_{up}, p_{up}\right) - \frac{1}{2} C_v^2 u_{dw,th}^2 \tag{5.23}$$

and:

$$h\left(T_{dw}, p_{dw}\right) = h\left(T_{up}, p_{up}\right) - C_v^2 \, \frac{p_{up} - p_{dw}}{\rho_f} \tag{5.24}$$

In order to apply Equations (5.20) and (5.24), it is necessary to express the fuel specific enthalpy as a function of T and p. The relationship among the specific enthalpy of the flow and its specific internal energy (e) is given by Equation (5.25):

$$h = e + \frac{p}{\rho} \tag{5.25}$$

It is important to note that, due to the small diameters involved in the injector internal flow, the heating induced by viscous dissipation (i.e. friction) along the orifices is deemed to be important [9–14]. Under the assumption of adiabatic flow, this heat is supposed to remain within the fluid, contributing to increase its internal energy. As a consequence, in the case of an isenthalpic expansion, the fluid temperature rises as it expands, according to Equation (5.25). In the case of the nozzle, for which the stagnation enthalpy is preserved, the temperature change also depends on the flow velocity change along the process.

Let us consider the general formulation for the specific enthalpy as a function of the fluid temperature and pressure:

$$\mathrm{d}h = \left(\frac{\partial h}{\partial T}\right)_p \mathrm{d}T + \left(\frac{\partial h}{\partial p}\right)_T \mathrm{d}p = c_p \mathrm{d}T + \frac{1 - \alpha T}{\rho} \mathrm{d}p \tag{5.26}$$

Note that the second term of the right hand side of Equation (5.26) is null for an ideal gas (for which $\alpha T = 1$), but cannot be neglected for a liquid. If the variation of the fluid properties (c_p, α and ρ) with respect to the pressure and temperature is known, Equation (5.26) can be integrated taking into account that the final result is independent on the integration path [15]. For an isenthalpic process ($\mathrm{d}h = 0$) this directly leads to the determination of the fluid temperature downstream of a restriction if the temperature upstream

and the pressure both upstream and downstream of the restriction are known, as explicitly shown by Equation (5.20). In AMESim, these quantities are given from the adjacent components. For processes that are not isenthalpic but for which the stagnation enthalpy is preserved, the fluid temperature variation will also depend on the flow velocity change across the process.

The fuel properties required by AMESim to determine the temperature change across a hydraulic restriction may be introduced with polynomial expressions as the ones obtained as part of this thesis and presented in Section 4.4. The particular application for the winter diesel fuel used in this thesis will be introduced in Section 5.3.

The comparison of the temperature changes across the control volume orifices predicted by the model against the results obtained from the experimental facility for the hydraulic characterization described in Section 4.3 (Figure 4.13) will be shown in Section 5.4. This comparison will allow to assess the limits of the suitability of the assumption of adiabatic flow through the injector.

5.2.4 Mixed hydraulic-mechanical components

The multi-domain nature of AMESim is reflected in components that share both mechanical and hydraulic parameters and variables. This is the case of elements on which the pressure on a fluid is responsible for the movement of a body due to the forces it generates on its surface. For instance, in a solenoid driven *common-rail* injector, some elements need to model how the fuel pressure forces drive the needle or the control valve. In AMESim, these components are represented by pistons, volumes or hydraulic valves.

Pistons and volumes

A *common-rail* injector constitutes a multi-domain system in which mechanical and hydraulic components, among others, transfer power and effort. A common situation in which these two domains are involved are the surfaces of the movable elements on which the high pressures of the fuel generate important pressure forces that drive them, governing the transient stages of the injector. As an example, the top surface of the rod-needle set (see Figure 5.3) generates a force downwards due to the pressure set in the control volume.

The elements used to model these forces in AMESim are the pistons and volumes. Figure 5.7(a) shows the sketch of a moving piston. Its representation in AMESim is shown in Figure 5.7(b). The velocity at which this component moves is usually computed from an associated mass component, whereas the

(a) Piston sketch (b) AMESim piston (c) Hydraulic chamber

Figure 5.7: Sketch of a moving piston together with the AMESim components corresponding to piston and hydraulic chamber.

pressure acting on it also comes from an adjacent component, usually modelled as a hydraulic chamber (Figure 5.7(c)).

In an AMESim hydraulic chamber with an initial volume V_0, each port i receives a volumetric flow rate $\dot{V}_i$ and a fluid volume V_i as inputs, whereas pressure is computed as an output in the following way:

$$\frac{\mathrm{d}p}{\mathrm{d}t} = \frac{\beta_{eff}(p) \sum_{i=1}^{nports} \dot{V}_i(p)}{V_0 + \sum_{i=1}^{nports} V_i} \tag{5.27}$$

The volumetric flow rate coming out from the piston element is:

$$\dot{V} = -U_b \frac{\pi}{4} \left(D_{pist}^2 - D_{rod}^2 \right) \tag{5.28}$$

And the force acting on the piston can be computed from the pressure in the adjacent chamber as:

$$F = F_{ext} - p \frac{\pi}{4} \left(D_{pist}^2 - D_{rod}^2 \right) \tag{5.29}$$

It is important to note that, for circular surfaces such as the needle top, the rod diameter is set to zero so that the piston area is computed accordingly. However, Equation (5.29) covers the general case in which this section is annular. Indeed, when a change in cross-sectional area occurs in the injector movable elements, such as the needle, the surface on which the pressure forces act is indeed an annular surface (see the needle-rod set of Figure 5.3). Hence, the changes in section in the movable elements may also be modelled as pistons.

Internal leakages and friction

An AMESim component computes a laminar hydraulic leakage between a cylindrical piston and its sleeve, together with the corresponding viscous friction. Figure 5.8 shows an example of geometry for this case.

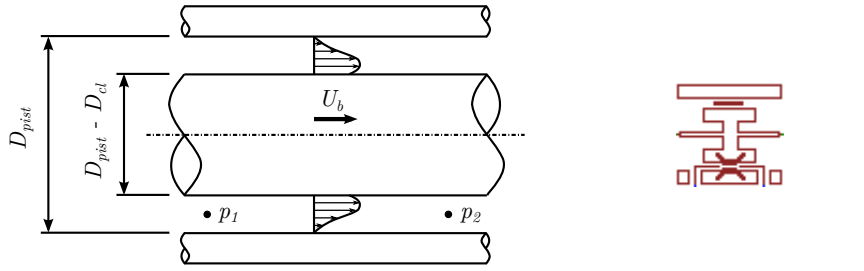

(a) Geometry sketch (b) AMESim component

Figure 5.8: Sketch of the geometry between a moving piston and its sleeve for leakage calculation purposes, together with the AMESim corresponding component.

Flow and friction due to Couette and Poiseuille phenomena are both taken into account, considering that the cylindrical piston may be moving with respect to the sleeve. In an AMESim model, this movement is transferred by an adjacent mass element through a mechanical connection. According to Blackburn *et al.* [16], under the assumptions of laminar flow, no eccentricity and a small clearance compared to the piston diameter, the volumetric flow rate through the leakage can be computed as:

$$\dot{V} = -\frac{\Delta p}{12\eta_f L}\left(\frac{D_{cl}}{2}\right)^3 \pi D_{pist} + \frac{U_b}{2}\frac{D_{cl}}{2}\pi D_{pist} \tag{5.30}$$

The force related to viscous friction is:

$$F_{fric} = -\Delta p\,\pi\frac{D_{cl}}{2}\frac{D_{pist}-D_{cl}}{2} + 4\pi\eta_f U_b L\left(\frac{D_{pist}}{D_{cl}} - 1\right) \tag{5.31}$$

Thus, the total forces on the piston are computed as:

$$F = F_{ext} - F_{fric} \tag{5.32}$$

Flow through variable section orifices

The hydraulic orifices treated previously had a constant geometrical area. However, in hydraulic systems, there are some elements where the area is a function of the displacement of a body as a consequence of the fluid pressure and/or the external forces, such as the valves. In the case of solenoid *common-rail* injectors, these elements are generally the nozzle seat, a command piston and the solenoid control valve. It is therefore necessary to properly model the area variations in order to obtain an accurate injector behaviour, not only in terms of fuel delivered but also regarding injector dynamics.

Several AMESim components represent different geometries in order to accurately model the area variations in those orifices, such as a plain seat, a ball seat or a conical seat.

- Plain seat valve
  Figure 5.9(a) shows a plain seat valve. As depicted in Figure 5.9(b), the effective area of the orifice discovered by the valve is determined as the lateral surface of a cylinder and depends on the valve lift l, which is imposed by the adjacent elements through mechanical connections:

$$A_{eff} = \pi D_s l \tag{5.33}$$

  where D_s is the seat throat diameter. This effective area is used to compute the volumetric flow rate $\dot{V}$ through the orifice according to

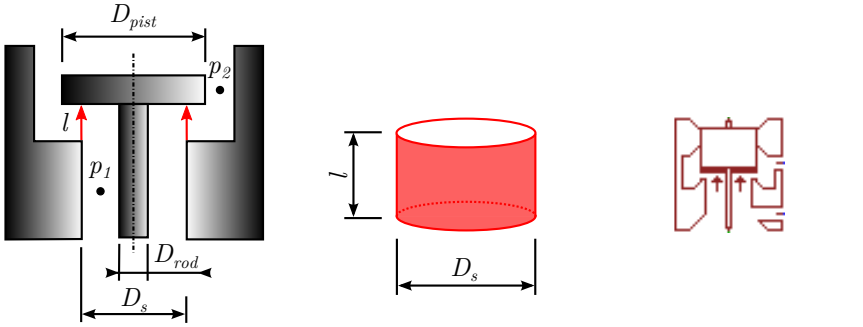

(a) Plain seat sketch (b) Effective area (c) AMESim component

Figure 5.9: Sketch of a plain seat valve geometry together with the effective area of the orifice and the corresponding AMESim component.

Equation (5.13). The discharge coefficient C_d is calculated with the hydraulic diameter of the variable section orifice as:

$$D_h = \frac{4A}{P} = 4l \tag{5.34}$$

Note that Equations (5.33) and (5.34) are valid if the valve lifts are small compared to the seat throat diameter D_s, which is usually true for *common-rail* injectors. From a certain value of valve lift, the throat area becomes more restrictive than the one discovered by the valve and it is then used for the calculations:

$$A_{throat} = \frac{\pi}{4}\left(D_s^2 - D_{rod}^2\right) \tag{5.35}$$

It is also considered that the surface delimiting the effective area of the orifice discovered by the valve splits the region ocuppied by the fluid into two separate regions. The first one is submitted to the pressure upstream of the valve, whereas the pressure downstream of the valve acts on the second one. However, AMESim allows the use of a transition (for instance, a linear pressure gradient or a user-defined profile) from one pressure to the other instead of a discrete jump. The resulting distribution of pressures is then used to calculate the forces exerted on the valve.

On the other hand, cavitation is not accounted for in variable section orifices.

- Ball seat valve

  Figure 5.10(a) shows the geometry of a ball seat valve. From Figure 5.10(b) it can be seen that, in this case, the area of the restriction introduced by the seat is determined by the curved surface of a truncated cone, as follows:

$$A_{eff} = \pi l \left(D_b + l\cos\alpha_b\right)\sin\alpha_b\cos\alpha_b \tag{5.36}$$

  where D_b is the ball diameter. In this case, the hydraulic diameter for the calculation of the discharge coefficient C_d through the theoretical Reynolds number, Re_{th}, is computed as follows:

$$D_h = \frac{4A}{P} = 4l\cos\alpha_b \tag{5.37}$$

  Equations (5.36) and (5.37) are used if the ball valve lift is small compared to the orifice diameter. This is the case of *common-rail* injectors:

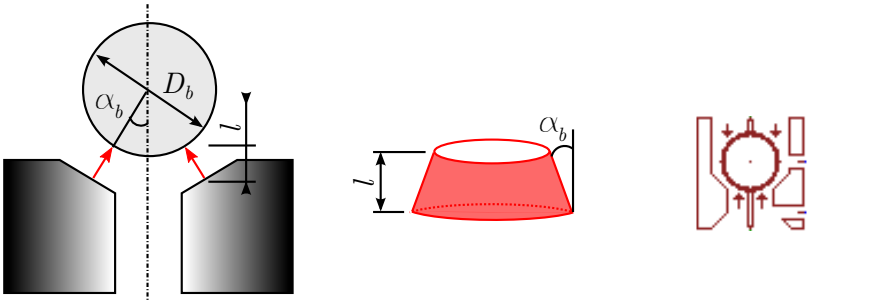

(a) Ball seat sketch (b) Effective area (c) AMESim component

Figure 5.10: Sketch of a ball seat valve geometry together with the effective area of the orifice and the corresponding AMESim component.

the solenoid injectors that use ball seat valves applied to the control valve usually involve ball diameters around 1.5 mm and maximum lifts around 50 µm.

As it happened for the plain seat valve, in order to compute the pressure forces on the ball, it is assumed that the truncated cone surface divides the region ocuppied by the fluid into two separate regions submitted to different pressures. The pressure upstream of the orifice acts on the first region, whereas the second one is submitted to the pressure downstream of the orifice.

- Conical seat valve

  Figure 5.11(a) sketches the geometry of a conical seat valve. In this case, there exist two regions of minimum flow area represented by the surfaces of truncated cones, as shown in Figure 5.11(b). The effective areas of these restrictions are calculated according to Hardenberg [17, 18]. The area at the lower side is given by Equation (5.38)

$$A_{eff,1} = \pi l \sin\frac{\alpha_c}{2} \frac{D_s - l\sin\frac{\alpha_c}{2}\left(\cos\frac{\alpha_c}{2} + \sin\frac{\alpha_c}{2}\tan\alpha_{p,1}\right)}{\cos\alpha_{p,1}} \tag{5.38}$$

  where $\alpha_{p,1}$ is the angle that the truncated cone shapes with respect to the perpendicular to the poppet, as seen in Figure 5.11(a):

$$\tan\alpha_{p,1} = M_1 - \sqrt{\left|M_1^2 - \frac{1}{2}\right|} \tag{5.39}$$

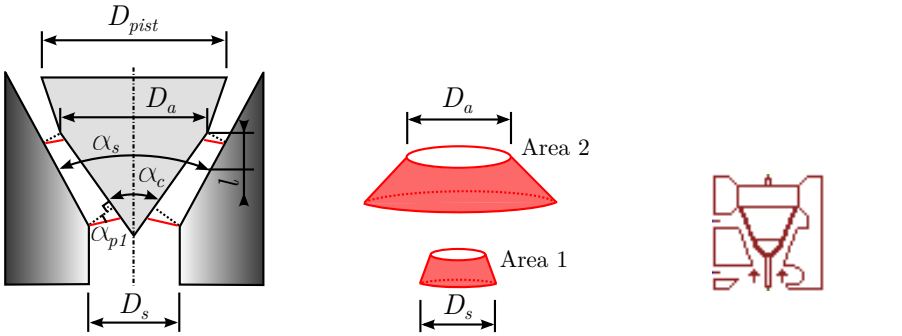

(a) Conical seat sketch (b) Effective areas (c) AMESim component

Figure 5.11: Sketch of a conical seat valve geometry together with the effective areas of the orifice and the corresponding AMESim component.

with M_1 given by:

$$M_1 = \frac{1}{4}\left[\frac{D_s}{l}\left(1 + \frac{1}{\tan^2\frac{\alpha_c}{2}}\right) - \frac{1}{\tan\frac{\alpha_c}{2}}\right] \tag{5.40}$$

On the other hand, the area of the truncated cone at the upper side is given by:

$$A_{eff,2} = \pi l \sin\frac{\alpha_s}{2}\frac{D_a + l\sin\frac{\alpha_s}{2}\left(\cos\frac{\alpha_s}{2} - \sin\frac{\alpha_s}{2}\tan\alpha_{p,2}\right)}{\cos\alpha_{p,2}} \tag{5.41}$$

with $\alpha_{p,2}$ analogous to $\alpha_{p,1}$:

$$\tan\alpha_{p,2} = M_2 - \sqrt{\left|M_2^2 - \frac{1}{2}\right|} \tag{5.42}$$

where M_2 is given by:

$$M_2 = \frac{1}{4}\left[\frac{D_a}{l}\left(1 + \frac{1}{\tan^2\frac{\alpha_s}{2}}\right) - \frac{1}{\tan\frac{\alpha_s}{2}}\right] \tag{5.43}$$

For a given situation, the actual effective flow area is the minimum among the previous two:

$$A_{eff} = \min\left(A_{eff,1}, A_{eff,2}\right) \tag{5.44}$$

The hydraulic diameter is simplified as:

$$D_h = \frac{4A_{eff}}{P} = 4l \sin\frac{\alpha_c}{2} \tag{5.45}$$

In any case, Equations (5.44) and (5.45) are used if the conical valve lift is small compared to the seat diameter D_s. For larger values of valve lift, the area calculated according to Equation (5.44) may exceed the throat area. In such an event, the highest restriction to the flow would be the throat area:

$$A_{throat} = \frac{\pi}{4} D_s^2 \tag{5.46}$$

This may be the case for the Bosch CRI 2.20 injector, in which the lower side of the needle is accurately modelled by a conical valve. In several situations the throat area will be the maximum restriction from a certain needle lift lower than its mechanical maximum (850 µm).

In this element, the two truncated cone surfaces divide the region occupied by the fluid into three, where different pressures are assumed to act in order to compute the forces on the valve. The pressure upstream of the restriction is directly taken from the adjacent element, whereas the other two regions are assumed to be subject to an average pressure among the upstream and downstream pressures. The transition among pressures is assumed by an exponential function that depends on the valve lift.

5.2.5 Electromagnetic phenomena modelled

In order to introduce the basic equations of electromagnetism, let us consider a ferromagnetic core wrapped by an electric coil with N_t turns, as shown in Figure 5.12.

When a current I flows through the coil, a magnetic flux Φ_B is induced inside the core.

$$\Phi_B = \int_A \boldsymbol{B} \cdot \mathrm{d}\boldsymbol{A} \tag{5.47}$$

where B is the magnetic flux density, describing the magnetic field. Hence, B may be seen as the amount of flux passing through an area element perpen-

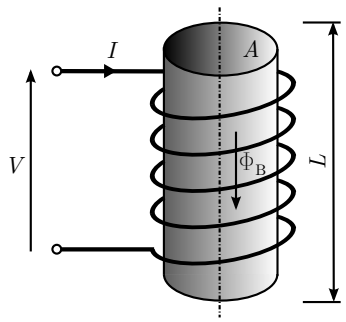

Figure 5.12: Ferromagnetic core wrapped by an electric coil.

dicular to the flux lines. If the flux is considered to be constant in a sectional area A of the coil, B can be rewritten as:

$$B = \frac{\Phi_B}{A} \tag{5.48}$$

The voltage V is related to the magnetic flux rate and the number of turns:

$$V = N_t \frac{\mathrm{d}\Phi_B}{\mathrm{d}t} \tag{5.49}$$

The force that drives flux through the magnetic material is known as *magnetomotive force* $\mathcal{F}$. The magnetomotive force around a closed loop is related to the magnetic field intensity H as follows:

$$\mathcal{F} = \oint \boldsymbol{H} \cdot \mathrm{d}\boldsymbol{L} \tag{5.50}$$

If the magnetic field intensity is constant along the path followed by the magnetic flux, Equation (5.50) can be rewritten as:

$$\mathcal{F} = HL \tag{5.51}$$

For a long coil, the magnetomotive force can also be easily calculated as:

$$\mathcal{F} = N_t I \tag{5.52}$$

A core material is characterized by the relation among the magnetic flux density B and the magnetomotive force. However, the relation among B and

the magnetic field intensity H is usually preferred due to its independence of the core geometry.

Soft ferromagnetic materials show no difficulty in being magnetized and demagnetized. Hence, their typical $B - H$ curve passes through the origin as depicted in Figure 5.13, showing no hysteresis. For low values of H, B is almost proportional to H. This relationship is often expressed as:

$$B = \mu H \tag{5.53}$$

where μ is the permeability. Equation (5.53) may also be expressed in terms of the permeability of vacuum μ_0 ($\mu_0 = 4\pi 10^{-7}$H/m) and the relative permeability of the material, μ_r:

$$B = \mu_0 \mu_r H \tag{5.54}$$

In this linear region, the magnetic reluctance $\mathcal{R}$ may be defined as:

$$\mathcal{R} = \frac{\mathcal{F}}{\Phi_B} = \frac{L}{\mu A} \tag{5.55}$$

This expression is commonly known as Hopkinson's law and is analogous to Ohm's law. Similarly, the magnetic permeance $\mathcal{P}$ is defined as the inverse of the magnetic reluctance:

$$\mathcal{P} = \frac{1}{\mathcal{R}} \tag{5.56}$$

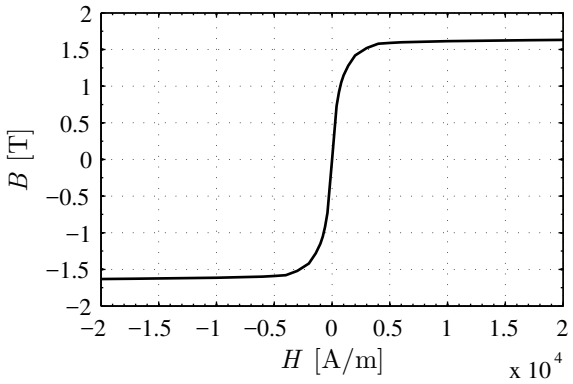

Figure 5.13: Typical $B - H$ curve for a soft ferromagnetic material.

Beyond the linear region of the $B - H$ curve, there is a transition zone where the core starts to saturate. For some other materials, such as hard ferromagnetic materials, the $B - H$ curve may present a hysteresis loop.

The elements modelled in AMESim to represent a *common-rail* injector solenoid actuated valve, such as the one present in the Bosch CRI 2.20 injector, are the solenoid itself (electric coil), the magnetic cores (axial and radial) and the air gap, as shown in Figure 5.14.

(a) Solenoid (b) Axial core (c) Radial core (d) Air gap

Figure 5.14: Representation of the AMESim components used to model a common-rail injector solenoid actuated valve.

Solenoid

The component employed in AMESim to model a solenoid calculates the magnetic flux through the coils by applying Equation (5.57):

$$\frac{\mathrm{d}\Phi_B}{\mathrm{d}t} = \frac{V + R\frac{\mathcal{F}}{N_t}}{N_t} \tag{5.57}$$

where R is the electrical resistance, whereas the term $\mathcal{F}/N_t$ is the electric current I through the solenoid, usually supplied from an adjacent component. In the case of a common-rail solenoid actuated injector, an external source directly delivers the electric current signal.

Magnetic core

Figure 5.15 sketches the typical arrangement of the magnetic side of a solenoid actuated *common-rail* injector control valve. The coil embedded in a magnetic core can be observed. The magnetic flux path is also shown, highlighting the fact that it trespasses the core both longitudinally (paths A and C) and radially (paths B and D). Hence, the AMESim elements shown in Figures 5.14(b) and 5.14(c) need to be used, respectively.

In these components, the geometry is defined through parameters introduced by the user. In the case of axial magnetic core elements, both the trespassed area and the length are directly specified as parameters. Concerning

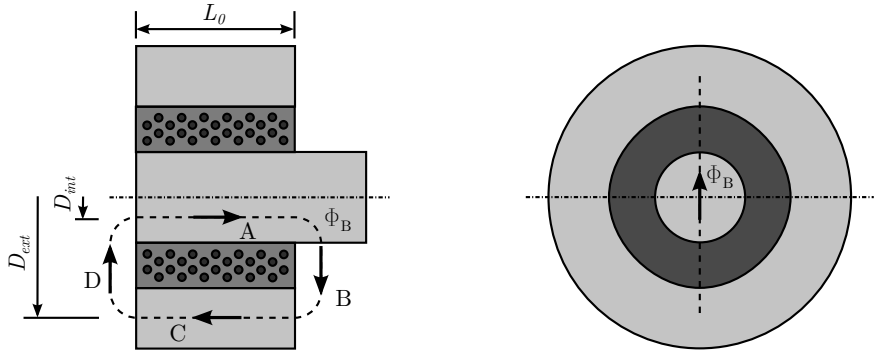

(a) Side view (b) Top view

Figure 5.15: Sketch of the magnetic flux path through the magnetic core in a solenoid actuated common-rail injector control valve. The embedded coils are also represented.

the radial magnetic core elements, their relevant area and length are computed from the reference length L_0 and the diameters D_{ext} and D_{int} specified in Figure 5.15, so that:

$$L = \frac{D_{ext} + D_{int}}{4} \ln\left(\frac{D_{ext}}{D_{int}}\right) \tag{5.58}$$

$$A = \pi L_0 \frac{D_{ext}}{D_{int}} \tag{5.59}$$

The magnetic flux Φ_B is given as an input from an adjacent component (typically the solenoid), whereas the magnetomotive force is computed as an output as follows.

The time derivative of the magnetomotive force can be derived from Equation (5.51):

$$\frac{\mathrm{d}\mathcal{F}}{\mathrm{d}t} = L\frac{\mathrm{d}H}{\mathrm{d}t} \tag{5.60}$$

The rate of change of the magnetic field intensity can be deduced from Equation (5.53):

$$\frac{\mathrm{d}H}{\mathrm{d}t} = \frac{1}{\mu}\frac{\mathrm{d}B}{\mathrm{d}t} \tag{5.61}$$

Differentiating Equation (5.48), the magnetic flux density time derivative can be computed from the rate of change of the magnetic flux given by the adjacent component and the core geometry:

$$\frac{\mathrm{d}B}{\mathrm{d}t} = \frac{1}{A}\frac{\mathrm{d}\Phi_B}{\mathrm{d}t} \tag{5.62}$$

Therefore, combining Equations (5.60) to (5.62), the magnetomotive force is calculated in a magnetic core AMESim component as:

$$\frac{\mathrm{d}\mathcal{F}}{\mathrm{d}t} = \frac{L}{\mu A}\frac{\mathrm{d}\Phi_B}{\mathrm{d}t} \tag{5.63}$$

Air gap

An air gap is a flux path included between two poles in a magnetic circuit. The motion of one or both of these poles alters the relation among the magnetic flux and the magnetomotive force in the circuit and induces a resistive force on the moving pole. This is illustrated in Figure 5.16, where one pole is fixed and the other one is movable. The velocity and displacement in each part of the gap are inputs from the adjacent components (the lift of the control valve, in the case of a *common-rail* injector), whereas the force due to the magnetic flux is computed as an output.

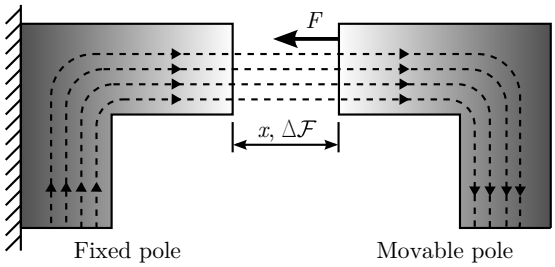

Figure 5.16: Sketch of an air gap with a fixed pole and a movable pole.

A flux passes through the gap and is associated with a magnetomotive force drop, $\Delta\mathcal{F}$. The reluctance associated to the gap is dependent on the gap width x. From Equation (5.55), this relation is written as:

$$\mathcal{R}(x) = \frac{\Delta\mathcal{F}}{\Phi_B} \tag{5.64}$$

The energy stored in the gap may be calculated from the magnetomotive force drop:

$$E = \int \Delta\mathcal{F}\left(\Phi_B, x\right)\, \mathrm{d}\Phi_B = \frac{\Phi_B^2}{2}\mathcal{R}(x) \tag{5.65}$$

Differentiating Equation (5.65), the force in the air gap can then be expressed as:

$$F = \left(\frac{\partial E}{\partial x}\right)_{\Phi_B} = \frac{\Phi_B^2}{2}\frac{\mathrm{d}\mathcal{R}}{\mathrm{d}x} \tag{5.66}$$

Hence, the time derivative of this force may be written as:

$$\frac{\mathrm{d}F}{\mathrm{d}t} = \left(\frac{\partial F}{\partial x}\right)_{\Phi_B}\frac{\mathrm{d}x}{\mathrm{d}t} + \left(\frac{\partial F}{\partial \Phi_B}\right)_{x}\frac{\mathrm{d}\Phi_B}{\mathrm{d}t} = \frac{\Phi_B^2}{2}\frac{\mathrm{d}^2\mathcal{R}}{\mathrm{d}x^2}\frac{\mathrm{d}x}{\mathrm{d}t} + \Phi_B\frac{\mathrm{d}\mathcal{R}}{\mathrm{d}x}\frac{\mathrm{d}\Phi_B}{\mathrm{d}t} \tag{5.67}$$

On the other hand, the rate of change of the magnetomotive force with respect to time is calculated as:

$$\frac{\mathrm{d}\mathcal{F}}{\mathrm{d}t} = \left(\frac{\partial \mathcal{F}}{\partial x}\right)_{\Phi_B}\frac{\mathrm{d}x}{\mathrm{d}t} + \left(\frac{\partial \mathcal{F}}{\partial \Phi_B}\right)_{x}\frac{\mathrm{d}\Phi_B}{\mathrm{d}t} = \Phi_B\frac{\mathrm{d}\mathcal{R}}{\mathrm{d}x}\frac{\mathrm{d}x}{\mathrm{d}t} + \mathcal{R}(x)\frac{\mathrm{d}\Phi_B}{\mathrm{d}t} \tag{5.68}$$

The submodel implemented by AMESim for an air gap with planar parallel poles of circular layout (as typical for *common-rail* solenoid actuated injectors given their cylindrical shape) relates the reluctance to the gap width x in the following way:

$$\mathcal{R} = \frac{1}{\mu_0 D_{pole}\left(\frac{\pi D_{pole}}{4x} + \zeta\right)} \tag{5.69}$$

where ζ is a correction factor that accounts for possible distortions of the magnetic flux that may be assumed to take a value of 0.58 for most industrial applications [19].

5.2.6 Numerical resolution of the equations

When developing one-dimensional models of physical systems, several kinds of equations need to be solved as shown along Section 5.2: ordinary differential

equations (ODEs), differential algebraic equations (DAEs) and partial differential equations (PDEs). As reviewed in Section 3.2, injection system modellers have traditionally used different solutions in this regard. In addition, a treatment needs to be given to handle discontinuities during a simulation.

In order to solve ODEs, two main groups of methods are used. On the one hand, Runge-Kutta methods, which use a fixed time step to solve the equations and are easier to implement, but are not appropriate for systems with numerical stiffness. On the other hand, Linear Multistep Methods (LMMs), which can use variable time steps and solve stiff problems, although they present some issues when treating discontinuities. One of the most known LMMs methods is the Gear method. Some algorithms to implement these methods are Adams, Gear and LSODA. DAEs can be solved through the DASSL algorithm, which is an extension of the Gear algorithm. Finally, PDEs are usually reduced to ODEs and solved through a simple temporal discretization via finite-difference methods, finite-element methods or the method of characteristics.

AMESim does not give the user the possibility to choose the integration algorithm. It automatically analyses the characteristics of the equations that describe the model in order to select an appropriate solution. If the model contains any implicit variables, the DASSL integration algorithm for DAEs is used. Otherwise, the LSODA integration algorithm for ODEs is utilized.

LSODA uses both non-stiff integration methods (Adams-Moulton multistep) and stiff integration methods (backward differentiation formulae multistep). The algorithm monitors the characteristics of the governing equations and switches from one method to the other accordingly. This capability allows LSODA to be an efficient solver independently of the characteristics of the equations.

DASSL solves the set of constraint equations and implicit equations by using specific Newton-base iterative methods. The user can choose between the LU algorithm (based on the Gaussian elimination method, which solves the system in a direct way) and a Krylov method (which minimises residuals on Kyrlov subspaces and then iterates over the subspaces towards the real solution of the initial system). In several occasions, the solution of DAEs may require the use of a preconditioner.

To solve PDEs, AMESim allows to choose among finite-difference methods or finite-element methods. Finally, in order to deal with discontinuities, AMESim employs a specific treatment in each component so that the numerical resolution of the equations is still robust without significantly increasing the simulation time.

5.3 Modelling of the Bosch CRI 2.20 injector

As stated earlier, the Bosch CRI 2.20 is the injector used as a basis for the study carried out in the present thesis. The computational model of this injector implemented to support and extend the findings from the experimental results is discussed in the present section.

For illustrative purposes, the model is divided in three parts: the injector holder (piece of the injector body that contains the control volume piece and the internal ducts to drive the fuel towards the nozzle), the solenoid valve and the nozzle. The implementation of the fuel properties is also described here, with special attention to the computation of the specific enthalpy, from which the temperature variations along the injector are determined.

5.3.1 Injector holder

Figure 5.17 shows a sketch of the injector holder together with its AMESim model representation. A first element (pressure and temperature source) provides the fuel inlet temperature, on the one hand, and simulates the high-pressure pump, on the other. Both variables have been assumed to be constant at this location.

The high-pressure pump raises the pressure in a volume that represents the *common-rail*. The rail is connected to the injector inlet by means of a high-pressure line (HPL), key on the pressure wave propagation. Right at the injector inlet, the flow travels through the high pressure filter (HPF), modelled as a flow restriction.

Once the fuel enters the injector, it passes through the line HL1 until it reaches a bifurcation: part of the fuel enters the injector control volume HV1 through the inlet orifice (also referred to as OZ orifice). The pressure in this volume is used to compute the pressure force on the upper part of the needle, mechanically modelled as the element P1. The flow is also allowed to leave the control volume through the HL2 line linked to the outlet orifice (referred to as OA orifice). This orifice is connected, in turn, to the HV2 volume that links the injector holder to the solenoid valve.

The rest of the fuel after the bifurcation downstream of the HL1 line travels to the nozzle through lines HL3, HL4 and HL5 in order to be injected into the cylinder. This fuel also encounters the volumes HV3 and HV4, where the pressure forces on other parts of the needle are computed.

It is important to note that the main parameters of the hydraulic lines are their length and diameter, as deduced from Section 5.2.3. For those cases in

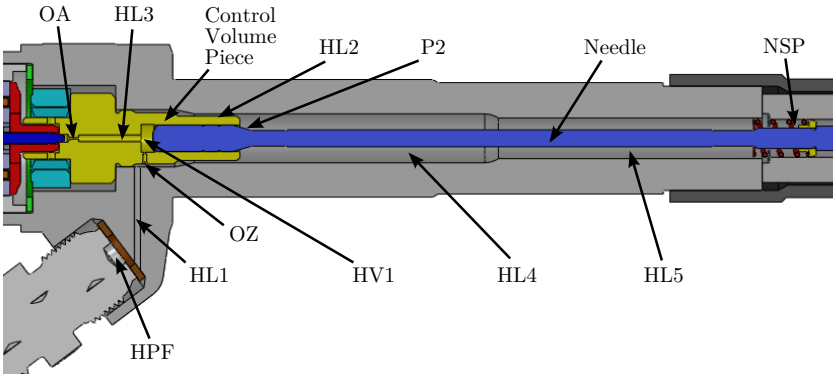

(a) Bosch CRI 2.20 injector holder sketch.

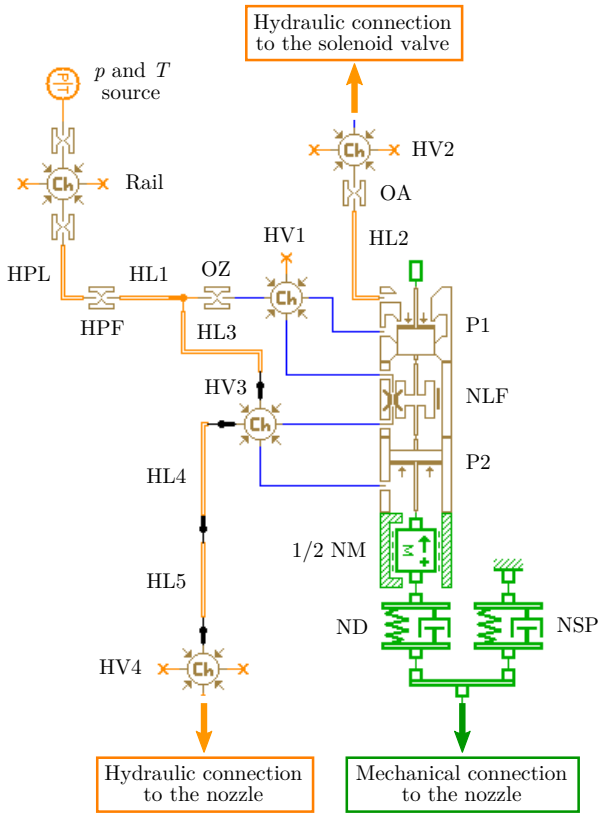

(b) AMESim model sketch of the Bosch CRI 2.20 injector holder.

Figure 5.17: Sketch of the Bosch CRI 2.20 injector holder together with its AMESim model representation.

which the hydraulic line is not circular (such as lines HL4 and HL5, which are annular ducts), the hydraulic diameter defined in Equation (5.15) has been used instead. In the particular case of an annular line, the hydraulic diameter is determined as:

$$D_{h,annulus} = \frac{4A}{P} = D_{ext} - D_{int} \tag{5.70}$$

As far as the mechanical elements of the injector holder are concerned, the upper part of the needle has been modelled by the elements P1, NLF, P2, 1/2 NM, ND and NSP. The piston P2 computes the pressure forces due to the change in cross-sectional area in the needle that generates an annular surface on which the pressure established in the HV3 volume acts, trying to push the needle upwards.

The element 1/2 NM accounts for half of the needle mass, since the other half has been linked to the nozzle part due to compatibility among AMESim elements (to properly establish the causality relations). In addition to the friction in the masses taken into account by the 1/2 NM element, as shown in Section 5.2.2, the NLF element accounts for internal leakages and viscous friction that take place due to the small clearance among the needle and the injector holder itself in certain parts of the injector. According to Equation (5.31), the friction forces in this component depend on the pressure difference across the element Δp and the fuel viscosity η_f. In the case of the needle, this pressure difference is the one set among the volumes HV1 (control volume) and HV3. During the normal operation of the injector, the pressure in the control volume depends on the pressure drop across the inlet orifice OZ, whereas the pressure in the HV3 volume is approximately the rail pressure, since no important flow restrictions are found in the high pressure filter or the HL1 and HL3 lines. Thus, the pressure drop in the control volume and the fuel viscosity are key on understanding the friction forces on the needle.

In addition, NSP represents the spring that tries to hold the needle against its seat and opposes to its lift. Finally, the element ND models the elastic deformation of the needle, especially relevant prior to the injection event as justified in Section 5.2.2.

A summary of the main parameters introduced in this part of the model is presented in Table 5.1. These parameters were gathered through the dimensional characterization described in Section 4.2. Details on the control volume orifices were presented in Sections 4.2 and 4.3 (Tables 4.2 and 4.4) and are therefore omitted in the table.

Hydraulic elements			
Element	$\boldsymbol{L}$ [mm]	$\boldsymbol{D_h}$ [mm]	$\boldsymbol{V_o}$ [mm^3]
Rail	-	-	2.4×10^4
HPL	300.0	2.5	-
HPF	-	0.8	-
HL1	7.38	1.38	-
HV1	-	-	13.5
HL2	8.75	1.1	-
HV2	-	-	1.85
HL3	17.05	1.0	-
HL4	40.64	5.18	-
HL5	49.9	3.84	-
HV3	-	-	81
HV4	-	-	25

Hydraulic-mechanical elements					
Element	$\boldsymbol{D_{pist}}$ [mm]	$\boldsymbol{D_{rod}}$ [mm]	$\boldsymbol{m}$ [g]	$\boldsymbol{k}$ [N/m]	$\boldsymbol{x_0}$ [mm]
P1	4.3	0	-	-	-
LF	4.3	4.292	-	-	-
P2	4.3	4.0	-	-	-
1/2 NM	-	-	4.6	-	-
ND	-	-	-	8.5×10^7	0
NSP	-	-	-	5.25×10^3	5.0

Table 5.1: Summary of the main parameters of the CRI 2.20 injector holder AMESim model.

5.3.2 Solenoid valve

A detail of the solenoid valve part of the injector is shown in Figure 5.18(a). Figure 5.18(b) shows a detail of the path followed by the magnetic flux around the solenoid coil. The AMESim sketch proposed in this thesis to model this part of the injector is shown in Figure 5.18(c).

The mechanical elements (piston) of the valve are in charge of avoiding any flow from the control volume (HV1) through the injector outlet orifice (OA) while the injector is not energized. When a current I (imposed by a signal generation component) arrives to the solenoid coil, it induces a magnetic flux through the magnetic core (represented by the elements SC1, SC2, SC3 and SC4). During its path around the coil, the magnetic flux crosses the air gap AG towards the upper side of the valve piston (SC2).

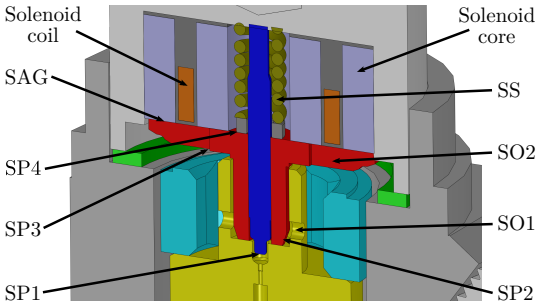

(a) Bosch CRI 2.20 solenoid valve sketch

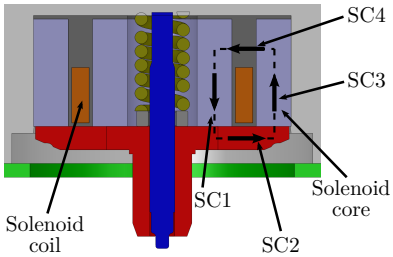

(b) Bosch CRI 2.20 magnetic path

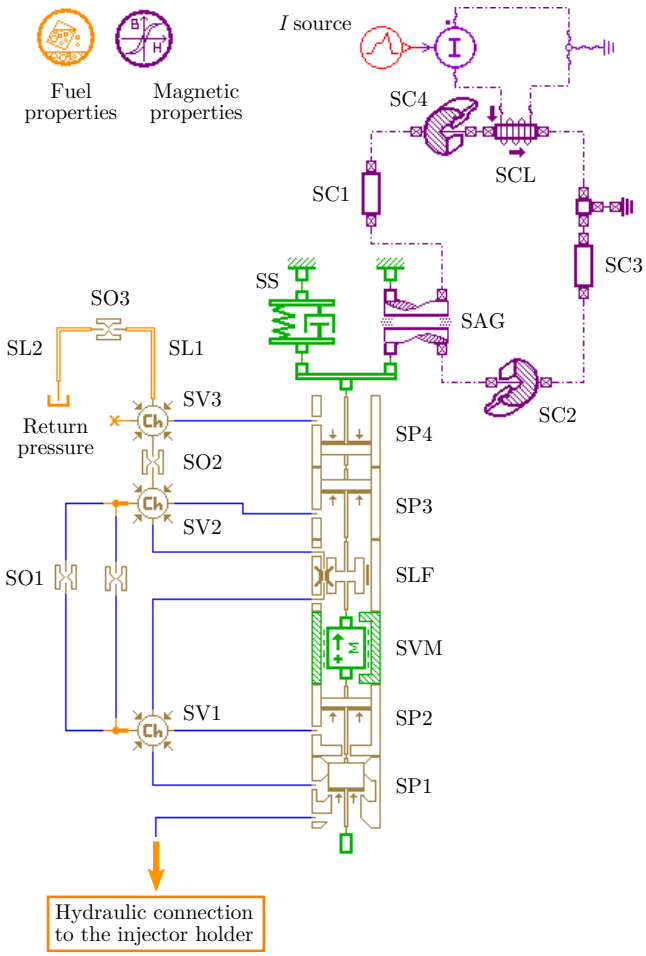

(c) AMESim model sketch of the Bosch CRI 2.20 solenoid valve

Figure 5.18: Sketch of the Bosch CRI 2.20 solenoid valve with a detail of the magnetic path together with its AMESim model representation.

The resulting magnetic flux is responsible for the generation of a force that attracts the valve piston, lifting it upwards and letting the fuel flow from the control volume through a variable section orifice whose cross-sectional area grows as the valve piston moves up. This variable section restriction has been modelled as the plain seat valve SP1, whose lift is limited to 25 µm, and is linked to the injector holder part of the model through the injector outlet orifice, OA. Therefore, once the injector is energized, the set consisting of the OA and SP1 orifices evacuates fuel from the control volume, thus dropping its pressure and letting the needle rise. This unlocks the nozzle orifices starting the fuel injection into the cylinder.

The fuel leaving the control volume through the solenoid control valve flows to the return line through the SO1 orifices carved at both sides of the upper part of the control volume piece. From there, it travels through the SO2 orifices, drilled on the valve piston upper surface, and leaves the injector through the lines SL1 and SL2 and the orifice SO3, which represent the fuel return duct. Along this path, the fuel also encounters the volumes SV1, SV2 and SV3, whose pressure acts on the pistons SP1, SP2, SP3 and SP4. The pressure on these elements is responsible for generating the forces that help opening or closing the solenoid control valve against the SP1 variable section orifice. These pistons, together with the solenoid valve mass (SVM), shape the valve piston mechanical part.

In addition, the SLF component accounts for the internal leakages and viscous friction taking place at this section of the injector, in a similar way to the one described for the needle in Section 5.3.1.

Once the injector stops being energized, the valve piston closes the variable section SO1 orifice thanks to the force imposed by the SS spring. From this moment, the spring force keeps the SO1 orifice locked, cutting the flow from the control volume. In this situation, the OZ orifice refills the control volume, restoring its pressure and making the needle close against the nozzle seat, cutting the injection.

A summary of the main parameters of the solenoid valve part of the Bosch CRI 2.20 injector model is shown in Table 5.2. The magnetic coil resistance was determined by means of a commercial digital multimeter, whereas the number of turns was found by cutting the solenoid valve in half and visualizing them through an optical microscope as described in Section 4.2.

Electromagnetic elements				
Element	$\boldsymbol{L}$ [mm]	$\boldsymbol{A}$ [mm^2]	$\boldsymbol{N_t}$ [-]	$\boldsymbol{R}$ [Ω]
SC1	6.725	51.25	-	-
SC2	3.0	108.38	-	-
SC3	6.725	136.07	-	-
SC4	3.0	108.38	-	-
SCL	-	-	40	7.46
SAG	0.08	31.82	-	-

Hydraulic elements			
Element	$\boldsymbol{L}$ [mm]	$\boldsymbol{D_h}$ [mm]	$\boldsymbol{V_o}$ [mm^3]
SV1	-	-	23.0
SO1	-	1.255	-
SV2	-	-	522.2
SO2	-	5.233	-
SV3	-	-	5.3
SL1	8.25	5.0	-
SO3	-	1.0	-
SL2	23.25	5.0	-

Hydraulic-mechanical elements					
Element	$\boldsymbol{D_{pist}}$ [mm]	$\boldsymbol{D_{rod}}$ [mm]	$\boldsymbol{m}$ [g]	$\boldsymbol{k}$ [N/m]	$\boldsymbol{x_0}$ [mm]
SP1	3.6	1.6	-	-	-
SP2	4.3	3.6	-	-	-
SVM	-	-	3.1	-	-
SLF	4.5	4.3	-	-	-
SP3	12.5	4.3	-	-	-
SP4	12.5	1.5	-	-	-
SS	-	-	-	3.807×10^4	1.5

Table 5.2: Summary of the main parameters of the CRI 2.20 solenoid valve AMESim model.

5.3.3 Nozzle

Figure 5.19 shows a detail of the nozzle part of the injector together with its AMESim equivalent sketch.

Fuel comes from the injector holder through the three parallel lines NL1 that result from the needle having a quasi-triangular cross-section. For each of these lines, an additional hydraulic orifice NO1 has been introduced due

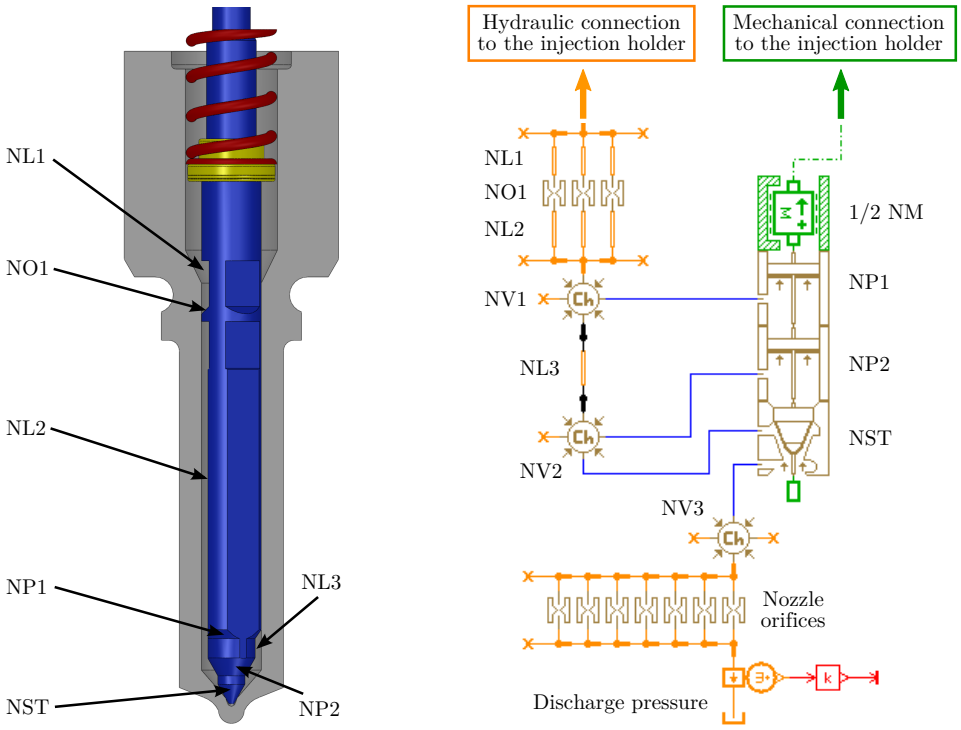

(a) Bosch CRI 2.20 nozzle sketch

(b) AMESim model sketch of the Bosch CRI 2.20 nozzle

Figure 5.19: Sketch of the Bosch CRI 2.20 nozzle together with its AMESim model representation.

to a sudden increase in the needle cross-section. This section of the needle (commonly referred to as *needle flaps*) generates an important restriction to the flow that may lead to important pressure changes.

After these orifices, the fuel keeps travelling along parallel ducts (NL2), until they encounter each other in the NV1 volume, from where it flows to the nozzle discharge orifices through the nozzle channel NL3. The volume at the lower part of the nozzle has been divided into the NV2 and NV3 volumes, since the latter exclusively represents the sac, considered from the needle seat point onwards.

The NV1 and NV2 volumes are associated to the pistons NP1 and NP2, which account for the pressure forces pushing the needle upwards. The nozzle seat NST has been represented by a conical valve seat element that takes into consideration both the needle tip and the seat. Therefore, this component

Hydraulic elements			
Element	$\boldsymbol{L}$ [mm]	$\boldsymbol{D_h}$ [mm]	$\boldsymbol{V_o}$ [mm^3]
NL1	3.5	0.7	-
NO1	-	0.37	-
NL2	20.75	0.7	-
NV1	-	-	2.68
NL3	5.0	0.5	-
NV2	-	-	6.36
NV3	-	-	0.3
Hydraulic-mechanical elements			
Element	$\boldsymbol{D_{pist}}$ [mm]	$\boldsymbol{D_{rod}}$ [mm]	$\boldsymbol{m}$ [g]
1/2 NM	-	-	4.6
NP1	4.0	3.16	-
NP2	3.16	1.81	-
NST	-	0.61	-

Table 5.3: Summary of the main parameters of the CRI 2.20 injector holder AMESim model.

simulates the flow through a variable section orifice and it also computes an additional pressure force associated to the sac (NV3 volume).

As stated in Section 5.3.1, half of the needle mass NM was associated to the injector holder part of the model. The other half of this mass is associated to the nozzle part. When the needle lifts, it discovers the 7 orifices of the nozzle, leading to the fuel being injected to a tank at a given backpressure.

The main parameters introduced into the nozzle part of the model are shown in Table 5.3. Details on the geometry of the nozzle orifices and their hydraulic performance were already given in Sections 4.2 and 4.3 and summarized in Tables 4.1 and 4.4.

The determination of the parameters associated to the variable section orifice represented by the nozzle seat element NST is especially critical due to their influence on the transient stages of the injection. Thanks to the dimensional characterization technique explained in Section 4.2, it is possible to obtain them by overlapping optical microscope pictures of both the needle and the nozzle silicone mould, as shown in Figure 5.20.

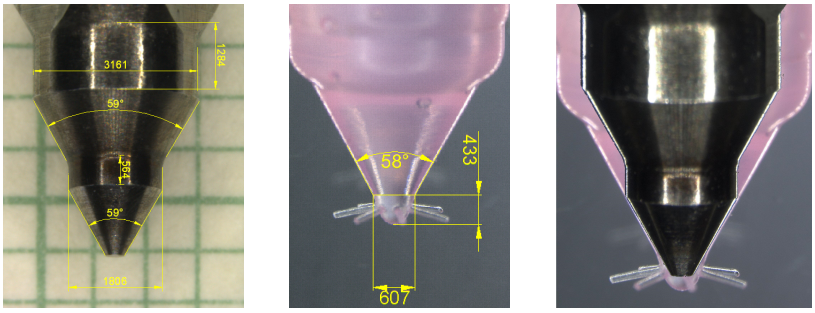

(a) Bosch CRI 2.20 needle picture

(b) Bosch CRI 2.20 nozzle silicone mould

(c) Overlapping

Figure 5.20: Overlapping of digital pictures from the Bosch CRI 2.20 needle and nozzle taken by an optical microscope.

5.3.4 Fuel properties

As stated in Section 4.3, the fuel used for both the injector hydraulic characterization and the experimental study of the present thesis was a winter diesel fuel. The computational model has therefore been implemented using this same fuel as a basis. The dependence of the fuel properties on the pressure and temperature has been introduced in AMESim through the polynomial expressions presented as a result of its experimental determination in Section 4.4. Thanks to these correlations, the computational code is able to introduce local changes in the fuel properties during a simulation.

In addition, as highlighted in Section 5.2.3, the temperature changes along a hydraulic element may be deduced from these fuel properties by means of Equation (5.18), where the enthalpy variations are computed according to Equation (5.26), reproduced here for illustrative purposes:

$$\mathrm{d}h = \left(\frac{\partial h}{\partial T}\right)_p \mathrm{d}T + \left(\frac{\partial h}{\partial p}\right)_T \mathrm{d}p = c_p \mathrm{d}T + \frac{1-\alpha T}{\rho}\mathrm{d}p \tag{5.71}$$

Thereby, Equation (5.71) may be applied to determine the map of specific enthalpy of a fuel if small variations of pressure and temperature are taken instead of differentials. Figure 5.21 shows the specific enthalpy map for the winter diesel fuel tested in the present thesis. As shown in Section 3.3.2, the fuel density was correlated with p and T (Equation (4.22)), whereas $c_p = f(T)$ was assumed to follow the same evolution as the ISO4113 test fluid, whose data

were reported by Chorazewski *et al.* [20]. The values of $\alpha = f(T)$ introduced in Equation (5.71) were calculated from the fuel density correlation as:

$$\alpha = -\frac{1}{\rho_f}\left(\frac{\partial \rho_f}{\partial T}\right) \tag{5.72}$$

Specific enthalpy data have been fitted to a polynomial equation as follows:

$$h\,(T,p) = G_0 + G_1\,(T - T_0) + G_2\,(T - T_0)^2 + G_3\,(p - p_0) + G_4\,(p - p_0)^2 + G_5\,(T - T_0)\,(p - p_0) \tag{5.73}$$

The coefficients of Equation (5.73) for the winter diesel fuel are shown in Table 5.4. The high value of the R^2 statistical confirms the reliability of this regression.

On the one hand, for an isenthalpic expansion ($\mathrm{d}h = 0$), such as the one assumed for the experimental measurements corresponding to the hydraulic characterization of the control volume orifices, Equation (5.73) can then be

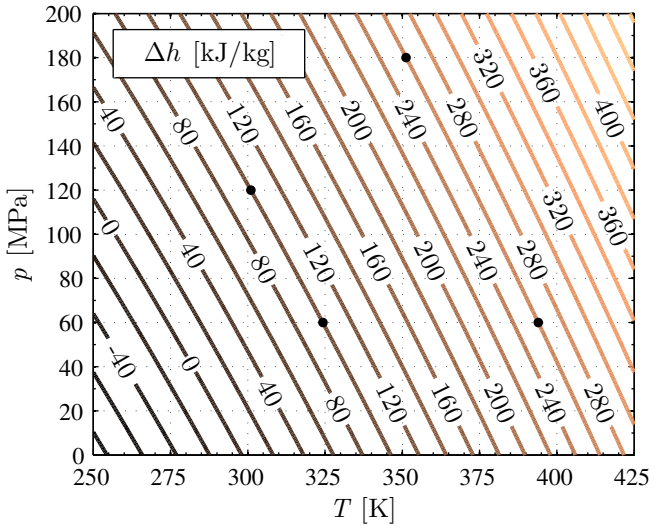

Figure 5.21: Fuel specific enthalpy evolution with respect to temperature and pressure. Reference: $T_0 = 298\,\mathrm{K}$; $p_0 = 0.1\,\mathrm{MPa}$.

G_1 [-]	$G_2 \cdot 10^3$ [-]	G_3 [-]	$G_4 \cdot 10^4$ [-]	$G_5 \cdot 10^4$ [-]	R^2 [-]
1.9465	2.5631	0.75714	2.2179	5.8989	0.99997

Table 5.4: Coefficients for the enthalpy correlation of Equation (5.73) *for the winter diesel fuel. Reference:* $T_0 = 298\,\mathrm{K}$*;* $p_0 = 0.1\,\mathrm{MPa}$.

directly used to determine the theoretical temperature change, solving Equation (5.20) for T_{dw}:

$$h\left(T_{dw}, p_{dw}\right) = h\left(T_{up}, p_{up}\right) \tag{5.74}$$

In this case, a look at Figure 5.21 clearly shows that the fuel warms upon expansion, since isenthalpic lines need to be followed. For instance, it can be seen that an isenthalpic expansion from 120 MPa to 60 MPa (which can be representative of the pressure drop in the control volume for $p_i = 120\,\mathrm{MPa}$) with an initial temperature of 300 K would lead to a temperature of 325 K ($\Delta T = 25\,\mathrm{K}$), or an isenthalpic expansion from 180 MPa to 60 MPa with an initial temperature of 351 K would lead to a temperature of 394 K ($\Delta T = 43\,\mathrm{K}$).

On the other hand, for the expansion taking place through the nozzle orifices under the assumption of adiabatic flow, the stagnation enthalpy must be preserved. Since the kinetic energy importantly increases along the orifice, the enthalpy must decrease in order to compensate for it according to Equation (5.24):

$$h\left(T_{dw}, p_{dw}\right) = h\left(T_{up}, p_{up}\right) - C_v^2 \frac{p_{up} - p_{dw}}{\rho_f} \tag{5.75}$$

In the particular case of the Bosch CRI 2.20 nozzle, the fact that cavitation was not found to take place allows to state that $C_a \approx 1$. Consequently, $C_v \approx C_d$ and Equation (5.75) may be rewritten as:

$$h\left(T_{dw}, p_{dw}\right) = h\left(T_{up}, p_{up}\right) - C_d^2 \frac{p_{up} - p_{dw}}{\rho_f} \tag{5.76}$$

From Equation (5.76) it follows that the temperature along the orifice may be increased or reduced depending on the magnitude of the velocity change, which in turn depends on the pressure drop across the orifice and the discharge coefficient.

5.4 Model validation

In order to ensure the applicability of the injector computational model and the reliability of its predictions, it is necessary to perform a complete validation against experimental results in a wide range of operating conditions. This procedure is described in the present section.

First, given their importance on the injector behaviour, the most important hydraulic restrictions of the Bosch CRI 2.20 injector (i.e. control volume and nozzle orifices) are validated independently. Next, the limitations of the assumption of adiabatic flow along the injector are assessed to check under which conditions the fuel temperature changes along the injector and the consequent variations in the fuel properties are not far from reality.

Finally, the complete injector model is validated by comparing the simulated ROI against experimental results for a wide range of operating conditions. Attention is also given to the predicted temporal evolution of the pressure at the high-pressure line among the rail and the injector, given its strong influence on the timing among injections when implementing multiple injection strategies. A satisfactory analysis would ensure that split injections can also be simulated to assess the impact of the thermal effects on their behaviour.

5.4.1 Flow through a single injector internal orifice

The behaviour of each of the most significant hydraulic restrictions of the Bosch CRI 2.20 injector (namely the control volume and nozzle orifices) was independently validated against the mass flow rate experimental results from the hydraulic characterization presented in Section 4.3.1.

The importance of this individual validation is highlighted considering that AMESim computes the discharge coefficient of an orifice as a function of the Reynolds number through an expression that slightly disagrees from the behaviour observed by researchers in the field. As described in Section 5.2.3 (Figure 5.5), the function introduced by AMESim implies that the maximum discharge coefficient is already reached for values of the theoretical Reynolds number close to the critical one. In most of the reported measurements in the literature (Table 2.2), however, this transition is smoother, as shown in Figure 2.11. It is therefore important to assess the impact of these discrepancies on the mass flow rate values predicted by the model in order to quantify the associated error.

In order to perform the individual validation of the control volume and nozzle orifices, the experimental facility used to carry out their hydraulic char-

acterization (described in Section 4.3.1) has been reproduced in AMESim, as shown in Figure 5.22. Simulations were performed for the same nominal operating conditions as the experimental tests, that were depicted in Table 4.3.

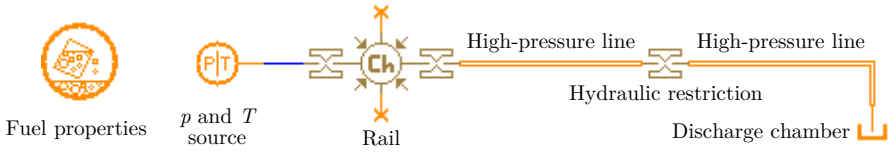

Figure 5.22: AMESim sketch of the experimental facility for the hydraulic characterization of injector internal orifices.

Figure 5.23 shows the results of the comparison among modelled and experimentally measured mass flow rate for the nozzle. The evolution of the mass flow rate with respect to the square root of the pressure drop is depicted for both the simulations and the experiments in Figure 5.23(a). Figure 5.23(b), in turn, represents the percentual deviations among the modelled and the experimentally observed mass flow rate ($\dot{m}_{f,mod}$ and $\dot{m}_{f,exp}$, respectively), defined as:

$$\varepsilon_{\dot{m},f} = \frac{\dot{m}_{f,mod} - \dot{m}_{f,exp}}{\dot{m}_{f,exp}} \cdot 100\,(\%) \tag{5.77}$$

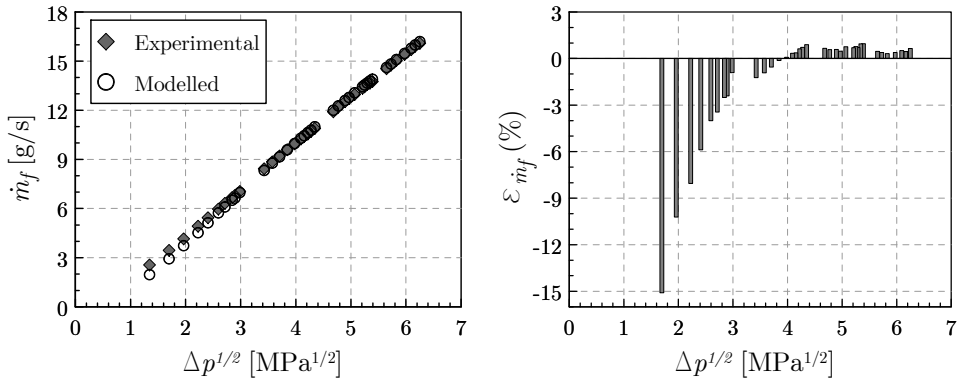

(a) Mass flow rate results (b) Deviations to experiments

Figure 5.23: Modelled mass flow rate through the Bosch CRI 2.20 nozzle compared against the experimental results.

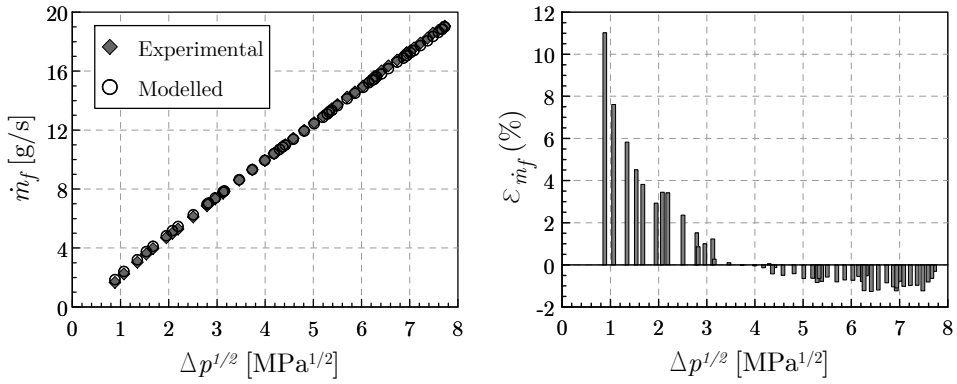

(a) Mass flow rate results (b) Deviations to experiments

Figure 5.24: Modelled mass flow rate through the Bosch CRI 2.20 inlet orifice compared against the experimental results. For illustrative purposes, only half of the tested points are shown.

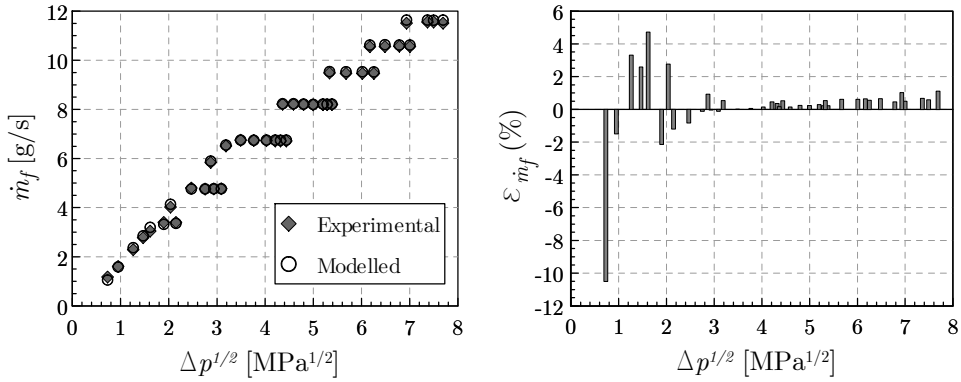

(a) Mass flow rate results (b) Deviations to experiments

Figure 5.25: Modelled mass flow rate through the Bosch CRI 2.20 outlet orifice compared against the experimental results. For illustrative purposes, only half of the tested points are shown.

As can be seen, results show an excellent agreement for most of the pressure conditions tested. The highest deviations are found for the lowest values of the pressure drop, where the mass flow rate is underestimated reaching deviations up to 15%. For values of $\Delta p^{1/2}$ higher than 3 (which mean pressure drops around 9 MPa, reached in the injector nozzle for the typical engine operating

conditions), the deviations are bounded below 1.5%, tending to overestimate the mass flow rate for large pressure drops.

Results corresponding to the validation of the behaviour of the control volume orifices are presented in Figures 5.24 and 5.25. In the case of the inlet orifice (Figure 5.24), the mass flow rate is overestimated by the model for low pressure drops, leading to deviations up to 11 % in the least favourable conditions. Again, for higher values of the pressure drop the deviations are bounded within a 2%, leading to a slight underestimation of the mass flow for large pressure drops.

Focusing on the outlet orifice, the analysis is similar. In this case, the deviations are bounded below 1% for most tested points. In addition, the model has proved to be able to accurately determine the critical cavitation conditions at each of the injection pressures tested. This implies that the values of mass flow rate corresponding to the collapse can also be predicted with precision.

5.4.2 Assumption of adiabatic flow through a diesel injector internal orifice

The assumption of adiabatic flow along the injector has been taken in the present thesis. As stated in Sections 5.2.3 and 5.3.4, the temperature variation through a flow restriction can be computed from the fuel enthalpy map (Figure 5.21) and the velocity change through the restriction. In the case of the flow through the control volume orifices, this velocity change is not deemed to be important given that the flow velocity in the injector ducts both upstream and downstream of the orifices is similar. Hence, the flow has been regarded to as isenthalpic ($\mathrm{d}h = 0$) and the temperature changes have been directly obtained from the aforementioned map following isenthalpic lines, according to Equations (5.73) and (5.74).

In any case, the limits of the extension of this hypothesis need to be assessed in order to ensure the reliability of the simulations performed by the computational model, given that local changes in temperature and pressure are taken into account in the calculations.

To this end, the theoretical values of temperature change through an injector control volume orifice computed assuming isenthalpic flow are compared in this section against the ones obtained from the hydraulic characterization with continuous flow described in Section 4.3.1 (recall Figure 4.13). It is important to remind that, in order to gather a wider set of results to guarantee the validaty of the assumption, the Denso G4S injector orifices were also tested.

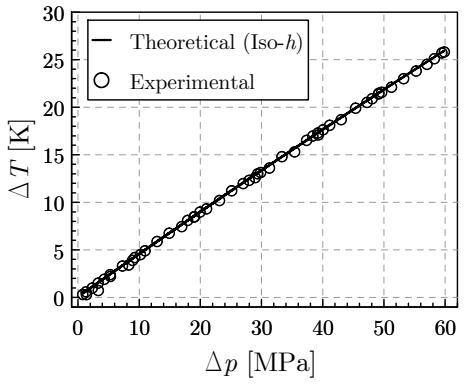

(a) Bosch inlet orifice

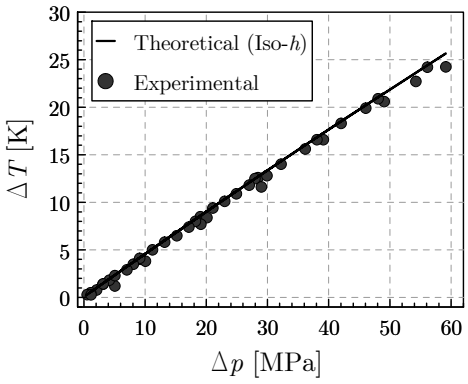

(b) Bosch outlet orifice

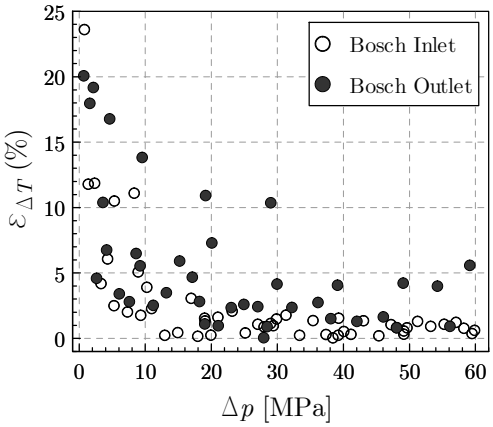

(c) Deviations to experiments

Figure 5.26: Experimental temperature changes across the Bosch CRI 2.20 control volume orifices compared against the theoretical results. For illustrative purposes, only half of the tested points are shown.

This also ensured that both cavitating and non-cavitating orifices were explored, allowing to assess the significance of the cavitation phenomenon in the adiabatic flow assumption.

Figure 5.26 shows the results corresponding to the Bosch CRI 2.20 control volume orifices. The comparisons among the evolution of the theoretical and the experimentally determined values of ΔT with respect to the pressure drop across the inlet and the outlet orifices are presented in Figures 5.26(a) and 5.26(b), respectively. As it can be seen, results fit the theoretical values almost

perfectly in both cases. Hence, the flow practically behaves as if it were isenthalpic and heat exchange with the surroundings does not seem to be significant, supporting the hypothesis of adiabatic flow. Deviations could also be attributed to uncertainties in the experimental measurements. In any case, it is important to note that the experimental ΔT registered is always slightly lower than the theoretical one. Since the fuel is considerably warmer than the ambient in all cases this means that, in the event of heat transfer being relevant, it is indeed transferred to the surroundings rather than the other way around.

Figure 5.26(c) shows the evolution of the percentual deviations ($\varepsilon_{\Delta T}$) among the theoretical temperature increase corresponding to an isenthalpic expansion and the experimental results. These deviations were calculated according to Equation (5.78), in a similar way to the ones for the mass flow rate individual validation.

$$\varepsilon_{\Delta T} = \frac{\Delta T_{th} - \Delta T_{exp}}{\Delta T_{th}} \cdot 100\,(\%) \tag{5.78}$$

Having a look at a given orifice in Figure 5.26(c), a decreasing trend is observed when Δp increases. This result is expected considering the higher flow velocities induced, which lead to lower residence times of the fuel in the injection orifice, thus preventing important heat exchange with the ambient. In addition, the differences are bounded for each orifice as long as the pressure drop is high enough. The most important differences in percentual terms take place for low values of Δp. In those cases, the flow may be laminar (the associated Re could be lower than the critical one), which means that viscous dissipation effects become relevant. These effects, located at the boundary layer, result in a decrease of the fuel velocity close to the wall (even though viscous heating induces higher fuel temperatures also close to the wall, which act in the sense of reducing the fuel viscosity thus damping the mentioned effect), thus increasing the fuel residence times in the channel. Hence, there may be enough time for the flow to lose heat to the surroundings.

It is also important to note that, if the Bosch CRI 2.20 injector orifices are compared among them, the observed deviations with the isenthalpic prediction in the case of the inlet orifice are bounded below 2 %, whereas they remain around 5 % in the case of the outlet orifice. On the one hand, these differences among orifices could be due to the lower diameter of the outlet orifice (259 µm as opposed to 290 µm). As stated in Section 4.3.1, despite the lower effective surface for heat exchange, the reduction in cross-sectional area leads to a higher portion of the flow being affected by the boundary layer. This generates

a reduction in flow velocity that enhances heat transfer. More generally, low diameters result in low values of Re that may also modify the flow regime and the orifice discharge capabilities, as it happened for low values of Δp. Hence, an orifice with low diameter may induce laminar flow for operating conditions for which a similar orifice with the same critical Reynolds number and a larger diameter already generates turbulent flow (please note that this affirmation may not hold if the values of Re_{crit} for both orifices importantly differ). On the other hand, the fact that the outlet orifice works under cavitating conditions for sufficiently high pressure drops may also be responsible for modifying the heat transfer features.

In order to further investigate these findings, the Denso G4S injector orifices were also studied in the present thesis. Figure 5.27 shows the comparison among experimental and theoretical values of the temperature change across these orifices. The observed trends with the pressure drop are in agreement with the ones reported for the Bosch orifices. However, even though the experimental results for the inlet and control valve orifices remain close to the theoretical values, the behaviour of the outlet orifice importantly departs from the isenthalpic assumption. While the deviations in the first cases remain lower than 5 % and 10 % for large pressure drops, respectively, they do not get much lower than 15 % for the outlet orifice. As suggested for the Bosch orifices, the deviations seem to scale well with the orifice diameter (274 µm for the inlet orifice, 198 µm for the control valve orifice and 102 µm for the outlet one). In addition, the minimum pressure drop at which the deviations get bounded is higher for this orifice with a lower diameter. This might be explained considering that higher pressure drops are needed to achieve sufficiently high values of the Reynolds number.

From the findings of Figures 5.26 and 5.27, it seems that several parameters (such as flow velocity, viscosity, orifice diameter - all of them linked through Re -, etc.) are involved in the proneness of the flow induced through an injector orifice to resemble an isenthalpic flow. Therefore, it may be interesting to relate these variables in a single parameter to qualitatively quantify their effects in a combined way. This parameter could provide a strong basis on which the hypothesis of adiabatic flow through the Bosch CRI 2.20 injector hydraulic restrictions could be confidently asseverated, allowing to rely on the results of the computational model developed in the present thesis. This task is performed in the following subsections.

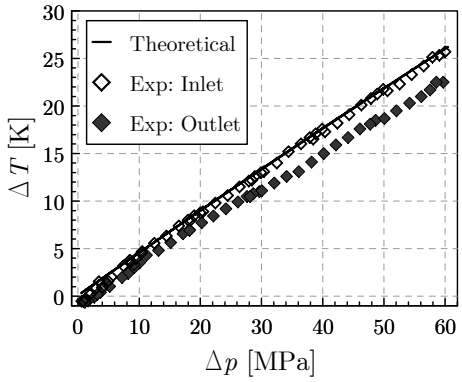

(a) Denso orifices

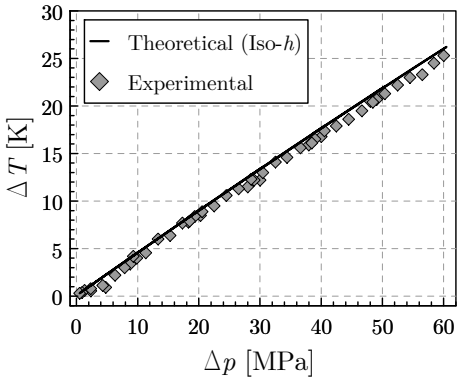

(b) Denso control valve

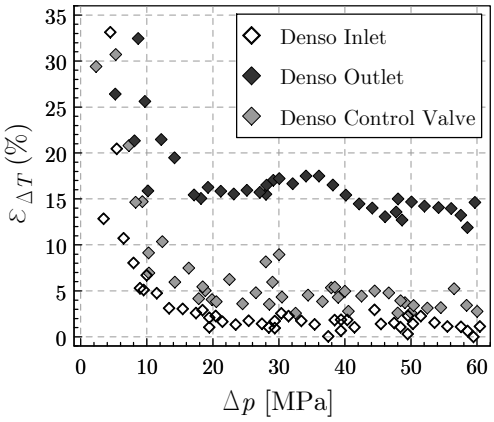

(c) Deviations to experiments

Figure 5.27: Experimental temperature changes across the Denso G4S control volume orifices compared against the theoretical results. For illustrative purposes, only half of the tested points are shown.

Derivation of a dimensionless parameter to quantify the proneness of an orifice to transfer heat with the surroundings

Let us consider a fluid travelling through a channel of length L and perimeter P, as depicted in Figure 5.28. The fluid enters the channel at a certain T_{up} temperature, and leaves with a different temperature, T_{dw}. At any location inside the channel, the fluid is allowed to exchange heat with the surroundings since there may be a difference among its temperature, T_f, and the channel wall temperature, T_w. In these conditions, without any additional external

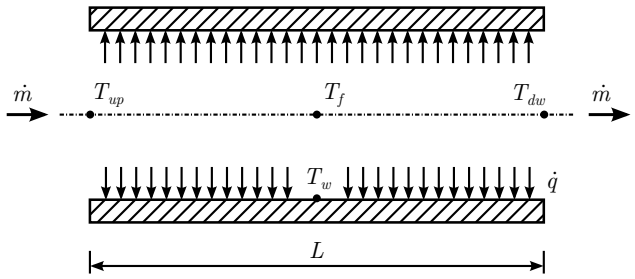

Figure 5.28: Scheme of flow through a circular duct with heat transfer to the surroundings.

work, the change in specific enthalpy of the fluid must equal the heat transferred, which yields:

$$\dot{m}c_p\left(T_{dw} - T_{up}\right) = h_c A_P\left(T_w - T_f\right) \tag{5.79}$$

where h_c is the convective heat transfer coefficient and A_P is the heat transfer area of the channel surface. It is then possible to define a dimensionless parameter (Ad) as the ratio among temperature changes:

$$Ad = \frac{\left(T_w - T_f\right)}{\left(T_{dw} - T_{up}\right)} = \frac{\dot{m}c_p}{h_c A_P} \tag{5.80}$$

Ad may be referred to as *adiabatic number* and it quantifies the temperature difference needed among the channel wall and the fluid in order for the fluid to increase its temperature in 1 K at the channel outlet. In other words, Ad measures the proneness of a flow to retain the heat within itself instead of transferring it to the surroundings. Thus, the higher the value of Ad, the closer to the theoretical adiabatic condition the flow will behave. Ad may be expressed in terms of other dimensionless groups:

$$Ad = \frac{\dot{m}c_p}{h_c A_P} = \frac{\rho A_0 u c_p}{PLh_c} = \frac{1}{4}\frac{D}{L}\frac{\rho u c_p}{h_c} = \frac{1}{4}\frac{D}{L}St^{-1} \tag{5.81}$$

where the concept of hydraulic diameter (equal to the channel diameter in a circular channel) as the ratio among the cross-sectional area A_0 and the perimeter P of the channel has been used. Thus, Ad is directly related to the diameter-to-length ratio of the channel and to the Stanton number, St,

which relates the heat transferred into a fluid through convection to its heat capacity. St can also be expressed as a function of Nu, Pr and Re so that:

$$Ad = \frac{1}{4}\frac{D}{L}St^{-1} = \frac{1}{4}\frac{D}{L}\frac{PrRe}{Nu} \tag{5.82}$$

Evaluation of the Ad number for the tested orifices

As pointed out by Equation (5.82), the derivation of Ad is consistent with the findings reported along this section for the control volume orifices of both the CRI 2.20 and the Denso G4S injectors: heat transfer to the surroundings is enhanced by low values of Re and low diameters for a given channel length.

It is now interesting to evaluate Ad for each of the tested conditions for all of the orifices in order to assess its usefulness. Since the thermocouples of the experimental setup described in Section 4.3.1 are located in the high pressure lines at a certain distance (16 cm) upstream and downstream of the orifices (recall Figure 4.7), and the diameter of these lines (5 mm) differs from the orifices diameter, Ad has been evaluated taking into account three different sections (also labelled in Figure 4.7):

- Section A: from the thermocouple upstream of the orifice to the entrance of the orifice test rig.
- Section B: from the entrance of the orifice test rig to its outlet.
- Section C: from the orifices test rig outlet to the location of the thermocouple downstream of the orifice.

Attending to the two ΔT involved in the generic definition of Ad (Equation (5.80)), its corresponding value among Sections A and C can be established from the following expression:

$$\frac{1}{Ad} = \frac{T_{dw} - T_{up}}{T_w - T_f} = \frac{\Delta T_C + \Delta T_B + \Delta T_A}{(T_w - T_f)} = \frac{1}{Ad_A} + \frac{1}{Ad_B} + \frac{1}{Ad_C} \tag{5.83}$$

Therefore, it may be stated that:

$$Ad = \frac{1}{\sum_{i=1}^{n} \frac{1}{Ad_i}} = \frac{1}{\sum_{i=1}^{n} \left(4\frac{L_i}{D_i}\frac{Nu_i}{Pr_i Re_i}\right)} \tag{5.84}$$

where n is the number of sections in which the distance among thermocouples is discretized. For each value of Δp tested in the experimental charac-

terization of the orifices, Re_i may be evaluated from the continuous mass flow measurements. Pr_i, in turn, can be easily calculated from the fuel properties:

$$Pr_i = \frac{\eta_{f,i} c_{p,i}}{k_{f,i}} \tag{5.85}$$

where k_f is the fuel thermal conductivity, which for the present investigation has been taken from a generic diesel fuel as reported in [15], considering its low variation from one fuel to another. With regard to the Nusselt number, empirical correlations that relate it to Re and Pr are readily available in the literature. In the present thesis, the correlation introduced by Sieder and Tate [21] has been used for laminar flow:

$$Nu = 1.86 \left(\frac{D}{L} RePr \right)^{\frac{1}{3}} \left(\frac{\eta_b}{\eta_w} \right)^{0.14} \tag{5.86}$$

where the last term, relating the fluid bulk viscosity (η_b) to the fluid viscosity at the wall (η_w), has been neglected. This assumption has been introduced, on the one hand, considering that the experimental measurements for the hydraulic characterization of the injector control volume orifices were performed at room temperature (293 K) and pressures up to 60 MPa. For values of pressure up to 60 MPa, variations in temperature lead to viscosity changes (recall Figure 4.34) that are not deemed to importantly affect the last term of Equation (5.86). On the other hand, given that the experimental measurements are taken by setting continuous flow, the fuel temperature and the wall temperature will not importantly differ. The significance of this last statement on the assumption of adiabatic flow and its suitability for studying injector internal flow will be discussed later.

In the case of turbulent flow, the correlation defined by Nusselt [22], valid for short tubes ($10 < L/D < 400$), has been used:

$$Nu = 0.036 Re^{0.8} Pr^{\frac{1}{3}} \left(\frac{D}{L} \right)^{\frac{1}{18}} \tag{5.87}$$

Equations (5.85) to (5.87) highlight the relevance of the fuel properties in the evaluation of Ad through Re, Pr and Nu. Given the changes in fuel pressure and temperature through sections A to C in the experiments, the fuel properties involved (ρ, η, c_p and k) were evaluated accordingly, as stated in Table 5.5. The criteria for the evaluation of Nu are also shown in the table.

Before showing how the deviations among fuel temperature changes predicted by a theoretical isenthalpic expansion and the experimental results

Section	Fuel properties	*Nu* correlation
A	Evaluated for p_{up} and T_{up}	Laminar flow (low velocity)
B	Evaluated for the average of p and T upstream and downstream of the orifice	Laminar flow if $Re < Re_{crit}$ Turbulent flow if $Re > Re_{crit}$
C	Evaluated for p_{dw} and T_{dw}	Laminar flow (low velocity)

Table 5.5: Criteria for the evaluation of the fuel properties and Nu at the different sections of the hydraulic characterization experimental setup.

scale with the Ad number, it is interesting to analyse the significance of cavitation. Figure 5.29 shows the evolution of $\varepsilon_{\Delta T}$ against Ad for all the tested points corresponding to the Bosch CRI 2.20 outlet orifice (Figure 5.29(a)) and the Denso G4S control valve orifice (Figure 5.29(b)). A distinction has been made among the operating points leading to cavitation conditions and those corresponding to non-cavitating conditions.

Focusing on the behaviour for non-cavitating conditions, a decreasing trend of the deviation with the Ad number is clearly observed for both cases. This fact agrees with the purpose of the Ad number definition and is expected since the lowest values of Ad correspond to low values of Re (Equation (5.82)), for which the flow along the orifice is laminar (recall Figure 4.12 from Section 4.3.1). In the experiments, these points are found for the lowest Δp

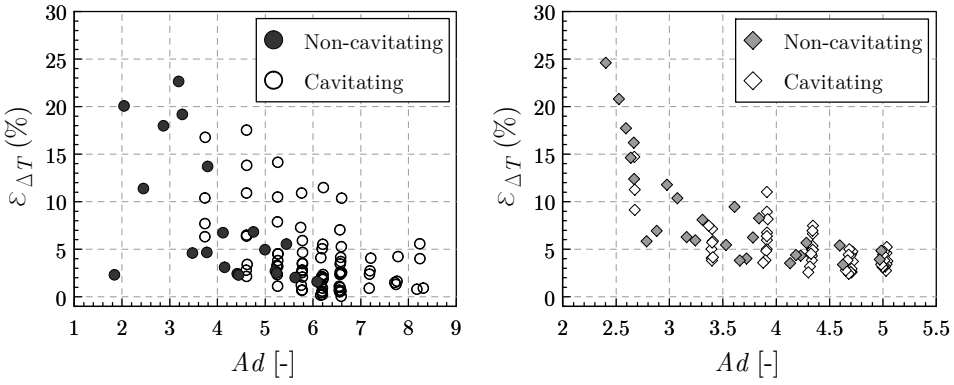

(a) Bosch CRI 2.20 outlet orifice

(b) Denso G4S control valve orifice

Figure 5.29: $\varepsilon_{\Delta T}$ against the Ad number for the Bosch CRI 2.20 outlet orifice and the Denso G4S control valve orifice. Points corresponding to both cavitating and non-cavitating conditions are represented.

values tested. In these conditions, the flow velocity is reduced, increasing the fuel residence time and allowing heat exchange with the surroundings. On the other hand, Ad increases for higher values of Δp, for which the flow gets turbulent and its velocity is increased, reducing the available time to transfer heat to the surroundings. With all, it can be seen that the operating conditions leading to Ad values higher than 4 lead in both cases to relatively low deviations compared to the theoretical ΔT corresponding to an isenthalpic expansion. Indeed, these deviations are bounded within a 10 % margin, making it possible to state that the flow nearly behaves as if it were adiabatic. In addition, $\varepsilon_{\Delta T}$ is generally lower for the Bosch CRI 2.20 outlet orifice than for the Denso control valve orifice. This is consistent with the Ad definition since the former generally leads to higher values of Ad than the latter due to its higher diameter.

Having a look at the cavitating conditions in Figure 5.29, the observed values of $\varepsilon_{\Delta T}$ are more scattered than those reported for non-cavitating conditions, and no general trend can be established. There seem to be groups of operating conditions that lead to the same value of Ad but register different levels of deviation (for instance, for $Ad \approx 5.2$ in the case of the Bosch orifice, there are operating conditions for which the deviation ranges among 2 and 15 %). Each of these groups correspond to a given value of upstream pressure and it has been checked that, for a given group, the deviation grows larger the higher the cavitation intensity (i.e., the lower the downstream pressure). Therefore, the flow behaviour importantly departs from being isenthalpic.

The higher deviations observed when the orifices work under cavitating conditions should not be attributed to the local cooling associated to the enthalpy of phase change, since several authors have shown its relatively low importance (in the order of tenths of a degree) [23]. However, they might be explained considering that the heat transfer parameters associated to the vapour bubbles (specifically the convective heat transfer coefficient h_c) importantly differ from those of the liquid phase [24]. Indeed, Bergman *et al.* [24] report an increase in h_c with the appearing vapour bubbles that would lead to lower effective Ad values, supporting the higher deviations found for cavitating conditions. Nevertheless, they also report a reduction in h_c if the vapour fraction increases modifying the cavitation regime so that the bubbles start to rearrange in films or sheets, which obstruct heat transfer among liquid and vapour. In any case, these considerations have not been taken into account in the evaluation of Ad given the difficulty to quantify the variations in h_c beforehand.

At this point, it is interesting to check the behaviour of all the orifices

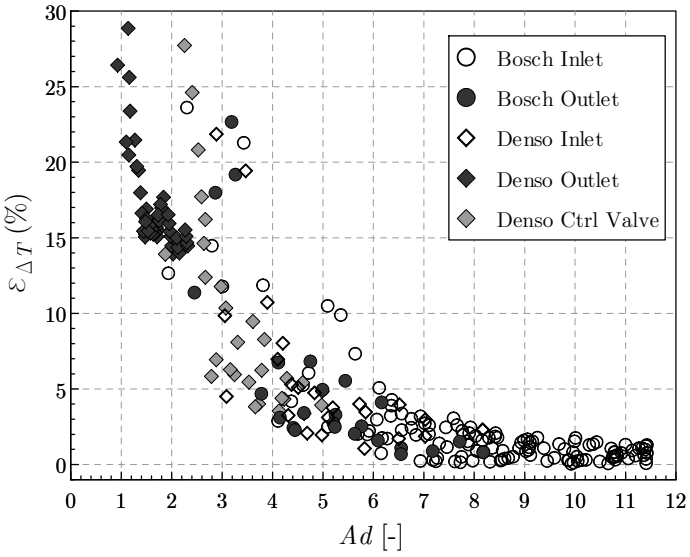

Figure 5.30: $\varepsilon_{\Delta T}$ against the Ad number for the all the tested orifices. Only the points corresponding to non-cavitating conditions are represented.

jointly. Figure 5.30 shows $\varepsilon_{\Delta T}$ plotted against Ad for all the orifices tested. Given the remarks on cavitating conditions, only the points corresponding to non-cavitating conditions are represented in the figure. The same decreasing trend that was reported for a given orifice is noticed. Given the Ad number definition, the orifices are effectively sorted by their outlet diameters (recall Table 4.2): the Denso G4S injector outlet orifice leads to the lowest values of Ad, followed by the Denso G4S control valve, Bosch CRI 2.20 outlet, Denso G4S inlet and Bosch inlet orifices, in this order. This scaling with the diameter was expected as explained earlier in the view of Figures 5.26 and 5.27. Thus, orifices that lead to low values of Ad, even for the higher Δp values tested, present high deviations with respect to the theoretical isenthalpic expansion. Hence, the deviations found for the Denso G4S outlet orifice are higher than 13 % even for its higher values of Ad. On the contrary, since the conditions tested for the Bosch CRI 2.20 inlet orifice never lead to low values of Ad, their deviations are bounded. In addition, the points of Figure 5.30 corresponding to different orifices tend to collapse for a given value of Ad, which highlights the usefulness of this number.

As it was found for a given orifice, it is possible to state in a more general way that the flow through orifices leading to high average values of Ad behaves in a nearly adiabatic manner (for instance, Ad values higher than 4 keep

the deviations bounded within a 10 % margin). Considering the Ad values induced by the Bosch CRI 2.20 control volume orifices, only the least favourable conditions (low pressure drops, not representative of the usual operation of the injector) lead to a high departure from the isenthalpic predictions. Therefore, it seems that the adiabatic assumption for the flow could be accurate enough for engineering purposes when dealing with the internal flow through the Bosch CRI 2.20 injector.

Critical analysis about the extension of the validity of the assumption of adiabatic flow along a diesel injector

It is important to state that the results here presented in terms of Ad have been obtained for specific conditions. As stated in Section 4.3.1, during the experimental measurements corresponding to the hydraulic characterization of the control volume orifices, both the fuel inlet temperature and the ambient temperature were controlled. In addition, the measurements were carried out by imposing continuous flow. Therefore, the fluid bulk temperature and the wall temperature were somewhat forced to remain close to each other, preventing heat transfer to the surroundings from occurring. In fact, these measurements for individual orifices were conceived to replicate the ones corresponding to the rate of injection of the whole injector (Section 4.3.2), which were also performed with a refrigerated injector holder trying to keep a controlled fuel temperature both at the inlet and at the injector walls. These ROI measurements were used as a basis to implement the computational model with the adiabatic assumption.

Anwyay, despite the fact that the fuel and the wall temperatures were kept close to each other in all the measurements described, it has been proved that certain combinations of orifice geometry (namely low diameter-to-length ratio) and working conditions (low pressure drops) may lead to the fluid not being able to retain the heat within itself when an expansion through a restriction generates a temperature rise. Instead, a significant amount of heat may be transferred to the surroundings through the line downstream of the restriction. It must also be noted that the total heat effectively transferred also depends on the length of this line (which indeed has been taken into account in the calculation of Ad). In the experiments, the length of this line was taken as 16 cm not only to ensure that the kinetic energy was preserved with respect to the one upstream of the restriction in order to assimilate the experimental findings to a theoretical isenthalpic evolution, but also to match the length of the Bosch CRI 2.20 line that feeds the nozzle, since it is characteristic of the length available by the injector to interact with the surroundings.

With the above considerations, the high values of Ad induced by the orifices of the injector of study (Bosch CRI 2.20) for most of its real operating conditions highlight that, under laboratory conditions in which the fuel temperature is controlled and the injector holder is refrigerated, the only temperature changes that can be expected from the injector inlet to the nozzle outlet are the ones corresponding to the internal evolution of the fluid (i.e. compressions, expansions, etc.).

Specifically, on the one hand, this finding validates the assumption of adiabatic flow implemented in the computational model used to conduct the study about the thermal effects on the injector internal behaviour in the present thesis. More generally, on the other hand, this fact may be of interest for experimentalists carrying out fundamental investigations about the injection process conducted in research facilities, such as rate of injection, spray momentum or spray visualization (including spray penetration or spreading angle, among others).

The next question that arises when dealing with this topic is the applicability of the aforementioned findings about the validity of the adiabatic assumption to real engine-like conditions. The limits of the extension of these findings are therefore assessed in the next subsection.

Remarks on the applicability of the assumption of adiabatic flow for engine-like operating conditions

The validity of the assumption of adiabatic flow for the controlled conditions of study reported in this thesis has been analysed. This includes the imposition of a similar temperature among the fluid and the wall that prevents heat transfer from importantly being transferred to the surroundings. In real engine-like operating conditions, however, an important temperature difference may be established among the fuel (stored in a tank far from the injector) and the injector walls (located close to the engine head, significantly warm during the engine operation).

Injection in real engine conditions, with fuel being injected into the cylinder in a pulsed manner and remaining at rest during the lapse among injections, is a highly transient phenomenon. This transiency, together with the amount of varied operating conditions that may be achieved during an engine run, obstructs the analysis of the problem. The approach taken in this section to determine whether heat transfer is relevant and, if so, quantify to what extent, is to compare the fuel residence time in the injector (t_{res}) to the characteristic time of heat transfer due to conduction from the injector walls to the fuel

(τ_k). Hence, a dimensionless parameter t_{Ad} may be directly defined as the ratio among times:

$$t_{Ad} = \frac{t_{res}}{\tau_k} \tag{5.88}$$

So that:

- If $t_{Ad} \ll 1$, the fuel residence time in the injector is way lower than the characteristic time of heat transfer and the fuel does not significantly modify its temperature during the time lapse among injections. Once an injection starts, the fuel will increase its temperature due to its internal evolution (i.e. expansions) or will cede heat to the ambient depending on the related Ad value, as analysed earlier. Anyway, low Ad values are not expected since low fuel residence times imply either high injection frequencies (limited to 4000 rpm in diesel engines) or large pressure gradients that would lead to high Ad numbers by definition. Therefore, the assumption of adiabatic flow does not seem to be compromised at any stage for low values of t_{Ad}.
- If $t_{Ad} \approx 1$, the fuel residence times are similar to the characteristic time of heat transfer and the fuel importantly changes its temperature during the lapse among injections. Hence, the temperature of the fuel inside the injector has enough time to get closer to the injector wall temperature prior to each injection event, thus departing from the fuel temperature right at the injector inlet. However, at the same time, this means that the temperature difference among the wall and the fluid is minimised by the time an injection starts. For this reason, again, the ability of the fuel to increase its temperature upon its internal expansions (constituting an adiabatic process) or to transfer this heat to the ambient will depend on the related values of the Ad number.
- If $t_{Ad} \gg 1$, the fuel residence times are way higher than the characteristic time of heat transfer and the fuel temperature by the time of a new injection already coincides with the injector wall temperature. This situation can only be generated by really low injection frequencies (not usual in diesel engines) or small pressure gradients that would imply low Ad numbers. As seen in the previous results about Ad, low values may lead to the fuel not being able to retain the temperature rises produced by its internal evolution through hydraulic restrictions even though the temperature difference among the wall and the fluid upstream of the restriction is negligible. In this case, the assumption of adiabatic flow during the injection would be no longer valid.

As a reference for the fuel residence time, t_{res}, the time needed for the injector to fully evacuate a fuel volume equivalent to the one of its internal lines has been considered. In the case of the Bosch CRI 2.20 injector, the dimensional characterization allowed to estimate this volume as $6\,cm^3$. Three extreme characteristic operating points of a typical passenger engine have been used to evaluate t_{res}, as shown in Table 5.6. The mass injected per stroke (m_i) is also shown, together with the number of injections needed to evacuate the injector internal volume. The times shown in the table were evaluated taking into account that, in a four-stroke diesel engine, the injection frequency is half of the engine speed, n_e. Additionally, three conditions corresponding to the ROI measurements of this thesis at room temperature ($T_i = 303\,K$), in which the injection frequency was set to 10 Hz (Section 4.3.2), are shown in the table for comparison purposes.

Engine-like conditions				
Condition	n_e [rpm]	m_i [mg/st]	**No. injections** [-]	t_{res} [s]
Low speed and load	1500	17	300	24.0
Maximum torque	2500	50	102	4.9
Maximum power	3750	40	128	4.1
ROI measurements conditions				
Condition	p [MPa]	**ET** [ms]	m_i [mg/st]	**No. injections** [-]	t_{res} [s]
Low p	40	0.5	5.25	972	97.2
Medium p	120	1.0	44.33	115	11.5
High p	180	2.0	116.14	44	4.4

Table 5.6: Sample of the time needed for the injector to evacuate a fuel volume equivalent to its own internal volume for different engine and laboratory characteristic conditions.

On the other hand, the characteristic time of heat transfer due to conduction from the injector walls (τ_k) has been estimated considering the simplified problem of transient radial conduction in an infinitely long solid cylinder as the one shown in Figure 5.31. The fluid temperature at the center of the cylinder initially takes a given value T_i, whereas the wall remains at its own temperature T_w. The fluid is considered to be at rest so that convection is negligible. The assumption of infinite length ensures one-dimensional conduction in the radial direction. Once the fluid temperature is let to evolve freely, it will modify its value $T(r)$ along the cylinder radial coordinate r, tending to approach the wall temperature. The hypotheses taken conform the scenario

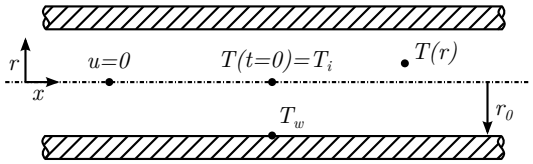

Figure 5.31: Scheme of an infinitely long cylinder containing fuel at rest.

on which heat transfer takes place in an easier way, thus leading to the minimum possible characteristic times for heat transfer, τ_k. Therefore, this results in a conservative estimation of t_{Ad}.

The aforementioned situation can be assimilated to the one present in the nozzle feeding duct of a diesel injector in the lapse among injections. Before an injection event, the fuel (which entered the injector at a certain temperature) remains at rest and is able to transfer heat to the injector walls (submitted to a different temperature) or receive it from them, depending on the sign of the temperature difference. For any radial position, this temperature difference may be defined as:

$$\theta\left(r\right) = T\left(r\right) - T_w \tag{5.89}$$

The solution of the problem of the transient radial conduction in an infinitely long solid cylinder is treated in Appendix 5.A. The general solution for $\theta(r,t)$ is given by:

$$\theta\left(r,t\right) = \sum_{n=1}^{\infty} \theta_n\left(r,t\right) = \sum_{n=1}^{\infty} \theta_i J_0\left(\lambda_n r\right) e^{-\lambda_n^2 \alpha_k t} \tag{5.90}$$

where θ_i is the initial temperature difference among the fluid and the wall ($\theta_i = T_i - T_w$), $J_0(z)$ is the Bessel function of first kind of order zero, λ_n are the eigenvalues of the problem and α_k is the fuel thermal diffusivity.

From Equation (5.90), it follows that the fluid temperature at the cylinder axis will exponentially tend to the wall temperature. As demonstrated in the appendix, a relaxation time $\tau_{k,1/j}$ may be defined as the time at which the temperature difference among the fluid at the cylinder axis and the wall, $\theta(0, \tau_{k,1/j})$ is reduced to $1/j$ of the initial difference ($\theta/\theta_i = 1/j$):

$$\tau_{k,1/j} = -\ln\left(\frac{1}{j}\right) \lambda_{inj} \tag{5.91}$$

where λ_{inj} is a constant of the problem defined by:

$$\lambda_{inj} = \frac{r_0^2}{2.4048^2 \alpha_k} \tag{5.92}$$

which corresponds to the relaxation time $\tau_{k,1/e}$ at which the temperature difference among the wall and the fluid at the cylinder axis has been reduced to a difference of $1/e$ times the initial one ($\approx 36.78\%$). As estimated in Appendix 5.A, this relaxation time may be approximated as 7.344 s for the Bosch CRI 2.20 injector.

Hence, t_{Ad} may be evaluated for the conditions depicted in Table 5.6 according to Equation (5.88), as summarized in Table 5.7 for 2 characteristic values of j for which $\tau_{k,1/j}$ has been determined: e and 20. For these values of j, the temperature difference among the wall and the fluid at the center of the nozzle feeding line have been reduced to a difference of 36.78% and 5%, respectively.

Engine-like conditions					
Condition	$\boldsymbol{t_{res}}$ [s]	$\boldsymbol{\tau_{k,1/e}}$ [s]	$\boldsymbol{t_{Ad}}$ [-]	$\boldsymbol{\tau_{k,1/20}}$ [s]	$\boldsymbol{t_{Ad}}$ [-]
Low speed and load	24.0		3.27		1.09
Maximum torque	4.9	7.34	0.67	22.0	0.22
Maximum power	4.1		0.56		0.19
ROI measurements conditions					
Condition	$\boldsymbol{t_{res}}$ [s]	$\boldsymbol{\tau_{k,1/e}}$ [s]	$\boldsymbol{t_{Ad}}$ [-]	$\boldsymbol{\tau_{k,1/20}}$ [s]	$\boldsymbol{t_{Ad}}$ [-]
Low p	97.2		13.24		4.42
Medium p	11.6	7.34	1.58	22.0	0.53
High p	4.4		0.60		0.20

Table 5.7: Evaluation of t_{Ad} for different engine and laboratory characteristic conditions.

As it can be seen, t_{Ad} is higher than 1 for the engine low speed and low load case. If $j = 20$ is taken as a reference, t_{Ad} is close to 1. Therefore, the fuel residence time within the injector is of the same order of the characteristic time of heat transfer from the surroundings by conduction. As stated earlier this implies that, in this condition, the temperature of the fuel inside the injector has enough time to get closer to the injector wall temperature prior to each injection event, departing from the fuel temperature right at the injector inlet. However, during a given injection, since the wall temperature and the

fluid temperature are close to each other, the considerations previously given about the adiabatic assumption with the *Ad* number are valid: if the *Ad* number (established by both the geometry of the injector restrictions and the induced operating conditions) is high, the low temperature difference among fluid and wall will prevent the fluid from further changing its temperature due to heat exchange, and only its own internal evolution will be able to modify its temperature. Hence, the assumption of adiabatic flow will still hold with the particularity that a certain temperature gap should be initially considered. On the contrary, if the established *Ad* number is low, the assumption of adiabatic flow during the injection event will not hold either despite the low temperature difference among fluid and wall.

For the rest of engine-like conditions depicted in Table 5.7, the associated t_{Ad} is lower than 1, but always within the same order of magnitude ($0.1 < t_{Ad} < 1$). This implies that the fuel residence times within the injector are lower than the characteristic time of heat transfer. Consequently, the time among injections is not enough for the fuel to completely acquire the temperature of the injector walls. Nevertheless, the fact that t_{Ad} remains in the order of 10^{-1} indicates that heat transfer is still relevant to an extent and a certain temperature change is expected before an injection event. During the injection event itself, the relative importance of heat transfer with respect to the temperature changes due to the fluid internal evolution will depend on the *Ad* number and the effective temperature difference set among the fluid and the wall.

Focusing on the ROI measurements conditions, similar conclusions can be extracted in the view of the results. During any experiments with diesel injectors, heat transfer may be relevant if the fuel temperature and the injector wall temperature importantly differ. However, most of the heat exchange is expected to take place in the lapse among injections, and may be accounted for in any calculations by introducing some corrections to the fuel initial temperature. In any case, the assumption of adiabatic flow is not compromised as long as two conditions are met. On the one hand, if the experiments are carried out in a controlled environment (typical of research facilities) in which both the fuel temperature at the injector inlet and the injector holder temperature are forced to closely match each other (as it was done for the measurements of the present thesis). On the other hand, if the *Ad* number imposed by both the geometry of the injector orifices and the operating conditions is high. Under these conditions, the fuel temperature changes along the injector may be exclusively attributed to its internal evolution across its most important hydraulic restrictions.

It should be noted that the purpose of this analysis is merely to provide crude numbers about the relative importance of heat transfer during the injection phenomenon. Therefore, the approach here taken has its inherent limitations. In reality, important temperature gradients along the injector walls may be present given the extremely high temperatures at which the nozzle tip is submitted, as opposed to the rest of the injector body. In addition, these temperature gradients may differ depending on the duration of the engine run. On the other hand, the constant λ_{inj} depends on the fuel properties and especially on the diameter of the ducts carrying the fuel to the nozzle. Hence, variations of this parameter are also present in reality due to the different diameters of each of the injector internal lines. In any case, this fact is not expected to condition the order of magnitude of the results here presented and the reasoning behind them.

5.4.3 Complete injector validation

Once the computational model has been partially validated by ensuring its ability to predict the individual behaviour of the injector internal orifices and assessing the limitations of the assumption of adiabatic flow, the accuracy of the predictions of the complete injector model should be tested for a wide range of operating conditions.

To this end, the ROI curves simulated by the computational model were compared to the ones experimentally obtained through the methodology explained in Section 4.3.2, which included a wide set of values of injection pressure, fuel temperature at the injector inlet and energizing time (recall Table 4.5).

Furthermore, the modelled evolution of the pressure at the injector inlet was also compared to the experimental measurements. This comparison allows to assess the capability of the model to describe the propagation of the pressure wave along the injector. A satisfactory comparison in this regard would ensure the proper prediction of the injector behaviour under multiple injection strategies.

A successful validation in the previous terms would also assure a precise matching of the total mass injected in the cylinder per each injection event. The proper prediction of this quantity is especially appreciated by both combustion modellers and engine manufacturers and operators. Hence, comparisons regarding this parameter are also shown in the present section, giving an additional indicator of the model accuracy.

Prediction of the ROI signal

Figure 5.31 shows the comparison among the mass flow rate curves simulated by the model and the ones obtained experimentally[1] according to the explanation given in Section 4.3.2. Each graph depicts results corresponding to the different injection pressures tested (40, 70, 120 and 180 MPa) for a given fuel temperature at the injector inlet. Three curves, corresponding to different energizing times (0.25, 0.5 and 1 ms), are depicted for each of the injection pressures and temperatures. Injections corresponding to an ET of 2 ms, which were taken to extract the steady mass flow rate along the injector, were removed from the validation given their scarce interest in real engine applications.

It can be seen that the model properly reproduces the injector behaviour for most of the tested conditions. The average steady mass flow rate follows the observed trends with injection pressure and temperature, although the instantaneous values are generally underpredicted for a first part of the injection and slightly overpredicted for the second part, corresponding to the oscillation produced by the injector closing.

Concerning the injection delay, deviations do not seem to be large, although a slightly early opening is observed for low fuel temperatures at the injector inlet, whereas it opens later than the experiments for the highest ones.

With regard to the injection duration, the trends are preserved in general. An underprediction of the duration is noticed for the shortest injections (ET = 0.25 ms), being more accused the higher the fuel temperature at the injector inlet. The opposite trend is revealed for the longest injections (ET = 1 ms), for which the injection duration tends to be more overestimated the higher the injection temperature.

The analysis of the opening slope reveals a good reproduction of reality by the model, which appropriately follows the observed trend with the injection temperature. The worst results are obtained for the lowest injection temperatures simulated, for which the model assumes a slower opening slope. This inaccuracy, in turn, results in a late reaching of the steady value of fuel mass flow rate.

Finally, the closing slope is also modelled in a proper manner, although the model predicts faster closings for the lowest injection pressures, especially at low temperatures.

[1]The complete analysis of the experimental results, including the influence of the fuel temperature on the injector rate of injection, will be shown in Chapter 6.

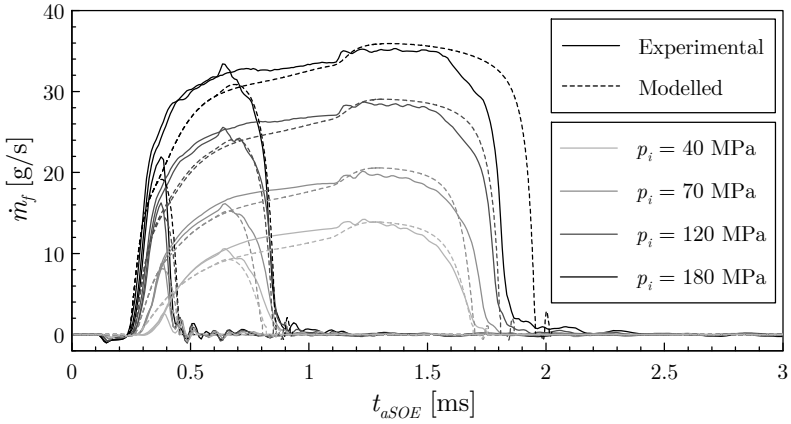

(a) $T_i = 253\,\mathrm{K}$

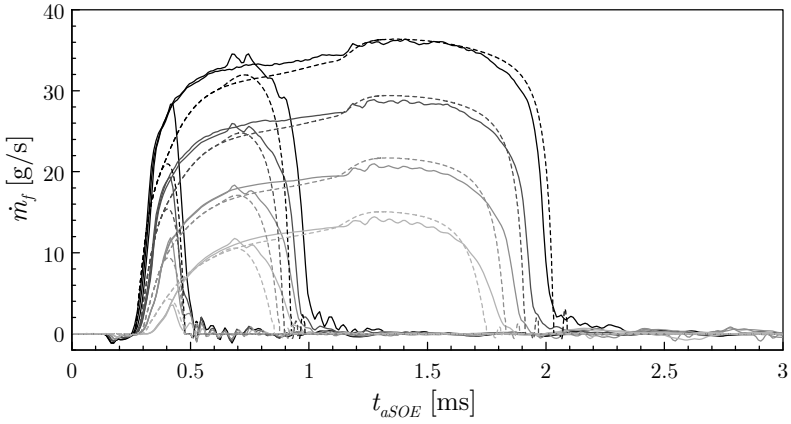

(b) $T_i = 273\,\mathrm{K}$

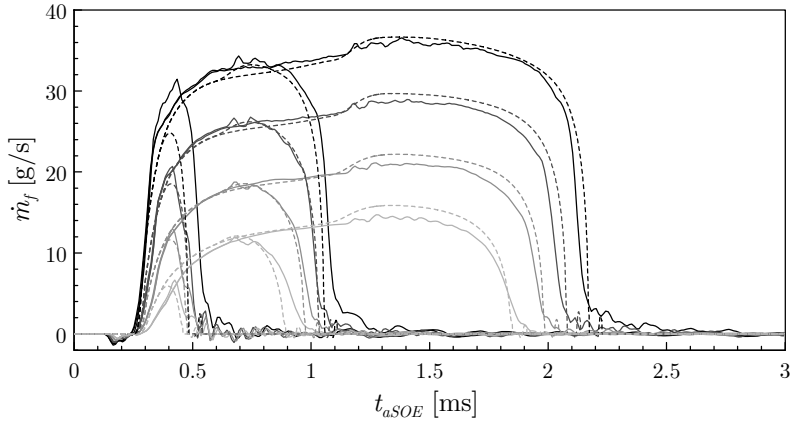

(c) $T_i = 303\,\mathrm{K}$

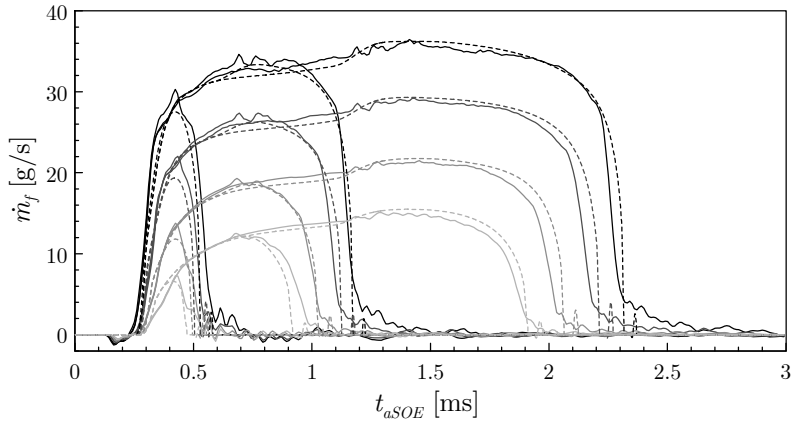

(d) $T_i = 353\,\mathrm{K}$

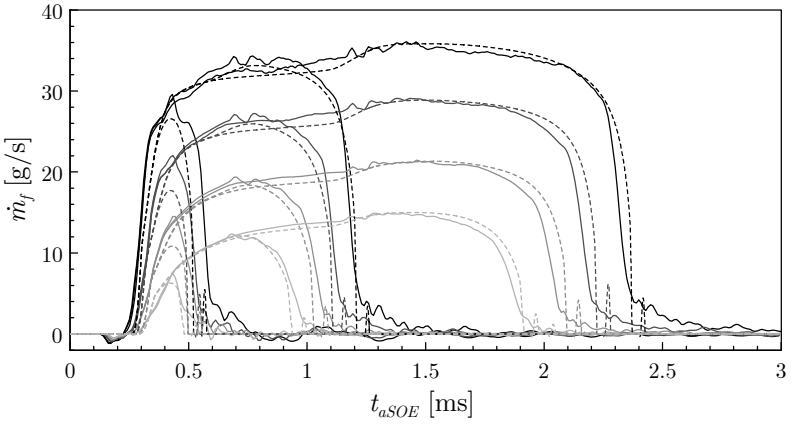

(e) $T_i = 373\,\mathrm{K}$

Figure 5.31: Comparison among modelled and experimental ROI curves.

Prediction of the pressure wave propagation

The propagation of the pressure wave generated by an injection event is of key importance when implementing multiple-injection strategies. Once an injection finishes, the induced pressure wave will affect the next injection event depending on the timing among injections.

Sample comparisons among the modelled and the experimental pressure evolution at the high-pressure line connecting the *common-rail* to the injector are shown in Figure 5.32. In order to assess the validity of the injector model for the widest possible range of operating conditions, points corresponding to

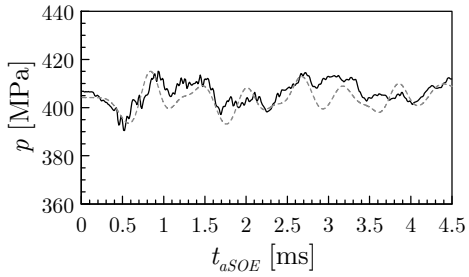

(a) $p_i = 40\,\text{MPa}$, $T_i = 373\,\text{K}$, ET $= 0.25\,\text{ms}$

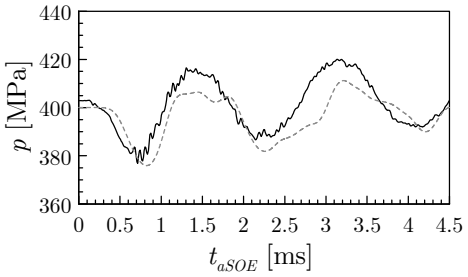

(b) $p_i = 40\,\text{MPa}$, $T_i = 373\,\text{K}$, ET $= 0.5\,\text{ms}$

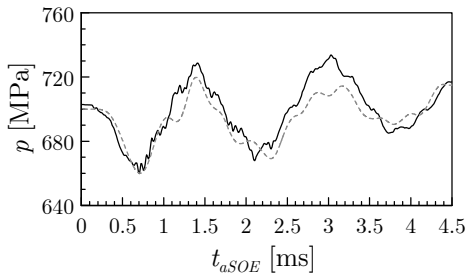

(c) $p_i = 70\,\text{MPa}$, $T_i = 353\,\text{K}$, ET $= 0.5\,\text{ms}$

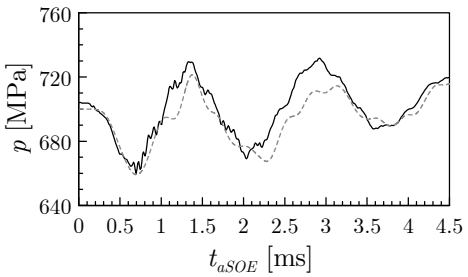

(d) $p_i = 70\,\text{MPa}$, $T_i = 303\,\text{K}$, ET $= 0.5\,\text{ms}$

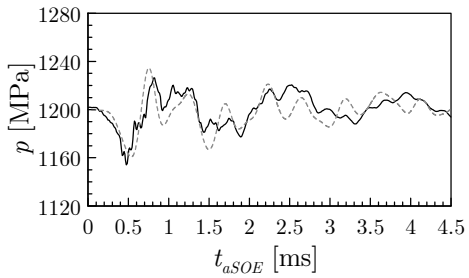

(e) $p_i = 120\,\text{MPa}$, $T_i = 303\,\text{K}$, ET $= 0.25\,\text{ms}$

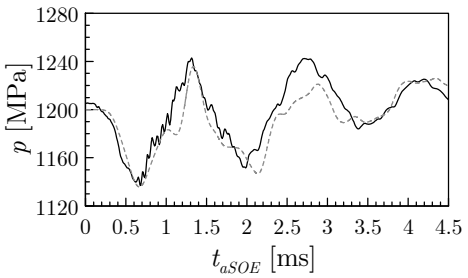

(f) $p_i = 120\,\text{MPa}$, $T_i = 303\,\text{K}$, ET $= 0.5\,\text{ms}$

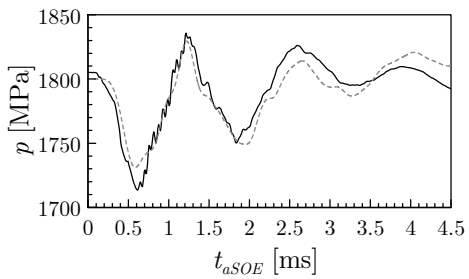

(g) $p_i = 180\,\text{MPa}$, $T_i = 253\,\text{K}$, ET $= 0.5\,\text{ms}$

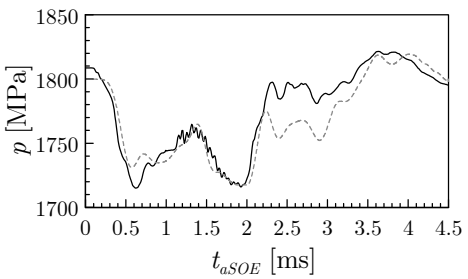

(h) $p_i = 180\,\text{MPa}$, $T_i = 253\,\text{K}$, ET $= 1\,\text{ms}$

Figure 5.32: Comparison among modelled (continuous) and experimental (dashed) pressure signal at the common-rail high-pressure line.

the extreme values of speed of sound in the ROI measurements (low pressures and high temperatures on the one hand, high pressures and low temperatures on the other) are depicted. Different energizing times are also shown.

As it can be seen, the model accurately represents the pressure evolution for most of the tested points. The first drop in pressure, which coincides with the injector opening, always takes place slightly later for the injection model. As highlighted by the points corresponding to ET = 0.5 ms, both the period and the amplitude of the oscillations are nicely predicted. The amplitude of the second pressure peak is slightly underestimated, although the differences seem to be reduced for the next peak.

Results for the extreme energizing times are less accurate especially in terms of amplitude, although the period of the oscillations seems to be properly modelled. The proper matching of this last parameter is essential, since it defines the trends followed by the mass injected by the post-injections depending on the dwell time among injections.

Prediction of the total mass injected per injection event

The ability of the model to predict the total mass injected by a single injection event (m_i) depends on the proper matching of the ROI signal and the pressure wave propagation, previously analysed. The reliability of the model was also quantitatively assessed in terms of this parameter. Figure 5.32 shows the comparison among the model and the experimental values.

As a consequence of the findings from Figures 5.31 and 5.32, results show a fair prediction for the majority of points studied. More than 90% of the points leading to masses higher than 10 mg per stroke are within a deviation margin lower than 10%. The points for which the highest deviations are produced generally correspond to the extreme cases of injection pressure and temperature tested.

Figure 5.32(b) show a detail of the injections corresponding to lower injected masses. In these cases, deviations in percentual terms are higher. This is expected considering that, for these small mass quantities, short deviations in absolute terms lead to a high percentage of deviation even if the injection rate shape is properly predicted. Nevertheless, 70% of the tested points still remain bounded within a 25% deviation margin.

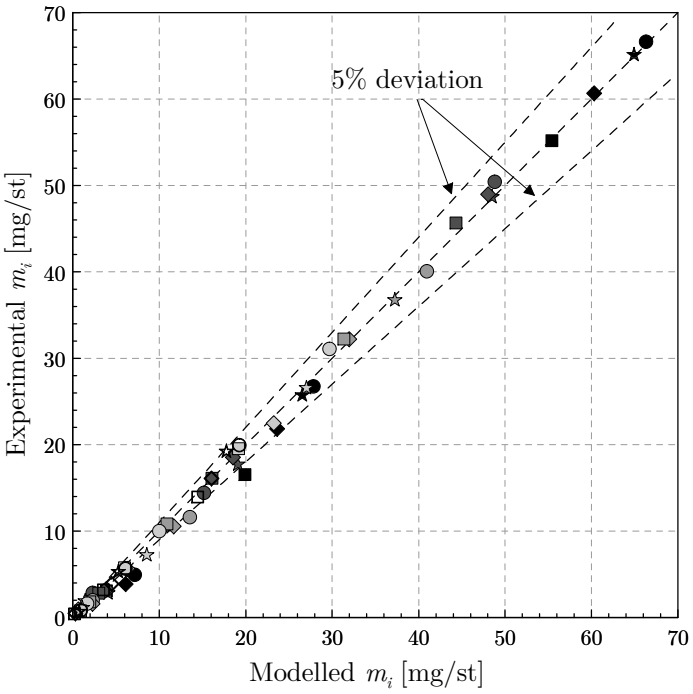

(a) All points tested

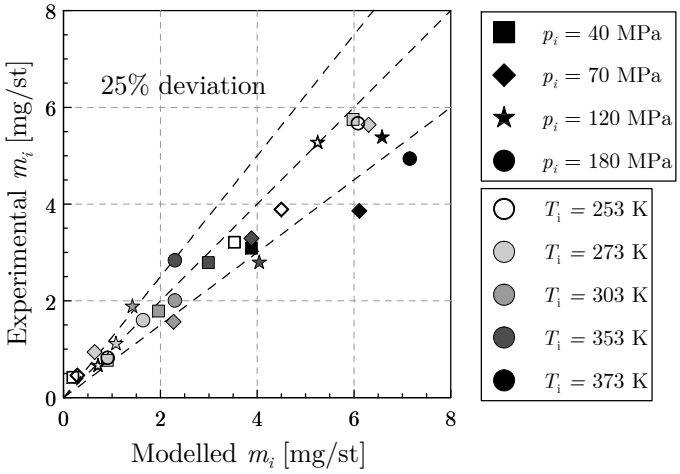

(b) Detail of the short injections

Figure 5.32: Comparison among modelled and experimental results for total mass injected per stroke.

5.A Appendix: Transient radial heating by conduction in an infinitely long cylinder

Considering a fluid at rest contained within the cylinder of infinite length depicted in Figure 5.31, heat transfer only takes place as conduction in the radial direction (one-dimensional). The equation describing the problem in cylindrical coordinates reads as follows:

$$\frac{1}{\alpha_k}\frac{\partial T}{\partial t} = \frac{1}{r}\frac{\partial}{\partial r}\left(r\frac{\partial T}{\partial r}\right) \tag{5.93}$$

where α_k is the fluid thermal diffusivity, defined as:

$$\alpha_k = \frac{k}{\rho c_p} \tag{5.94}$$

Subject to the following boundary conditions:

$$T = T_w \qquad \text{at } r = r_0 \tag{5.95}$$

$$\frac{\partial T}{\partial r} = 0 \qquad \text{at } r = 0 \tag{5.96}$$

and the initial condition:

$$T = T_i \qquad \text{for } t = 0 \tag{5.97}$$

The variable θ may be introduced as the temperature difference among the fluid at a location r from the cylinder axis and the wall:

$$\theta = T(r) - T_w \tag{5.98}$$

Equation (5.93) may then be rewritten as:

$$\frac{1}{\alpha_k}\frac{\partial \theta}{\partial t} = \frac{\partial^2 \theta}{\partial r^2} + \frac{1}{r}\frac{\partial \theta}{\partial r} \tag{5.99}$$

subject to:

$$\theta = 0 \qquad \text{at } r = r_0 \tag{5.100}$$

$$\frac{\partial \theta}{\partial r} = 0 \qquad \text{at } r = 0 \tag{5.101}$$

$$\theta = \theta_i \qquad \text{for } t = 0 \tag{5.102}$$

Equation (5.99) may be solved through separation of variables by defining the functions $\mathbb{R}$ and $\mathbb{T}$, which are only function of r and t, respectively. Hence:

$$\theta\left(r,t\right)=\mathbb{R}\left(r\right)\mathbb{T}\left(t\right) \tag{5.103}$$

which yields:

$$\frac{1}{\alpha_k\mathbb{T}}\frac{\mathrm{d}\mathbb{T}}{\mathrm{d}t}=\frac{1}{\mathbb{R}}\left(\frac{\mathrm{d}^2\mathbb{R}}{\mathrm{d}r^2}+\frac{1}{r}\frac{\mathrm{d}\mathbb{R}}{\mathrm{d}r}\right)=-\lambda^2 \tag{5.104}$$

where λ is a separation constant.

Equation (5.104) may then be separated into two equations for $\mathbb{R}$ and $\mathbb{T}$:

$$\frac{\mathrm{d}\mathbb{T}}{\mathrm{d}t}+\lambda^2\alpha_k\mathbb{T}=0 \tag{5.105}$$

$$\frac{\mathrm{d}^2\mathbb{R}}{\mathrm{d}r^2}+\frac{1}{r}\frac{\mathrm{d}\mathbb{R}}{\mathrm{d}r}+\lambda^2\mathbb{R}=0 \tag{5.106}$$

which, considering that $\mathbb{R}(r_0)=0$ and that R must be bounded at $r=0$, have the following general solutions:

$$\mathbb{T}=Ce^{-\lambda^2\alpha_k t} \tag{5.107}$$

$$\mathbb{R}=B'J_0\left(\lambda r\right) \tag{5.108}$$

where C and B' are constants to be determined through the boundary conditions and $J_0(z)$ is the Bessel function of first kind of order zero of the argument given by:

$$J_0\left(z\right)=1-\frac{z^2}{\left(1\,!\right)^2 2^2}+\frac{z^4}{\left(2\,!\right)^2 2^4}-\frac{z^6}{\left(3\,!\right)^2 2^6}+\cdots \tag{5.109}$$

The solution for θ may then be rewritten as:

$$\theta=Be^{-\lambda^2\alpha_k t}J_0\left(\lambda r\right) \tag{5.110}$$

where $B=B'C$ and λ are constants to be determined from the boundary and initial conditions. From the initial condition ($\theta=\theta_i$ at $t=0$ and, for instance, $r=0$) if follows that:

$$B=\theta_i \tag{5.111}$$

From the boundary condition defined by Equation (5.100), it results that:

$$\theta_i J_0 (\lambda r_0) = 0 \tag{5.112}$$

This requires that $J_0(\lambda r_0) = 0$, which defines the eigenvalues and eigenfunctions for this problem. The eigenvalues are thus given as the roots of:

$$J_0 (\lambda_n r_0) = 0 \tag{5.113}$$

The first roots of the problem are shown in Table 5.8

n	Root	Value
1	$\lambda_1 r_0$	2.4048
2	$\lambda_2 r_0$	5.5201
3	$\lambda_3 r_0$	8.6537
4	$\lambda_4 r_0$	11.7915
5	$\lambda_5 r_0$	14.9309

Table 5.8: First roots of the Bessel function of first kind of order zero appearing in Equation (5.113).

A particular solution of the problem is then:

$$\theta_n (r,t) = \mathbb{R}_n (r)\, \mathbb{T} (t) = \theta_i J_0 (\lambda_n r)\, e^{-\lambda_n^2 \alpha_k t} \tag{5.114}$$

Superposition of particular solutions yields the more general solution:

$$\theta (r,t) = \sum_{n=1}^{\infty} \theta_n (r,t) = \sum_{n=1}^{\infty} \mathbb{R}_n (r)\, \mathbb{T} (t) = \sum_{n=1}^{\infty} \theta_i J_0 (\lambda_n r)\, e^{-\lambda_n^2 \alpha_k t} \tag{5.115}$$

Determination of the relaxation time of the solution

From Equations (5.114) and (5.115), given the negative exponent of the solution of the problem, it is easy to see that the fluid temperature at the cylinder axis ($T(0,t)$) will exponentially tend to the wall temperature. It is then possible to determine a relaxation time τ_k for which the $T(0,\tau)$ has almost reached this asymptotic condition.

Having a look at Table 5.8, it follows that the first root ($\lambda_1 r_0 = 2.4048$) leads to the longer relaxation time and must be the one used in its determination. Focusing at the cylinder axis ($r = 0$) where $J_0 = 1$, the first particular solution from Equation (5.114) yields:

$$\frac{\theta\,(0,t)}{\theta_i} = e^{-\lambda_1 \alpha_k t} \tag{5.116}$$

From where the time may be isolated:

$$t = -\ln\left(\frac{\theta\,(0,t)}{\theta_i}\right)\frac{r_0^2}{2.4048^2\alpha_k} \tag{5.117}$$

At this point, the relaxation time $\tau_{k,1/j}$ may be defined as the time at which the temperature difference among the fluid at the cylinder axis and the wall, $\theta(0,\tau_{k,1/j})$ is reduced to $1/j$ of the initial difference ($\theta/\theta_i = 1/j$):

$$\tau_{k,1/j} = -\ln\left(\frac{1}{j}\right)\frac{r_0^2}{2.4048^2\alpha_k} \tag{5.118}$$

The last parameters in Equation (5.118) may be grouped in a constant of the problem which, given the application in the present thesis, has been labelled as λ_{inj}:

$$\tau_{k,1/j} = -\ln\left(\frac{1}{j}\right)\lambda_{inj} \tag{5.119}$$

It is important to note that, by definition, λ_{inj} corresponds to the relaxation time $\tau_{k,1/e}$, at which the temperature difference among wall and fluid at the cylinder axis has been reduced to a difference of $1/e$ times the initial one ($\approx 36.78\%$).

Estimation of a suitable value for λ_{inj}

In order to correctly estimate the order of magnitude of the characteristic times of heat transfer by radial conduction τ_k in an injector duct by means of Equation (5.119), it is necessary to compute a reasonable value of λ_{inj}.

On the one hand, a suitable value of r_0 must be introduced. Given its high volume and its influence on the nozzle internal flow, the duct feeding the injector nozzle may be taken as a reference. In the particular case of the Bosch CRI 2.20 injector, this duct contains the lines HL1, HL3, HL4 and HL5

defined in Figure 5.17. The line HL5 has an average hydraulic diameter among them. Its value, 3.84 mm, will be considered representative for the problem. Hence, $r_0 \approx 1.9\,\text{mm}$.

On the other hand, α_k must be computed for a diesel fuel according to Equation (5.94) at representative injection conditions of temperature and pressure. The density has been determined in the present thesis for the winter diesel fuel used in the experiments, as shown in Section 4.4.2. Values of c_p were accepted from reported data for the ISO4113 fuel [20] (Sections 4.4.2 and 5.3.4), whereas k_f was extracted from the literature for a standard diesel fuel [15] (Section 5.4.2).

Figure 5.33 shows the variation of α_k with the temperature and pressure for a diesel fuel calculated with the previous remarks. As it can be observed, this property does not significantly vary for the depicted conditions, remaining in the same order of magnitude. Hence, a value of $\alpha_k = 8.5 \times 10^{-8}\,\text{m}^2/\text{s}$ will be taken as representative for all conditions without introducing important changes in the estimated value of λ_{inj}.

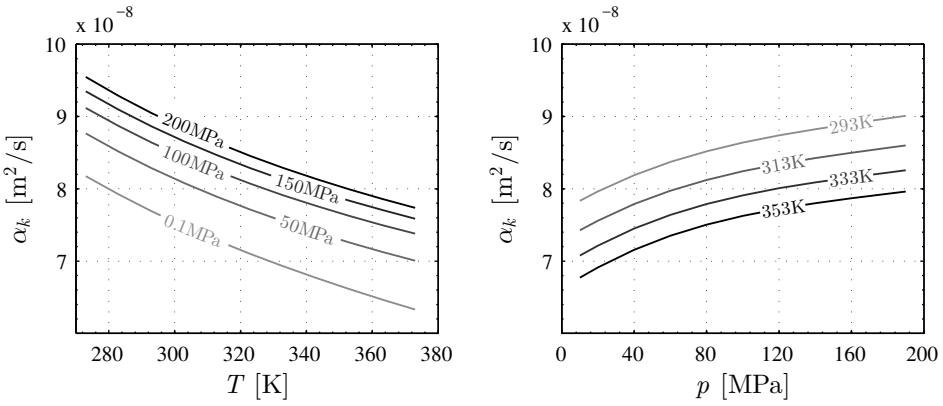

(a) Isobaric curves (b) Isothermal curves

Figure 5.33: Thermal diffusivity curves for a typical diesel fuel.

With the above considerations, a characteristic value for λ_{inj} may be estimated:

$$\lambda_{inj} = \frac{r_0^2}{2.4048^2 \alpha_k} \approx \frac{\left(1.9 \times 10^{-3}\,\text{m}\right)^2}{2.4048^2 \cdot 8.5 \times 10^{-8}\,\text{m}^2/\text{s}} = 7.344\,\text{s} \tag{5.120}$$

References

[1] LMS. *Imagine.Lab AMESim v.10. User's manual*. 2010.

[2] KARNOPP, D., MARGOLIS, D., and ROSENBERG, R. *System Dynamics - Modeling, Simulation and Control of Mechatronic Systems*. New Jersey, NJ: John Wiley & Sons, 2012. ISBN: 978-0-470-88908-4.

[3] KARNOPP, D. "Computer Simulation of Stick-Slip Friction in Mechanical Dynamic Systems". *Journal of Dynamic Systems, Measurement, and Control*, vol. 107.1 (1985), p. 100. ISSN: 00220434. DOI: 10.1115/1.3140698.

[4] ADLER, U. and BAUER, H. *Automotive Handbook*. 3rd ed. Stuttgart: Robert Bosch GmbH, 1995. ISBN: 1-56091-918-3.

[5] DESANTES, J. M., ARRÈGLE, J., and RODRÍGUEZ, P. J. "Computational model for simulation of Diesel Injection systems". *SAE Technical Paper 1999-01-0915* (1999). DOI: 10.4271/1999-01-0915.

[6] MOODY, L. and PRINCETON, N. "Friction Factors for Pipe Flow". *Transactions of the ASME*, vol. 66.8 (1944), pp. 671–684.

[7] NURICK, W. H. "Orifice Cavitation and Its Effect on Spray Mixing". *Journal of Fluids Engineering*, vol. 98.4 (1976), p. 681. ISSN: 00982202. DOI: 10.1115/1.3448452.

[8] SOTERIOU, C., ANDREWS, R., and SMITH, M. "Direct Injection Diesel Sprays and the Effect of Cavitation and Hydraulic Flip on Atomization". *SAE Technical Paper 950080* (1995). DOI: 10.4271/950080.

[9] THEODORAKAKOS, A., STROTOS, G., MITROGLOU, N., ATKIN, C., and GAVAISES, M. "Friction-induced heating in nozzle hole microchannels under extreme fuel pressurisation". *Fuel*, vol. 123.x (2014), pp. 143–150. ISSN: 00162361. DOI: 10.1016/j.fuel.2014.01.050.

[10] STROTOS, G., KOUKOUVINIS, P., THEODORAKAKOS, A., GAVAISES, M., and BERGELES, G. "Transient heating effects in high pressure Diesel injector nozzles". *International Journal of Heat and Fluid Flow*, vol. 51 (2015), pp. 257–267. ISSN: 0142727X. DOI: 10.1016/j.ijheatfluidflow.2014.10.010.

[11] XU, B., OOI, K. T., MAVRIPLIS, C., and ZAGHLOUL, M. E. "Evaluation of viscous dissipation in liquid flow in microchannels". *Journal Of Micromechanics And Microengineering*, vol. 13.1 (2003), pp. 53–57. ISSN: 0960-1317. DOI: 10.1088/0960-1317/13/1/308.

[12] Koo, J. and Kleinstreuer, C. "Viscous dissipation effects in microtubes and microchannels". *International Journal of Heat and Mass Transfer*, vol. 47.14-16 (2004), pp. 3159–3169. ISSN: 00179310. DOI: 10.1016/j.ijheatmasstransfer.2004.02.017.

[13] Morini, G. L. "Viscous heating in liquid flows in micro-channels". *International Journal of Heat and Mass Transfer*, vol. 48.17 (2005), pp. 3637–3647. ISSN: 00179310. DOI: 10 . 1016 / j . ijheatmasstransfer.2005.01.011.

[14] Han, D. and Lee, K.-J. "Viscous dissipation in micro-channels". *Journal of Mechanical Science and Technology*, vol. 21.12 (2007), pp. 2244–2249. ISSN: 1738-494X. DOI: 10.1007/BF03177486.

[15] Kolev, N. I. "Thermodynamic and transport properties of diesel fuel". *Multiphase Flow Dynamics 3: turbulence, gas absorption and release, diesel fuel properties*. 3rd editio. Springer Verlag, 2007. Chap. 13, pp. 293–327. ISBN: 978-3-540-71443-9.

[16] Blackburn, J., Reethof, G., and Shearer, J. *Fluid Power Control*. Cambridge MA: The MIT Press, 1960. ISBN: 9780262020060.

[17] Hardenberg, H. "The geometrical flow cross section of hole nozzles for direct injection Diesel engines". *MTZ worldwide*, vol. 45.10 (1984), pp. 427–429.

[18] Hardenberg, H. "The needle lift dependency of flow coefficients of holes nozzles for direct injection Diesel engines". *MTZ worldwide*, vol. 46.4 (1985), pp. 143–146.

[19] Kallenbach, E. et al. *Elektromagnete*. 4th ed. Wiesbaden: Vieweg+Teubner Verlag, 2012, p. 432. ISBN: 978-3-8348-0968-1. DOI: 10.1007/978-3-8348-8297-4.

[20] Chorazewski, M. et al. "Thermophysical properties of Normafluid (ISO 4113) over wide pressure and temperature ranges". *Fuel*, vol. 105 (2013), pp. 440–450. ISSN: 00162361. DOI: 10.1016/j.fuel.2012.05.059.

[21] Sieder, E. N. and Tate, G. E. "Heat Transfer and Pressure Drop of Liquids in Tubes". *Industrial and Engineering Chemistry*, vol. 28 (1936), pp. 1429–1435. ISSN: 0019-7866. DOI: 10.1021/ie50324a027.

[22] Nusselt, W. "Der Wärmeaustausch zwischen Wand und Wasser im Rohr". *Forschung auf dem Gebiete des Ingenieurwesens*, vol. 2.9 (1931), pp. 309–313. ISSN: 0015-7899. DOI: 10.1007/BF02583210.

[23] FRANC, J.-P. "The Rayleigh-Plesset equation: a simple and powerful tool to understand various aspects of cavitation". *Fluid Dynamics of Cavitation and Cavitating Turbopumps*. Vol. 496. Vienna: Springer, 2007, pp. 1–41. ISBN: 978-3-211-76668-2. DOI: 10.1007/978-3-211-76669-9_1.

[24] BERGMAN, T. L., LAVINE, A. S., INCROPERA, F. P., and DEWITT, D. P. *Fundamentals of Heat and Mass Transfer*. 7th ed. New York, NY: John Wiley & Sons, 2011. ISBN: 978-0470917855.

Chapter 6

Analysis of the influence of the thermal effects on the injector performance

6.1 Introduction

The aim of the present thesis is to analyse the influence of the thermal effects on the performance of a diesel injector by means of a combined experimental and computational approach. Once the experimental tools have been presented (Chapter 4) together with partial results that ensured a proper implementation of the computational model of a Bosch CRI 2.20 injector (as described in Chapter 5), it is time to benefit from the potential of this approach to try to address the problem. This task is treated in the present chapter.

In order to carry out the analysis, the effect of the fuel temperature at the injector inlet on the ROI is first analysed exclusively through the experimental measurements. Once the experimental findings are reasoned and discussed, results generated by the computational model are analysed in order to confirm and extend the purely experimental observations by looking at the injector internal features. This includes the obtaining of the fuel temperature evolution along the injector, which affects the flow regime through the hydraulic restrictions due to changes in the fuel properties, allowing a deeper understanding

of injector dynamics than the one gained by means of the sole experimental measurements.

Considering the requirements of the modern automotive systems, the significance of the reported findings on multiple injection strategies is also explored. In this sense, the combined effect of the fuel temperature at the injector inlet and the rail pressure on the ability of the injector to allow split injections is studied in this chapter.

6.2 Experimental results

As a first approach to the assessment of the thermal effects on the injection process, the effect of the fuel temperature at the injector inlet on the injector behaviour is studied by analysing the ROI curves experimentally obtained as described in Section 4.3.2.

6.2.1 ROI curves

The experimentally determined temporal evolution of the ROI is shown in Figure 6.1 for all the measured conditions (recall Table 4.5). Each graph represents an injection pressure, for which all the tested fuel temperatures at the injector inlet (T_i) are depicted. Results for $T_i = 353\,\mathrm{K}$ have been omitted in the figure due to the similarities with the 373 K case.

The effect of the inlet fuel temperature can be appreciated in the figure. Influence on the opening slope and injection delay will be analysed in following sections, but it can already be seen that it seems more relevant at low injection pressures. Similarly, the steady-state mass flow is more affected by temperature at low injection pressures. This fact is also analysed in Section 6.2.2.

Anyway, the most important effect of the initial fuel temperature that can be appreciated is the injection duration. It can be seen that it is noticeably reduced at low temperatures, as other authors also found for solenoid-operated injectors [1–3]. In the case of the Bosch CRI 2.20, this can be directly explained due to the ballistic nature of the injector. As it was shown in Section 4.4.4, the fuel absolute viscosity decreases with the fuel temperature. This results in a lower friction of the needle against the fuel during the injector opening stage, which leads to higher maximum needle lifts achieved the higher the fuel temperature. Thus, during the closing stage, the needle falls from a higher position when the fuel temperature is increased. Since the effect of the fuel temperature on the closing slope seems almost negligible, this fact leads to a higher time for the needle to close against its seat and cut the injection.

It is also important to mention that the effect of the fuel temperature on the injection duration seems to be more important at the lowest temperature (253 K), for which the injection duration is reduced in a much more substantial way as compared to the 273 K case. Recalling Figure 4.34 and according to Kouzel's equation (Equation (4.27)), this is due to the fact that the fuel absolute viscosity grows exponentially when the fuel temperature decreases, whereas the influence of the temperature on viscosity is not as important for higher temperatures.

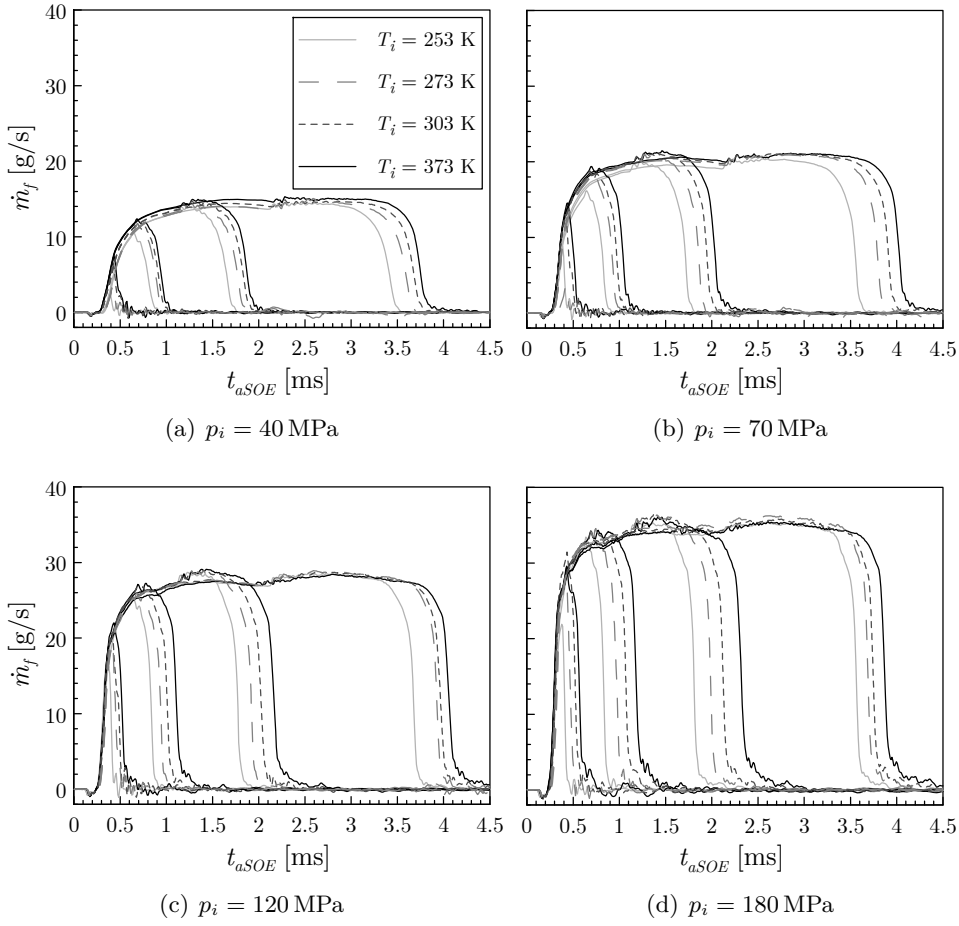

Figure 6.1: Experimental ROI curves for the tested conditions. All the tested energizing times are represented. Results for T_i = 353 K are omitted in the figure for illustrative purposes.

6.2.2 Steady-state ROI

Information concerning the values of steady-state ROI has been extracted for the tested points with an ET of 2 ms, as explained in Section 4.3.2 (Figure 4.17). The obtained values are listed in Table 6.1 and represented in Figure 6.2, both against the square root of the pressure drop for each tested value of fuel temperature at the injector inlet (Figure 6.2(a)) and against this fuel temperature for each injection pressure (Figure 6.2(b)).

	Steady-state $\dot{m}_f$ [g/s]			
T_i [K] / p_i [MPa]	40	70	120	180
253	14.09	19.79	27.76	34.56
273	14.20	20.31	27.94	35.37
303	14.43	20.49	27.89	34.94
353	14.74	20.69	27.99	34.87
373	14.93	20.58	27.67	34.64

Table 6.1: Steady-state values of mass flow rate for the different tested conditions with ET = 2 ms.

The steady-state mass flow rate increases almost linearly with the square root of the pressure drop, as expected [4, 5]. This fact also points out that the nozzle does not work under cavitating conditions in any case, as it was deduced from the nozzle specific hydraulic characterization presented in Section 4.3.1.

Focusing on the influence of T_i on the steady-state mass flow rate for a given injection pressure, Figure 6.2 also reveals that, at low injection pressures, the steady-state mass flow rate increases with the fuel temperature, with a difference of about 6% among the extreme cases. However, this trend is not noticed at higher injection pressures, for which the differences among temperatures do not seem to be as relevant in percentage terms.

In order to analyse these results, it is important to note that there are two mechanisms with opposed effects through which the fuel temperature and pressure influence the steady-state mass flow, as can be deduced recalling Equation (2.19). On the one hand, a mass flow rate decrease is expected the higher the fuel temperature given the lower densities induced at any pressure (recall Figure 4.30). On the other hand, the mass flow rate also depends on the discharge coefficient. As explained in Section 2.3.4, the discharge coefficient grows asymptotically with the Reynolds number, which in turn depends on the fuel density and viscosity.

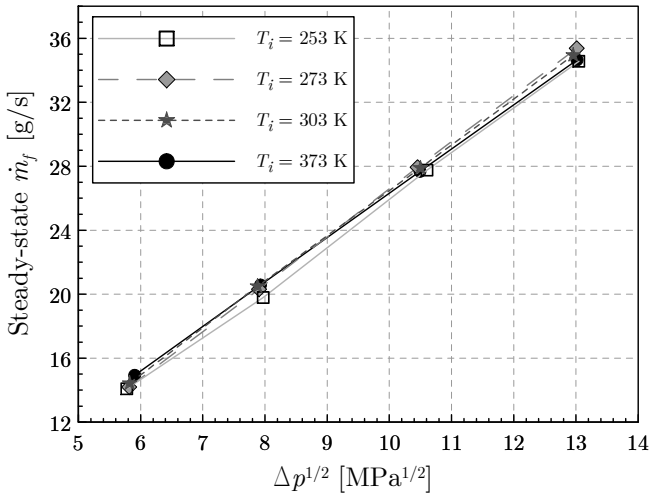

(a) Evolution against $\Delta p^{1/2}$ for the different values of T_i tested.

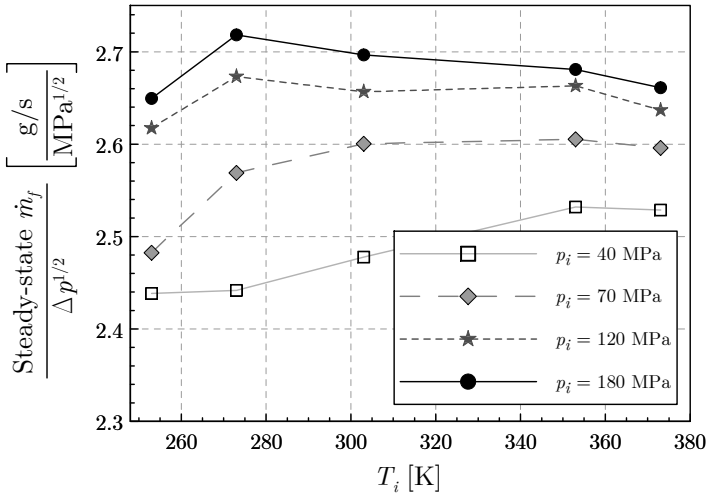

(b) Evolution against T_i for the different values of p_i tested. Values are normalized with $\Delta p^{1/2}$.

Figure 6.2: Evolution of the steady-state mass flow rate with the injection pressure and the fuel temperature at the injector inlet.

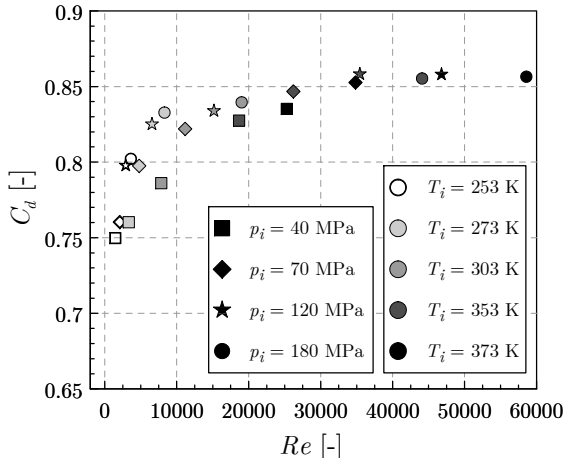

Figure 6.3: Injector discharge coefficient evolution against Re for the different tested conditions.

Figure 6.3 shows the evolution of the injector C_d against Re for the tested conditions. The discharge coefficient values were determined according to Equation (2.19), whereas the fuel properties used for the calculation of Re were taken at the discharge conditions, assuming at this point that the fuel temperature does not significantly change from the injector inlet to the nozzle outlet[1]. The expected asymptotic growth of C_d with Re for non-cavitating orifices is observed. It can be seen that, for high temperatures and high injection pressures, the high Re leads to the nozzle orifices working in the turbulent zone, with only slight variations in C_d due to the fact that the velocity profile is nearly uniform and the friction losses along the orifice are minimised, as stated in Section 2.3.4. However, the nozzle is working in the laminar-turbulent transition zone for the lowest Re values tested, which are obtained for the lowest injection pressures and the lowest temperatures within the injector operating conditions. In this region, the flow velocity profile in the nozzle is not uniform and there is a boundary layer along part of the nozzle orifices whose thickness directly increases the losses due to friction. This induces a lower effective area for the flow together with a lower effective velocity near the wall, resulting in lower values of both C_a and C_v, which in turn lead to the lower values of C_d appreciated.

[1]The fuel temperature variations along the injector cannot be determined by purely experimental means. As stated in Chapter 5, the computational model allows to estimate the fuel temperature variations along the injector. Results concerning these variations from the injector inlet to the nozzle outlet are presented in Section 6.3.

In summary, the trends observed in Figure 6.2 can be explained in view of the previous reasoning. At low injection pressures, the temperature effects on the flow regime lead to high variations in the discharge coefficient, able to overcome the steady-state mass flow rate reduction due to the density decrement when the temperature increases. When the fuel injection pressure is higher and the flow gets more turbulent, except for the case of $T_i = 253\,\mathrm{K}$, the variation of the discharge coefficient with the temperature is not as important and it is not able to invert the trend established by the density effect. In these situations, both conflicting effects of the fuel temperature seem to have the same importance and no particular trend can be established, obtaining virtually the same steady-state mass flow for all temperatures (variations among the extreme cases for $p_i = 120\,\mathrm{MPa}$ are only 1.1%.). This fact is aligned with the findings reported by Dernotte *et al.* [6–8], who established the injection pressure of 85 MPa as a reference value from which the effects of fuel density and viscosity compensate. That is also the reason why the steady-state mass flow at $T_i = 273\,\mathrm{K}$ stops taking one of the lowest values at low pressure to be the highest one at high pressure. However, at $T_i = 253\,\mathrm{K}$ the Re values are low even at the highest injection pressure, making the nozzle work in the laminar-turbulent transition. This explains why the highest steady-state stage mass flow rates are not obtained for this temperature (which would be expected by the sole influence of the density), being achieved for $T_i = 273\,\mathrm{K}$ instead, for which the discharge coefficient is not as substantially modified by pressure as the density is.

6.2.3 Injector dynamics

Injector dynamics can also be analysed from the experimental ROI measurements. Figure 6.4 shows a detail of the first instants of the ROI curves, depicted to analyse the impact of the initial fuel temperature at the injector inlet on the opening stage.

It can be observed that the fuel temperature does not importantly affect the opening slope of the mass flow rate curve at any injection pressure. However, it can be seen that it directly affects the injection delay t_d, defined in Section 4.3.2 (Figure 4.17). The evolution of t_d with the injection pressure for the different injection temperatures tested is shown in Figure 6.5. It can be seen that the injection delay is reduced when the injection pressure increases. This result agrees with those reported by other authors [9] and is expected since the injector opening takes place due to an unbalance of pressure forces above and below the needle. This unbalance is higher the higher the injection pressure.

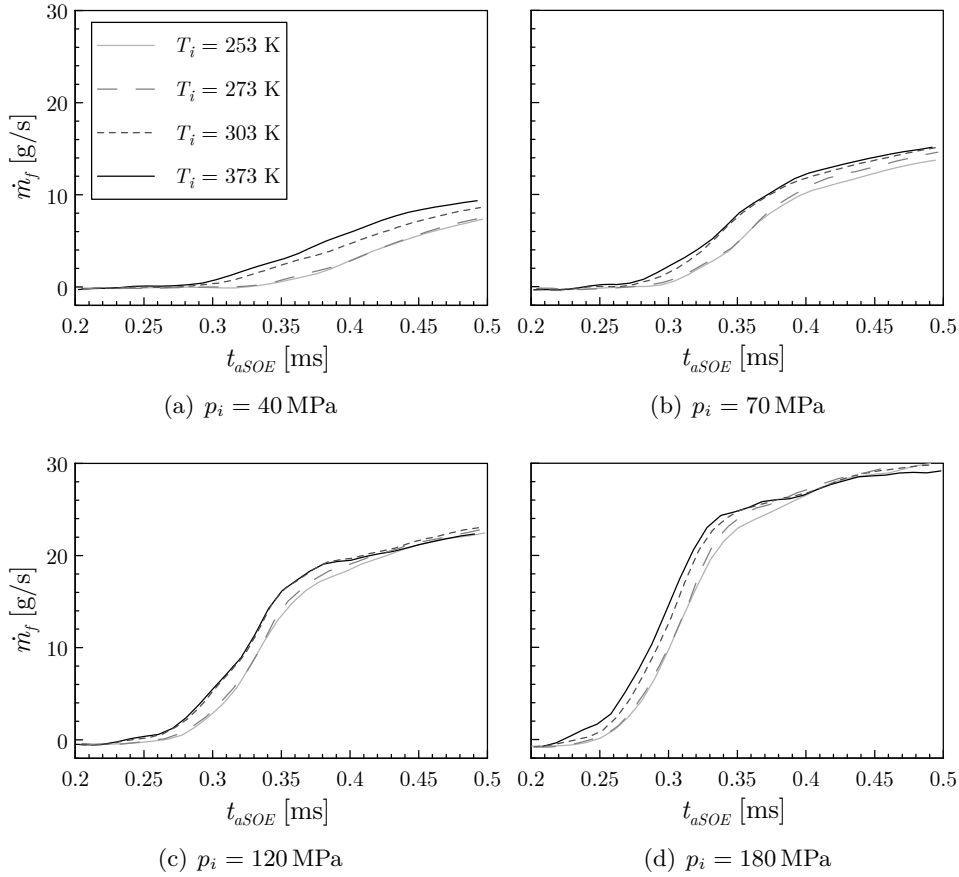

Figure 6.4: Detail of the ROI curves to highlight the injector behaviour on the opening stage. Only points corresponding to $ET = 1$ ms are represented. Results for $T_i = 353$ K are omitted in the figure for illustrative purposes.

Focusing on a given injection pressure, it can be seen that, in general, the injection delay is reduced when T_i increases. This can be explained due to the fact that another parameter influencing needle dynamics is the fuel viscosity, since it is directly related to the viscous forces that oppose the needle movement. As already established in Section 4.4.4, the viscosity is reduced the higher the temperature is (Figure 4.34). This influence is more important at low temperatures, for which the viscosity varies exponentially. This is the reason why the differences in injection delay among temperatures are more significant at low pressures, where the needle opening is governed by the friction forces induced by fuel viscosity, as opposed to the higher injection pres-

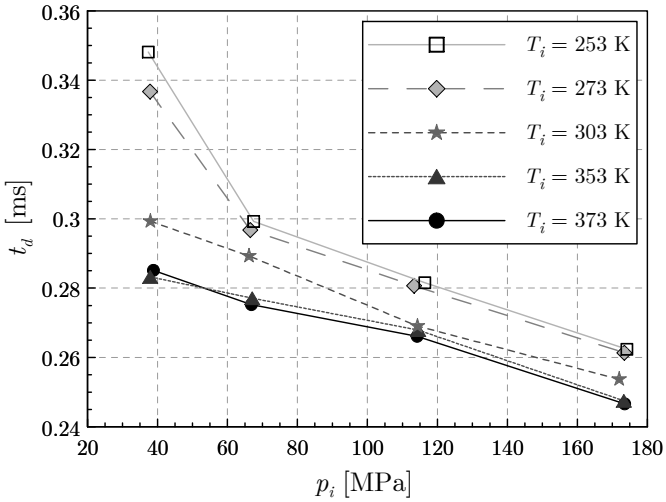

Figure 6.5: Evolution of the injection delay with the injection pressure for the different tested fuel temperatures at the injector inlet.

sures, where needle dynamics is more importantly dominated by the pressure unbalance and the differences in injection delay get gradually reduced.

As already commented in Section 6.2.1 due to its high visibility in the ROI curves, the injection duration is highly affected by the fuel temperature due to the ballistic nature of the Bosch CRI 2.20 injector and the different values of maximum lift achieved by the needle. Figure 6.6 summarizes the results of injection duration (t_{inj}), processed as defined in Section 4.3.2 (Figure 4.17).

As intuition dictates considering that the injector is ballistic, the injection time increases linearly with the energizing time for a given injection pressure and fuel initial temperature, since each of these conditions leads to a different value of maximum needle lift from which the needle has to fall in order to close against its seat. Nevertheless, the highest injection pressure ($p_i = 180\,\text{MPa}$) exhibits an exception to this trend when the injector is energized in the range of 1 to 2 ms. This fact could be explained if the injector reached its maximum lift for those conditions, possibility that will be analysed in Section 6.3 in the view of the computational model simulations. It is also important to highlight that the most important differences in injection time among temperatures take place for the coldest conditions, from 253 to 273 K. This fact can also obey to the fuel viscosity exponentially increasing at the lowest temperatures.

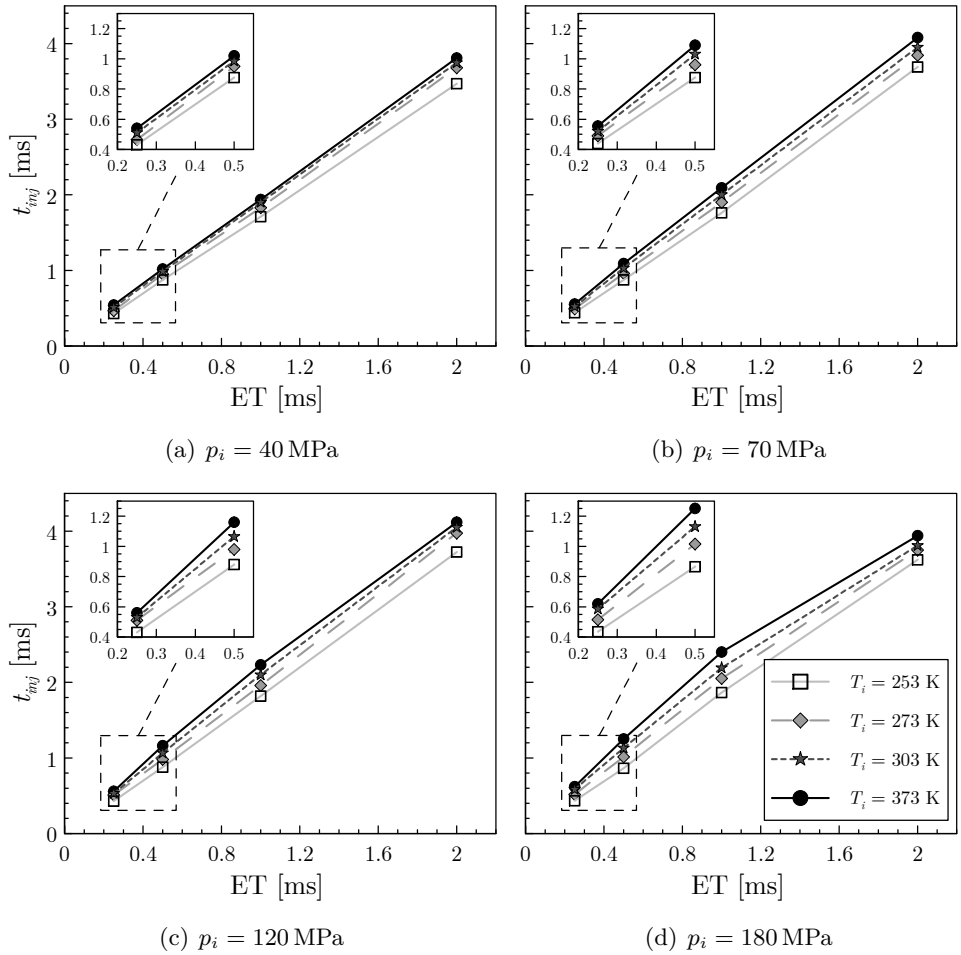

(a) $p_i = 40\,\text{MPa}$ (b) $p_i = 70\,\text{MPa}$

(c) $p_i = 120\,\text{MPa}$ (d) $p_i = 180\,\text{MPa}$

Figure 6.6: Injection time as a function of ET for the tested conditions. Results for $T_i = 353\,\text{K}$ are omitted in the figure for illustrative purposes.

6.2.4 Total mass injected per stroke

The total mass injected per stroke (m_i) from the experiments was determined by integrating the corresponding ROI curve and comparing it to the weight measured by the scale, as explained in Section 4.3.2. Figure 6.7 shows the results for each tested condition.

The observed trends are similar to those found for the injection duration and analysed in Section 6.2.3 (Figure 6.6). This fact makes it possible to state that the highest effect through which the fuel initial temperature influences

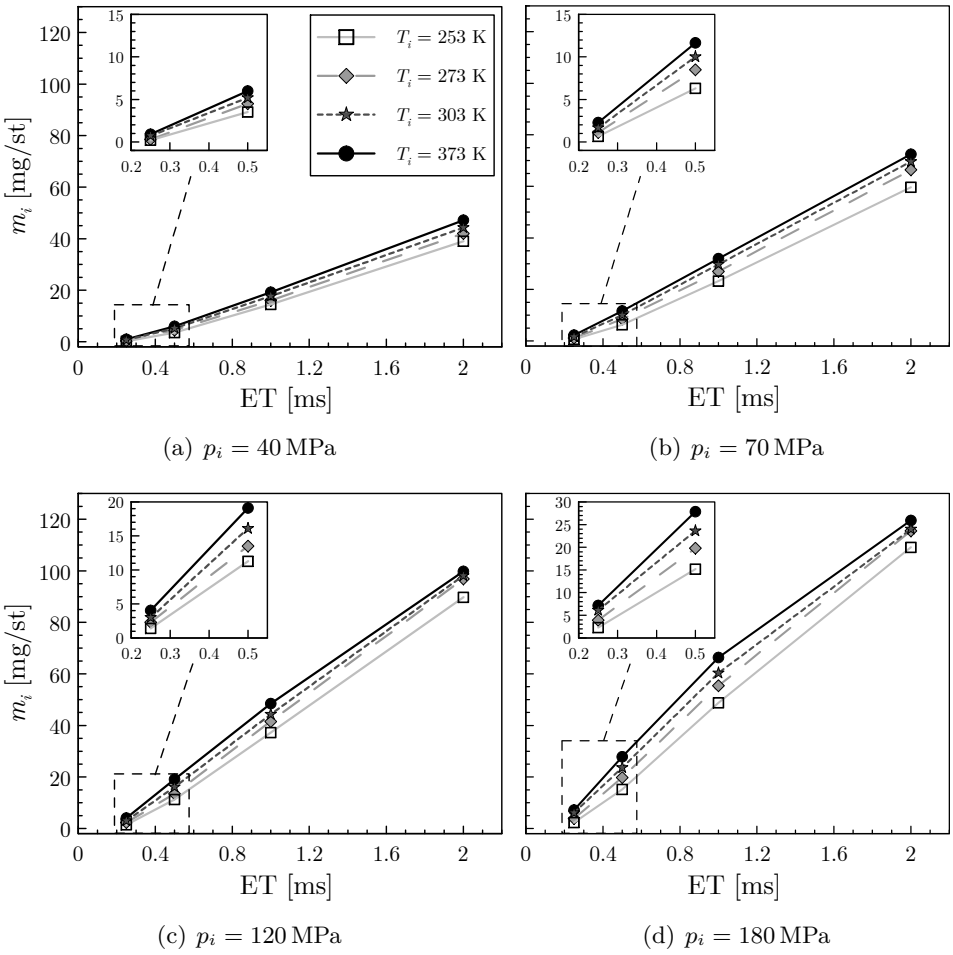

Figure 6.7: Total mass injected per stroke as a function of ET for the tested conditions. Results for T_i = 353 K are omitted in the figure for illustrative purposes.

the injected mass is injection duration, overcoming the effects on injection delay or steady-state mass flow rate that have already been discussed along the present section. Therefore, a reduction in fuel temperature at the injector inlet results in lower mass quantities injected into the cylinder. This influence is more significant at sub-zero temperatures due to the high influence on the fuel viscosity. This fact should not be neglected due to its importance during cold start, where it could be desirable for the ECU to act in order to enlarge the energizing times for a given condition so that the quantities of fuel burnt

are not resented. As a matter of fact, differences ranging from 70% to 80% have been reported among the extreme temperatures at all pressures and an energizing time of 0.5 ms. These differences are still important at higher energizing times (1 ms) where the mass flow rate remains stabilized for a longer period, ranging from 30% to 40% among the extreme temperatures at all pressures.

6.3 Computational model results

Section 6.2 dealt with the analysis of the influence of the fuel temperature at the injector inlet on the rate of injection curves by means of experimental measurements. Even though the analysis of the experiments allowed to extract useful information, a look at the injector internal features would result in a deeper understanding of the reasons behind those observations. In addition, it could provide some extra information that is not achievable by purely experimental means. To this end, results from the computational model are presented and discussed in this section.

The temperature variations determined through the most important injector hydraulic restrictions are first analysed. These temperature changes result in variations in the fuel properties that, in turn, establish the flow regime across the restrictions controlling injector dynamics. Hence, the resulting flow regime in the orifices is identified for each operating condition, allowing to determine the conditions for which the pressure in the control volume drops in a quicker way. This evolution of the pressure in the control volume, together with the viscous forces opposing the needle movement, will help justifying the needle lift laws for each operating condition, also presented.

Additionally, since the simulated propagation of the pressure wave along the injector has been validated, multiple injection strategies are also explored. The influence of the inlet fuel temperature and its variations inside the injector on the mass injected by each separated injection is assessed in this chapter. Moreover, the critical dwell time below which two subsequent injections are not completely separated is also determined for each operating condition.

6.3.1 Temperature changes along the injector

Injector dynamics is controlled by the flow through the control orifices. In order to determine the flow regime established in each of them for the injector operating conditions, it is necessary to determine the fuel temperature changes across them. Results in this regard for the Bosch CRI 2.20 inlet orifice, the outlet orifice and the nozzle are presented in this section.

Inlet orifice (OZ)

Figure 6.8 shows the temporal evolution of the temperature change across the Bosch CRI 2.20 inlet orifice for some of the injector operating conditions, corresponding to an ET of 1 ms (all the tested injection pressures for $T_i = 273$ and 373 K). Given its location, the temperature upstream of this orifice can be assumed as equal to T_i at all times.

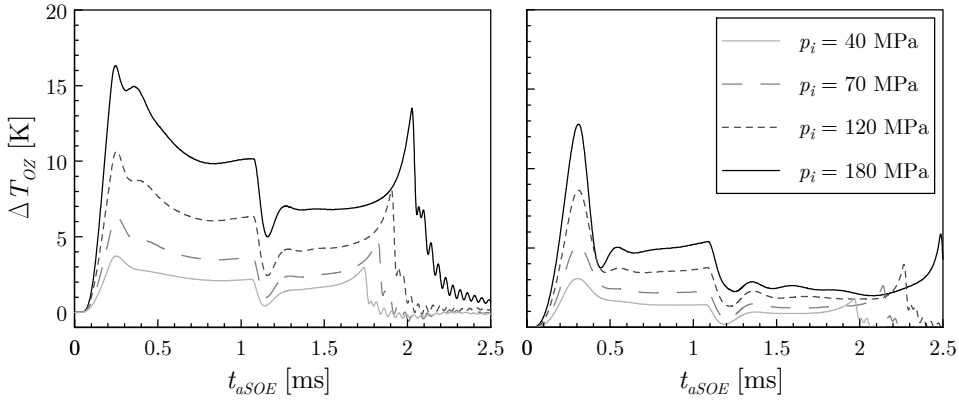

(a) $T_i = 273$ K (b) $T_i = 373$ K

Figure 6.8: Temporal evolution of the temperature change across the inlet orifice. ($ET = 1$ ms).

As can be seen, the fuel temperature always increases through the orifice. Considering that this restriction generates a pressure drop in the control volume, this is consistent with the reasoning made in Section 5.3.4 in the view of Figure 5.21 and Equation (5.74) about the fuel temperature increasing upon an isenthalpic expansion. Hence, in general terms, the temperature rise is more important the higher the injection pressure, since the absolute pressure drop across the orifice also gets larger. In addition, it can be observed that the temperature rise is not constant during the injection. After a first peak taking place for $t_{aSOE} \approx 0.3$ ms coinciding with the injector opening stage (recall Figure 6.1), ΔT gets less important during the injection. This is due to the pressure upstream of the orifice decreasing once a higher amount of fuel bypasses the OZ orifice and leaves the injector through the nozzle feeding line and the nozzle orifices. As a result, the pressure drop through the OZ orifice is less important. Once the injector stops being energized and the pressure in the control volume is restored, the pressure drop across the OZ orifice is even lower, generating the valley in the temperature increase curve

seen at $t_{aSOE} \approx 1.2\,\text{ms}$. At this point, the needle starts falling, leaving more room in the control volume for the fuel, which keeps being introduced through the OZ orifice. This orifice still generates a pressure drop responsible for the temperature rise observed until the injector is effectively closed.

Another interesting finding is that, for a given pressure, the temperature increase is more important the lower the upstream temperature. In order to analyse all the operating conditions jointly, Figure 6.9 shows the maximum temperature increase across the orifice for each of them, also focusing on the experiments for ET = 1 ms since they allow the achievement of steady conditions. The maximum temperature increase has been chosen as a reference since it coincides with the injector opening stage, as stated. For this reason, it will also be taken as the relevant temperature in following sections in order to analyse injector dynamics through the flow regime set along the orifice.

Figure 6.9 shows the validity of the previous statements. The maximum temperature rise is more important the higher the injection pressure, due to the larger absolute pressure drop in the control volume. In addition, for a given pressure, the temperature increases more importantly the lower the upstream temperature. This fact can be attributed to two reasons. On the one hand, the isenthalpic lines of the enthalpy map (Figure 5.21) are not completely parallel. The slope of these lines is more abrupt the higher the fuel temperature. Hence, for a given pressure drop, the temperature rise upon an isenthalpic expansion is lower the larger the initial temperature. On the other hand, the orifice could

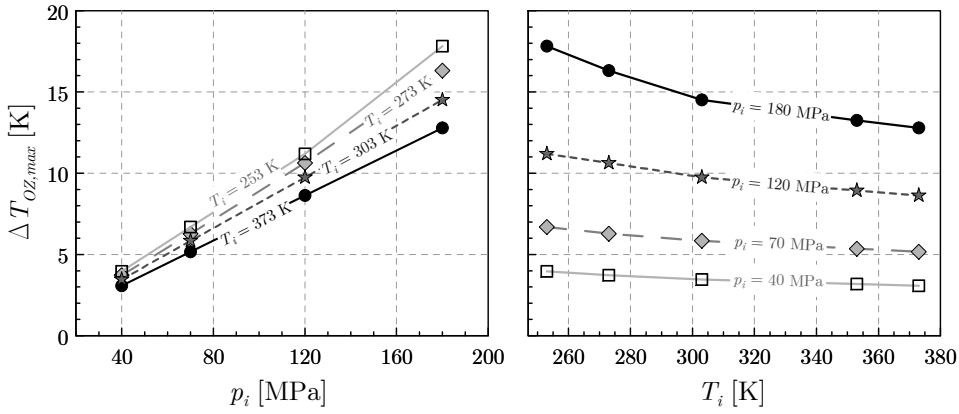

(a) $\Delta T_{OZ,max} = f(p_i)$ (b) $\Delta T_{OZ,max} = f(T_i)$

Figure 6.9: Maximum temperature change across the inlet orifice. (ET = 1 ms).

work under a different flow regime at low temperatures. The higher viscosities associated at these temperatures could induce a laminar regime with a lower discharge coefficient (Figure 2.11) that would imply higher losses through the orifice. As a consequence, the pressure drop in the control volume would be larger in relative terms, generating a higher temperature rise across the inlet orifice. This reasoning would also explain the fact that the nearly linear trend of $\Delta T_{OZ,max}$ with T_i is not respected at the highest injection pressures, given the combined effect of pressure and temperature on the fuel viscosity that is expected to reduce the Reynolds and the discharge coefficient consequently. In any case, this reasoning will be confirmed in the next sections once the pressure drop across the control volume and the flow regime established for each orifice are analysed.

Outlet orifice (OA)

Analogously to what was done for the inlet orifice, Figure 6.10 shows the temporal evolution of the temperature change across the outlet orifice for some sample operating conditions. In this case, the temperature upstream of the orifice coincides with the one downstream of the inlet orifice dealt with in Figures 6.8 and 6.9. Hence, the global temperature change from the injector inlet to the fuel return line is the addition of both values of ΔT.

In this case, fuel only travels effectively across the orifice while the electrovalve is open (Figure 5.18). During this period, the temperature increase

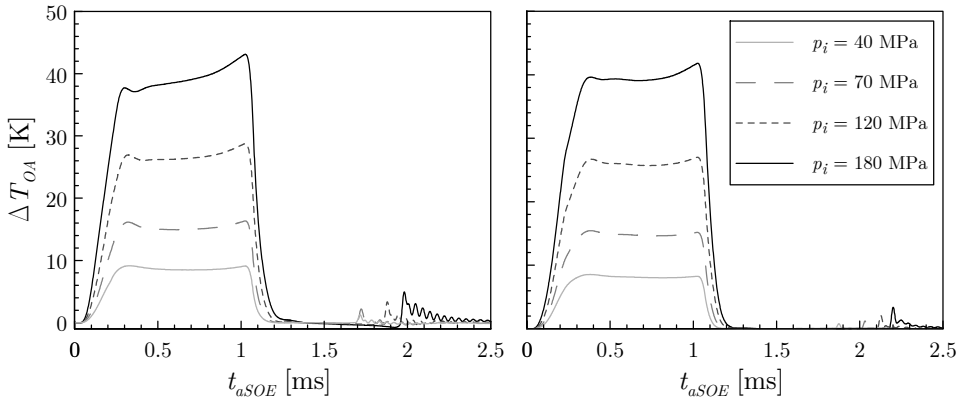

(a) $T_i = 253\,\mathrm{K}$ (b) $T_i = 303\,\mathrm{K}$

Figure 6.10: Temporal evolution of the temperature change across the outlet orifice. ($ET = 1\,\mathrm{ms}$).

is almost constant with time. As it can be seen, the magnitude of the temperature rise in these cases is higher than the ones reported for the inlet orifice. This is justified due to the larger pressure drop expected across this orifice for the injector operating conditions, since the fuel is discharged from the control volume to the return side of the injector. The return is at atmospheric pressure and the OA orifice is the highest restriction to its flow, since the SO1 and SO2 orifices and the SP1 variable section orifice (Figure 5.18) are not as small. This means that most of the pressure drop from the control volume to atmospheric pressure is generated by the OA orifice itself. Figure 6.11 exemplifies this statement: for $p_i = 40\,\text{MPa}$, the pressure downstream of the OA orifice reaches about 8 MPa ($\Delta p \approx 32\,\text{MPa}$, as seen in Figure 6.11(a)), whereas for $p_i = 120\,\text{MPa}$, its lowest value achieves around 20 MPa ($\Delta p \approx 100\,\text{MPa}$, Figure 6.11(b)). Therefore, the absolute pressure drop achieved is higher the larger the injection pressure, thus justifying the findings from Figure 6.10 for which the temperature rise grows higher with the injection pressure.

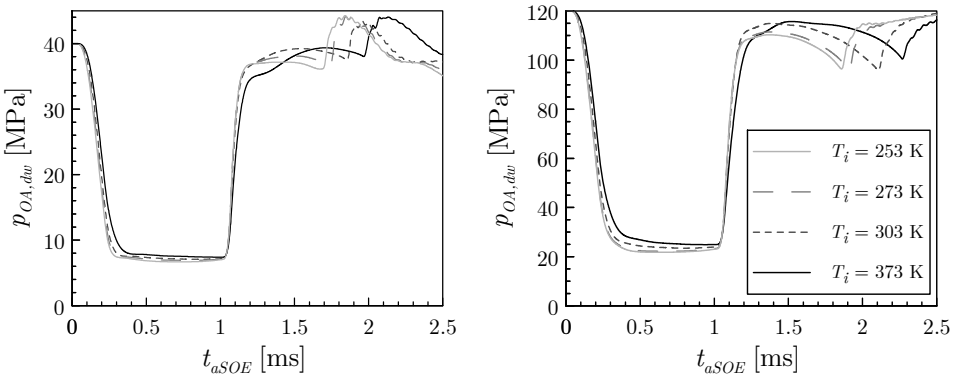

(a) $p_i = 40\,\text{MPa}$ (b) $p_i = 120\,\text{MPa}$

Figure 6.11: Temporal evolution of the pressure downstream of the outlet orifice. Results for $T_i = 353\,\text{K}$ are omitted in the figure for illustrative purposes. ($ET = 1\,\text{ms}$).

A joint look at Figures 6.10(a) and 6.10(b) also shows that the initial temperature at the injector inlet (T_i) does not importantly affect the temperature rise across the outlet orifice. In order to extend this finding to the rest of operating conditions, Figure 6.12 shows the maximum temperature rise across the orifice for all of them. In this case, these values of $\Delta T_{OA,max}$ are representative of both the opening and closing stages.

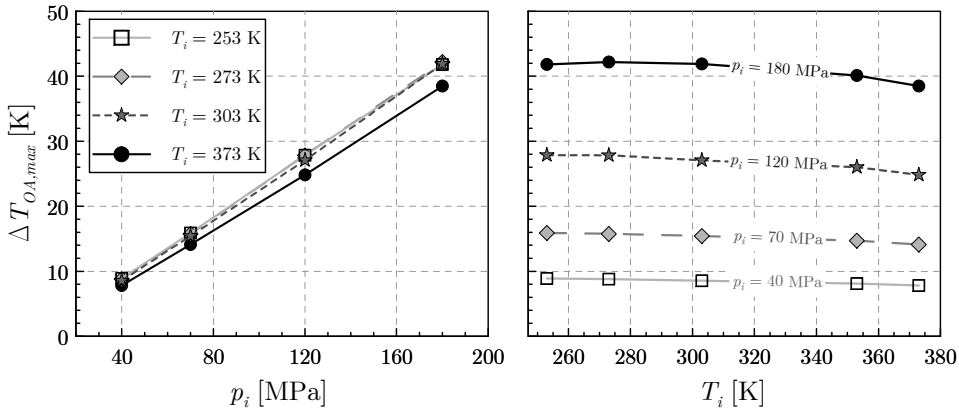

(a) $\Delta T_{OA,max} = f(p_i)$ (b) $\Delta T_{OA,max} = f(T_i)$

Figure 6.12: Maximum temperature change across the outlet orifice. (ET = 1 ms).

As it can be seen, the temperature rise across this orifice is mostly governed by p_i, with the already stated marginal influence of T_i. This low influence of T_i on the temperature rise could be explained considering that the outlet orifice is prone to cavitate. Given the relatively high pressure drops established across this orifice, cavitation could be present for all the operating conditions. This means that the discharge coefficient would not be dependent on the Reynolds number (which is influenced by the different fuel properties imposed by each temperature and pressure condition) but rather on the cavitation number *CN*, as stated in Section 2.3.4. Considering that *CN* exclusively depends on the pressure ratio among upstream and downstream pressure, and that this pressure drop from the control volume to the atmospheric pressure is splitted proportionally among the OA orifice and the SP1, SO1 and SO2 orifices (as seen comparing Figures 6.11(a) and 6.11(b)), *CN* could take similar values regardless of the injection pressure, not significantly changing the orifice discharge coefficient. Therefore, the low differences among temperature rise observed for the different values of T_i could be attributed either to these only marginal differences in C_d, or even to the fact that the isenthalpic lines in the enthalpy map are not strictly parallel to each other. Another factor that should be taken into account in this regard is that the temperature upstream of the OA orifice has already been submitted to the temperature change through the OZ orifice. Hence, the different temperature rises induced in these orifice depending on the injection temperature and pressure also affect the starting temperature for the expansion across the OA orifice.

Nozzle feeding line

Before reaching the nozzle itself, the fuel travels through the nozzle feeding ducts, encountering the NO1 restrictions as an important constraint to the flow (see Figures 5.17 and 5.19). This might impose significant pressure losses together with an associated temperature change that would need to be taken into account to determine the conditions right upstream of the nozzle.

Figure 6.13 shows the temporal evolution of the pressure drop from the rail to the NV2 volume (recall Figure 5.19), together with its associated temperature increase, for some of the injector operating conditions. The figure

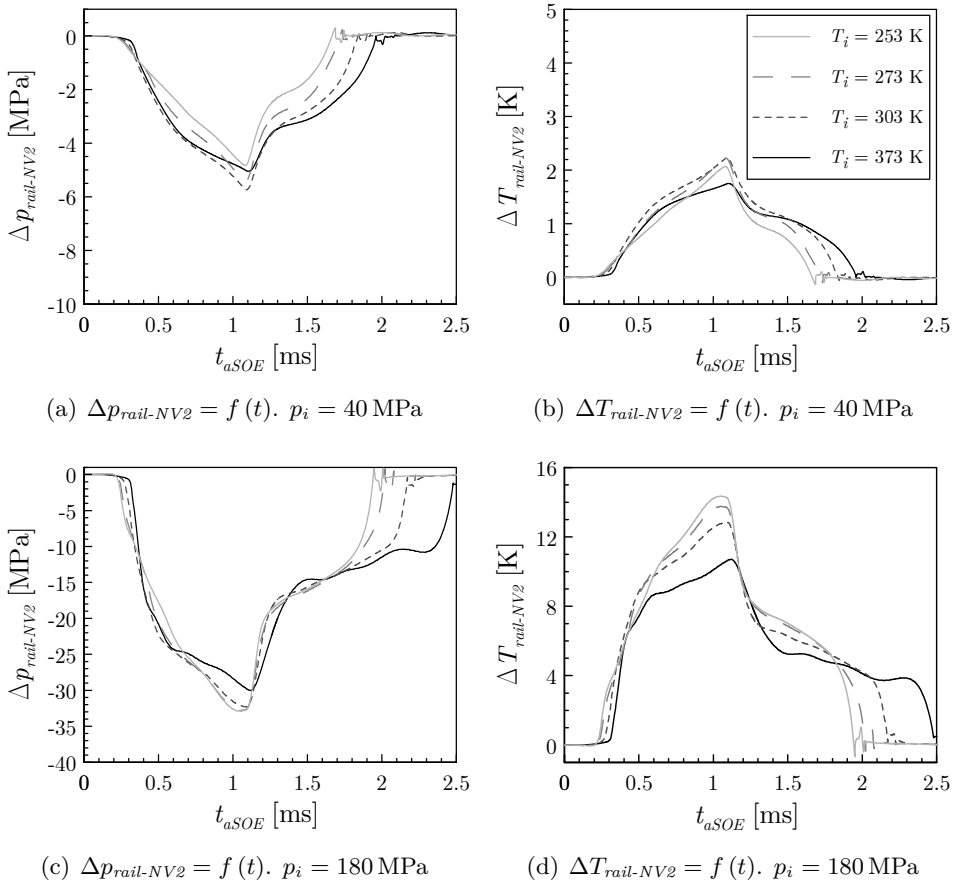

(a) $\Delta p_{rail\text{-}NV2} = f(t)$. $p_i = 40\,\text{MPa}$

(b) $\Delta T_{rail\text{-}NV2} = f(t)$. $p_i = 40\,\text{MPa}$

(c) $\Delta p_{rail\text{-}NV2} = f(t)$. $p_i = 180\,\text{MPa}$

(d) $\Delta T_{rail\text{-}NV2} = f(t)$. $p_i = 180\,\text{MPa}$

Figure 6.13: Temporal evolution of the pressure and temperature changes from the rail to the NV2 volume. Results for $T_i = 353\,\text{K}$ are omitted in the figure for illustrative purposes. ($ET = 1\,\text{ms}$).

illustrates that the maximum pressure drops from the rail to the NV2 volume range from around 5.5 MPa for the lowest injection pressure tested to 30 MPa for the highest one. These maximum pressure drops occur when the electrovalve stops being energized. The associated temperature increase ranges from around 2 K to 14 K, respectively.

Figure 6.14 summarizes the values of the maximum temperature rise along the nozzle feeding line. As it can be seen, the magnitude of the temperature rise is not important at low injection pressure, although it is not negligible for medium injection pressures and above. No significant influence of T_i is observed for the low pressure cases, although differences are noticed as the injection pressure rises. In this sense, the temperature rise is always higher the lower the fuel temperature at the injector inlet. The reasons for this behaviour are analogous to the ones described for the OZ orifice.

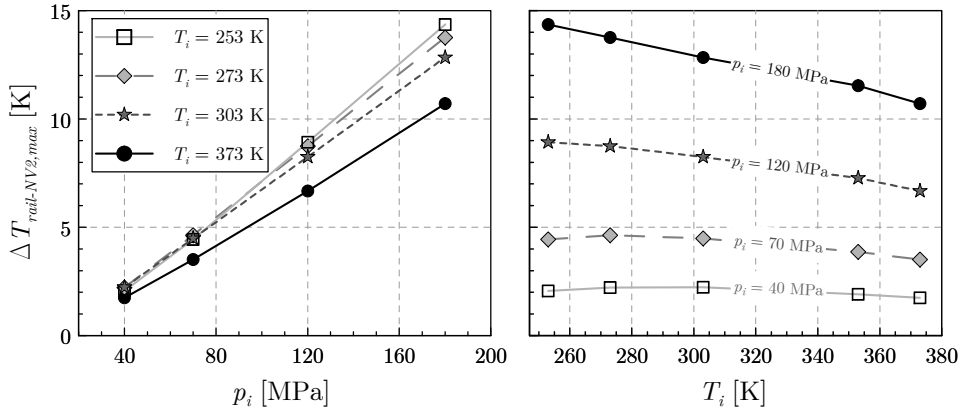

(a) $\Delta T_{rail\text{-}NV2,max} = f(p_i)$ (b) $\Delta T_{rail\text{-}NV2,max} = f(T_i)$

Figure 6.14: Maximum temperature change across the nozzle feeding line. ($ET = 1$ ms).

Nozzle

As stated in Section 5.2.3, the adiabatic flow through the nozzle cannot be treated to as isenthalpic, due to the important change in kinetic energy across it. In this case, the first law states that the stagnation enthalpy is conserved.

Equation (5.76), reproduced here for illustrative purposes, shows that the temperature downstream of the nozzle orifices depends not only on the fuel specific enthalpy, but also on the pressure drop across the nozzle, the discharge

coefficient and the fuel density[2]. It is important to remind here that Equation (6.1) was derived under the assumptions of adiabatic flow and no net work done on or by the system. This last assumption may not hold for low values of needle lift, for which the needle may exchange mechanical work with the flow established through the nozzle. On the other hand, the discharge coefficient of the nozzle orifices is not constant along the injection event, depending on the Reynolds number (which in turn varies along the transient stages of the injection as the needle moves discovering the orifices).

$$h\left(T_{dw}, p_{dw}\right) = h\left(T_{up}, p_{up}\right) - C_d^2 \frac{p_{up} - p_{dw}}{\rho_f} \tag{6.1}$$

With the above considerations, in order to illustrate the whole scenario about the possible temperature changes along the nozzle, Figure 6.15 represents the steady-state ($t_{aSOE} = 1\,\text{ms}$ for the ET $= 1\,\text{ms}$ cases) temperature change[3] as a function of C_d for the different operating conditions tested (hence, the steady values of T_{up} and p_{up} passed by the nozzle feeding line - lines HL1 to NL3 in Figures 5.17 and 5.19 - are accounted for for each operating condition). The values of ΔT were normalized with the maximum temperature increase detected ($\Delta T_{nozzle,max} = 71.4\,\text{K}$), found for $T_i = 253\,\text{K}$ and $p_i = 180\,\text{MPa}$ with $C_d = 0$.

The figure shows that, in steady-state conditions, the fuel temperature increases across the nozzle for low values of C_d, due to the important losses associated. This temperature increase is less important as C_d increases. Indeed, there is a value of C_d for which the low losses and high velocities result in the fuel being subcooled rather than heated. A similar result has already been reported in the literature by Strotos *et al.* [10, 11].

The transitional C_d among heating and cooling in steady-state conditions is slightly lower than the nozzle orifices maximum discharge coefficient. Hence, situations for which the fuel cools upon expansion through the nozzle may be present in reality. As can be seen in Figure 6.15, the fuel is expected to heat more importantly the lower the fuel temperature at the injector inlet (T_i) for low values of C_d. On the one hand, as it happened for the control volume orifices, this may be attributed to the fact that the isenthalpic lines

[2]In this work, the fuel density in Equation (6.1) was taken at a mean pressure and mean temperature among the ones found at the inlet and the outlet of the nozzle.

[3]It is important to note that, given the 1D approach followed, these values correspond to the fuel bulk temperature. In reality, the fuel temperature is expected to vary in the radial direction, being heated in the wall vicinities where the friction losses are located (boundary layer) and being subcooled near the orifices axes.

in the enthalpy map (Figure 5.21) are not completely parallel, leaving more room for heating upon expansion the lower the upstream temperature. On the other hand, this can also be related to the different values of pressure and temperature set upstream of the nozzle after the losses through the nozzle feeding line. The effect of T_i on the temperature rise through the nozzle also leads to the transitional discharge coefficient among heating and cooling (whose variability depending on the injection pressure is represented as shaded

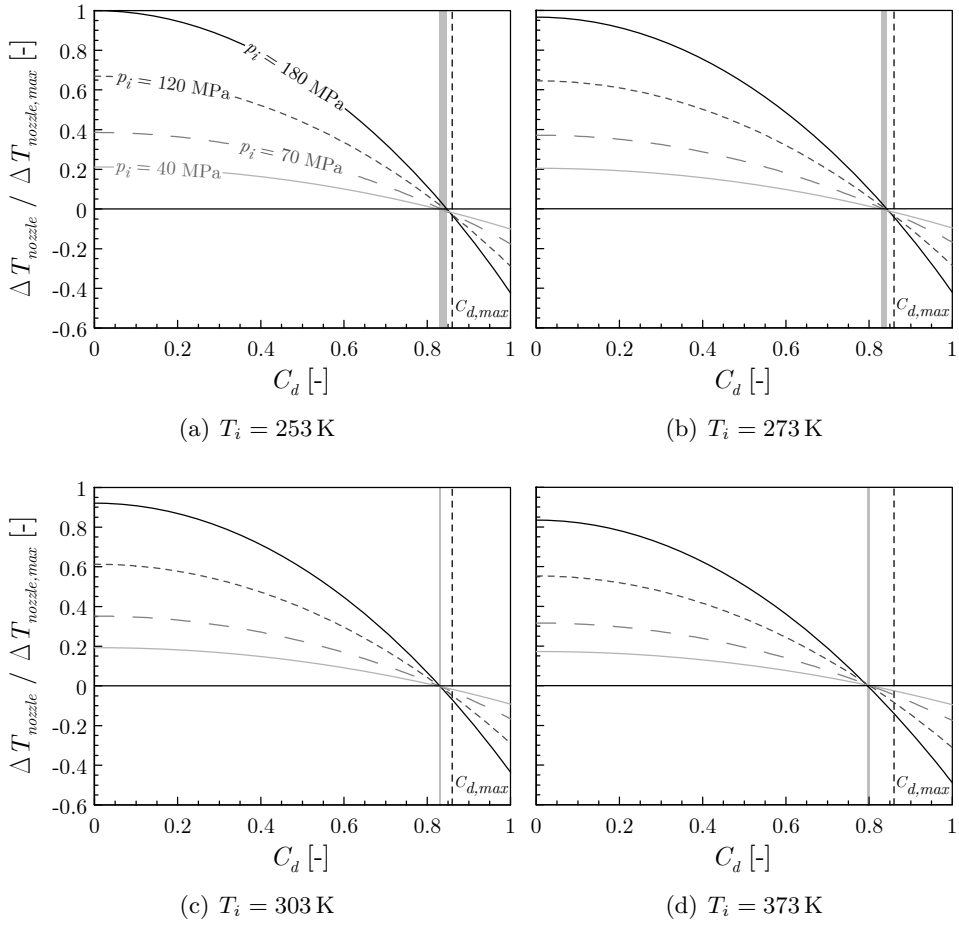

(a) $T_i = 253\,\mathrm{K}$ (b) $T_i = 273\,\mathrm{K}$

(c) $T_i = 303\,\mathrm{K}$ (d) $T_i = 373\,\mathrm{K}$

Figure 6.15: Steady-state temperature change across the nozzle as a function of the discharge coefficient. Values normalized with $\Delta T_{nozzle,max} = 71.4\,\mathrm{K}$, found for $T_i = 253\,\mathrm{K}$ and $p_i = 180\,\mathrm{MPa}$. The orifices $C_{d,max}$ is also represented. The shaded bands highlight the transitional C_d for which the flow stops being heated and is subcooled instead. ($ET = 1\,\mathrm{ms}$, $t_{aSOE} = 1\,\mathrm{ms}$).

vertical bands) being lower the higher the value of T_i. Hence, the difference among this transitional C_d and $C_{d,max}$ gets higher, leaving room for a more important cooling effect the higher T_i.

In the view of these observations, the fuel temperature is expected to increase across the nozzle during the injector opening and closing transient stages. The low needle lifts impose a restriction to the flow that results in a lower effective cross-sectional area (i.e. lower effective diameter) of the orifices, lower Reynolds number and higher losses that lead to low values of discharge coefficient.

Once steady conditions are achieved, the discharge coefficient is expected to become higher and the pressure drop across the nozzle reaches the conditions for which the temperature changes were displayed in Figure 6.15. Therefore, for those combinations of p_i and T_i leading to values of Re for which $C_{d,max}$ is achieved, the fuel will be subcooled during the steady-state stage. This also means that there will be a transitional time during the injection event (corresponding to a certain needle lift) from which fuel stops being heated to be subcooled after the opening, and another transition from where the fuel stops being subcooled to be heated again during the closing stage. Nevertheless, due to the influence of pressure and temperature on the fuel properties, there may be combinations of p_i and T_i leading to Re values lower than the critical one, so that the nozzle orifices work in the laminar-turbulent transition even during the steady-state stage. In these cases, even though to a lower extent than during the transient stages, the fuel might kept being heated during the whole injection event. In addition, the operating conditions for which steady conditions are not achieved (i.e. low ET) will result in the fuel being importantly heated at all times.

In order to better illustrate the aforementioned effects, Figure 6.16 shows the modelled temporal evolution of the fuel temperature variations along the nozzle for the operating conditions tested. Nevertheless, as stated earlier, the values of ΔT have been calculated from assumptions that are not realistic for low values of needle lift, since the external work might not be neglected in the first law Equation ((5.18)). Hence, the values here presented for the injection opening and closing transient stages are only shown for illustrative purposes and should not be relied on quantitatively. For this reason, only the cases of ET = 1 ms are represented, since they lead to the achievement of the steady conditions for which the temperature predictions are assumed to be valid.

The figure illustrates the aforementioned facts, showing that the flow can be expected to be heated during the opening and closing stages, and that it may be cooled or heated during the steady-state stage depending on the

pressure drop through the nozzle and the flow regime established through its orifices. In addition, injections with a low energizing time may mostly be submitted to the heating associated to the transient stage.

In order to focus on the steady-state conditions, Figure 6.17 summarizes the temperature variation through the nozzle for $t_{aSOE} = 1\,\text{ms}$ for the points with ET $= 1\,\text{ms}$ shown in Figure 6.16.

As it can be seen, fuel generally cools upon expansion through the nozzle from a certain value of fuel temperature at the injector inlet, regardless of the injection pressure. Moreover, for these temperatures, the magnitude of

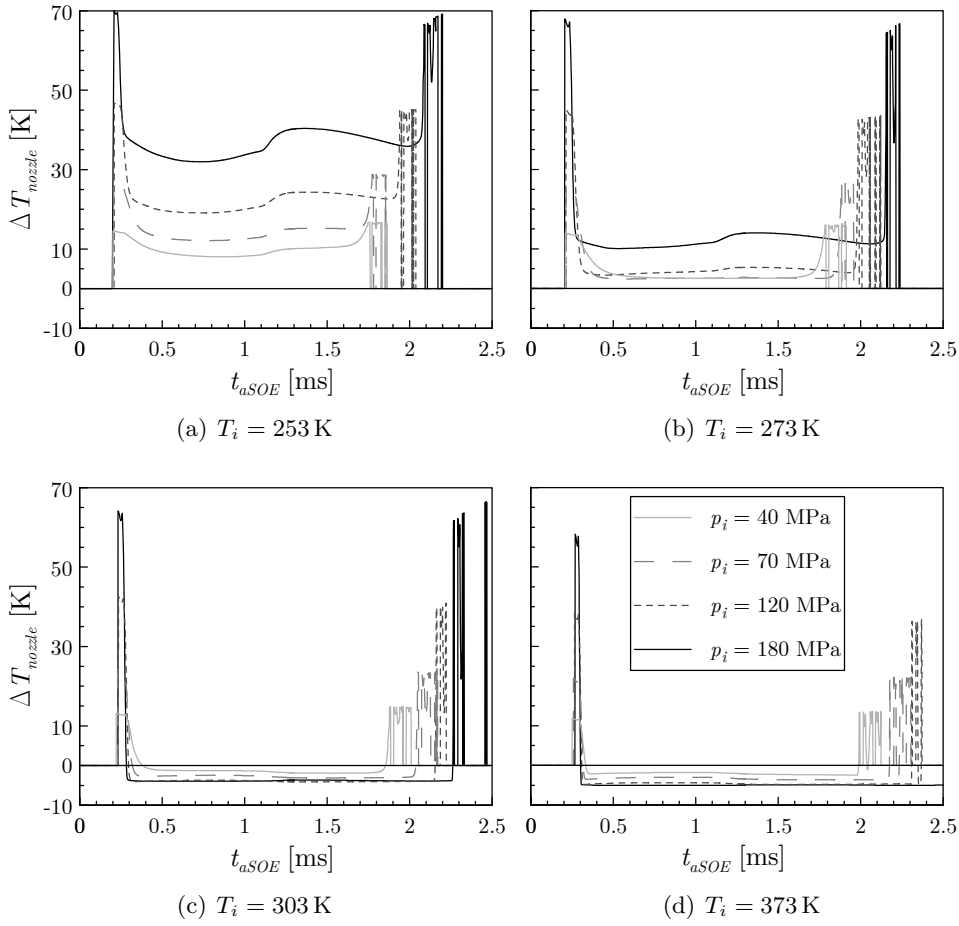

(a) $T_i = 253\,\text{K}$ (b) $T_i = 273\,\text{K}$

(c) $T_i = 303\,\text{K}$ (d) $T_i = 373\,\text{K}$

Figure 6.16: Temporal evolution of the temperature change across the nozzle. ($ET = 1\,\text{ms}$).

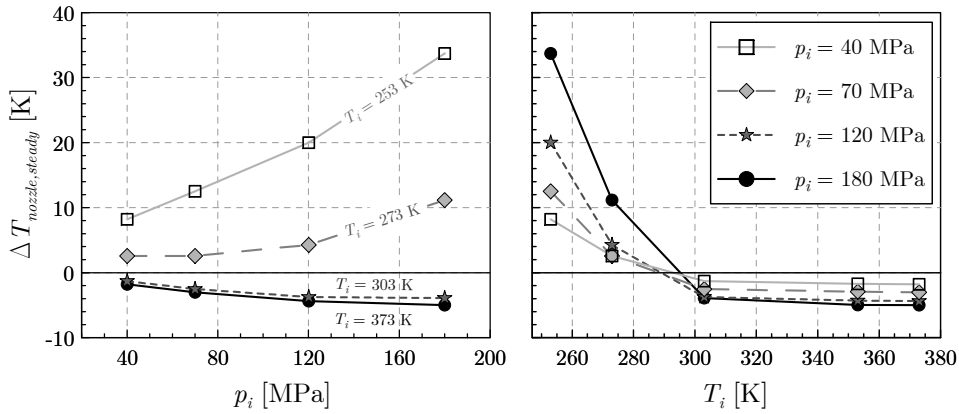

(a) $\Delta T_{nozzle,steady} = f(p_i)$ (b) $\Delta T_{nozzle,steady} = f(T_i)$

Figure 6.17: Temperature change along the nozzle for steady-state conditions ($t_{aSOE} = 1$ ms for points with $ET = 1$ ms).

the fuel cooling does not importantly depend on the injection pressure. This may be explained if the turbulent flow regime had already been reached for these conditions. Hence, the induced C_d values would be close to $C_{d,max}$ and not significantly vary among conditions. As suggested by Figures 6.16(c) and 6.16(d), differences among injection pressures are small for these values of C_d. In addition, a slightly higher cooling is observed in Figure 6.17 for $T_i = 373$ K. This fact can be justified considering that the C_d showing the transition among the cooling and heating effects departs more importantly from $C_{d,max}$ the higher the fuel temperature, as seen in Figure 6.15.

For cold conditions, nevertheless, the fuel heats upon expansion through the nozzle. In addition, this heating is more important the higher the injection pressure. Again, this could be justified by the flow regime established through the nozzle orifices. If they are working in the laminar-turbulent transition zone, Figure 6.16 suggests that the temperature increase is more important the higher the injection pressure and the lower T_i. The non-linear trends observed with pressure and temperature for the lowest temperatures tested ($T_i = 253$ K and $T_i = 273$ K) could be expected if C_d is not constant for a given temperature. This may be the case considering the exponential increase of fuel viscosity when both high pressures and low temperatures are combined (Figure 4.34).

Summarizing the previous effects for steady-state conditions, it may be stated that:

- From a given fuel temperature at the injector inlet among $T_i = 273\,\mathrm{K}$ and $T_i = 303\,\mathrm{K}$ (usual room temperatures), the fuel stops being heated along the nozzle to be cooled instead. In any case, the magnitude of this cooling is not high regardless of the injection pressure. Considering the addition of the heating effect observed along the nozzle feeding line from the injector inlet to the NV2 volume (Figures 6.13 and 6.14), it is possible to state that the fuel does not significantly change its temperature from the injector inlet to the nozzle outlet in steady-state conditions.
- In cold conditions (below $T_i = 273\,\mathrm{K}$) the fuel is heated along the injector due to the observed effects both through the nozzle feeding line and the nozzle itself. The magnitude of this heating, which is more important the lower the fuel temperature and the higher the injection pressure, may importantly affect the flow conditions downstream of the nozzle, especially considering the high sensitivity of the fuel viscosity to changes in fuel temperature for cold conditions.

Given its interest for both engine modellers and experimentalists, this result constitutes one of the main contributions of this thesis. In any case, this analysis will be confirmed in Section 6.3.2 in the view of the flow regime established in the nozzle orifices for each operating condition.

6.3.2 Flow regime established through the injector orifices

The temperature variations along the injector presented in Section 6.3.1 are deemed to strongly affect the flow regime through the orifices, due to the significant changes induced in the fuel properties (namely fuel density and viscosity). This dependency is reciprocal, since the flow regime also influences the fuel heating in turn through variations in the discharge coefficient. In the case of the control orifices, variations in C_d imply the establishment of different pressure drops across them. With regard to the nozzle, variations in C_d directly affect the specific enthalpy loss that determines the temperature change.

It is then interesting to analyse the hydraulic parameters established both in the nozzle orifices and in the control volume ones. As far as the nozzle orifices are concerned, this may also allow to explain the differences in steady-state ROI observed through the experiments. In the case of the control orifices, the hydraulic parameters imposed by the induced flow regime play a key role on injector dynamics, since they determine the ability to effectively generate the pressure drop in the control volume and to restitute the original pressure in order to drive the needle.

Nozzle orifices

Figure 6.18 shows the discharge coefficient of the nozzle orifices modelled as a function of Re_{th}[4]. Depending on the pressure drop and the temperature established across the orifice, the injector operating conditions lead to a value of Re_{th} for these orifices, which in turn induces a certain discharge coefficient. The values established for each of the tested operating conditions once the steady-state stage is reached are shown in the figure.

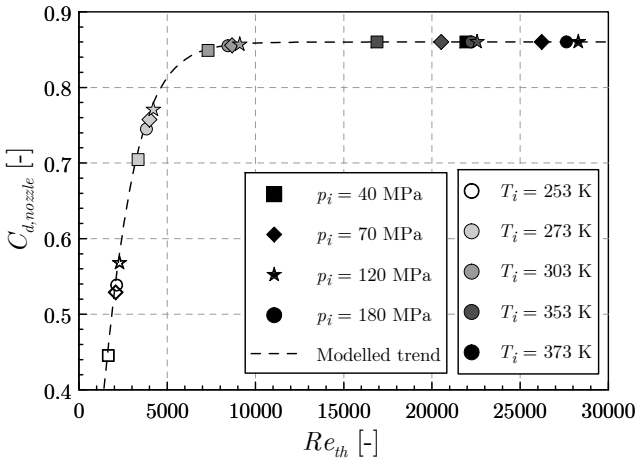

Figure 6.18: Predicted discharge coefficient for the nozzle orifices according to the flow regime set during the steady-state stage at the tested operating conditions. ($t_{aSOE} = 1$ ms for points with $ET = 1$ ms).

As can be seen, the highest values of temperature at the injector inlet (T_i) lead to the nozzle working in the turbulent regime regardless of the injection pressure. This is clearly seen for $T_i = 353$ K and $T_i = 373$ K. The transitional regime is established in the case of $T_i = 303$ K, for which the injection pressure does not play a significant role either. This value of temperature is observed to define the transition among laminar and turbulent regime along the orifices. For lower values of T_i, the laminar or the transitional regimes are always induced due to the high fuel viscosities associated (recall Figure 4.34), and the variations in injection pressure strongly modify the injector discharge coefficient through the Reynolds number, both by means of the effective velocity and the fuel viscosity again.

[4]Recall that the theoretical Reynolds number, defined in Equation (5.14), is the variant used by AMESim to establish the actual discharge coefficient during a simulation

One fact that draws attention is that Re_{th} does not always increase with the injection pressure. From a certain value of p_i, the extremely large increase in fuel viscosity provoked by high pressures (recall Figure 4.34) is able to counteract the increase in theoretical flow velocity induced by the pressure drop, thus generating low values of Re_{th}. Hence, as shown in Figure 6.18, the discharge coefficient for $p_i = 180\,\text{MPa}$ is always lower than the one achieved for $p_i = 120\,\text{MPa}$ (for intermediate values of T_i, it may be even below the one corresponding to $p_i = 70\,\text{MPa}$). This is an important finding, since this observation would not have been possible if the fuel properties had been regarded to as constant along the injector, as it is the standard approach in *common-rail* injection systems modelling (recall Section 3.2). Indeed, this fact was not noticed when introducing Figure 6.3[5], derived from the experiments, since the fuel properties used to determine Re were evaluated at the discharge conditions.

Anyway, these apparently conflicting observations still allow to explain the trends of the steady-state mass flow rate with the pressure and temperature experimentally observed and reported in Figure 6.2. For a given injection pressure, an increase in temperature from cold conditions up to 303 K tends to increase the steady-state mass flow rate due to the higher discharge coefficient induced by the flow regime. This trend was not experimentally observed for $p_i = 120\,\text{MPa}$ and $p_i = 180\,\text{MPa}$, for which a reduction in steady-state mass flow rate was reported when going from $T_i = 273\,\text{K}$ to $T_i = 303\,\text{K}$. This fact may be attributed to the variation of C_d with Re along the laminar-to-turbulent transition being smoother in reality than the one predicted by AMESim through Equation (5.16). Hence, the high gaps in C_d seen in Figure 6.18 among these conditions may be less important in reality, not becoming large enough to overcome the reduction in fuel density when the temperature is increased. From this temperature of 303 K onwards, the turbulent regime is set. According to the modelled C_d trend, the maximum discharge coefficient is already achieved and the only differences in steady-state mass flow rate are due to density. Therefore, this mass flow rate would decrease when increasing the temperature. The experimental trends reported in Figure 6.2(b), however, show that the steady-state mass flow rate still increases with temperature for some injection pressures. This could also be explained considering that, in reality, the discharge coefficient would still tend asymptotically to its maximum value. Thus, the higher Re associated to an increase in fuel temperature

[5]It is important to mention that Figure 6.3 depicts the injector discharge coefficient with respect to the real Re, whereas Figure 6.18 deals with the nozzle orifices exclusively, taking the theoretical Re as a reference to analyse the simulations carried out through the computational model.

through viscosity would still generate an increase in C_d able to overcome the effect of density.

On the other hand, the explanation of the trends of the fuel temperature variations across the nozzle in steady-state conditions (Figure 6.17) reported in Section 6.3.1 may also be confirmed in the view of the flow regime induced in the nozzle orifices. The fact that these variations do not importantly differ among injection pressures from a temperature of $T_i = 303\,\mathrm{K}$ is justified considering that $C_{d,max}$ is almost reached. For cold conditions, the fuel heats upon expansion through the nozzle orifices, which responds to the orifices working under the laminar regime. In addition, the non-linear trend with the pressure for these cold temperatures may be explained considering that C_d does not always increase with the injection pressure for a given fuel temperature.

The possibility of carrying out the previous reasonings exemplifies the potential of combining the experimental approach with computational modelling. It is important to note that the temperature variation along the nozzle orifices depends on the discharge coefficient, as established by Equation (6.1). This coefficient, in turn, depends on the fuel properties induced by the injector operating temperature and pressure together with the temperature variations along the injector. This recursive problem may only be completely analysed by computational means.

Inlet orifice (OZ)

As stated earlier, the control volume orifices strongly affect injector dynamics. During the opening stage, the OA orifice is uncovered and becomes responsible for evacuating the fuel from the control volume, whereas the losses through the OZ orifice, which is always active, determine the pressure drop in this volume. During the closing stage, the OA orifice is locked and the discharge capabilities of the OZ orifice determine the ability of the control volume to recover its pressure. Attention to the discharge coefficients of both orifices must then be given in order to shed light on these phenomena, keeping in mind that the OZ orifice is not expected to cavitate for any of the engine operating conditions due to its high conicity (recall Section 4.2) and the high pressures set downstream, whereas the OA orifice is prone to cavitate given its cylindrical shape and the high pressure drops found through it.

Figure 6.19 shows the modelled discharge coefficient of the inlet orifice as a function of Re_{th}. The values of Re_{th} and C_d associated to the orifice for the tested operating conditions are also represented over the curve.

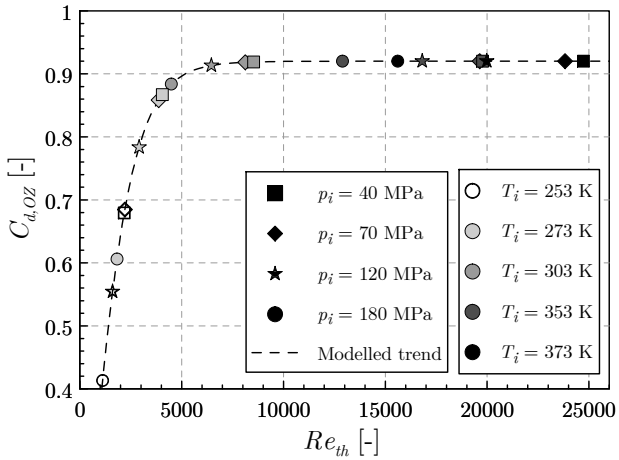

Figure 6.19: Predicted discharge coefficient for the inlet orifice according to the flow regime set during the opening stage at the tested operating conditions. ($ET = 1$ ms).

As it happened for the nozzle orifices, no influence of the fuel temperature at the injector inlet is found from a certain temperature value. Hence, for $T_i = 353$ K and $T_i = 373$ K, the maximum discharge coefficient is already reached regardless of the injection pressure. The value of $T_i = 303$ K makes the orifice work in the laminar-to-turbulent transition, although the induced values of Re_{th} are high enough to avoid a significant influence of the injection pressure either. For colder conditions, however, the orifice is submitted to the laminar flow regime and the changes induced by the injection pressure in Re_{th} result in important changes in the discharge coefficient.

As opposed to the nozzle orifices, for which C_d generally grows with the injection pressure, except for the case of $p_i = 180$ MPa that could lead to values lower than the ones found for $p_i = 120$ MPa (Figure 6.18), in this case Re_{th} is generally higher the lower the injection pressure. This is justified considering that the flow through the OZ orifice is driven by the pressure difference among the injection pressure and the one established in the control volume (as opposed to the nozzle orifices, which are submitted to a pressure difference that covers most of the pressure drop among the rail and the discharge pressure). Therefore, an increase in injection pressure importantly reduces Re_{th} through the exponential increment induced in fuel viscosity. This effect of larger values of p_i on Re_{th} overcomes the one due to the associated increase in theoretical flow velocity, since the pressure drop in the control volume does not grow with p_i in such an important proportion.

These observations allow to explain the trends reported in Figure 6.9 about the influence of p_i and T_i on the temperature increase across the OZ orifice. For the injection pressures of $p_i = 40\,\text{MPa}$ and $p_i = 70\,\text{MPa}$, the differences in maximum temperature rise across the orifice were similar among the extreme temperatures. This is justified considering that the induced values of C_d are within the same range in both conditions (from $C_d \approx 0.68$ to $C_{d,max}$, as shown in Figure 6.19). For higher values of p_i, however, the high fuel viscosities lead to more extreme values of C_d being swept (as low as 0.4 for $p_i = 180\,\text{MPa}$ and $T_i = 253\,\text{K}$). This induces major losses across the orifice, resulting in a larger pressure drop that in turn generates a higher temperature rise.

As advanced through these explanations, the flow regime established in the OZ orifice strongly influences the pressure drop generated in the control volume, which is in turn responsible for lifting the needle. Therefore, the analysis of injector dynamics carried out in Section 6.3.3 will also benefit from the observations presented in the present section.

Outlet orifice (OA)

Figure 6.20 depicts the predicted discharge coefficient of the outlet orifice during the opening stage. The points are represented over the curves corresponding to the behaviour of C_d modelled as a function of Re (for non-cavitating

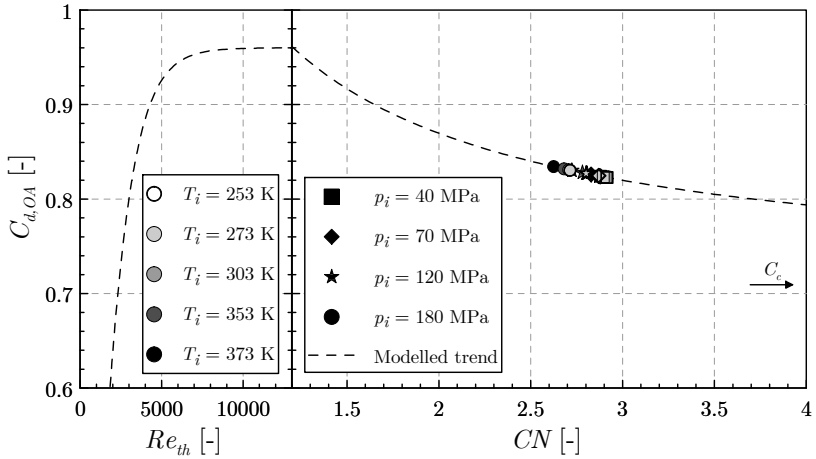

Figure 6.20: Predicted discharge coefficient for the outlet orifice according to the flow regime set during the opening stage at the tested operating conditions. ($ET = 1\,\text{ms}$).

conditions) and CN (for the cavitating ones), depending on the conditions induced by the tested injection pressures and fuel temperatures at the injector inlet. As it can be seen, the orifice is cavitating ($CN > CN_{crit}$) for all the tested conditions, although the non-cavitating part of the curve has been kept for illustrative purposes.

The figure shows that similar values of CN are imposed by all the injector operating conditions. As advanced in Section 6.3.1, this is due to the fact that the flow experiences subsequent pressure drops downstream of the orifice due to the presence of other restrictions (SO1 and SO2 orifices and the SP1 variable section orifice, see Figure 5.18) before reaching the atmospheric pressure at the return line. Hence, the total pressure drop among the control volume and the atmospheric pressure is splitted proportionally when the injection pressure increases.

In any case, it can be seen that the resulting cavitation number in the OA orifice is higher the lower the injection pressure and the fuel temperature at the injector inlet. This results in variations in C_d from around 0.82 (low pressure and low temperature) to 0.84 (high pressure and high temperature). Despite the low differences among these extreme values, they explain the fact that the established pressure drop across the OA orifice while it is unlocked is larger the lower T_i, since the lower discharge coefficient associated leads to higher pressure losses.

6.3.3 Injector dynamics analysis

As the experimental ROI curves demonstrated, the operation of the Bosch CRI 2.20 injector leads to different injection durations depending on the fuel injection pressure and temperature (Figure 6.6). In Section 6.2.3, these differences were attributed to the ballistic nature of the injector, since the varied operating conditions lead to different upper values of needle lift from which the needle has to fall in order to close against its seat. The present section aims at the observation of the injector internal features by means of the implemented model in order to fully understand these differences.

Figure 2.4 showed a simplified sketch of the injector depicting the main phenomena involved during the transient stages of the injection. On the one hand, injector dynamics is influenced by the force ($F_{\Delta p}$) due to the pressure difference between the upper part of the needle (control volume, HV1 in Figure 5.17) and its lower part. This pressure difference is governed by the performance of the control volume orifices analysed in Section 6.3.2, since the flow rate through them determines both the ability to generate the pressure

drop at the control volume when the solenoid valve is energized (making the needle rise discovering the nozzle orifices) or to restore it when the injector stops being energized (making the needle close against its seat). On the other hand, needle dynamics is influenced by the force (F_{fric}) generated by viscous friction in the clearance between the needle and the injector wall, especially when this clearance is small. This force is opposed to the needle movement and therefore to the force generated by the pressure unbalance, so that:

$$F_{needle} = F_{\Delta p} - F_{fric} \tag{6.2}$$

The viscous friction force F_{fric} depends on fuel viscosity, as stated by Equation 5.31, which in turn depends on fuel temperature and pressure. These phenomena will be hereby analysed and linked to the needle lift evolution during the injection event, which should explain the findings from the experimental ROI measurements.

Analysis of the evolution of the pressure in the control volume

Figure 6.21 shows the evolution of the pressure in the control volume for the whole range of injection pressures and temperatures at the injector inlet studied, focusing on the cases of ET = 1 ms. The figure shows that, for any injection pressure condition, the depression generated in the control volume during the opening stage occurs earlier and achieves a greater magnitude the lower the fuel temperature.

This result can be explained due to the different flow regime established at both control orifices depending on the injector operating conditions. As reported in Section 6.3.2, the range of values taken by the discharge coefficient of the OA orifice is not wide (Figure 6.20). In the case of the OZ orifice, however, important differences were seen depending on the injector operating conditions. Figure 6.19 showed that, for a given injection pressure, the discharge coefficient is lesser the lower the fuel temperature. This implies higher losses through the orifice that result in an earlier and larger pressure drop, explaining the trends observed in Figure 6.21.

On the other hand, Figure 6.21 shows that it takes longer for the control volume to restore its pressure the higher the value of T_i once the injector stops being energized. At this instant, the OA orifice is locked and the OZ orifice is responsible for re-establishing the pressure in the volume. Hence, this behaviour may be justified by the mass flow rate through the orifice. Even though the discharge coefficient is higher for high values of T_i, the pressure drop that it induces across the orifice is lower, resulting in a lesser theoretical

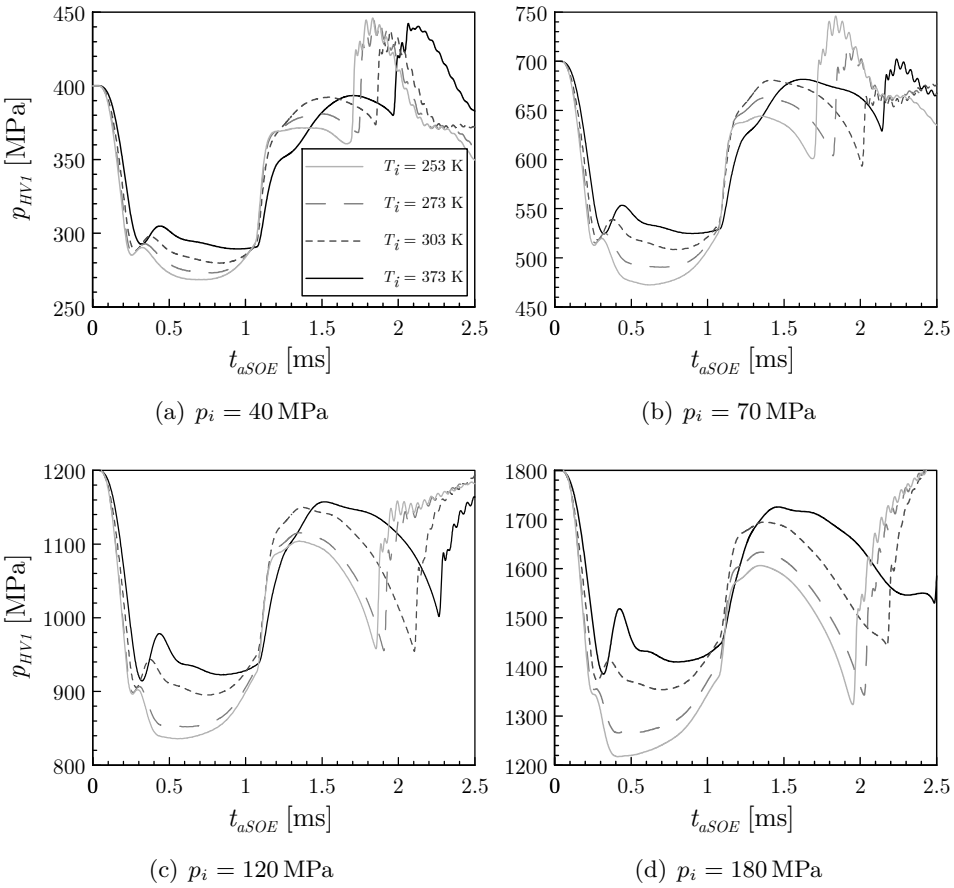

(a) $p_i = 40\,\mathrm{MPa}$ (b) $p_i = 70\,\mathrm{MPa}$

(c) $p_i = 120\,\mathrm{MPa}$ (d) $p_i = 180\,\mathrm{MPa}$

Figure 6.21: Temporal evolution of the pressure in the control volume for the operating conditions tested. Results for $T_i = 353\,\mathrm{K}$ are omitted for illustrative purposes. ($ET = 1\,\mathrm{ms}$).

flow velocity. In addition, the fuel density is considerably lower when compared to the one at cold conditions. These two factors are able to overcome the sole effect of the discharge coefficient and lead to small mass flow rates through the orifice. As a consequence, longer times are needed for the control volume to restore the rail pressure, as observed.

It is important to note that the sole effect of the discussed control volume orifices hydraulic parameters would lead to a faster response of the injector at low temperatures, due to the more accused pressure drop at the control volume that generates a higher unbalance at both sides of the needle.

Analysis of the friction force opposing the needle movement

As shown by Equation (5.31), reproduced here for illustrative purposes, the friction forces appearing on the needle when trying to lift it through the fuel depend both on the pressure drop along the needle and on the fuel viscosity, with opposed effects. It is therefore interesting to determine which of the two terms in the equation plays a more significant role in the needle of a diesel injector.

$$F_{fric} = -\Delta p\,\pi \frac{D_{cl}}{2}\frac{D_{pist}-D_{cl}}{2} + 4\pi\eta_f U_b L\left(\frac{D_{pist}}{D_{cl}}-1\right) \tag{6.3}$$

Figure 6.22 shows the value of the ratio among the term of Equation (6.3) that depends on the fuel viscosity η_f, (labelled as $F_{fric,\eta}$) and the one that depends on the pressure drop (named $F_{fric,\Delta p}$) along part of an injection event for some of the tested conditions. The figure only shows the time range corresponding to the stage in which the needle is rising. The lowest and highest values of injection pressure have been chosen for the comparison since they are expected to lead to the most extreme values of the studied terms.

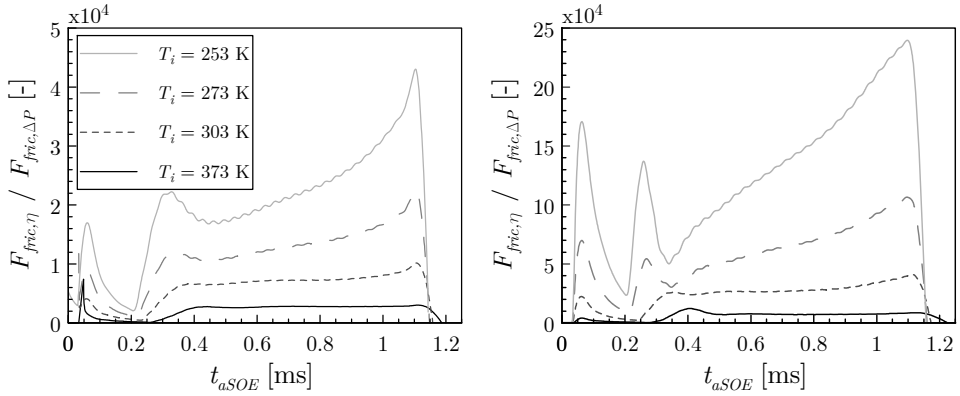

(a) $p_i = 40\,\text{MPa}$ (b) $p_i = 180\,\text{MPa}$

Figure 6.22: Temporal evolution of the ratio among the viscous force on the needle generated by fuel viscosity and the one induced by the pressure drop along the needle. Results for $T_i = 353\,\text{K}$ are omitted for illustrative purposes. ($ET = 1\,\text{ms}$).

As it can be seen, the term related to fuel viscosity when generating friction forces is several orders of magnitude higher than the one related to the pressure drop. In addition, its influence is even more important the lower the fuel

temperature at the injector inlet and the higher the injection pressure, due to the high viscosities associated (Figure 4.34). Hence, it is possible to state that the net effect of increasing the fuel temperature is a reduction in the friction force, which would in turn act in the sense of a faster needle opening.

In the view of the previous considerations, only this finding will be taken into account when analysing the total force on the needle (Equation (6.2)) through the combination of the observations regarding the pressure drop in the control volume and the friction forces generated upon needle movement.

Combined effect of the control volume pressure drop and friction forces on needle dynamics

At this point, it is interesting to analyse how the observed differences in pressure evolution in the control volume and viscous friction are translated into needle movement. As pointed out by Figure 6.21, a lower fuel temperature would lead to a faster injector opening if only the pressure forces were considered. However, it would lead to a slower opening by the sole effect of viscous friction. As stated in Section 3.4, these opposed effects of the fuel temperature on injector dynamics have already been reported in the literature [2, 12–14].

Figure 6.23 depicts the needle lift evolution obtained from the simulations for the whole range of injection pressures and temperatures tested in order to analyse the net effect of both phenomena. Needle lift values are normalised with respect to the mechanical limit of the injector (850 µm).

The figure shows that the time at which the injector closes depends on the fuel temperature at the injector inlet, as deduced from the experimental measurements. For each injection pressure, it is observed that the needle starts to rise earlier the lower the fuel temperature. In the absence of needle movement and therefore of friction forces acting on the needle, this fact is in agreement with the findings from Figure 6.21 about the pressure in the control volume dropping faster and to a larger extent the lower the fuel temperature. However, the slopes of the curves reveal that the injector opening is slower the lower the fuel temperature. This result is also aligned with the previous findings. Once the needle moves, friction forces proportional to the fuel viscosity appear, opposing this movement. Given the significant increase in fuel viscosity at low temperatures (and especially at high injection pressures, for which Figure 6.23 shows the higher differences in opening slope), this soon results in the needle moving slower for cold conditions. Indeed, it can be seen that once the needle reaches among 5 to 10% of its maximum lift, which takes place at around $t_{aSOE} = 0.4\,\text{ms}$, it has already reached upper positions the higher the fuel temperature.

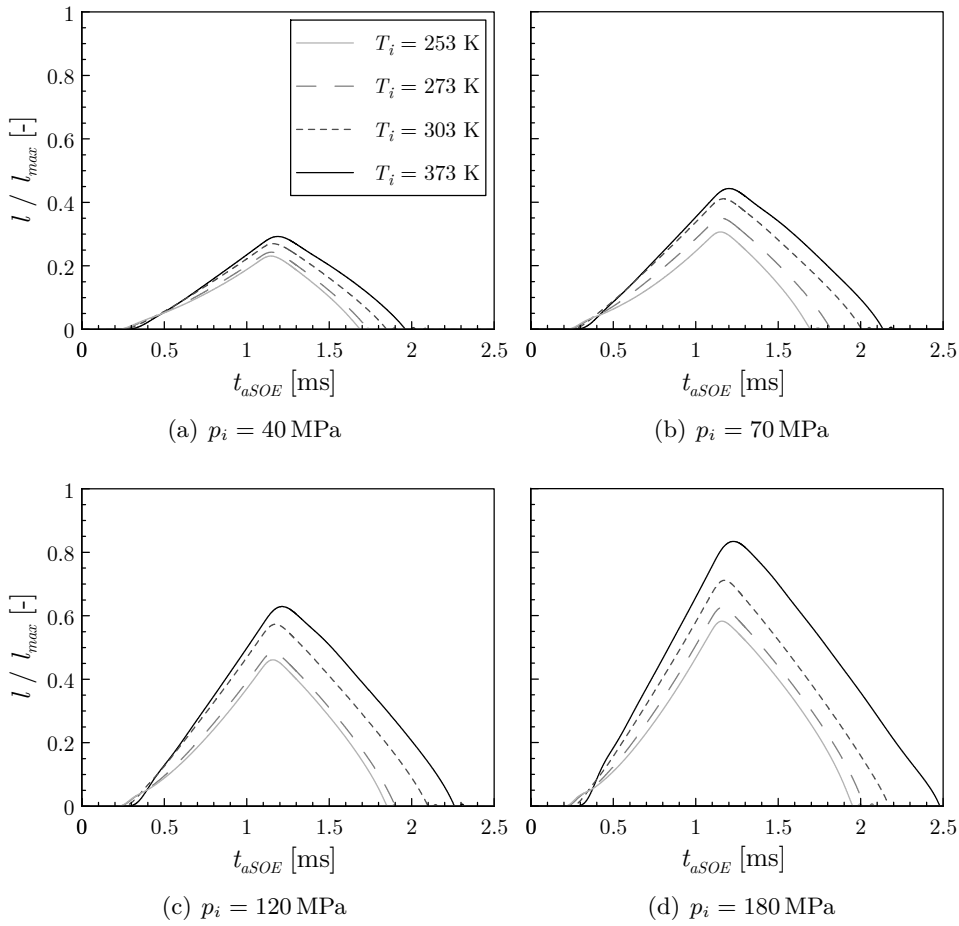

(a) $p_i = 40\,\text{MPa}$ (b) $p_i = 70\,\text{MPa}$

(c) $p_i = 120\,\text{MPa}$ (d) $p_i = 180\,\text{MPa}$

Figure 6.23: Temporal evolution of the needle lift for the operating conditions tested. Values normalized with $l_{max} = 850\,\mu\text{m}$. Results for $T_i = 353\,\text{K}$ are omitted for illustrative purposes. ($ET = 1\,\text{ms}$).

On the other hand, as expected, the effect of the injection pressure on the opening stage is to achieve faster rates. This is explained considering the larger pressure drops achieved in the control volume in absolute terms (Figure 6.21), which generate a higher unbalance among the pressures at the lower and the upper side of the needle.

Figure 6.23 also shows that a slower needle opening results in lower top positions reached by the needle during an injection event. Hence, during the closing stage, the needle falls from these lower positions for low injection

temperatures, which results in shorter times needed for the needle to close against its seat and cut the injection. This confirms the injection duration trends pointed out from the experimental measurements and pointed out in Figure 6.6.

In this regard, it is also interesting to point out that the time at which the top position is reached by the needle in each condition varies depending on the fuel temperature, being achieved later the higher the value of T_i. This finding may be justified in the view of Figure 6.21, where it was observed that the pressure in the control volume was restored more slowly the higher the fuel temperature due to the lower mass flow rates imposed by the lower densities induced.

This reasoning might also be valid to explain the slightly slower closing found for high values of T_i. Once the needle lifts, it reduces the fuel volume at the upper part of the needle. When the needle falls back towards its seat, this volume is increased again. Hence, it needs to be *refilled* with fuel in order to restore the pressure. For high values of T_i, the taller top positions reached by the needle result in a higher volume that needs to be *refilled* during the closing in order to restore the initial pressure. However, these high values of T_i result in lower fuel densities that reduce the mass flow rate employed to that end.

In any case, an acceleration in the needle closing is observed at the end of the injection for most conditions. This acceleration, especially relevant at cold conditions, has also been reported by other authors in the literature. Moon *et al.* [15] observed this increase in needle speed through an X-ray imaging technique, and relate it to the sudden decrease of sac pressure due to flow restriction from the needle at low needle lifts. This phenomenon is known as *throttling* effect of the needle. The higher restriction (i.e. lower effective discharge coefficient) generates a higher pressure drop through the needle seat. Consequently, the sac pressure decreases. This results in an even higher unbalance among the pressure forces at the upper and the lower sides of the needle, abruptly increasing the needle speed. According to Moon *et al.*, this effect is more accused for nozzles with a large number of holes. Wang *et al.* [3] also noticed through ROI measurements that this phenomenon was especially important for cold fuel temperature conditions. They reasoned that the major friction induced by high viscosity could curb the fuel flow generating an even higher pressure drop in the sac.

In order to summarize some of the previous trends and finish explaining the experimentally reported findings about injection duration and total mass

injected per stroke, Figure 6.24 shows the highest position reached by the needle for all the simulated operating conditions.

The expected trends in the view of Figure 6.23 are followed. The needle lifts faster the higher the pressure and the fuel temperature at the injector inlet. The exception to this trend is noticed at low injection pressures ($p_i = 40\,\text{MPa}$ and $p_i = 70\,\text{MPa}$), for which the low fuel temperatures lead to higher lifts reached for the shortest energizing times (ET = 0.25 ms). These points correspond to conditions for which the slower needle velocity expected due to

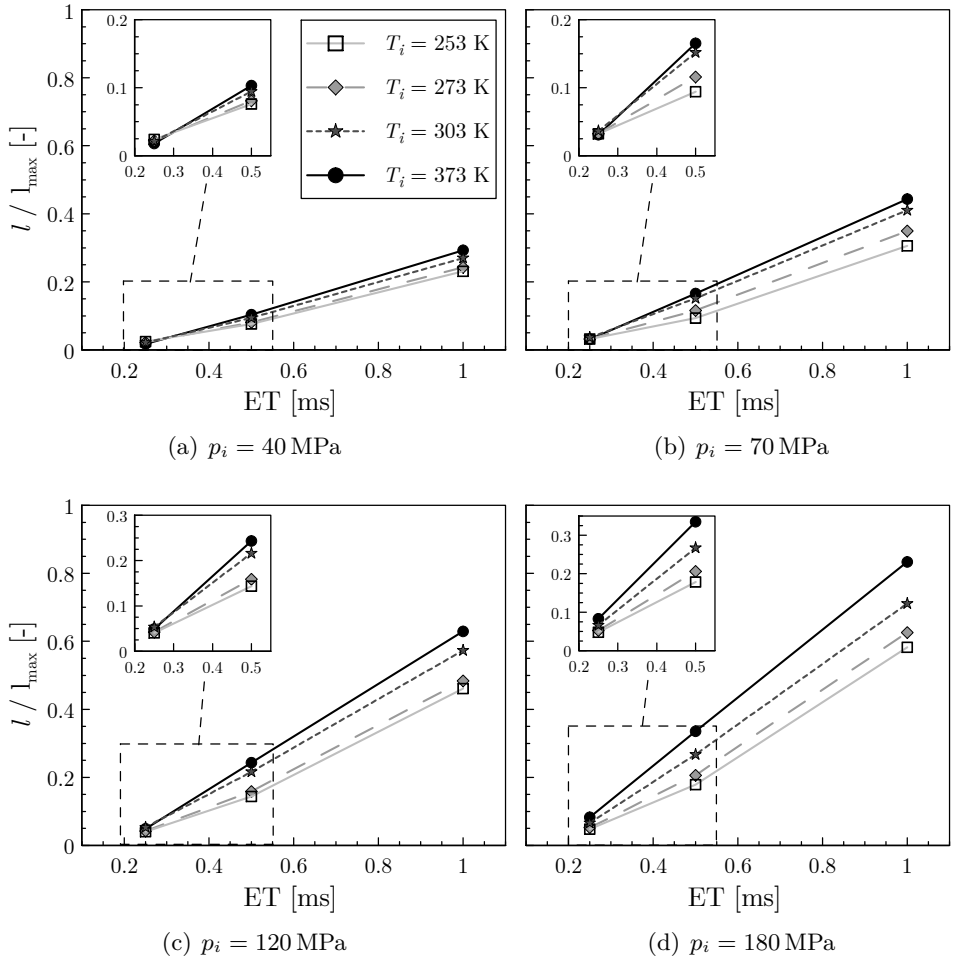

(a) $p_i = 40\,\text{MPa}$ (b) $p_i = 70\,\text{MPa}$

(c) $p_i = 120\,\text{MPa}$ (d) $p_i = 180\,\text{MPa}$

Figure 6.24: Maximum needle lift for the operating conditions tested. Values normalized with $l_{max} = 850\,\mu\text{m}$.

high viscosity at low temperature still does not overcome the faster opening due to the higher pressure unbalance among the upper and the lower sides of the needle generated due to the lower discharge coefficient of the OZ orifice. This explanation also justifies the fact that the maximum needle position achieved is not linear with ET for $T_i = 253\,\mathrm{K}$ and $T_i = 273\,\mathrm{K}$, as opposed to the linear trend observed for $T_i > 303\,\mathrm{K}$.

Another interesting fact that must be commented is that the needle almost reaches its maximum lift for the longest injections of $p_i = 180\,\mathrm{MPa}$ and $T_i = 373\,\mathrm{K}$. In fact, with the observed linear trend with ET, this maximum would be reached for any T_i for values of ET lower than 2 ms. Indeed, these conditions were experimentally tested. This fact would explain the observations concerning injection duration (Figure 6.6) and total mass injected per stroke (Figure 6.7), for which the observed trends with ET were not respected at the highest injection pressure and longest energizing times. If the needle had reached its maximum lift for those conditions, the needle would have fallen from the same position in all cases and the only effect on injection duration would be the one due to the needle closing speed, related to the aforementioned phenomena.

6.3.4 Behaviour under multiple injections

As stated in Section 2.2.1, *common-rail* systems have allowed the introduction of multiple injection strategies, which consist of performing several consecutive injections in one cycle.

The influence of the operating conditions on the hydraulic performance of the Bosch CRI 2.20 injector under multiple strategies is examined in this section by means of the implemented computational model. In order to analyse this influence, several electric dwell times among injections have been tested. The electric dwell time (DT), defined in Figure 6.25, is the temporal separation among the end of the energizing pulse of an injection and the beginning of the pulse of the subsequent injection.

The time needed for the injector to stop delivering fuel once the energizing signal has ended cannot be neglected, especially for a ballistic injector, for which the needle still needs to fall from the position it reached (for instance, Figure 6.6 showed that an ET = 1 ms leads to injection durations of about 2 ms). Hence, if DT is too small, an overlapping among two subsequent injections may take place, preventing them from being splitted. A sample of this statement for several tested conditions is shown in Figures 6.26 (for pilot plus main injection strategies) and 6.27 (for main plus post injection sequences).

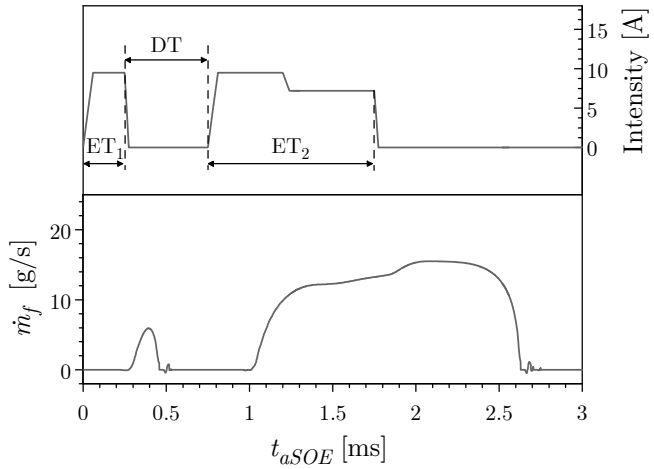

Figure 6.25: Definition of the electric dwell time (DT).

It is therefore interesting to determine the critical dwell time that allows to obtain two separate injections. In the particular case of the Bosch CRI 2.20 injector, an important influence of the pressure and temperature on the highest needle lift achieved (and therefore on the injection duration) has been reported along this chapter. Thus, the injector operating conditions are expected to strongly affect the critical dwell time through fuel properties variations.

In addition, Figures 6.26 and 6.27 show an important influence of the dwell time on the amount of fuel delivered by the second injection, more accused for the main plus post injection case. The pressure wave induced by the opening of the injector for the first injection is responsible for this phenomenon. As seen in Figure 5.32, the pressure at the injector inlet still oscillates once the injector is effectively closed. Similarly, the pressure at the nozzle inlet (volume NV2, see Figure 5.19) takes some time to be stabilized after a given injection. This is exemplified in Figure 6.27, where the temporal evolution of the pressure in the NV2 volume corresponding to the simulation of the single injection case equivalent to the main injection is also represented. Hence, if the injector is reenergized during this period, the new injection will introduce a higher or lower amount of fuel mass than its single injection equivalent depending on the instantaneous value of pressure at the nozzle inlet. The instantaneous pressure unbalance among this volume and the control volume also affects needle opening and injection duration, although it has been checked that the phasing among these signals does not significantly modify the second injection for realistic values of t_{aSOE}.

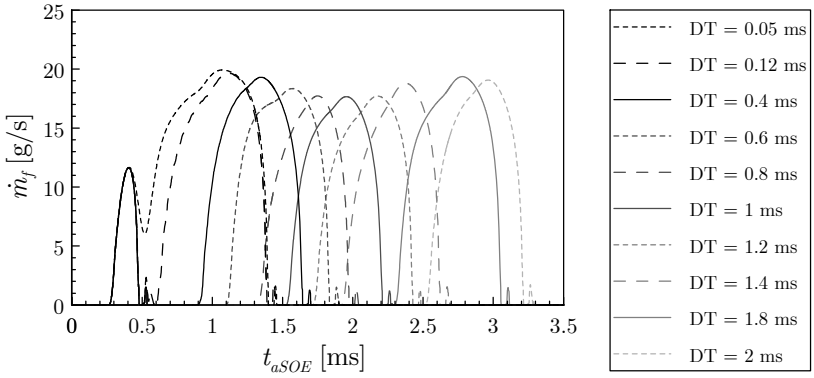

(a) $p_i = 70\,\text{MPa}$, $T_i = 303\,\text{K}$, $ET_1 = 0.25\,\text{ms}$, $ET_2 = 0.5\,\text{ms}$.

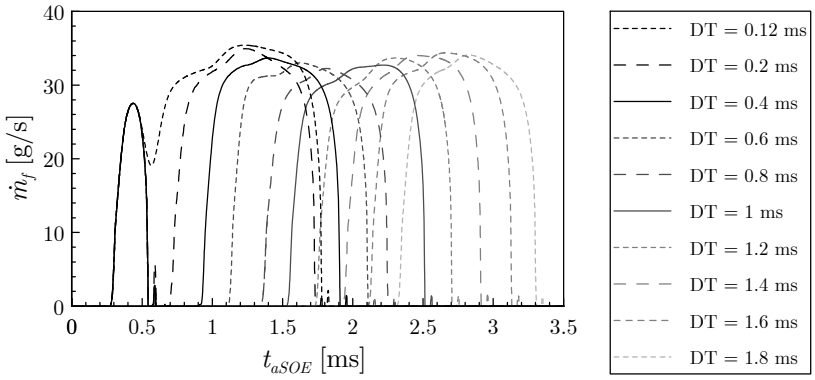

(b) $p_i = 180\,\text{MPa}$, $T_i = 353\,\text{K}$, $ET_1 = 0.25\,\text{ms}$, $ET_2 = 0.5\,\text{ms}$.

Figure 6.26: Modelled injection rate for pilot plus main injection strategies.

As reviewed in Section 3.4, pressure wave propagation is influenced by the fuel speed of sound and bulk modulus. In this way, both the amplitude and period of the pressure oscillations in the NV2 volume will depend on fuel temperature and pressure. Therefore, the injector operating conditions are expected to affect the total mass injected by the second injection as it happened for the critical dwell time.

The influence of the injector operating conditions on the aforementioned features related to multiple injection strategies are analysed next. The injection conditions selected for the study are the same ones that were dealt with for the single injection strategies (Sections 6.3.1 to 6.3.3). Both pilot plus main injection strategies and main plus post injection sequences are analysed.

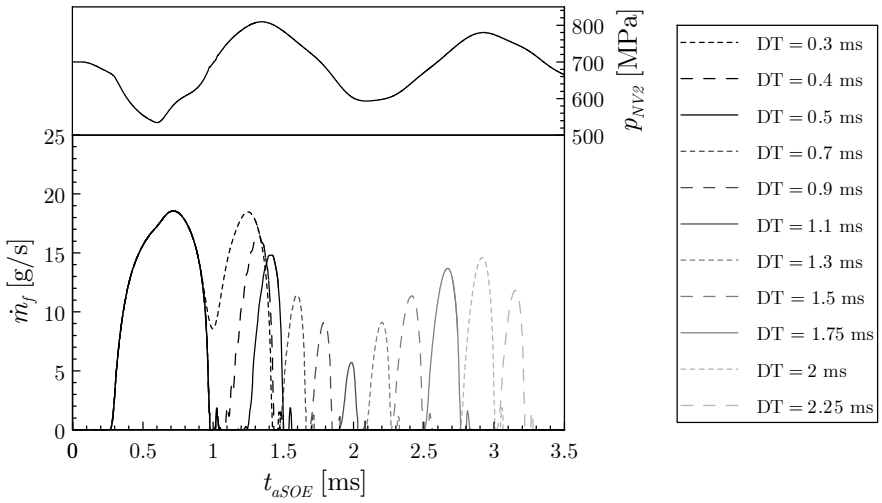

(a) $p_i = 70\,\text{MPa}$, $T_i = 303\,\text{K}$, $ET_1 = 0.5\,\text{ms}$, $ET_2 = 0.25\,\text{ms}$.

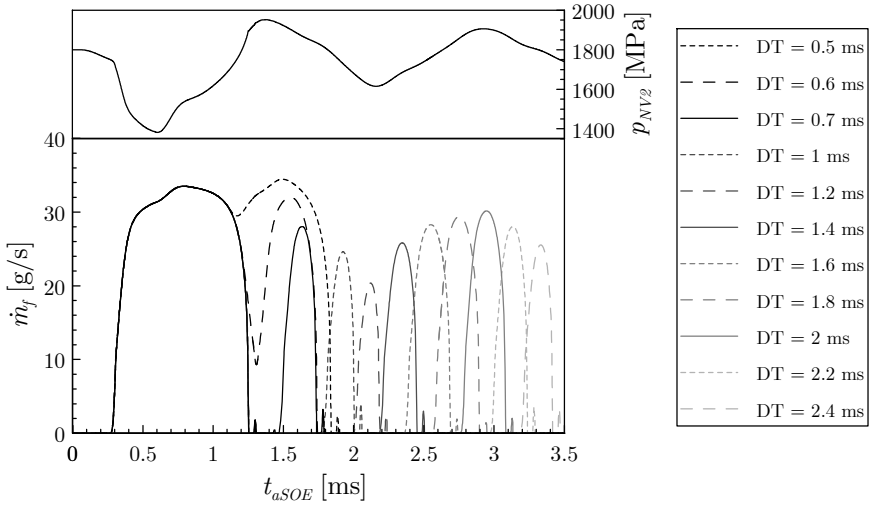

(b) $p_i = 180\,\text{MPa}$, $T_i = 353\,\text{K}$, $ET_1 = 0.5\,\text{ms}$, $ET_2 = 0.25\,\text{ms}$.

Figure 6.27: Modelled injection rate for main plus post injection strategies. The evolution of the pressure in the NV2 volume (upstream of the nozzle orifices) corresponding to the single injection case equivalent to the main injection is also represented.

Influence of the operating conditions on the critical dwell time

The characteristic time at which two desired injections stop being overlapped to be effectively separated has been determined for each of the tested values of fuel temperature at the injector inlet and injection pressure. An ET of 0.5 ms has been considered for the main injection, whereas ET = 0.25 ms has been taken for the secondary one (either pilot or post injection), so that their corresponding single injections modelled were validated against experimental results (Section 5.4).

The information about the critical dwell time is depicted in Figure 6.28 for the pilot plus main injection strategies, both against the injection pressure for all the values of T_i tested and against the fuel temperature at the injector inlet for all the injection pressures tested. As it can be seen, the injector may be reenergized shortly after the first pulse is finished. In general, a larger separation among energizing pulses is required the higher the injection pressure and the higher the fuel temperature.

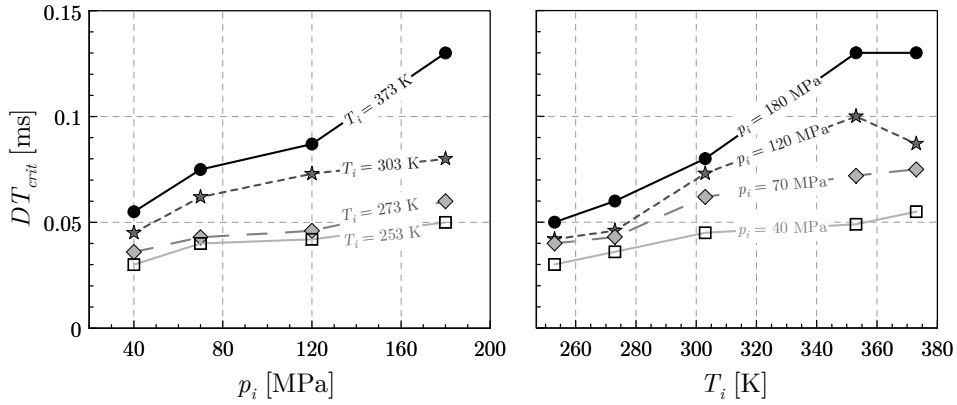

(a) $DT_{crit} = f(p_i)$ (b) $DT_{crit} = f(T_i)$

Figure 6.28: Critical dwell time for the pilot plus main injection strategies. ($ET_1 = 0.25$ ms, $ET_2 = 0.5$ ms).

This result is consistent with the trends in injection duration found experimentally (Figure 6.6). These trends were justified in Section 6.2.3 and confirmed in Section 6.3.3 due to the different upper positions reached by the needle depending on the fuel pressure and temperature, which also result in less time needed for the needle to travel back to its seat. On the one hand, low temperatures induce higher viscosities that result in lower needle velocities

and short top positions reached by it, resulting in a lower injection duration. On the other hand, high pressures for a given fuel temperature lead to a larger pressure unbalance among the upper and the lower sides of the needle, resulting in higher needle velocities and larger injection durations. The injection duration of the first injection directly establishes the critical dwell to separate the next one.

As seen in Figure 6.28, DT_{crit} is not completely linear with pressure and temperature, and the analysed trends are not respected for the whole set of tested conditions. This may be attributed to two minor effects influencing the injector opening of the second injection to a lower extent. On the one hand, the pressure oscillations in several parts of the injector, which may lead to slight variations in the pressure unbalance at both sides of the needle resulting in different injection delays for this second injection. On the other hand, the injector delay itself was reported to decrease the higher the injection pressure and fuel temperature (Figure 6.5). Hence, under these conditions the needle starts moving again earlier for the second injection, needing lower dwell times to get independent injections. This effect of the injection pressure on the critical dwell time is opposed to the one analysed earlier due to its influence on the duration of the first injection.

With regard to the main plus post injection strategies, the analogous results are shown in Figure 6.29. The same trends commented for the pilot plus main injection sequences are observed, since the factors influencing the

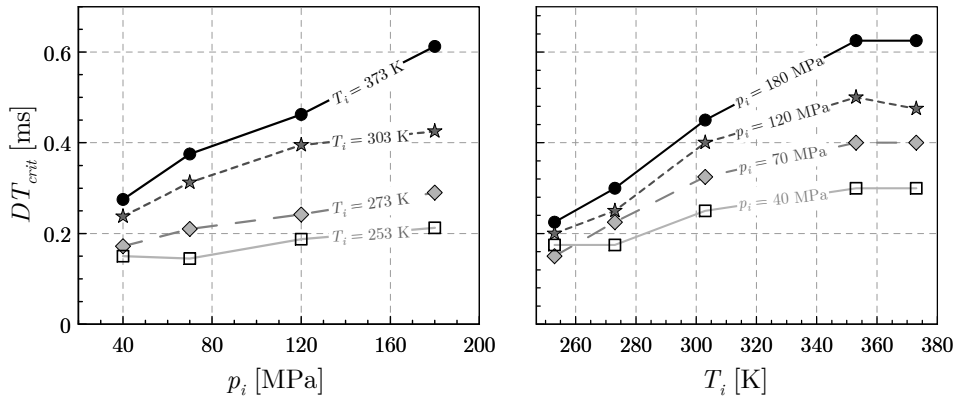

(a) $DT_{crit} = f(p_i)$ (b) $DT_{crit} = f(T_i)$

Figure 6.29: Critical dwell time for the main plus post injection strategies. ($ET_1 = 0.5$ ms, $ET_2 = 0.25$ ms).

process remain the same. However, comparatevely higher values of DT_{crit} are exhibited, due to the virtually linear trend of the duration of the first injection with the energizing time (Figure 6.6). As commented in Section 6.2.3, this trend was observed due to the ballistic nature of the injector, given the upper positions achieved by the needle. This reasoning remains true unless the mechanical limit has already been reached, which is not the case for the values of ET tested.

Influence of the operating conditions on the mass injected by a second injection

As suggested by Figures 6.26 and 6.27, another aspect suitable to be studied is the effect of the first injection on the mass injected by the second injection event. This effect has been quantified for different DT values (higher than DT_{crit}) for each tested condition of pressure and temperature.

The results obtained for the different operating conditions tested for the pilot plus main injection strategies are shown in Figure 6.30. Mass values injected by the main injection are normalised with respect to the ones corresponding to their equivalent single injection cases.

As it can be seen, the mass values are highly influenced for short dwell times in all cases, leading to masses that can even increase in 40% those of the single injection. This result, already observed by Salvador *et al.* [14], is attributed to the pressure overshoot that takes place in the NV2 volume right after the first injection event (as can be observed in Figure 6.27). After a certain value of DT, this influence gets lower, obtaining masses that oscillate from about 80% to 115% of the values corresponding to the single injection. The oscillations depending on DT are induced by the fluctuation of the pressure in the NV2 volume, as explained earlier in the view of Figure 6.27. Hence, the amount of fuel delivered by the main injection may be enhanced or reduced by the effect of the pilot one.

A strong influence of the fuel temperature at the injector inlet is observed on the phasing of the oscillations of the normalised mass with respect to DT. In general, the decrease of the normalised mass with DT takes place at earlier dwell times for the lowest temperatures. This may be attributed to the higher values of fuel speed of sound and bulk modulus observed at these temperatures (Section 4.4), which reduce the period of the pressure fluctuations in the NV2 volume once the injector is closed. On the other hand, comparing Figures 6.30(a) to 6.30(d), the injection pressure does not seem to have such an important influence on the results as the fuel temperature.

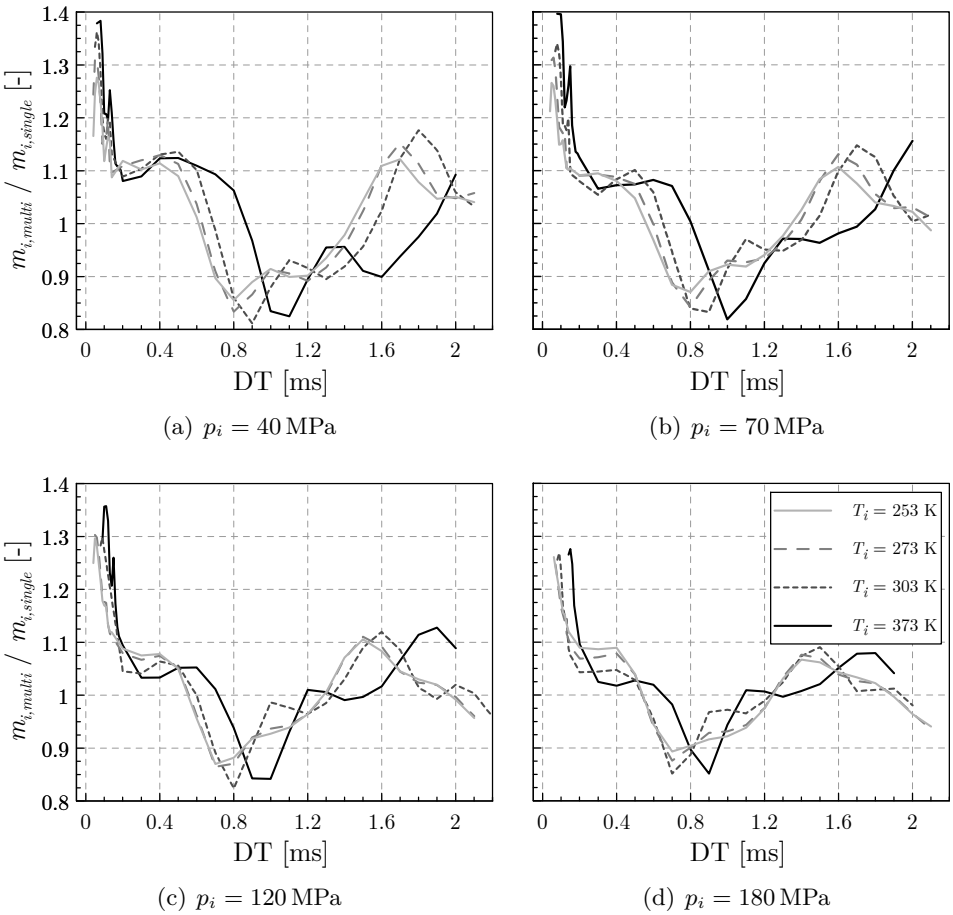

(a) $p_i = 40\,\text{MPa}$ (b) $p_i = 70\,\text{MPa}$

(c) $p_i = 120\,\text{MPa}$ (d) $p_i = 180\,\text{MPa}$

Figure 6.30: Fuel mass injected during the main injection for the operating conditions tested for pilot plus main injection strategies. Values normalized with the mass injected by a single injection equivalent to the main injection. ($ET_1 = 0.25\,\text{ms}$, $ET_2 = 0.5\,\text{ms}$).

It can be observed that the variability of the mass delivered depending on DT seems to be damped the higher the injection pressure and the lower T_i. This influence of the fuel temperature on the variability of mass injected by a second injection was already reported by Wang *et al.* [3], who attributed it to the addition of the effects of shorter injection duration and longer injection delay induced by low temperatures.

Figure 6.31 shows the analogous results for the main plus post injection strategies tested. Similar observations to the ones made for the pilot plus

main injection case may be pointed out, although the relative influence of the interaction among injections is higher, as it was already noticed through Figures 6.26 and 6.27. This is due to the pressure in the NV2 volume being perturbated to a larger extent the longer the first injection. Hence, masses almost 400% higher than the analogous ones for single injections may be delivered by the post injection, whereas the variability of the mass delivered depending on DT after this initial peak ranges from 10% to 200%.

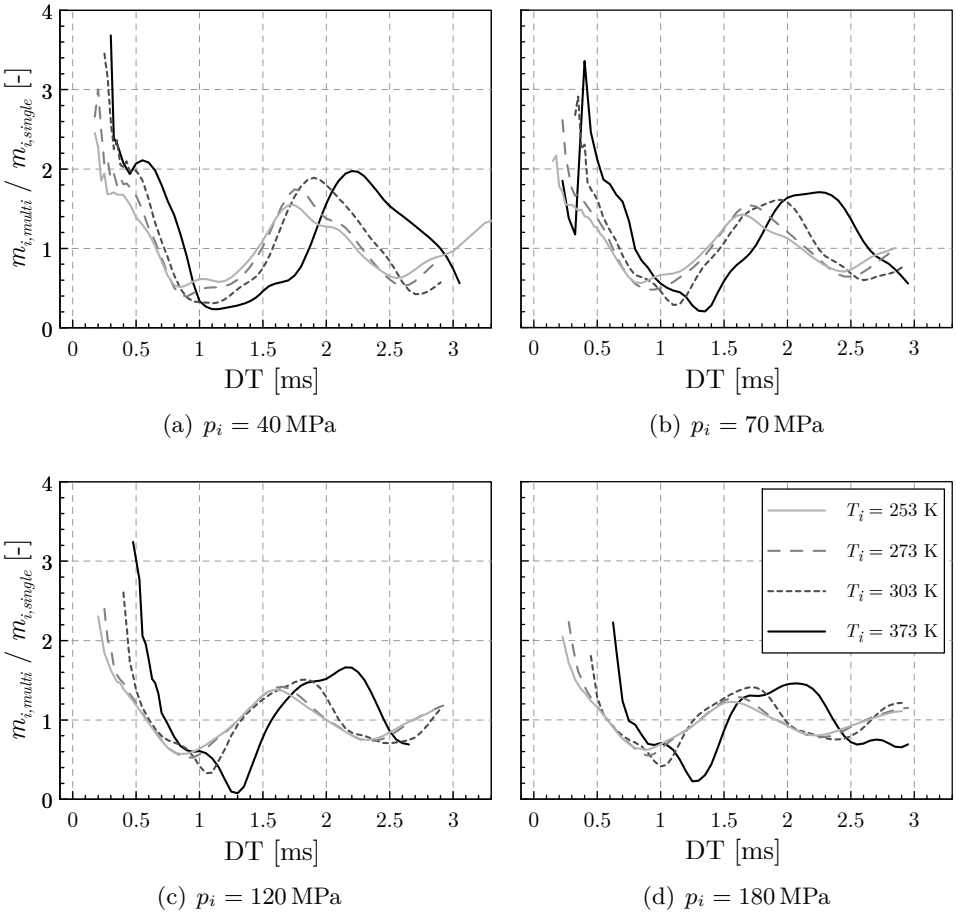

(a) $p_i = 40\,\mathrm{MPa}$ (b) $p_i = 70\,\mathrm{MPa}$

(c) $p_i = 120\,\mathrm{MPa}$ (d) $p_i = 180\,\mathrm{MPa}$

Figure 6.31: Fuel mass injected during the post injection for the operating conditions tested for main plus post injection strategies. Values normalized with the mass injected by a single injection equivalent to the post injection. ($ET_1 = 0.5\,\mathrm{ms}$, $ET_2 = 0.25\,\mathrm{ms}$).

References

[1] KEGL, B. and HRIBERNIK, A. "Experimental Analysis of Injection Characteristics Using Biodiesel Fuel". *Energy & Fuels*, vol. 20.5 (2006), pp. 2239–2248. ISSN: 0887-0624. DOI: 10.1021/ef060285m.

[2] PARK, Y. et al. "Effects of diesel fuel temperature on fuel flow and spray characteristics". *Fuel*, vol. 162 (2015), pp. 1–7. ISSN: 00162361. DOI: 10.1016/j.fuel.2015.09.008.

[3] WANG, Z., DING, H., WYSZYNSKI, M. L., TIAN, J., and XU, H. "Experimental study on diesel fuel injection characteristics under cold start conditions with single and split injection strategies". *Fuel Processing Technology*, vol. 131 (2015), pp. 213–222. ISSN: 03783820. DOI: 10.1016/j.fuproc.2014.10.003.

[4] PAYRI, R., SALVADOR, F., GIMENO, J., and NOVELLA, R. "Flow regime effects on non-cavitating injection nozzles over spray behavior". *International Journal of Heat and Fluid Flow*, vol. 32.1 (2011), pp. 273–284. ISSN: 0142727X. DOI: 10.1016/j.ijheatfluidflow.2010.10.001.

[5] PAYRI, R., SALVADOR, F. J., GIMENO, J., and GARCIA, A. "Flow regime effects over non-cavitating diesel injection nozzles". *Proceedings of the Institution of Mechanical Engineers, Part D: Journal of Automobile Engineering*, vol. 226.1 (2012), pp. 133–144. ISSN: 0954-4070. DOI: 10.1177/0954407011413056.

[6] DERNOTTE, J., HESPEL, C., FOUCHER, F., HOUILLÉ, S., and MOUNAÏM-ROUSSELLE, C. "Influence of physical fuel properties on the injection rate in a Diesel injector". *Fuel*, vol. 96 (2012), pp. 153–160. ISSN: 00162361. DOI: 10.1016/j.fuel.2011.11.073.

[7] DERNOTTE, J. et al. "Experimental Study of the Influence of Fuel Properties on the Diesel Injection Process in Non-Vaporizing Conditions". *ILASS - Europe 2011, 24th European Conference on Liquid Atomization and Spray Systems*. Estoril, Portugal, 2011, pp. 1–10.

[8] DERNOTTE, J., HESPEL, C., HOUILLE, S., FOUCHER, F., and MOUNAIM-ROUSSELLE, C. "Influence of Fuel Properties on the Diesel Injection Process in Nonvaporizing Conditions". *Atomization And Sprays*, vol. 22.6 (2012), pp. 461–492. ISSN: 1044-5110. DOI: 10.1615/AtomizSpr.2012004401.

[9] Armas, O., Martínez-Martínez, S., Mata, C., and Pacheco, C. "Alternative method for bulk modulus estimation of Diesel fuels". *Fuel*, vol. 167 (2016), pp. 199–207. issn: 00162361. doi: 10.1016/j.fuel.2015.11.067.

[10] Strotos, G., Koukouvinis, P., Theodorakakos, A., and Wang, L. "Fuel heating in high pressure diesel nozzles". *THIESEL 2014 Conference on Thermo- and Fluid Dynamic Processes in Direct Injection Engines*. Valencia, Spain, 2014.

[11] Strotos, G., Koukouvinis, P., Theodorakakos, A., Gavaises, M., and Bergeles, G. "Transient heating effects in high pressure Diesel injector nozzles". *International Journal of Heat and Fluid Flow*, vol. 51 (2015), pp. 257–267. issn: 0142727X. doi: 10.1016/j.ijheatfluidflow.2014.10.010.

[12] Payri, R., Salvador, F. J., Gimeno, J., and Bracho, G. "Effect of fuel properties on diesel spray development in extreme cold conditions". *Proceedings of the Institution of Mechanical Engineers. Part D, Journal of Automobile Engineering*, vol. 222.9 (2008), pp. 1743–1753. issn: 0954-4070. doi: 10.1243/09544070JAUTO844.

[13] Payri, R., Salvador, F. J., Gimeno, J., and Bracho, G. "Understanding Diesel Injection Characteristics in Winter Conditions". *SAE Technical Paper 2009-01-0836* (2009). doi: 10.4271/2009-01-0836.

[14] Salvador, F. J., Gimeno, J., De la Morena, J., and Carreres, M. "Using one-dimensional modeling to analyze the influence of the use of biodiesels on the dynamic behavior of solenoid-operated injectors in common rail systems: Results of the simulations and discussion". *Energy Conversion and Management*, vol. 54.1 (2012), pp. 122–132. issn: 01968904. doi: 10.1016/j.enconman.2011.10.007.

[15] Moon, S. et al. "Effect of the number and position of nozzle holes on in- and near-nozzle dynamic characteristics of diesel injection". *Fuel*, vol. 150 (2015), pp. 112–122. issn: 00162361. doi: 10.1016/j.fuel.2015.01.097.

Chapter 7

Conclusions and future works

7.1 Conclusions

The influence of the thermal effects on the performance of a *common-rail* diesel injector has been investigated along this thesis through a combined experimental and computational approach. Experiments were carried out in different facilities, not only to directly evaluate the injector behaviour, but also to provide a strong basis to implement and validate a 1D computational model of the injector that could serve to the purpose of getting a deeper insight into the studied topic. While the purely experimental approach only allows to collect data downstream of the injector, the model makes it possible to analyse its internal features to confirm and extend the findings gathered from the experiments.

The main objectives that were summarized to give answer to the problem included: the estimation of the fuel temperature variations along the injector, the determination of the influence of those variations on the fuel thermodynamic properties relevant to the injection process, and their induced effects on injector dynamics and injection rate shaping.

In order to decide the logical steps that needed to be taken to give answer to these objectives, a literature review was carried out first. A view to the state of the art would ensure a proper approach to the problem by identifying the relevant phenomena that should be accounted for. In addition, results reported by other authors would provide a reasonable basis for comparison

with the ones derived from the present thesis. The following conclusions could be extracted as a result from this literature review:

- The most relevant fuel properties for the diesel injection process are the speed of sound, density, bulk modulus and viscosity.
- It is possible to experimentally determine the significant variation of the aforementioned properties within the range of pressure and temperature conditions relevant for *common-rail* injection systems.
- Many authors reported the strong influence of these properties on both the internal flow (rate of injection, momentum flux, cavitation pattern and appearance, injection delay and duration) and spray development (spray penetration, spreading angle, droplet size and liquid core length), especially at very low temperatures.
- Despite this important influence, most modellers assume the flow inside the injector as isothermal. Only a few researchers have implemented a local variation of the fuel temperature and pressure inside the injector, treating the flow as adiabatic.
- None of the authors that introduced the adiabatic hypothesis for the injector internal flow paid attention to the limits of the validity of this assumption.

Once the literature review was carried out, and given the strong influence of the fuel properties on the injection rate and injector dynamics, it was clear that the computational approach would require the introduction of local variations of fuel temperature and pressure inside the injector. Moreover, in the case of injector dynamics, the extent of the influence of the fuel properties (especially fuel viscosity) also depends on the injector technology. Given the ballistic nature of the injector of study (Bosch CRI 2.20), these effects were expected to be magnified. In order to ensure the applicability of the model, in addition, an assessment of the extension of the validity of the assumption of adiabatic flow inside the injector should also be performed.

The methodology followed in this thesis to give answer to the objectives must then be highlighted, given the high experimental load needed both to gather results and to ensure a proper implementation of a model able to locally modify the fuel pressure and temperature and take into account their effect on the fuel properties. In this regard, this thesis benefited from the application of several experimental techniques:

- A dimensional characterization of the injector by means of silicone moulds of its internal ducts and orifices, visualized thanks to optical and scanning electron microscopes.

- A hydraulic characterization of the injector internal orifices, both in terms of their mass flow rate capabilities and the quantification of the temperature increase across them. This characterization, carried out thanks to an experimental facility that allowed to establish continuous flow across the orifices, offered a strong basis to implement the computational model and to validate the hypothesis of adiabatic flow.
- A hydraulic characterization of the injector as a whole by means of an IRDCI, which allowed to obtain the ROI curves under a wide range of operating conditions, including cold start (injection pressures from 40 MPa to 180 MPa, fuel temperatures at the injector inlet from 253 K to 373 K and energizing times from 0.25 ms to 2 ms). Special attention had to be given to the fuel temperature control thanks to a setup that included the use of a climatic chamber and injector holder cooling. The results from these experiments were not only profitable for the study itself, but also for the validation of the 1D model.
- A characterization of the relevant fuel thermodynamic properties (namely speed of sound, density and bulk modulus) at high pressure, thanks to a speed of sound measurement facility that made use of the propagation of a pressure wave along a *common-rail* system. Again, the fuel temperature was carefully controlled in order to obtain a wide set of results of use for the injector relevant conditions. Fuel viscosity was measured at ambient pressure and estimated at high pressure through a correlation from the literature.

Results from the ROI measurements already allowed to extract useful information about the influence of the fuel temperature on the injector performance, both in terms of steady-state mass flow injected and injector dynamics:

- The steady-state mass flow rate increases almost linearly with the square root of the pressure drop, since the nozzle orifices do not cavitate. At low injection pressures (40 MPa), it increases with the fuel temperature, although differences among temperatures do not seem to be relevant at higher injection pressures. This is due to the opposed influence of the two main parameters through which temperature and pressure influence the steady-state mass flow, namely fuel density and flow regime. The former decreases the higher the fuel temperature, whereas low values of Re (favoured by low fuel temperatures) induce the laminar flow regime reducing the discharge coefficient.
- No significant influence of the fuel temperature at the injector inlet on the injector opening slope has been noticed, although a higher injection delay was found the lower the fuel temperature. This influence is more

important at low injection pressures. This result is explained considering that there are two different factors driving the needle: the pressure unbalance among its upper and lower sides and the friction forces induced by fuel viscosity, which is more important the lower the fuel temperature. Needle opening is governed by the former factor at high pressures, whereas the viscous forces gain importance at low injection pressures.

- The injection duration is importantly reduced the lower the fuel temperature at the injector inlet. This is the most remarkable effect of the fuel temperature on the ROI curves of the Bosch CRI 2.20 injector, which is explained due to its ballistic nature. Fuel viscosity decreases with fuel temperature, resulting in a lower friction among fuel and needle during the injector opening. This, in turn, results in higher top positions being reached by the needle the higher the fuel temperature. Hence, during closing, the needle falls from an upper position, leading to a higher time for the needle to close against its seat.
- The effect of fuel temperature on the closing slope seems almost negligible, reinforcing the previous effect.
- The important differences in injection duration depending on the operating condition also result in important deviations among total mass injected into the cylinder during an injection event.

The experimental measurements carried out for this thesis also allowed to implement the injector computational model. The AMESim commercial platform, based on the Bond Graph technique, was utilized to this end. The main features of the model include:

- Local variations of the fuel pressure and temperature along the injector. The hypothesis of adiabatic flow was assumed to this end, and implemented thanks to the experimental characterization of the fuel at high pressure.
- Local variations of the flow regime across the injector internal orifices. In this sense, the discharge coefficient of each hydraulic restriction was determined depending on the theoretical Reynolds number set at each time step.
- Prediction of the appearance of cavitation inside the orifices, including its associated losses.
- Elastic deformation of the injector movable elements, key in order to predict the injector hydraulic delay (time lapse among the start of energizing and effective start of injection).

- Pressure wave propagation along the injector internal ducts, including the associated attenuation by friction. This feature allowed the possibility of simulating multiple injection strategies.

The validity of this model was tested against the previous experimental results for their wide range of operating conditions. This validation was not only performed in terms of ROI adequacy, but also in terms of individual behaviour of the orifices and pressure wave propagation. Special attention was given to the assessment of the extension of the validity of the assumption of adiabatic flow inside the injector during an injection event. In this regard, a dimensionless parameter (Ad) was derived establishing the temperature difference needed among the internal duct wall and the fuel in order for the fuel to increase its temperature in 1 K at the channel outlet. Thus, high values of Ad are expected to hinder any heat exchange processes. About this parameter:

- Ad may be expressed in terms of other dimensionless groups, namely the length-to-diameter ratio and St, which in turn may be expressed as a function of Pr, Re and Nu. This last dimensionless number was estimated through available correlations that relate it to Pr and Re.
- Through this parameter, it was deduced that heat exchange to the surroundings is theoretically minimised the lower the length-to-diameter ratio and the higher Re and Pr, this last group strictly depending on the fuel. Therefore, the ability of the injector to exchange heat with the surroundings during an injection event exclusively depends on its internal geometry and the operating conditions.
- The dependency of the heat transfer features on Re may be explained through the flow regime. High pressure drops lead to high velocities that result in less time available for heat transfer to take place. However, low pressure drops establish a laminar flow regime that favours viscous dissipation, reducing the flow velocity close to the wall and favouring heat exchange. Similarly, low diameters may induce low values of Re resulting in laminar flow and a higher portion of the flow being affected by the boundary layer.
- The injector internal hydraulic restrictions generate important pressure drops and are responsible for driving the flow. Hence, the proneness of the injector to exchange heat with the surroundings could be assessed by evaluating the Ad parameter for the conditions experimentally tested during the hydraulic characterization of the orifices under continuous flow. The three control orifices of the Denso G4S injector were also tested in order to provide a larger set of results for comparison.

- It was found that values of Ad higher than 4 lead to the experimentally observed temperature changes across the orifices departing less than 10% from the theoretical predictions performed under the assumption of adiabatic flow. Hence, for combinations of orifice geometry and pressure drops across the orifices (established by the injector operating conditions) leading to these values of Ad, the hypothesis of adiabatic flow leads to accurate enough results for engineering purposes.
- In the particular case of the Bosch CRI 2.20 injector, its orifices induce high values of Ad except for low pressure drops, which are not representative of the usual operation of the injector. Therefore, any temperature variation in the flow due to its internal evolution can be assumed to remain within the fluid. This is not the case of the Denso G4S injector, for which a given orifice leads to low values of Ad regardless of the operating conditions.
- The trends reported for non-cavitating conditions have not been found if cavitation takes place along the orifices. The changes in convective heat transfer coefficient induced by the presence of vapour bubbles difficult the analysis in these conditions.

The Ad parameter was found useful to quantify the proneness of the injector to exchange heat with the ambient during an injection event. Comparisons with the experiments were based on measurements in continuous flow that favoured the establishment of similar temperatures at the wall and the fuel, hindering the heat transfer process.

However, injection in a real engine is performed in a pulsed manner and may be regarded to as a highly transient phenomenon. During the time lapse among injections, the fuel remains at rest and heat exchange could become significant, especially taking into account that an important temperature difference may be established among the fuel and the injector walls. An analysis about the limits of the extension of the assumption of adiabatic flow taking into account these considerations was also performed. To this end, the ratio t_{Ad} among the fuel residence time in the injector and the characteristic time of heat transfer due to conduction from the injector walls was assessed. In this regard:

- For low engine speed and low load, the fuel residence time within the injector is of the same order of the characteristic time of heat transfer to the surroundings by conduction. In this condition, the fuel temperature inside the injector has enough time to get close to the injector wall temperature prior to each injection event, departing from the fuel temperature at the injector inlet. During a given injection, since the wall

temperature and the fluid temperature are already close to each other, the considerations given about the *Ad* number are valid.

- For the rest of engine-like conditions, the fuel residence times within the injector are an order of magnitude lower than the characteristic times of heat transfer. Therefore, the time among injections is not enough for the fuel to completely acquire the temperature of the injector walls. Heat transfer still may slightly modify the fuel temperature before an injection event, whereas the relative importance of heat transfer during the injection depends on *Ad*.
- Concerning ROI measurements such as the ones conducted as a basis for this investigation, the assumption of adiabatic flow is not compromised as long as they are carried out in a controlled environment in which the fuel temperature at the injector inlet and the injector holder temperature are forced to match each other. Otherwise, heat transfer may be relevant during the time lapse among injections depending on the injection frequency. In any case, its importance during the injection event depends on the *Ad* parameter.

Once the validity of the predictions of the computational model was ensured for the particular case of study, its results could be used in combination with the ones from the experimental ROI measurements in order to quantify the importance of the thermal effects on the injector hydraulic behaviour. The first results that were analysed correspond to the fuel temperature variations along the injector. In this regard:

- In the case of the control orifices, the adiabatic assumption allowed to treat the flow as isenthalpic. For this reason, it was proved that the fuel warms upon expansion across these orifices. This increase is more important the higher the injection pressure due to the larger absolute pressure drops established.
- Concerning the inlet orifice (OZ), temperature variations up to 18 K were found for the operating conditions tested. The magnitude of the temperature increase is higher for low values of fuel temperature at the injector inlet. This behaviour was attributed to two main reasons. On the one hand, the isenthalpic lines of the fuel enthalpy map (which represents the fuel enthalpy as a function of temperature and pressure) are not completely parallel, being more abrupt the higher the fuel temperature. On the other hand, the laminar flow regime is established at low temperatures due to the higher viscosities associated.
- With regard to the outlet orifice (OA), the temperature rise is more important than the one found for the inlet orifice (OZ), increasing up

to 42 K. This was justified given the larger pressure drops established across this orifice for the injector operating conditions, since the fuel is discharged from the control volume to the return side of the injector, which does not have any comparable restriction. In this case, as opposed to what was stated about the OZ orifice, the fuel temperature at the injector inlet does not importantly affect the temperature rise across the orifice for a given pressure. This could be explained since all the operating conditions induce cavitation in the orifice due to the large pressure drops across it. No important differences in terms of discharge coefficient were found in this orifice once cavitation appears.

- A relatively important temperature increase (up to 14 K for the highest pressure and lowest temperature tested) takes place in the nozzle feeding line due to the restriction generated by the needle flaps, which induces important pressure losses.
- As far as the nozzle orifices are concerned, the flow cannot be regarded to as isenthalpic due to the important velocity variations along it. In this case, the stagnation enthalpy can be assumed to be preserved during the expansion. Thus, the specific enthalpy loss associated to the velocity increase may be estimated as a function of the discharge coefficient. This hypothesis, however, does not hold during the opening and closing transient stages of the injection, since an external mechanical work exerted by the needle could be relevant. Anyway, it was observed that the fuel heats along the nozzle during the transient stages of the process, whereas it may be heated or subcooled during the steady-state stage depending on the discharge coefficient achieved (i.e. flow regime).
- Specifically, it was observed that, from a given fuel temperature at the injector inlet among 273 K and 303 K, the fuel stops being heated along the nozzle during the steady-state stage and starts being cooled instead. The magnitude of this cooling is only about 5 K regardless of the injection pressure, since the turbulent regime is already achieved. This result, together with the heating appearing in the nozzle feeding line, makes it possible to conclude that the fuel does not significantly change its temperature from the injector inlet to the nozzle outlet in these conditions. In colder conditions, however, the fuel is heated due to the low discharge coefficients associated to the higher viscosities induced. In this case, the heating is more important the higher the injection pressure, since pressure further increases the fuel viscosity reducing Re and, consequently, the orifices discharge coefficient. A heating of 34 K was reported in the most extreme conditions tested (253 K and 180 MPa).

These temperature variations along the injector, in turn, affect the flow regime established across each of the hydraulic restrictions, which was also analysed in order to explain the injector dynamics behaviour. In this regard:

- Needle dynamics is influenced by the pressure unbalance established among its upper and its lower side once the injector is energized. For a given injection pressure, the depression generated in the control volume during the opening stage occurs earlier and achieves a greater magnitude the lower the fuel temperature, since the laminar or the transitional regime are established across the OZ orifice. This results in a lower discharge coefficient that generates higher pressure losses across the orifice, further reducing the pressure in the control volume. The influence of the OA orifice is not as significant due to the fact that cavitation appears for all the injector operating conditions.
- Once the needle starts moving, its lifting velocity not only depends on the pressure unbalance at both sides of the needle, but also on the viscous friction opposing the needle movement. This effect is more important the lower the fuel temperature, due to the important increase in viscosity.
- If it were only for the pressure unbalance at both sides of the needle, it would rise earlier the lower the fuel temperature at the injector inlet. Indeed, this has been observed from the simulated needle lift law. However, once the needle starts moving, the viscous forces gain relevance and the opening slope gets slower. Early after the opening (once the needle reaches among 5% to 10% of its maximum mechanical lift), the needle has already reached upper positions the higher the fuel temperature. This allows to explain the observed differences in injector duration reported from the ROI measurements.

The proper reproduction of the pressure propagation by the model also allowed to study the injector behaviour under multiple injections. In this regard:

- Fuel properties influence the critical dwell time that allows to totally separate two subsequent injections. In general, this time is higher the higher the fuel temperature and the injection pressure. This result is related to the previously mentioned effects of the fuel temperature and pressure on the injection duration, since the needle falls from an upper position in these conditions, needing more time to close against its seat after the electrovalve stops being energized.
- The timing among injections affects the total mass injected by the second injection in a different way depending on the injection pressure and the

fuel temperature at the injector inlet, due to the different induced values of speed of sound and bulk modulus. In addition, the variability in fuel mass injected depending on the dwell time is more accused the lower the fuel temperature.

- The interaction among injections is higher the longer the energizing time of the first injection, due to the higher pressure perturbation induced. Hence, the effect of the fuel properties on multiple injections behaviour is more important for main plus post injection strategies than for pilot plus main injection sequences.

7.2 Future works

Along the present thesis, the flow inside the *common-rail* injector has been exhaustively analysed by means of a combined experimental and computational approach. The development of a model that considers local variations of pressure and temperature along the injector and the analysis of its implications on the injector internal flow represents a contribution to the field. However, certain questions still remain open and should be further investigated in order to gain a better understanding of the injection phenomenon.

On the one hand, from the experimental point of view, some additional tasks would help to shed more light on the topic:

- Measurement of fuel viscosity at high pressure. Even though the fuel speed of sound, density and bulk modulus were determined at high pressure through an experimental procedure, the fuel viscosity was only measured at atmospheric pressure, using an existing correlation to estimate its variation with pressure. Indeed, a falling body viscometer was designed and built as part of the present thesis, although it could not be used due to current technological limitations. Fuel viscosity has proved to be an especially relevant property for the injector operation. A more accurate estimation would in turn improve the accuracy of the flow regime calculations and the model predictions concerning injector dynamics.
- Characterization of other relevant fuel properties. The experimental fuel characterization carried out in this thesis comprised the fuel properties more relevant for the injection process. Although to a lower extent, some other properties influence the topics dealt with in the present thesis, namely the specific heat capacities or the thermal conductivity. Were needed in the present work, values corresponding to similar fuels were used. This included the derivation of the fuel density at high pressure

or the estimation of the Ad parameter. The measurement of the specific fuel used for the investigation would undoubtedly improve the accuracy of the results.

- Study of the influence of cavitation on the assumption of adiabatic flow. The Ad parameter derived in the present thesis depends on the convective heat transfer coefficient, which varies depending on the intensity of cavitation. The inclusion of this variation could extend the conclusions about the validity of the assumption of adiabatic flow to cavitating conditions and would allow a deeper understanding of its significance.
- Characterization of the spray for the operating conditions considered in this work. It would help to understand the significance of the effects discussed in this thesis on the air-fuel mixing and combustion processes. This would give an idea of the range of variation of the engine performance, noise and emissions depending on the fuel temperature at the injector inlet.

On the other hand, from the computational point of view, the following tasks are proposed:

- Inclusion of heat transfer capabilities in the model. Even though the assumption of adiabatic flow seems to be reliable for the case of study, it is not completely applicable to some engine-like conditions, since heat transfer may be relevant during the time lapse among injections. Fuel temperature variations associated to this stage could be taken into account to completely extend the validity of this model to real conditions.
- Coupling the 1D model with a 3D CFD tool for internal nozzle flow simulation with the adiabatic assumption. The results of this thesis allow to provide boundary conditions for this kind of simulation, including needle lift laws and values of temperature and pressure (including its oscillations) at the nozzle inlet. Indeed, a bidirectional coupling would allow to further improve the accuracy of the 1D model. The fulfillment of this task would provide the three-dimensional flow pattern along the nozzle, including the velocity and temperature profile. These results, in turn, could be useful to understand the spray development.
- Coupling the injector flow model with a spray model. Again, the present work constitutes a good basis to supply proper boundary conditions for spray simulation, including the mass flow and fuel temperature at the nozzle outlet. As it has been commented for the experimental spray visualization, this task would provide a clear understanding of the implications of the topics dealt with in the present study.

Additionally, it must also be noted that this study approached the particular problem of the Bosch CRI 2.20 injector, which is a solenoid-actuated injector of ballistic nature. It would be interesting to conduct a similar study concerning other kinds of injector, in order to assess and compare the relative importance of the thermal effects on the injection process depending on the injector technology.

Bibliography

Adler, U. and Bauer, H. *Automotive Handbook*. 3rd ed. Stuttgart: Robert Bosch GmbH, 1995. ISBN: 1-56091-918-3, (*cited on: Chap.5-p.190*).

Agarwal, A. K. et al. "Effect of fuel injection pressure and injection timing of Karanja biodiesel blends on fuel spray, engine performance, emissions and combustion characteristics". *Energy Conversion and Management*, vol. 91 (2015), pp. 302–314. ISSN: 01968904. DOI: 10.1016/j.enconman.2014.12.004, (*cited on: Chap.1-p.2, Chap.3-pp.107,110,111,112*).

Alliévi, L. and Dubs, R. *Allgemeine Theorie über die veränderliche Bewegung des Wassers in Leitungen*. Ed. by R. Dubs and V. Bataillard. Berlin, Heidelberg: Springer Berlin Heidelberg, 1909. ISBN: 978-3-642-51953-6. DOI: 10.1007/978-3-642-52015-0, (*cited on: Chap.3-p.85*).

Altieri, L. and Tonoli, A. "Piezoelectric Injectors for Automotive Applications: Modeling and Experimental Validation of Hysteretic Behavior and Temperature Effects". *Journal of Dynamic Systems, Measurement, and Control*, vol. 135.1 (2012), p. 011005. ISSN: 0022-0434. DOI: 10.1115/1.4006627, (*cited on: Chap.2-p.25, Chap.3-p.95*).

Amoia, V., Ficarella, A., and Laforgia, D. "A Theoretical Code to Simulate the Behavior of an Electro-injector for Diesel Engines and Parametric Analysis". *SAE Technical Paper 970349* (1997). DOI: 10.4271/970349, (*cited on: Chap.3-pp.90,93*).

Appeldoorn, J. K. "A Simplified Viscosity-Pressure-Temperature Equation". *SAE Paper 630139* (1963). DOI: 10.4271/630139, (*cited on: Chap.3-p.105*).

Aquing, M. et al. "Composition analysis and viscosity prediction of complex fuel mixtures using a molecular-based approach". *Energy & Fuels*, vol. 26.4 (2012), pp. 2220–2230. issn: 08870624. doi: 10.1021/ef300106z, (*cited on: Chap.3-pp.99,104*).

Arai, M., Tabata, M., Hiroyasu, H., and Shimizu, M. "Disintegrating Process and Spray Characterization of Fuel Jet Injected by a Diesel Nozzle". *SAE Technical Paper 840275* (1984). doi: 10.4271/840275, (*cited on: Chap.2-p.63*).

Arai, M., Shimizu, M., and Hiroyasu, H. "Similarity between the breakup lengths of a high speed liquid jet in atmospheric and pressurized conditions". *In ICLASS-91, Gaithersburg, Maryland.* 1991, (*cited on: Chap.2-p.59*).

Arcoumanis, C., Badami, M., Flora, H., and Gavaises, M. "Cavitation in real-size multi-hole Diesel injector nozzles". *SAE Technical Paper 2000-01-1249* (2000). doi: 10.4271/2000-01-1249, (*cited on: Chap.1-p.2, Chap.2-p.44*).

Arcoumanis, C. and Fairbrother, R. J. "Computer Simulation of Fuel Injection Systems for DI Diesel Engines". *SAE Technical Paper 922223* (1992). doi: 10.4271/922223, (*cited on: Chap.3-pp.87,89*).

Arcoumanis, C., Flora, H., Gavaises, M., Kampanis, N., and Horrocks, R. "Investigation of cavitation in a vertical multi-hole Diesel injector". *SAE Technical Paper 1999-01-0524* (1999). doi: 10.4271/1999-01-0524, (*cited on: Chap.2-p.29*).

Arcoumanis, C., Gavaises, M., Bostock, P. G., and Horrocks, R. W. "Evaluation of Pump Design Parameters in Diesel Fuel Injection Systems". *SAE Technical Paper 950078* (1995). doi: 10.4271/950078, (*cited on: Chap.3-pp.87,89*).

Arcoumanis, C., Gavaises, M., Yamanishi, M., and Oiwa, J. "Application of a FIE Computer Model to an In-Line Pump-Based Injection System for Diesel Engines". *SAE Technical Paper 970348* (1997). doi: 10.4271/970348, (*cited on: Chap.3-pp.86,87,89*).

Arcoumanis, C., Gavaises, M., Abdul-Wahab, E., and Moser, V. "Modeling of Advanced High-Pressure Fuel Injection Systems for Passenger Cars Diesel Engines". *SAE Technical Paper 1999-01-0910* (1999). doi: 10.4271/1999-01-0910, (*cited on: Chap.3-pp.91,93*).

Arcoumanis, C., Gavaises, M., and French, B. "Effect of fuel injection processes on the structure of Diesel sprays". *SAE Technical Paper 970799* (1997). doi: 10.4271/970799.

Armas, O., Martínez-Martínez, S., Mata, C., and Pacheco, C. "Alternative method for bulk modulus estimation of Diesel fuels". *Fuel*, vol. 167 (2016), pp. 199–207. issn: 00162361. doi: 10.1016/j.fuel.2015.11.067, (*cited on: Chap.3-pp.99,103, Chap.4-p.177, Chap.6-p.267*).

Arpaia, A., Catania, A., Ferrari, A., and Spessa, E. "Development and Application of an Advanced Numerical Model for CR Piezo Indirect Acting Injection Systems". *SAE Technical Paper 2010-01-1503* (2010). doi: 10.4271/2010-01-1503, (*cited on: Chap.3-pp.92,95*).

Arrègle, J. "Análisis de la estructura y dinámica interna de chorros Diesel". PhD thesis. Universitat Politècnica de València, 1997, (*cited on: Chap.1-p.4*).

Asihmin, V. I., Geller, Z. I., and Skobel'cyn, Y. A. "Discharge of a real fluid from cylindrical orifices". *Oil Industry*, vol. 9 (1961), pp. 135–172, (*cited on: Chap.2-p.36*).

Assael, M. J., Oliveira, C. P., Papadaki, M., and Wakeham, W. A. "Vibrating-Wire Viscometers for Liquids at High Pressures". *International Journal of Thermophysics*, vol. 13.4 (1992), pp. 593–615. issn: 0195928X. doi: 10.1007/BF00501943, (*cited on: Chap.3-pp.97,103*).

ASTM D1217-15, Standard Test Method for Density and Relative Density (Specific Gravity) of Liquids by Bingham Pycnometer. West Conshohocken, PA, 2015. doi: 10.1520/D1217-15, (*cited on: Chap.4-p.171*).

ASTM D1298-12b, Standard Test Method for Density, Relative Density, or API Gravity of Crude Petroleum and Liquid Petroleum Products by Hydrometer Method. West Conshohocken, PA, 2012. doi: 10.1520/D1298-12B, (*cited on: Chap.4-p.170*).

ASTM D445-15a, Standard Test Method for Kinematic Viscosity of Transparent and Opaque Liquids (and Calculation of Dynamic Viscosity). West Conshohocken, PA, 2015. doi: 10.1520/D0445-15A, (*cited on: Chap.4-p.180*).

ASTM D7806-12, Standard Test Method for Determination of the Fatty Acid Methyl Ester (FAME) Content of a Blend of Biodiesel and Petroleum-Based Diesel Fuel Oil Using Mid-Infrared Spectroscopy. West Conshohocken, PA, 2012. doi: 10.1520/D7806-12, (*cited on: Chap.4-p.160*).

Audonnet, F. and Pádua, A. A. H. "Simultaneous measurement of density and viscosity of n-pentane from 298 to 383 K and up to 100 MPa using a vibrating-wire instrument". *Fluid Phase Equilibria*, vol. 181.1-2 (2001), pp. 147–161. issn: 03783812. doi: 10.1016/S0378-3812(01)00487-3, (*cited on: Chap.3-pp.98,104*).

Bae, C., Yu, J., Kang, J., Kong, J., and Lee, K. O. "Effect of Nozzle Geometry on the Common-Rail Diesel Spray". *SAE Technical Paper 2002-01-1625* (2002). doi: 10.4271/2002-01-1625, (*cited on: Chap.2-p.29*).

Ball, S. J. and Trusler, J. P. M. "The speed of Sound and derived thermodynamic properties of n-hexane and n-hexadecane at temperatures between 298 K and 373 K and pressures up to 100 MPa". *International Journal of Thermophysics*, vol. 22.2 (2001), pp. 427–443, (*cited on: Chap.3-pp.98,100, Chap.4-p.167*).

Bardi, M. "Partial needle lift and injection rate shape effect on the formation and combustion of the Diesel spray". PhD thesis. Valencia (Spain): Universitat Politècnica de València, 2014. doi: 10.4995/Thesis/10251/37374, (*cited on: Chap.1-p.4, Chap.2-p.25*).

Bazyn, T. and Koci, C. "The Effect of Jet Spacing on the Combustion Characteristics of Diesel Sprays". *THIESEL 2014 Conference on Thermo- and Fluid Dynamic Processes in Direct Injection Engines*. Valencia, Spain, 2014, (*cited on: Chap.2-p.50*).

Becchi, G. A. "Analytical Simulation of Fuel Injection in Diesel Engines". *SAE Technical Paper 710568* (1971). doi: 10.4271/710568, (*cited on: Chap.3-pp.86,88*).

Bell, I. H., Wronski, J., Quoilin, S., and Lemort, V. "Pure and pseudo-pure fluid thermophysical property evaluation and the open-source thermophysical property library coolprop". *Industrial and Engineering Chemistry Research*, vol. 53.6 (2014), pp. 2498–2508. issn: 08885885. doi: 10.1021/ie4033999, (*cited on: Chap.3-p.96, Chap.4-pp.165,166,174*).

Belmon, L., Gonard, R., and Clarenc, P. "Simulation of Thermal Behaviour of Closed Loop Common Rail Injection Systems". *Diesel- und Benzindirekteinspritzung V*. Ed. by H. Tschoke. Essen: Haus der Technik, 2009. Chap. 6. isbn: 978-3-8169-2867-6, (*cited on: Chap.3-pp.92,95*).

Belonenko, V. "Application of a Micro- (p, V, T) apparatus for measurement of liquid densities at pressures up to 500 MPa". *The Journal of Chemical Thermodynamics*, vol. 32 (2000), pp. 1203–1219. issn: 00219614. doi: 10.1006/jcht.1999.0604, (*cited on: Chap.3-pp.98,101*).

Benajes, J., Molina, S., González, C., and Donde, R. "The role of nozzle convergence in diesel combustion". *Fuel*, vol. 87.10-11 (2008), pp. 1849–1858. issn: 00162361. doi: 10.1016/j.fuel.2007.12.016, (*cited on: Chap.2-p.49*).

Benajes, J., Payri, R., Molina, S., and Soare, V. "Investigation of the Influence of Injection Rate Shaping on the Spray Characteristics in a Diesel Common Rail System Equipped with a Piston Amplifier". *Journal of Fluids Engineering*, vol. 127.6 (2005), p. 1102. ISSN: 00982202. DOI: 10.1115/1.2062767, (*cited on: Chap.2-p.23*).

Benedict, R. *Fundamentals of temperature, pressure and flow measurements*. Ed. by W.-I. Publication. 3rd. USA, 1984. ISBN: 0-471-89383-8, (*cited on: Chap.2-p.36*).

Bergman, T. L., Lavine, A. S., Incropera, F. P., and DeWitt, D. P. *Fundamentals of Heat and Mass Transfer*. 7th ed. New York, NY: John Wiley & Sons, 2011. ISBN: 978-0470917855, (*cited on: Chap.5-p.237*).

Bergstrand, P. and Denbratt, I. "The Effects of Multirow Nozzles on Diesel Combustion". *SAE Technical Paper 2003-01-0701* (2003). DOI: 10.4271/2003-01-0701, (*cited on: Chap.2-p.50*).

Bergwerk, W. "Flow pattern in diesel nozzle spray holes". *Proceedings of the Institution of Mechanical Engineers*, vol. 173 (1959), pp. 655–660. ISSN: 0020-3483. DOI: 10.1243/PIME_PROC_1959_173_054_02, (*cited on: Chap.2-pp.39,43,49*).

Bermudez, V., Payri, R., Salvador, F. J., and Plazas, A. H. "Study of the influence of nozzle seat type on injection rate and spray behavior". *ImechE. Journal of automobile engineering*, vol. 219.5 (2005), pp. 677–689. ISSN: 0954-4070. DOI: 10.1243/095440705X28303, (*cited on: Chap.2-p.29*).

Bianchi, G. M., Falfari, S., Brusiani, F., and Pelloni, P. "Advanced Modelling of a New Diesel Fast Solenoid Injector and Comparison with Experiments". *SAE Technical Paper 2004-01-0019* (2004). DOI: 10.4271/2004-01-0019, (*cited on: Chap.3-pp.91,94*).

Bianchi, G. M., Falfari, S., Parotto, M., and Osbat, G. "Advanced modeling of common rail injector dynamics and comparison with experiments". *SAE Technical Paper 2003-01-0006* (2003). DOI: 10.4271/2003-01-0006, (*cited on: Chap.2-p.28, Chap.3-pp.91,92,94*).

Bianchi, G. M., Falfari, S., Pelloni, P., Filicori, F., and Milani, M. "A Numerical and Experimental Study Towards Possible Improvements of Common Rail Injectors". *SAE Technical Paper 2002-01-0500* (2002). DOI: 10.4271/2002-01-0500, (*cited on: Chap.3-p.94*).

Bianchi, G. M., Pelloni, P., Filicori, F., and Vannini, G. "Optimization of the Solenoid Valve Behavior in Common-Rail Injection Systems". *SAE Technical Paper 2000-01-2042* (2000). DOI: 10.4271/2000-01-2042, (*cited on: Chap.3-pp.91,94*).

Bianchi, G., Falfari, S., Pelloni, P., Kong, S.-C., and Reitz, R. D. "Numerical Analysis of High-Pressure Fast-Response Common Rail Injector Dynamics". *SAE Technical Paper 2002-01-0213* (2002). DOI: 10.4271/2002-01-0213, (*cited on: Chap.3-p.94*).

Bianchi, G. et al. "Numerical Investigation of Critical Issues in Multiple-Injection Strategy Operated by a New CR Fast-Actuation Solenoid Injector". *SAE Technical Paper 2005-01-1236* (2005). DOI: 10.4271/2005-01-1236, (*cited on: Chap.3-pp.92,94*).

Blackburn, J., Reethof, G., and Shearer, J. *Fluid Power Control*. Cambridge MA: The MIT Press, 1960. ISBN: 9780262020060, (*cited on: Chap.5-p.200*).

Bode, J. "Zum Kavitationseinfluss auf den Zerfall von Flüssigkeitsstrahlen". PhD thesis. Göttingen, Germany, 1991, (*cited on: Chap.2-p.59*).

Boehman, A. L., Morris, D., Szybist, J., and Esen, E. "The Impact of the Bulk Modulus of Diesel Fuels on Fuel Injection Timing". *Energy & Fuels*, vol. 18.6 (2004), pp. 1877–1882. ISSN: 0887-0624. DOI: 10.1021/ef049880j, (*cited on: Chap.3-pp.98,102,109,112, Chap.4-p.170*).

Boehner, W. and Hummel, K. "Common rail injection system for commercial Diesel vehicles". *SAE Technical Paper 970345* (1997). DOI: 10.4271/970345, (*cited on: Chap.2-p.17*).

Bosch, W. "The Fuel Rate Indicator: a New Measuring Instrument for Display of the Characteristics of Individual Injection". *SAE Technical Paper 660749* (1966). DOI: 10.4271/660749, (*cited on: Chap.4-p.152*).

Boudy, F. and Seers, P. "Impact of physical properties of biodiesel on the injection process in a common-rail direct injection system". *Energy Conversion and Management*, vol. 50.12 (2009), pp. 2905–2912. ISSN: 01968904. DOI: http://dx.doi.org/10.1016/j.enconman.2009.07.005, (*cited on: Chap.3-p.113*).

Bracho, G. "Experimental and theoretical study of the direct diesel injection process at low temperatures". PhD thesis. Universitat Politècnica de València, 2011, (*cited on: Chap.1-p.4, Chap.3-pp.99,112, Chap.4-p.161*).

Brennen, C. "An oscillating-boundary-layer theory for ciliary propulsion". *Journal of Fluid Mechanics*, vol. 65.04 (1974), pp. 799–824. ISSN: 0022-1120. DOI: 10.1017/S0022112074001662, (*cited on: Chap.2-p.59*).

Bridgman, P. W. *The physics of high pressure*. Dover Publications, 1931. ISBN: 9780486627120, (*cited on: Chap.3-pp.96,103*).

Brown, G. W. and McCallion, H. "Simulation of an injection system with delivery pipe cavitation using a digital computer". *Proceedings of the Institution of Mechanical Engineers, Conference Proceedings*, vol. 182.12 (1967), pp. 206–216. ISSN: 0367-8849. DOI: 10.1243/PIME_CONF_1967_182_374_02, (*cited on: Chap.3-pp.85,88*).

Brunner, M. and Ruf, H. "Contribution to the problem of starting and operating diesel vehicles at low temperatures". *Proceedings of the Institution of Mechanical Engineers, Automobile Division*, vol. 13.1 (1959), pp. 124–154. ISSN: 0367-8822. DOI: 10.1243/PIME_AUTO_1959_000_019_02, (*cited on: Chap.3-p.106*).

Brusiani, F., Falfari, S., and Pelloni, P. "Influence of the diesel injector hole geometry on the flow conditions emerging from the nozzle". *Energy Procedia*, vol. 45 (2014), pp. 749–758. ISSN: 18766102. DOI: 10.1016/j.egypro.2014.01.080, (*cited on: Chap.2-p.49*).

Caika, V., Sampl, P., and Greif, D. "Integrated 1D/2D/3D Simulation of Fuel Injection and Nozzle Cavitation". *SAE Technical Paper 2013-24-0006*, vol. 2013-24-00 (2013), pp. 1544–1552. ISSN: 19463936. DOI: 10.4271/2013-24-0006, (*cited on: Chap.3-pp.92,95*).

Canaan, R., Dec, J., Green, R., and Daly, D. "The influence of fuel volatility on the liquid-phase fuel penetration in a heavy-duty D.I. Diesel engine". *SAE Technical Paper 980510* (1998). DOI: 10.4271/980510, (*cited on: Chap.2-p.63*).

Catalano, L. A., Tondolo, V. A., and Dadone, A. "Dynamic rise of pressure in the common-rail fuel injection system". *SAE Technical Paper 2002-01-0210* (2002). DOI: 10.4271/2002-01-0210, (*cited on: Chap.3-pp.91,93*).

Catania, A. E., Dongiovanni, C., and Mittica, A. "Implicit Numerical Model of a High-Pressure Injection System". *Journal of Engineering for Gas Turbines and Power*, vol. 114.3 (1992), pp. 534–543. ISSN: 07424795. DOI: 10.1115/1.2906622, (*cited on: Chap.3-p.89*).

Catania, A. E., Dongiovanni, C., Mittica, A., Badami, M., and Lovisolo, F. "Numerical Analysis Versus Experimental Investigation of a Distributor-Type Diesel Fuel-Injection System". *Journal of Engineering for Gas Turbines and Power*, vol. 116.4 (1994), pp. 814–830. ISSN: 07424795. DOI: 10.1115/1.2906890, (*cited on: Chap.3-p.89*).

Catania, A. E., Ferrari, A., Manno, M., and Spessa, E. "Thermal Effect Simulation in High-Pressure Injection System Transient Flows". *SAE Technical Paper 2004-01-0532* (2004). doi: 10.4271/2004-01-0532, (*cited on: Chap.3-pp.91,94*).

Catania, A. E., Ferrari, A., and Spessa, E. "Temperature variations in the simulation of high-pressure injection-system transient flows under cavitation". *International Journal of Heat and Mass Transfer*, vol. 51 (2008), pp. 2090–2107. issn: 00179310. doi: 10.1016/j.ijheatmasstransfer.2007.11.032, (*cited on: Chap.1-p.2, Chap.3-pp.91,94*).

Catania, A. E., Ferrari, A., and Manno, M. "Development and Application of a Complete Multijet Common-Rail Injection-System Mathematical Model for Hydrodynamic Analysis and Diagnostics". *Journal of Engineering for Gas Turbines and Power*, vol. 130.6 (2008), p. 062809. issn: 07424795. doi: 10.1115/1.2925679, (*cited on: Chap.3-pp.91,94*).

Catania, A. E., Ferrari, A., Manno, M., and Spessa, E. "Experimental Investigation of Dynamics Effects on Multiple-Injection Common Rail System Performance". *Journal of Engineering for Gas Turbines and Power*, vol. 130.3 (2008), p. 032806. issn: 07424795. doi: 10.1115/1.2835353, (*cited on: Chap.1-p.2*).

Catania, A. E., Dongiovanni, C., Mittica, A., Negri, C., and Spessa, E. "Study of Automotive Diesel Injection-System Dynamics Under Control". *SAE Technical Paper 962020* (1996). doi: 10.4271/962020, (*cited on: Chap.3-pp.87,89*).

Catania, A. E. and Ferrari, A. "Advanced Mathematical Modeling of Electronic Unit-Injector Systems for Heavy Duty Diesel Engine Application". *SAE International Journal of Commercial Vehicles*, vol. 1.1 (2008), pp. 134–151. issn: 1946391X. doi: 10.4271/2008-01-1195, (*cited on: Chap.3-p.94*).

Caudwell, D. R., Trusler, J. P. M., Vesovic, V., and Wakeham, W. A. "The viscosity and density of n-dodecane and n-octadecane at pressures up to 200 MPa and temperatures up to 473 K". *International Journal of Thermophysics*, vol. 25.5 (2004), pp. 1339–1352. issn: 0195928X. doi: 10.1007/s10765-004-5742-0, (*cited on: Chap.3-pp.98,104*).

Caudwell, D. R., Trusler, J. P. M., Vesovic, V., and Wakeham, W. A. "Viscosity and Density of Five Hydrocarbon Liquids at Pressures up to 200 MPa and Temperatures up to 473 K". *Journal of Chemical Engineering Data*, vol. 54 (2009), pp. 359–366. issn: 0021-9568. doi: 10.1021/je800417q, (*cited on: Chap.3-pp.98,104*).

Chan, R. K. Y. and Jackson, D. A. "An automated falling-cylinder high pressure laser-Doppler viscometer". *Journal of Physics E: Scientific Instruments*, vol. 18.6 (1985), pp. 510–515. ISSN: 0022-3735. DOI: 10.1088/0022-3735/18/6/011, (*cited on: Chap.3-pp.97,104*).

Chang, C. T. and Farrell, P. V. "A study on the effects of fuel viscosity and nozzle geometry on high injection pressure Diesel spray characteristics". *SAE Technical Paper 970353* (1997). DOI: 10.4271/970353, (*cited on: Chap.3-pp.107,112*).

Chaves, H., Knapp, M., Kubitzek, A., and Obermeier, F. "Experimental study of cavitation in the nozzle hole of diesel injectors using transparent nozzles". *SAE Technical Paper 950290* (1995). DOI: 10.4271/950290, (*cited on: Chap.2-pp.39,45*).

Chaves, H. and Obermeier, F. "Correlation between light absorption signals of cavitating nozzle flow within and outside of the hole of a transparent Diesel injection nozzle". *Proc. 15th ILASS-Europe, Toulouse, July 5-7.* 1999, pp. 224–229, (*cited on: Chap.2-p.60*).

Chehroudi, B., Chen, S.-H., Bracco, F. V., and Onuma, Y. "On the Intact Core of Full-Cone Sprays". *SAE Technical Paper 850126* (1985). DOI: 10.4271/850126, (*cited on: Chap.2-p.63*).

Chorazewski, M. et al. "Thermophysical properties of Normafluid (ISO 4113) over wide pressure and temperature ranges". *Fuel*, vol. 105 (2013), pp. 440–450. ISSN: 00162361. DOI: 10.1016/j.fuel.2012.05.059, (*cited on: Chap.3-p.99, Chap.4-pp.173,174, Chap.5-pp.223,257*).

Colebrook, C. F. "Turbulent flow in pipes, with particular reference to the transition region between the smooth and rough pipe laws". *Journal of the Institution of Civil Engineers*, 4 (1939), pp. 133–156. ISSN: 0368-2455. DOI: 10.1680/ijoti.1939.13150, (*cited on: Chap.2-pp.26,27*).

Coppo, M. and Dongiovanni, C. "Experimental Validation of a Common-Rail Injector Model in the Whole Operation Field". *Journal of Engineering for Gas Turbines and Power*, vol. 129.2 (2007), pp. 596–608. ISSN: 07424795. DOI: 10.1115/1.2432889, (*cited on: Chap.3-pp.91,95*).

Coppo, M., Dongiovanni, C., and Negri, C. "Numerical Analysis and Experimental Investigation of a Common Rail-Type Diesel Injector". *Journal of Engineering for Gas Turbines and Power*, vol. 126.4 (2004), pp. 874–885. ISSN: 07424795. DOI: 10.1115/1.1787502, (*cited on: Chap.2-p.28*).

Correas, D. "Estudio teórico-experimental del chorro libre Diesel isotermo". PhD thesis. Valencia: E.T.S. Ingenieros Industriales. Universidad Politécnica de Valencia, 1998, (*cited on: Chap.2-p.61*).

Dandridge, A. and Jackson, D. A. "Measurements of viscosity under pressure: a new method". *Journal of Physics D: Applied Physics*, vol. 14.5 (1981), pp. 829–831. ISSN: 0022-3727. DOI: 10.1088/0022-3727/14/5/012, (*cited on: Chap.3-pp.97,104*).

Daridon, J., Lagrabette, A., and Lagourette, B. "Speed of sound, density, and compressibilities of heavy synthetic cuts from ultrasonic measurements under pressure". *The Journal of Chemical Thermodynamics*, vol. 30.5 (1998), pp. 607–623. ISSN: 00219614. DOI: 10.1006/jcht.1997.0330, (*cited on: Chap.3-pp.97,100,101,102, Chap.4-pp.167,170,175,179*).

Dauge, P., Baylaucq, A., Marlin, L., and Boned, C. "Development of an Isobaric Transfer Viscometer Operating up to 140 MPa. Application to a Methane + Decane System". *Journal of Chemical & Engineering Data*, vol. 46.4 (2001), pp. 823–830. ISSN: 0021-9568. DOI: 10.1021/je000371v, (*cited on: Chap.3-pp.98,103*).

Dávila, M. J. and Martin Trusler, J. "Thermodynamic properties of mixtures of N-methyl-2-pyrrolidinone and methanol at temperatures between 298.15K and 343.15K and pressures up to 60MPa". *The Journal of Chemical Thermodynamics*, vol. 41.1 (2009), pp. 35–45. ISSN: 00219614. DOI: 10.1016/j.jct.2008.08.003, (*cited on: Chap.3-pp.98,100,101,102,106*).

De la Garza, O. "Estudio de los efectos de la cavitación en toberas de inyección diesel sobre el proceso de inyección y el de formación de hollín". PhD thesis. Valencia (Spain): Universitat Politècnica de València, 2012. DOI: 10.4995/Thesis/10251/18153, (*cited on: Chap.1-p.4*).

De la Morena, J. "Estudio de la influencia de las características del flujo interno en toberas sobre el proceso de inyección Diesel en campo próximo". PhD thesis. Universidad Politécnica de Valencia, 2011, (*cited on: Chap.1-p.4, Chap.2-pp.40,59,60,63,64*).

Dechoz, J. and Rozé, C. "Surface tension measurement of fuels and alkanes at high pressure under different atmospheres". *Applied Surface Science*, vol. 229.1-4 (2004), pp. 175–182. ISSN: 01694332. DOI: 10.1016/j.apsusc.2004.01.057, (*cited on: Chap.3-pp.98,106*).

DeJuhasz, K. J. "Graphical analysis of transient phenomena in linear flow". *Journal of the Franklin Institute*, vol. 223.5 (1937), pp. 643–654. ISSN: 00160032. DOI: 10.1016/S0016-0032(37)91917-3, (*cited on: Chap.3-p.85*).

Delacourt, E., Desmet, B., and Besson, B. "Characterisation of very high pressure Diesel sprays using digital imaging techniques". *Fuel*, vol. 84.7-8 (2005), pp. 859–867. doi: 10.1016/j.fuel.2004.12.003, (*cited on: Chap.2-p.62*).

Dent, J. C. "A basis for comparison of various experimental methods for studying spray penetration". *SAE Technical Paper 710571* (1971). doi: 10.4271/710571, (*cited on: Chap.2-p.60*).

Dernotte, J., Hespel, C., Foucher, F., Houillé, S., and Mounaïm-Rousselle, C. "Influence of physical fuel properties on the injection rate in a Diesel injector". *Fuel*, vol. 96 (2012), pp. 153–160. issn: 00162361. doi: 10.1016/j.fuel.2011.11.073, (*cited on: Chap.3-pp.108,112, Chap.6-p.267*).

Dernotte, J., Hespel, C., Houille, S., Foucher, F., and Mounaim-Rousselle, C. "Influence of Fuel Properties on the Diesel Injection Process in Nonvaporizing Conditions". *Atomization And Sprays*, vol. 22.6 (2012), pp. 461–492. issn: 1044-5110. doi: 10.1615/AtomizSpr.2012004401, (*cited on: Chap.1-p.2, Chap.3-pp.108,111,112, Chap.6-p.267*).

Dernotte, J. et al. "Experimental Study of the Influence of Fuel Properties on the Diesel Injection Process in Non-Vaporizing Conditions". *ILASS - Europe 2011, 24th European Conference on Liquid Atomization and Spray Systems*. Estoril, Portugal, 2011, pp. 1–10, (*cited on: Chap.3-pp.108,111,112, Chap.6-p.267*).

Desantes, J. M., Payri, R., Pastor, J. M., and Gimeno, J. "Experimental characterization of internal nozzle flow and diesel spray behavior. Part I: Nonevaporative conditions". *Atomization And Sprays*, vol. 15.5 (2005), pp. 489–516. issn: 1044-5110. doi: 10.1615/AtomizSpr.v15.i5.20, (*cited on: Chap.2-p.45*).

Desantes, J., Payri, R., Salvador, F., and Gil, A. "Development and validation of a theoretical model for diesel spray penetration". *Fuel*, vol. 85.7-8 (2006), pp. 910–917. issn: 00162361. doi: 10.1016/j.fuel.2005.10.023, (*cited on: Chap.2-pp.61,64*).

Desantes, J. M., Arrègle, J., Lopez, J. J., and Hermens, S. "Experimental Characterization of Outlet Flow for Different Diesel Nozzle Geometries." *SAE Technical Paper 2005-01-2120*, 2005-01-2120 (2005). doi: 10.4271/2005-01-2120, (*cited on: Chap.2-p.49*).

Desantes, J. M., Arrègle, J., Pastor, J. V., and Delage, A. "Influence of the fuel characteristics on the injection process in a D.I. Diesel engine". *SAE Technical Paper 980802* (1998). doi: 10.4271/980802, (*cited on: Chap.3-pp.107,111,112*).

Desantes, J. M., Arrègle, J., and Rodríguez, P. J. "Computational model for simulation of Diesel Injection systems". *SAE Technical Paper 1999-01-0915* (1999). doi: 10.4271/1999-01-0915, (*cited on: Chap.3-pp.91,93, Chap.5-p.190*).

Desantes, J. M., García-Oliver, J. M., Pastor, J. M., and Ramírez-Hernández, J. G. "Influence of nozzle geometry on ignition and combustion for high-speed direct injection diesel engines under cold start conditions". *Fuel*, vol. 90.11 (2011), pp. 3359–3368. issn: 00162361. doi: 10.1016/j.fuel.2011.06.006, (*cited on: Chap.1-p.2*).

Desantes, J. M., Pastor, J. V., Payri, R., and Pastor, J. M. "Experimental characterization of internal nozzle flow and diesel spray behavior. Part II: Evaporative conditions". *Atomization and Spray*, vol. 15.5 (2005), pp. 517–543. issn: 1044-5110. doi: 10.1615/AtomizSpr.v15.i5.20, (*cited on: Chap.2-p.62*).

Desantes, J. M., Payri, R., Garcia, A., and Manin, J. "Experimental Study of Biodiesel Blends' Effects on Diesel Injection Processes". *Energy & Fuels*, vol. 23.6 (2009), pp. 3227–3235. issn: 0887-0624. doi: 10.1021/ef801102w, (*cited on: Chap.3-pp.108,111,112*).

Desantes, J. M., Payri, R., Garcia-Oliver, J. M., and Salvador, F. J. "A contribution to the understanding of isothermal diesel spray dynamics". *Fuel*, vol. 86.7-8 (2007), pp. 1093–1101. issn: 00162361. doi: 10.1016/j.fuel.2006.10.011, (*cited on: Chap.2-p.65*).

Desantes, J. M., Payri, R., Salvador, F. J., and Gimeno, J. "Measurements of spray momentum for the study of cavitation in diesel injection nozzles". *SAE Technical Paper 2003-01-0703*, vol. 2003-01-07 (2003). doi: 10.4271/2003-01-0703, (*cited on: Chap.2-p.45*).

Desantes, J. M., Payri, R., Salvador, F. J., and Manin, J. "Influence on Diesel Injection Characteristics and Behavior Using Biodiesel Fuels". *SAE Technical Paper 2009-01-0851*, vol. 4970.2009-01-0851 (2009). doi: 10.4271/2009-01-0851, (*cited on: Chap.3-pp.108,111,112*).

Desantes, J. M., Salvador, F. J., Carreres, M., and Martinez-Lopez, J. "Large-eddy simulation analysis of the influence of the needle lift on the cavitation in diesel injector nozzles". *Proceedings of the Institution of Mechanical Engineers, Part D: Journal of Automobile Engineering*, vol. 229.4 (2014), pp. 407–423. ISSN: 0954-4070. DOI: 10.1177/0954407014542627, (*cited on: Chap.2-p.29*).

Desantes, J. M., Salvador, F. J., Lopez, J. J., and De la Morena, J. "Study of mass and momentum transfer in diesel sprays based on X-ray mass distribution measurements and on a theoretical derivation". *Experiments in Fluids*, vol. 50.2 (2011), pp. 233–246. ISSN: 07234864. DOI: 10.1007/s00348-010-0919-8, (*cited on: Chap.2-p.65*).

Digesu, P., Ficarella, A., Laforgia, D., Bruni, G., and Ricco, M. "Diesel Electro-injector: A Numerical Simulation Code". *SAE Technical Paper 940193* (1994). ISSN: 07424795. DOI: 10.1115/1.2815466, (*cited on: Chap.3-pp.90,91,93*).

Digesu, P. and Laforgia, D. "Diesel Electro-injector: A Numerical Simulation Code". *Journal of Engineering for Gas Turbines and Power*, vol. 117.4 (1995), pp. 792–798. ISSN: 07424795. DOI: 10.1115/1.2815466, (*cited on: Chap.3-pp.90,91,93*).

Dindar, C. and Kiran, E. "Reliable method for determination of the velocity of a sinker in a high-pressure falling body type viscometer". *Rev. Sci. Instrum.* Vol. 73.10 (2002), pp. 3664–3670. ISSN: 0034-6748. DOI: 10.1063/1.1505100, (*cited on: Chap.3-pp.98,103*).

Dober, G., Guerrassi, N., and Karimi, K. "Mixture Preparation and Combustion Analysis , a Key Activity for Future Trends in Diesel Fuel Injection Equipment". *SIA Diesel Powertrain International Conference*. Rouen, 2012, (*cited on: Chap.2-pp.24,50*).

Dober, G. et al. "The Impact of Injection Strategies on Emissions Reduction and Power Output of Future Diesel Engines". *SAE Technical Paper 2008-01-0941*, vol. 2008.724 (2008). DOI: 10.4271/2008-01-0941, (*cited on: Chap.2-p.23*).

Dohle, U., Kampmann, S., Hammer, J., Wintrich, T., and Hinrichsen, C. "Advanced Diesel Common Rail Systems for Future Emission Legislation". *International Conference on Automotive Technologies-ICAT* (2004), pp. 109–113, (*cited on: Chap.2-p.23*).

Douhéret, G., Davis, M. I., Reis, J. C. R., and Blandamer, M. J. "Isentropic Compressibilities—Experimental Origin and the Quest for their Rigorous Estimation in Thermodynamically Ideal Liquid Mixtures". *ChemPhysChem*, vol. 2.3 (2001), pp. 148–161. ISSN: 1439-4235. DOI: 10.1002/1439-7641(20010316)2:3<148::AID-CPHC148>3.0.CO;2-J, (*cited on: Chap.3-p.102*).

Duncan, A. M., Pavlicek, N., Depcik, C. D., Scurto, A. M., and Stagg-Williams, S. M. "High-pressure viscosity of soybean-oil-based biodiesel blends with ultra-low-sulfur diesel fuel". *Energy and Fuels*, vol. 26.11 (2012), pp. 7023–7036. ISSN: 08870624. DOI: 10.1021/ef3012068, (*cited on: Chap.3-p.99*).

Duncan, A. M. et al. "High-pressure viscosity of biodiesel from soybean, canola, and coconut oils". *Energy & Fuels*, vol. 24.10 (2010), pp. 5708–5716. ISSN: 08870624. DOI: 10.1021/ef100382f, (*cited on: Chap.3-p.99*).

Dymond, J. H., Glen, N. F., and Isdale, J. D. "Transport properties of nonelectrolyte liquid mixtures-VII. Viscosity coefficients for isooctane and for equimolar mixtures of isooctane + n-octane and isooctane + n-dodecane from 25 to 100??C at pressures up to 500 MPa or to the freezing pressure". *International Journal of Thermophysics*, vol. 6 (1985), pp. 233–250. ISSN: 0195928X. DOI: 10.1007/BF00522146, (*cited on: Chap.3-pp.97,103*).

Dymond, J. H., Robertson, J., and Isdale, J. D. "Transport Properties of Nonelectrolyte Liquid Mixtures - III. Viscosity Coefficients for the n-Octane + n-Dodecane and Equimolar Mixtures of n-Octane + n-Dodecane and n-Hexane + n-Dodecane from 25 to 100°C at Pressures up to the Freezing Pressure or 500 M". *International Journal of Thermophysics*, vol. 2.2 (1981), pp. 133–154. ISSN: 0195928X, (*cited on: Chap.3-pp.97,103*).

Dymond, J. H., Young, K. J., and Isdale, J. D. "Transport properties of nonelectrolyte liquid mixtures-II. Viscosity coefficients for the n-hexane + n-hexadecane system at temperatures from 25 to 100°C at pressures up to the freezing pressure or 500 MPa". *International Journal of Thermophysics*, vol. 1.4 (1980), pp. 345–373. ISSN: 0195928X. DOI: 10.1007/BF00516563, (*cited on: Chap.3-pp.97,103*).

Dzida, M. and Prusakiewicz, P. "The effect of temperature and pressure on the physicochemical properties of petroleum diesel oil and biodiesel fuel". *Fuel*, vol. 87.10-11 (2008), pp. 1941–1948. ISSN: 00162361. DOI: 10.1016/j.fuel.2007.10.010, (*cited on: Chap.3-pp.98,101,102,106*).

Eifler, W. "Untersuchungen zur Struktur des instationären Dieselöleinspritzstrahles in Düsennahbereich mit der Methode der Hochfrequenz-Kinematografie". PhD thesis. Universität Kaiserslautern, Germany, 1990, (*cited on: Chap.2-p.59*).

El-Erian, M. F. "Simulation and control of transient flow in the diesel injection system". PhD thesis. University of Michigan, 1972.

El-Erian, M. F., Wylie, E. B., and Bolt, J. A. "Analysis and Control of the Transient Flow in the Diesel Injection System. Part I - The Analytical Control Method.pdf". *SAE Technical Paper 730661* (1973). DOI: 10.4271/730661.

El-Erian, M. F., Wylie, E. B., and Bolt, J. A. "Analysis and Control of the Transient Flow in the Diesel Injection System. Part II - Design Results of Controlled After-Injection". *SAE Technical Paper 730662* (1973). DOI: 10.4271/730662.

Erlach, H., Chmela, F., Cartellieri, W., and Herzog, P. "Pressure Modulated Injection and Its Effect on Combustion and Emissions Ofa Hd Diesel Engine". *SAE transactions*, 412 (1995). DOI: 10.4271/952059, (*cited on: Chap.1-p.2*).

Espey, C. and Dec, J. E. "The effect of TDC temperature and density on the liquid-phase fuel penetration in a D.I. Diesel engine". *SAE Technical Paper 952456* (1995). DOI: 10.4271/952456, (*cited on: Chap.2-p.63*).

Fairbrother, R. J. "Computer Simulation of Fuel Injection for Direct-Injection Diesel Engines". PhD thesis. Imperial College London, 1994, (*cited on: Chap.3-pp.86,87,89*).

Falfari, S. et al. "Assessment of a Simplified Model of Common Rail Injector for Getting Proper Boundary Conditions for 3D Simulations of the Combustion Process in HSDI Diesel Engines". *61 Congresso Nazionale ATI - Perugia 12-15 Settembre 2006*. 2006, pp. 3–7, (*cited on: Chap.3-pp.92,94*).

Favennec, A. G. "Analyse d'un Système d'Injection Directe Diesel de Type Common Rail". PhD thesis. Université de Lyon, 1999, (*cited on: Chap.3-p.93*).

Ficarella, A. and Laforgia, D. "Injection characteristics simulation and analysis in Diesel engines". *Meccanica*, vol. 28.3 (1993), pp. 239–248. ISSN: 0025-6455. DOI: 10.1007/BF00989127, (*cited on: Chap.3-p.89*).

Ficarella, A., Laforgia, D., and Cipolla, G. "Investigation and Computer Simulation of Diesel Injection System With Rotative Pump". *Journal of Engineering for Gas Turbines and Power*, vol. 112.3 (1990), pp. 317–323. ISSN: 07424795. DOI: 10.1115/1.2906497, (*cited on: Chap.3-pp.86,87,89*).

Ficarella, A., Laforgia, D., and Landviscina, V. "Evaluation of Instability phenomena in a common rail injection system for high speed Diesel engines". *SAE Technical Paper 1999-01-0192*, 724 (1999). DOI: 10.4271/1999-01-0192, (*cited on: Chap.3-pp.90,92,93*).

Ficarella, A. and Laforgia, D. "Contribution To The Simulation Of Injection System For Reciprocating Internal Combustion Engines". *SAE Technical Paper 885016* (1988). DOI: 10.4271/885016, (*cited on: Chap.3-p.89*).

Fox, T. A. and Stark, J. "Characteristics of Miniature Short-Tube Orifice Flows". *Proceedings of the Institution of Mechanical Engineers, Part C: Journal of Mechanical Engineering Science*, vol. 203.5 (1989), pp. 351–358. ISSN: 0954-4062. DOI: 10.1243/PIME_PROC_1989_203_124_02, (*cited on: Chap.2-p.48*).

Fox, T. A. and Stark, J. "Discharge coefficients for miniature fuel injectors". *Proceedings of the Institution of Mechanical Engineers, Part G: Journal of Aerospace Engineering*, vol. 203.17 (1989), pp. 75–78. ISSN: 0954-4100. DOI: 10.1243/PIME_PROC_1989_203_056_01, (*cited on: Chap.2-pp.35,48*).

Franc, J.-P. "The Rayleigh-Plesset equation: a simple and powerful tool to understand various aspects of cavitation". *Fluid Dynamics of Cavitation and Cavitating Turbopumps*. Vol. 496. Vienna: Springer, 2007, pp. 1–41. ISBN: 978-3-211-76668-2. DOI: 10.1007/978-3-211-76669-9_1, (*cited on: Chap.5-p.237*).

Freitas, S. V. D. et al. "Measurement and prediction of high-pressure viscosities of biodiesel fuels". *Fuel*, vol. 122 (2014), pp. 223–228. ISSN: 00162361. DOI: 10.1016/j.fuel.2014.01.031, (*cited on: Chap.3-pp.99,103*).

Fresco, G. P., Klaus, E. E., and Tewksbury, E. J. "Measurement and Prediction of Viscosity-Pressure Characteristics of Liquids". *Journal of Lubrication Technology*, vol. 91.3 (1969), pp. 451–457. ISSN: 00222305. DOI: 10.1115/1.3554960, (*cited on: Chap.3-p.105*).

Fukui, K., Asakuma, Y., and Maeda, K. "Determination of liquid viscosity at high pressure by DLS". *Journal of Physics: Conference Series*, vol. 215 (2010), p. 012073. ISSN: 1742-6596. DOI: 10.1088/1742-6596/215/1/012073, (*cited on: Chap.3-pp.99,104*).

Ganippa, L. C., Andersson, S., and Chomiak, J. "Transient measurements of discharge coefficients of Diesel nozzles". *SAE Technical Paper 2000-01-2788* (2000). DOI: 10.4271/2000-01-2788, (*cited on: Chap.2-p.37*).

GANSER, M. A. "Common rail injectors for 2000 bar and beyond". *SAE Technical Paper 2000-01-0706* (2000). DOI: 10.4271/2000-01-0706, (*cited on: Chap.1-p.2*).

GAVAISES, M. and ANDRIOTIS, A. "Cavitation Inside Multi-hole Injectors for Large Diesel Engines and Its Effect on the Near-nozzle Spray Structure". *SAE Technical Paper 2006-01-1114* (2006). DOI: 10.4271/2006-01-1114, (*cited on: Chap.1-p.2*).

GAVAISES, M., ANDRIOTIS, A., PAPOULIAS, D., MITROGLOU, N., and THEODORAKAKOS, A. "Characterization of string cavitation in large-scale Diesel nozzles with tapered holes". *Physics of Fluids*, vol. 21.5 (2009), p. 052107. ISSN: 10706631. DOI: 10.1063/1.3140940, (*cited on: Chap.2-p.29*).

GIMENO, J. "Desarrollo y aplicación de la medida del flujo de cantidad de movimiento de un chorro Diesel". PhD thesis. Universitat Politècnica de València, 2008, (*cited on: Chap.1-p.4, Chap.2-pp.19,32,37,40,61*).

GLASSEY, S. F., STOCKNER, A. R., and FLINN, M. A. "HEUI - A New Direction for Diesel Engine Fuel Systems". *SAE Technical Paper 930270* (1993). DOI: 10.4271/930270, (*cited on: Chap.2-p.24*).

GONZÁLEZ, C. A. "Estudio de la influencia de la geometría de la tobera de inyección en la combustión y emisión de contaminantes de un motor diesel". PhD thesis. Universitat Politècnica de València, 2005, (*cited on: Chap.1-p.4*).

GOYAL, M. "Modular Approach to Fuel Injection System Simulation". *SAE Technical Paper 780162* (1978). DOI: 10.4271/780162, (*cited on: Chap.3-pp.86,88*).

GRAVESEN, P., BRANEBJERG, J., and JENSEN, O. S. "Microfluidics-a review". *Journal of Micromechanics and Microengineering*, vol. 3.4 (1993), pp. 168–182. ISSN: 0960-1317. DOI: 10.1088/0960-1317/3/4/002, (*cited on: Chap.2-p.33*).

GU, F. and BALL, A. D. "Diesel injector dynamic modelling and estimation of injection parameters from impact response Part 1: modelling and analysis of injector impacts". *Proceedings of the Institution of Mechanical Engineers, Part D: Journal of Automobile Engineering*, vol. 210.44 (1996), pp. 293–302. ISSN: 0954-4070. DOI: 10.1243/PIME_PROC_1996_210_276_02, (*cited on: Chap.3-p.89*).

Gu, F., Ball, A. D., and Rao, K. K. "Diesel injector dynamic modelling and estimation of injection parameters from impact response part 2: prediction of injection parameters from monitored vibration". *Proceedings of the Institution of Mechanical Engineers, Part D: Journal of Automobile Engineering*, vol. 210.44 (1996), pp. 303–312. ISSN: 0954-4070. DOI: 10.1243/PIME_PROC_1996_210_277_02, (*cited on: Chap.3-p.89*).

Gullaksen, J. "Simulation of Diesel Fuel Injection Dynamics Using MATLAB". *SAE Technical Paper 2004-01-2966* (2004). DOI: 10.4271/2004-01-2966, (*cited on: Chap.3-p.94*).

Gumus, M., Sayin, C., and Canakci, M. "The impact of fuel injection pressure on the exhaust emissions of a direct injection diesel engine fueled with biodiesel–diesel fuel blends". *Fuel*, vol. 95.1 (2012), pp. 486–494. ISSN: 00162361. DOI: 10.1016/j.fuel.2011.11.020, (*cited on: Chap.1-p.2, Chap.3-p.107*).

Ha, J. Y. et al. "Investigation on the initial part and the spray formation delay of Diesel spray". *SAE Technical Paper 830451* (1983). DOI: 10.4271/830451, (*cited on: Chap.2-p.64*).

Halderman, J. and Linder, J. *Automotive Fuel and Emissions Control Systems*. Prentice Hall, 2011. ISBN: 978-0132542920, (*cited on: Chap.2-p.15*).

Hall, G. W. "Analytical determination of the discharge characteristics of cylindrical-tube orifices". *Journal of Mechanical Engineering Science*, vol. 5.1 (1963), pp. 91–97. ISSN: 0022-2542. DOI: 10.1243/JMES_JOUR_1963_005_013_02, (*cited on: Chap.2-p.36*).

Han, D. and Lee, K.-J. "Viscous dissipation in micro-channels". *Journal of Mechanical Science and Technology*, vol. 21.12 (2007), pp. 2244–2249. ISSN: 1738-494X. DOI: 10.1007/BF03177486, (*cited on: Chap.2-p.26, Chap.5-p.197*).

Hardenberg, H. "The geometrical flow cross section of hole nozzles for direct injection Diesel engines". *MTZ worldwide*, vol. 45.10 (1984), pp. 427–429, (*cited on: Chap.5-p.203*).

Hardenberg, H. "The needle lift dependency of flow coefficients of holes nozzles for direct injection Diesel engines". *MTZ worldwide*, vol. 46.4 (1985), pp. 143–146, (*cited on: Chap.5-p.203*).

Hay, P. and Jones, P. L. "Comparison of the various correlations for spray penetration". *SAE Technical Paper 720776* (1972). DOI: 10.4271/720776, (*cited on: Chap.2-p.60*).

HAYWARD, A. T. J. "Compressibility equations for liquids: a comparative study". *British Journal of Applied Physics*, vol. 18.7 (1967), pp. 965–977. ISSN: 0508-3443. DOI: 10.1088/0508-3443/18/7/312, (*cited on: Chap.3-p.102*).

HAYWARD, A. T. J. "How to measure the isothermal compressibility of liquids accurately". *Journal of Physics D: Applied Physics*, vol. 4.7 (1971), pp. 938–950. ISSN: 00223727. DOI: 10.1088/0022-3727/4/7/308, (*cited on: Chap.3-p.102, Chap.4-pp.169,170*).

HE, L. and RUIZ, F. "Effect of cavitation on flow and turbulence in plain orifices for high-speed atomization". *Atomization and Sprays*, vol. 5 (1995), pp. 569–584. DOI: 10.1615/AtomizSpr.v5.i6.30, (*cited on: Chap.2-p.45*).

HERMENS, S. "Influence of Diesel injector nozzle geometry on the injection and combustion process". PhD thesis. Universitat Politècnica de València, 2007, (*cited on: Chap.1-p.4*).

HEYWOOD, J. B. *Internal Combustion Engine Fundementals*. McGraw Hill, 1988. ISBN: 007028637X, (*cited on: Chap.1-p.1, Chap.2-p.13, Chap.3-p.107*).

HIROYASU, H. and ARAI, M. "Structures of Fuel Sprays in Diesel Engines". *SAE Technical Paper 900475* (1990). DOI: 10.4271/900475, (*cited on: Chap.2-pp.55,61,63*).

HIROYASU, H. "Spray breakup mechanism from the hole-type nozzle and its applications". *Atomization and Sprays*, vol. 10.3-5 (2000), pp. 511–527. ISSN: 1044-5110. DOI: 10.1615/AtomizSpr.v10.i3-5.130, (*cited on: Chap.2-p.59*).

HO, C.-M. and GUTMARK, E. "Vortex induction and mass entrainment in a small-aspect-ratio elliptic jet". *Journal of Fluid Mechanics*, vol. 179 (1987), p. 383. ISSN: 0022-1120. DOI: 10.1017/S0022112087001587, (*cited on: Chap.2-p.50*).

HONG, J. G., KU, K. W., KIM, S. R., and LEE, C. W. "Effect of cavitation in circular nozzle and elliptical nozzles on the spray characteristic". *Atomization and Sprays*, vol. 20.10 (2010), pp. 877–886. ISSN: 10445110. DOI: 10.1615/AtomizSpr.v20.i10.40, (*cited on: Chap.2-p.50*).

HUSBERG, T., MANENTE, V., EHLESKOG, R., and ANDERSSON, S. "Fuel Flow Impingement Measurements on Multi-Orifice Diesel Nozzles". *SAE Technical Paper 2006-01-1552* (2006). DOI: 10.4271/2006-01-1552, (*cited on: Chap.2-p.37*).

Hussain, F. and Husain, H. S. "Elliptic jets. Part 1. Characteristics of unexcited and excited jets". *Journal of Fluid Mechanics*, vol. 208 (1989), p. 257. ISSN: 0022-1120. DOI: 10.1017/S0022112089002843, (*cited on: Chap.2-p.50*).

Idelchik, I. E. *Memento des pertes de charge*. Eyrolles Paris, 1968, (*cited on: Chap.2-p.49*).

Irving, J. B. and Barlow, A. J. "An automatic high pressure viscometer". *Journal of Physics E: Scientific Instruments*, vol. 4.3 (1971), pp. 232–236. ISSN: 0022-3735. DOI: 10.1088/0022-3735/4/3/017, (*cited on: Chap.3-pp.97,103*).

ISO 12937:2000, Petroleum products – Determination of water – Coulometric Karl Fischer titration method. Geneva, 2000, (*cited on: Chap.4-p.160*).

ISO 2719:2002, Determination of flash point – Pensky-Martens closed cup method. Geneva, 2002, (*cited on: Chap.4-p.160*).

Johnson, T. V. "Vehicular Emissions in Review". *SAE International Journal of Engines*, vol. 5.2 (2012), pp. 2012–01–0368. ISSN: 1946-3944. DOI: 10.4271/2012-01-0368, (*cited on: Chap.2-p.18*).

Judy, J., Maynes, D., and Webb, B. W. "Characterization of frictional pressure drop for liquid flows through microchannels". *International Journal of Heat and Mass Transfer*, vol. 45.17 (2002), pp. 3477–3489. ISSN: 00179310. DOI: 10.1016/S0017-9310(02)00076-5, (*cited on: Chap.2-p.26*).

Kallenbach, E. et al. *Elektromagnete*. 4th ed. Wiesbaden: Vieweg+Teubner Verlag, 2012, p. 432. ISBN: 978-3-8348-0968-1. DOI: 10.1007/978-3-8348-8297-4, (*cited on: Chap.5-p.211*).

Kampmann, S., Dittus, B., Mattes, P., and Kirner, M. "The influence of hydro grinding at VCO nozzles on the mixture preparation in a D.I. diesel engine". *SAE Technical Paper 960867* (1996). DOI: 10.4271/960867, (*cited on: Chap.2-p.49*).

Kao, C.-C. and Shih, A. J. "Form measurements of micro-holes". *Measurement Science and Technology*, vol. 18.11 (2007), pp. 3603–3611. ISSN: 0957-0233. DOI: 10.1088/0957-0233/18/11/045, (*cited on: Chap.2-p.47*).

Karnopp, D., Margolis, D., and Rosenberg, R. *System Dynamics - Modeling, Simulation and Control of Mechatronic Systems*. New Jersey, NJ: John Wiley & Sons, 2012. ISBN: 978-0-470-88908-4, (*cited on: Chap.5-p.188*).

KARNOPP, D. "Computer Simulation of Stick-Slip Friction in Mechanical Dynamic Systems". *Journal of Dynamic Systems, Measurement, and Control*, vol. 107.1 (1985), p. 100. ISSN: 00220434. DOI: 10.1115/1.3140698, (*cited on: Chap.5-p.189*).

KASHIWAGI, H. and MAKITA, T. "Viscosity of twelve hydrocarbon liquids in the temperature range 298-348 K at pressures up to 110 MPa". *International Journal of Thermophysics*, vol. 3.4 (1982), pp. 289–305. ISSN: 0195928X. DOI: 10.1007/BF00502346, (*cited on: Chap.3-pp.97,104*).

KASTENGREN, A. L. et al. "Engine Combustion Network (ECN): Measurements of Nozzle Geometry and Hydraulic Behavior". *Atomization and Sprays*, vol. 22.12 (2012), pp. 1011–1052. ISSN: 1044-5110. DOI: 10.1615/AtomizSpr.2013006309, (*cited on: Chap.2-p.47*).

KATO, T., KOYAMA, T., SASAKI, K., and MORI, K. K. "Common Rail Fuel Injection System for Improvement of Engine Performance on Heavy Duty Diesel Engine". *SAE Technical Paper 980806* (1998). DOI: 10.4271/980806, (*cited on: Chap.2-p.17*).

KEGL, B. "An Improved Mathematical Model of Conventional FIE Processes". *SAE Technical Paper 950079* (1995). DOI: 10.4271/950079, (*cited on: Chap.3-p.89*).

KEGL, B. "Biodiesel usage at low temperature". *Fuel*, vol. 87 (2008), pp. 1306–1317. ISSN: 00162361. DOI: 10.1016/j.fuel.2007.06.023, (*cited on: Chap.3-pp.109,112*).

KEGL, B. and HRIBERNIK, A. "Experimental Analysis of Injection Characteristics Using Biodiesel Fuel". *Energy & Fuels*, vol. 20.5 (2006), pp. 2239–2248. ISSN: 0887-0624. DOI: 10.1021/ef060285m, (*cited on: Chap.3-pp.109,110,112, Chap.6-p.262*).

KENT, J. C. and BROWN, G. M. "Nozzle Exit Flow Characteristics for Square-edged and Rounded Inlet Geometries". *Combustion Science and Technology*, vol. 30.1-6 (1983), pp. 121–132. ISSN: 0010-2202. DOI: 10.1080/00102208308923615, (*cited on: Chap.2-p.35*).

KESKINEN, K., KAARIO, O., TILLI, A., HULKKONEN, T., and LARMI, M. "Improving the Accuracy of 1-D Fuel Injection Modeling". *SAE Technical Paper 2012-01-1256* (2012). DOI: 10.4271/2012-01-1256, (*cited on: Chap.3-p.95*).

Khasanshin, T. S., Shchamialiou, A. P., and Poddubskij, O. G. "Thermodynamic Properties of Heavy n-Alkanes in the Liquid State: n-Dodecane". *International Journal of Thermophysics*, vol. 24.5 (2003), pp. 1277–1289. ISSN: 0195928X. DOI: 10.1023/A:1026199017598, (*cited on: Chap.3-pp.98,102,106*).

Khasanshin, T. S. and Shchemelev, A. P. "Sound Velocity in Liquid n-Alkanes". *High Temperature*, vol. 39.1 (2001), pp. 60–67. ISSN: 0018151X. DOI: 10.1023/A:1004170530517, (*cited on: Chap.3-p.98*).

Kiełczyński, P. et al. "Ultrasonic evaluation of thermodynamic parameters of liquids under high pressure". *IEEE Transactions on Ultrasonics, Ferroelectrics, and Frequency Control*, vol. 62.6 (2015), pp. 1122–1131. ISSN: 0885-3010. DOI: 10.1109/TUFFC.2015.007053, (*cited on: Chap.3-pp.99,100,102*).

Kiijärvi, J. "Diesel fuel injection system simulation". PhD thesis. Helsinki University of Technology, 2003. ISBN: 9512266571, (*cited on: Chap.3-p.86*).

Kiss, T. and Wolverton, M. A. "Analytical Comparison of 2 and 3 Way Digital Valves for Use on Direct Needle Control Fuel Injectors". *SAE Technical Paper 2004-01-0032* (2004). DOI: 10.4271/2004-01-0032, (*cited on: Chap.3-pp.91,92,94*).

Knight, B. E. "Fuel-Injection system calculations". *Proceedings of the Institution of Mechanical Engineers, Automobile Division*, vol. 14.1 (1960), pp. 25–33. ISSN: 0367-8822. DOI: 10.1243/PIME_AUTO_1960_000_009_02, (*cited on: Chap.3-pp.85,88*).

Kolev, N. I. "Thermodynamic and transport properties of diesel fuel". *Multiphase Flow Dynamics 3: turbulence, gas absorption and release, diesel fuel properties*. 3rd editio. Springer Verlag, 2007. Chap. 13, pp. 293–327. ISBN: 978-3-540-71443-9, (*cited on: Chap.5-pp.197,235,257*).

Koo, J. and Kleinstreuer, C. "Viscous dissipation effects in microtubes and microchannels". *International Journal of Heat and Mass Transfer*, vol. 47.14-16 (2004), pp. 3159–3169. ISSN: 00179310. DOI: 10.1016/j.ijheatmasstransfer.2004.02.017, (*cited on: Chap.2-p.26, Chap.5-p.197*).

Kouzel, B. "How pressure affects liquid viscosity". *Hydrocarbon Process. Petrol Refiner*, vol. 44 (3) (1965), p. 120, (*cited on: Chap.3-p.105, Chap.4-p.181*).

Kull, E. and Krüger, G. "Correlation of spray symmetry with mass and momentum of multihole diesel nozzles". *THIESEL 2004 Conference on Thermo and Fluid-dynamic Processes in Diesel Engines*. Valencia, Spain, 2004, pp. 7–10, (*cited on: Chap.2-p.37*).

Kumar, K., Gaur, R. R., Garg, R. D., and Gajendra Babu, M. K. "A Finite Difference Scheme for the Simulation of a Fuel Injection System". *SAE Technical Paper 831337* (1983). DOI: 10.4271/831337, (*cited on: Chap.3-pp.86,88*).

Lapuerta, M., Armas, O., and Rodríguez-Fernández, J. "Effect of biodiesel fuels on diesel engine emissions". *Progress in Energy and Combustion Science*, vol. 34.2 (2008), pp. 198–223. ISSN: 03601285. DOI: 10.1016/j.pecs.2007.07.001, (*cited on: Chap.3-p.107*).

Lee, C.-w., Kim, I., Koo, K.-w., Park, J., and Lee, Y. "Experimental study of the effects of nozzle hole geometry for a DI diesel engine". *ICLASS 2006*. Kyoto, 2006, (*cited on: Chap.2-p.50*).

Lee, J. H., Cho, S., Lee, S. Y., and Bae, C. "Bouncing of the diesel injector needle at the closing stage". *Proceedings of the Institution of Mechanical Engineers, Part D: Journal of Automobile Engineering*, vol. 216.8 (2002), pp. 691–700. ISSN: 0954-4070. DOI: 10.1177/095440700221600807, (*cited on: Chap.3-pp.91,92,93*).

Lee, J. W. et al. "Effect of piezo-driven and solenoid-driven needle opening of common-rail diesel injectors on internal nozzle flow and spray development". *International Journal of Engine Research*, vol. 7.6 (2006), pp. 489–502. ISSN: 1468-0874. DOI: 10.1243/14680874JER00806, (*cited on: Chap.2-p.21*).

Lee, W.-K. K., Fezzaa, K., and Wang, J. "Metrology of steel micronozzles using x-ray propagation-based phase-enhanced microimaging". *Applied Physics Letters*, vol. 87.8 (2005), p. 84105. ISSN: 00036951. DOI: 10.1063/1.2034099, (*cited on: Chap.2-p.46*).

Lefebvre, A. H. *Atomization and Sprays*. CRC Press, 1988. ISBN: 9780891166030, (*cited on: Chap.2-p.51*).

Leidenfrost, W. "Measurements of thermophysical properties". *Measurements in Heat Transfer*. Ed. by E. R. G. Eckert and R. J. Goldstein. 2nd editio. New York: Hemisphere Publishing Corporation, 1976. Chap. 11. ISBN: 0-89116-652-1, (*cited on: Chap.3-p.106*).

Lichtarowicz, A., Duggins, R. K., and Markland, E. "Discharge coefficients for incompressible non-cavitating flow through long orifices". *Journal of Mechanical Engineering Science*, vol. 7.2 (1965), pp. 210–219. ISSN: 0022-2542. DOI: 10.1243/JMES_JOUR_1965_007_029_02, (*cited on: Chap.2-pp.35,36,47, Chap.4-p.148*).

Lindström, M. "Injector Nozzle Hole Parameters and their Influence on Real DI Diesel Performance". PhD thesis. KTH, 2009, (*cited on: Chap.2-pp.29,37*).

Liu, B., Jia, M., and Peng, Z. "An investigation of multiple-injection strategy in a Diesel PCCI combustion enginee". *SAE Technical Paper 2010-01-1134* (2010). DOI: 10.4271/2010-01-1134, (*cited on: Chap.2-p.60*).

LMS. *Imagine.Lab AMESim v.10. User's manual.* 2010, (*cited on: Chap.4-p.150, Chap.5-p.185*).

Lopez, J. J., Salvador, F. J., Garza, O. A. de la, and Arrègle, J. "Characterization of the pressure losses in a common rail diesel injector". *Proceedings of the Institution of Mechanical Engineers Part D-Journal of Automobile Engineering*, vol. 226.D12 (2012), pp. 1697–1706. ISSN: 0954-4070. DOI: 10.1177/0954407012447020, (*cited on: Chap.2-p.28*).

Macian, V., Bermudez, V., Payri, R., and Gimeno, J. "New technique for determination of internal geometry of a Diesel nozzle with the use of silicone methodology". *Experimental Techniques*, vol. 27.April (2003), pp. 39–43. ISSN: 0732-8818. DOI: 10.1111/j.1747-1567.2003.tb00107.x, (*cited on: Chap.2-pp.45,48,49, Chap.4-p.150*).

Macian, V., Payri, R., Margot, X., and Salvador, F. J. "A CFD analysis of the influence of diesel nozzle geometry on the inception of cavitation". *Atomization and Sprays*, vol. 13 (2003), pp. 579–604. ISSN: 1045-5110. DOI: 10.1615/AtomizSpr.v13.i56.80.

Marcer, R. et al. "Coupling 1D System AMESim and 3D CFD EOLE models for Diesel Injection Simulation Renault". *ILASS - Europe 2010, 23rd Annual Conference on Liquid Atomization and Spray Systems*. September. 2010, pp. 1–10, (*cited on: Chap.3-pp.92,95*).

Marcic, M. "Computer Simulation of the Diesel Fuel Injection Nozzle". *SAE Technical Paper 930925* (1993). DOI: 10.4271/930925, (*cited on: Chap.3-p.88*).

Marcic, M. "Calculation of the Diesel Fuel Injection Parameters". *SAE Technical Paper 952071* (1995). DOI: 10.4271/952071, (*cited on: Chap.3-p.88*).

Marcic, M. and Kovacic, Z. "Computer Simulation of the Diesel Fuel Injection System". *SAE Technical Paper 851583* (1985). doi: 10.4271/851583, (*cited on: Chap.3-pp.87,88*).

Marcic, S., Marcic, M., and Praunseis, Z. "Computer Simulation of the Common Rail Accumulator Fuel-Injection System". *Journal of Mechanical and Automobile Engineering*, vol. 1.1 (2016), pp. 1–15, (*cited on: Chap.3-p.95*).

Martí Gómez-Aldaraví, P. "Development of a computational model for a simultaneous simulation of internal flow and spray break-up of the diesel injection process". PhD thesis. Valencia (Spain): Universitat Politècnica de València, 2014. doi: 10.4995/Thesis/10251/43719.

Martínez López, J. "Estudio computacional de la influencia del levantamiento de aguja sobre el flujo interno y el fenómeno de la cavitación en toberas de inyección diésel". PhD thesis. Valencia (Spain): Universitat Politècnica de València, 2013. doi: 10.4995/Thesis/10251/29291, (*cited on: Chap.1-pp.2,4, Chap.2-pp.29,32,39, Chap.3-p.92*).

Matsumoto, S., Yamada, K., and Date, K. "Concepts and Evolution of Injector for Common Rail System". *SAE Technical Paper 2012-01-1753* (2012). doi: 10.4271/2012-01-1753, (*cited on: Chap.2-pp.23,24*).

Matsumoto, S. et al. "4 th Generation Diesel Common Rail System: Realizing Ideal Structure Function for Diesel Engine". *SAE Technical Paper 2013-01-1590* (2013). doi: 10.4271/2013-01-1590, (*cited on: Chap.2-p.23*).

Matsuoka, S., Yokota, K., Kamimoto, T., and Igoshi, M. "A Study of Fuel Injection Systems in Diesel Engines". *SAE Technical Paper 760551* (1976). doi: 10.4271/760551, (*cited on: Chap.3-pp.86,88*).

Mohan, B., Yang, W., and Chou, S. K. "Fuel injection strategies for performance improvement and emissions reduction in compression ignition engines - A review". *Renewable and Sustainable Energy Reviews*, vol. 28.x (2013), pp. 664–676. issn: 13640321. doi: 10.1016/j.rser.2013.08.051, (*cited on: Chap.1-p.2, Chap.2-p.17*).

Molina, S., Salvador, F. J., Carreres, M., and Jaramillo, D. "A computational investigation on the influence of the use of elliptical orifices on the inner nozzle flow and cavitation development in diesel injector nozzles". *Energy Conversion and Management*, vol. 79 (2014), pp. 114–127. issn: 01968904. doi: 10.1016/j.enconman.2013.12.015, (*cited on: Chap.2-p.50*).

Mollenhauer, K. and Tschoke, H. *Handbook of Diesel Engines*. Ed. by K. Mollenhauer and H. Tschöke. 1st ed. Berlin, Heidelberg: Springer Berlin Heidelberg, 2010, p. 636. isbn: 978-3-540-89082-9. doi: 10.1007/978-3-540-89083-6, (*cited on: Chap.2-pp.15,29, Chap.3-p.96*).

Monyem, A., Van Gerpen, J. H., and Canakci, M. "The Effect of Timing and Oxidation on Emissions from Biodiesel-Fueled Engines". *Transactions of the ASAE*, vol. 44.1 (2001), pp. 35–42. issn: 2151-0059. doi: 10.13031/2013.2301, (*cited on: Chap.3-p.107*).

Moody, L. and Princeton, N. "Friction Factors for Pipe Flow". *Transactions of the ASME*, vol. 66.8 (1944), pp. 671–684, (*cited on: Chap.5-p.192*).

Moon, S. et al. "Effect of the number and position of nozzle holes on in- and near-nozzle dynamic characteristics of diesel injection". *Fuel*, vol. 150 (2015), pp. 112–122. issn: 00162361. doi: 10.1016/j.fuel.2015.01.097, (*cited on: Chap.2-p.50, Chap.6-p.297*).

Moreno, E. "Contribución a la simulación del sistema de inyección de combustible de un motor diesel de inyección indirecta". PhD thesis. Universidad Politécnica de Madrid, 1999. isbn: 8482402609, (*cited on: Chap.3-p.86*).

Morini, G. L. "Viscous heating in liquid flows in micro-channels". *International Journal of Heat and Mass Transfer*, vol. 48.17 (2005), pp. 3637–3647. issn: 00179310. doi: 10.1016/j.ijheatmasstransfer.2005.01.011, (*cited on: Chap.5-p.197*).

Mugele, R. A. and Evans, H. D. "Droplet Size Distribution in Sprays". *Industrial & Engineering Chemistry*, vol. 43.6 (1951), pp. 1317–1324. doi: 10.1021/ie50498a023, (*cited on: Chap.2-p.64*).

Mulemane, A. et al. "Comparing cavitation in Diesel injectors based on different modeling approaches". *SAE Technical Paper 2004-01-0027* (2004). doi: 10.4271/2004-01-0027, (*cited on: Chap.3-p.94*).

Muñoz, A. "Análisis y Simulación de los Sistemas de Inyección de Combustible de los Motores Diesel Equipados con Bomba en Línea". PhD thesis. Universidad Politécnica de Madrid, 1987, (*cited on: Chap.3-p.88*).

Naber, J. D. and Siebers, D. L. "Effect of gas density and vaporization on penetration and dispersion of Diesel sprays". *SAE Technical Paper 960034*, vol. 105.412 (1996), pp. 82–111. doi: 10.4271/960034, (*cited on: Chap.1-p.2, Chap.2-pp.37,61,62,63*).

Nakayama, Y. "Action of the Fluid in the Air-Micrometer : 1st Report, Characteristics of Small-Diameter Nozzle and Orifice". *Bulletin of JSME*, vol. 4.15 (1961), pp. 507–515. ISSN: 1881-1426. DOI: 10.1299/jsme1958.4.507, (*cited on: Chap.2-p.36*).

Nayfeh, A. H. "Nonlinear Stability of a Liquid Jet". *Physics of Fluids*, vol. 13.4 (1970), p. 841. ISSN: 00319171. DOI: 10.1063/1.1693025, (*cited on: Chap.2-p.54*).

Ndiaye, E. H. I., Bazile, J. P., Nasri, D., Boned, C., and Daridon, J. L. "High pressure thermophysical characterization of fuel used for testing and calibrating diesel injection systems". *Fuel*, vol. 98 (2012), pp. 288–294. ISSN: 00162361. DOI: 10.1016/j.fuel.2012.04.005, (*cited on: Chap.3-pp.99,100,101,102,103,105*).

Nikolić, B. D., Kegl, B., Marković, S. D., and Mitrović, M. S. "Determining the speed of sound, density, and bulk modulus of rapeseed oil, biodiesel, and diesel fuel". *Thermal Science*, vol. 16.2 (2013), pp. 505–514. ISSN: 03549836. DOI: 10.2298/TSCI120426187N, (*cited on: Chap.3-pp.99,100*).

Nishimura, T., Satoh, K., Takahashi, S., and Yokota, K. "Effects of Fuel Injection Rate on Combustion and Emission in a DI Diesel Engine". *SAE Technical Paper 981929*. 1998. DOI: 10.4271/981929, (*cited on: Chap.1-p.1*).

Nurick, W. H. "Orifice Cavitation and Its Effect on Spray Mixing". *Journal of Fluids Engineering*, vol. 98.4 (1976), p. 681. ISSN: 00982202. DOI: 10.1115/1.3448452, (*cited on: Chap.2-pp.39,40, Chap.5-p.194*).

Nusselt, W. "Der Wärmeaustausch zwischen Wand und Wasser im Rohr". *Forschung auf dem Gebiete des Ingenieurwesens*, vol. 2.9 (1931), pp. 309–313. ISSN: 0015-7899. DOI: 10.1007/BF02583210, (*cited on: Chap.5-p.235*).

Ohnesorge, W. V. "Formation of Drops by nozzles and the breakup of liquid jets". *ZAMM - Journal of Applied Mathematics and Mechanics*, vol. 16.6 (1936), pp. 355–358. ISSN: 00442267. DOI: 10.1002/zamm.19360160611, (*cited on: Chap.2-p.54*).

Oliveira, C. M. B. P. and Wakeham, W. A. "The viscosity of five liquid hydrocarbons at pressures up to 250 MPa". *International Journal of Thermophysics*, vol. 13.5 (1992), pp. 773–790. ISSN: 0195-928X. DOI: 10.1007/BF00503906, (*cited on: Chap.3-pp.97,103*).

On type-approval of motor vehicles and engines with respect to emissions from heavy duty vehicles (Euro VI) and on access to vehicle repair and maintenance information and amending Regulation (EC) No 715/2007 and Directive 2007/46/EC and repealing Directi. Official Journal of the European Union. Regulation. 2009, (*cited on: Chap.1-p.1*).

Onorati, A. "Prediction of the Acoustical Performances of Muffling Pipe Systems by the Method of Characteristics". *Journal of Sound and Vibration*, vol. 171.3 (1994), pp. 369–395. ISSN: 0022460X. DOI: 10.1006/jsvi.1994.1127, (*cited on: Chap.3-p.86*).

Palomar, J. M. and Ruiz, J. J. "Análisis y Predicción del Comportamiento de una Bomba de Inyección Rotativa en Función de las Actuaciones Sobre Sus Parámetros Fundamentales". *Anales de Ingeniería Mecánica*, vol. 11.1 (1997), pp. 143–150, (*cited on: Chap.3-p.89*).

Park, S. H., Yoon, S. H., and Lee, C. S. "Effects of multiple-injection strategies on overall spray behavior, combustion, and emissions reduction characteristics of biodiesel fuel". *Applied Energy*, vol. 88.1 (2011), pp. 88–98. ISSN: 0306-2619. DOI: http://dx.doi.org/10.1016/j.apenergy.2010.07.024, (*cited on: Chap.1-pp.1,2, Chap.2-p.17*).

Park, Y. et al. "Effects of diesel fuel temperature on fuel flow and spray characteristics". *Fuel*, vol. 162 (2015), pp. 1–7. ISSN: 00162361. DOI: 10.1016/j.fuel.2015.09.008, (*cited on: Chap.3-pp.108,109,110,112, Chap.6-pp.262,295*).

Paton, J. M. and Schaschke, C. J. "Viscosity measurement of biodiesel at high pressure with a falling sinker viscometer". *Chemical Engineering Research and Design*, vol. 87.11 (2009), pp. 1520–1526. ISSN: 02638762. DOI: 10.1016/j.cherd.2009.04.007, (*cited on: Chap.3-pp.98,103,104*).

Payri, F., Payri, R., Salvador, F., and Martínez-López, J. "A contribution to the understanding of cavitation effects in Diesel injector nozzles through a combined experimental and computational investigation". *Computers & Fluids*, vol. 58 (2012), pp. 88–101. ISSN: 00457930. DOI: 10.1016/j.compfluid.2012.01.005, (*cited on: Chap.2-p.49*).

Payri, F., Bermúdez, V., Payri, R., and Salvador, F. J. "The influence of cavitation on the internal flow and the spray characteristics in diesel injection nozzles". *Fuel*, vol. 83.4-5 (2004), pp. 419–431. ISSN: 00162361. DOI: 10.1016/j.fuel.2003.09.010, (*cited on: Chap.1-p.2, Chap.2-pp.45,49,61, Chap.3-p.110, Chap.4-p.148*).

PAYRI, F. and DESANTES, J. M. *Motores de combustion interna alternativos*. Editorial Reverte, 2011. ISBN: 978-84-291-4802-2, (*cited on: Chap.1-pp.1,2, Chap.2-pp.13,14,17,52*).

PAYRI, F., PAYRI, R., BARDI, M., and CARRERES, M. "Engine combustion network: Influence of the gas properties on the spray penetration and spreading angle". *Experimental Thermal and Fluid Science*, vol. 53.September 2015 (2014), pp. 236–243. ISSN: 08941777. DOI: 10.1016/j.expthermflusci.2013.12.014, (*cited on: Chap.2-p.61*).

PAYRI, F., PAYRI, R., SALVADOR, F. J., and GIMENO, J. "Influence of Nozzle Geometry on Spray Characteristics in Non-Evaporative and evaporative conditions". *SAE Technical Paper 2007-24-0023* (2007). DOI: 10.4271/2007-24-0023, (*cited on: Chap.1-p.1*).

PAYRI, R., CLIMENT, H., SALVADOR, F. J., and FAVENNEC, A. G. "Diesel Injection System Modelling. Methodology and Application for a First-generation Common Rail System". *Proceedings of the Institution of Mechanical Engineers, Part D: Journal of Automobile Engineering*, vol. 218.1 (2004), pp. 81–91. ISSN: 0954-4070. DOI: 10.1243/095440704322829191, (*cited on: Chap.3-pp.91,94,113*).

PAYRI, R., GARCIA-OLIVER, J. M., BARDI, M., and MANIN, J. "Fuel temperature influence on diesel sprays in inert and reacting conditions". *Applied Thermal Engineering*, vol. 35 (2012), pp. 185–195. ISSN: 1359-4311. DOI: 10.1016/j.applthermaleng.2011.10.027, (*cited on: Chap.3-pp.111,112,113*).

PAYRI, R., GARCIA-OLIVER, J. M., SALVADOR, F. J., and GIMENO, J. "Using spray momentum flux measurements to understand the influence of diesel nozzle geometry on spray characteristics". *Fuel*, vol. 84.5 (2005), pp. 551–561. ISSN: 00162361. DOI: 10.1016/j.fuel.2004.10.009, (*cited on: Chap.1-p.1, Chap.2-pp.36,37,45,46*).

PAYRI, R., GIL, A., PLAZAS, A. H., and GIMENEZ, B. "Influence of Nozzle Seat Type on Internal Flow of Convergent Nozzles". *SAE Tehnical Paper 2004-01-2010* (2004). DOI: 10.4271/2004-01-2010, (*cited on: Chap.2-p.29*).

PAYRI, R., GIMENO, J., VIERA, J. P., and PLAZAS, A. H. "Effect of Partial Needle Lift on the Hydraulic and Evaporative Performance Characteristics of a Common rail Diesel Fuel Injector". *THIESEL 2012 Conference on Thermo- and Fluid Dynamic Processes in Diesel Engines*. Valencia, Spain, 2012, pp. 1–19, (*cited on: Chap.2-p.25*).

Payri, R., Guardiola, C., Salvador, F. J., and Gimeno, J. "Critical cavitation number determination in Diesel injection nozzles". *Experimental Techniques*, vol. 28.3 (2004), pp. 49–52. doi: 10.1111/j.1747-1567.2004.tb00164.x, (*cited on: Chap.2-pp.30,45, Chap.3-p.110*).

Payri, R., Molina, S., Salvador, F. J., and Gimeno, J. "A study of the relation between nozzle geometry, internal flow and sprays characteristics in diesel fuel injection systems". *KSME International Journal*, vol. 18.7 (2004), pp. 1222–1235. issn: 1226-4865. doi: 10.1007/BF02983297, (*cited on: Chap.2-p.45*).

Payri, R., Salvador, F., Gimeno, J., and Bracho, G. "The effect of temperature and pressure on thermodynamic properties of diesel and biodiesel fuels". *Fuel*, vol. 90.3 (2011), pp. 1172–1180. issn: 00162361. doi: 10.1016/j.fuel.2010.11.015, (*cited on: Chap.1-p.2, Chap.3-pp.99,100,102,108, Chap.4-pp.161,177*).

Payri, R., Salvador, F., Gimeno, J., and Novella, R. "Flow regime effects on non-cavitating injection nozzles over spray behavior". *International Journal of Heat and Fluid Flow*, vol. 32.1 (2011), pp. 273–284. issn: 0142727X. doi: 10.1016/j.ijheatfluidflow.2010.10.001, (*cited on: Chap.6-p.264*).

Payri, R., Salvador, F. J., Gimeno, J., and Bracho, G. "A new methodology for correcting the signal cumulative phenomenom on injection rate measurements". *Experimental Techniques*, vol. 32.February (2008), pp. 46–49. issn: 07328818. doi: 10.1111/j.1747-1567.2007.00188.x, (*cited on: Chap.4-p.158*).

Payri, R., Salvador, F. J., Gimeno, J., and Bracho, G. "Effect of fuel properties on diesel spray development in extreme cold conditions". *Proceedings of the Institution of Mechanical Engineers. Part D, Journal of Automobile Engineering*, vol. 222.9 (2008), pp. 1743–1753. issn: 0954-4070. doi: 10.1243/09544070JAUTO844, (*cited on: Chap.3-pp.108,109,111,112, Chap.6-p.295*).

Payri, R., Salvador, F. J., Gimeno, J., and Bracho, G. "Understanding Diesel Injection Characteristics in Winter Conditions". *SAE Technical Paper 2009-01-0836* (2009). doi: 10.4271/2009-01-0836, (*cited on: Chap.3-pp.108,109,111,112, Chap.6-p.295*).

Payri, R., Salvador, F. J., Gimeno, J., and De la Morena, J. "Effects of nozzle geometry on direct injection diesel engine combustion process". *Applied Thermal Engineering*, vol. 29.10 (2009), pp. 2051–2060. ISSN: 13594311. DOI: 10.1016/j.applthermaleng.2008.10.009, (*cited on: Chap.2-p.32*).

Payri, R., Salvador, F. J., Gimeno, J., and De la Morena, J. "Study of cavitation phenomena based on a technique for visualizing bubbles in a liquid pressurized chamber". *International Journal of Heat and Fluid Flow*, vol. 30.4 (2009), pp. 768–777. ISSN: 0142727X. DOI: 10.1016/j.ijheatfluidflow.2009.03.011, (*cited on: Chap.2-p.49*).

Payri, R., Salvador, F. J., Gimeno, J., and De la Morena, J. "Influence of injector technology on injection and combustion development, Part 1: Hydraulic characterization". *Applied Energy*, vol. 88.4 (2011), pp. 1068–1074. ISSN: 0306-2619. DOI: 10.1016/j.apenergy.2010.10.012, (*cited on: Chap.1-p.1*).

Payri, R., Salvador, F. J., Gimeno, J., and De la Morena, J. "Influence of injector technology on injection and combustion development, Part 2: Combustion analysis". *Applied Energy*, vol. 88.4 (2011), pp. 1130–1139. ISSN: 0306-2619. DOI: 10.1016/j.apenergy.2010.10.012, (*cited on: Chap.1-p.1*).

Payri, R., Salvador, F. J., Gimeno, J., and Garcia, A. "Flow regime effects over non-cavitating diesel injection nozzles". *Proceedings of the Institution of Mechanical Engineers, Part D: Journal of Automobile Engineering*, vol. 226.1 (2012), pp. 133–144. ISSN: 0954-4070. DOI: 10.1177/0954407011413056, (*cited on: Chap.2-p.48, Chap.6-p.264*).

Payri, R., Salvador, F. J., Marí-Aldaraví, P., and Martínez-López, J. "Using one-dimensional modeling to analyze the influence of the use of biodiesels on the dynamic behavior of solenoid-operated injectors in common rail systems: Detailed injection system model". *Energy Conversion and Management*, vol. 54.1 (2012), pp. 90–99. ISSN: 01968904. DOI: 10.1016/j.enconman.2011.10.007, (*cited on: Chap.2-p.28, Chap.3-pp.91,92,95*).

Payri, R., Tormos, B., Salvador, F., and Plazas, A. "Using one-dimensional modelling codes to analyse the influence of diesel nozzle geometry on injection rate characteristics". *International Journal of Vehicle Design*, vol. 38.1 (2005), p. 58. ISSN: 0143-3369. DOI: 10.1504/IJVD.2005.006605, (*cited on: Chap.3-pp.91,94,113*).

Peiner, E., Balke, M., and Doering, L. "Form measurement inside fuel injector nozzle spray holes". *Microelectronic Engineering*, vol. 86.4-6 (2009), pp. 984–986. ISSN: 01679317. DOI: 10.1016/j.mee.2008.12.016, (*cited on: Chap.2-p.47*).

Peleties, F., Segovia, J. J., Trusler, J. P. M., and Vega-Maza, D. "Thermodynamic properties and equation of state of liquid di-isodecyl phthalate at temperature between (273 and 423) K and at pressures up to 140 MPa". *Journal of Chemical Thermodynamics*, vol. 42.5 (2010), pp. 631–639. ISSN: 00219614. DOI: 10.1016/j.jct.2009.12.002, (*cited on: Chap.3-pp.99,100,101,102,103,106*).

Peleties, F. and Trusler, J. P. M. "Viscosity of liquid di-isodecyl phthalate at temperatures between (274 and 373) K and at pressures up to 140 MPa". *Journal of Chemical and Engineering Data*, vol. 56.5 (2011), pp. 2236–2241. ISSN: 00219568. DOI: 10.1021/je101256z, (*cited on: Chap.3-pp.99,100,101,102,103*).

Plamondon, E. and Seers, P. "Development of a simplified dynamic model for a piezoelectric injector using multiple injection strategies with biodiesel/diesel-fuel blends". *Applied Energy*, vol. 131 (2014), pp. 411–424. ISSN: 03062619. DOI: 10.1016/j.apenergy.2014.06.039, (*cited on: Chap.3-pp.92,95*).

Plazas, A. H. "Modelado unidimensional de inyectores common-rail Diesel". PhD thesis. Valencia: Universitat Politècnica de València, 2005, (*cited on: Chap.1-pp.2,4, Chap.3-pp.92,94, Chap.4-p.139*).

Plesset, M. "The Dynamics of Cavitation Bubbles". *ASME Journal of Applied Mechanics*, vol. 16 (1949), pp. 277–282, (*cited on: Chap.2-p.39*).

Pogulyaev, Y., Baitimerov, R., and Rozhdestvenskii, Y. "Detailed Dynamic Modeling of Common Rail Piezo Injector". *Procedia Engineering*, vol. 129 (2015), pp. 93–98. ISSN: 18777058. DOI: 10.1016/j.proeng.2015.12.014, (*cited on: Chap.3-pp.92,95*).

Potz, D., Chirst, W., and Dittus, B. "Diesel nozzle: The determining interface between injection system and combustion chamber". *THIESEL 2000 Conference on Thermo and Fluid-dynamic Processes in Diesel Engines*. Valencia, Spain, 2000, (*cited on: Chap.2-pp.30,49*).

Rakopoulos, C. and Hountalas, D. "A simulation analysis of a DI diesel engine fuel injection system fitted with a constant pressure valve". *Energy Conversion and Management*, vol. 37.2 (1996), pp. 135–150. ISSN: 01968904. DOI: 10.1016/0196-8904(95)00176-E, (*cited on: Chap.3-p.89*).

RAMAMURTHI, K. and NANDAKUMAR, K. "Characteristics of flow through small sharp-edged cylindrical orifices". *Flow Measurement and Instrumentation*, vol. 10.3 (1999), pp. 133–143. ISSN: 09555986. DOI: 10.1016/S0955-5986(99)00005-9, (*cited on: Chap.2-p.48*).

RANDALL, L. N. "Rocket Applications of the Cavitating Venturi". *Journal of the American Rocket Society*, vol. 22.1 (1952), pp. 28–38. ISSN: 1936-9964. DOI: 10.2514/8.4412, (*cited on: Chap.2-p.40*).

RANZ, W. E. "Some experiments on orifice sprays". *The Canadian Journal of Chemical Engineering*, vol. 36.4 (1958), pp. 175–181. ISSN: 00084034. DOI: 10.1002/cjce.5450360405, (*cited on: Chap.2-p.62*).

REITZ, R. D. "Atomisation and other breakup regimes of a liquid jet". PhD thesis. Ph.D. Thesis, Princeton University, 1978, (*cited on: Chap.2-p.55*).

REITZ, R. D. "Mechanism of atomization of a liquid jet". *Physics of Fluids*, vol. 25.10 (1982), p. 1730. ISSN: 00319171. DOI: 10.1063/1.863650, (*cited on: Chap.2-pp.53,58*).

REITZ, R. D. and BRACCO, F. B. "On the dependence of spray angle and other spray parameters on nozzle design and operating conditions". *SAE Technical Paper 790494* (1979). DOI: 10.4271/790494, (*cited on: Chap.2-p.62*).

REYNOLDS, O. "An Experimental Investigation of the Circumstances Which Determine Whether the Motion of Water Shall Be Direct or Sinuous, and of the Law of Resistance in Parallel Channels". *Philosophical Transactions of the Royal Society of London*, vol. 174 (1883), pp. 935–982, (*cited on: Chap.2-p.26*).

RODRIGUEZ, P. "Modelado del comportamiento hidrodinámico de sistemas de inyección directa Diesel". PhD thesis. Valencia: Universitat Politècnica de València, 2001, (*cited on: Chap.1-pp.2,4, Chap.3-pp.92,93*).

RODRÍGUEZ-ANTÓN, L. M., APARICIO, C., GUIGNON, B., and SANZ, P. D. "Volumetric properties at high pressure of waste oil methyl ester compared with diesel oil". *Fuel*, vol. 87.10-11 (2008), pp. 1934–1940. ISSN: 00162361. DOI: 10.1016/j.fuel.2007.10.006.

RODRÍGUEZ-ANTÓN, L. M., CASANOVA-KINDELAN, J., and TARDAJOS, G. "High Pressure Physical Properties of Fluids used in Diesel injection systems". *SAE Paper 2000-01-2046*, vol. 2000-01-20 (2000). DOI: 10.4271/2000-01-2046.

RODRÍGUEZ-ANTÓN, L. M. "Simulación de sistemas de inyección Diesel mediante la técnica del Bond Graph". PhD thesis. Universidad Politécnica de Madrid, 1996.

Roth, H., Gavaises, M., and Arcoumanis, C. "Cavitation initiation, its development and link with flow turbulence in diesel injector nozzles." *SAE Technical Paper 2002-01-0214* (2002). DOI: 10.4271/2002-01-0214, (*cited on: Chap.2-p.45*).

Ruiz, F. "A few useful relations for cavitating orifices". *In Proceedings of International Conference on Liquid Atomizations and Spray System. ICLASS-91, Gaithersburg, Maryland, 15-18 July.* 1991, pp. 595–602, (*cited on: Chap.2-p.58*).

Ruiz, F. "Turbulence inside a cavitating injector orifice: a different animal". *ILASS-Americas.* 1998, pp. 133–137, (*cited on: Chap.2-p.58*).

Ruiz, S. "Estudio teórico-experimental de los procesos de atomización y de mezcla en los chorros Diesel D.I." PhD thesis. Valencia: E.T.S. Ingenieros Industriales. Universidad Politécnica de Valencia, 2003, (*cited on: Chap.1-p.4*).

Rutland, D. and Jameson, G. "Theoretical prediction of the sizes of drops formed in the breakup of capillary jets". *Chemical Engineering Science*, vol. 25.11 (1970), pp. 1689–1698. ISSN: 00092509. DOI: 10.1016/0009-2509(70)80060-4, (*cited on: Chap.2-p.54*).

Růžička, V. and Domalski, E. S. "Estimation of the Heat Capacities of Organic Liquids as a Function of Temperature using Group Additivity. I. Hydrocarbon Compounds". *Journal of Physical and Chemical Reference Data*, vol. 22.3 (1993), p. 597. ISSN: 00472689. DOI: 10.1063/1.555923, (*cited on: Chap.3-p.106*).

Růžička, V., Zábranský, M., and Majer, V. "Heat capacities of organic compounds in liquid state II. C1 to C18 n-alkanes". *Journal of Physical and Chemical Reference Data*, vol. 20.2 (1991), p. 405. ISSN: 00472689. DOI: 10.1063/1.555883, (*cited on: Chap.3-pp.97,106*).

Saint-guirons, H., Alliez, J., Lagourette, B., and Xans, P. "High pressure guided falling body viscometer. Representation of alkanes viscosity as a function of temperature and pressure". *High Pressure Research*, vol. 8.1-3 (1992), pp. 419–422. ISSN: 0895-7959. DOI: 10.1080/08957959108260694.

Salvador, F. J. "Estudio teórico experimental de la influencia de la geometría de toberas de inyección Diésel sobre las características del flujo interno y del chorro". PhD thesis. Universitat Politècnica de València, 2003, (*cited on: Chap.1-pp.1,4, Chap.2-pp.35,36,39,40,45,49,59, Chap.3-p.110, Chap.4-pp.139,150*).

Salvador, F. J., Carreres, M., Jaramillo, D., and Martínez-López, J. "Comparison of microsac and VCO diesel injector nozzles in terms of internal nozzle flow characteristics". *Energy Conversion and Management*, vol. 103 (2015), pp. 284–299. ISSN: 01968904. DOI: 10.1016/j.enconman.2015.05.062, (*cited on: Chap.2-p.29*).

Salvador, F. J., Carreres, M., Jaramillo, D., and Martínez-López, J. "Analysis of the combined effect of hydrogrinding process and inclination angle on hydraulic performance of diesel injection nozzles". *Energy Conversion and Management*, vol. 105 (2015), pp. 1352–1365. ISSN: 0196-8904. DOI: 10.1016/j.enconman.2015.08.035, (*cited on: Chap.2-p.49*).

Salvador, F. J., Gimeno, J., De la Morena, J., and Carreres, M. "Using one-dimensional modeling to analyze the influence of the use of biodiesels on the dynamic behavior of solenoid-operated injectors in common rail systems: Results of the simulations and discussion". *Energy Conversion and Management*, vol. 54.1 (2012), pp. 122–132. ISSN: 01968904. DOI: 10.1016/j.enconman.2011.10.007, (*cited on: Chap.2-p.28, Chap.3-pp.92,95,109, Chap.6-pp.295,305*).

Salvador, F. J., Hoyas, S., Novella, R., and Martinez-Lopez, J. "Numerical simulation and extended validation of two-phase compressible flow in diesel injector nozzles". *Proceedings of the Institution of Mechanical Engineers, Part D: Journal of Automobile Engineering*, vol. 225.4 (2011), pp. 545–563. ISSN: 0954-4070. DOI: 10.1177/09544070JAUTO1569, (*cited on: Chap.1-p.2*).

Salvador, F. J., Martínez-López, J., Caballer, M., and De Alfonso, C. "Study of the influence of the needle lift on the internal flow and cavitation phenomenon in diesel injector nozzles by CFD using RANS methods". *Energy Conversion and Management*, vol. 66 (2013), pp. 246–256. ISSN: 01968904. DOI: 10.1016/j.enconman.2012.10.011, (*cited on: Chap.3-pp.108,111,112*).

Salvador, F. J., Martínez-López, J., Romero, J., and Roselló, M. "Influence of biofuels on the internal flow in diesel injector nozzles". *Mathematical and Computer Modelling*, vol. 54.7-8 (2011), pp. 1699–1705. ISSN: 08957177. DOI: 10.1016/j.mcm.2010.12.010, (*cited on: Chap.3-pp.113,114*).

Salvador, F. J., Plazas, A. H., Gimeno, J., and Carreres, M. "Complete modelling of a piezo actuator last-generation injector for diesel injection systems". *International Journal of Engine Research*, vol. 15.1 (2014), pp. 3–19. ISSN: 1468-0874. DOI: 10.1177/1468087412455373, (*cited on: Chap.2-pp.21,22,26,28, Chap.3-pp.92,95*).

Salvador, F. J., Ruiz, S., Gimeno, J., and De la Morena, J. "Estimation of a suitable Schmidt number range in diesel sprays at high injection pressure". *International Journal of Thermal Sciences*, vol. 50.9 (2011), pp. 1790–1798. ISSN: 12900729. DOI: 10.1016/j.ijthermalsci.2011.03.030, (*cited on: Chap.2-p.65*).

Salvador, F. J., Ruiz, S., Salavert, J., and De La Morena, J. "Consequences of using biodiesel on the injection and air-fuel mixing processes in diesel engines". *Proceedings of the Institution of Mechanical Engineers, Part D: Journal of Automobile Engineering*, vol. 227.8 (2013), pp. 1130–1141. ISSN: 09544070. DOI: 10.1177/0954407012463667.

Sangiah, D. K. and Ganippa, L. C. "Application of spray impingement technique for characterisation of high pressure sprays from multi-hole diesel nozzles". *International Journal of Thermal Sciences*, vol. 49.2 (2010), pp. 409–417. ISSN: 12900729. DOI: 10.1016/j.ijthermalsci.2009.08.001, (*cited on: Chap.2-p.37*).

Sargent, L. B. "Pressure-Viscosity Coefficients of Liquid Lubricants". *A S L E Transactions*, vol. 26.1 (1983), pp. 1–10. ISSN: 0569-8197. DOI: 10.1080/05698198308981471, (*cited on: Chap.3-p.105*).

Sayin, C., Gumus, M., and Canakci, M. "Influence of injector hole number on the performance and emissions of a di diesel engine fueled with biodiesel-diesel fuel blends". *Applied Thermal Engineering*, vol. 61.2 (2013), pp. 121–128. ISSN: 13594311. DOI: 10.1016/j.applthermaleng.2013.07.038, (*cited on: Chap.2-p.50*).

Schaschke, C., Fletcher, I., and Glen, N. "Density and Viscosity Measurement of Diesel Fuels at Combined High Pressure and Elevated Temperature". *Processes*, vol. 1.2 (2013), pp. 30–48. ISSN: 2227-9717. DOI: 10.3390/pr1020030, (*cited on: Chap.3-pp.99,101,103*).

Schlichting, H. and Gersten, K. *Boundary layer theory*. 4th editio. McGraw-Hill, 1979. ISBN: 0-07-055334-3, (*cited on: Chap.2-p.33*).

Schmidt, D. P. "Cavitation in Diesel Fuel Injector Nozzles". PhD thesis. Wisconsin: University of Wisconsin - Madison, 1997, (*cited on: Chap.2-p.45*).

Schmidt, D. P. and Corradini, M. L. "The internal flow of diesel fuel injector nozzles: a review". *International Journal of Engine Research*, vol. 2.1 (2001), pp. 1–22. ISSN: 1468-0874. DOI: 10.1243/1468087011545316, (*cited on: Chap.1-p.1, Chap.2-p.41*).

Schmidt, D. P., Rutland, C. J., and Corradini, M. L. "A numerical study of cavitating flow through various nozzle shapes". *SAE Technical Paper 971597* (1997). doi: 10.4271/971597, (*cited on: Chap.2-p.39*).

Schöppe, D. et al. "Delphi Common Rail system with direct acting injector". *MTZ worldwide*, vol. 69.10 (2008), pp. 32–38. issn: 2192-9114. doi: 10.1007/BF03226918, (*cited on: Chap.2-p.24*).

Seykens, X. and Somers, L. "Detailed modeling of common rail fuel injection process". *Journal of Middle European* (2005), pp. 30–39, (*cited on: Chap.1-p.2, Chap.3-pp.92,94*).

Seykens, X., Somers, L., and Baert, R. "Modelling of common rail fuel injection system and influence of fluid properties on process". *In: Proceedings of VAFSEP, Dublin, Ireland; July 6-9,* July (2004), pp. 6–9, (*cited on: Chap.3-pp.92,94*).

Shi, J., Guerrassi, N., Dober, G., Karimi, K., and Meslem, Y. "Complex physics modelling of diesel injector nozzle flow and spray supported by new experiments". *THIESEL 2014 Conference on Thermo- and Fluid Dynamic Processes in Direct Injection Engines.* Valencia, Spain, 2014, (*cited on: Chap.3-p.114*).

Siebers, D. L. "Liquid-phase fuel penetration in diesel sprays". *SAE Technical Paper 980809* (1998). doi: 10.4271/980809, (*cited on: Chap.1-p.2, Chap.2-pp.63,64*).

Siebers, D. L. "Scaling liquid-phase fuel penetration in diesel sprays based on mixing-limited vaporization". *SAE Technical Paper 1999-01-0528* (1999). doi: 10.4271/1999-01-0528, (*cited on: Chap.2-p.64*).

Sieder, E. N. and Tate, G. E. "Heat Transfer and Pressure Drop of Liquids in Tubes". *Industrial and Engineering Chemistry*, vol. 28 (1936), pp. 1429–1435. issn: 0019-7866. doi: 10.1021/ie50324a027, (*cited on: Chap.5-p.235*).

So, B. Y. C. and Klaus, E. E. "Viscosity-Pressure Correlation of Liquids". *A S L E Transactions*, vol. 23.4 (1980), pp. 409–421. issn: 0569-8197. doi: 10.1080/05698198008982986, (*cited on: Chap.3-p.105*).

Sobel, D. R. and Lehrach, R. P. C. "A Hydro-Mechanical Simulation of Diesel Fuel Injection Systems". *SAE Technical Paper 870432* (1987). doi: 10.4271/870432, (*cited on: Chap.3-pp.86,87,88*).

Som, S., Aggarwal, S. K., El-Hannouny, E. M., and Longman, D. E. "Investigation of nozzle flow and cavitation characteristics in a diesel injector". *Journal of Engineering for Gas Turbines and Power*, vol. 132 (2010), p. 42802. ISSN: 07424795. DOI: 10.1115/1.3203146, (*cited on: Chap.3-p.113*).

Som, S., E., D., I., A., and Aggarwal, S. "Influence of Nozzle Orifice Geometry and Fuel Properties on Flow and Cavitation Characteristics of a Diesel Injector". *Fuel Injection in Automotive Engineering*. InTech, 2012. ISBN: 978-953-51-0528-2. DOI: 10.5772/38900, (*cited on: Chap.2-p.49, Chap.3-p.113*).

Som, S., Longman, D., Ramírez, A., and Aggarwal, S. "A comparison of injector flow and spray characteristics of biodiesel with petrodiesel". *Fuel*, vol. 89.12 (2010), pp. 4014–4024. ISSN: 00162361. DOI: 10.1016/j.fuel.2010.05.004.

Som, S., Ramirez, A. I., Longman, D. E., and Aggarwal, S. K. "Effect of nozzle orifice geometry on spray, combustion, and emission characteristics under diesel engine conditions". *Fuel*, vol. 90.3 (2011), pp. 1267–1276. ISSN: 00162361. DOI: 10.1016/j.fuel.2010.10.048, (*cited on: Chap.2-p.49*).

Soteriou, C., Andrews, R., and Smith, M. "Direct Injection Diesel Sprays and the Effect of Cavitation and Hydraulic Flip on Atomization". *SAE Technical Paper 950080* (1995). DOI: 10.4271/950080, (*cited on: Chap.2-pp.35,40,43,59, Chap.5-p.194*).

Sou, A., Hosokawa, S., and Tomiyama, A. "Cavitation in Nozzles of Plain Orifice Atomizers with Various Length-To-Diameter Ratios". *Atomization and Sprays*, vol. 20.6 (2010), pp. 513–524. ISSN: 1044-5110. DOI: 10.1615/AtomizSpr.v20.i6.30, (*cited on: Chap.2-p.48*).

Sou, A., Hosokawa, S., Tomiyama, A., and Akio, T. "Effects of cavitation in a nozzle on liquid jet atomization". *International Journal of Heat and Mass Transfer*, vol. 50.17-18 (2007), pp. 3575–3582. DOI: 10.1016/j.ijheatmasstransfer.2006.12.033, (*cited on: Chap.2-p.59*).

Sou, A., Tomiyama, A., Hosokawa, S., Nigorikawa, S., and Maeda, T. "Cavitation in a Two-Dimensional Nozzle and Liquid Jet Atomization (LDV Measurement of Liquid Velocity in a Nozzle)". *JSME International Journal Series B*, vol. 49.4 (2006), pp. 1253–1259. ISSN: 1340-8054. DOI: 10.1299/jsmeb.49.1253, (*cited on: Chap.2-p.45*).

Strotos, G., Koukouvinis, P., Theodorakakos, A., and Wang, L. "Fuel heating in high pressure diesel nozzles". *THIESEL 2014 Conference on Thermo- and Fluid Dynamic Processes in Direct Injection Engines*. Valencia, Spain, 2014, (*cited on: Chap.3-p.114, Chap.6-p.280*).

Strotos, G., Koukouvinis, P., Theodorakakos, A., Gavaises, M., and Bergeles, G. "Transient heating effects in high pressure Diesel injector nozzles". *International Journal of Heat and Fluid Flow*, vol. 51 (2015), pp. 257–267. ISSN: 0142727X. DOI: 10.1016/j.ijheatfluidflow.2014.10.010, (*cited on: Chap.3-p.114, Chap.5-p.197, Chap.6-p.280*).

Suh, H. K., Park, S. H., and Lee, C. S. "Experimental investigation of nozzle cavitating flow characteristics for diesel and biodiesel fuels". *International Journal of Automotive Technology*, vol. 9.2 (2008), pp. 217–224. ISSN: 1229-9138. DOI: 10.1007/s12239-008-0028-3, (*cited on: Chap.3-pp.110,112*).

Suh, H. K. and Lee, C. S. "Effect of cavitation in nozzle orifice on the Diesel fuel atomization characteristics". *International Journal of Heat and Fluid Flow*, vol. 29 (4).4 (2008), pp. 1001–1009. ISSN: 0142727X. DOI: 10.1016/j.ijheatfluidflow.2008.03.014, (*cited on: Chap.1-p.2*).

Surhone, L. M., Tennoe, M. T., and Henssonow, S. F. *Rayleigh- Taylor Instability*. Vdm Verlag, 2010. ISBN: 9786131104077, (*cited on: Chap.2-p.58*).

Takeda, Y., Keiichi, N., and Keiichi, N. "Emission characteristics of premixed lean Diesel combustion with extremely early staged fuel injection". *SAE Technical Paper 961163* (1996). DOI: 10.4271/961163, (*cited on: Chap.2-p.60*).

Tamaki, N., Shimizu, M., and Hiroyasu, H. "Enhancement of the atomization of a liquid jet by cavitation in a nozzle hole". *Atomization and Sprays*, vol. 11.2 (2001), p. 14. ISSN: 1044-5110. DOI: 10.1615/AtomizSpr.v11.i2.20, (*cited on: Chap.2-p.59*).

Tat, M. E. and Van Gerpen, J. H. *Measurement of Biodiesel Speed of Sound and Its Impact on Injection Timing*. Tech. rep. 4. National Renewable Energy Laboratory (NREL), 2003, (*cited on: Chap.3-pp.109,112*).

Tat, M. E. et al. "The speed of sound and isentropic bulk modulus of biodiesel at 21°C from atmospheric pressure to 35 MPa". *Journal of the American Oil Chemists' Society*, vol. 77.3 (2000), pp. 285–289. ISSN: 0003-021X. DOI: 10.1007/s11746-000-0047-z, (*cited on: Chap.3-pp.97,100,102*).

Theodorakakos, A., Mitroglou, N., and Gavaises, M. "Simulation of heating effects in cavitating flows through Diesel fuel injectors caused by extreme fuel pressurisation". *8th international symposium on cavitation*. Singapore, 2012, (*cited on: Chap.3-p.113*).

Theodorakakos, A., Strotos, G., Mitroglou, N., Atkin, C., and Gavaises, M. "Friction-induced heating in nozzle hole micro-channels under extreme fuel pressurisation". *Fuel*, vol. 123.x (2014), pp. 143–150. ISSN: 00162361. DOI: 10.1016/j.fuel.2014.01.050, (*cited on: Chap.3-p.113, Chap.5-p.197*).

Tinprabath, P., Hespel, C., Chanchaona, S., and Foucher, F. "Influence of biodiesel and diesel fuel blends on the injection rate under cold conditions". *Fuel*, vol. 144 (2015), pp. 80–89. ISSN: 00162361. DOI: 10.1016/j.fuel.2014.12.010, (*cited on: Chap.3-pp.108,110,112*).

Torda, T. P. "Evaporation of drops and breakup of sprays". *Astronautica Acta*, vol. 18 (1973), pp. 383–393, (*cited on: Chap.2-p.55*).

Venegas, O. "Estudio del fenómeno de la cavitación en la inyección Diesel mediante la visualización del flujo interno en orificios transparentes." PhD thesis. Valencia (Spain): Universitat Politècnica de València, 2014. DOI: 10.4995/Thesis/10251/37375, (*cited on: Chap.1-p.4*).

Vergnes, C., Foucher, F., and Mounaim-Rousselle, C. "Discharge coefficients for a diesel injector during cold starting conditions". *Atomization and Sprays*, vol. 19.7 (2009), pp. 621–631. ISSN: 1044-5110. DOI: 10.1615/AtomizSpr.v19.i7.20, (*cited on: Chap.3-pp.108,110,112*).

Von Kuensberg Sarre, C., Kong, S.-c., and Reitz, R. D. "Modeling the effects of injector nozzle geometry on diesel sprays". *SAE Technical Paper 1999-01-0912*, 724 (1999). DOI: 10.4271/1999-01-0912, (*cited on: Chap.1-p.1, Chap.2-pp.48,49*).

Wakuri, Y. et al. "Studies of the penetration of a fuel spray in a Diesel Engine". *Bulletin of JSME*, vol. 3.9 (1960), pp. 123–130. ISSN: 0029-0270. DOI: 10.1299/kikai1938.25.820, (*cited on: Chap.2-p.60*).

Wan, Y. and Peters, N. "Scaling of spray penetration with evaporation". *Atomization and Sprays*, vol. 9.2 (1999), pp. 111–132. DOI: 10.1615/AtomizSpr.v9.i2.10, (*cited on: Chap.2-p.61*).

Wang, X., Huang, Z., Kuti, O. A., Zhang, W., and Nishida, K. "Experimental and analytical study on biodiesel and diesel spray characteristics under ultra-high injection pressure". *International Journal of Heat and Fluid Flow*, vol. 31.4 (2010), pp. 659–666. ISSN: 0142727X. DOI: 10.1016/j.ijheatfluidflow.2010.03.006, (*cited on: Chap.3-pp.111,112*).

Wang, Z., Ding, H., Wyszynski, M. L., Tian, J., and Xu, H. "Experimental study on diesel fuel injection characteristics under cold start conditions with single and split injection strategies". *Fuel Processing Technology*, vol. 131 (2015), pp. 213–222. ISSN: 03783820. DOI: 10.1016/j.fuproc.2014.10.003, (*cited on: Chap.3-pp.108,109,110,112, Chap.6-pp.262,297,306*).

Wannenwetsch, P. and Egler, W. "A User-Friendly Program System for Digital Simulation of Hydraulic Equipment". *SAE Technical Paper 850532* (1985). DOI: 10.4271/850532, (*cited on: Chap.3-pp.87,88*).

White, F. M. *Fluid mechanics*. 5th editio. McGraw-Hill, 2003. ISBN: 9780071215664, (*cited on: Chap.2-pp.33,34*).

Wierzba, A. "Deformation and breakup of liquid drops in a gas stream at nearly critical Weber numbers". *Experiments in Fluids*, vol. 9.1-2 (1990), pp. 59–64. ISSN: 0723-4864. DOI: 10.1007/BF00575336, (*cited on: Chap.2-pp.56,57*).

Wu, C. S., Klaus, E. E., and Duda, J. L. "Development of a Method for the Prediction of Pressure-Viscosity Coefficients of Lubricating Oils Based on Free-Volume Theory". *Journal of Tribology*, vol. 111.1 (1989), p. 121. ISSN: 07424787. DOI: 10.1115/1.3261861, (*cited on: Chap.3-p.105*).

Wu, K.-J., Su, C.-C., Steinberger, R. L., Santavicca, D. A., and Bracco, F. V. "Measurements of the Spray Angle of Atomizing Jets". *Journal of Fluids Engineering*, vol. 105.4 (1983), p. 406. ISSN: 00982202. DOI: 10.1115/1.3241019, (*cited on: Chap.2-p.62*).

Wylie, E. B., Bolt, J. A., and El-Erian, M. F. "Diesel Fuel Injection System Simulation and Experimental Correlation". *SAE Technical Paper 710569* (1971). DOI: 10.4271/710569, (*cited on: Chap.3-pp.86,88*).

Xu, B., Ooi, K. T., Mavriplis, C., and Zaghloul, M. E. "Evaluation of viscous dissipation in liquid flow in microchannels". *Journal Of Micromechanics And Microengineering*, vol. 13.1 (2003), pp. 53–57. ISSN: 0960-1317. DOI: 10.1088/0960-1317/13/1/308, (*cited on: Chap.2-p.26, Chap.5-p.197*).

Xu, M. and Hiroyasu, H. "Development of a new optical technique for measuring Diesel spray penetration". *SAE Technical Paper 902077* (1990). DOI: 10.4271/902077, (*cited on: Chap.2-p.64*).

Yamaoka, K. and Saito, A. "Computer Technique for Evaluation of Cavitation Characteristics of Certain Phases of Fuel Injection in Fuel Injection System". *SAE Technical Paper 730663* (1973). DOI: 10.4271/730663, (*cited on: Chap.3-pp.86,88*).

Yamaoka, K., Saito, A., Abe, N., and Okazaki, M. "Analysis of Bypass Control Fuel Injection Systems for Small Diesel Engines by Digital Computer". *SAE Technical Paper 730664* (1973). DOI: 10.4271/730664, (*cited on: Chap.3-p.88*).

Ye, S. et al. "Réalisation d'un dispositif de mesure de la vitesse et de l'atténuation d'ondes ultrasonores dans des liquides sous pression". *Revue de Physique Appliquée*, vol. 25.6 (1990), pp. 555–565. ISSN: 0035-1687. DOI: 10.1051/rphysap:01990002506055500, (*cited on: Chap.3-pp.97,100, Chap.4-p.161*).

Yuen, M.-C. "Non-linear capillary instability of a liquid jet". *Journal of Fluid Mechanics*, vol. 33.01 (1968), p. 151. ISSN: 0022-1120. DOI: 10.1017/S0022112068002429, (*cited on: Chap.2-p.54*).

Yunyi, G., Changwen, L., Yezhou, H., and Zhijun, P. "An Experimental Study on Droplet Size Characteristics and Air Entrainment of Elliptic Sprays". *SAE Technical Paper 982546* (1998). DOI: 10.4271/982546, (*cited on: Chap.2-p.50*).

Zábranský, M. "Heat Capacity of Liquids: Critical Review and Recommended Values. Supplement I". *Journal of Physical and Chemical Reference Data*, vol. 30.5 (2001), p. 1199. ISSN: 00472689. DOI: 10.1063/1.1407866, (*cited on: Chap.3-p.106*).

Zábranský, M., Kolská, Z., Růžička, V., and Domalski, E. S. "Heat capacity of liquids: Critical review and recommended values. Supplement ii". *Journal of Physical and Chemical Reference Data*, vol. 39.1 (2010), pp. 3–404. ISSN: 00472689. DOI: 10.1063/1.3182831, (*cited on: Chap.3-p.106*).

Zeh, D. et al. "Bosch Diesel Injection Technology – Response for Every Vehicle Class Production : Light Vehicles 1) World by Region". *23 Aachener Kolloquium*. Aachen, 2014, (*cited on: Chap.1-p.3*).

Zeng, M. and Schaschke, C. "High Pressure Falling Sinker Liquid Viscosity Determination without Supplementary Density Data: A New Approach". *International Journal of Chemical Engineering* (2009), pp. 1–8. ISSN: 1687-806X. DOI: 10.1155/2009/747592, (*cited on: Chap.3-pp.98,103*).

Zheng, M. and Kumar, R. "Implementation of multiple-pulse injection strategies to enhance the homogeneity for simultaneous low-NOx and -soot diesel combustion". *International Journal of Thermal Sciences*, vol. 48.9 (2009), pp. 1829–1841. ISSN: 12900729. DOI: 10.1016/j.ijthermalsci.2009.02.009, (*cited on: Chap.1-p.2, Chap.2-p.17*).